Annual Report

of

The Institute Of Physics

Academia Sinica

Volume 9 December 1979

The Institute of Physics, Academia Sinica

Taipei, Taiwan, Republic of China

中央研究院物理研究所集刊

編 輯 委 員 會

The Annual Report is published annually by the Institute of Physics, Academia Sinica, Taipei, Taiwan 115, Republic of China.

本集刊每年出版一次

非賣品

中央研究院

物理研究所集刊

第九卷

發行人：林爾康

編輯者：中央研究院物理研究所集刊編輯委員會

出版者：中央研究院物理研究所　臺北市南港區

印刷者：大地印刷廠

電話：九七一二二四四・九七一二二六六

中華民國六十八年十二月出版

中央研究院物理研究所集刊

第 九 卷

中央研究院物理研究所印行

CONTENTS 目 錄

ARTICLES

ABSTRACT

THE EXCITED STATES IN ^{82}Kr BY THE β-DECAY OF 35h ^{82}Br*

G. C. Kiang (江祀成), L. L. Kiang** (李 琳), D. Wang (王 定)
E. K. Lin (林炳康) and B. Cheng** (程 斌)

Institute of Physics Academia Sinica

Abstract

The energy levels of ^{82}Kr populated by the β-decay of 35h ^{82}Br have been investigated with a 43 cm^3 Ge(Li) detector, a Ge(Li)-NaI(Tl) coincidence spectrometer and a NaI(Tl)-NE102A Fast/Slow coincidence circuit. A total of 30 gamma rays were observed, and the directional correlation of 554-619 keV, 554-1318 keV, 776-698 keV, 776-1043 keV, 776-1318 KeV, 827-1043 keV cascades have been measured. The lifetime of the excited states at 776.3-, 1474-, 1820-, 2093 keV have also been obtained.

With the energies, intensities and the multipole mixing ratios of the γ-rays in ^{82}Kr, the partial transition rate and the reduced transition probabilities have been deduced for various transitions. The main square deformation β_0^2 of ^{82}Kr has also been deduced.

1. INTRODUCTION

The γ-transitions in ^{82}Kr nucleus following the β-decay of the ^{82g}Br and ^{82m}Br have been studied rather extensively during the past years[1-10]. With the advent of the high energy-resolution Ge(Li) spectrometers, a considerable large amount of informations expecially on the weak γ-rays have been found to establish the presently acceptable decay scheme.

The even-even nucleus of ^{82}Kr with 36 protons and 46 neutrons, are far from the magic numbers. Early in 1956, Waddell and Jensen[7] described the excited states of ^{82}Kr nucleus in terms of vibrational levels. These levels have also been interpreted by Klema et al.[11] and Simons et al.[12] as rotor model with rotation-vibration interaction.[13] Shortly, Etherton and Kelley[4] obtained the ratio of B(E2) for the 698 keV and 1474 keV transitions from the second 2^+ level as 60 ± 10, which is fairly in agreement with the value of non-axiality parameter $\gamma \simeq 30°$ obtained by Klema et al..[13]

The present investigations were undertaken to test the energy level scheme and the γ-transitions energies of the ^{82}Kr nucleus. Of special interests were the lifetimes of some of the excited states at 776.3, 1474, 1820 and 2093 keV. Together with the informations about the γ-transition energies, intensities, branching ratios, angular correlation functions, and total conversion coefficients, it is possible to deduce the B(E2) transition probabilities.

* Work Supported by the National Science Council, R.O.C.

** Dept. of Physics, National Tsing Hua Univ. Hsinchu, Taiwan, R.O.C.

2. EXPERIMENTALS

2-1. Source Preparation

The ^{82}Br sources were produced by thermal neutron irradiation of nature bromine (49% ^{79}Br and 51% ^{82}Br) in the form of NH_4Br in the Tsing Hua reactor. The irradiation time was 10 min. in neutron flux of 10^{12} neutron/cm/sec. A small piece of the activated ^{82}Br of about 10 mg was stuck at the end of a small ($\sim$1 mm diameter) stick to keep it as a point source. The source will be allowed to decay for two days to let the 4.5h ^{80m}Br die off before measurements.

2-2. The Gamma Ray Single Spectra

The Gamma-ray single spectra of ^{82}Br were measured by a ORTEC 43 cm^3 ture coax Ge(Li) detector with energy resolution (FWHM) about 3 keV for the 1332 keV ^{60}Co gamma ray. The signals were amplified by a CI-1412 research amplifier and recorded with a CI-8700 4096 multichannel analyzer. The photopeak efficiency versus the gamma energies for the Ge(Li) detector and energy calibration have been measured previously[15] in this laboratory.

In order to reduce the natural background and avoid the interference of the β-particles, an 1 cm thick lead cup with 5 cm thick acrylic plate was used to shield the detector. The source was placed at 10-, 15-, 25 cm from the surface of the detector separately during the course of measurement in order to identify the summing effect.

2-3. The Coincidence Spectra and the Directional Correlation

In the coincidence measurements, a 43 cm^3 ORTEC Ge(Li) detector and a 7.6 cm $\times$ 7.6 cm NaI(T1) crystal were used. The signals of selected γ-lines from the NaI(T1) branch was in coincidence with the signals of Ge(Li) branch to operate the time-to-pulse-height converter, which was employed to gate the linear signals of Ge(Li). Four coincidence spectra gated at 554-, 776-, 1043- and 1437 keV were measured.

Directional correlation measurements were carried out with the same system under the same condition, except for the NaI(T1) detector which was turned around the source, and the Ge(Li) detector was kept fixed. Five correlation functions of the 544-1317 keV, 554-619 keV, 776-1317 keV, 776-698 keV, 827-1403 keV cascades were obtained from $\theta = 90°$ to $\theta = 180°$, with an angle of increment of $\Delta\theta = 10°$. In order to improve the accuracy, each run was measured three times. The source-to-detector distance was kept 15 cm for both of the

two detectors. The measured data have been normalized by the decay law and have been corrected to the known ^{60}Co $4^+(2)2^+(2)0^+$ cascade transition for the geometrical errors.

2-4. The Lifetime Measurements

The lifetimes of the 776.3-, 1474-, 1820- and 2093 keV Levels of ^{82}Kr nucleus were measured with the conventional delayed coincidence technique[15]. A 5 cm × 3 cm NE 102A plastic scintillator coupled with 56 AVP photomultiplier and the ORTEC 269 photo base served as a detector, the other detector was a 5 cm × 5 cm NaI(T1) scintillator which was also connected to a 56 AVP photomultiplier and ORTEC 269 photo base. The time resolution of the system was 700 ps. for ^{60}Co cascade transitions. Details of the electronic system and time calibration have been given previously[14].

3. RESULTS

3-1. Single and coincidence spectra

Fig. 1 shows the typical gamma-ray spectrum in the γ-energy region of 180 keV to 2614 keV. The gamma-ray single spectra were obtained with a ORTEC 43 cm^3 coaxial Ge(Li) detector. In order to determine the summing effects of this detector, measurements were made at three different detector-to-source distances of 5-, 10-, 15 cm respectively. The relative intensities of the gamma-rays extracted from these spectra are listed in Table 1. The gamma ray energies were determined from a calibration curve which was determined from a series of well known gamma-rays in ^{133}Ba, ^{22}Na, ^{137}Cs, ^{60}Co and some of the natural background. Most of the observed γ-peaks in the spectra agree with the previous works[8, 9, 10]. Two of the obvious speaks at 1820 keV and 2093 keV were identified as due to the summing effects.

TABLE I

Nuclear Data Sheet(a)	E. Liukkonen et al. (b)	Subramanian Raman (c)	Meredith & Meyer (d)	Present Work		Assiginment (keV)	
				Energy (keV)	Int.	From	To
92.2	92.22±.5	92.19±.02	92.19				
101	101.0 ±.5	100.9	100.89				
			129			(2555.92)	(2426.6)
138	137.1±.3	137.4	137.4			(2093)	(1956)
183.9±.3			179.8	180.78 ±1.5	0.6 ±0.003	2829	2647.8
221.4	221.5±.3	221.4 ±.03	221.411	221.4 ±1.3	30.2 ±0.01	2648	2426

TABLE I (Cont.)

Nuclear Data Sheet(a)	E. Liukkonen et al. (b)	Subramanian Raman (c)	Meredith & Meyer (d)	Present Work		Assiginment (keV)	
				Energy (keV)	Int.	From	To
274	273.5±.3	273.42±.03	273.419	273.03 ±0.8	12.5 ±0.01	2093.8	1820.3
			280.7	281.8 ±2.1	0.6 ±0.01	2827.5	2545.7
295							
320			332.9				
			345.6			1820.3	1474.8
	401.0±1.5	401.12	401.12	400.76 ±1.2	1.47 ±.03	2827.9	2426.5
480				480.8 ±1.5	2.61 ±.05	1956.3	1474.8
554.3±.1	554.2±.2	554.32±.2	554.32	554.32 ±0.8	900 ±.10	2426.7	2093
				599			
602.0	606.8±.1	606.32±.02	606.3	605.43 ±0.6	15.7 ±.5	2426.7	1820.3
619.0	619.3±.4	619.05	619.054	618.89 ±0.5	651 ±2.0	2093.8	1474.8
			692.7				
698.4	698.2±.4	698.32±0	698.32	698.25 ±0.8	376.8 ±.10	1474.8	776.3
		711.1	726.8	723.8 ±0.8	1.0 ±.01	2545.7	1820.3
	736 ±1.5	736.62	735.62	734.58 ±0.6	2.4 ±.05	2555.9	1820.3
776.8±.1	776.3±.3	776.49±.4	776.489	776.28 ±0.5	1000	776.3	g.s.
827.2±.0	827.6±.4	827.81±.3	827.81	827.39 ±0.6	273.2 ±8	2426	1820.3
951	952.4±1.0	952.12	952.12	952.5 ±0.5	2.9 ±0.5	2426.5	1474.8
1010 ±1.0	1007.7±0.8	1007.57±0.9	1007.568	1007.66 ±0.5	12.6 ±0.8	2554.72	1474.8
1044 ±1.2	1043.8±.4	1043.98±.3	1043.98	1043.98 ±0.5	342.2 ±10	1820.3	776.3
	1073.2	1072.57	1072.57	1070.7 ±0.5	0.82 ±.03	2545.7	1474.8
1084	1081.5±.6	1081.05	1081.35	1081.3 ±0.8	6.01 ±0.5	2555.9	1474.8
	1180.5±.6	1180.10	1173.9	1172.8 ±0.6	7.85 ±0.8	2426.7	1474.8
1317.2±.2	1317.9±.4	1317.47	1317.475	1318.1 ±0.7	290 ±10	2093.8	776.3
			1356.22	1351.2 ±0.8	0.66 ±0.3	2827.5	1474.8
			1426.82				
1474.8±.2	1474.4±.2	1474.2 ±.08	1474	1474.82 ±0.5	203.8 ±10	1474.8	g.s.
1651	1649.8±.8	1650.29	1650.20	1650.3 ±0.3	7.24 ±.03	2426.7	776.3
	1768.9±.8	1770.97		1769.44 ±0.4	0.24 ±.03	2545.7	776.3
1728	1779.5±.1	1779.58	1779.58	1780.5 ±0.3	1.11 ±0.3	2555.5	776.3
1822.6±1				(1820.3) ±0.4	0.94 ±.05	1820.3	g.s.
1874 ±4	1871.0±.8	1871.6		1872.8 ±0.6	1.5 ±.2	2426.7	776.3
1959 ±4	1957 ±2	1956.5	1956.5				
2056	2051 ±2			(2051.7) ±0.6	0.1	2827.5	1474.8
				(2093.9) ±0.5	0.8 ±.1	2093	g.s.

(a) A. Artna, Nuclear Data Sheets, B1-4-103 (1966).

(b) E. Liukkonen, et al., Nucl. Phys. A138 (1969) 163.

(c) S. Raman, Phys. Rev. C **2**, 6, 2176 (1970).

(d) G. R. Meredith and R. Y. Meyer, Nucl. Phys A142 (1970) 513.

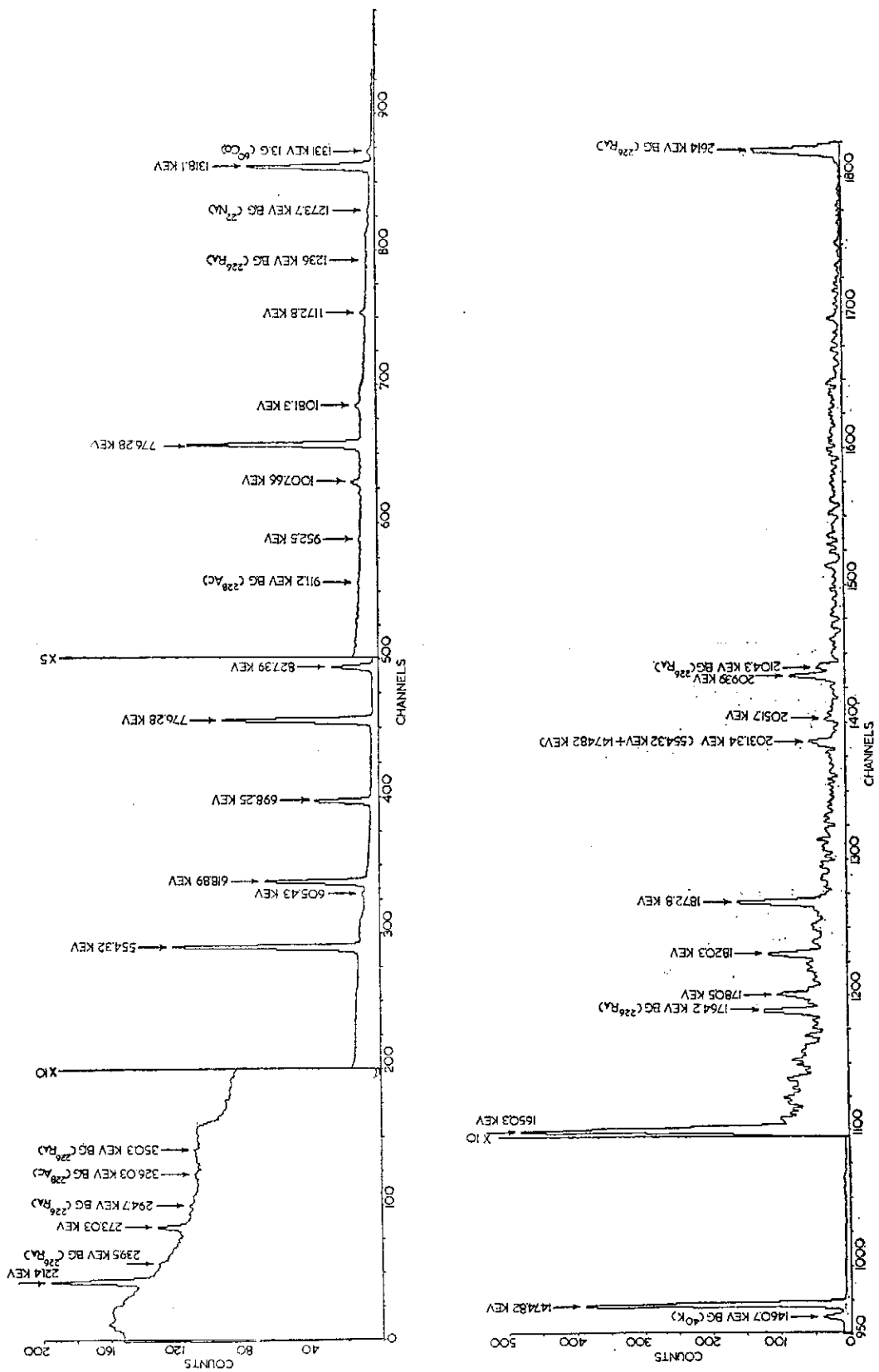

FIG. 1. Gamma-ray spectrum of ^{82}Br taken with 43 cm^3 Ge(Li) detector in the energy region 980-2614 keV.

The decay scheme obtained from the analysis of the single and coincidence spectra is shown in fig. 2.

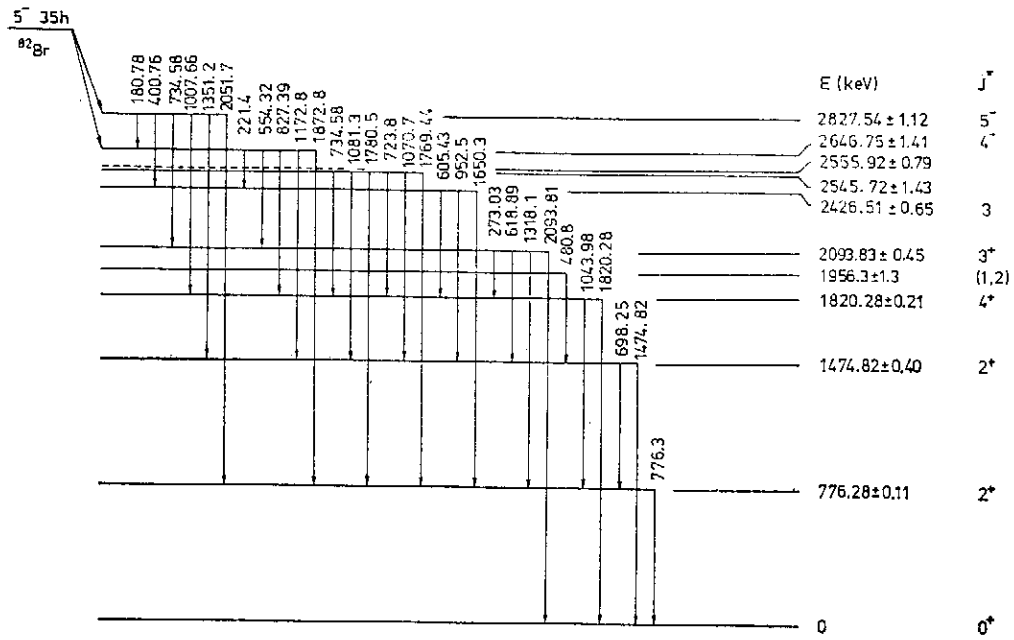

FIG. 2. The level scheme of ^{82}Kr in the decay of 35h 82h ^{82}Br.

Fig. 3 shows two Ge(Li)-NaI(T1) coincidence spectra, which were obtained respectively with gating at 776.3 keV (Fig. 3A) and at 1474 keV (Fig. 3B). In Fig. 3B, a clear peak appeard at 1620 channel which corresponds to E 1173 keV, since there is no such peak showed up in Fig. 3A, the 1173 keV γ-ray is likely due to the transition of 2674 keV state to 1474 keV state. The other coincidence spectra gated at 554 keV and 1043 keV were in agreement with the work of E. Linkkonen et al.[9]

3-2. The Directional Correlation Functions

The measured directional functions of 554-619 keV, 554-1317 keV, 698-776 keV, 1043-776 keV, 1317-776 keV and 1043-776 keV, cascades are shown in Fig. 4. All of the data have been corrected by the finite angle correction[13] and with a least-square fitting for

$$W(\theta) = 1 + A_2P_2(\cos\theta) + A_4P_4(\cos\theta)$$

The values of the fitted A_2 and A_4 for each said cascades are listed in Table 3. It is seen that the results obtained are pretty close to the values obtained by Etherton and Kelly[4].

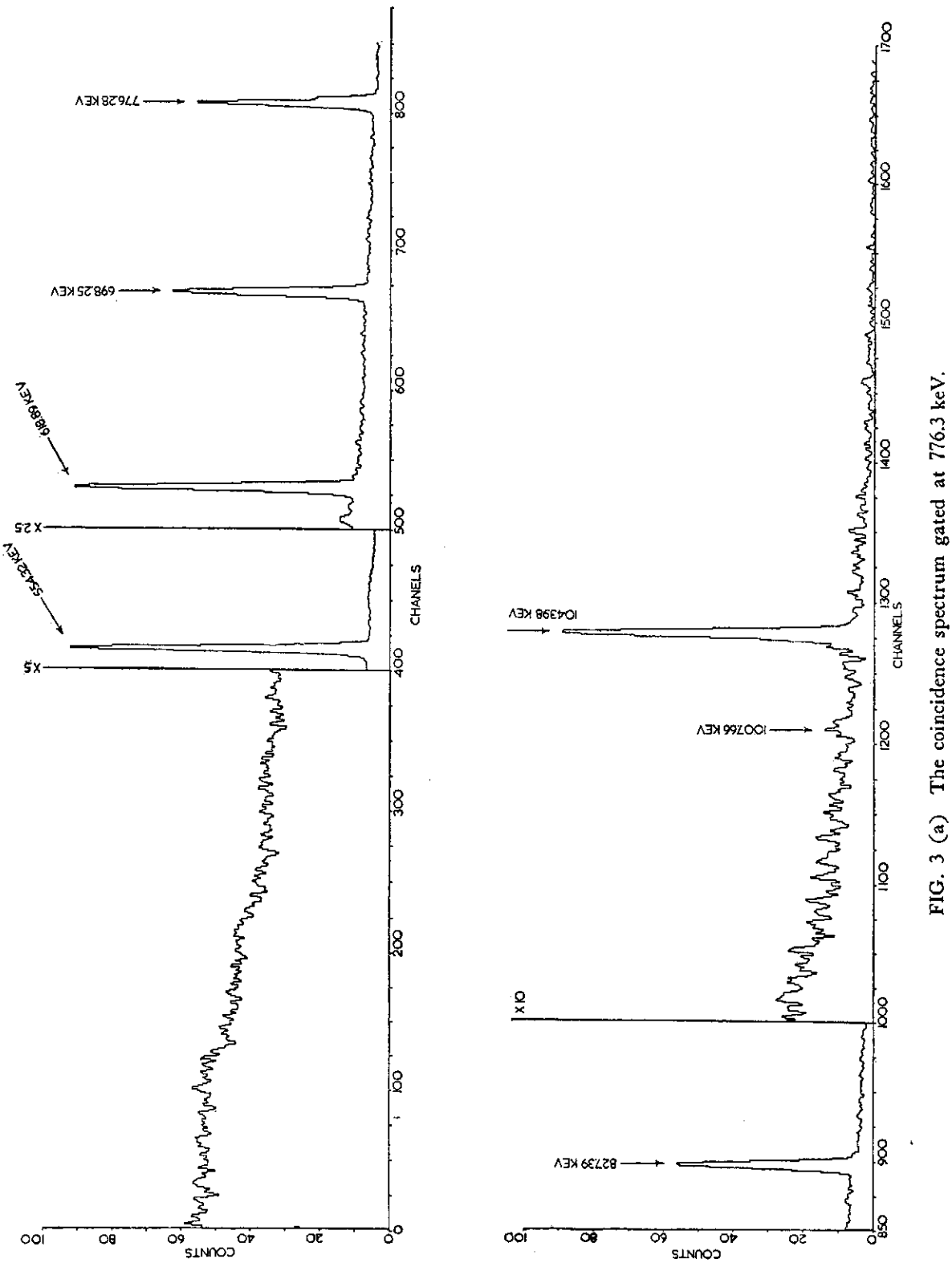

FIG. 3 (a) The coincidence spectrum gated at 776.3 keV.

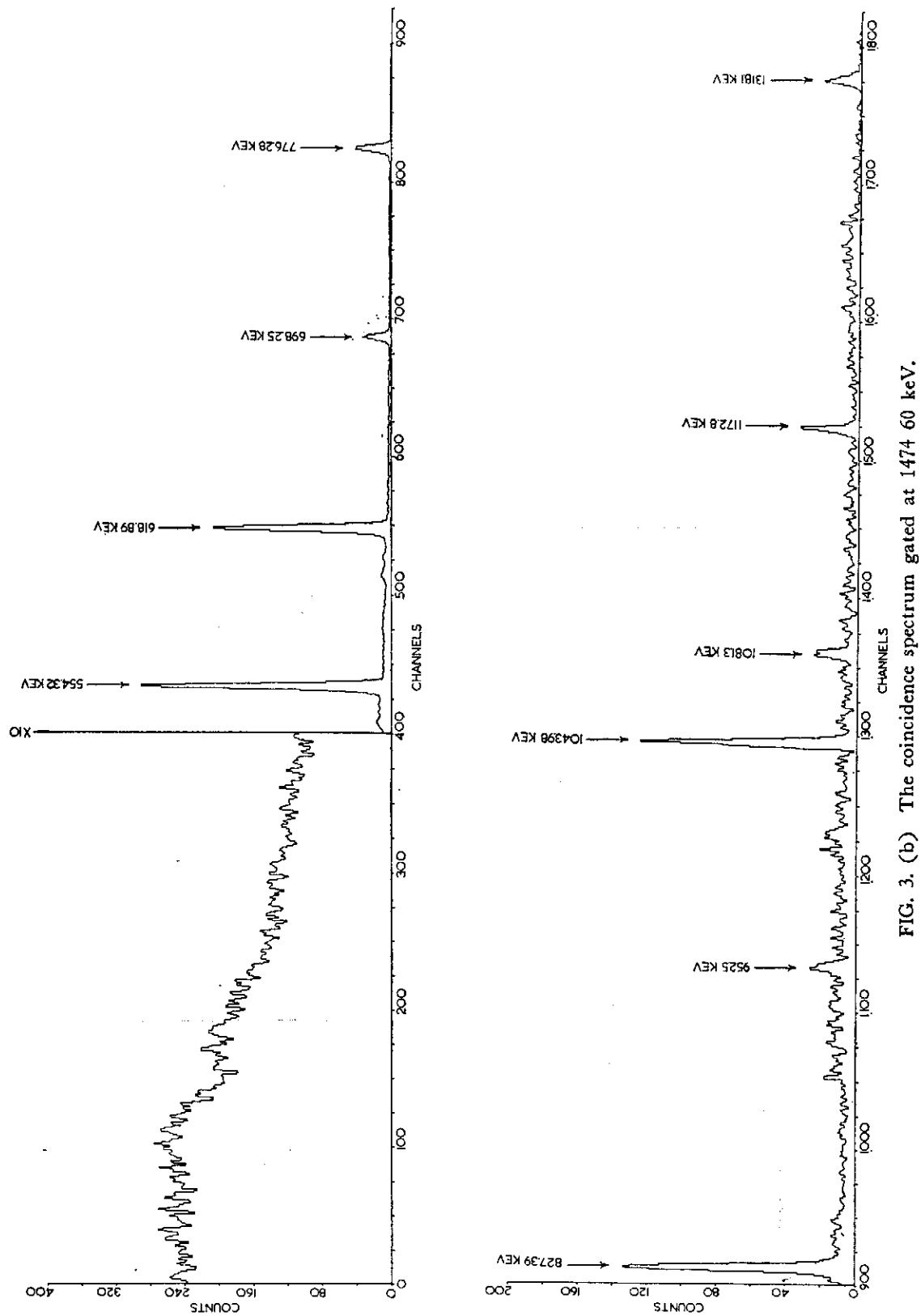

FIG. 3. (b) The coincidence spectrum gated at 1474.60 keV.

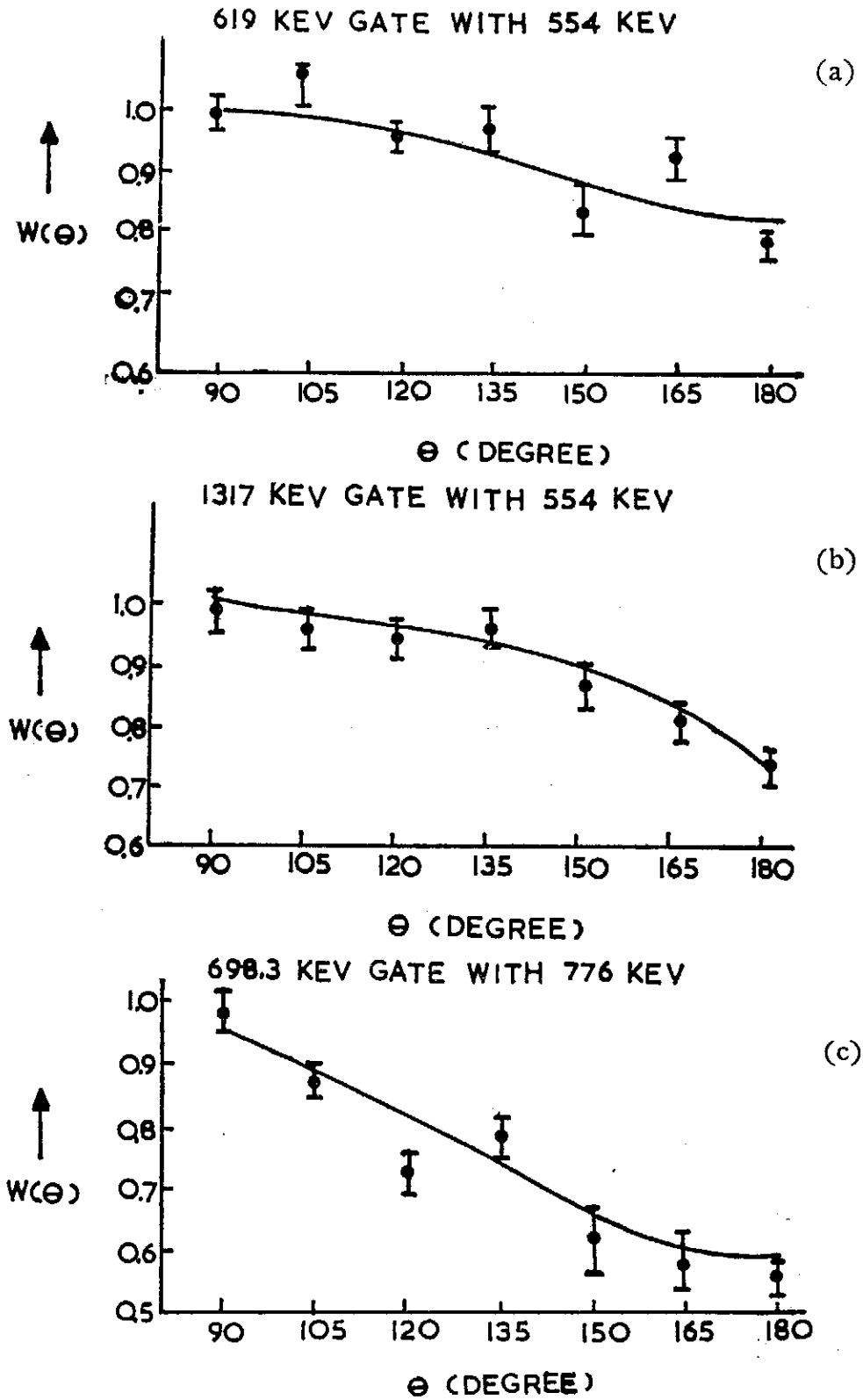

FIG. 4. The fitted directional correlation function and experimental data, (a) 554-619 keV cascade; (b) 554-1317 keV cascade, (c) 698-776 keV cascade; (d) 1043-776 keV cascade, (e) 1317-776 keV cascade (f) 1043-776 keV cascade.

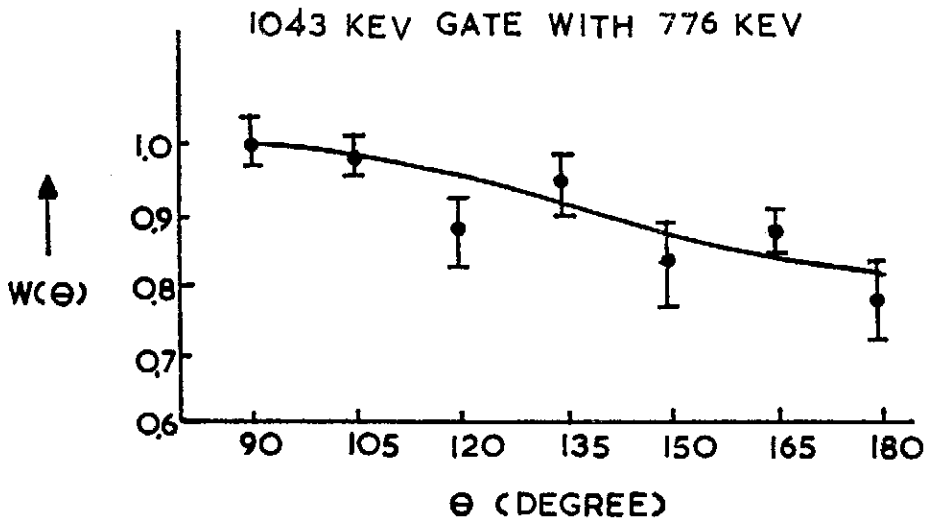
1043 KEV GATE WITH 776 KEV
W(Θ)
1.0
0.9
0.8
0.7
0.6
90
105
120
135
150
165
180
Θ (DEGREE)

(d)

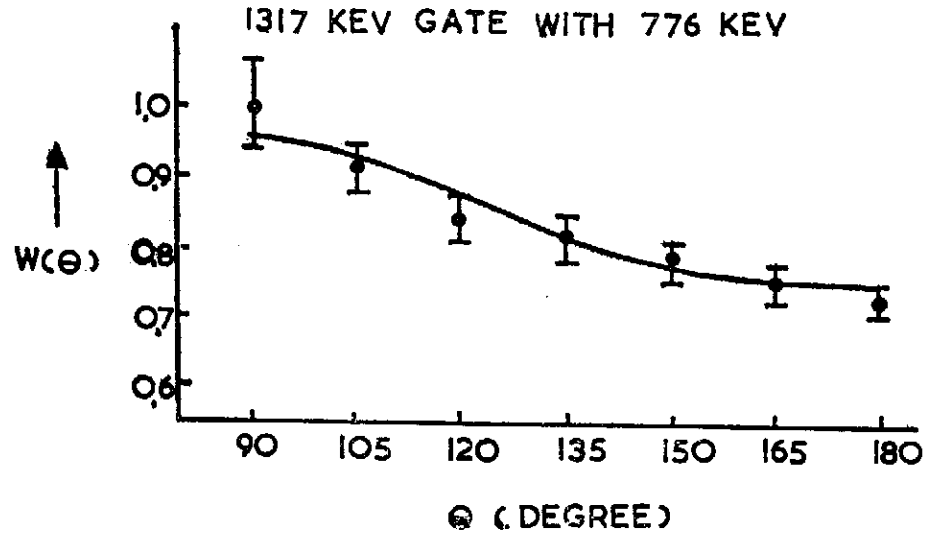
1317 KEV GATE WITH 776 KEV
W(Θ)
1.0
0.9
0.8
0.7
0.6
90
105
120
135
150
165
180
Θ (DEGREE)

(e)

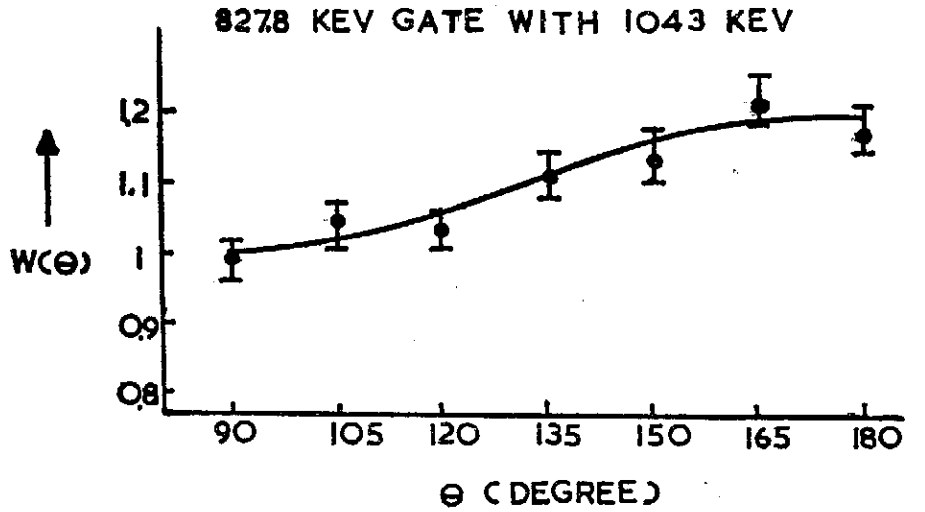
827.8 KEV GATE WITH 1043 KEV
W(Θ)
1.2
1.1
1
0.9
0.8
90
105
120
135
150
165
180
Θ (DEGREE)

(f)

3-3. The Lifetime Measurements

In measuring the lifetime of the 776.3 keV state, the energy window for the 5.08 cm (D) × 5.08 cm (L) NaI(T1) crystal was set at 776.3 ± 30 keV. And the window set for the NE 102A detector was set between 660 keV and 1200 keV. In this energy region, both the 698 keV and 1044 keV transitions should be in coincidence with the 776.3 keV transition. The time spectrum obtained is shown in Fig. 5. The mean values of the half-life in the measurement is

$$T_{1/2}(776.3 \text{ keV level}) = (1.016094 \pm 0.0193) \times 10^{-12} \text{ sec}$$

For the measurement of the lifetime of the 1474.3 keV level, the 698 keV γ-line was selected for the NaI(T1) detector, and the energy window was set in the 500~1100 keV region for the NE 102A detector. The 698 keV transition from 1474 keV level to the first excited state of 776.3 keV was in coincidence with the 619.3-, 952- and 1081 keV gamma rays. The time spectrum is shown in Fig. 6. And the mean value of the half-life of the 1474 keV level was deduced from the third moment method[20] in three independent measurement to be:

$$T_{1/2}(1474.3 \text{ keV level}) = (0.87720 \pm 0.1262) \times 10^{-12}\text{sec}$$

Figs. 7 and 8 show the time spectra recorded in the lifetime measurements of 1820 keV and 2093 keV level respectively. According to the level scheme of ^{82}Kr nucleus in the β-decay of 35h. ^{82}Br, the strong. γ-transition leading to the 1820 keV level is 827.4 keV γ-ray and the γ-transition from the 1820 keV level is 1043.8 keV γ-ray. The energy window settings were 827 ± 20 keV for NaI(T1) detector, and 900~1200 keV for NE 102A detector in the Slow/Fast coincidence measurement, the mean value of the half-life at the 1820 keV level is found to be.

$$T_{1/2}(1820 \text{ keV level}) = (0.956434 \pm 0.0284) \times 10^{-12}\text{sec}$$

Since the γ-transitions leading to the 2093 keV level is 554.2 keV γ-ray, and the γ-transitions from 2093 keV level are 237-, 273.5-, 619.3- and 1317 keV, we set the window of NaI(T1) detector at 554 ± 20 KeV, and the window of NE 102A between 500~1400 keV. The time spectrum obtained from the lifetime measurement of 2093 keV level is shown in Fig. 8. The deduced mean value of this level is

$$T_{1/2}(2093 \text{ keV level}) = (1.21902 \pm 0.1696) \times 10^{-12}\text{sec}$$

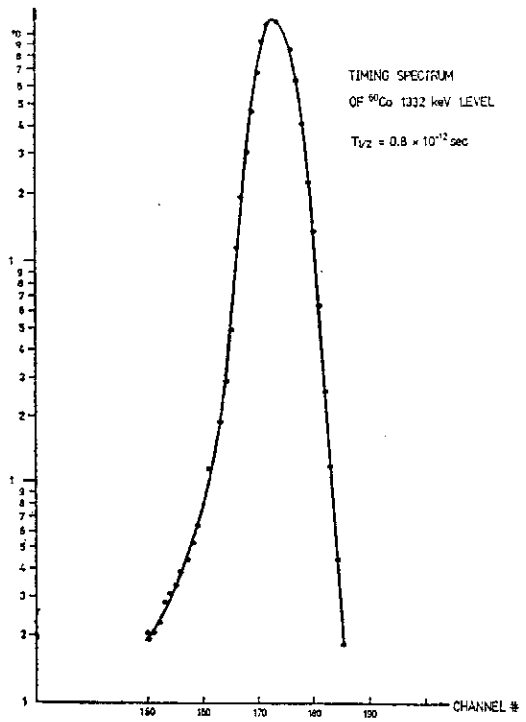

FIG. 5. A prompt coincidence curve made with ^{60}Co at the same experimental conditions with other time spectra for time standard.

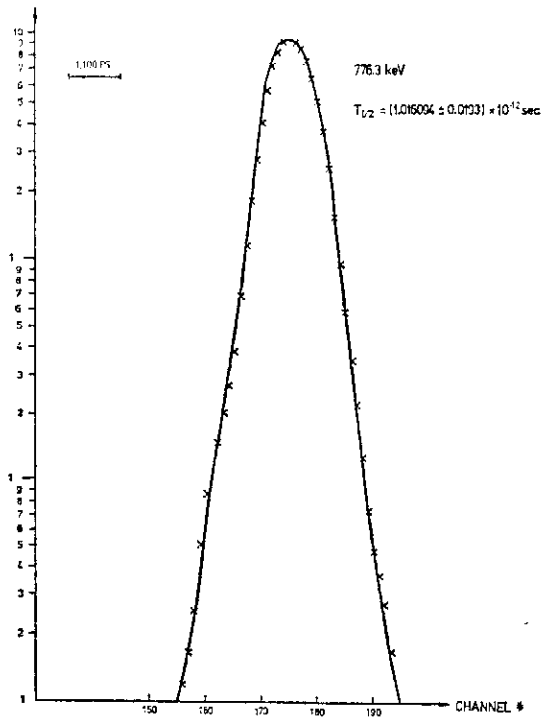

FIG. 6. Time distribution of coincidence between both of the 698 keV, 1044 keV and 776.3 keV. A prompt coincidence curve made with ^{60}Co at the same experimental condition.

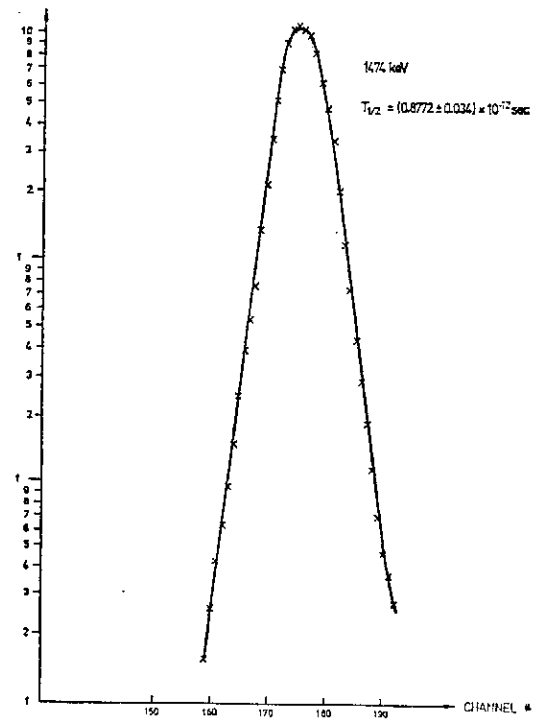

FIG. 7. Results of the lifetime measurements of the 1474 keV level.

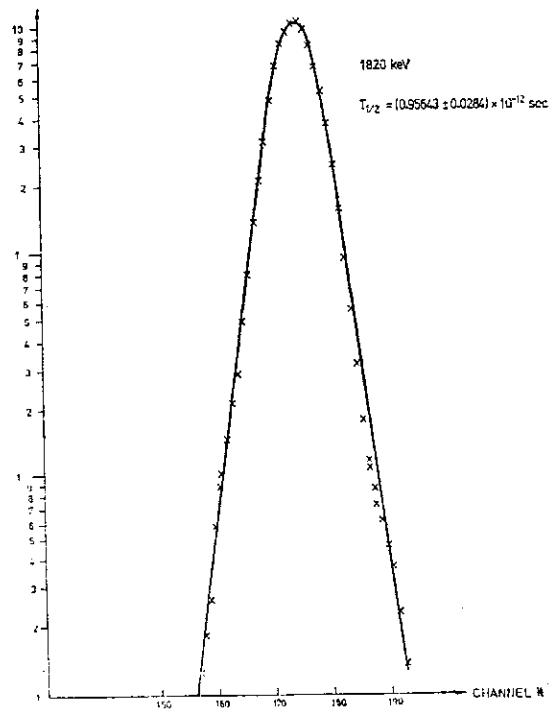

FIG. 8. The delayed coincidence spectrum of the 827-1043 keV γ-γ cascade in ^{82}Kr.

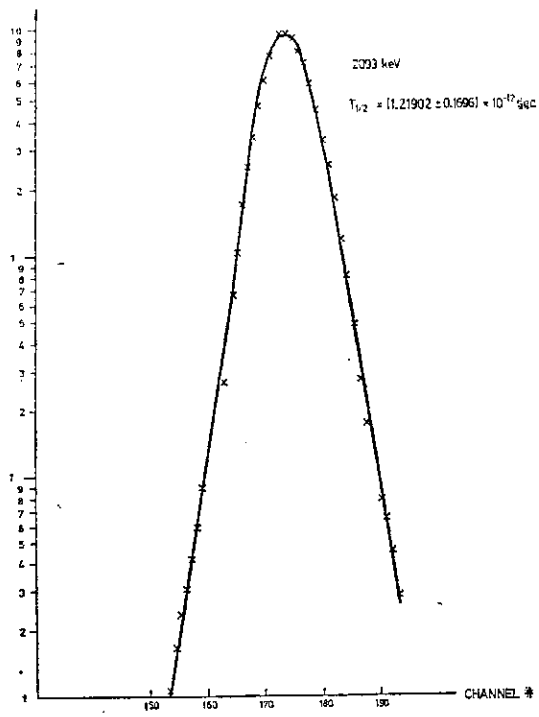

FIG. 9. The time spectrum of the measurement for the lifetime of 2093 keV level in ^{82}Kr.

4. DISCUSSION

It is interesting to check the level scheme of ^{82}Kr nucleus. Fig. 2 shows our results in which most of the assignments for the γ-transition agree with the previous work except the 1173 keV γ-ray. Raman[2] and Liukkonen et al.[9]. assigned the 1173 keV γ-ray as the transition between 1956.8 keV and 776.3 keV states. However, in the present coincidence measurements, we found that the 1173 keV γ-peak appears in the 1474 keV γ-ray gated spectrum (fig. 3B) but not appears in the 776.3 keV γ-ray gated spectrum (fig. 3A). Accordingly the 1173 keV γ-ray is favorably attributed to the transition between 2648 keV state and 1474 keV state of ^{82}Kr. This assignment is in agreement with the results of Meredith and Meyer[6].

In the directional correlation measurements, all the data have been corrected with the finite solid angle correction[13]. Due to the considerably shorter half-life of the γ-decay of ^{82}Kr, the data have also been corrected by the decay law. In Table 2, we list the correlation coefficients obtained from the present experiment together with the proposed transition modes.

In the evaluation for the lifetime of the excited states of ^{82}Kr nucleus, the time spectra obtained from the delayed coincidence measurements as shown

TABLE II Summary of ^{82}Kr Angular Correlation Data

Cascade Energies (keV)	Correlation Coefficients				Proposed Transition Mode
	A_2		A_4		
554.3—618.9	−0.1072	±0.015	−0.0136	±0.0035	4+(1)3+(1,2)2+
554.3—1318.1	−0.06167	±0.0015	−0.02907	±0.0008	4(1,2)3(1,2)2
	−0.065	±0.012*	−.007	±0.0028*	
776.3—698.25	−0.26918	±0.031	+0.2751	±0.021	2(1,2)2(2)0
	−0.265	±0.025*	+0.249	±0.014*	
776.3—1043.9	−0.1123	±0.06	+0.06181	±0.026	4(2,3)2(2)0
	+0.095	±0.018*	+0.042	±0.044*	
776.3—1318.1	−0.0183	±0.009	−0.0586	±0.006	3(1,2)2(2)0
	−0.027	±0.007*	−0.079	±0.014*	
827 —1043	+0.14192	±0.04	−0.0221	±0.025	4(1,2)4(2,3)2
	+0.190	±0.027*	−0.028	±0.047*	

* Ref. 4.

in figs. 5-10 were analyzed by the modified third moment method[16, 20]. By which, we calculated the third-moments of each required time spectra according to Weaver and Bell[18], and then normalized each of the third moment of the required time spectra to the third moment of the known half-life (0.8ps) of the 1332 keV state of ^{60}Co nucleus. This procedure gives the possible way to extend the measurable range of the delayed coincidence method down to $\tau \sim 10^{-13}$sec. Without introducing much errors[20].

According to our results of the measured half-life of (2^+) 776.3-, (2^+) 1474-, (4^+) 1820- and (3^+) 2093 keV states, we calculated the partial transition rate P(E2) and the reduced transition probabilities B(E2) for each of the E2 transition γ-rays. The values of P(E2) and B(E2) are listed in Table 3. The internal conversion coefficients, brancing ratios and multipole mixing ratios used for the calculation are partially taken from refs. 4 and 22.

The reduced transtion probability of the 2^+ first excited state to the 0^+ ground state of ^{82}Kr we obtained is 0.19729×10^{-48} e^2 cm^4, which is about 5 times larger than the value of B(E2) = $(0.041 \pm 0.006)e^2 \times 10^{-48}$cm^4 by Beard[22] from the nuclear resonance-fluorescente scattering experiment. It is noted that our measured value of the half-life of the 776.3 (2^+) first excited state $T_{1/2}(1.016 \pm 0.019) \times 10^{-12}$sec is also shorter then that of Beard's $\tau = 6.9\ 1.1) \times 10^{-12}$ sec as deduced from the average resonance fluorescence cross-section.

TABLE III

Excited State (keV)	Transition Energy (keV)	$\delta^2 = [\frac{I(E2)}{I(M2)}]$	Internal Coefficient ($\times 10^{-3}$)	P(E2) (10^{12} Sec^{-1})	B(E2) ($e^2 \times 10^{-48}$) cm^4
776.28	776.28	∞	0.822	0.6816	0.1973
1474	698.25	9	1.046	1.0247	0.19504
	1474.82	∞	0.188	1.8750	0.003141
1820	1043.98	∞	0.419	0.724414	0.04773
2093	1318.1	19	0.245	0.2057	0.04238
	618.89	4	1.4	0.2739	0.245818

(a) Ref. 1, (b), (c) Ref. 4.

Beard also predicated the lower limit for the mean lifetime of the 1474 keV 4^+ excited state of ^{32}Kr as 1.2×10^{-12}sec. Our measured value $T_{1/2} = (0.87772 \pm 0.1252) \times 10^{-12}$sec for the 1474 keV 4^+ state is pretty close to the Beard limit.

Using the values of $P(E2: 2^+ \rightarrow 0^+)$ and $\beta(E2: 2^+ \rightarrow 0^+)$, we also obtained the deformation parmeter $\beta = 0.4252$ and the intrinsic quadrupole moment $0_0 = 3.149$b with the nuclear radius of $R_0 = 1.2\ A^{1/3}$fm. The calculated values are some what larger than the values of $\beta = 0.2$ and $Q_0 = 1.5$b as deduced by Etherton and Kelly who adopted the value of B(E2) obtained by Beard[4].

According to the Davydov and Filippov's non-axial rotator model, Klema, Mallmann and Day[11] have shown that the energy of 4^+ state at 1820 keV can be described in terms of the ratio of the energies of the 2^+ at 1474 keV and 2^+ at 776.3 keV states. And they obtained the parameters $\gamma = 27.7^0 \pm 0.01^0$, $\mu = 0.450 \pm 0.002$. They also obtained the non-axiality parameter $\gamma = 29.0^0 \pm 0.1^0$ and the non-adiabaticity parameter $\mu = 0.38 \pm 0.02$ for the 3^+ state at 2093 keV state. From our data the ratio of B(E2) for the 698 keV transition $(2^{+\prime} \rightarrow 2^+)$ and the 1474 keV transition $(2^{+\prime} \rightarrow 0^+)$ from the second 2^+ state at 1474 keV is found to be

$$\frac{B(E2;\ 2^{+\prime} \rightarrow 2^+)}{B(E2;\ 2^{+\prime} \rightarrow 0^+)} = \frac{0.195}{0.031} = 62 \pm 2$$

This is in good agreement with the values of 60 ± 10 obtained by Etherton and Kelly[4]. This value corresponds to $\gamma = 27.13^0$ which is comparable within error to the values of $\gamma = 27.1^0 \pm 0.1^0$ obtained by Klema et al[11]. Another

ratio of B(E2) for the transitions from the 3^+ state at 2094 keV to the $2^{+\prime}$ state at 1474 keV and 2^+ state at 776.3 keV is calculated as

$$\frac{B(E2;\ 3^+\rightarrow 2^{+\prime})}{B(E2;\ 3^+\rightarrow 2^+)} = \frac{0.0042}{0.2458} = 0.0172 \pm 0.0003$$

Compared to the value of 0.017 ± 0.005 obtained by Etherton and Kelly[4] the agreement is seem to be good also. The corresponding γ value ($\gamma = 27.3^0$) agrees well with the results of Klema et al.[11]

The authors wish to thank Dr. C. W. Wang of the Institute of Physics, Academic Sinica for his valuable and helpful discussions.

REFERENCES

(1) C. M. Lederer, J. M. Hollander, I. Perlman, Table of Isotopes, 6th Ed., John Wiley & Sons Inc. 1967
A. Artna, Nuclear Data Sheets B1-4-103 (1966)
(2) S. Raman, Nucl. Phys. **A90** (1967) 508
(3) E. S. Kenney and S. Raman, Bull. Am. Phys. Soc. 10 (1965) 588
(4) R. C. Etherton, W. H. Kelly, Nucl. Phys. **84** (1966) 129
(5) F. H. H. Hsu and C. S. Wu, Nucl. Phys. **A94** (1967) 205
(6) G. R. Meredith and R. Y. Meyer, Nucl. Phys. **A142** (1970) 513
(7) R. C. Waddell and E. N. Jensen, Phys. Rev. 102 (1956) 816
(8) S. Raman, Phys. Rev. **C2** (1970) 2176
(9) E. Liukkonen, J. Hattual and A. Anttila, Nucl. Phys. **A138** (1969) 163
(10) S. Raman, J. Pinajian, Nucl. Phys. **A125** (1969) 129
(11) E. D. Klema, C. A. Mallmann and P. Day Nucl. Phys. **25** (1961) 266
(12) L. Simon, S. Bergstom and A. Anttila, Nucl. Phys. **54** (1964) 683
(13) D. C. Camp and A. L. Van Lehn, Nucl. Instr. and Meth. **76** (1969) 192
(14) A. S. Davydov and A. A. Chaban, Nucl. Phys. **20** (1960) 499
(15) G. C. Kiang, T. Wang, B. Chen, and E. K. Lin, Ann. Rept., Inst. of Phys. Academia Sinica Vol. 6, 1976, 945
(16) T. Sundstrom, Nucl. Instr. & Meth. **16** (1962) 153
(17) P. Sparrman and F. Falk, Arkiv. for Fysik Bd 32 nr 24 (1966)
(18) R. S. Weaver and R. E. Bell, Nucl. Instr. & Meth. **9** (1960) 149
(19) Nuclear Data sheet, NSC 59-1-73
(20) G. C. Kiang, L. L. Kiang and W. C. Wang to be published
(21) A. S. Davydov and G. F. Filippov, Nucl. Phys. **8** (1958) 237
(22) K. Sieghahn, Editor, α-, β- and γ-Ray Spectroscopy, Vol. 2. p. 1639

A PRELIMINARY STUDY ON THE EXCITED STATES OF ^{154}Gd NUCLEUS*

G. C. KIANG (江紀成), D. WANG (王 定), C. W. WANG (王建萬)
and
E. K. LIN (林爾康)

Institute of Physics Academia Sinica

Abstract

A preliminary study on the excited states of ^{154}Gd is reported. A weak γ-ray of 966 keV is determined as the transition from 1650 keV state to the 680 keV state. A decay schame of the ^{154}Gd nucleus is proposed.

The excited states of ^{154}Gd nucleus have been investigated extensively in the past years[1-7]. Since the strong deformed nucleus like ^{154}Gd exhibits the properties of vibrational band mixing[6, 7]. We do have interest to study it carefully.

The ^{154}Eu activity was obtained by the thermal neutron irradiation of the enriched ^{153}Eu isotope (0.55% ^{151}Eu and 99.45% ^{153}Eu) in the Tsing Hua Reactor at National Tsing Hua University. The γ-source was prepared as a point source. The γ-ray single spectra of ^{153}Eu were measured by a ORTEC 43 cm^3 true coax Ge(Li) detector with energy resolution (FWHM) about 2.5 keV for the 1332 keV ^{60}Co gamma ray. The signals were amplified by a CI-1412 research amplifier and recorded with a Canbara 80 4096 multichannel analyzer. In the coincidence measurements, a 7.6 cm × 7.6 cm NaI(Tℓ) crystal and the said Ge(Li) detector were used. The signals of the selected γ-lines from the NaI(Tℓ) branch was in coincidence with the signals of Ge(Li) branch to operate the time-to-pulse-height converter which was employed to gate the linear signals of Ge(Li) detector.

The typical γ-ray single spectrum in the γ-ray energy region of 180 keV to 1800 keV was obtained by a 3 hr. measurement. The spectrum is shown in Fig. 1. The relative intensities of the γ-rays extracted from the spectrum are listed in Table 1. The gamma-ray energies were determined from a second order calibration curve which was obtained from a series well known gamma-rays in ^{133}Ba, ^{22}Na, ^{137}Cs, ^{60}Co and some of the natural background. Most of the γ-rays in the spectrum agree with the previous work[7], except the weak peak located at 1776 channel which corresponding to 966 keV according to our calibration. (Shown in Fig. 2)

According to Whitlock et al[2] a weak γ-ray of 964.5 keV was considered

* Work supported by the National Science Council, R.O.C..

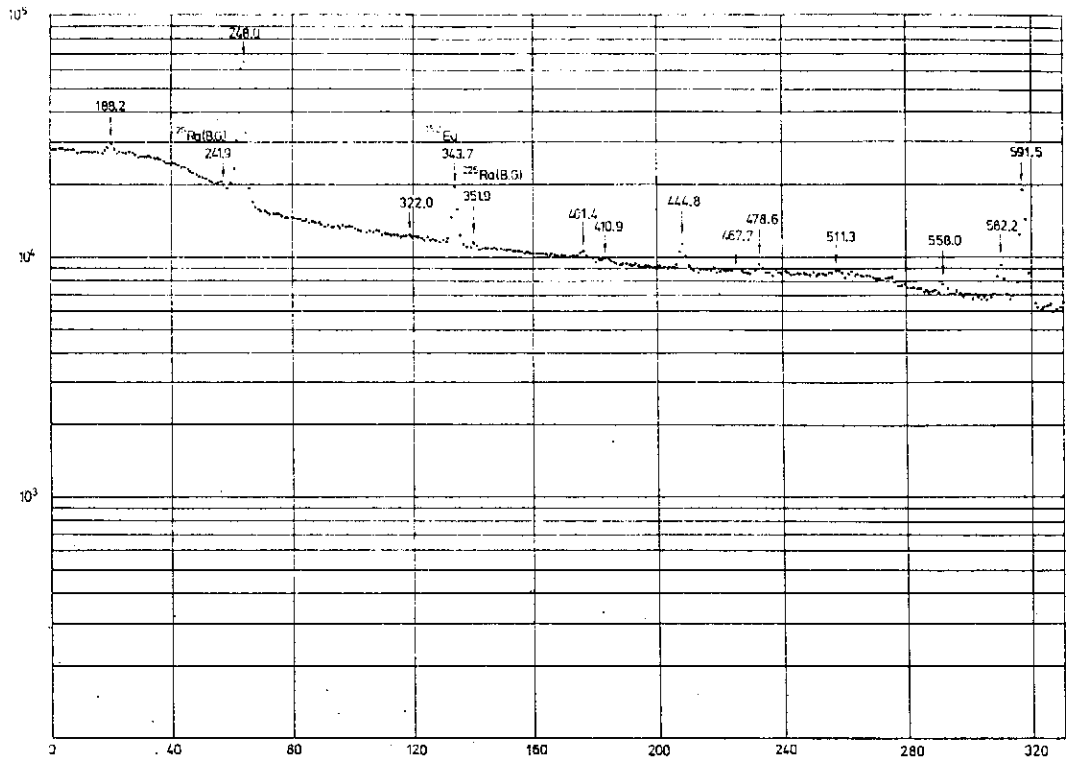
248.0
189.2
241.9
343.7
351.9
322.0
401.4
410.9
444.8
467.7
478.6
511.3
558.0
582.2
591.5
0
40
80
120
160
200
240
280
320

Fig. 1

(a)

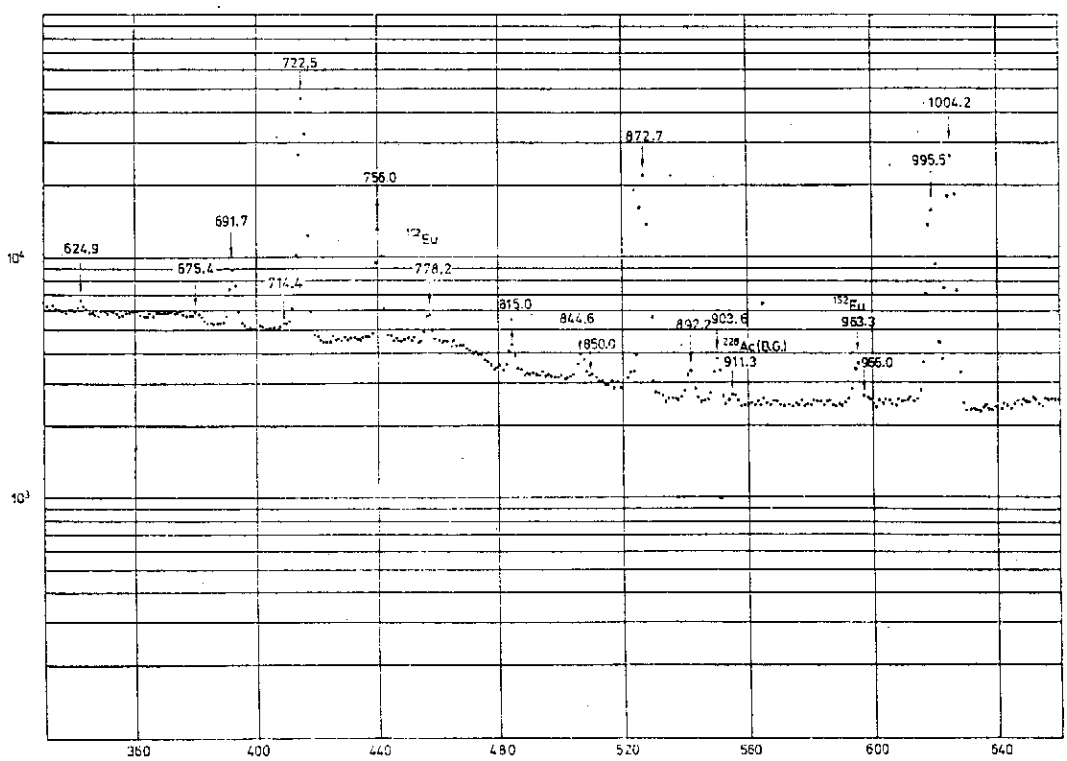
722.5
756.0
691.7
624.9
675.4
714.4
778.2
815.0
844.6
850.0
872.7
892.2
903.6
911.3
963.3
966.0
1004.2
995.5
360
400
440
480
520
560
600
640

Fig. 1

(b)

Fig. 1 (c)

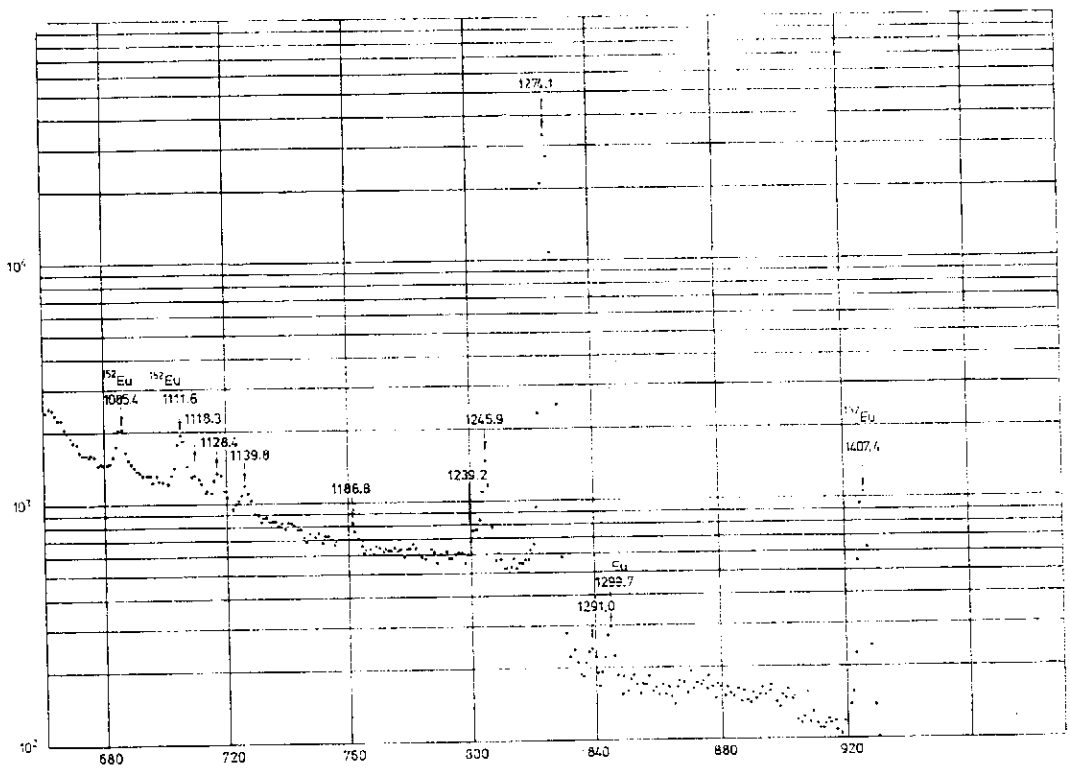

Fig. 1 (d)

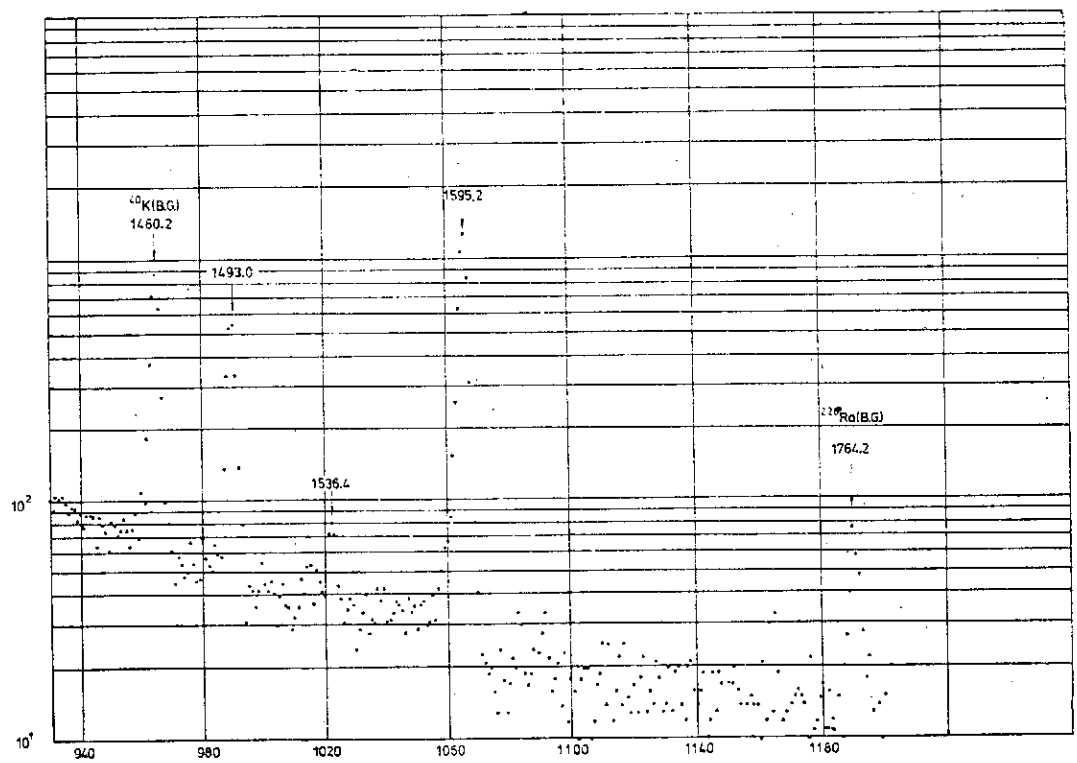

FIG. 1. The typical γ-ray single spectrum.

Table 1. The relative intensities of the γ-rays obained from the γ-ray single spectrum of ^{154}Eu.

Transition			
Eγ (KeV)	from	to	I (relative intensity)
188.2±0.5	1719.1	1531.0	5.77±0.07
248.2±0.5	370.5	123.0	120.1 ±0.3
322.0±0.4	1719.1	1397.2	0.30±0.02
401.4±0.3	1397.2	995.8	2.24±0.05
410.9±0.3	1661.3	1251.3	1.84±0.04
444.8±0.3	815.2	370.5	6.09±0.08
467.7±0.3	1719.1	1251.3	0.30±0.02
478.6±0.3	1719.1	1240.8	1.58±0.04
511.3±0.3	1558.3	1047.3	0.30±0.02
558.0±0.3	680.3	123.0	1.79±0.04
582.2±0.3	1397.2	815.2	5.94±0.08
591.5±0.3	1719.1	1127.1	30.2 ±0.2
624.9±0.3	995.8	370.5	1.55 ±0.04
675.4±0.3	1047.3	370.5	0.67±0.03
691.7±0.3	815.2	123.0	9.05±0.1
714.4±0.3	1531.0	815.2	0.42±0.02
722.5±0.3	1719.1	995.8	101.4 ±0.3
756.0±0.3	1127.1	370.5	21.3 ±0.2
815.0±0.3	815.2	0	2.32±0.05
844.6±0.3	1661.3	815.2	2.82±0.05
850.0±0.3	1531.0	680.3	0.82±0.03
872.7±0.3	995.8	123.0	50.2 ±0.2
892.2±0.4	1263.2	370.5	2.12±0.05
903.6±0.4	1719.1	815.2	3.17±0.05
966.0±0.5	1645.9	680.3	<0.05
995.5±0.5	995.8	0	38.4 ±0.2
1004.2±0.5	1127.1	123.0	64.5 ±0.2
1118.3±0.5	1240.8	123.0	0.29±0.02
1128.4±0.5	1251.3	123.0	0.80±0.03
1139.8±0.5	1263.2	123.0	0.83±0.03
1186.8±0.5	1558.3	370.5	0.32±0.02
1239.2±0.6	1240.8	0	0.11±0.01
1245.9±0.6	1617.2	370.5	3.27±0.05
1274.1±0.6	1397.2	123.0	100±0.3
1291.0±0.7	1661.3	370.5	0.15±0.01
1493.0±0.7	1617.2	123.0	1.70±0.04
1536.4±0.7	1661.3	123.0	0.11±0.01
1595.2±0.7	1719.1	123.0	4.38±0.04

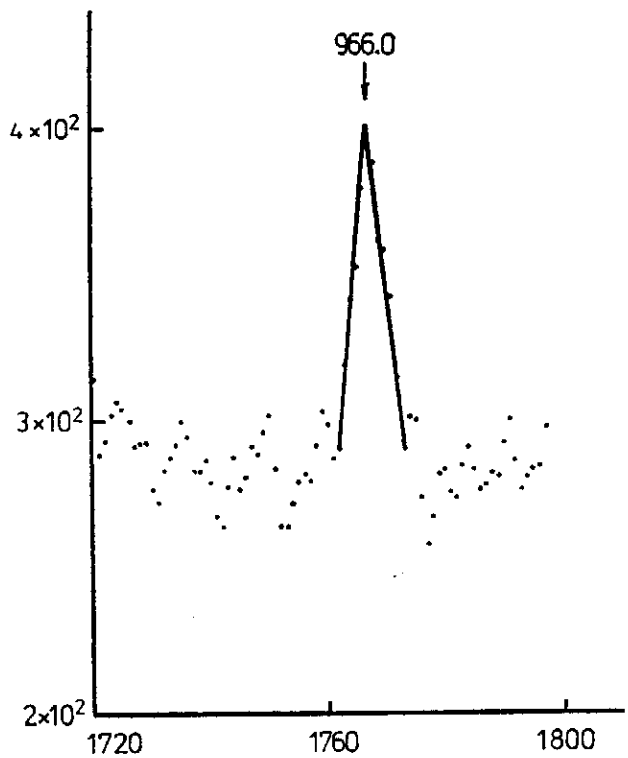

FIG. 2. A part of the coincidence spectrum obtained by gating at 557.6±10 keV.

as emitted by the impurity of ^{152}Eu. However, in check with the coincidence measurement, a peak appears at channel "1767" which corresponding to 966 keV. It is most likely that the 996 keV γ-ray arise due to the transition between 1650 keV state to 680 keV state of the ^{154}Gd nucleus. Based on a simple analysis, a proposed decay schame is constructed and shown in Fig. 3.

More experimental works such as the coincidence measurements directional correlation measurements, and the lifetime measurements for each of the excited states of ^{154}Gd will be continued to carry out, in order to get more informations about the structure of the strong deformed nucleus of ^{154}Gd.

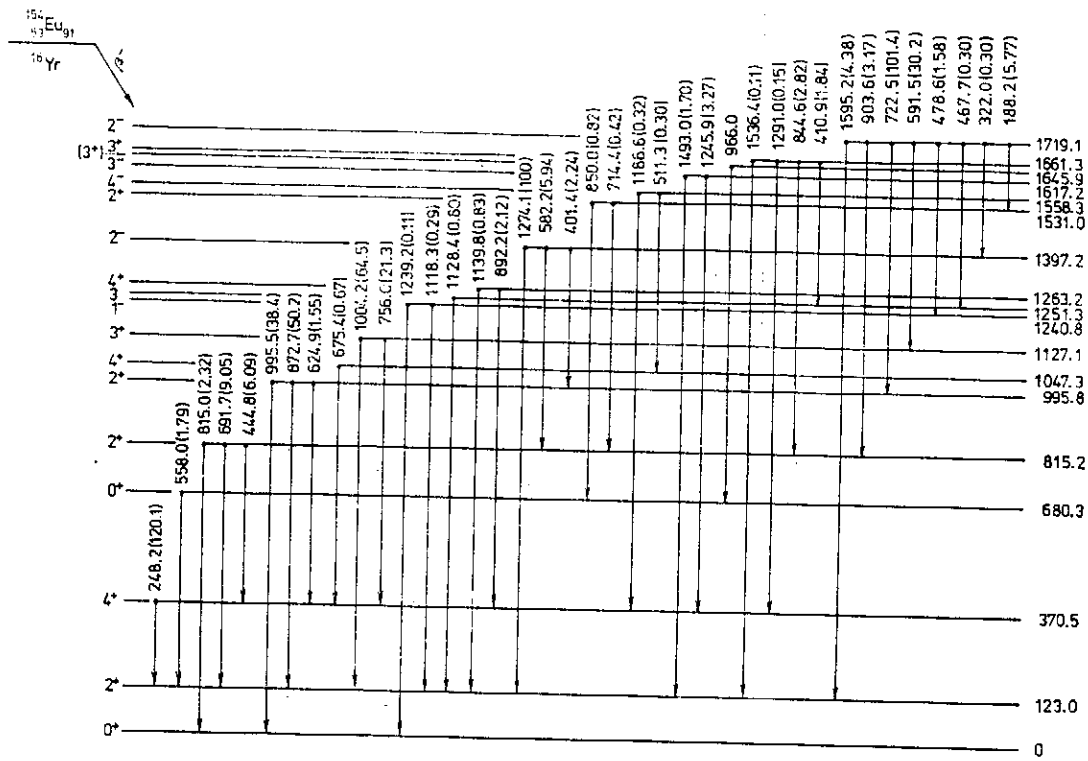

FIG. 3. A proposed decay schame of the ^{154}Gd nucleus.

REFERENCES

(1) C. M. Lederer, J. M. Hollander and I. Perlman, 'Table of Isotopes', 6th Ed. John Wiley & Sons, Inc. 1968.
(2) L. C. Whitlock, J. H. Hamilton and A. V. Ramaya, Phys. Rev. **C3**, 313 (1970).
(3) W. H. Brantely, J. H. Hamilton, T. Katoh and E. F. Zganjar, Nucl. Phys. A1118 (1968) 677.
(4) L. L. Riedinger, N. R. Johnson and J. H. Hamilton, Phys. Rev. Lett. **19**, 21 (1967), 1243.
(5) J. H. Hamilton, A. V. Ramaya, L. C. Whitlock, Phys. Rev. Lett. **23**, 20 (1969) 1178.
(6) J. H. Hamilton, A. V. Ramayya and L. C. Whitlock, ibid **22**, 2 (1969) 65.
(7) R. A. Meyer, Phy. Rev. **170**, 4 (1968) 1089.

NOTE ON MOMENTS ANALYSIS FOR THE DELAYED COINCIDENCE MEASUREMENTS

G. C. Kiang (江纪成), L. L. Kiang *(李 琳), and C. W. Wang (王建成)

Institute of Physics, Academia Sinica

Abstract

Based on Weaver and Bell's Theory, a simple method for analyzing the time spectra obtained by the delayed coincidence measurements was introduced. By using this method, several examples of analysis for the known half-lives were presented. It is believed that this method may extend the measurable range of the delayed coincidence down to 10^{-12} sec. or less.

Short lifetimes of excited states of nuclei are frequently measured by means of delayed coincidence method with a time-to-pulse-height converter in combination with a multichannel analyzer. And the evaluation of the lifetime from the measured curve can be made by many ways such as the well known slope method[1], the moments method[2, 3] etc. However, if the lifetime of the inquiried excited state is shorter than 10^{-11} sec the methods mentioned above will not be able to evaluate the lifetime accurately.

Here, we would like to introduce a new, simple but convience and quite accuracy method for analyzing the time spectra obtained from the delayed coincidence measurements. It is the possible way to extend the measurable range down to 10^{-12} sec. and not introduce much errors.

Based on the centroid shift method of Bay[2], Weaver and Bell[4] developed their method, which only need a rough knowledge of the shape of the prompt curve P(x) but not the position of its centroid. According to Bay[2], the relationship between the measured delayed curve F(x) and the prompt curve P(x) is

$$M_n(F)=\sum_{i=0}^{n}\frac{n!}{i!(n-i)!}M_{n-i}(P)M_i(\omega) \qquad (1)$$

$$M_n(F)=\int_{-\infty}^{\infty}X^nF(x)dx$$

where, $M_n(F)$ is the n-th moment of $F(\infty)$ and,

$$\omega(t)=\tau^{-1}\exp(-t/\tau) \qquad (t>0)$$

For n = 1, 2, and 3, we have the following relations,

$$M_1(F)=\tau+M_1(P) \qquad (2)$$

$$M_2(F)=\tau^2+M_2(P) \qquad (3)$$

* Department of Physics, National Tsing Hua University.

$$M_3(F) = 2\tau^3 + M_3(P)$$

Weaver and Bell[4] pointed out that when the prompt curve P(x) is an "unobserved". It may define the centroid of the delayed curve F(x), from (2) as.

$$M_1^*(F) = 0 \qquad (5)$$

then the quantity $M_3^*(P)$ is very small and even be neglible. In such a case, the mean lifetime can be obtained from the delayed curve F(x) only

$$\tau = [\ \tfrac{1}{2} M_3^*(F)\ ]^{1/3}.$$

Based on Weaver and Bells method, we chose the known half-life $T_{1/2} = 0.8$ ps[5] ^{60}Co 1332 keV excited state as our time standard. That was we measured the time spectrum of the 1332 keV state of ^{60}Co (Fig. 1) with the delayed coincidence method. Then normalized the whole peak area to unit. A computer code was prepared to help finding it's centroid with $M_1^*(F) = 0$. About this centroid we evaluated the third moment as well as the lifetime τ in number of channels. The same procedure was applied on the required time spectrum and the lifetime may evaluate from the simple formula

$$\frac{\tau_1}{0.8\text{ps}} = \frac{\tau_2}{T_{1/2}}$$

Several known half-life excited states, such as the first state of ^{82}Kr ($T_{1/2} = 1 \times 10^{-12}$ sec)[6], the second excited state of ^{154}Gd ($T_{1/2} = 4 \times 10^{-11}$ sec) and the first excited state of ^{122}Te ($T_{1/2} = 8 \times 10^{-12}$ sec)[5] have been used for the test of the method. Figs. (2), (3) and (4) wasn the time spectra obtained by the delayed coincidence measurements of the excited states respectively. The results of the analysis wes shewn show in Table 1. In comparision with the known halflives, our results of the analysis are quite good, especially for the short halflives arround 10^{-12} sec. And the errors would not be larger than the 3rd moment method[4].

More measurements for the other known half-lives states will be given in order to test the accuracy and the reliability of the analysis method.

REFERENCES

(1) T. D. Newton, Phys. Rev. 78, 490 (1950)
(2) Z. Bay, Phys. Rev. 77, 419 (1950)
(3) P. Sparrman and F. Falk, Arkiv Fur Physik Bd. 32 nr. 24
(4) R. S. Weaver and R. E. Bell Nucl. Instr. & Meth. 9, 143 (1960)
(5) C. M. Lederer, J. M. Hollander, I. Perlman, 'Table of Isotopes' 6th Ed. John Wiley & Sons, 1967.
(6) G. C. Kiang et al. to be published.

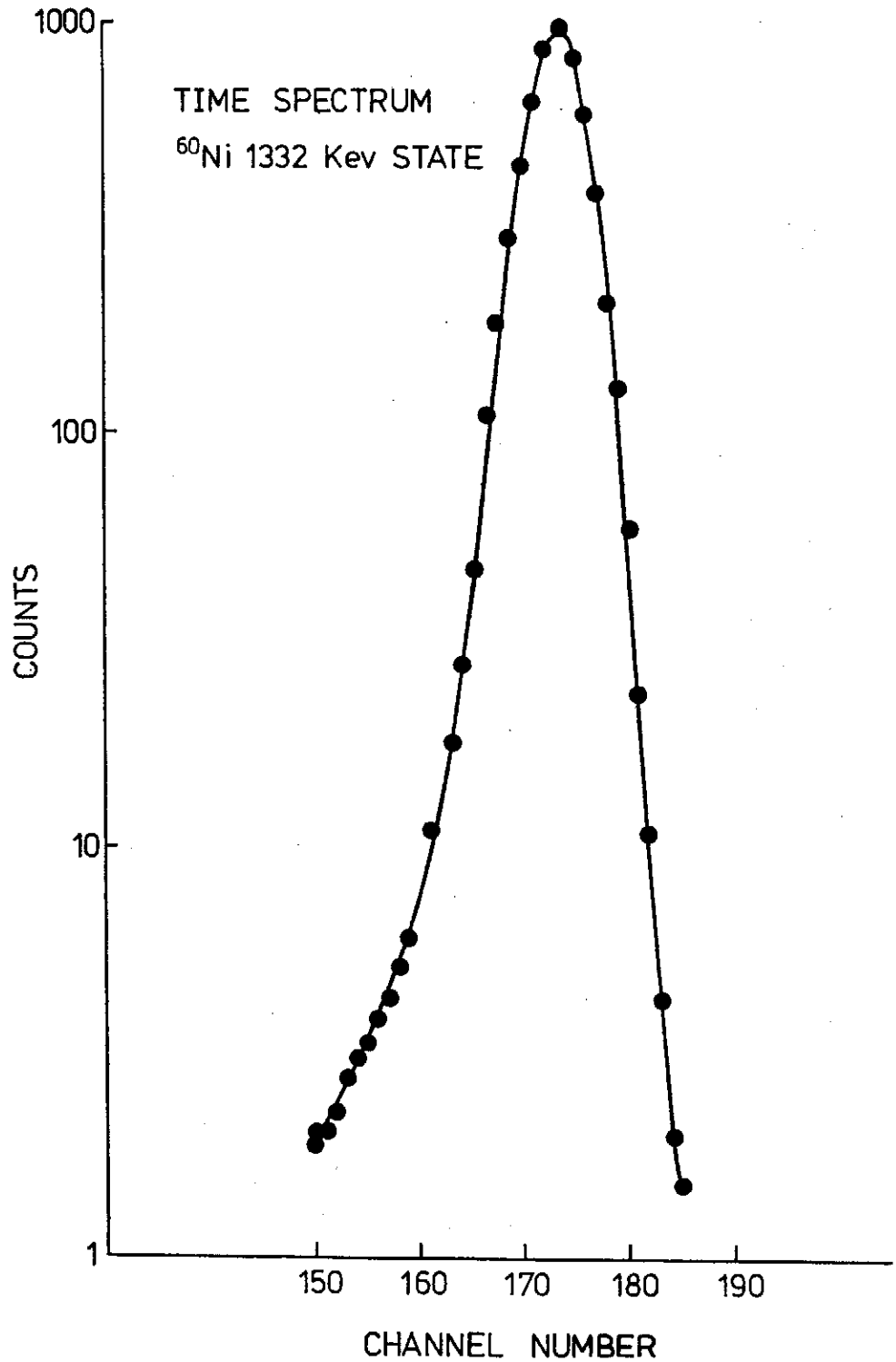

FIG. 1. The time spectrum of the 1332 keV state of ^{60}Ni nucleus obtained by the delayed coincidence method. This spectrum was analyzed with 3rd moment method as times standard.

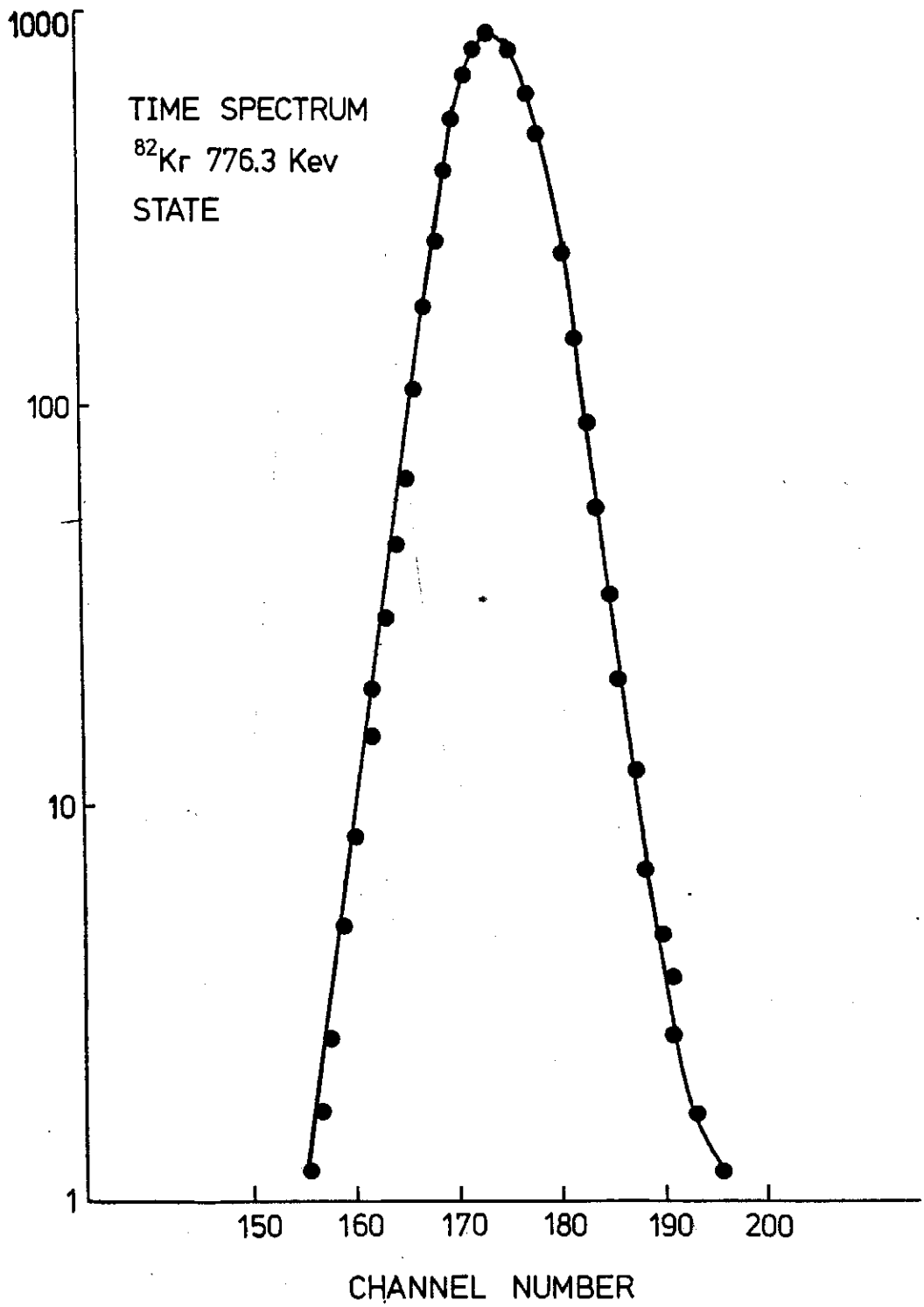

FIG. 2. The time spectrum of the ^{82}Kr 776.3 KeV state.

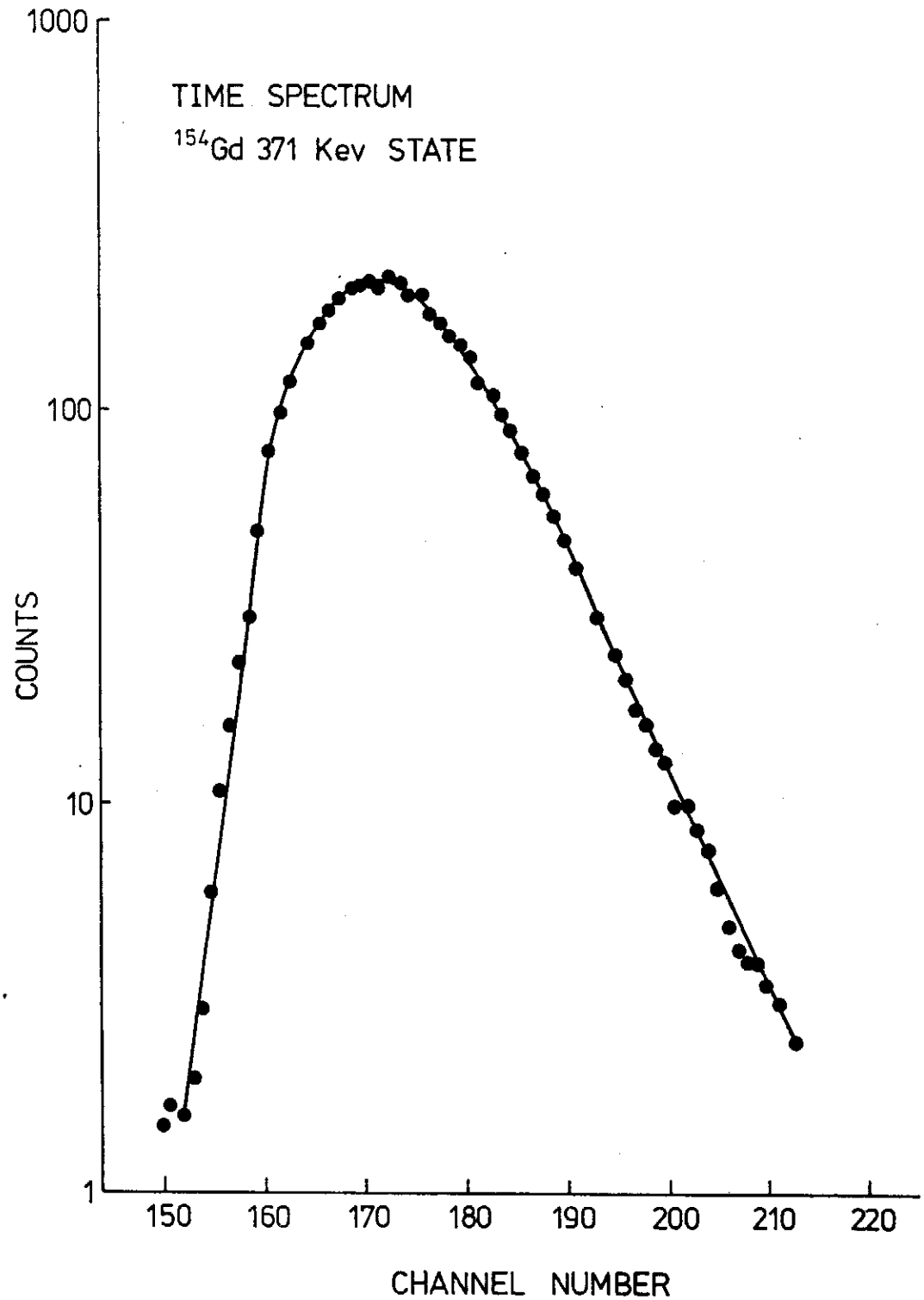

FIG. 3. The time spectrum of ^{154}Gd 371 keV state.

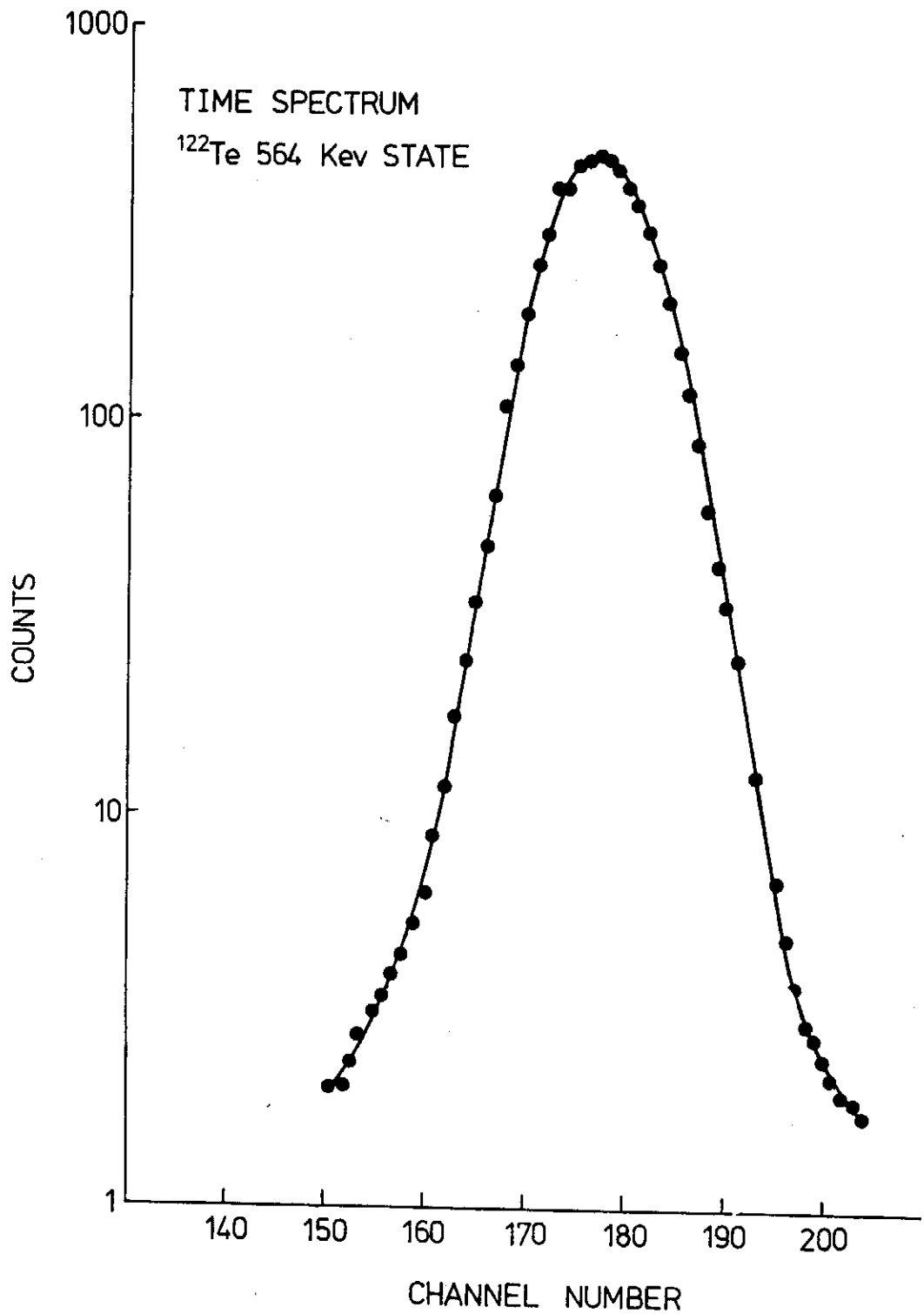

FIG. 4. The time spectrum of ^{122}Te 564 keV state.

TABLE 1

Nuclei	State (MeV)	Half-life* (sec)	Half-life obtained by our method (sec)
^{82}Kr	0.776	1.01×10^{-12}*	1.0×10^{-12}
^{124}Gd	0.371	4×10^{-11}+	3.2×10^{-11}
^{122}Te	0.564	8×10^{-12}+	6×10^{-12}

*Ref. 6. G. C. Kiang et al, to be published.

+Ref. 5. C. M. Lederer, J. M. Hollander, I. Perlman, 'Table of Isotopes' 6th Ed. Jonn Wiley and Sons, 1967

本所新竹及南港地區原子核實驗室中伽瑪背景之分析

江紀成、李琳*、王建萬、梁靈平、王　定

中央研究院物理研究所

摘　　要

量度本所南港及新竹地區原子核實驗室內自然背景伽瑪線譜，分析各伽瑪線峯之來源及相對强度，作爲實驗工作時之參考。建築用砂，及澳洲鐵礦砂之伽瑪線譜，亦予以分析，並略加討論。

壹、緒　　言

由於宇宙射線，及存於自然界中之長生命期（life time）的放射性同位素，核爆後的輻射塵；甚或是人爲因素等所造成的放射性污染。在我們的生活環境中，或多或少，有若干放射性存在。這種微量的放射性，對人們的生活起居，固然不構成威脅。然而，若存在於實驗室中，尤其是放射性量度實驗室，或原子核物理實驗室，則對靈敏而精確的放射性量度儀器，會造成若干嚴重的干擾，影響到實驗的精確；形成研究工作上的困擾。這種自然存在的，所謂「背景放射性」（background radiation）可謂無所不在，防不勝防。即使連構成輻射偵檢器的材料中也含有微量的放射性物質[1,2]，在度量放射線能譜時也隨之出現。因此，一般放射性或原子核物理實驗室，均把背景放射性的認定及量度，作爲必要的工作之一，以免在實驗中造成錯覺，影響分析[2]。

本所原子核物理小組，除在南港本所，設有一伽瑪射線實驗室，從事慢中子捕獲伽瑪射線的量度，以研究原子核構造；在新竹清華大學，亦有一中子物理實驗室，除從事快中子物理的研究外，亦量取伽瑪線譜，作原子核構造之研究工作。因此，這兩個實驗室對伽瑪背景均有瞭解之必要。新竹實驗室，爲求其對 14.1 MeV 快

* 清華大學物理系

中子之屏蔽，其實驗區與計數、控制室之隔牆，以90公分之加强混凝土分兩層築成；面向快中子源部分，混凝土中細沙以½澳洲鐵礦砂取代，面向控制室方面，混凝土中之細砂，以½之硼砂取代；形成特有之快中子屏蔽體。其餘牆壁及屋頂，亦爲厚度爲48公分之混凝土築成，應該對外來宇宙射線等有較佳之屏蔽力。然而，在量取伽瑪背景射線時，發現新竹實驗室之背景伽瑪射線，多達30餘條，大致說來，其能量之分佈在 15 KeV 至 2700 KeV 間。至於南港實驗室，則所量得之伽瑪線譜，顯示背景伽瑪射線較少，在20條左右，能量分佈在 230 KeV 至 1800 KeV 間。因此，伽瑪背景射線之來源，澳洲鐵礦砂、拌合水泥之河砂等，均在考慮之列。

貳、實驗過程與結果

在本實驗中，我們以 43 cm^3 高分鑑率之同軸鋰（鋰）偵檢器，量取伽瑪線譜；此項偵檢器，對 ^{60}Co 1332 KeV 伽瑪射線之分鑑率爲 2.3 KeV，伽瑪線譜之記錄，則以 CI-8700 型 4096 多頻分析儀爲之。我們作了下述幾種度量：

(1)無試料時，連續量取伽瑪線譜 500 分鐘。

(2)取拌合水泥用砂一公斤，分置爲塑膠袋中，環置於偵檢器四週，連續量取伽瑪線譜， 500 分鐘。

(3)以澳洲鐵礦砂一公斤作試料， 分裝爲塑膠袋中， 幾何安排如 (2)， 連續量取500分鐘。

(4)偵檢器，以厚度爲 5-10 cm 鉛塊，完全屏蔽，量取伽瑪線譜500分鐘。

上述的四種伽瑪線譜，分別示之如圖 1 至圖 4。這此所譜上的伽瑪能峯，經分析後，就其來源及强度，分別列之如表一及表二。由表中我們可以看出，新竹實驗室中的自然背景伽瑪線，一共發現有34個能峯，伽瑪能量由 154 KeV 至 2614 KeV。南港實驗室中線量得的自然背景伽瑪能峯數較少，有 19 個；能量分配，自 241 KeV 至 2614 KeV。在表一中，我們把由鉀—40核種來的，能量爲 1460.8 KeV 的伽瑪射線，定爲强度爲 100， 以表在同一能譜中，其他伽瑪線的相對强度。在表二中， 我們把由自然背景中量得的鉀-40 ， 1460.75 KeV 的伽瑪射線 ； 定爲强度爲 100 以表出，在河砂，澳洲鐵礦砂爲試料，及加鉛塊屏蔽後所得的能譜，其中伽瑪射線的相對强度。由這些分析、比較中，我們發現若干有趣的問題。其一是，背景伽瑪線，都來自自然界生成的放射性核種。例如，屬於鈾系的 ^{226}Ra ；屬於釷系的

^{212}Bi (或稱 ThC) ，^{208}Tl (或稱 The[11]) 及 ^{228}Ac (或稱 ThD)。其他的還有鉀—40，錳—56等。由表一及表二，我們也可以看出，在以河砂作試料，所量得的能譜中，鈾系 ^{226}Ra 來的伽瑪射線，其相對强度，並未因河砂的屏蔽作用而減少，屬於釷系的 ^{212}Bi 伽瑪線峯，也有類似的情形。因此，我們有理由相信，在拌合水泥的河砂中有若干天然放射性核種存在。至於在自然背景及砂的伽瑪能譜中，有錳-54 835 KeV 的線峯出現，則可能是實驗室中，有少量錳—54 污染的緣故。

與其他地區所得的自然背景伽瑪線譜相比較[2,3]，新竹地區實驗室的伽瑪自然背景相當高，核種來源固然類似，但伽瑪線峯的數目則多，可能係分析較周密的緣故。一般言之，鉛屏蔽爲對伽瑪射線，最有效的屏蔽之一，但却無法對自然背景作澈底的消除 (見圖4)[2]，故一般原子核實驗室，均應對其自然背景能譜，作一澈底地量度與瞭解。

參 考 文 獻

(1) W. J. Price, Nuclear Radiation Detection, Taiwan Print, 1958 p. 192

(2) C. E. Coothamel, 'Applied Gamma-Ray Spectrometry' 2nd Ed. Completely Revised and enlarged by F. Adams and R. Dams, Pergaman Press, 1970, p. 165

(3) 翁寶山、許俊男、張鴻讚，原子能委員會彙報，第11卷，5期 (16) (民國六十四年)

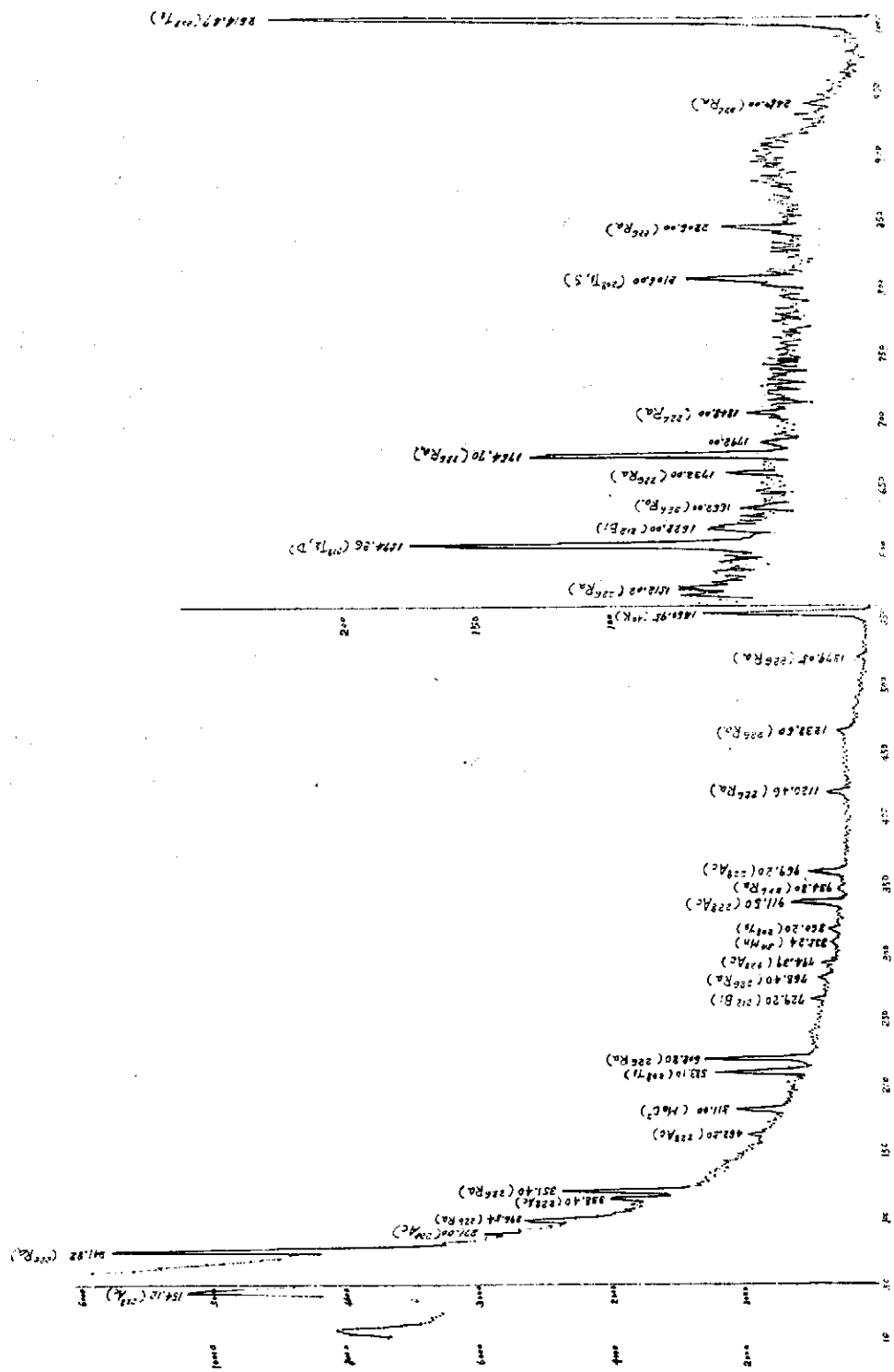

圖 1. 新竹實驗室伽瑪自然背景能譜（量取時間 500 分種）

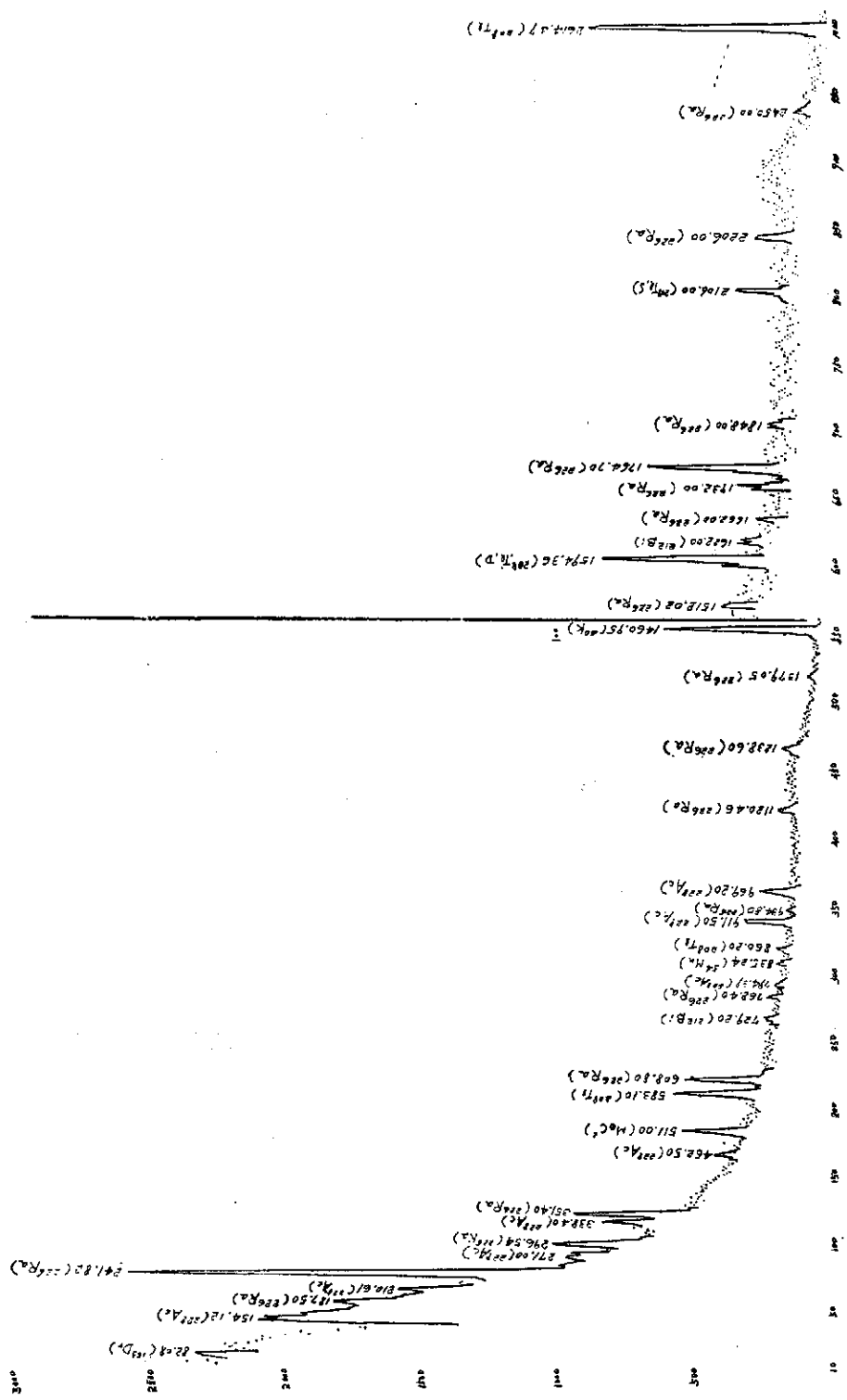

圖 2. 新竹實驗室伽瑪射線能譜，試料爲河砂

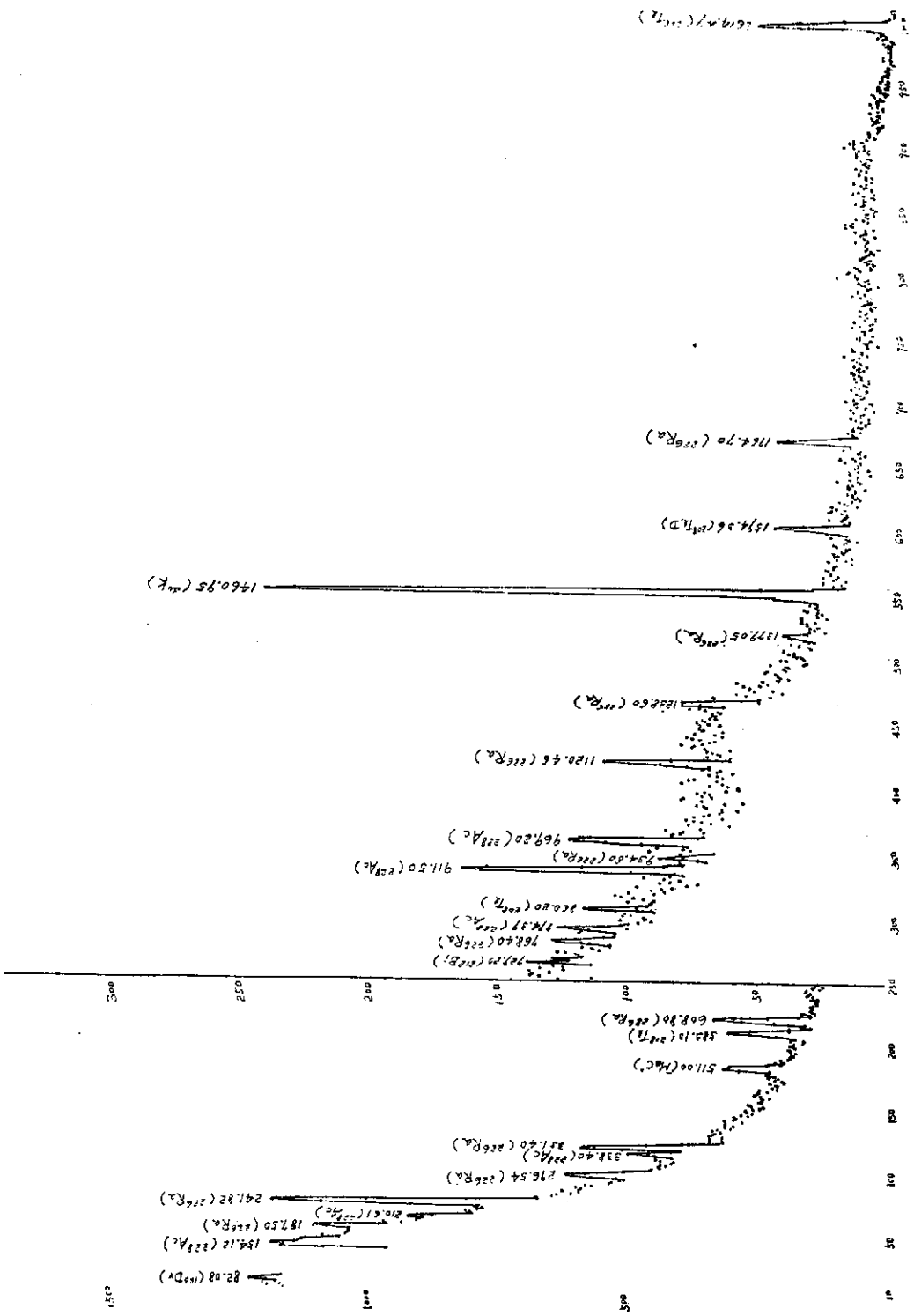

圖 3. 新竹實驗室伽瑪射線能譜，試料爲澳洲鐵磺砂

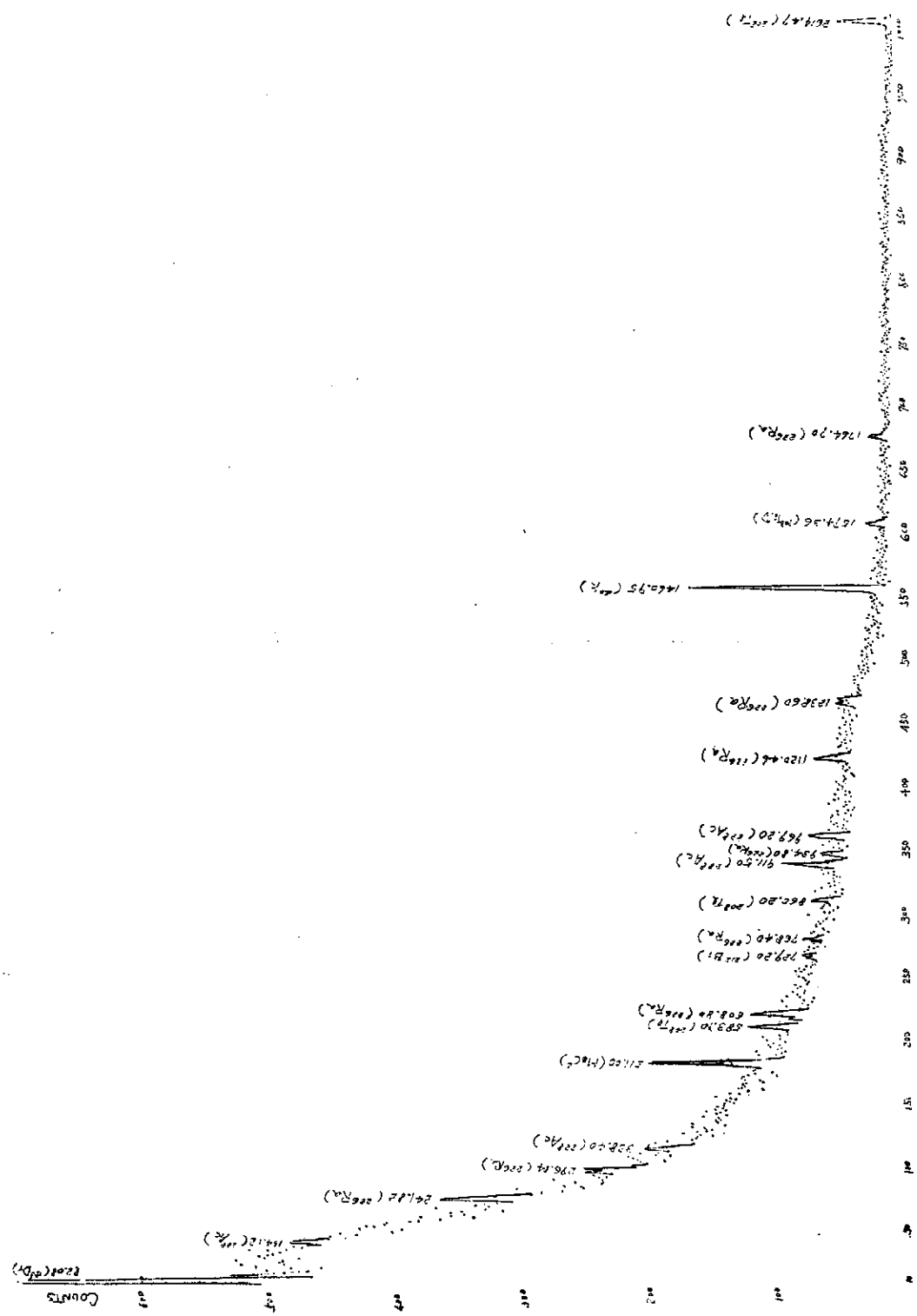

圖 4. 新竹實驗室自然背景伽瑪射線線譜，加 1 吋鉛塊屏蔽後。

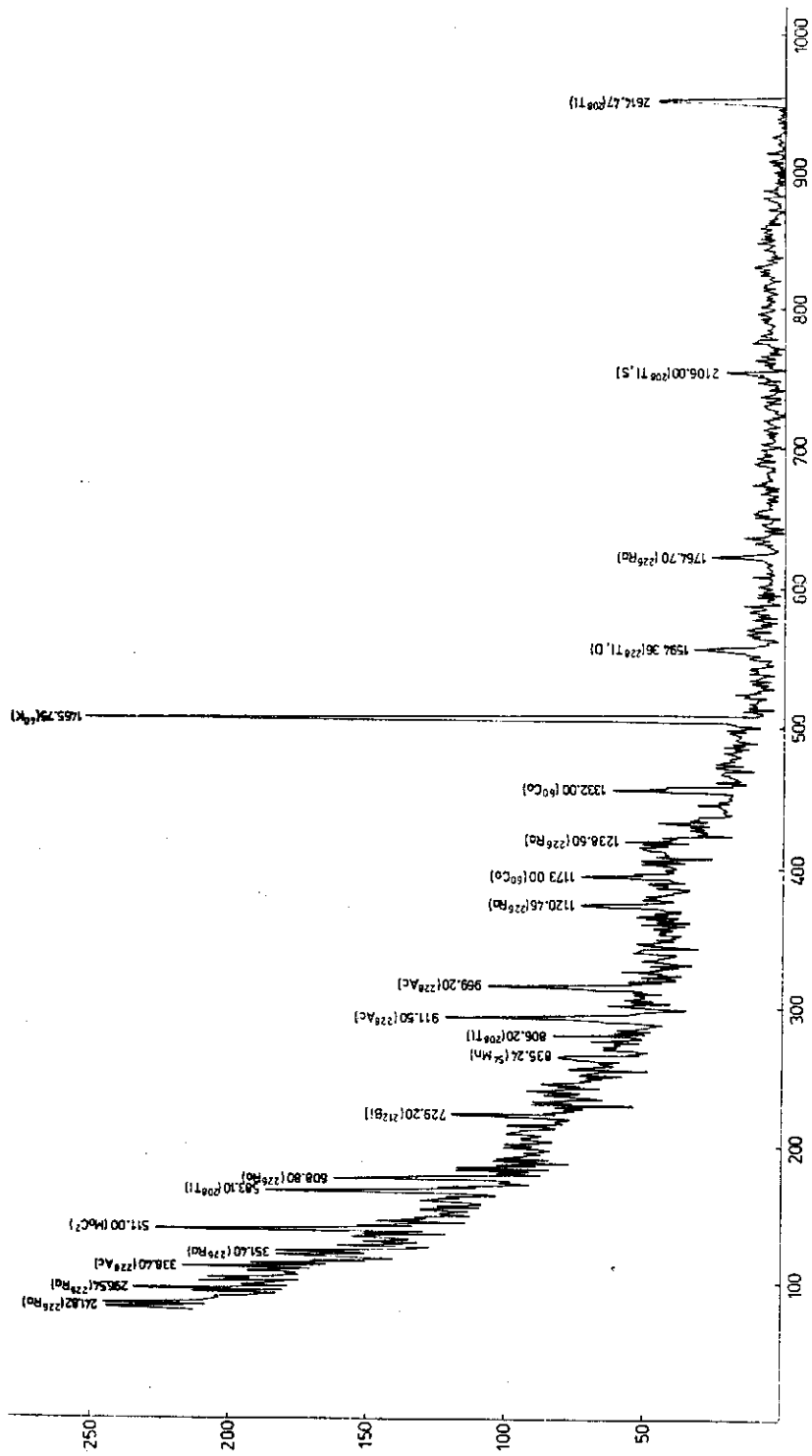

圖 5. 南港實驗室伽瑪自然背景能譜

表一、新竹及南港地區，本所原子核實驗室內，伽瑪背景強度之比較，以 1460.95 KeV，鉀 —40伽瑪射線之強度為 100。

能量 (KeV)	新竹實驗室 相對強度				南港實驗室* 自然背景	來源
	自然背景	砂	鐵砂	鉛		
154.12	324.74	95.6	96.36	97.5	—	^{228}Ac
187.50	—	97.6	98.49	—	—	^{226}Ra
210.61	—	116.2	108.05	—	—	^{228}Ac
241.82	306.18	255.2	224.35	144.96	72.19	^{226}Ra
271.00	156.73	61.77	—	—	—	^{228}Ac
296.54	103.79	80.63	100.19	32.87	36.43	^{226}Ra
338.40	154.57	90.86	79.68	44.84	17.16	^{228}Ac
351.40	156.43	49.84	197.08	—	36.43	^{226}Ra
462.50	16.88	22.58	—	—	—	^{228}Ac
511.00	62.61	63.56	43.02	59.05	29.96	MoC?
583.10	82.93	58.68	87.86	22.52	33.65	^{208}T$_\ell$
608.80	81.74	51.35	103.05	46.93	30.86	^{226}Ra
729.20	27.20	15.27	15.28	10.40	11.30	^{212}Bi
768.40	23.38	7.75	11.22	14.56	—	^{226}Ra
794.39	10.13	5.74	6.3	—	—	^{228}Ac
835.24	5.00	7.2	—	—	6.31	^{54}Mn
860.20	15.63	10.16	10.08	13.32	7.42	^{208}T$_\ell$
911.50	34.46	41.20	41.69	25.97	18.89	^{228}Ac
934.80	4.58	6.53	11.68	11.32	—	^{226}Ra
969.20	24.44	24.21	20.40	22.35	17.24	^{228}Ac
1,120.46	13.49	9.93	14.4	18.68	7.00	^{226}Ra
1,238.60	12.41	13.81	18.95	10.06	3.88	^{226}Ra
1,379.05	3.31	3.85	5.9	—	—	^{226}Ra
1,460,95	100.00	100.00	100.00	100.00	100.00	^{40}K
1,512.02	3.06	4.27	—	—	—	^{226}Ra
1,594.36	14.14	8.9	12.11	7.06	10.53	^{208}T$_\ell$D
1,622.00	5.15	0.9	—	—	—	^{212}Bi
1,662.00	2.06	1.63	—	—	—	^{226}Ra
1,732.00	2.82	5.37	—	—	—	^{226}Ra
1,764.70	9.37	9.66	14.15	12.37	8.84	^{226}Ra
1,792.00	1.71	—	—	—	—	B_i?
1,848.00	1.84	3.03	—	—	—	^{226}Ra
2,106.00	4.85	5.93	—	—	5.21	^{208}T$_\ell$S
2,206.00	2.60	5.93	—	—	—	^{226}Ra-
2,450.00	2.22	4.01	—	—	—	^{226}Ra-
2,614.47	18.53	18.39	27.33	24.74	13.62	^{208}T$_\ell$

* 能譜量取時間 100 分鐘。

表二、新竹及南港地區，本所原子核實驗室內，伽瑪射線強度之比較，以自然背景中 1460.95 KeV 鉀—40伽瑪射線之強度為100。

能量 (KeV)	新竹清大實驗室 相對強度				來源
	自然背景	砂	鐵砂	鉛	
154.12	324.74	69.44	30.42	19.37	^{228}Ac
187.50	—	70.94	31.16	—	^{226}Ra
210.61	—	84.26	34.14	—	^{228}Ac
241.82	306.18	185.24	71.12	28.69	^{226}Ra
271.00	156.73	44.86	—	—	^{228}Ac
296.54	103.79	59.01	31.65	6.48	^{226}Ra
338.40	154.57	66.11	25.20	8.80	^{228}Ac
351.40	156.43	36.48	30.86	—	^{226}Ra
462.50	16.88	16.01	20.1	20.1	^{228}Ac
511.00	62.61	46.19	13.66	11.68	MoC^{2}
583.10	82.93	42.78	27.77	4.50	^{208}T$_{\ell}$
608.80	81.74	37.36	32.62	9.29	^{226}Ra
729.20	27.20	11.19	4.82	2.11	^{212}Bi
768.40	23.38	5.66	3.09	2.93	^{226}Ra
794.39	10.13	4.15	2.57	—	^{228}Ac
835.24	5.00	5.25	—	—	^{54}Mn
860.20	15.63	7.64	3.31	2.57	^{208}T$_{\ell}$
911.50	34.46	23.92	10.54	5.12	^{228}Ac
934.80	4.58	4.95	3.71	2.19	^{226}Ra
969.20	24.44	17.58	6.42	4.47	^{228}Ac
1,120.46	13.49	7.51	4.55	1.84	^{226}Ra
1,238.60	12.41	10.11	2.82	2.06	^{226}Ra
1,279.05	3.31	2.82	1.87	—	^{226}Ra
1,460.95	100.00	58.06	25.28	15.77	^{40}K
1,512.02	3.06	3.06	—	—	^{226}Ra
1,594.36	14.14	6.53	3.82	1.38	^{208}T$_{\ell}$ (D)
1,622.00	5.15	1.11	—	—	^{212}Bi
1,632.00	2.06	0.95	—	—	^{226}Ra
1,732.00	2.82	3.12	—	—	^{226}Ra
1,764.70	9.37	5.61	3.58	1.95	^{22} Ra
1,792.00	1.71	—	—	—	
1,848.00	1.84	1.76	—	—	^{226}Ra
2,106.00	4.85	3.44	—	—	^{60}Co
2,206.00	2.60	3.44	—	—	^{226}Ra
2,450.00	2.22	2.33	—	—	^{226}Ra
2,614.47	18.53	10.68	6.91	3.90	^{208}T$_{\ell}$

THE QUASI-FREE $(\alpha,2\alpha)$ REACTION INDUCED BY 140 MeV ALPHA PARTICLES ON ^{9}Be, ^{12}C, ^{16}O and ^{20}Ne

C. W. WANG, N. S. CHANT, P. G. ROOS,
A. NADASEN, and T. A. CAREY

Department of Physics and Astronomy
University of Maryland, College Park, Maryland 20742

Abstract

Measurements of the $(\alpha, 2\alpha)$ reaction on ^{9}Be, ^{12}C, ^{16}O and ^{20}Ne targets at $E_{\alpha}=140$ MeV were made at 20 angle pairs. The quasi-free knockout mechanism appears to dominate the reaction. The experimental data were analyzed with distorted wave impulse approximation calculations. The factorization approximation employed in the calculations was tested explicitly and found to be valid. The shapes of the calculated energy sharing spectra are in satisfactory agreement with the data. The predicted absolute cross sections were found to be very sensitive to the cluster core bound state radius parameter, and a bound state radius $R=2.52\ A_c^{1/3}$ fm is necessary to obtain absolute spectroscopic factors consistent with existing theoretical values. Several possible explanations for this excessive value are suggested. Comparisons are made with other alpha knockout and transfer reactions.

I. INTRODUCTION

Quasi-free knockout reactions have proved to be a powerful tool for the investigation of nuclear structure. Since the first experiment studying (p, 2p) reactions on light nuclei,[1] a considerable amount of experimental and theoretical work has been carried out on this subject. In situations where the quasi-free knockout reaction mechanism dominates, the (p, 2p) reaction can provide two types of information.[1-6] Firstly, the proton hole states in nuclei can be investigated, and secondly, one can study off-energy-shell p-p interactions. Similar information about nucleon clusters in nuclei can be obtained using quasi-free cluster knockout reactions.[4]

In this paper we present studies of alpha clustering using the $(\alpha, 2\alpha)$ reaction at 140 MeV. In recent years alpha clustering in 1p and 2s1d shell nuclei has been studied using a variety of nuclear reactions. The (d, ^{6}Li), (^{3}He, ^{7}Be), (α, ^{8}Be), (^{6}Li, d), (^{7}Li, t) and (^{16}O, ^{12}C) alpha transfer reactions[7-13] have been studied and analyzed using distorted wave Born approximation (DWBA) and coupled channel Born approximation (CCBA) calculations.[14] However, most of these analyses are limited to extracting relative alpha spectroscopic factors. The (p, pα) quasi-free knockout reaction has been investigated in several works.[15-18] Analyses of the experimental results at an incident energy of 100 MeV have shown that the plane wave impulse approximation (PWIA)

* Present address: Institute of Physics, Academia Sinica.

reaction model is inadequate but that the data are well described by distorted wave impulse approximation (DWIA) calculations.[19-21] In these analyses the extracted *absolute* alpha cluster spectroscopic factors are found to be in good agreement with theoretical calculations.[22, 23]

The $(\alpha, 2\alpha)$ quasi-free knockout reaction on 1p and 2s1d shell nuclei has also been studied by other groups. Results for the $^{6,7}Li(\alpha, 2\alpha)$ reaction at $E_\alpha = 50$ to 80 MeV[24, 25] have been analyzed using the PWIA. Also a reaction mechanism study of $^{9}Be(\alpha, 2\alpha)$ at $E_\alpha = 40$ to 60 MeV has been reported.[26, 27] In addition, data have been obtained for the $^{20}Ne(\alpha, 2\alpha)$ reaction at $E_\alpha = 78$ MeV[28] and analyzed using the PWIA. Recently, Sherman, et al.,[29, 30] have carried out extensive measurements of the $(\alpha, 2\alpha)$ reaction on nine nuclei from ^{12}C to ^{66}Zn at $E_\alpha = 90$ MeV. Finally the ^{16}O, $^{28}Si(\alpha, 2\alpha)$ reactions have been studied at 0.65 and 0.85 GeV.[31]

The most complete $(\alpha, 2\alpha)$ study is the work of Sherman, et al., at 90 MeV which poses some interesting problems. Using an approximate parameterized form for the distorted waves[32] quite good agreement was obtained with the shape of the energy sharing spectra and the results were insensitive to the type of bound state wave function used. The alpha spectroscopic factors obtained from this analysis are 2.9 ± 0.4 and 2.9 ± 0.5 for $^{12}C(\alpha + {}^{8}Be(g.s.))$ and $^{16}O(\alpha + {}^{12}C$ (g.s.)), respectively, which should be compared to the theoretical values of 0.55 and 0.23 obtained by Kurath.[22] However, for the $^{16}O(\alpha, 2\alpha)^{12}C$ data of Sherman, et al., calculations by Chant and Roos,[19] using an exact partial wave expansion of the distorted waves and a Woods-Saxon bound state wave function with parameters chosen to reproduce the rms radius of ^{16}O, yield absolute spectroscopic factors roughly 100 times the theoretical prediction. In spite of this unexpected result, the ratio S_{0+}/S_{2+} of the spectroscopic factors for ^{12}C(g.s.) and the first excited state of ^{12}C(4.43 MeV, 2^+) was found to be 1/8, fairly close to the value 1/5.7 of Kurath. At $E_\alpha = 850$ MeV, Chant and Roos obtained a value of 1.8 for S_α which is an upper limit since many levels contributed due to poor binding energy resolution of the experiment.[31]

Studies[33, 34] of $^{16}O(\alpha, 2\alpha)^{12}C$(g.s.) at $E_\alpha = 25$ MeV and ^{16}O, $^{20}Ne(p, p\alpha)$ at $E_p = 46.8$ MeV showed that the alpha removal reaction at these energies is dominated by sequential processes, while in the systematic study of Sherman, et al.,[29, 30] at $E_\alpha = 90$ MeV the quasi-free knockout mechanism appeared to dominate. Nevertheless, since the difficulties in Sherman's approximate DWIA analysis and in the exact DWIA treatment of Chant and Roos may arise from the presence of competing processes at this energy, we chose to study the $(\alpha, 2\alpha)$ reaction at a higher energy, $E_\alpha = 140$ MeV, in the hope that the reaction mechanism might be more easily understood and hence more reliable nuclear

structure information obtained. Results for ^{9}Be, ^{12}C, ^{16}O and ^{20}Ne targets are presented. The experimental details and results are presented in Sec. II. A DWIA analysis of the data is presented in Sec. III. An important feature of this section is a series of explicit tests to the factorization approximation employed in the analysis which serve to establish the validity of the assumed reaction mechanism. As a prerequisite to a comparison of experimental and theoretical values for the alpha cluster spectroscopic factors it is important to be aware of the sensitivity of the results to the various parameters associated with the DWIA calculations. Thus, in Sec. III we also present studies of these sensitivities together with comparison of our results with theoretical predictions and the other experimental studies. Finally the implications of our results are discuseed in Sec. IV.

II. EXPERIMENT

A. General Description

A 140 MeV alpha beam from the University of Maryland sector-focused isochronous cyclotron was focused at the center of a 1.5 m diameter scattering chamber. The beam spot at the center of the target was 2mm × 2mm with an angular divergence of 5mr. Beam currents ranged from 15 nA to 100 nA depending on the detector angles.

The outgoing alpha particles were detected by two identical counter telescopes which were mounted coplanar with and on opposite sides of the beam. Each telescope consisted of a 300 μ silicon surface barrier ΔE detector followed by a 4 mm Si(Li) E detector mounted at 45° to provide an effective thickness of 5.65 mm which is sufficient to stop 140 MeV alpha particles. The solid angles subtended by the detectors were 1.35 and 1.39 msr, respectively.

For the ^{9}Be runs a self-supporting foil of 2.52 mg/cm^{2} thickness was used. For the other measurements, high purity ^{16}O, and Ethane (C_2H_6) and isotopically enriched ^{20}Ne gases were used in a 12 cm diameter gas cell. The typical pressure was about 1 atmosphere. In order to define the gas target thickness and to prevent particles scattered by the gas cell windows from entering the detector telescopes, a double slit collimator system was used in front of each telescope. The overall angular resolution provided by the slit system was 1.9° and 2.8°, respectively.

Details of the experimental setup are discussed in Ref. 35. Briefly fast timing signals from the ΔE preamplifiers provided start and stop signals for a time-to-amplitude converter in order that real and accidental coincidences could be simultaneously stored. The timing resolution was approxsmately 3ns. In addition a slow coincidence was required between the four detectors and the

TAC signal. The analogue signals from the four detectors and the TAC signal were gated by the slow coincidence and fed to analogue-to-digital converters interfaced to an IBM 360 44 computer. Dead time losses were determined using a four-fold pulser unit triggered at a rate proportional to the beam current.

All ADC data were written, event by event, on magnetic tape for off-line reanalysis. In addition a very flexible data handling code permitted on-line calibration, particle identification, random coincidence subtraction and one and two dimensional array accumulation.

On reanalysis two-dimensional spectra were constructed for the parameters F_3 vs. T_1 where T_1 is the total energy deposited in one telescope and $F_3 = T_1+T_2+T_3$. Here T_2 is the energy deposited in the second telescope and T_3 the (computed) residual nucleus recoil energy. Clearly $F_3 = T_0 - B$ where T_0 is the incident kinetic energy and B the alpha binding energy in the target. Thus we refer to distributions of the parameter F_3 as "binding energy" spectra. Each F_3 vs. T_1 spectrum was gated by the computer generated particle identification functions to correspond to alpha-alpha coincidences and random events were subtracted. The counts in each F_3 vs. T_1 spectrum were summed along the kinematic line for each final state in the residual nucleus in bins of $\Delta T_1 = 2.4$ MeV. The resulting spectra were plotted as a function of T_1 yielding the energy sharing cross section $\frac{d^3\sigma}{d\Omega_1 d\Omega_2 dT_1}$.

The errors in the calculated cross sections are predominantly statistical. An error evaluation showed the errors due to other sources such as random subtraction, solid angles, target thickness, gas pressure and temperature, current integrator, slit scattering, dead time correction and bin size measurements, could be neglected relative to the statistical errors.

B. Experimental Results

The $(\alpha, 2\alpha)$ reaction yields were measured for ^{20}Ne, ^{16}O, ^{12}C and ^{9}Be targets at 20 angle pairs with an incident energy $E_\alpha = 140$ MeV. Table I shows the data taken in the experiment, where q_{min} is the allowed minimum recoil momentum of the residual nucleus for the ground state transition. All but three of these angle pairs permit $q_{min} = 0$. At these so-called "quasi-free" angle pairs the reaction can proceed leaving the residual nucleus at rest.

The binding energy spectra for ^{20}Ne, ^{16}O, ^{12}C and $^{9}Be(\alpha, 2\alpha)$ reactions at symmetric quasi-free angles are shown in Fig. 1. Each binding energy spectrum shows a prominent isolated peak corresponding to the ground state of the residual nucleus. In the $^{20}Ne(\alpha, 2\alpha)^{16}O$ spectrum, a peak corresponding to the 6.05 and 6.13 MeV doublet of ^{16}O is also rather clear. Other states, due to poor counting

TABLE I

Target	θ_1/θ_2	q_{min}(MeV/c)	Target	θ_1/θ_2	q_{min}(MeV/c)
^{20}Ne	43.71°/-43.71°	0	^{12}C	62.21°/-23.0°	0
	49.39°/-38.0°	0			
	57.20°/-30.0°	0	^{9}Be	44.19°/-44.19°	0
	63.82°/-23.0°	0		47.39°/-41.0°	0
				50.38°/-38.0°	0
^{16}O	43.16°/-43.16°	0		54.85°/-33.5°	0
	55.97°/-30.0°	0		58.30°/-30.0°	0
	63.82°/-23.0°	10		61.25°/-27.0°	0
^{12}C	43.11°/-43.11°	0		64.65°/-23.5°	0
	49.15°/-37.0°	0		40.0°/-40.0°	69
	55.86°/-30.0°	0		36.0°/-36.0°	125

statistics, could not be identified. In the $^{16}O(\alpha, 2\alpha)^{12}C$ spectrum, the 2^+ (4.43 MeV) peak is comparable in magnitude to that of the ^{12}C(g.s.) transition. In addition, a broad peak corresponding to the 4^+ (14.0 MeV) is evident. The ground and first excited states of ^{8}Be are smeared somewhat in the binding energy spectrum. This is largely due to a slight gain shift of the detector telescopes and some nonlinearity of the F_3 functions in the F_3 vs. T_1 spectra. However, the two dimensional F_3 vs. T_1 spectrum used to calculate the cross section had a much clearer separation of the two states. For $^{9}Be(\alpha, 2\alpha)^{5}He$ reaction, no ^{5}He state other than the ground state is seen in the binding energy spectrum.

The energy sharing spectrum for the transition leaving the residual nucleus in its ground state was extracted for each target and angular setting. Three additional spectra for $^{20}Ne(\alpha, 2\alpha)^{16}O$ (6 MeV), $^{16}O(\alpha, 2\alpha)^{12}C$ (4.43 MeV), and $^{12}C(\alpha, 2\alpha)^{8}Be$ (2.9 MeV) at the symmetric quasi-free angle pair were also obtained.

The g.s. energy sharing spectra for the symmetric quasi-free angle pairs are presented in Fig. 2. There are several systematic features which characterize these spectra. Firstly, the maximum in each quasi-free angle pair spectrum comes at the minimum recoil momentum of the residual nucleus. An arrow in each spectrum indicates this point. Secondly, the structure of the spectra is characterized by a broad, smooth bump which is characteristic of the quasi-free knockout mechanism for $L=0$ transitions.[36] Spectra for non-symmetric angle pairs, two of which are shown in Fig. 3, are very similar and the full width at the half maximum (FWHM) of the spectrum for each target is essentially independent of the particular angle pair when plotted against the momentum of the recoil nucleus rather than outgoing particle energy. The approximate

widths are: 70 MeV/c for $^{20}Ne(\alpha, 2\alpha)^{16}O$(g.s.), 90 MeV/c for $^{16}O(\alpha, 2\alpha)^{12}C$(g.s.), 90 MeV/c for $^{12}C(\alpha, 2\alpha)^{8}Be$(g.s.), and 70 MeV/c for $^{9}Be(\alpha, 2\alpha)^{5}He$(g.s.).

When one of the detector angles is less than 30° strong contributions from mechanisms other than knockout are evident. For example in Fig. 3(a) for $^{20}Ne(\alpha, 2\alpha)$ at $\theta_1/\theta_2 = 63.82°/-23°$, a large yield is observed on the lower energy side of the quasi-free distribution. There is no well defined peak, although in Fig. 3(b) for the ^{16}O target there is evidence of sequential alpha decay following inelastic scattering to levels in the target nucleus centered around 20 MeV excitation. In this excitation region many alpha decay channels are open and cannot be resolved in the experiment.

III. ANALYSIS

A. DWIA Calculations

The theoretical analysis of the data was performed using the distorted wave impulse approximation code written by Chant and Roos.[19] The differential cross section for the reaction $A(\alpha, 2\alpha)B$ for the knockout of an alpha particle with total angular momentum J and orbital angular momentum L is given by

$$\frac{d^3\sigma^{LJ}}{d\Omega_1 d\Omega_2 dT_1} = KF \times S_{LJ} \times \frac{d\sigma}{d\Omega}\bigg|_{\alpha-\alpha} \times \sum_{\Lambda} \left| T_{BA}^{\alpha L\Lambda} \right|^2 \qquad (1)$$

where KF is a kinematic factor, $\frac{d\sigma}{d\Omega}\Big|_{\alpha-\alpha}$ is the two body $\alpha-\alpha$ cross section, and S_{LJ} is the cluster spectroscopic factor for specific L and J. The quantity

$$T_{BA}^{\alpha L\Lambda} = \frac{1}{(2L+1)^{1/2}} \int \chi_2^{(-)*}(\vec{r})\chi_1^{(-)*}(\vec{r})\chi_0^{(+)}(\gamma\vec{r})\phi_{L\Lambda}^{\alpha}(\vec{r})d\vec{r} \qquad (2)$$

where the $\chi_i^{(*)}$ are distorted waves, $\gamma = B/A$ and $\phi_{L\Lambda}^{\alpha}(\vec{r})$ is the bound state wave function of the alpha cluster in the target nucleus. We refer to this quantity as the "distorted momentum distribution", since in the limit of no distortion $T_{BA}^{\alpha L\Lambda}$ reduces to $\phi_{L\Lambda}^{\alpha}$ in a momentum representation at the point $\vec{q} = -\vec{p}_B$. In practice we shall see that distortion effects are quite severe for the present data.

It is important to note that Eq. (1) employs a factorized impulse approximation in which the two-body cross section enters as a multiplicative factor rather than as a t-operator within the integrand of Eq. (2). Thus the integration over what is properly a fully off-energy-shell matrix element is replaced by the half off-shell value at the asymptotic kinematics. Furthermore, in practice we make the additional approximation of replacing $\frac{d\sigma}{d\Omega}\Big|_{\alpha-\alpha}$ by the corresponding quantity determined from a measured (on-shell) two body cross section. In analyzing (p, pα) data at 100 MeV, Roos, et al.,[17] found little error arose

from the neglect of half off-shell effects although there was some breakdown in the factorization approximation. This problem is investigated for the present data in Sec. III. B.

B. Factorization Test

In order to test our description of the assumed reaction mechanism we first divided the measured experimental cross sections at $P_B=0$ by the kinematic factor KF. According to Eq. (1) we have

$$\frac{d^3\sigma}{d\Omega_1 d\Omega_2 dT_1}/KF = \{S_\alpha |\phi(-\vec{p}_B)|^2\} \left.\frac{d\sigma}{d\Omega}\right|_{\alpha-\alpha} \qquad (3)$$

In principle S_α is constant. In addition, explicit DWIA calculations of the quantity $|\phi(-\vec{p}_B)|^2$ varied by less than $\pm 10\%$ at the $p_B=0$ point over the entire angular range studied for all four targets. Thus, in the factorized DWIA, the ratio constructed in Eq. (3) should be proportional to the two-body cross section $d\sigma/d\Omega|_{\alpha-\alpha}$ to within this accuracy. Results are shown in Fig. 4 for all four targets studied plotted as a function of the two-body c.m. scattering angle. Also shown are measured free $\alpha-\alpha$ cross sections at 120 and 140 MeV lab energy.[37, 38] As indicated in Fig. 4, since the struck alpha particle is bound, the effective scattering energy (in the final state) is less than 140 MeV. It is found that, for all four targets, the ratios $(d^3\sigma/d\Omega_1 d\Omega_2 dT_1)/KF$ can be normalized to lie between the free cross sections at 120 and 140 MeV and that the angular variation of the data points follows the free cross sections very closely over almost three orders of magnitude.

The result of the preceding series of factorization tests with the quasi-free angular distribution data is encouraging. However, there is no free $\alpha-\alpha$ scattering data available at energies between 120 and 140 MeV and the uncertainties in the extracted half-shell cross sections are quite large. In order to choose a suitable energy for the free $\alpha-\alpha$ cross section which is used to replace the half-shell cross section, three possible prescriptions were examined. On-shell $\alpha-\alpha$ cross sections were obtained by interpolation at energies: a) $E=T_f$, b) $E=1/2(T_f+T_i)$, and c) $E=T_i$. Using these cross sections the ratio of the experimental three-body cross section at $p_B=0$ and the product $KF \cdot \frac{d\sigma}{d\Omega}$ is compared with the calculated $|\phi(0)|^2$ at each angle for each of the (α, 2α) reactions under investigation. Differences between the three prescriptions are not large. However, a careful comparison of the extracted $|\phi(0)|^2$ obtained from the on-shell cross section at the three different energies with the calculated $|\phi(0)|^2$ shows that the T_f prescription gives slightly better consistency between the experimental and calculated results. This result is in agreement with other

investigations and with the result that the final energy prescription arises as the first term of a multiple scattering expansion based on the Fadeev equations.[39] It thus is used throughout the ensuing analyses.

These tests have been carried out with different sets of distorting and bound state parameters. The factorization characteristics are found to be insensitive to the distorting and bound state parameters.

C. Comparison of DWIA Calculations with Experiment

In order to carry out the DWIA calculations it is necessary to evaluate both the distorted wave functions and the bound cluster "wave function" appearing in the integrand of Eq. (2). The latter quantity, $\phi^{a}_{LA}(\vec{r})$, more properly represents the result of projecting the target nucleus wave function onto the product of the residual nucleus wave function and the internal wave function of an alpha particle in its ground state. Following common practice in both knockout and transfer reaction analyses we have replaced $\phi^{a}_{LA}(r)$ in our calculations by an eigenfunction of a Woods-Saxon potential with an energy eigenvalue equal to the alpha particle separation energy. The principle quantum number N is chosen on the basis of conservation of oscillator shell model quanta. Thus where the

$$2(N-1)+L=\sum_{i=1}^{4}2(n_i-1)+\ell_i \qquad (4)$$

n_i and ℓ_i are individual nucleon principal quantum numbers and orbital angular momenta respectively. Thus, assuming $(1s^4)$ $(1p^n)$ configurations for $A \leq 16$, $L=0(2)$ transitions must have $N=3(2)$. For ^{20}Ne, if we assume an initial $(1s^4)$ $(1p^{12})$ $(2s1d)^4$ configuration, $L=0(2)$ transitions have $N=5(4)$.

Initially calculations were carried out using bound state potential parameters yielding a potential consistent with the known r.m.s. radii of the target nuclei. For the ^{16}O target the parameters used are listed in Table II. The values ($R=1.22\times 12^{1/3}$ fm, $a=0.76$ fm) are quite similar to the results of a folding procedure which was used successfully in an earlier analysis[17] of the (p, pα) reaction at 100 MeV. Also listed in Table II are potentials used for the incident and emitted alpha particles. Our notation is such that, for example, *C139* is a potential obtained by fitting $\alpha+$ ^{12}C elastic scattering at a laboratory energy of 139 MeV. Notice that our use of $\alpha+$ ^{12}C potential parameters is consistent with the formal result[40] that the projectile-ejectile interaction is, in principle, included to all orders via the two-body t-matrix.

Using the parameters C139/C139/C139 for the incident/emitted/emitted alpha particles for ^{16}O($(\alpha, 2\alpha)^{12}$C(g.s.) at 140 MeV the shapes of the experimental distributions at three different angle pairs were reasonably well reproduced.

TABLE II. Optical Potential Parameters[a] for $^{16}O(\alpha, 2\alpha)^{12}C$(g.s.) Test

Set Series	V_0[b]	r_0	a	r_c	W_0	r_0'	a′	Ref.
B.S.[c]	72.5	1.22	0.76	1.24				
A	108.1	1.22	0.76	1.26	16.9	1.85	0.47	52
B	114.0	1.22	0.80	1.26	13.8	1.91	0.50	52
C	151.9	1.24	0.665	1.4	28.05	1.24	0.64	53
D	216.8	1.3	0.58	1.4	38.05	1.5	0.32	53

a) The optical potential is defined to be
$V_{opt} = -V_0 f(r, r_0, a) - i\, w_0 f(r, r_0', a') + V_c$
where $f(r, r_0, a) = [1+\exp\{(r-r_0A^{1/3})/a\}]^{-1}$; A is the target mass;
V_c is the Coulomb potential of a uniform charged sphere of radius $r_cA^{1/3}$.

b) V_0 and W_0 in MeV: r_0, r_0', a, a′, and r_c in fm.

c) Bound state.

Typical results are shown in Fig. 2. Somewhat surprisingly, however, the extracted spectroscopic factor S_α was approximately 25, more than 100 times the theoretical value of 0.23 predicted in the Kurath shell model calculations.[22] This result is similar to that obtained by Chant and Roos[19] in their DWIA analysis of the 90 MeV (α, 2α) data. Noting that, at $p_B=0$, the emitted alpha particle kinetic energies are each about 66 MeV the sets C139/C104/C104, C104/C104/C104, C139/C56/C56 were tried. However, these calculations produced a variation in the spectroscopic factor of less than a factor of three. Finally, to allow for the energy variation of the emitted alphas in the exit channel (between 40 and 90 MeV) calculations were carried out using the various combinations of potentials listed above with real potential strengths readjusted to yield volume integrals J/4A corrected for an energy dependence of $-1.3\ E_{cm}$ where E_{cm} is the c.m. energy. This is consistent with the observed variation of the real volume integral in the range $30 < E < 160$ MeV and $4 < A < 60$. In all cases the extracted spectroscopic factors were at least 30 times larger than the theoretical value.

A similar study[41] by Jain and Sarma of the sensitivity of the spectroscopic factor extracted from the 90 MeV $^{16}O(\alpha, 2\alpha)^{12}C$ data[29, 30] to the choice of optical parameters has been reported. These authors correctly point out that the optical parameters selected for the original calculations of Chant and Roos[19] are not in good agreement with appropriate elastic scattering data (being in fact obtained from fits to slightly heavier targets). By selecting optical parameters from the work of Pehl,[42] Jain and Sarma obtain improved fits to the relevant elastic scattering data and obtained a spectroscopic factor only about five times the theoretical value. We have carried out additional calculations which suggest that this reduction in S_α is a consequence not of the detailed improvements in

the elastic scattering fits but rather of the fact that, in his early wore, Pehl reported the shallowest potential from among the various discrete ambiguities. Specifically the potential of Ref. 42 has V=33 MeV and J/4A roughly one fourth of the value derived from the energy dependence described above. In the light of more recent work[43] we argue that this choice is unphysical and does not satisfactorily remove the large discrepancy in S_α which we have noted.

Similar problems are encountered for the other targets. Initial calculations reproduced the shapes of the $(\alpha, 2\alpha)$ distributions but gave spectroscopic factors of 9 for ^{9}Be, 11 for ^{12}C and 27 for ^{20}Ne which are much larger than the theoretical values[22, 23] of 0.57, 0.55 and 0.21 respectively. As found for ^{16}O reasonable variations in distorting parameters failed to remove the disagreement between theory and experiment.

Next a test of the sensitivity of the calculations to the bound state parameters was carried out. The results were found to be relatively insensitive to the diffuseness parameter "a" and to the Coulomb radius r_c. Variation of the bound state radius parameter r_o produced no change in the shape of the energy sharing distribution, but resulted in significant changes in the predicted magnitude. To illustrate this effect we have plotted in Fig. 5 the distorted momentum distribution at $p_B=0, |\phi(0)|^2$, as a function of the bound state radius parameter r_o for $^{16}O(\alpha, 2\alpha)^{12}C$(g.s.) at $\theta_1=-\theta_2=43.16°$. In these calculations the distorting parameter set was C139/C139/C139. For the bound state, the parameters a and r_c were fixed at 0.76 fm and 1.3 fm respectively while the potential strength was readjusted at each value of r_o to yield a solution with the empirical alpha separation energy. It is seen that the magnitude of $|\phi(0)|^2$ is increased by a factor of approximately 120 on changing r_o from 1.2 fm to 2.52 fm which thus serves to reduce the extracted spectroscopic factor to approximately 0.23, the anticipated value.

It should be noted that the value $r_o=2.52$ fm for $^{16}O(\alpha, 2\alpha)^{12}C$(g.s.) does not lead to noticeable deterioration in the fit to the shape of the energy sharing distribution. However, the associated 3S wave function has an r.m.s. radius of 4.37 fm while the r.m.s. radius of the potential is 3.56 fm. Both values are well in excess of the empirical r.m.s. radius of 2.65 fm for ^{16}O. Although the value $r_o=2.52$ fm may seem excessive it is important to note that comparable values have been used in analyses of alpha-transfer reactions in order to reproduce the experimental absolute cross sections (that is to obtain absolute spectroscopic factors in agreement with shell model theories). For example, the authors of Refs. 11 and 12 used bound state well radii of $R=2.0A_c^{1/3}$ fm and $R=1.2(A_c^{1/3}+4^{1/3})$ fm respecively, where A_c is the mass number of the core. These values are equivalent to $r_o=2.0$ and 2.05 fm for ^{16}O in our parameterization.

Our decision to characterize the enhanced (α, 2α) cross sections by an increased value of r_0 thus has the merit of consistency with transfer reaction analyses and is clearly preferable to the introduction of unphysical optical potentials in *both* knockout and transfer analyses. Nevertheless, it is a somewhat arbitrary device. We shall return to the question of the implications of this choice in Sec. III. F. For the present we choose $r_0 = 2.52$ fm for all targets studied in order to investigate the resultant fits to the energy sharing distributions as well as the deduced spectroscopic factors.

Calculated energy sharing spectra for all four ground state transitions at the symmetric quasi-free angle pair are shown in Fig. 2. The optical parameters used are listed in Table III. It should be noted that, with the exception of ^{9}Be, these are pure L=0 transitions. For ^{9}Be, as we have discussed previously,[17] roughly equal admixtures of 3S and 2D transitions are expected. These terms add incoherently and the curve shown in Fig. 2 is the summed result. As found for (p, pα) at 100 MeV the 2D admixture has little effect.

TABLE III. Optical Potential Parameters[a] for Final Calculations

Reaction	System	V_0[b]	r_0	a	r_c	w_0	r_0'	a′	r_{rms}	J/4A	Ref.
^{9}Be(α, 2α) ^{5}He	α+^{9}Be	72.63	1.36	0.765	1.3	23.8	1.36	0.765		329	54
	α+^{5}He	72.63	1.36	0.765	1.3	23.8	1.36	0.765		396	54
	B.S.[c]	36.69	2.52	0.765	1.3				4.74	806	
^{12}C(α, 2α) ^{8}Be	α+^{12}C	108.1	1.22	0.76	1.26	16.9	1.85	0.47		356	52
	α+^{8}Be	108.1	1.22	0.76	1.26	16.9	1.75	0.47		402	52
	B.S.	35.80	2.52	0.655	1.26				4.03	700	
		38.51[d]									
^{16}O(α, 2α) ^{12}C	α+^{16}O	108.1	1.22	0.76	1.26	16.9	1.85	0.47		330	52
	α+^{12}C	108.1	1.22	0.76	1.26	16.9	1.85	0.47		356	52
	B.S.	30.50	2.52	0.7825	1.26				4.37	604	
		35.13[d]									
^{20}Ne(α, 2α) ^{16}O	α+^{20}Ne	110.6	1.22	0.82	1.3	17.9	1.77	0.63		338	55
	α+^{16}O	110.6	1.22	0.82	1.3	17.9	1.77	0.63		358	55
	B.S.	46.34	2.52	0.78	1.3				5.44	892	

a) The optical potential is defined to be $V_{opt} = -V_0 f(r, r_0, a) - iW_0 f(r, r_0', a') + V_c$ where $f(r, r_c, a) = [1 + \exp\{(r - r_0 A^{1/3})/a\}]^{-1}$; A is the target mass; V_c is the Coulomb potential of a uniform sphere of radius $r_0 A^{1/3}$.

b) V_0 and W_0 in MeV; r_0, r_0', a, a′, r_c, and r_{rms} in fm; J/4A in MeV-fm^3.

c) Bound state

d) When the core is left in its first excited state.

In general agreement between theory and experiment in Fig. 2 is good. Comparable agreement is also apparent in Fig. 3 in which results are shown for the ground state transitions at asymmetric angle paris.

D. Spectroscopic Factors: Ground State Transitions

The ground state spectroscopic factors extracted from our 140 MeV data are shown in Table IV together with theoretical values obtained from structure calculations employing shell model[22] and SU_3 model[23] approaches. All data sets have been included with the exception of the $\pm 36°$ angle pair for ^{9}Be which was poorly reproduced in the DWIA calculations. This difficulty can be attributed to the fact that this angle pair involves much higher momentum components in the alpha wave function than any other angle pair chosen. Specifically, the minimum value of p_B is 125 MeV/c which is to be compared with a distorted momentum distribution width of ± 70 MeV/c for ^{9}Be. As a result the knockout cross section is suppressed, and accuracy in treating the bound state and distorted waves becomes more crucial. Also competing reaction mechanisms may play a more significant role.

From Table IV it is seen that the extracted spectroscopic factors for each target vary between $\pm 20\%$ and $\pm 30\%$ over the angular range studied. The uncertainties attached to the average spectroscopic factors quoted are merely standard deviations of the angular variations. Clearly many sources of relative and absolute errors have been ignored.

Agreement between theory and experiment is generally good. Clearly our choice of $r_o = 2.52$ fm guarantees this result for ^{16}O. However, it is seen that this choice, made arbitrarily for the other targets, leads to an excellent description of the *relative* strengths for the four targets.

As a further test of our chosen bound state geometry, calculations were carried out for $(\alpha, 2\alpha)$ data obtained by other groups at lower energies. Results for the four targets under discussion are compared with our 140 MeV results in Table V. For ^{9}Be$(\alpha, 2\alpha)^5$He(g.s.) data at $E_\alpha = 55$, 49.2, and 42.8 MeV[26, 27] have been analyzed. It is surprising that at these low energies, where the quasi-free knockout reaction mechanism may be less dominant and the free $\alpha - \alpha$ cross sections oscillate, we obtain an experimental spectroscopic factor consistent with that from 140 MeV data to within about 50%. The results of the same analysis of ^{12}C data at $E_\alpha = 90$ MeV[29, 30] and ^{16}O data at 90 MeV[29, 30] 52.5 and 46 MeV[26, 27] and ^{20}Ne data at 78 MeV[28] are also shown in Table V. The results from the ^{12}C and ^{16}O data at 90 MeV are consistent with the results from our own data to within a factor of 3. For the ^{16}O data at around 50 MeV the

TABLE IV. Spectroscopic Factrs for Angle Pairs (θ_1/θ_2) Extracted by Means of the DWIA Analysis. The Average $< S_{\alpha}^{exp} >$ is a Statistical Average of all Angle Pairs.

Reaction	θ_1/θ_2	S_{α}^{exp}	$< S_{\alpha}^{exp} >$	S_{α}^{theory}	Ref.
^{9}Be(α, 2α)^{5} He(g. s.)	44.19°/-44.19°	0.656			
	47.39°/-41.0°	0.930			
	50.38°/-38.0°	0.574		0.57	22
	54.85°/-33.5°	0.635			
	58.39°/-30.0°	0.579	0.633±0.120		
	61.25°/-27.0°	0.622			
	64.65°/-23.5°	0.540			
	40.0°/40.0°	0.527			
^{12}C(α, 2α)^{8} Be(g. s.)	43.11°/-43.11°	0.641		0.674	47
	49.15°/-37.0°	0.682		0.55	22
	55.86°/-30.0°	0.421	0.558±0.107	0.285	23
	62.21°/-23.0°	0.487		0.759	56
				0.675	56
^{16}O(α, 2α)^{12} C(g. s.)	43.16°/-43.16°	0.209		0.295	47
	55.97°/-30.0°	0.304		0.23	22
	63.82°/-23.0°	0.222	0.244±0.046	0.296	23
				0.333	56
				0.296	56
^{20}Ne(α, 2α)^{16} O(g. s.)	43.71°/-43.71°	0.157			
	49.39°/-38.0°	0.235		0.21	23
	57.20°/-30.0°	0.220	0.202±0.029	0.182	47
	63.82°/-23.0°	0.196			
^{12}C(α, 2α)^{8} Be(2.9 MeV)	43.16°/-43.16°	1.74	1.74	0.72	22
				0.592	23
^{16}O(α, 2α)^{12} C(14.43 MeV)	43.11°/-43.11°	1.26	1.26	1.31	22
				1.48	23

agreement is within a factor of 4. For ^{20}Ne at 78 MeV agreement with our 140 MeV result is within the experimental error. Considering the original disagreement of over a factor of 100, these differences are not large.

The optical model parameters used for the lower energy calculations are the same as those listed in Table III. We have not investigated the sensitivity of the lower energy results to the choice of distorting potentials. Clearly there are large uncertainties and a more consistent description might be possible. An important ingredient of any improved analysis would be a more systematic treatment of the energy dependence of the alpha optical potential.

TABLE V. Spectroscopic Factors S_α^{exp} Extracted by Means of the DWIA Analysis at Symmetric Quasi-free Angle Pairs

Reactions	Eα(MeV)	S_α^{exp}	$< S_\alpha^{exp} >$ Eα=140 MeV
$^{9}Be(\alpha, 2\alpha)^{5}$ He(g. s.)	55	0.820 ±0.082	
	49.2	0.655 ±0.068	0.633
	42.8	0.936 ±0.156	
$^{12}C(\alpha, 2\alpha)^{8}$ Be(g. s.)	90	0.196 ±0.014	0.558
$^{16}O(\alpha, 2\alpha)^{12}$ C(g.s.)	90	0.0942±0.011	
	52.5	0.982 ±0.225	0.244
	46	0.687 ±0.125	
$^{20}Ne(\alpha, 2\alpha)^{16}$ O(g.s.)	78.6	0.149 ±0.017	0.202

E. Transitions to the First Excited States of ^{8}Be and ^{12}C

The overlaps of $^{12}C \rightarrow \alpha + {}^{8}Be$ (2.9 MeV, 2^+) and $^{16}O \rightarrow \alpha + {}^{12}C$ (4.43 MeV, 2^+) have also been investigated with the quasi-free knockout reactions $^{12}C(\alpha, 2\alpha)^{8}Be$(2.9 MeV) and $^{16}O(\alpha, 2\alpha)^{12}C$ (4.43 MeV) at angles 43.11°/−43.11° and 43.16°/−43.16° respectively. The measured energy sharing spectra are shown in Fig. 6. The distorting parameters and bound state radius and diffuseness parameters of the DWIA analysis are the same as those for the ground state transitions. Both states have spin and parity 2^+. The principal quantum number N=2 and orbital angular momentum quantum number L=2 are used for the analyses in both cases. The calculated energy sharing distributions can roughly reproduce the experimental data in the region where the two outgoing alpha particle energies are not very different. However, the overall fits are disappointing.

Alpha spectroscopic factors were extracted by comparing the data with the DWIA calculations near the minimum recoil momentum regions. The results are compared with theoretical estimates obtained using a 1p shell model[22] and by considering the nuclei as alpha chains,[23] in Table IV. The consistency between the experimental and theoretical values for the $^{16}O \rightarrow \alpha + {}^{12}C$ (4.43 MeV) transition is remarkable while for the $^{12}C \rightarrow \alpha + {}^{8}Be$ (2.9 MeV) transition agreement is within a factor of 3. A difficulty in this case is the possibility of L=0 contributions to the transition which are permitted owing to the unbound nature of the final state and which may be present in (p, pα) data for the same transition.[17] Clearly data with improved statistics coupled with further reaction mechanism studies for the excited states are needed.

F. The Alpha Cluster Bound State Wave Function

In the preceding sections we have seen that DWIA calculations for the

(α, 2α) reaction at 140 MeV are relatively insensitive to reasonable changes in the distorting potentials but are strongly dependent on the choice of bound state wave function $\phi^{a}_{LA}(\vec{r})$. Specifically, if we accept the theoretical absolute spectroscopic factors quoted as being correct to better than an order of magnitude, calculations using a bound state radius parameter $r_o \sim 1.22$ fm seriously underestimate the observed absolute cross section. Such a choice for r_o is "reasonable" in that the resultant wave function and potential have r.m.s. radii similar to the empirical target r.m.s. radii. In fact, in order to reproduce the observed cross sections the apparently excessive value of $r_o = 2.52$ fm is needed. This choice leads to reasonable predicted absolute cross sections for all four targets at 140 MeV without deterioration in the fits to the shapes of the distributions. In addition, consistent absolute cross sections are obtained at lower energies (at least to within a factor of 2-3).

This behavior is in marked contrast to studies[17] of (p, pα) and (p, d ^{3}He) reactions at 100 MeV on ^{9}Be and ^{12}C and in more recent studies[44, 45] at the same energy on ^{16}O and ^{20}Ne. These authors used values of $r_o \sim 1.1-1.3$ fm which is close to a folding model geometry and thus quite different from our value of $r_o = 2.52$ fm. However, as pointed out elsewhere[46] the predicted distorted momentum distributions for these (p, pα) transitions are not very sensitive to the radius parameter of the alpha-core bound state. Thus in Ref. 46 we noted that S_α for ^{16}O(p, pα)^{12}C(g.s.) at 100 MeV changes by less than a factor of 2 when r_o is changed from 1.2 fm to 2.3 fm.

Some of these features can be understood in terms of the radial localization of these reactions. By integrating $T^{\alpha LA}_{BA}$ of Eq. (2), from r to infinity one obtains a calculated differential cross section $\sigma(r)$, which is a measure of the contribution to the reaction in the range from r to infinity. The differende $\Delta\sigma = \sigma(r) - \sigma(r+\Delta r)$ is thus a measure of the contribution to the reaction in the range from r to $r+\Delta r$. From a histogram of these differences against r one can investigate the reaction contribution from different values of r. Fig. 7 shows the histogram for ^{16}O(α, 2α)^{12}C(g.s.) at $\theta_1/\theta_2 = 43.16°/-43.16°$, $p_B = 0$, and $E_\alpha = 140$ MeV. For the case of bound state radius parameter $r_o = 1.22$ fm, one observes a dramatic interference near the region $r \sim r_o A_c^{1/3}$. It is this calculation which seriously underestimates the experimental absolute cross section. Also shown in Fig. 7 is the corresponding histogram for $r_o = 2.52$ fm, which leads to agreement with experiment. It is seen that the reaction is now localized to a region near 6.5 fm and that the interference region has been eliminated. At the lower end of Fig. 7 is the corresponding diagram for ^{16}O(p, pα)^{12}C(g.s.) at 100 MeV using $r_o = 1.3$ fm and $a = 0.65$ fm. These parameters lead to calculations in good agreement with experiment.[44] Here we see that the reaction is no longer

localized in the extreme tail of the bound state wave function and it is this feature which accounts for the more modest sensitivity to r_o.

As mentioned briefly in Sec. III. C. our choice of $r_o = 2.52$ fm is not inconsistent with the values used in alpha transfer reactions. Firstly the $(\alpha, {}^8Be)$ reaction study of Ref. 11 obtained absolute alpha spectroscopic factors for eight 1p shell nuclei using an alpha core bound state radius parameter $r_o = 2.0$ fm. Secondly, the analysis of the $^{12}C(^{16}O, {}^{20}Ne)^8Be$ reaction data[12] used an $\alpha - {}^{16}O$ bound state radius $R = 1.2(16^{1/3} + 4^{1/3})$ fm, which corresponds to $r_o = 1.96$ fm in our notation, to reproduce the experimental data. Thirdly, in analyzing the $^{16}O(d, {}^6Li)^{12}C$ reaction Nagel and Koshel[14] were obliged to use a bound state radius $R = 1.27(12^{1/3} + 4^{1/3})$ fm (which corresponds to $r_o = 2.15$ fm in our notation) in order to reproduce the magnitude of the experimental cross section. These authors pointed out that the magnitude of the calculated cross section increased by a factor of 18 when the bound state radius changed from $1.25 \times 12^{1/3}$ fm to the above value. This is to be compared with a factor of about 24 for a corresponding change in our $^{16}O(\alpha, 2\alpha)^{12}C$(g.s.) analysis. Finally, two groups[47, 48] have investigated the $({}^3He, {}^7Be)$ reaction on 1p and 2s1d shell nucle i and extracted relative alpha-spectroscopic factors. The authors of Ref. 47 used $r_o = 1.2$ fm for $^7Be \rightarrow {}^3He + \alpha$ while Audi et al.,[48] used a bound state radius $R = 1.25\ (A_c^{1/3} + 4^{1/3})$ fm. The results of Audi et al., are more consistent with the spectroscopic factors obtained in SU_3.

We have seen that while reasonable bound state geometry parameters work well for (p, pα), most alpha transfer analyses and the $(\alpha, 2\alpha)$ reaction at 140 MeV incident energy or less require bound state wave functions enhanced in the nuclear surface by up to an order of magnitude. The device we have selected to achieve this end, namely an increase in r_o, probably has no intrinsic significance. For example, as an alternative, we could have arbitrarily reduced the calculated cluster binding energy.

Yet another approach is that suggested by B. K. Jain[49] who was able to reproduce both the shapes and absolute magnitudes of the 90 MeV data of Ref. 30 using a strong absorption model with a radius parameter $R = 1.15(A^{1/3} + 4^{1/3})$ fm where A is the target mass number. Unfortunately the success of the strong absorption model calculations do not greatly clarify the situation and more physical explanations for the apparent enhancement of $\phi^{\alpha}_{L\Lambda}(r)$ are needed.

IV. DISCUSSION AND CONCLUSIONS

The present $(\alpha, 2\alpha)$ data suggest the dominance of the quasi-free knockout mechanism. The energy sharing data are well described by the DWIA calculations. Perhaps more importantly the angular dependence of the three-body cross

section is in excellent agreement with that obtained in free $\alpha+\alpha$ scattering. However, in spite of consistency with alpha-transfer analyses, the necessity of using bound state radii yielding rms radii sigificantly in excess of those expected is disturbing. Two possible explanations are suggested.

First one might conclude that surface clustering exists in excess of that predicted by the simple shell model calculations considered so far. To examine this question we have considered the treatment of the ^{16}O ground state by Brown and Green[50] who include 2p-2h and 4p-4h admixtures. We expect an increased yield over our 0p-0h calculation, since these components lead to 4S and 5S bound state wave functions, respectively. Using the amplitudes of Brown and Green we obtain an enhancement in the DWIA cross section of only a factor of 3.5. In fact, any combination of the various components is insufficient to explain the present data using a bound state radius near $r_o \simeq 1.2$ fm.

Thus more pronounced correlation effects than included in the calculations of Ref. 50 seem to be implied by the present data. However this result is not at variance with the general success of structure calculations such as Ref. 50. Referring to Fig. 7 we see that nuclear radii of 6 to 7 fm appear to be responsible for the (α, 2α) yield. In this region for the targets studied, nuclear densities are well below 1% of central density and it is only here that alpha clustering of order 100 times shell model estimates are implied by the data. In this regard it is of interest to compare the present results with charge distributions obtained in model independent analyses of electron scattering data. Using the bound alpha cluster wave function obtained with $r_o = 2.52$ fm we can estimate the charge densities at $r = 6-7$ fm implied by the (α, 2α) data. These are clearly crude estimates. However, it is interesting to note that the results are comparable to (or even exceed) values obtained from electron scattering. For example, for ^{12}C at $r = 7$ fm, Sick[51] obtained $\rho(r)/\rho(o) \sim 2.5 \times 10^{-4}$ from analysis of low momentum transfer electron scattering data whereas our ^{12}C(α, 2α)^{8}Be results is $\rho(r)/\rho(o) \sim 3.5 \times 10^{-4}$. Thus the ($\alpha$, 2α) data seems to imply that most of the nuclear matter at these very low densities has coalesced into alpha clusters.

As an alternative explanation of the present results we can consider alpha clustering in the surface region *induced* by the projectile. This would correspond to inelastic scattering to states with large alpha parentage followed by knockout. This is an appealing possibility since there exist (at least in ^{16}O) states near the alpha threshold[46] strongly excited in inelastic scattering. Thus, the second step would consist of knocking out an alpha particle weakly bound to the residual nucleus (and therefore having a large asymptotic tail). Unfortunately, no calculations for such processes exist at present. It is worth noting that not

only is it necessary to fit the energy sharing distribution, both in shape and magnitude but also such calculations must reproduce the angular dependence of the $(\alpha, 2\alpha)$ cross section. As we have seen this is in excellent agreement with free $\alpha+\alpha$ scattering and thus seems to imply a one-step process. This feature of our data may well prove decisive since one might speculate that dominance of two-step processes would lead to some broadening of the angular distribution. Lastly, similar levels must exist in all four nuclei studied despite their rather different nuclear structure, since all show the same basic effect. Notice also that such calculations must reproduce the alpha-transfer data, since similar bound state geometries are needed in those analyses.

We are indebted to the operators and staff of the University of Maryland Cyclotron for their assistance in obtaining stable and reproducible beams. Calculations were carried out using the facilities of the University of Maryland Computer Science Center. Provision of time is gratefully acknowledged. This research was supported in part by the National Science Foundation.

REFERENCES

1. O. Chamberlain and E. Segré, Phys. Rev. **87**, 81 (1952).
2. J. M. Wilcox and B. J. Moyer, Phys. Rev. **99**, 875 (1955).
3. H. Tyrén, P. Hillman, and Th. A. J. Maris, Nuovo Cimento **6**, 1507 (1957); Nucl. Phys. **7**, 1 & 10 (1958); Phys. Rev. Lett. **5**, 107 (1960).
4. M. Riou, Rev. Mod. Phys. **37**, 375 (1965).
5. I. E. McCarthy, Rev. Mod. Phys. **37**, 388 (1965).
6. G. Jacob and Th. A. J. Maris, Rev. Mod. Phys. **38**, 121 (1966); Rev. Mod. Phys. **45**, 6 (1973).
7. J. D. Cossairt, *et al.*, Nucl. Phys. **A261**, 373 (1976).
8. D. J. Pisano and P. D. Parker, Phys. Rev. C **14**, 375 (1976).
9. M. E. Cobern, D. J. Pisano, and P. D. Parker, Phys. Rev. C **14**, 491 (1976).
10. N. Anantaraman, *et al.*, Phys. Rev. Lett. **35**, 1131 (1975).
11. G. J. Wozniak, D. P. Stahel, J. Cerney, and N. A. Jelley, Phys. Rev. C **14**, 815 (1976).
12. H. Yoshida, Phys. Lett. **47B**, 411 (1973).
13. K. Bethge, Ann. Rev. Nucl. Sci., **20**, 255 (1970).
14. P. Nagel and R. D. Koshel, Phys. Rev. C **14**, 1667 (1976).
15. A. N. James and H. G. Pugh, Nuci. Phys. **42**, 441 (1963).
16. B. Gottschalk and S. L. Kannenberg, Phys. Rev. C **2**, 24 (1970).
17. P. G. Roos, *et al.*, Phys. Rev. C. **15**, 69 (1977).
18. A. A. Cowley, *et al.*, Phys. Rev. C **15**, 1650 (1977).
20. N. S. Chant and P. G. Roos, in *Proceedings of the Second International conference on Olustering Phenomena in Nuclei, College Park, 1575*, edited by D. A. Goldberg, J. B. Marion, and S. J. Wallace, (ERDA Technical Information Center, Oak Ridge, Tennessee).

21. P. G. Roos and N. S. Chant, in *Proceeding of the Second International Conference on Clustering Phenomena in Nuclei, College Park, 1975,* edited by D. A. Goldberg, J. B. Marion, and S. J. Wallace, (ERDA Technical Information Center, Oak Ridge, Tennessee).
22. D. Kurath, Phys. Rev. C **7**, 1390 (1973).
23. M. Ichimura, A. Arima, E. C. Halbert, and T. Terasawa, Nucl. Phys. **A204** 225 (1973).
24. J. W. Watson, *et al.*, Nucl. Phys. **A172**, 513 (1971).
25. M. Jain, P. G. Roos, H. G. Pugh, and H. D. Holmgren, Nucl. Phys. **A153**, 49 (1970); H. G. Pugh, *et al.*, Phys. Rev. Lett. **22**, 408 (1969).
26. A. Guichard, *et al.*, Phys. Rev. C **4**, 700 (1971).
27. P. Gaillard, *et al.*, Phys. Rev. Lett. **25**, 593 (1970).
28. M. B. Epstein, D. J. Margaziotis, N. S. P. King, and T. A. Cahill, Phys. Rev. C **9**, 581 (1974).
29. J. D. Sherman, Ph. D. thesis, University of California, Berkeley, 1973 (LBL.1690).
30. J. D. Sherman, D. L. Hendrie, and M. S. Zisman, Phys. Rev. C **13** (1976).
31. O. Chirapatpimol, *et al.*, Nucl. Phys. **A264**, 379 (1976).
32. I. E. McCarthy and D. L. Pursey, Phys. Rev. **122**, 578 (1961).
33. A. W. Parker, J. S. Allen, R. L. Yerke, and V. G. Scotland, Phys. Rev. **174**, 1093 (1968).
34. M. Epstein, *et al.*, Phys. **178** 169g).
35. C. W. Wang, Ph.D. thesis, University of Maryland, 1978 (unpublished).
36. H. D. Holmgren, Int. Conf. on Clustering Phenomena in Nuclei, Bochum, 17 (1969).
37. A. Nadasen, *et al.*, Phys. Rev. C **18**, 2792 (1978); P. Frisbee, Ph.D. thesis, University of Maryland, 1972 (unpublished).
38. P. Darriulat, G. Igo, H. G. Pugh, and H. D. Holmgren, Phys. Rev. **137**, B315 (1965).
39. E. F. Redish, G. J. Stephenson, Jr., and G. M. Lerner, Phys. Rev. C **2**, 1665 (1970).
40. D. F. Jackson and T. Berggren, Nucl. Phys. **62**, 353 (1965).
41. A. K. Jain and N. Sarma, *Clustering Aspects of Nuclear Reactions,* Winnipeg 1978, paper B12, edited by W. T. H. Van Oers, J. P. Svenne, J. S. C. McKee and W. R. Falk (American Institute of Physics 1978), p. 568.
42. R. H. Pehl, Ph.D. thesis, 1963, UCRL 10993 (unpublished).
43. See for example D. A. Goldberg and S. M. Smith, Phys. Rev. Lett. **33**, 715 (1974); P. Gaillard, *et al.*, Nucl. Phys. **A131**, 353 (1969).
44. T. A. Carey, Ph.D. thesis, University of Maryland, 1979 (unpublished).
45. N. S. Chant, *Clustering Aspects of Nucleyr, Structure and Nuclear Reactions,* Winnipeg 1978, edited by W. T. H. Van Oers, J. P. Svenne, J. S. C. McLee, and W. R. Falk (American Institute of Physics 1978) p. 415.
46. N. S. Chant, P. G. Roos, and C. V. Wang, Phys. Rev. C **17**, 8 (1978).
47. C. Détraz, H. H. Duhm, and H. Hafner, Nucl. Phys. **A147**, 588 (1970).
48. G. Audi, C. Détraz, M. Langevin, and F. Pougheon, Nucl. Phys. **A237**, 300 (1975).
49. B. L. Jain, Nucl. Phys. **A314**, 51 (1979).
50. G. E. Brown and A. M. Green, Nucl. Phys. **75**, 401 (1966).

51. I. Sick, Nucl. Phys. **A218**, 509 (1974).
52. S. M. Smith, *et al.*, Nucl. Phys. **A207**, 273 (1973).
53. P. Gaillard, *et al.*, Nucl. Phys. **A131**, 353 (1969).
54. S. Matsuki, *et al.*, J. Phys. Soc. Japan **26**, 1344 (1969).
55. H. Rebel, *et al.*, Nucl. Phys. **A182**, 145 (1972).
56. H. H. Gutbrod, H. Yoshida, and R. Bock, Nucl. Phys. **A165**, 240 (1971); P. Beregi, N. S. Zelenskaja, V. N. Neudatchin, and Yu. F. Smirnov, Nucl. Phys. **66** 513 (1965).

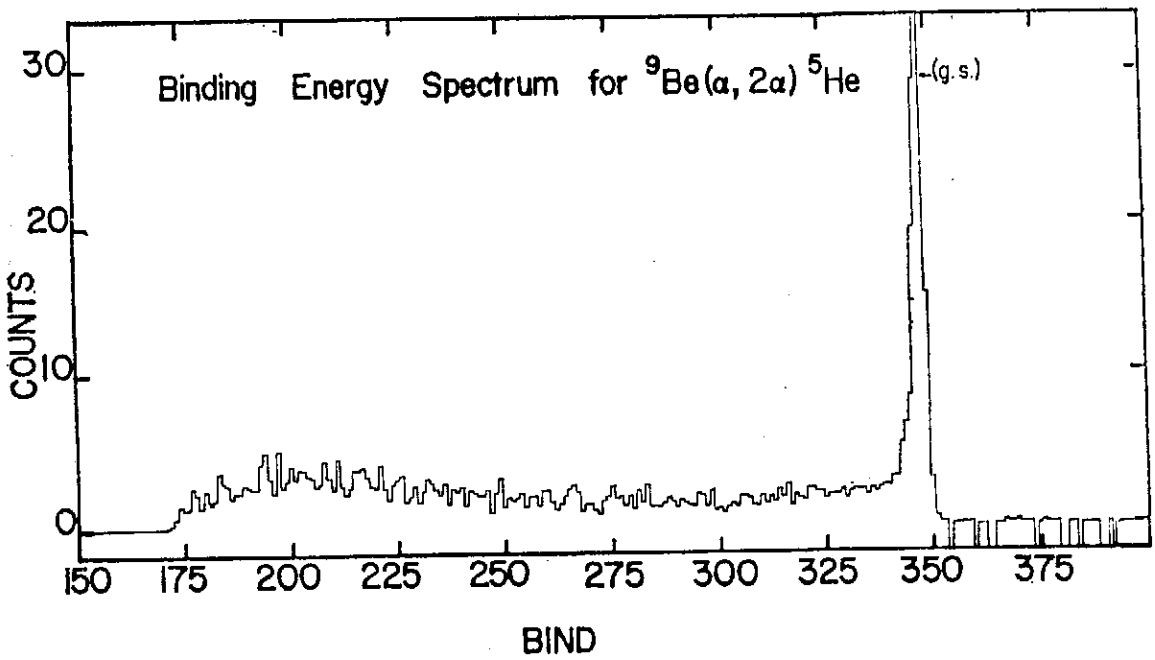

Fig. 1 (a) Binding Energy Spectrum for ^{9}Be (α, 2α)^{5} ^{5}He Reaction.

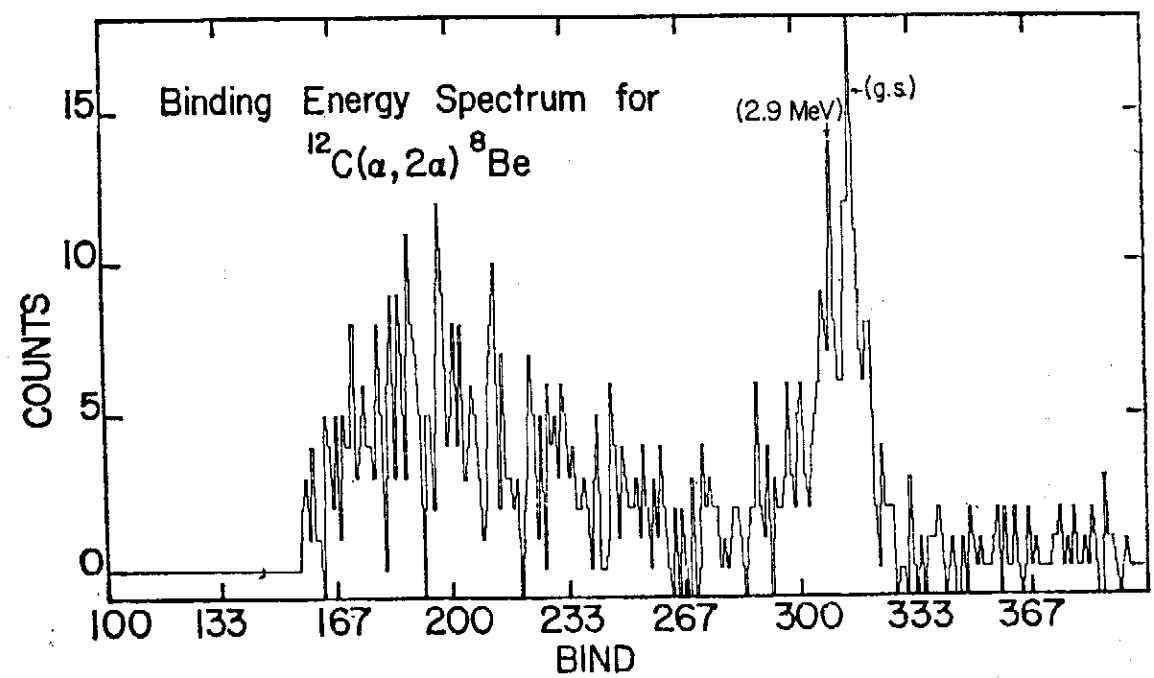

Fig. 1 (b) Binding Energy Spectrum for ^{12}C (α, 2α) ^{8}Be Reaction.

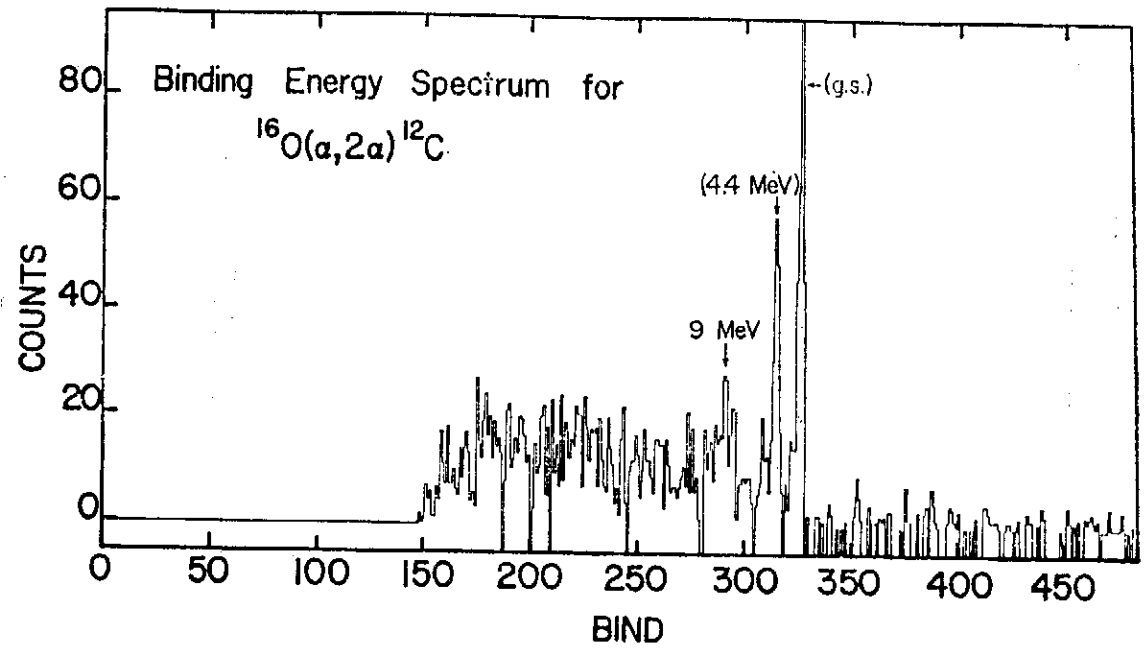

Fig. 1 (c) Binding Energy Spectrum for ^{16}O (α, 2α) ^{12}C Reaction.

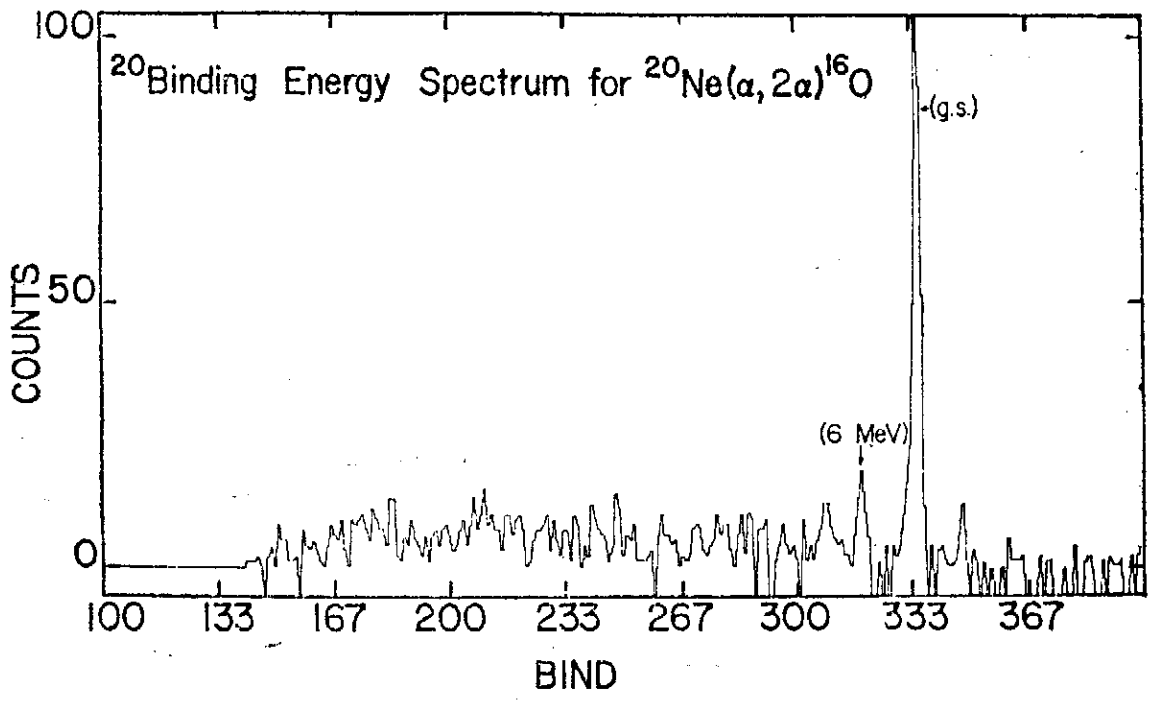

Fig. 1 (d) Binding Energy Spectrum for ^{20}Ne (α, 2α) ^{16}O Reaction.

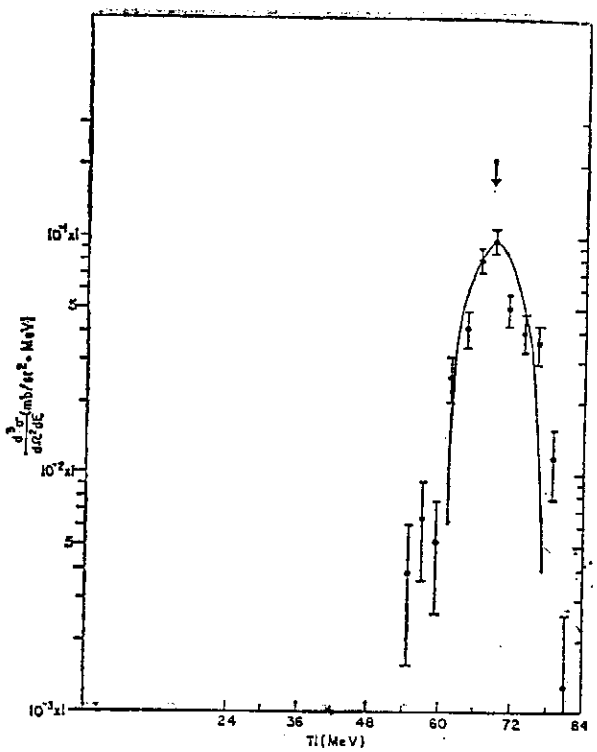

Fig. 2 (a) Energy Sharing Spectrum for ^{9}Be(α, 2α) ^{5}He (g.s.) at θ_1/θ_2=44.19°/−44.19°.

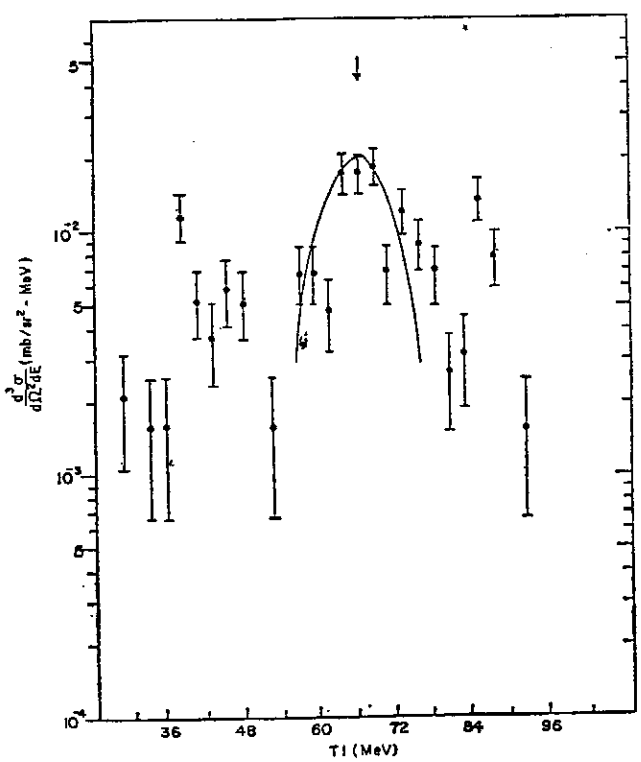

Fig. 2 (b) Energy Sharing Spectrum for ^{12}C(α, 2α) ^{8}Be(g.s.) at θ_1/θ_2=43.11°(−43.11°.

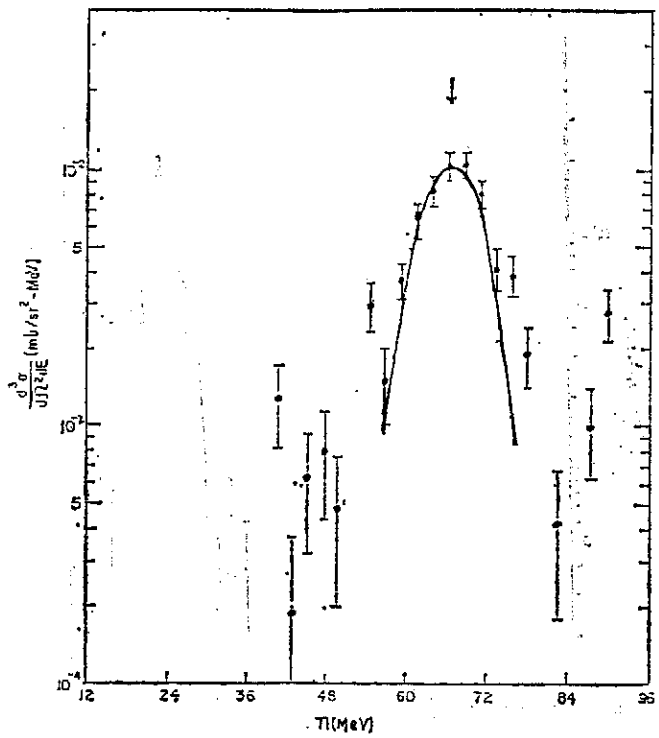

Fig. 2 (c) Energy Sharing Spectrum for $^{16}O(\alpha, 2\alpha)^{12}C(g.s.)$ at $\theta_1/\theta_2=43.16°/-43.16°$.

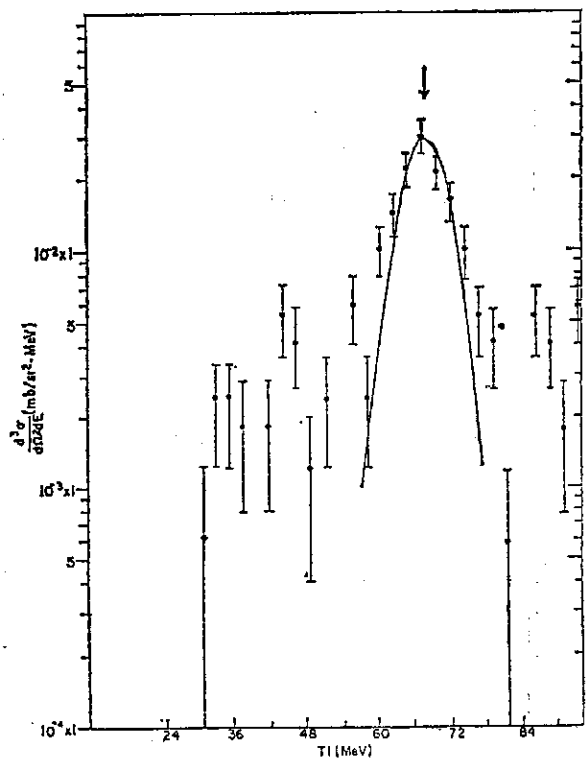

Fig. 2 (d) Energy Sharing Spectrum for $^{20}Ne(\alpha,°.\ 2\alpha)^{16}$ O(g.s.) at $\theta_1/\theta_2=43.71°/-43.71$

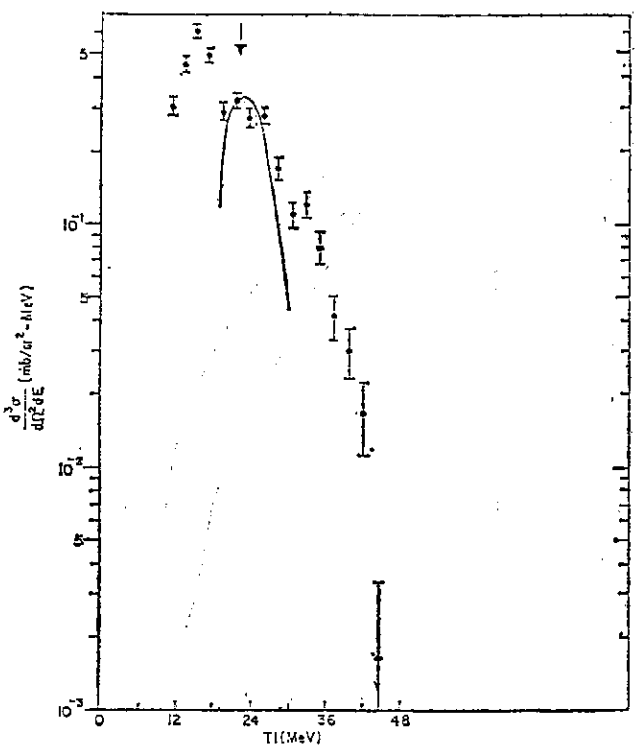

Fig. 3 (a) Energy Sharing Spectrum for ^{16}O(α, 2α) ^{12}C(g.s.) at θ_1/θ_2=63.82°/−23°.

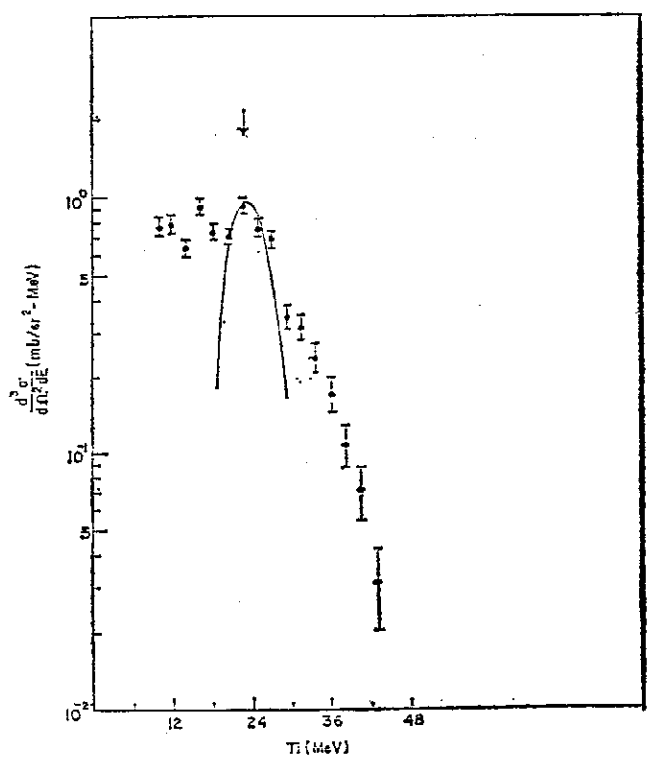

Fig. 3 (b) Energy Sharing Spectrum for ^{20}Ne(α, 2α) ^{16}O(g.s.) at θ_1/θ_2=63.82°−23°.

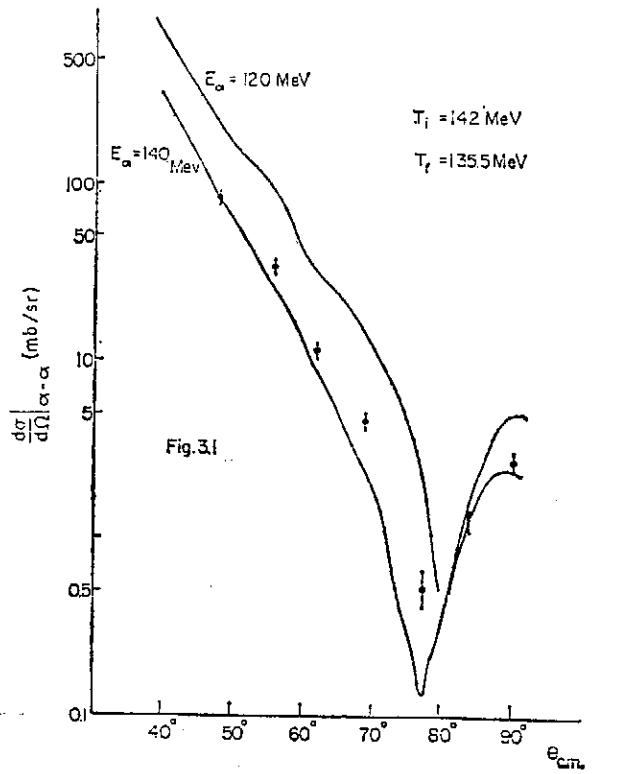

Fig. 4 (a) Half-shell $\alpha-\alpha$ Cross Section Extracted from the $^{9}Be(\alpha, \alpha)$ ^{5}He(g.s.) Data at 140 MeV.

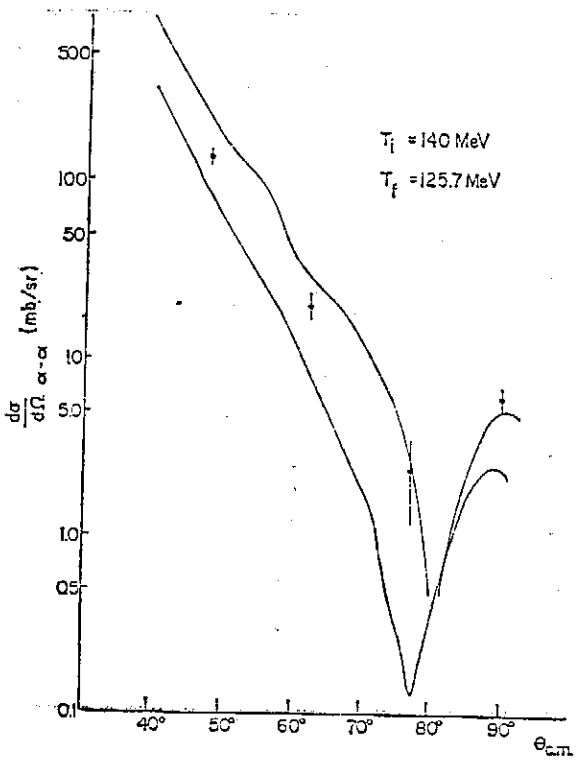

Fig. 4 (b) Half-shell $\alpha-\alpha$ Cross Section Extracted from the $^{12}C(\alpha, 2\alpha)$ ^{8}Be(g.s.) Data at 140 MeV.

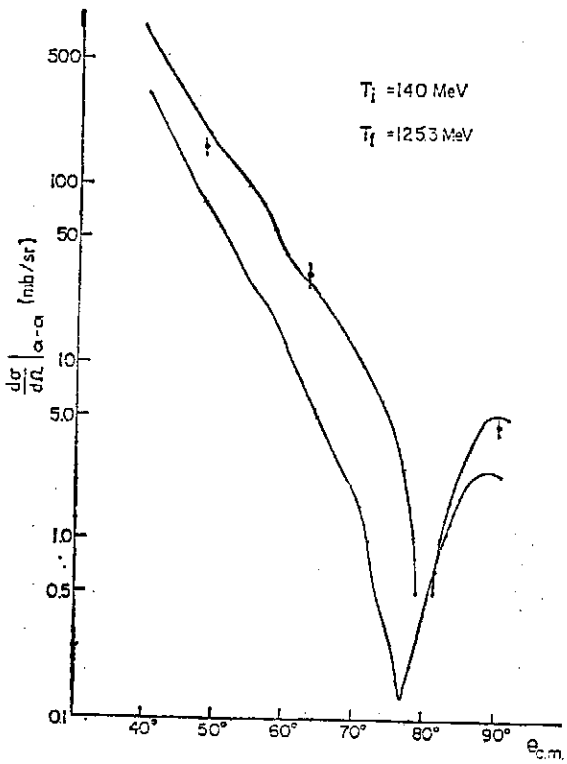

Fig. 4 (c) Half-shell $\alpha-\alpha$ Cross Section Extracted from the ^{16}O(α, 2α) ^{12}C(g.s.) Data at 140 MeV.

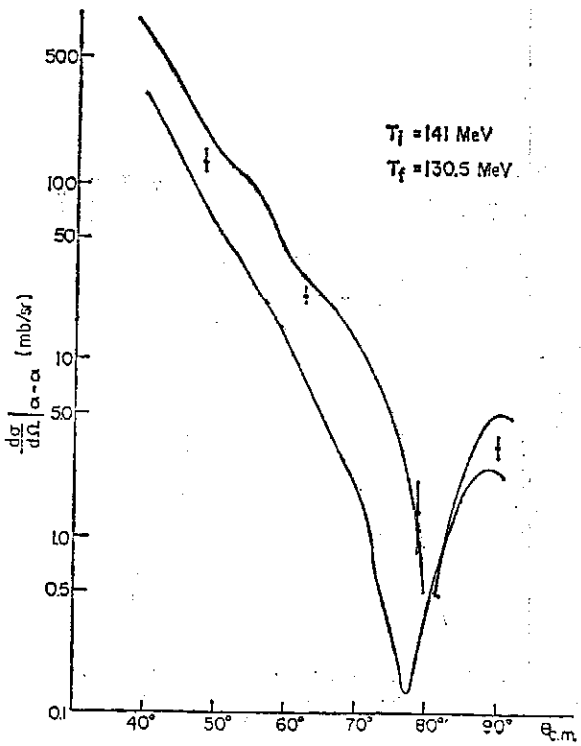

Fig. 4 (d) Half-shell $\alpha-\alpha$ Cross Section Section Extr acted from the ^{20}Ne(α, 2α) ^{16}O(g.s.) Data at 140 MeV.

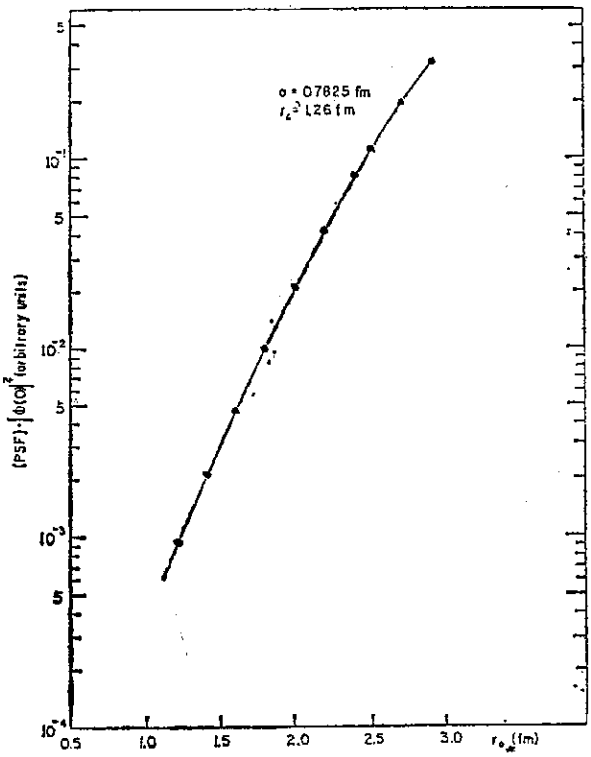

Fig. 5. Dependence of the (PSF) • | $\phi(0)$ |² on Bound State Radius Parameter r_0 for $^{16}O(\alpha, 2\alpha)$ ^{12}C(g.s.) at E=140 MeV.

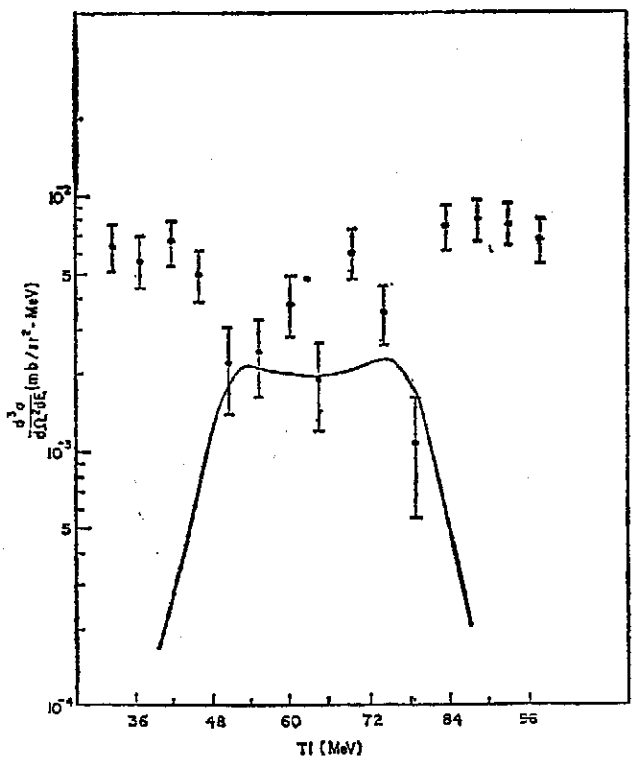

Fig. 6 (a) Energy Sharing Spectrum for $^{12}C(\alpha, 2\alpha)$ ^8Be(2.9 MeV) at θ_1/θ_2=43.11°/−43.11°.

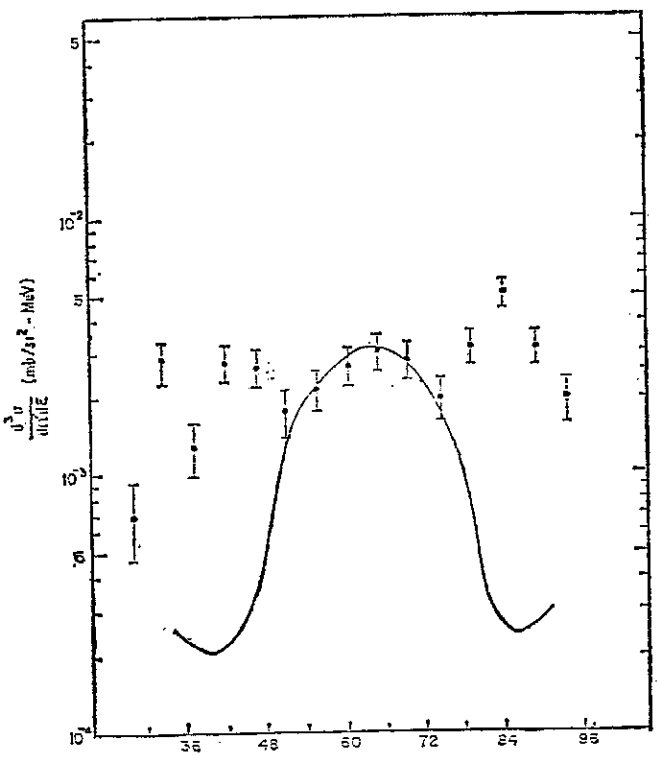

Fig. 6 (b) Energy Sharing Spectrum for $^{16}O(\alpha, 2\alpha)\ ^{12}C(4.4$ MeV) at $\theta_1/\theta_2 = 43.16°/-43.16°$.

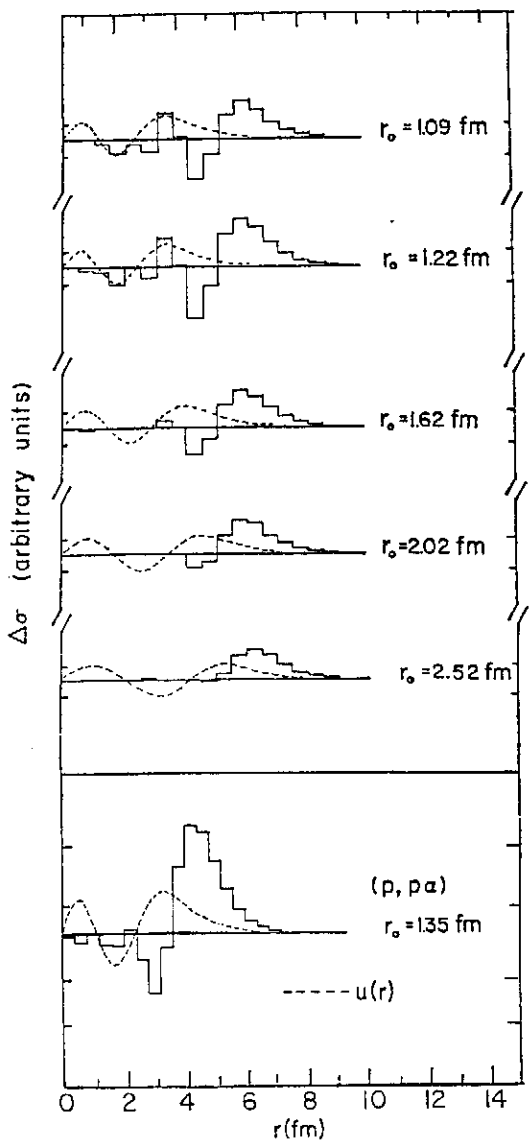

Fig. 7. Surface Localization of $^{16}O(\alpha, 2\alpha)\ ^{12}C(g.s.)$, $E_\alpha = 140$ MeV, $\theta_1/\theta_2 = 43.16°/-43.16°$ for various r_0

PHASE-SHIFT ANALYSIS OF α-^{12}C ELASTIC SCATTERING DATA AT ENERGRIES E_α = 5. and 6. MeV

C. W. Wang (王建萬), G. C. Kiang (江紀成), L. P. Liang (梁靈平), M. W. Lee (李明威)
D. Wang (王 定), L. L. Kiang (李 琳), E. K. Lin (林爾康)

Abstract

Elastic scattering of α-particles from ^{12}C target has been measured at $E_\alpha = 5.$ and 6. MeV. The results have been interpreted by a real phase-shift analysis. The phase shift of each partial wave has been compared with other work.

The phase-shift analysis of α-^{12}C elastic scattering data at energies below ^{15}N+p threshold had been reported by Clark et al[1]. Resonance states of ^{16}0 at excitation energies below 12.05 MeV had also been studied by Larson and Tombrello[2] and by other authors[3,4] via the α-^{12}C scattering experiments. The phase shifts extracted by these authors are not quite consistent with each other. The purposes of this work are two-folds. Firstly, we are trying to interpret the low energy α-^{12}C scattering data with real phase-shift analysis. This is part of our current study about low energy α-scattering on light nuclei. Secondly, we are trying to solve the inconsistency of the results obtained by the authors just mentioned.

The particle-nucleus elastic scattering differential cross section in the CM system may be expressed in terms of real phase shifts δ_ℓ by[5]

$$\frac{d\sigma}{d\Omega} = \frac{1}{k^2}\Big| -\frac{1}{2}\eta\csc^2\left(\frac{1}{2}\theta\right)] + \sum_\ell (2\ell+1)P_\ell(\cos\theta)\exp[i(2\alpha_\ell+\delta\ )]\sin\delta_\ell \Big|^2$$

where $\alpha_\ell = \sum_{m=1}^{\ell} \tan^{-1}(\eta/m)$, $\alpha_0 = \arg\Gamma(1+i\eta)$

and η is the charge parameter and k is the wave number associated with relative motion. In this work, we have used a conventional χ^2-fit of the experimental and theoretical angular distribution to extract the phase shifts δ_ℓ at laboratory energies $E_\alpha = 5.$ and 6. MeV. The optimal results are shown in Figs. 1 and 2 for incident energies 6. and 5. MeV respectively. The extracted phase shifts together with χ^2 are shown in Table 1.

TBBLE I

E_α(MeV)	δ_0	δ_1	δ_2	δ_3	δ_4	δ_5	χ^2
6.	− 37.71°	115.3°	347.7°	101.0°	172.3°	− 0.05°	0.86ϕ
5.	− 6.80	− 185.9°	− 253.6°	138.3°	170.4°	− 1.54°	7.28

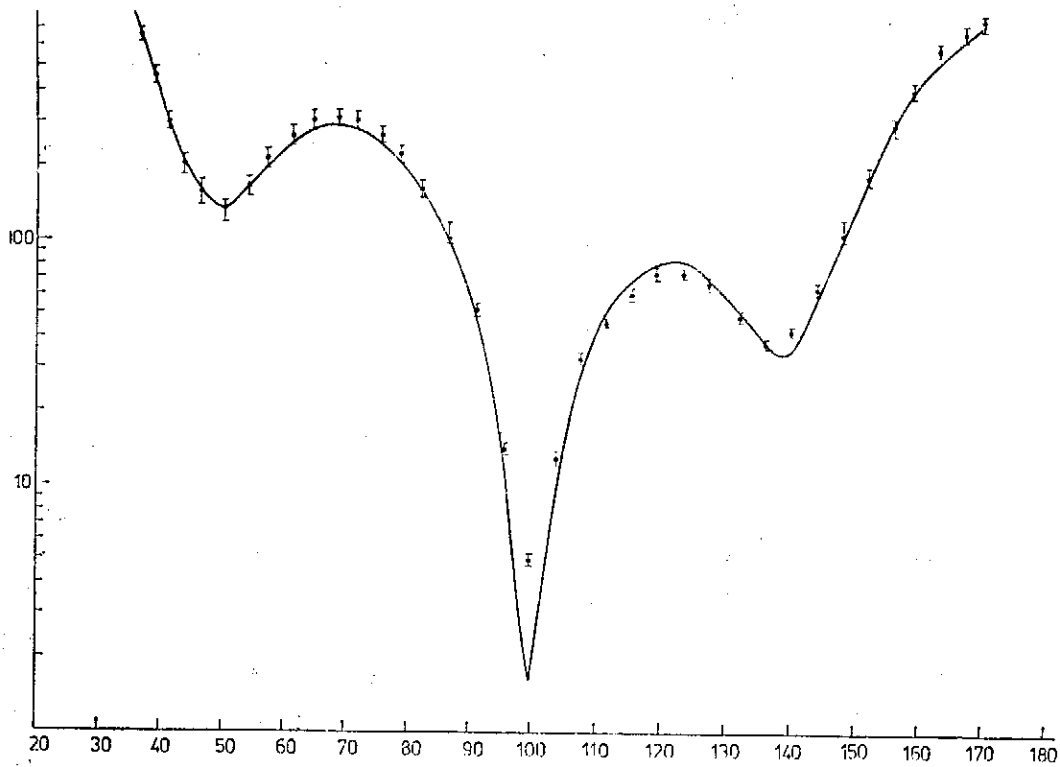

FIG. 1. $E\alpha = 6.$ MeV

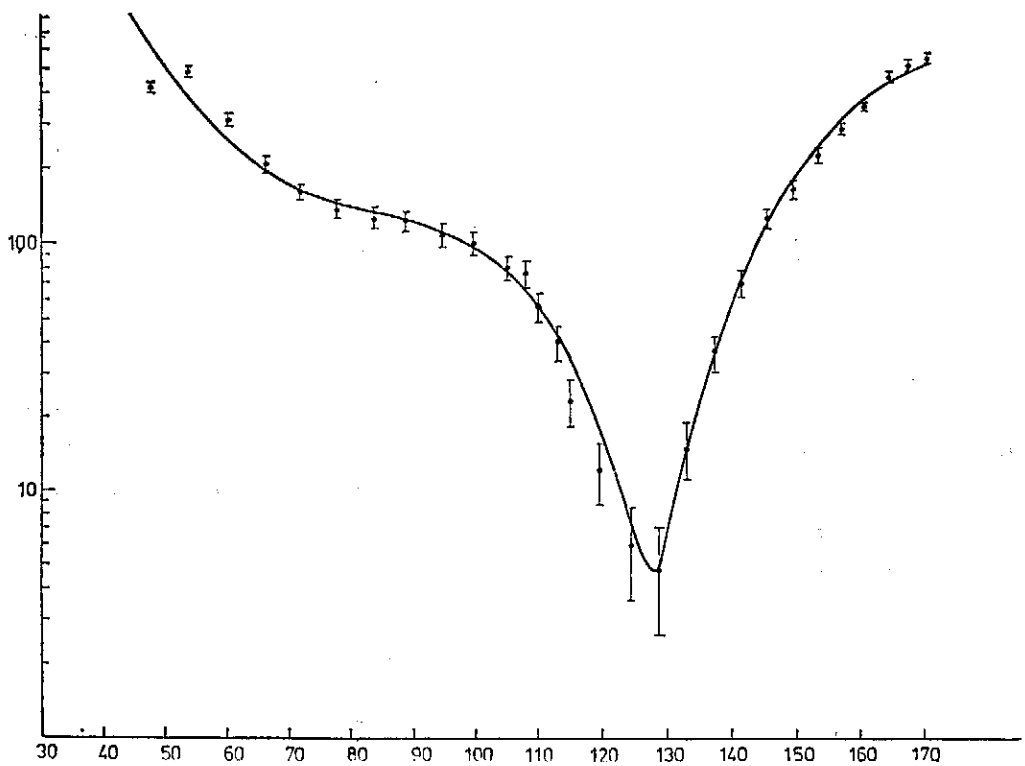

FIG. 2. $E\alpha = 5.0$ MeV

For the case of $E_\alpha = 6$. MeV, additional inelastic channel ($E_x = 4.43$ MeV) is open. A complex phase-shift analysis should be performed. However, the inelastic cross section is found to be very small in comparing with the elastic one at the energy studied. Thus we expect that real phase-shift analysis is acceptable. The results shown in the Figures and Table are quite good. The phase shifts for 6. MeV scattering are consistent with those obtained by Clark et al.[1] The χ^2 for 5. MeV fitting seems to be too big. Refined fittings are in process.

REFERENCES

(1) G. J. Clark et al., NP A110 (1968) 481
(2) J. D. Larson and T. A. Tombrello, PR 147 (1966) 760
(3) C. Miller Janes et al., NP 37 (1962) 1
(4) J. W. Bittner and R. D. Moffat, PR 96 (1954) 374
(5) R. R. Roy and B. P. Nigam, Nuclear Physics (1970).

A SIMPLE NUCLEAR E2 TRANSITION MODEL OF $2_1^+ \rightarrow 0_1^+$ TRANSITION FOR EVEN-EVEN NUCLEI

C. W. Wang (王建萬), G. C. Kiang (江紀成),
L. L. Kiang (李 琳)* C. C. Hsu (徐竹村), and E. K. Lin (林爾康)

Institute of Physics Academia Sinica
Nankang, Taipei, Taiwan, The Republic of China

Abstract

A simple model for nuclear E2 transition from 2_1^+ to 0_1^+ states for even-even nuclei has been proposed. Transition probabilities based on this model have been deduced. The lifetimes of the 2_1^+ states have been calculated and compared with experimental results. The ratios of these two values fall into a region from 0.3 to 3 for most nuclei.

The theory of electromagnetic multipole transitions between two nuclear states had been well established by using the long wave length approximation[1]. In that formulism, the transition probabilities are proportional to the square of the matrix elements of the nuclear electric or magnetic multipole operators which contain the structural information about the nuclear states. The E2 transition probabilities predicted by the simple shell-model calculation of Weisskopf[2] are some order of two magnitude smaller than the experimental results for most nuclei. Refined calculations for specific nucleus have been reported[3]. Collective model calculations have also been made[4].

In this report we present a model for nuclear E2 transitions between 2_1^+ and 0_1^+ states of the even-even nuclei. Assuming that the interaction of a nucleus and a radiation field could be thought of as a point charge of mass $M=Am$, (m is the nucleon mass, and charge is Ze), moving in a potential $V(\vec{r}) = -V_0 + \frac{1}{2}M\omega_0^2 r^2$, if the wave length of the field is much larger then the nuclear dimension, where V_0 and ω_0 are parameters. The nuclear E2 transition, $2_1^+ \rightarrow 0_1^+$, is then corresponding to the transition of this system from the $n=2$ state, n being the oscillator quantum number, to the ground state. From this arguement and the electric quadrupole operator

$$\hat{Q}_{2\mu} = \sum_{j=1}^{A} [e_j r^2 Y^*_{2\mu}(\theta_j, \phi_j) + i\, g_{sj}\, \mu_0 (\frac{\omega}{c})\, (2+1)^{-1} \vec{\sigma}_j \times \vec{r}_j \cdot \vec{\nabla}\, (r^2 Y^*_{2\mu})_j)$$

$$\sim \sum_{j=1}^{Z} [e r_j^2 Y^*_{2\mu}(\theta_j, \theta_j)] = Z e r^2 Y^*_{2\mu}(\theta, \phi) \qquad (1)$$

and the harmonic oscillator wave functions

$$|n\ell m> = R_{n\ell}(r) Y_{\ell m}(\theta, \phi)$$

* Dept. of Physics, Tsing Hua University, Hsinchu, Taiwan, R.O.C.

the $2_1^+ \rightarrow 0_1^+$ transition probability becomes

$$T_{fi} = \frac{8\pi(2+1)}{2[(2\cdot 2+1)!!]} \frac{1}{\hbar} \left(\frac{\hbar\omega}{\hbar c}\right)^5 |<000|(Zer^2 Y^*_{2\mu})|22m>|^2 \quad (2)$$

for specific m and μ. By carrying out equation (2) explicitly and averaging over the initial states and summing over the final states, we obtain

$$T(2_1^+ \rightarrow 0_1^+, E2) = \frac{cZ^2}{80} \cdot \frac{e^2}{\hbar c}\left(\frac{\hbar\omega}{\hbar c}\right]^5 \frac{1}{\alpha^2} \quad (3)$$

where $\alpha = M\omega_0/(2\hbar)$. The characteristic angular freqency ω_0 can be determined by considering that the energy of the emitted gamma ray is $\hbar\omega = E(n=2) - E(n=0) = 2\hbar\omega_0$. Thus $\omega_0 = \omega/2$. The parameter V_0 plays no role in the transition probability calculation. Substituting the universal constants and ω_0 in equation (3), we reach

$$T(2_1^+ \rightarrow 0_1^+, E2) = 2.5199 \times 10^{12} Z^2 (\hbar\omega)^3/A^2 \quad \text{sec}^{-1} \quad (4)$$

with $\hbar\omega$ measured in MeV. There is no free parameter in the expression (4). The mean lifetimes of the 2_1^+ states have been calculated based on equation (4) and compared with the experimental results for even-even nuclei (stable and unstable) from A = 12 to A = 206. The ratios of these two results τ_{cal}/τ_{exp}, without the correction due to internal convertion, are shown in Fig. 1. The

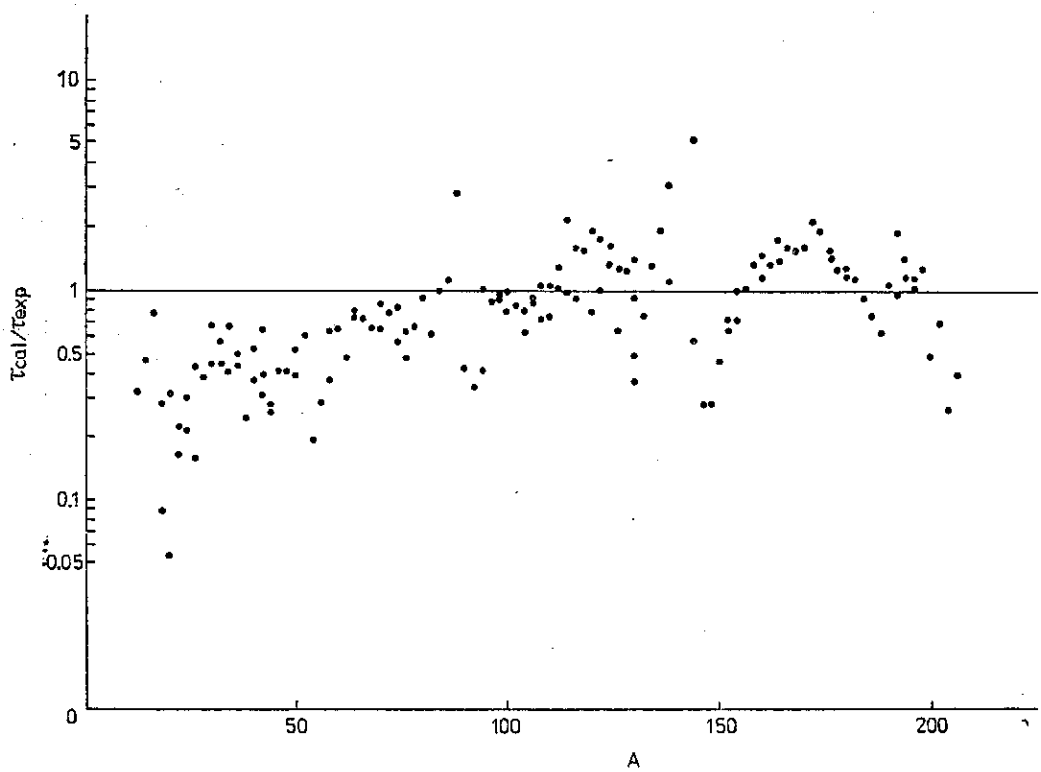

FIG. 1. Ratios of calculated and experimental life times, $\alpha = Am\omega/(4\hbar)$

calculated and experimental values are nicely consistent with each other to within a factor of 3 with fewer exceptions.

Recently, Hsu et al[5] have suggested that pure vibrational nuclear states were due to the vibration of the nuclear center-of-mass. These authors have also proposed a size parameter $\lambda = M\omega_A/(2\hbar) = 0.083A^{1/3}$ fm^{-2} from an averaging point of view. The calculations based on that arguement have been made by Kiang et al[6]. They have obtained an expression for transition probability mathematically the same as equation (3) with λ corresponding to our α. By using their size parameter for our α, the results (again without the correction due to internal convertion) are qualitively in agreement with our results as shown in Fig. 2.

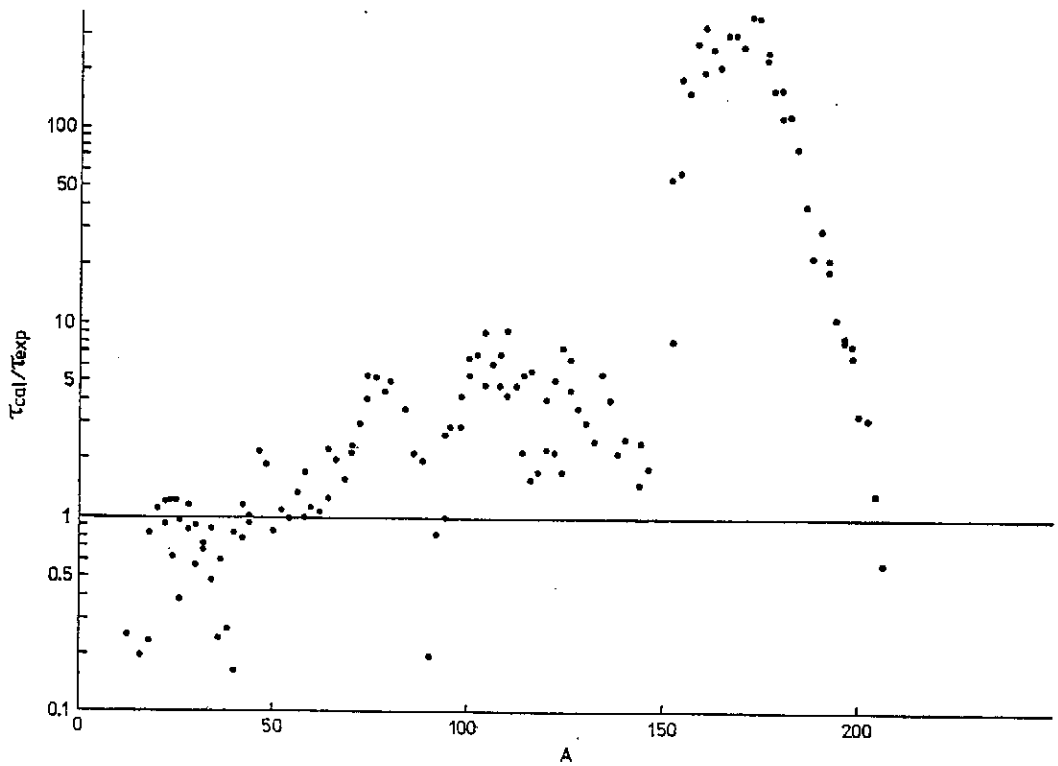

FIG. 2. Ratios of calculated and experimental lifetimes, $\alpha = 0.083A^{1/3}$ fm^2

REFERENCES

(1) e.g. de Shalit and Feshbah, Theoretical Nuclear Physics, Vol. 1. chapter VIII, John Wiley and Soas, Inc. 1974
(2) V. F. Weisskopf, Phys. Rev. 83, 1073 (1951)
(3) e.g. H. C. Chiang et al, to be published at J. Phys. G
(4) e.g. Eisenberg and Greiner, Nuclear Models, North-Holland Publishing, 1970
(5) C. C. Hsu et al, to be published
(6) L. L. Kiang et al, Private Commuication

THE REDUCED E2 TRANSITION PROBABILITIES OF THE ONE PHONON STATES TO THE GROUND STATES OF EVEN-EVEN VIBRATIONAL NUCLEI

L. L. Kiang (李 琳)*, G. C. Kiang (江纪成)+, C. W. Wang+ (王建萬)+
and
C. C. Hsu (徐竹村)*+

National Tsing Hua University
and
Institute of Physics Academia Sinica

Abstract

Based on the harmonic oscillator potential the reduced E2 transition probabilities B(E2) of one phonon states to the ground states and the half-lives $T_{1/2}$ of the one phonon state of the even-even vibrational nuclei have been calculated. In comparison with the experimental data, the ratios are in the range of 0.2~1.3 and 0.8~7 respectively.

The interaction in a doorway state and a nucleon in a more complicated states of the nuclei has already been discussed by Hsu[1, 2] and Hsu and Gonsior[3]. These authors proposed that owing to the vibration of the nucleons, the center of mass of the nucleus could be assumed to be a harmonic oscillator which is oscillating in a vibrational potential

$$V(r) = -A < V_d >_0 + \tfrac{1}{2} M\omega_A{}^2 r^2 \qquad (1)$$

where, $< V_d >_0$ is the averaged interaction potential between the nucleons in the different state with the value of ~8 keV. A is the number of nucleons of the nuclei. The second term is the potential of the assumed oscillator in the position r relative to the equilibrium point.

The electromagnetic transitions between one phonon state and ground state of the even-even vibrational nuclei are pure E2 mode. Due to the fluctuation of the nucleon density, we assumed that the oscillating nucleus has a very simple kind of charge distribution, and the electric quadrupole moment operator is approximately

$$\hat{Q}_{2\mu} = \sum_j e_j r_j^2 \, Y^*_{2\mu}(\theta, \phi) \qquad (2)$$

where r_j is the position of the charged nucleons to the equilibrium point. The reduced E2 transition probability for an electric quadrupole transition from the i state to the f state is

$$B(E2) = \frac{1}{2I_i + 1} \sum_{if} \left| < f | \hat{Q}_{2\mu} | i > \right|^2 \qquad (3)$$

* Dept. of Physics National Tsing Hua Univ.
+ Institute of Physics, Academia Sinica

where I_i is the augular quantum number of the state. And the transition probability for emission of a photon of energy $\hbar\omega$ from the one phonon state to the ground state is

$$T(E2;\ 2^+ \rightarrow 0) = \frac{4\pi}{75}\frac{1}{\hbar}\left(\frac{\omega}{c}\right)^5 B(E2;\ 2^+ \rightarrow 0^+) \qquad (4)$$

The wave function of the harmonic Oscillator is

$$\psi_{n\ell m} = R_{n\ell}(r)Y_{\ell m}(\theta,\ \phi) \qquad (5)$$

where $$R_{n\ell} = N_{n\ell}\ \exp(-\lambda r^2)\ r^{\ell+1}\nu_{n\ell}(2\lambda r^2) \qquad (6)$$

and $N_{n\ell}$ are the normalization factors,

$\nu_{n\ell}$ are the associated Legurerre polynormals,

λ is the size paramerter and $\lambda = \frac{M\omega_A}{2\hbar}$

According to equation (3), we calculated the reduced E2 transition probabilities B(E2) for the vibrational even-even nuclei in the mass region of $54 \leq A \leq 80$, $96 \leq A \leq 148$ and $188 \leq A \leq 206$ which were taken from the literature[4]. We also calculated the half-lives $T_{1/2}$ of the one phonon states of the vibrational nuclei from the E2 transition probabslities which were obtained from eq. (4). The results are shown in Table 1. In this table, we listed the nuclei of $A > 54$, which were similar in the excited states with the other vibrational nuclei in ref.(4). The $A > 54$ nuclei were chosen from the 'Table of Isotopes' of C. M. Lederer et al.[6].

TABLE I

Elements	1-phonon state 2^+-energy[MeV]	B(E2) exp $2^+ \rightarrow 0^+$ (10^{-50} cm^{4}e^2)	B(E2) cal $2^+ \rightarrow 0^+$ (10^{-50} cm^{4}e^2)	B(E2)cal / B(E2)exp	$T_{1/2}$ exp 2^+ ps	$T_{1/2}$ cal 2^+ ps	$T_{1/2}$ cal / $T_{1/2}$ exp
$^{104}Ru_{44}$	0.358				54	131.8	2.44
$^{104}Pd_{46}$	0.555				9.8	32.4	3.3
$^{106}Pd_{46}$	0.512				12	42.8	3.56
$^{108}Pd_{46}$	0.434				25	73	2.92
^{110}Pd	0.374	17.6	6.53	0.37	45	118.5	2.63
$^{106}Cd_{48}$	0.633				6	20.8	3.46
$^{108}Cd_{48}$	0.633				5.3	20	3.77
$^{110}Cd_{48}$	0.658	10	2.3	0.23	5	19.9	3.98
$^{112}Cd_{48}$	0.617	10.9	2.52	0.23	6.2	25	4.
$^{114}Cd_{48}$	0.558	11	3	0.27	9.9	35.1	3.54
$^{116}Cd_{48}$	0.513	12	3.4	0.28	12	46.8	3.9
$^{120}Te_{52}$	0.560	11	3.12	0.23	10	32.8	3.28
$^{122}Te_{52}$	0.564	13	3	0.19	7.6	33.2	4.37
$^{124}Te_{52}$	0.603				9	28.1	7.15

The Reduced E2 Transition Probabilities of the One Phonon States to the Ground States of Even-Even Vibrational Nuclei

(Continued)

Elements	1-Phonon state 2^+-energy[MeV]	B(E2) exp $2^+ \rightarrow 0^+ (10^{-50}\ cm^4e^2)$	B(E2) cal $2^+ \rightarrow 0^+ (10^{-50}\ cm^4e^2)$	$\frac{B(E2)cal}{B(E2)exp}$	$T_{1/2}$ exp 2^+ ps	$T_{1/2}$ cal 2^+ ps	$\frac{T_{1/1\ cal}}{T_{1/2\ exp}}$
$^{126}Te_{52}$	0.667	10.6	2.0	0.19	3.8	21.4	5.63
$^{128}Te_{52}$	0.743	8.3	1.56	0.19	2.9	16.0	5.51
$^{130}Te_{52}$	0.840				2.0	11.4	5.7
$^{144}Nd_{60}$	0.695	6.0	1.9	0.32	8.0	18.6	2.32
$^{146}Nd_{60}$	0.455	5.0	4.26	0.58	58.0	66.9	1.15
$^{148}Nd_{60}$	0.300				210.0	230.0	1.09
$^{188}Os_{76}$	0.155	72.0	35.5	0.5	710.0	1031.0	1.45
$^{190}Os_{76}$	0.186	52.0	20.13	0.4	425.0	852.0	2.0
$^{22}Ne_{10}$	1.274	0.64	0.66	1.03	2.7	2.57	0.95
$^{26}Mg_{12}$	1.81				0.5	0.86	1.72
$^{48}Ti_{22}$	0.99	1.4	1.0	0.71	4.2	6.0	1.43
$^{50}Cr_{24}$	0.79	3.0	2.0	0.67	6.2	9.8	1.58
$^{52}Cr_{24}$	1.443				0.64	1.7	2.65
$^{54}Cr_{24}$	0.835	1.14	1.48	1.3	12	9.5	0.79
$^{54}Fe_{26}$	1.41						
$^{56}Fe_{26}$	0.845	1.22	1.57	1.28	8.3	8.3	1
$^{58}Fe_{26}$	0.805	3.1	1.62	0.52	5.4	10.3	1.9
$^{64}Zn_{30}$	0.990	2.5	1.17	0.47	2.3	5.0	2.17
$^{66}Zn_{30}$	1.039	2.14	1.0	0.47	2.17	4.67	2.15
$^{68}Zn_{30}$	1.078	2.0	0.87	0.44	1.6	4.4	2.75
$^{70}Zn_{30}$	0.887	3.2	1.22	0.4	3.2	8.44	2.63
$^{74}Se_{34}$	0.635	4.2	2.73	0.65	13.0	20.0	1.54
$^{76}Se_{34}$	0.559	8.8	3.35	0.38	13.87	31.0	2.23
$^{78}Se_{34}$	0.614	7.2	2.63	0.37	8.95	24.6	2.73
$^{80}Se_{34}$	0.666	4.6	2.13	0.46	9.65	20.3	2.1
$^{96}Ru_{44}$	0.838				2.7	8.9	3.29
$^{98}Ru_{44}$	0.654				5.0*	19.2	3.84
$^{100}Ru_{44}$	0.540	11.4	3.5	0.3	11.0	35.5	3.22
$^{102}Ru_{44}$	0.473				16.0	55.0	3.43
$^{192}Os_{76}$	0.206	40.0	19.3	0.48	280.0	610.0	2.18
$^{192}Pt_{78}$	0.316				27.2	189.0	6.95
$^{194}Pt_{78}$	0.328	39.0	7.84	0.2	45.0	177.0	3.93
$^{196}Pt_{78}$	0.356	25.0	6.5	0.26	36.0	143.0	3.97
$^{198}Pt_{78}$	0.405	27.0	4.93	0.18	19.0	100.6	5.29
$^{196}Hg_{80}$	0.426				14.0*	77.5	5.53
$^{198}Hg_{80}$	0.412	22.0	5.0	0.22	22.2	91.0	4.1
$^{200}Hg_{80}$	0.368				59.0	128.3	2.17
$^{202}Hg_{80}$	0.440	10.6	4.2	0.39	27.5	77.7	2.82
$^{204}Hg_{80}$	0.430				80.0	85.0	1.06
$^{206}Pb_{82}$	0.803	1.2	1.28	10.6	7.7	13.2	1.71

*REF. 6

The experimental values of $B(E2)_{exp}$ and $T_{1/2exp}$ are taken from ref. (5). The ratios of the calculated $B(E2)_{theo}$ and the experimental $B(E2)_{exp}$ are shown in fig 1. The ratios of $T_{\frac{1}{2}theo}/T_{\frac{1}{2}exp}$ are shown in fig. 2. Examine both of the figures, we find that the variations of the $B(E2)_{theo}/B(E2)_{exp}$ and $T_{\frac{1}{2}theo}/T_{\frac{1}{2}exp}$ are in the range of 0.2～1.3 and 0.8～7 respectively, which is good enough to be accepted.

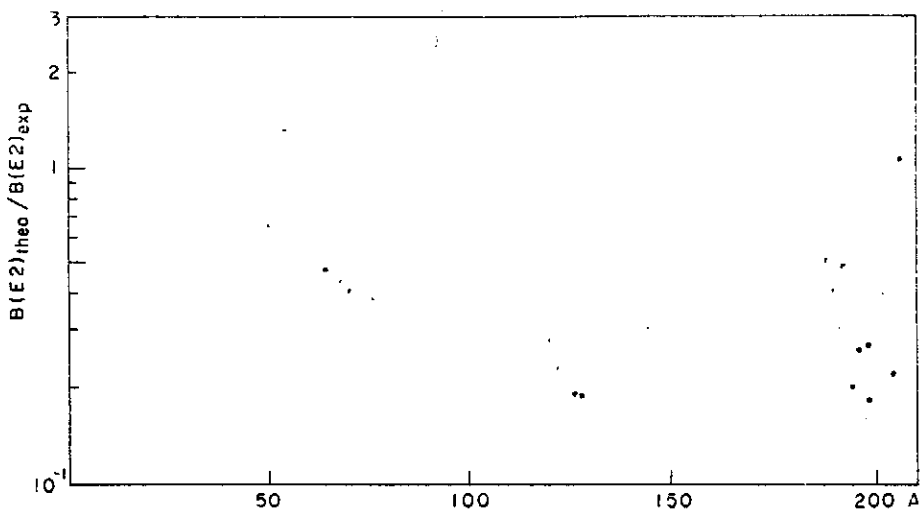

FIG. 1 The ratios of the calculated $B(E2)_{theo}$ and the experimental $B(E2)_{exp}$ versus the mass number A.

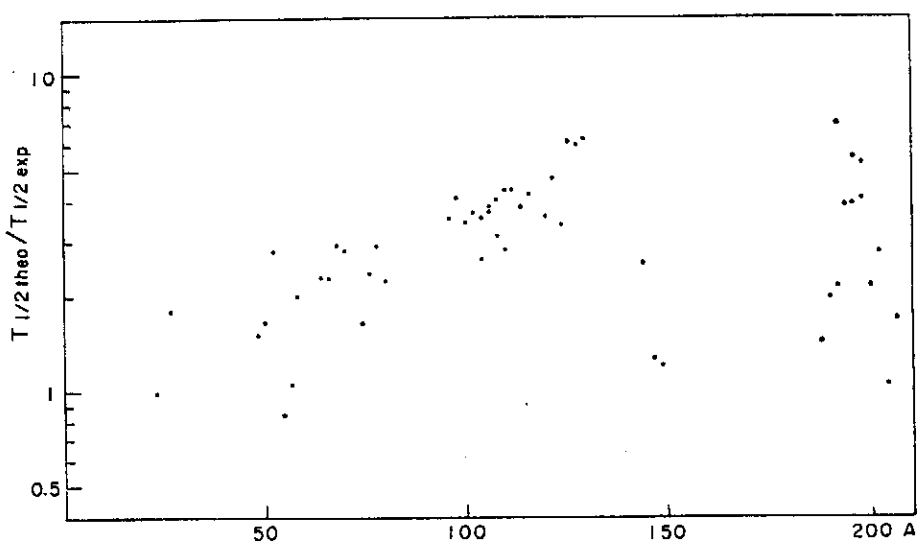

FIG. 2 The ratios of the calculated $T_{1/2theo}$ and the experimental $T_{1/2exp}$ versus the mass number A.

Since the nucleon density fluctuation may induce a surface vibration[3], which causes the nucleus going to deform. This deformation may change the

potential V(r) from a real harmonic oscillator potential[2], the wave function which we used for calculation should be corrected by the perturbation theory in order to have better match for the experimental results. The determination of the deformation parameters for the vibrational nuclei are in processing.

REFERENCES

(1) C. C. Hsu, Phys. Rev. **C** 14, 402, 1967
(2) C. C. Hsu, J. Phys. **G**. Nucl. Phys. **4**, L165, 1978
(3) C. C. Hsu, B. Gonsior, to be published
(4) J. M. Eisenberg and W. Greiner, 'Nuclear Models' p. p. 66, North Holland Published Co. 1970
(5) L. Seighahn, Editor, 'α-, β- and γ-Ray Spectroscopy', Vol. 2, p, 1599, North Holland Published Co. 1968
(6) C. M. Lederer., I. M. Hollander, I. Perlman, 'Table of Isotopes'. 6th Ed. John Wiley & Sons Inc. 1967

ELECTRICAL RESISTIVITY AND CRYSTALLIZATION OF METALLIC GLASSES $Fe_{84}B_{16}$ and $Fe_{84}B_{13}Si_3$

YEONG DER YAO

Institute of Physics, Academia Sinica
Taipei, Taiwan, 115, R. O. C.
and
SHUI TIEN LIN
Department of Physics, National Cheng Kung University
Tainan, Taiwan, 700, R. O. C.

Abstract

Electrical resistivity (ρ) of metallic glasses $Fe_{84}B_{16}$ and $Fe_{84}B_{13}Si_3$ have been measured as a function of temperature (T) between 78 K and 1010 K. The ρ vs. T curves, obtained with specified warming and cooling rates, show that such curves are sensitive probes of the crystallization process. Within the experimental error, no anomalies in the ρ behavior can be seen at the Curie temperature of each metallic glass.

INTRODUCTION

In recent years, metallic glasses have received considerable experimental and theoretical attention[1-5]. These materials are interesting from both the fundamental and applied viewpoints. Because of various superior mechanical, magnetic and electrical properties, in comparison with those of the crystalline state, metallic glasses form a class of technological important materials. These materials are essentially metastable substances. Therefore, each metallic glass should possesses a specific lifetime at a particular temperature. Obviously, it is very important to understand the lifetimes, stability and crystallization etc. of metallic glasses.

On physical grounds it can be expected that the electrical resistivity (ρ) is a sensitive property to structural changes. Specifically, at the crystallization temperature (T_x) the quantity ρ decreases drastically and exhibits specific characteristics which can be useful for understanding the crystallization processes. In this paper we report our investigation between 78 and 1010 K on two ferromagnetic metallic glasses ($Fe_{84}B_{16}$ and $Fe_{84}B_{13}Si_3$).

GLASSY STATE AND CRYSTALLIZATION

In principle, a liquid, when cooled either crystallizes or becomes a glass below its melting temperature (Tm). The structure and physical properties of the glassy state below the glass temperature (Tg) depend on previous thermal history. One particularly important aspect is the cooling rate used for the preparation of the material which can cause structural relaxation effects[6] when

the glassy material is heated towards Tg. Therefore, the preparation of amorphous metallic materials is extremely important for the subsequent studies of their properties.

Upon crystallization the internal energy (E), the viscosity (η), and the specific volume (v) change discontinuously while these properties change rapidly but continuously with the temperature if the crystallization is bypassed. Associated with this transition, certain other properties, such as the specific heat, electrical resistivity etc. also change dramatically.

Details of crystallization, such as temperature and time dependences, microstructures, their stability and transformation, etc., have not been extensively and completely studied. Thus, it is obvious that a systematic investigation on well-selected glassy systems are definitely needed.

EXPERIMENTAL RESULT AND DISCUSSION

We would like to start our electrical resistivity studies on metallic glasses by measuring the electrical resistivity of $Fe_{84}B_{16}$ and $Fe_{84}B_{13}Si_3$ between 78 °K and 1010 °K. Our results and their significance are presented below.

Ribbon samples of $Fe_{84}B_{16}$ and $Fe_{84}B_{13}Si_3$ were prepared by Prof. Lin during his visiting in University of Pennsylvania (U.S.A.) recently. Electrical resistivity of ribbons of $Fe_{84}B_{16}$ and $Fe_{84}B_{13}Si_3$ was measured using the facility described before[7]. These two samples were mounted together on a sample holder for the resistivity measurements. The behavior of the electrical resistivity of $Fe_{84}B_{16}$ and $Fe_{84}B_{13}Si_3$ as a function of temperature between 78 and 1010 °K is shown in Fig. 1. The rate of temperature increased from 78 to 300 °K and from 300 to 500 °K was roughly 2 K/min. Between 500 and 800 °K the temperature was increased roughly with the rate of 1 K/min. Above 800 °K the temperature increasing rate changed to roughly 2 K/min again.

The crystallization in $Fe_{84}B_{16}$ starts at about 625 °K at which ρ begins to decrease with increasing T. The crystallization processes is characterized by a single and sharp ρ drop of 42 $\mu\Omega$cm which terminates at about 700 °K. The crystallization process in $Fe_{84}B_{13}Si_3$ starts at about 610 °K. Above this temperature ρ drops rapidly with increasing T. The size of the ρ drop, which terminates at about 720 °K, is 43 $\mu\Omega$cm. Near the temperature of 751 °K, a second crystallization process seems to occur by a sharp ρ drop of 11 $\mu\Omega$cm which terminates at about 770 °K. When temperatures are further increased, ρ continues to increase. After reaching approximately 1010 °K, temperatures were decreased with a rate roughly about 2.5 K/min down to 300 °K. The ρ data in this region show typical behavior of a crystalline material.

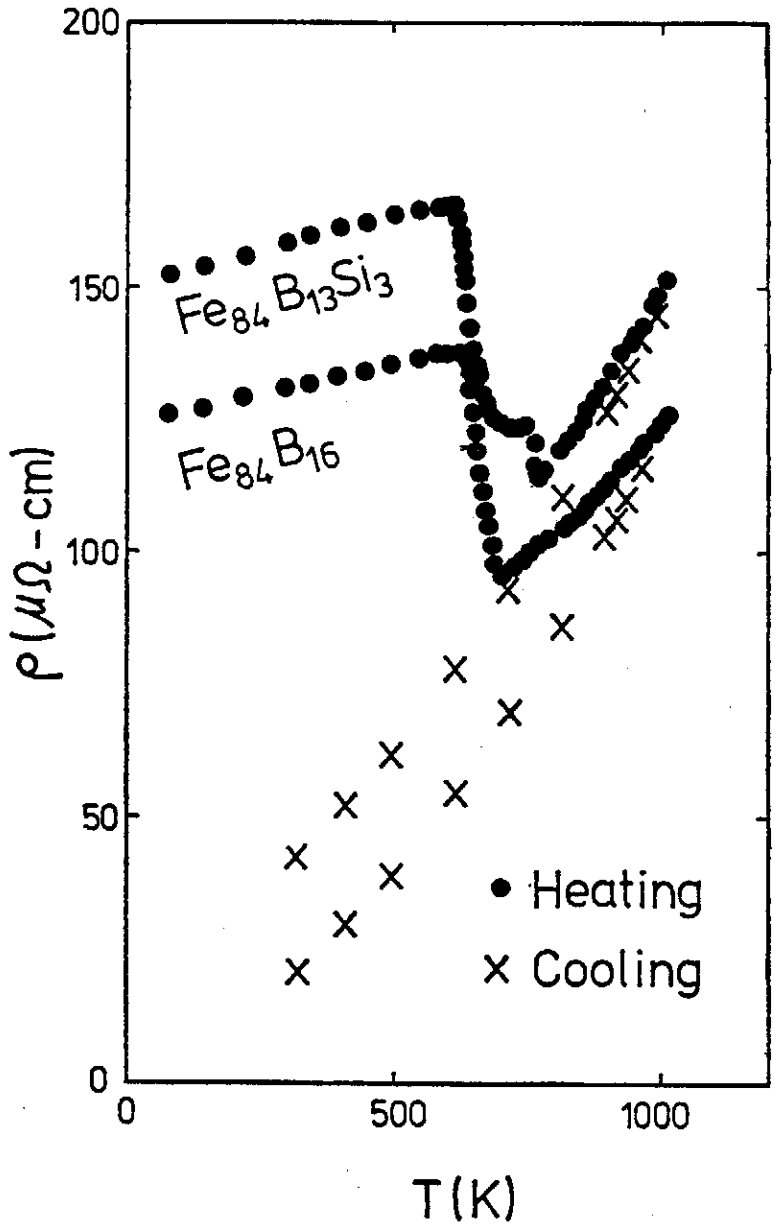

FIG. 1. Electrical resistivity of $Fe_{84}B_{16}$ and $Fe_{84}B_{13}Si_3$ between 78 and 1010 K.

According to the DSC studys[6] of these samples with a heating rate of 20 K/min, there are two crystallization processes for both $Fe_{84}B_{16}$ and $Fe_{84}B_{13}Si_3$. In $Fe_{84}B_{16}$, the first crystallization temperature is 675 °K; and the second crystallization occurs at 731 °K. For $Fe_{84}B_{13}Si_3$, the first crystallization starts at 678 °K and the second appears at 793 °K. The second crystallization process of $Fe_{84}B_{16}$ did not shown up in the resistivity measurement. This may be explained by either one of the following two statements: 1, the metastable phase in metallic glass may be absent if slow heating rates are used. 2, the

two crystallization processes of $Fe_{84}B_{16}$ are too close to distinguish by the electrical resistivity technique. Further experimental results are definitely needed for clarifying these arguments. It is clear that, in general, the transition from the glassy state to the crystalline state is a complicated process. It may lead to a fine grained crystalline but compositionally homogeneous body or, by phase separation, to a variety of two or more phase structures. For example, the crystallization processes of $Fe_{80}B_{20}$ reported by Chien and Hasegawa[9] are complex. After crystallization using heating rate of 20 K/min, $Fe_{80}B_{20}$ is transformed predominantly into Fe_3B. This is a postulated compound because of its structural instability. At higher temperatures Fe_3B phase completely disappears, and Fe_2B and α-Fe are the resultant equilibrium crystalline phases.

The above data clearly indicate that the glass temperature (Tg) of a metallic glass can be approached experimentally from the amorphous side by using very fast heating rates. However, if slower heating is used, an amorphous material will crystallize at some temperature (Tx) which is lower than Tg.

It is obvious from Fig. 1 that the presence of 3 at. % Si increases the value of the electrical resistivity at room temperature by about 27 $\mu\Omega$m at amorphous state and 21 $\mu\Omega$cm at crystalline state; and decreases the crystallization temperature by about 15K.

According to Lin[8] the Curie temperature (Tc) of $Fe_{84}B_{16}$ is 585 °K; Tc of $Fe_{84}B_{13}Si_3$ is 572 °K. However, our electrical resistivity data shown, at least within experimental error, no anomalous behavior in the ρ vs T curve which could be associated with the ferromagnetic-paramagnetic transition. It appears that this behavior may be typical for all amorphous materials.

In summary, our experimental data clearly show that the electrical resistivity can serve as a very sensitive probe for studies of crystallization in amorphous materials. Further systematic investigations on these glassy systems are now in progress in our laboratories and will be reported elsewhile.

Acknowledgement: The authors are grateful to the National Science Council of the Republic of China for the financial support of this research work.

REFERENCES

1. A. K. Sinha, Phys. Rev. B. **1**, 4541 (1970)
2. E. Hauser, R. J. Zirke, J. Tauc, J. J. Hauser and S. R. Nagel, Phys. Rev. Lett. **40**, 1733 (1978)
3. H. S. Chen, J. Appl. Phys. **49**, 4595 (1978)
4. J. C. Phillips, Phys. Rev. Lett. **42**, 1151 (1979)
5. T. Kemeny, I. Vincze, B. Fogarassy and S. Arajs, Phys. Rev. B **20**, 476 (1979)
6. H. S. Chen, Mat. Sci. Eng. **25**, 59 (1976)
7. Y. D. Yao and J. H. Tsai, Chinese J. Phys. **16**, 189 (1978)

8. S. T. Lin, Private communication.
9. C. L. Chien and R. Hasegawa, "Mösbauer Study of a Glassy $Fe_{80}B_{20}$ Ferromagnet", in *Amorphous Magnetism II*, edited by R. A. Levy and R. Hasegawa (Plenum Publishing Company, New York, 1977), p. 289

AN EXPERIMENTAL STUDY ON ANTHRACENE

Y. D. YAO, C. CHIANG and C. Y. YOUNG

Institute of Physics, Academia Sinica
Nankang, Taipei, 115 Taiwan, R. O. C.

Abstract

Anthracene thin films were prepared by dissolving anthracene in proper solvent. We intend to study the switching phenomenon of anthracene thin film prepared by this method and comparing it with that prepared by evaporation method reported by Elsharkawi and Kao[1]. The metal-insulator transition has not been found in our samples yet. More samples will be prepared. Experiments on these will be reported later.

Carbon chain systems of the polyene type have attracted great interest recently because of the possibility of occurrence of phenomenon such as metal-insulator transition etc.. The electric conductivity of carbon chain systems can be changed many orders of magnitude either by doping with diverse substances[2] or by selecting proper film thickness[1]. Anthracene is one of the carbon chain systems which has been extensively studied for fluorescence and switching phenomena (1, 3, 4, 5).

In this short note, we reported further study about the anthracene thin film prepared by dissolving anthracene in proper solvent. We intend to study the switching phenomenon of anthracene film prepared by evaporation method reported by Elsharkawi and Kao[1] using this method. This method seems to be more convenient than the evaporation method. According to Elsharkawi and Kao, anthracene film was prepared by vacuum sublimation of high-purity anthracene crystal at 70°C, and the temperature of the substrate had to be kept at-120°C during sublimation. After sublimation the film was kept in the chamber filled with dry nitrogen at a pressure of 5×10^{-3} torr to avoid volatilization when it was annealed slowly from -120°C to room temperature. In the present study, benzene was chosen to be the proper solvent. The solubility of anthracene in benzene is 5g per 100g benzene. The vapor pressure of benzene at 20°C is abount 75 mmHg. For benzene, the boiling temperature is about 80°C; and the melting temperature is about 5.5°C. However, for anthracene, the boiling temperature is about 350°C; and the melting temperature is about 215°C. The above physical properties show that the solution of anthracene in benzene can be used to prepare anthracene thin films at room temperature.

High-purity anthracene (standard for elementary analysis) was purchased from E. Merck Co. (Germany). About twenty samples were prepared by the solution of anthracene in pure benzene. The solution was dropped onto a flat

glass substrate on which several gold or copper stripes of 0.2mm in width and about 5 mm in separation had already been fixed to form the base electrodes. Let the benzene solvent be vaporized and repeated this procedure several times, then another gold or copper striper were mounted on the top of the sample as the electrodes. The the electrodes stripes and the base electrodes stripes are perpendicular to each other. Finally, the solution was again dropped onto the top of the sample for several times for the purpose of making good contacts. The film thickness is about 0.1 mm measured with an accurate vernier. A voltage/current reference source (North Hill, Model TC-100.2 BR) was used as a constant voltage supplier. The current through the samples was measured by an electrometer (Keithley Instruments, Model 610C). Our experimental result is presented below.

Figure 1 shows the typical D.C. current-voltage (I-V) characteristics of our samples. We did not observe a sharp increase in current with the applied voltage between 0 and 100 volts. This means that the switching and memory phenomena have not been observed in our samples. The electrical resistivity calculated from our experimental data is roughly in the order of $10^9\Omega$-cm which is definitely in the insulator region. The next step we plan to do is to prepare more samples with thickness less than 5 μm under the technique described in this note, and to extend the voltages to higher values. Experiments on these will be reported later.

REFERENCES

1. A. R. Elsharkwai and K. C. Kao, J. Phys. Chem. Solids **38**, 95 (1977).
2. C. K. Chiang, C. R. Fincher, Y. W. Park, A. J. Heepar, H. Shirakawa, E. J. Louis, S. C. Gau and A. G. MacDiarmid, Phys. Rev. Lett. **39**, 1098 (1977).
3. W. Helfrich and W. G. Schnider, Phys. Rev. Lett. **14**, 229 (1965).
4. W. Hwang and K. C. Kao, J. Chem. Phys. **58**, 3521 (1973).
5. C. Chiang, Ann. Rep. Inst. Phys. Acad. Sin. **8**, 61 (1978).

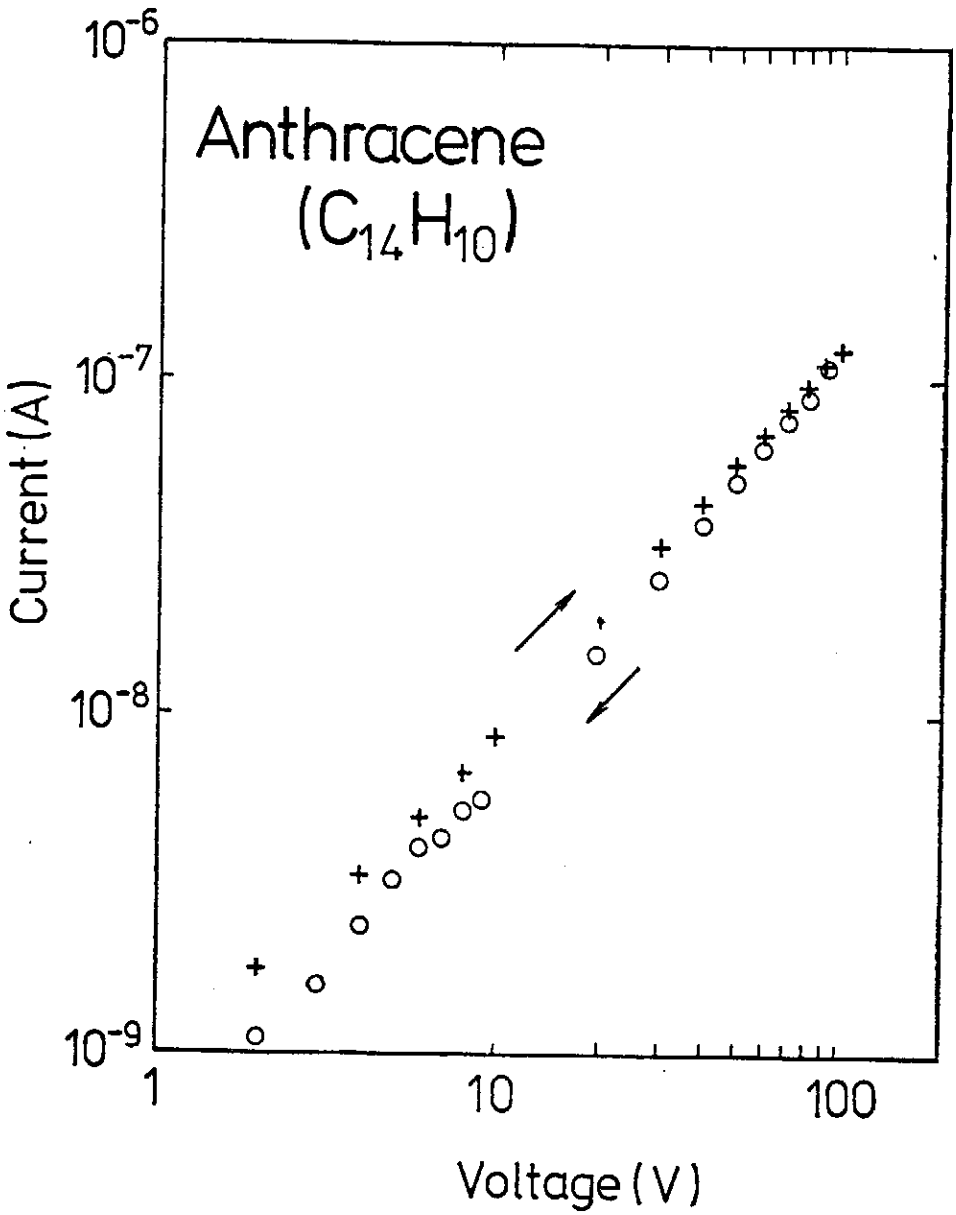

FIG. 1. Typical D. C. current-voltage characteristics at room temperature for our anthracene film samples with thickness around 0. 1 mm.

ANISOTROPY OF MAGNETORESISTIVITY OF NI-RICH NI-CU AND NI-SI ALLOYS

YEONG DER YAO

Institute of Physics, Academia Sinica
Nankang, Taipei, Taiwan, R. O. C.

Abstract

Measurements are reported on the anisotropy of the magnetoresistivity of Ni-rich Ni-Cu and Ni-Si alloys as a function of applied magnetic fields (up to 12 KG) at liquid nitrogen temperature. Our results imply that Smit spin mixing type of mechanism is the dominant one in our Ni-Cu and Ni-Si alloy systems

I. INTRODUCTION

The galvanomagnetic phenomena occur whenever a conductor carrying an electric current is placed in a magnetic field; and these effects have been extensively studied since quite a long time ago[1-4]. Recently, the interest in these effects has been renewed[5] because of the practical applications of bubble memory read outs and tape readers etc.. Magnetoresistance in magnetic alloys has been the subject of current interests[6-10].

The resistivity anisotropy is characteristic of ferromagnetic metals and does not occur in non-magnetic metals. Generally, two extreme situations can be distinguished for the resistivity anisotropy; i.e. the saturation magnetization of the ferromagnetic metal is either parallel or perpendicular to the electrical current. Such an anisotropy is generally recognized as originating in spin-orbit coupling effects and various types of mechanism have been proposed to explain the relation between the spin-orbit coupling.

In this paper, we present a study of the anisotropy of the magneto-resistivity of a series of Ni-rich Ni-Cu and Ni-Si alloys in magnetic fields up to 12 K Gauss at the liquid nitrogen temperature.

II. EXPERIMENTAL CONSIDERATION

One pure nickel, two nickel-copper alloys containing 5.0 and 10.0 wt.% copper and three nickel-silicon alloys containing 0.2, 0.73 and 1.66 wt.% silicon were prepared by a laboratory arc melter. Both nickel (99.999%) and copper (99.999%) used for these alloys was purchased from Electronic Space Products. Silicon used for this study is also 99.999% pure. After repeated melting the ingots were sealed in silica tubes under about 1/5 atmosphere pressure of hilium

gas at room temperature, annealed at 900 °C for several days and then furnace cooled. From these ingots, samples in the form of rectangular parallelepipeds were cut by hand using a diamond saw. The surfaces of the samples were polished using files and sandpapers. The electrical resistivity of these samples was determined using the conventional four-probe technique. A seven inches laboratory electromagnet (O. S. Walker Company) was used to produce the magnetic fields. The magnetic field was applied parallelly as well as transversally to the measuring current of the samples.

III. RESULTS AND DISCUSSION

For a fully magnetized ferromagnetic polycrystalline alloys, the electrical resistivity can be written as

$$\rho(\mathrm{B},\ \theta)=\bar{\rho}_0+(\cos^2\theta-\tfrac{1}{3})\,\overline{\Delta\rho}+\delta\rho\ (\mathrm{B},\ \theta) \qquad (1)$$

where θ is the angle between the current direction and the macroscopic magnetization of the sample. The last term represents the ordinary Lorentz force magnetoresistivity; the second term is due to the spontaneous anisotropy of resistivity, $\overline{\Delta\rho}$; the first term is due to all other effects. To separate the terms experimentally, the sample resistivity is measured as a function of applied magnetic field for $\theta=0$ and $\pi/2$. Then, the curves for $\rho_{11}(\mathrm{B})$ and $\rho_{\perp}(\mathrm{B})$ above technical saturation are extrapolated back to $\mathrm{B}=0$, eleminating the Lorentz term. We define the resistivity anisotropy ratio as

$$\frac{\overline{\Delta\rho}}{\bar{\rho}}=\frac{\rho_{11}(\mathrm{B}\to 0)-\rho_{\perp}(\mathrm{B}\to 0)}{\bar{\rho}} \qquad (2)$$

with $\bar{\rho}=\frac{1}{3}\left[\rho_{11}(\mathrm{B}\to 0)+2\rho_{\perp}(\mathrm{B}\to 0)\right]$

In this study, the electrical resistivities were all measured at liquid nitrogen temperature (78 °K). For the convenience of our experimental process, we let $\Delta\rho=\rho_{\mathrm{H=H}}-\rho_{\mathrm{H=O}}$; this is the difference of the resistivities between applied magnetic field H and zero applied magnetic field. Here, we must note that the value of $\rho_{\mathrm{H=O}}$ depends on the magnetic history of the sample and is generally different from $\bar{\rho}$. Eq. (2) can be rewritten as

$$\frac{\overline{\Delta\rho}}{\bar{\rho}}=\frac{\Delta\rho_{11}(\mathrm{B}\to 0)-\Delta\rho_{\perp}(\mathrm{B}\to 0)}{\bar{\rho}} \qquad (3)$$

Fig. 1 shows the difference of the electrical resistivities between applied magnetic field H and zero applied magnetic field of our Ni-Cu samples containing 0.0, 5.0 and 10.0 wt.% Cu at 78 °K as a function of H for both $\mathrm{H}\,//\,\mathrm{I}$ and $\mathrm{H}\perp\mathrm{I}$, where I is the current through the sample measured. $\Delta\rho$ of Ni-Si samples containing 0.20, 0.73 and 1.66 wt.% Si at 78 °K as a function of H for both

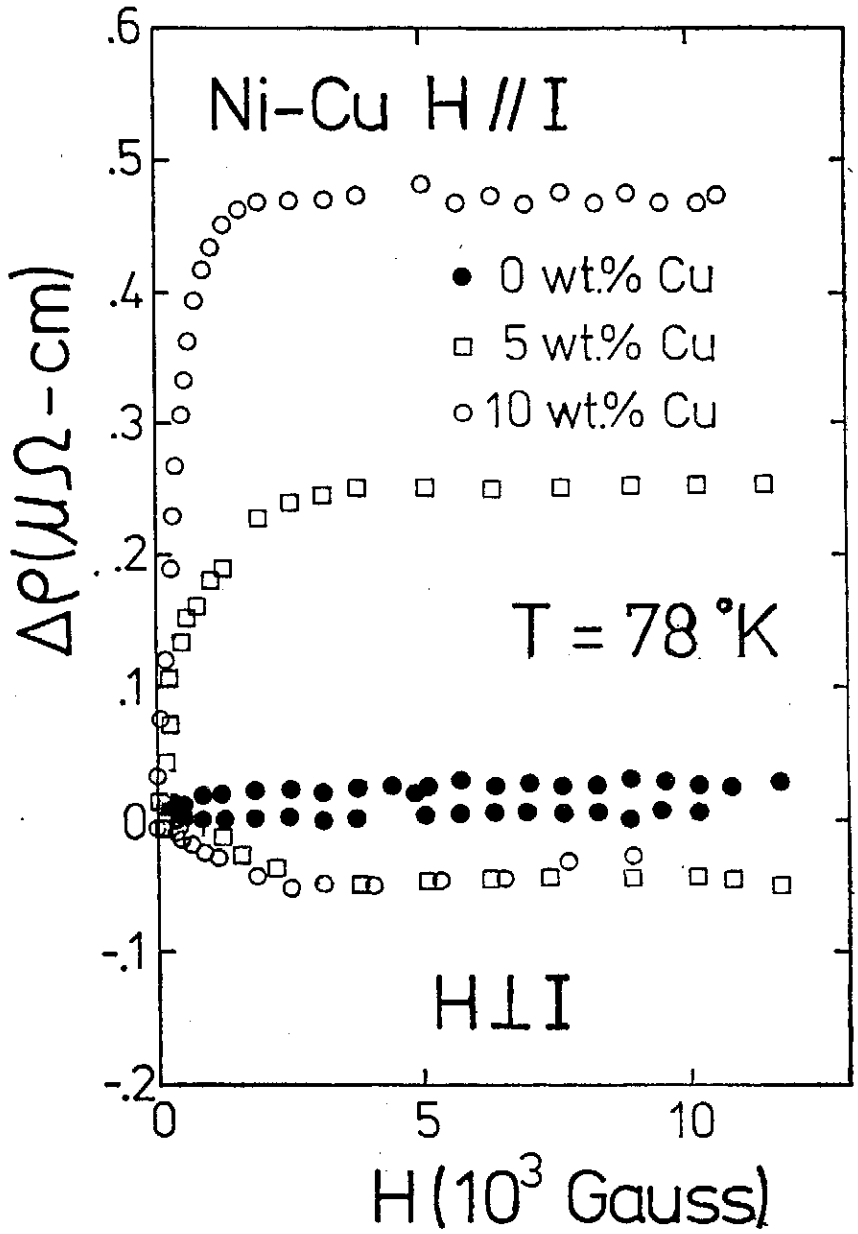

FIG. 1. $\Delta\rho$ of Ni and Ni-Cu alloys as a function of H at 78 °K.

H // I and H $\perp$ I are presented in Fig. 2. From these two figures, we find that $\Delta\rho$ of Ni-Cu samples containing 5.0 and 10.0 wt.% Cu is quite large comparing with that of pure Ni and Ni-Si samples.

Table I shows our experimental values of $\bar{\rho}$, $\overline{\Delta\rho}$ and $\overline{\Delta\rho}/\bar{\rho}$ for all the samples prepared for this study. We know that, in a ferromagnetic alloy, spin up($\uparrow$) and spin down($\downarrow$) electrons (i.e. spin parallel and antiparallel to the magnetization) carry current in parallel and we can define at T=0 specific residual resistivities $\rho_0\uparrow$ and $\rho_0\downarrow$. The ratio $\alpha=\rho_0\downarrow/\rho_0\uparrow$ for many Ni and Fe alloys has

been analysed in terms of a two-current model[5]. According to Dorleijn[5], $\rho_0\downarrow = 3.8$ $\mu\Omega$cm/at.% and $\rho_0\uparrow = 1.3$ $\mu\Omega$cm/at.% for Ni-Cu alloys; $\rho_0\downarrow = 6.4$ $\mu\Omega$cm/at.% and $\rho_0\uparrow = 5.0$ $\mu\Omega$cm/at.% for Ni-Si alloys. Therefore, $\alpha \approx 2.9$ for Ni-Cu alloys and $\alpha \approx 1.3$ for Ni-Si alloys. Roughly speaking, (since the liquid nitrogen temperature is not low enough to show exactly) our data imply that the resistivity anisotropy ratio of our Ni-Cu and Ni-Si alloys is roughly proportional to $(\alpha - 1)$. This means Smit spin mixing type of mechanism[11] is the dominant one in our Ni-Cu and Ni-Si alloy systems. Usually, in alloys where α is less

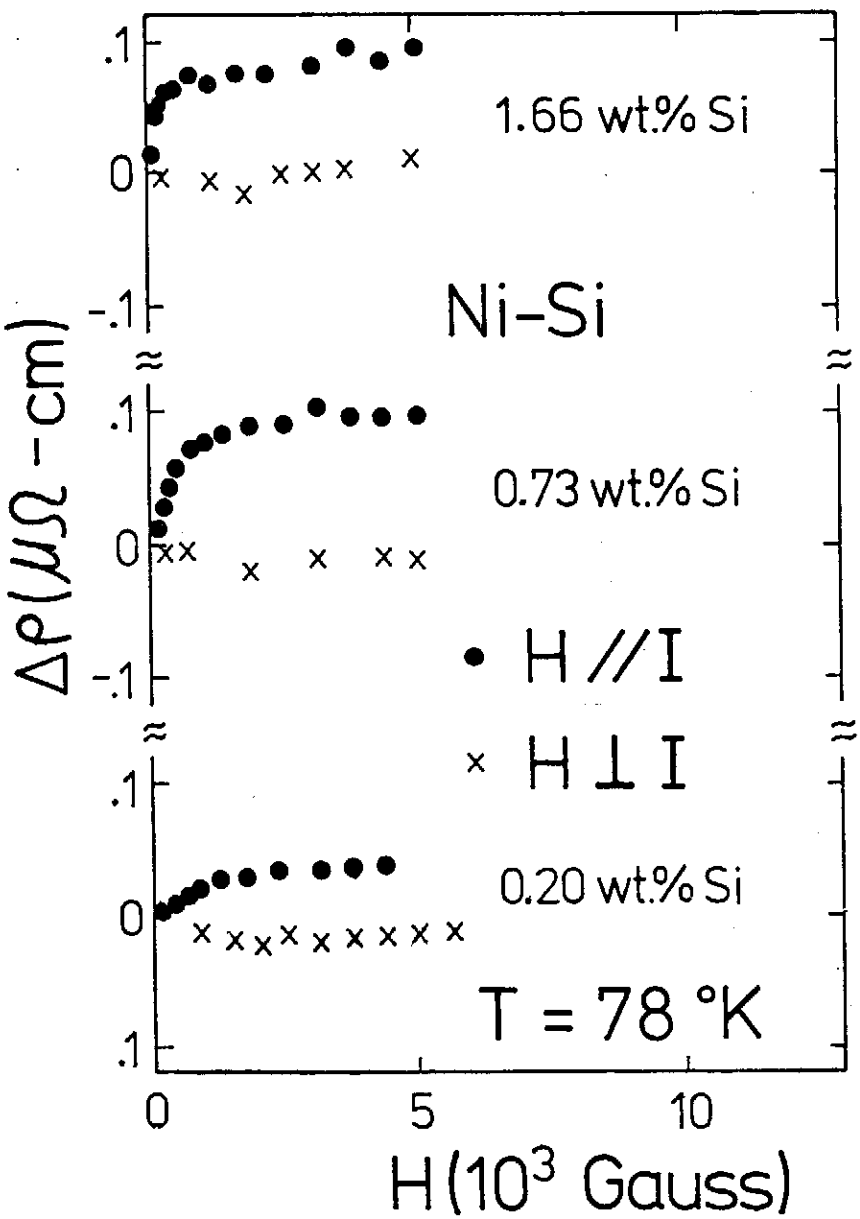

FIG. 2. $\Delta\rho$ of Ni-Si alloys as a function of H at 78 °K.

TABLE I. Experimental values of $\overline{\rho}$, $\overline{\Delta\rho}$ and $\overline{\Delta\rho}/\overline{\rho}$ for Ni-Si and Ni-Cu alloys at 78°K

Alloys	$\overline{\rho}$ ($\mu\Omega$-cm)	$\overline{\Delta\rho}$ ($\mu\Omega$-cm)	$\overline{\Delta\rho}/\overline{\rho}$
Ni	0.77±0.01	0.02±0.02	0.026±0.026
Ni-0.20 wt.% Si	2.10±0.01	0.05±0.02	0.024±0.010
Ni-0.73 wt.% Si	5.30±0.01	0.09±0.02	0.017±0.004
Ni-i.66 wt.% Si	11.08±0.01	0.08±0.02	0.007±0.002
Ni-5.0 wt.% Cu	4.86±0.01	0.29±0.02	0.060±0.004
Ni-10.0 wt.% Cu	8.38±0.01	0.54±0.02	0.064±0.003

Acknowledgement: The author is grateful to the National Science Cuoncil, Republic of China for the financial support of this work. The assistance in laboratory by Mr. W. J. Ueng is greatly appreciated.

than 1, the anisotropy is always quite small and there are always large deviations from the $(\alpha-1)$ rule. These studies for other systems with values of α both greater and less than 1 are now in progress and will be reported later.

REFERENCES

1. J. -P. Jan, Sol. State Phys. Eds. F. Seitz and D. Turnbull (Academic, N. Y. 1957) Vol. 5 p. 1.
2. I. M. Lifshits, J. Phys. Chem. Solids, **44**, 11 (1958).
3. I. M. Lifshits and A. M. Kosevich, J. Phys. Chem. Solids, **4**, 1 (1958)
4. A. C. Beer, *Galvanomagnetic Effects in Semiconductors,* (Academic, N. Y. 1963)
5. J. W. F. Dorleijn, Philips Res. Repts. **31**, 287 (1976)
6. K. Ueda, J. Phys. Soc. Japan **43**, 1497 (1977)
7. T. Fukui, J. Phys. Soc. Japan **45**, 1507 (1978)
8. K. Usami, J. Phys. Soc. Japan **45**, 466 (1978)
9. S. P. McAlister, L. R. Lupton and C. M. Hurd, Solid St. Comm. **25,** 903 (1978)
10. R. N. Ross, D. C. Price and G. Williams, J. Mag. Mag. Mat. **10**, 59 (1979)
11. J. Smit, Physica **16**, 612 (1951)

ANNEALING STUDY IN GLASSY Fe_{84} B_{16}

Y. D. YAO, S. T. LIN* and W. J. UENG

Institute of Phosics, Academia Sinica
Nankang, Taipei, Taiwan, R. O. C.

Abstract

Metallic glasses are essentially metastable substances. It can be expected that the lifetime will be a function of temperature since the crystallization is a thermally activated process. A short period of time of annealing effect for glassy Fe_{84} B_{16} is reported here. This is just a beginning of our systematic investigations about the lifetime of metallic glasses.

Metallic glasses are essentially metastable substances. It can be expected that the lifetime will be a function of temperature since the crystallization is a thermally activated process. Usually, the end of life of an amorphous material is defined as the onset of crystallization. The available data[1-7] of the time for start of crystallization as a function of temperature are shown in Fig. 1. These data clearly define the maximum fabrication and operating time-temperature exposures. For example, the crystallization of $Fe_{80}B_{20}$ will start (a linear Arrhenius extrapolation is assumed) at 175°C after 550 years, or at 200°C after 25 years.

The electrical resistivity (ρ) can serve as a very sensitive probe for studies of crystallization in amorphous materials. Starting from this short note, we will continue to investigate the lifetime of the metallic glasses by means of the electrical resistivity technique.

The equipments used for this study were constructed by Dr. Yao. Stripes of amorphous $Fe_{84}B_{16}$ were sealed into the silica tubes which can be either evacuated for filled with helium gas. After being evacuated, the silica tubes is always filled with helium gas kept at a pressure of approximate one atmosphere for all the temperatures. This is to improve the thermal coupling between the stripes and their environments. Each sample was annealed at selected temperature for specific periods of time. The periods of time are additive for each specific temperature of annealing. After each aging, the electrical resistivity was measured at room temperature.. Fig. 2 and Fig. 3 are results of our data. ρ_0 is the electrical resistivity at room temperature before annaling. The normalized electrical resistivity (ρ/ρ_0) as a function of annealing time at different annealing temperatures is shown in Fig. 2. Except the annealing temperature at approxi-

* Present address: Department of Physics, National Cheng Kung University, Tainan, Taiwan, 700, R. O. C.

mate 400°C, the electrical resistivity did not change manifestly within 30 minutes. Fig. 3 shows the normalized electrical resistivity as a function of annealing time within 30 minutes at approximate 400°C. After 30 minutes of annealing, the normalized electrical resistivity decrease approximately 35%. Further study of these annealing effects are in progress in our laboratory; and results of systematic investigations about the lifetime of metallic glasses will be reported lator.

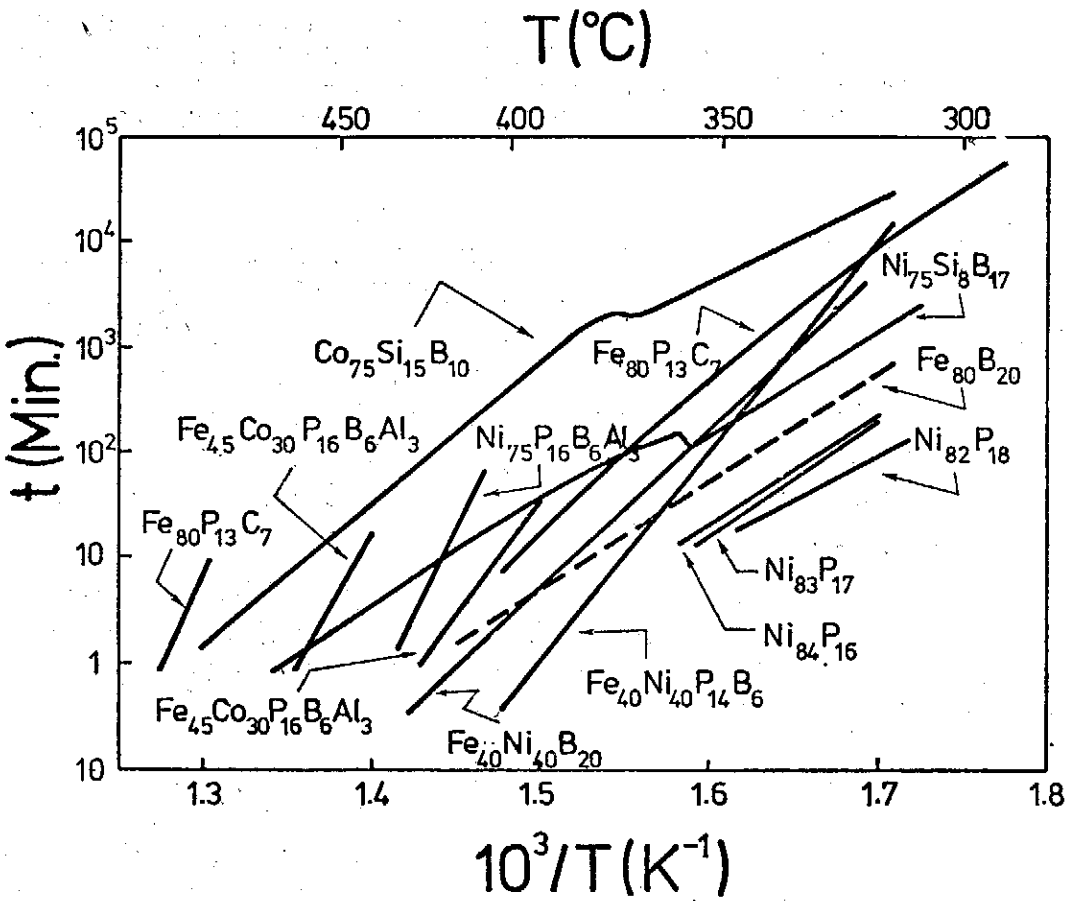

FIG. 1. Time for start of crystallization as a function of temperature.

REFERENCES

1. T. Masumoto, Y. Waseda, H. Kumura and A. Inoue, Sci. Repts. Res. Inst. Tohoku Univ. **A26**, 21 (1970)
2. T. Masumoto and R. Maddin, Mat. Sci. Eng. **19**, 1 (1975)
3. W. G. Clements and B. Cantor, Proc. Sec. Int. Conf. on Rapidly Quenched Metals, Section I, eds. N. J. Grant and B. C. Giessen (MIT Press, Cambridge, 1976) p. 267.
4. E. Caleman, Mat. Sci. Eng. **23**, 161 (1976)
5. F. E. Luborsky, Mat. Sci. Eng. **28**, 139 (1977)
6. M. G. Scott and P. Ramachandrarao, Mat. Sci. Eng. **29**, 137 (1977)
7. F. E. Luborsky, P. G. Frischmann and L. A. Johnson, J. Mag. Mag. Mat. **8**, 318 (1978).

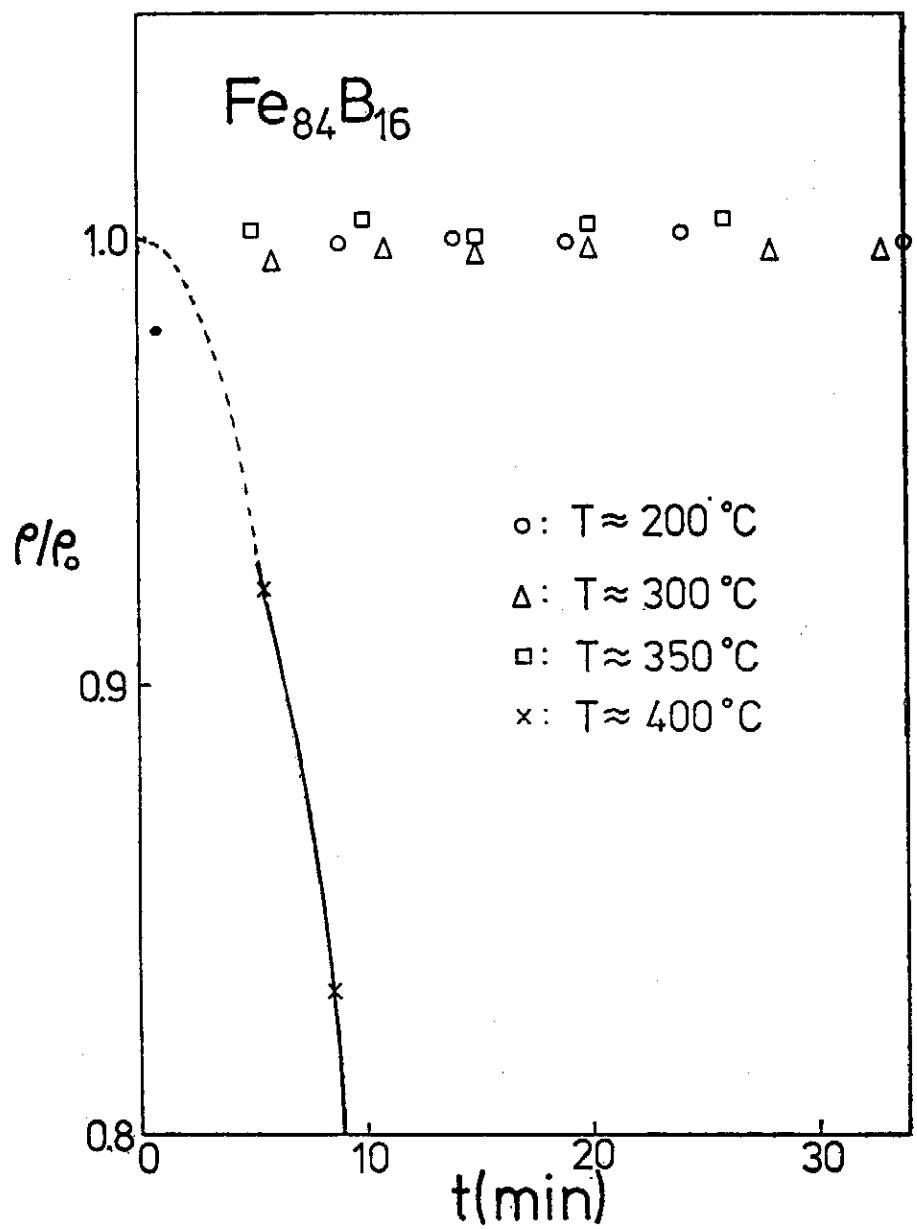

FIG. 2. Normalized electrical resistivity of Fe_{84} B_{16} as a function of annealing time. o: T ≈ 200 °C, Δ: T ≈ 300 °C, □: T ≈ 350 °C and ×: T ≈ 400 °C.

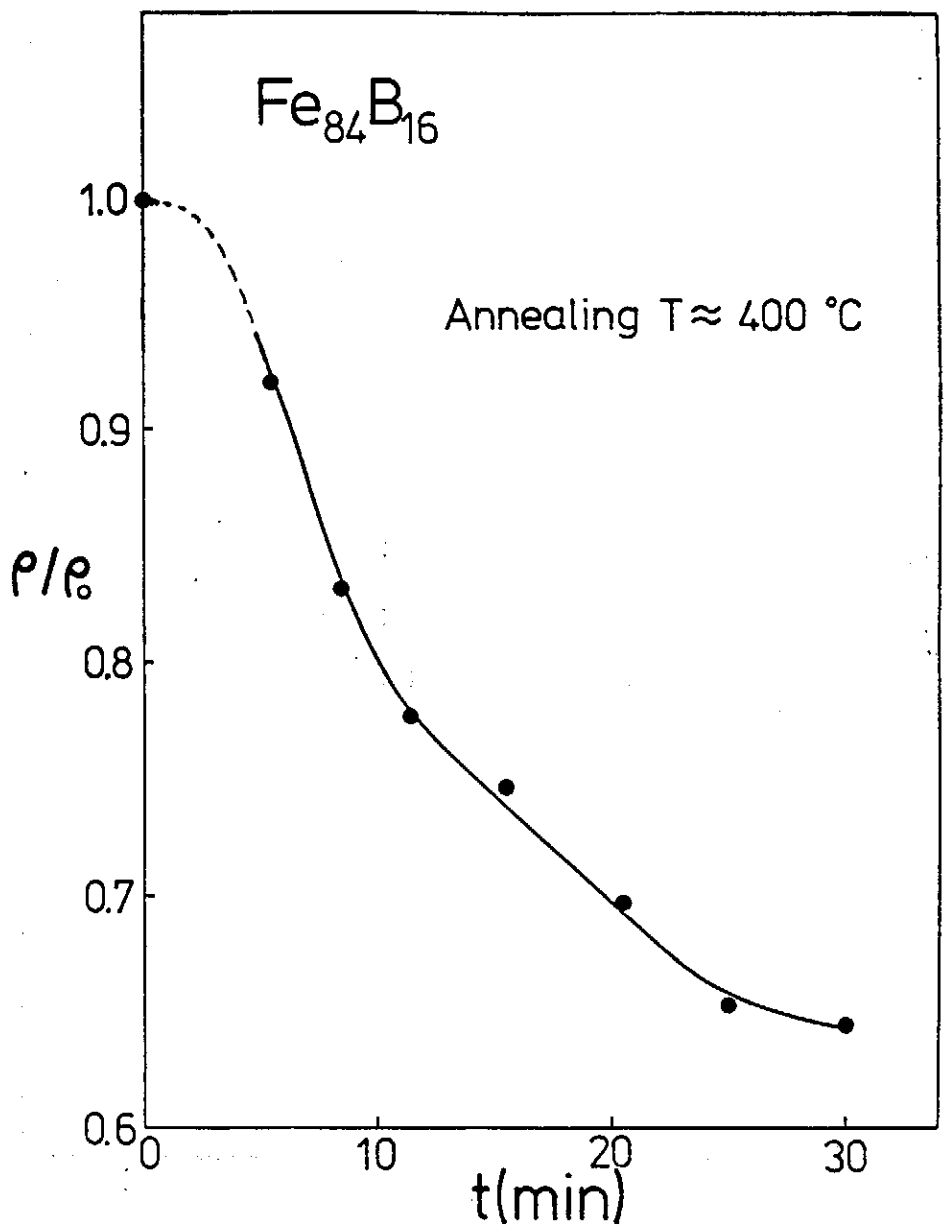

FIG. 3. Normalized electrical resistivity of $Fe_{84}B_{16}$ as a function of annealing time at 400 °C.

MAGNETIC PHASE TRANSITION IN NI-RICH NI-SI ALLOYS

JIN NAN LIN

Kuen Shan Institute of Technology, Tainan, Taiwan. R. O. C.

YEONG DER YAO

Institute of Physics, Academia Sinica, Taipei, Taiwan, R. O. C.

Abstract

The electrical resistivity, ρ, of a set of Ni-Si alloys containing 0.00, 0.20, 0.73, and 1.66 wt.% Si has been studied as a function of the absolute temperature, T, between 300 and 700 °K. Our experimental data show that each of the ρ vs. T curves exhibits a well-defined knee in the critical region of the magnetic phase transition. The concentration dependence of the Curie temperatures of these Ni-Si alloys has been determined from ($d\rho/dT$) vs. T etc. analyses.

I. INTRODUCTION

During recent years there has been intense interest in the behavior of various physical systems[1] in the vicinity of the phase transitions. It is well known that electrical resistivity measurements on a ferromagnetic system provide useful information about their magnetic phase transition etc.[2] According to Fisher and Langer[3], Richard and Geldart[4], the magnetic component of $d\rho/dT$ above the Curie temperature, T_c, should vary like the magnetic specific heat. This means that it is proportional to $\varepsilon^{-\alpha}$, where $\varepsilon = |T-T_c|/T_c$ and α is the specific heat critical exponent. Below T_c, $d\rho/dT$ should be proportional to $\varepsilon^{2\beta-1}$, where β is the critical index for the spontaneous magnetization. The divergence is positive both above and below T_c. The Curie temperature occurs at which $d\rho/dT$ diverges and there is no cusp in the ρ vs. T curve. Recently Su et al[5-8] basing on the itinerant model and band calculation of pure nickel, show that $d\rho/dT$ is divergent linearly and positively below T_c.

In this paper, we present a study of the electrical resistivity of nickel-rich nickel-silicon alloys containing 0.00, 0.20, 0.73 and 1.66 wt.% Si as a function of temperature between 300°K and 700 °K, and try to get further information about ferromagnetic alloy systems. Our experimental procedure and results as well as their significance are presented below.

II. EXPERIMENTAL PROCEDURE

The nickel-silicon alloys were prepared by means of a laboratory arc melter which was construced by Dr. Yao. It is a water-cooled type melter. A commercial rectified D.C. welding unit (the maximum power comsumption is 12 KW) is used as the electrical power suply.

Before melting, the chamber has to be cleaned and vacuum pumped. Due to the limited amount of metal available and the limited size of the copper base of the arc melter, the total weight of one batch of the material to be melted is about 5 to 7 grams. Each ingot was turned over and remelted two or three times to ensure homogeneous distribution of the impurity solute. In most cases the weight losses assured about 5% accuracy of the nominal impurity concentration.

After melting, the ingots were sealed in quartz tubes under 1/5 atmosphere pressure of helium gas at room temperature and annealed at 900°C for three days. From these ingots, samples in the form of rectangular parallelepipeds were cut by hand using a diamond saw. The surfaces of the samples were polished using files and sandpapers. Typical sample dimensions were roughly $2 \times 3 \times 20$ (units in mm).

Four nickel-silicon alloy samples containing 0.00, 0.20, 0.73 and 1.66 wt.% silicon were prepared for this study. Four copper electrodes were lightly spot-welded to each sample. The center two copper electrodes are the potential leads; the other two are the current leads. The width, thickness and distance between the potential leads were determined by means of a very accurate vernier caliper.

The equipments for the electrical resistivity measurements include the high vacuum system, the high-accurate temperature control system and the precision potentiometer system with necessary accessories etc. etc.. Those experimental equipments had been already set up by Dr. Yao before this study. The electrical resistivity of the above four Ni-Si samples was determined using the conventional four-probe technique. Temperatures between 300°K and 700°K were achieved achieved in a Marshall vacum furnace.

III. RESULTS AND DISCUSSION

Fig. 1 shows the values of ρ of our Ni-Si alloys as a function of Si content at 78°K. The increase in the electrical resistivity is about 7.2 $\mu\Omega$-cm per wt.% of Si at 78°K. This plot confirm the expected good quality of the alloys prepared by the methods described above. Fig. 2 shows the electrical resistivity of our Ni-Si alloys containing 0.00, 0.20, 0.73 and 1.66 wt.% Si between 300 and 700°K. It is obvious that the ρ vs. T curve undergoes an abrupt slope change which results from the ferromagnetic-paramagnetic phase transitions.

Fig. 3 presents the temperature dependece of the deviation from Matthiessen's rule, DMR or $\Delta\rho$, for three nickel-silicon alloys containing 0.20, 0.73 and 1.66 wt.% silicon. Values of $\Delta\rho$ were obtained by subtracting the electrical resistivity of the pure Ni from the electrical resistivity of the particular Ni.Si alloy. Mathematically, let:

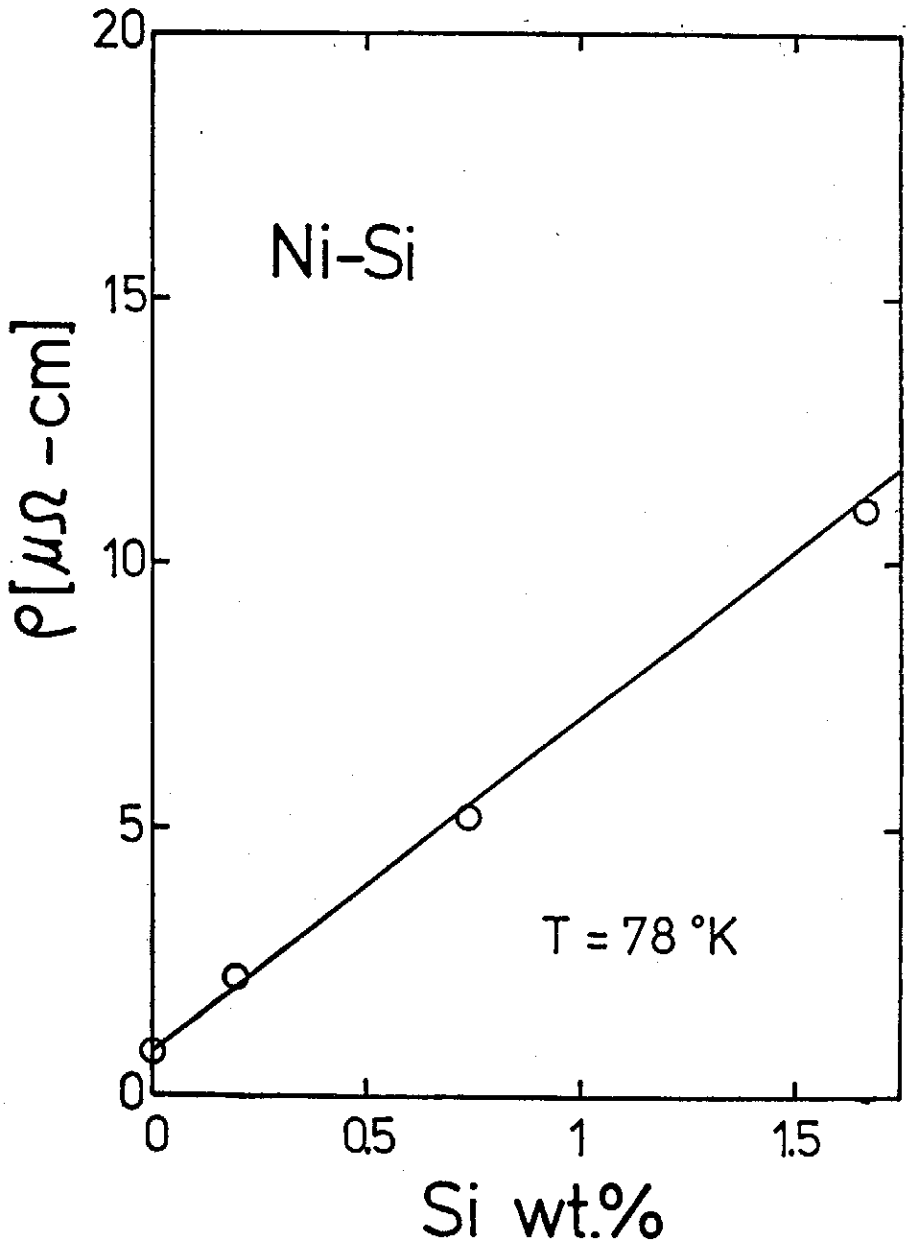

FIG. 1. Electrical resistivity of Ni-Si alloys as a function of silicon concentration at 78 °K.

$$\Delta\rho'(T_c) = \left[\frac{d\Delta\rho(T)}{dT}\right]_{T=T_c} = \lim_{\delta T \to 0} \frac{\Delta\rho(T_c+\delta T)-\Delta\rho(T_c)}{\delta T} \tag{1}$$

$$\Delta\rho_+'(T_c) = \lim_{\delta T \to 0^+} \frac{\Delta\rho(T_c+\delta T)-\Delta\rho(T_c)}{\delta T} \tag{2}$$

$$\Delta\rho_-'(T_c) = \lim_{\delta T \to 0^-} \frac{\Delta\rho(T_c+\delta T)-\Delta\rho(T_c)}{\delta T} \tag{3}$$

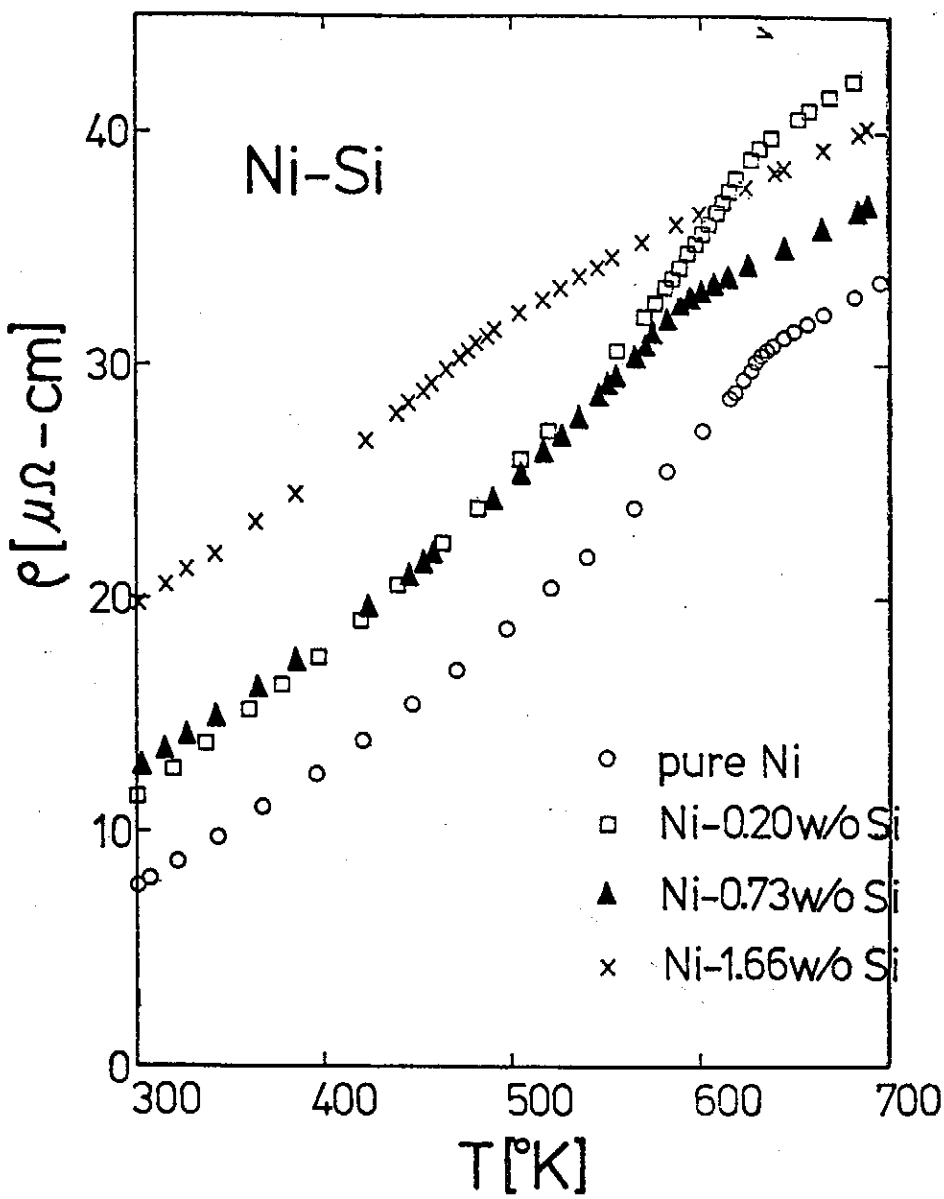

FIG. 2. Electrical resistivity of Ni-Si alloys as a function of temperature between 300 °K and 700 °K.

These three functions are called, respectively, the derivative, the derivative on the right, and the derivative on the left of $\Delta\rho(T)$ at $T=T_c$. And $\Delta\rho'$ (Tc) does not exist means that $\Delta\rho'_+(T_c) \neq \Delta\rho'_-(T_c)$. From figure 3, $\Delta\rho$ exhibits that $(d\Delta\rho/dT)$ does not exist at T_c. The arrows in figure 3 indicate T_c of the particular alloy and the crossed arrow shows the value of T_c for pure nickel. Below T_c of the particular alloy, $\Delta\rho$ increases smoothly with increasing T. Above T_c of the particular alloys, $\Delta\rho$ changes slowly and smoothly with increasing T. However, between T_c of pure nickel and T_c of the particular alloy, $\Delta\rho$ decreases much faster

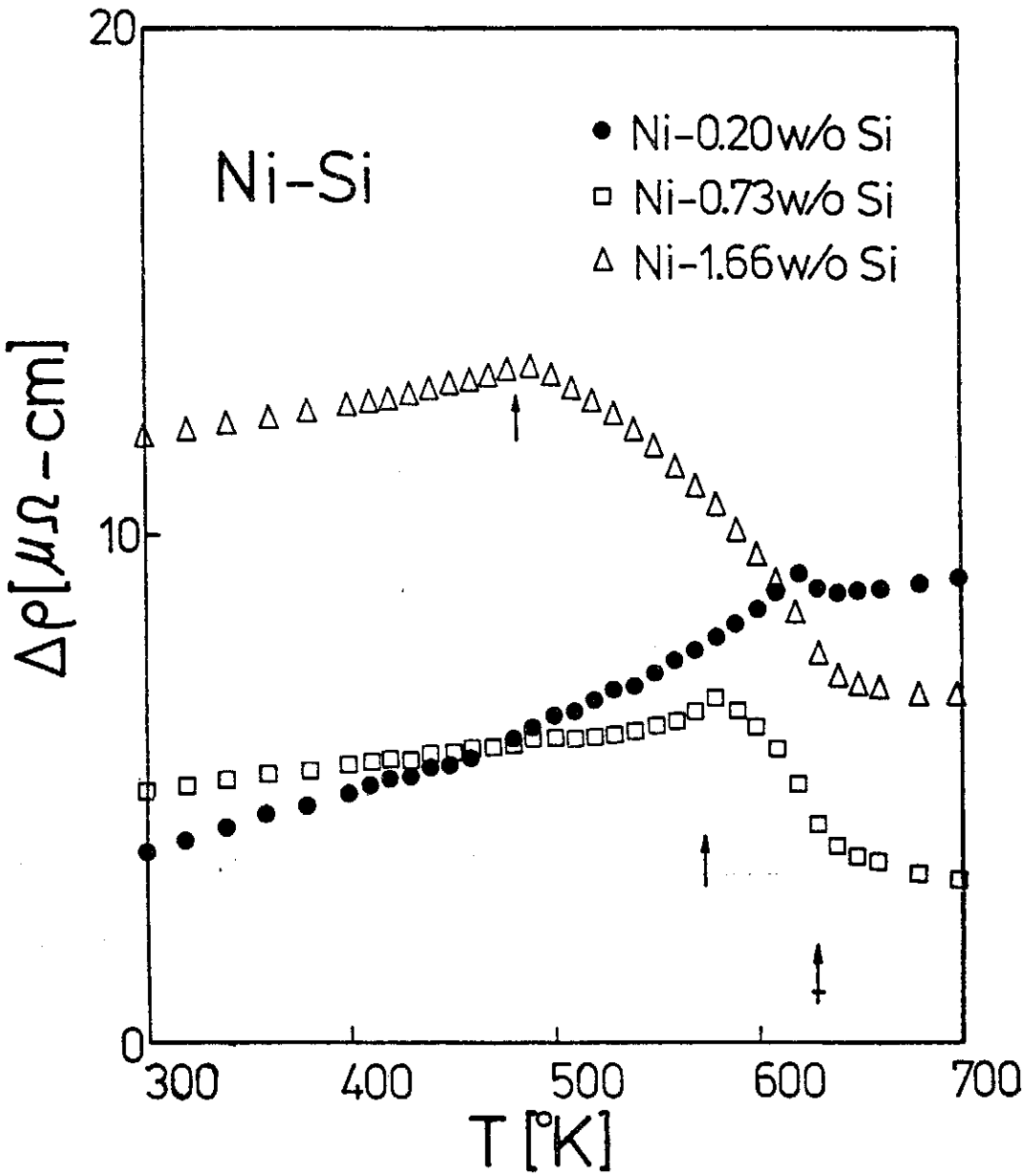

FIG. 3. $\Delta\rho(T)$ as a function of T for Ni-Si alloys between 300 °K and 700 °K.

with increasing T than that above T_c of pure nickel. It is clear that $\Delta\rho$ is continuous through the Curie temperatures, even $\Delta\rho_+'(T_c) \neq \Delta\rho_-'(T_c)$.

Fig. 4 shows the temperature dependence of the temperature derivative of the DMR, $d\Delta\rho/dT$, of our nickel-silicon alloy system. For each curve, $d\Delta\rho/dT$ was obtained from the $\Delta\rho$ (T) data by point-by-point differentiation using a computer. On each curve, there are two points that $\Delta\rho_+'(T_c) \neq \Delta\rho_-'(T_c)$, one point is the Curie temperature of the particular Ni-Si alloy and the other is the Curie temperature of pure Ni. According to the theoretical analyses[3-8], $d\Delta\rho/dT$ should be

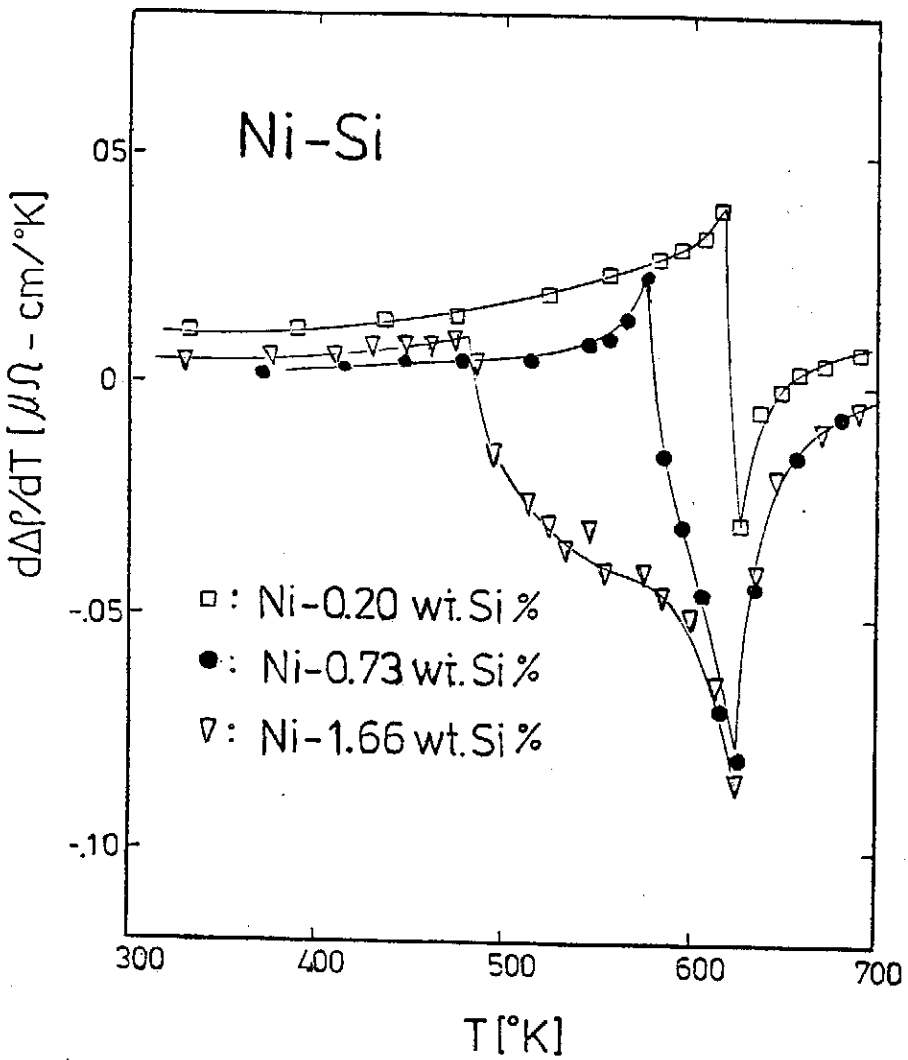

FIG. 4. $d\Delta\rho/dT$ as a function of T for Ni-Si alloys between 300 °K and 700 °K.

divergent positively near T_c of Ni-Si alloys and divergent negatively near T_c of pure nickel. However, from the experimental point of view, or figure 4, we would rather say that the two points of T_c occur at the maximum and minimum of each $d\Delta\rho/dT$ vs. T curve, respectively. Below T_c of a particular alloy $d\Delta\rho/dT$ increases slowly with increasing T. Between the T_c's of the particular alloy and the pure nickel, $d\Delta\rho/dT$ decreased quite fast with increasing T. Above T_c of the pure nickel, $d\Delta\rho/dT$ increasing very fast within a few degrees and appears to become quite flat thereafter. Evidently, we can conclude that the $d\Delta\rho/dT$ method gives results identical to those obtained by conventional methods.

Fig. 5 presents $d\rho/dT$ vs. T curves of these Ni-Si alloys in the temperature range between 300°K and 700°K. The Curie temperature is determined from this plot ast he temperature at which $d\rho/dT$ diverges. These $d\rho/dT$ vs. T plots

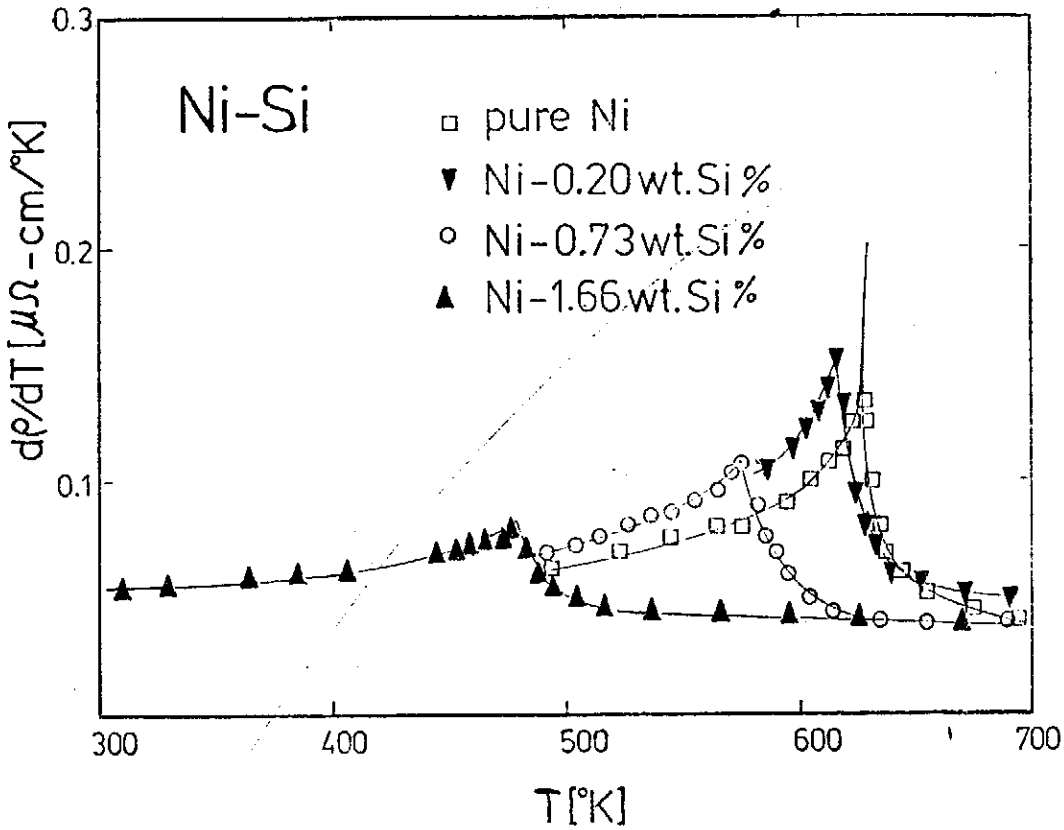

FIG. 5. $d\rho/dT$ as a function of T for Ni-Si alloys between 300 °K and 700 °K.

for the above alloys are quite similar to that shown for the pure Ni by Craig et. al.[9]. The values of T_c determined from above are shown in Fig. 6. The Curie temperature decreases monotonically with increasing Si concentration.

IV. CONCLUSION

One of the important properties of a ferromagnetic system is its Curie temperature. In this paper, we experimentally conclude that the Curie temperature of the Ni-Si alloys containing up to 1.66 wt.% of Si is monotonically decreased from about 627°K for pure Ni to about 480°K for Ni-1.66 wt.% Si.

V. ACKNOWLEDGMENT

Jin Nan Lin is grateful to Dr. Yeong Der Yao at the Institute of Physics, Academia Sinica for his encouragement, guidance and tremendous help throughout this research work. Special thanks go to Mr. W. J. Ueng for his assistance during this research work. Finally, Mr. Lin wishes to thank the Institute of Physics, Academia Sinica for allowing space and facilities in this research.

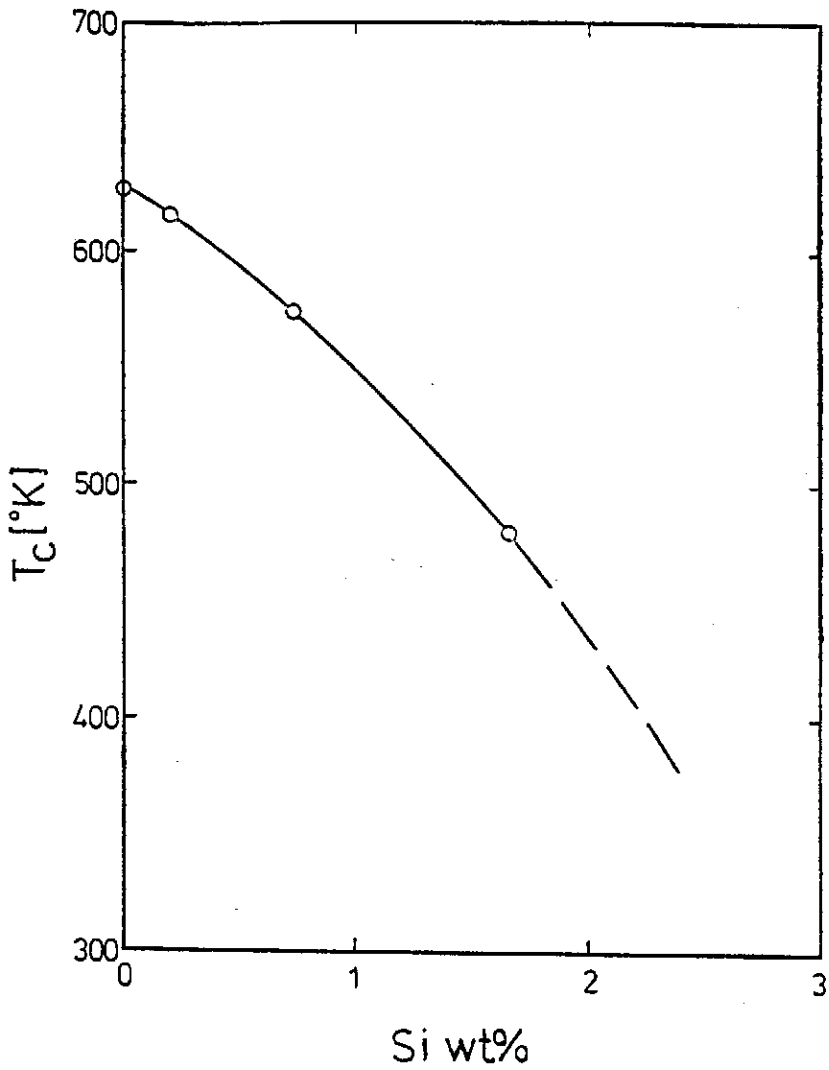

FIG. 6. T_C of Ni-Si alloys as a function of Si concentration.

REFERENCES

1. M. P. Kawatra and J. I. Budnick, Int. J. Magn. **1**, 61 (1970)
2. Y. D. Yao and J. H. Tsai, Chin. J. Phys. **16**, 189 (1978)
3. M. E. Fisher and J. S. Langer, Phys. Rev. Lett. **20**, 665 (1968)
4. T. G. Richard and D. J. W. Geldart, Phys. Rev. Lett. **30**, 290 (1973)
5. D. R. Su and T. M. Wu, J. Low Temp. Phys. **19**, 481 (1975)
6. D. R. Su, J. Low Temp. Phys. **24**, 701 (1976)
7. C. D. Hu and D. R. Su, J. Low Temp. Phys. **31**, 527 (1978)
8. D. R. Su, Nuovo Cimento **46B**, 315 (1978)
9. P. P. Craig, W. I. Goldburg, T. A. Kitchens and J. I. Budnick, Phys. Rev. Lett. **19**, 1334 (1967)

A THEORY OF McCOLLOUGH EFFECT AND CONTINGENT AFTER EFFECT

CHUN CHIANG (蔣 忻 儒)

Institute of Physics Academia Sinica
Nankang, Taipei, Taiwan, The Repnblic of China

Abstract

A model is advanced to explain the McCollough effect and the contingent motion after-effect. This model is based on the coupling of two units at the inspection stage, each of which sensitive to a particular feature of the stimuli. In the testing stage, the stimulus induces the excitation of the other feature detector through coupling to the state compatible to the previous inspecting stimulus, and the new incoming feature in reference to this state gives rise the after-effect. Comparision with other theories is discussed.

The McCollough effect (McCollough, 1965) is the effect that when viewing alternatively red/horizontal and green/vertical grids for some time, the achromatic vertically lined grid appears pinksh coloration and the achromatic horizontally lined grid appears greenish coloration.

Even though a lot of experimental data on this effect have been obtained, the theoretical explanation is still in question (Skobo et al., 1975). Of the many theories, two classes of theories may be classified. The first class of theory, orginally proposed by McCollugh (1965) and extended by many others, assumes that the effect arises due to chromatic adaptation of color coded edge detectors. With the inspection of red/horizontal lines, the chromatic component of the horizontal units for red is adapted, thus the achromatic test pattern presented later will appear tinged green by the unadapted horizontal detectors. The same reasoning applies to the appearance of pinkish coloration of achromatic vertical. However, this model has been criticized that too many properties have to be assigned to this color coded edge-detector (Murgh, 1976). Also, Murgh (1979, 1975, 1974, 1972, 1969) has reported some other data which are not compatible with this model.

The second class of theories attributes the McCollough effect to "a learning process by which the pairing of a color with a specific grid orientation produces an association in which the grid orientation comes to evoke the response of the visual system to the color" (Murgh, 1979). Furthermore, the lined grid in inspection was viewed as the conditioned stimulus and the color functions as the unconditioned stimulus. However, the learning process and the condition process imply that the effect can be taught by instructions without actually

requiring the inspection process; also, as remared by Mayhew and Anstis (1972), if it is due to learning, then the effect should be able to be contingent on shape such as triangles or disks. This seems not to be the case. In the following, a new model is presented which seems to be able to alleviate the above mentioned defects.

THEORY

Visual system consistes of many individual feature detectors or sensors, which normally detect each in-comming features. However, this is the passive response of our visual system. In order to perceive the in-comming signals through the detector, the visual system also consists of active response, this active response consists of subjective controller and follower (or filter) as shown in Fig. 1. The subjective controller exerts a concious control of the components of the visual spstem to match the signals and the matched components for the signals are termed the follower or the filter and the perception space is the detected signals filtered through this filter, namely, the in-comming signals minus the matched signals in the filter. This model has been used to explain the motion after effect (Chiang, 1978).

For the present situation, when two different features, feature A and feature B in the signal are repeatedly presented in the "inspection stage"; the matched filter for feature A, namely the filter A, and the matched filter feature B, namely the filter B, are coupled together. Also, the controller for feature A and the controller for feature B are coupled together as well. The coupling is due to the correlation of simultaneous firing of neurons for two different featurers. In the testing stage, with the signal containing feature A and a neutral feature, the filter A and controller for feature A are rapidly activated and thus feature A is perceived in the perception space. However, due to the coupling process, the firing of neurons for filter A will induce the firing of neurons for filter B even though feature B is not presented in the signals. Concequently the perceived "neutral feature" will be the "neutral feature" minus the "feature B" and this gives rise the contingent after effect.

Some experimental evidences can support above coupling induction process. For example, Hebb (1949) found that the firing of neurons in a "cell assembly" can affect the probability that other cells will fire. Also, Leppmann and Allen (1973) have reported that when test patterns are presented for brief periods, the exposure time required to identify the form of the pattern is less than that required for subjects to identify the color aftereffect; this fact supports the view that filter A is activated first, and filter B is activated latter by the coupling and induction process. Further support of the above model may

be judged by the cases for which this model can explain.

Case (a) McCollough Effect, the orientation contingent color after-effect:

In this effect, the inspection stimuli are the vertically orientated red and blace strips alternating with horizontically orientated green and black strips. Thus the feature follower for vertical black strip is coupled with the feature follower for red color and the feature follower for horizontal black strip is coupled with feature follower for green color in the visual system (see Fig. 1). In test stage, with the viewing of vertical black strip and white color, the vertical black strips induce the feature follower for red color through previous coupling mechanism, thus the white color goes through this red color filter (or the white color in reference to this red color) gives the green sensation. Similar explanation applies to the red sensation for viewing the horizontal black strip and white color.

Case (b) Color contingent motion after-effect (rotating spirals):

The inspection stimuli are spirals rotating clockwise in red background alternating with black spirals rotating counter clockwise in yellow background (Mayhew and Austis, 1972). According to Chiang's theory of motion after-effect (1978), the follower for the motion in the visual system should be a trisient. In the inspection stage, the follower follows the rotating stimulus starting from motionless in the beginning to full rotation and to abrupt stopping and then rotates in reverse direction. The coupling features are: red color (or yellow color) in follower A is coupled to transient clockwise rotation (or transient counter-clockwise rotation) in follower B. Furthermore, the switching of color from one color to the other (or from clockwise rotation to counter-clockwise rotation) in stimuli requires great concious effort in the subjective controller to cope with; thus in the present situation, the act of switching to red color (or yellow color) in the subjective controller A is also coupled to the act of initiating the clockwise rotation (or the counter-clockwise rotation) in the subjective controller B.

In the test stage, with the presentation of stationary spirals in red light, the stimulus of red light sets the follower A to conform to the red light, and since the red color in follower A was coupled to clockwise rotation in follower B, thus the stationary spirals will appear to rotate counter-clockwise in reference to this clockwise rotation of follower B. However, the coupled follower B is transient and will disappear gradually, thus the apparent rotation of the stationary stimulus will also be a transient and disappear gradually. Since the "switching" of color is also coupled to the "initiating" of the rotation in the subjective

controller, thus even though the apparent counter-clockwise rotation will gradually disappeare in the background of red light, the act of new switching of color to red light in subsequent test can again initiate the clockwise rotation of follower B and the stationary stimulus can appear to rotate counter-clockwisely again. With the similar argument, the stationary spirals will appear to rotate clockwisely in yellow light. Thus, these coupling of color with motion and the coupling of switching of color with the initiating of rotation together may explain the observed facts (Mayhew and Austis, 1972), namely, the color dependence of the direction of the apparent rotation, the gradual disappearence of the apparent rotation and the renewed apparent rotation with the switching of the color.

Case (c) Space contingent motion after-effect (moving strips):

The inspection stimuli are narrow spaced strips downward and medimum spaced strips moving upward (Mayhew and Austis, 1972). The coupling features are: narrow strips are coupled to the downward motion and medium strips are coupled to the upward motion. Thus in testing, the stationary narrow strips should appear to move upward according to the above theory and the stationary medium strips should appear to move downward. This is observed. Mayhew and Austis (1972) also reported that for some subjects, with the inspection of medium spaced strips and broad spaced strips (instead of narrow spaced strips and medium spaced strips), the "medium" spaced strips will appear to move upward (instead of downward) and "broad" spaced strips (which have not been presented in the inspection) will appear to move downward; and in general, this kind of transposed space contingent motion aftereffect occurred only if a rest period of about 20 min. was given between the inspection and test procedures. No explanation was given to this phenomenon. It is postulated here that in the inspection stage, not only the actual physical and physiological space of strips was coupled to the motion, but the impression of "broad" or "narrow" of the space was also coupled to the motion. Thus in the inspection stage, both the space of the narrow strips and the impression of being relative narrow are coupled to the downward motion and the space of the medium strips and the impression of being relative broad are coupled to the upward motion. Concequently, with the stimulli of stationary medium strips and broad strip in the test stage, the medium strip (the impression of being relative narrower) will appear to move upward and the broad strip (the impression of being relative broader) will appear to move downward. However, this kind of coupling takes time to develope, since the impression of the strips being broad or narrow requires the brain to interpretate, and the process of interpretation and its subsequent coupling with motion take time. Whereas the coupling of the

actual sensed space with the motion does not require interpretation, thus does not need time to develope. Also, since attention was concentrated in perceiving the motion in the inspection stage and there is not enough time for the brain to interprete the strips being broad or medium and to make strong coupling in the inspection stage. For these two reasons, the transposed space contingent motion after-effect can not show up right after the inspection stage and have to wait for 20 min. to show up. Thus the usuall aftereffect can apper right away and the motion aftereffect with transposition will take about 20 min. to develope. The above theory of contingent after effect may not only explain the examples given above, it may also explain many other experimental findings.

DISCUSSION

While there are many theories advanced in the past (see review by Skobo et al, 1975), it might be appropriate to compare some of those theories with the present one. For the edge-detection model and the single-unit model (McCollough, 1966; Fidell, 1970; Teft and Clark, 1968, Hepler, 1968), it was postulated that there is a single neural unit sensitive to two stimuli. In the present theory, it is the coupling of two units sensitive to each stimulus that leads to the after-effect, in stead of one unit sensitive to two stimulli. Murch (1972) proposed that "color adaptation in conjunction with a specific line orientation" might be an apropriate way to describe the the physiological correlates of the McCollough effect, the fatigued opponent-process color receptors in the lateral geniculate nuclus would "feed into" cortical units having orientation sensitivity; achromatic spatial patterns would appear colored because the lines were processed through fatigued color units on their way to the orientation detectors. Murch (1972) also suggest that the McCollough effect involves only the adaption and fatiguing of color, but probably does not involve a fatiguing of orientation-sensitive units. Skobot et al (1975) however questioned that why exposure to chromatic gratings could produce no longlasting fatigue of the orientation-detecting mechanism and yet, at the same time, would fatigue color units for a period of weeks. In the present theory, while it also proposes that the orientation elicites the aftereffect, similar to Murch's model, however, it does not use the notion of adaptation, and after-effect is due to the coupling, which is induced by the simutaneous firing of some neurons by other nuurons. This coupling is at a more basic stage and does not necessarily involve the retrival of the information from the memory. Therefore, this theory is also different from the pure learning or condition theory.

REFERENCES

Chiang, C. (1978) A theory of motion after-effect. Jap. Psychol. Res. **20**, 101-104.

Fidell, L. K. S. (1970) Orientation specificity in chromatic adaptation of human "edge ketectors". Percept. & Psychophys. **8**, 235-237.

Hebb, D. O. (1949) The organization of behavior, New York: Wiley.

Hepler, N. (1968) Color: A motion contingent after-effect. Science, **162**, 376-377.

Leppmann, P. K. and Allen, D. B. (1973) Further studies of form-specific chromatic aftereffects. paper presented at the meeting of the Optical Society of America Rochester, New York October.

Mayhew, J. E. W. and Austis, S. M. (1972) Movement after-effects contingent on color, intensity, and pattern. Percept. & Psychophys. **12**, 77-85.

McCollough C. (1965) Color adaptation of edge detectors in the human visual system. Science **149**, 1115-1116.

Murgh G. M. (1969) Size judgments of McCollough afterimages. J. Exp. Psychol. **81**, 44-48.

Murgh G. M. (1972) Binocular relationships in a size and color orientation specific aftereffect. J. Exp. Psychol. **93**, 30-34.

Murgh G. M. (1974) Color contingent motion after-effects: single or multiple levels of processing. Vision Res. **14**, 1181-1184.

Murgh G. M. (1975) Orientation specific colored after-effects are classically conditioned responses. paper presented at association for research in Vision and Ophthalmology, Sarasota, Fla.

Murgh G. M. (1976) Classical conditioning of the McCollough effect: temporal parameters. Vision Res. **16**, 615-619.

Murgh G. M. (1979) The role of test pattern background hue in the MuCollugh effect. Vision Res. **19**, 939-942.

Teft, L. W. & Clark, F. T. (1968) The effects of stimulus density on orientation specific after-effects of color adaptation. Psychonomic Sci. **11**, 265-266.

Skowbo, S., Timney B. N., Gentry T. A. and Morant R. B. (1975) McCollough Effects: Experimental findings and theoretical accounts. Psychol. Bull. **82**, 497-510.

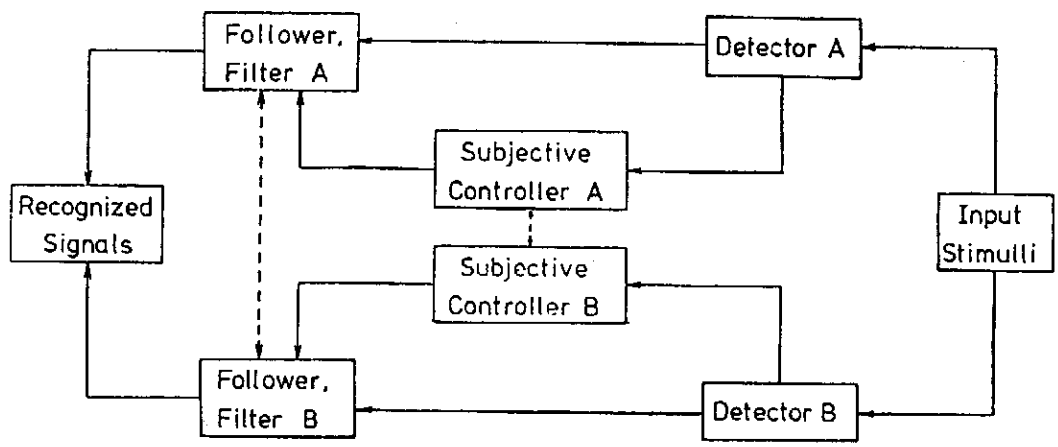

Fig. 1. A block diagram showing the perception and coupling of the units in the visual system sensitive for two different features of the stimulli. The sign→indicates the direction of flow and the sign←----indicates the coupling of two units.

MECHANISM OF MEMORY AND SWITCHING PROCESS IN AMORPHOUS THIN FILM

CHUN CHIANG (蔣 忻 儒)

Institute of Physics Academia Sinica
Nankang, Taipei, Taiwan, R. O. C.

Abstract

The mechanism of transition from one state to the other is proposed to explain the electric switching and memory phenomenon in thin film made of organic or inorganic material. An equation is derived.

Memory and switching process are of keen interest not only for its scientific curiosity, but also for its potential vast industrial applications. Nature also provides living examples of switching process such as nerve membrane excitation, etc. Thus it would be of vast interest to explore the switching mechanism for biologist, physicist, electrical engineer, and find the similarity and the difference of the switching mechanism among the biological membrane, organic thin film and the inorganic thin film.

Despite intensive research in recent years[1, 2, 3, 4, 5] no electronic theory has been developed to the stage that quantitative calculation and prediction can be made to the threshold behavior of amorphous thin film. Recently, a quantitative switching theory[6] has been given for the organic thin film with dipoles, a quantitative theory has also been given for the nerve excitation and action potential[7, 8]. This articie will report a novel switching mechanism in amorphos thin film and comparision of switching mechanism with other type of films can be made.

I propose that there are two stable configurations exist in the amorphous thin film (Fig. 1), configuration I at energy E_1 may transform to configuration II at energy E_2 through a barrier ($E_1 < E_2$), and the conductivities of these configurations are different. The difference between configuration I and configuration II may be due to the positional variation of the atoms, the variation of the number of the bonding atoms, the changing of the bonding state such as from p-orbital to d-orbital or from lone pair to bonding[9], or from neutral dangling bond to positive and negative dangling bond[10, 11] or a conbination of above situations. Furthermore, depending on the relative position of the atoms, the bond angle and bond distance among atoms may vary and thus the barrier and the configuration II may have several energy states as indicated in Fig. 1. Also, I assume that a current I passing through the film may elevate the energy of the configuration I and II by the amount k_1 I and k_2 I resgectively, where

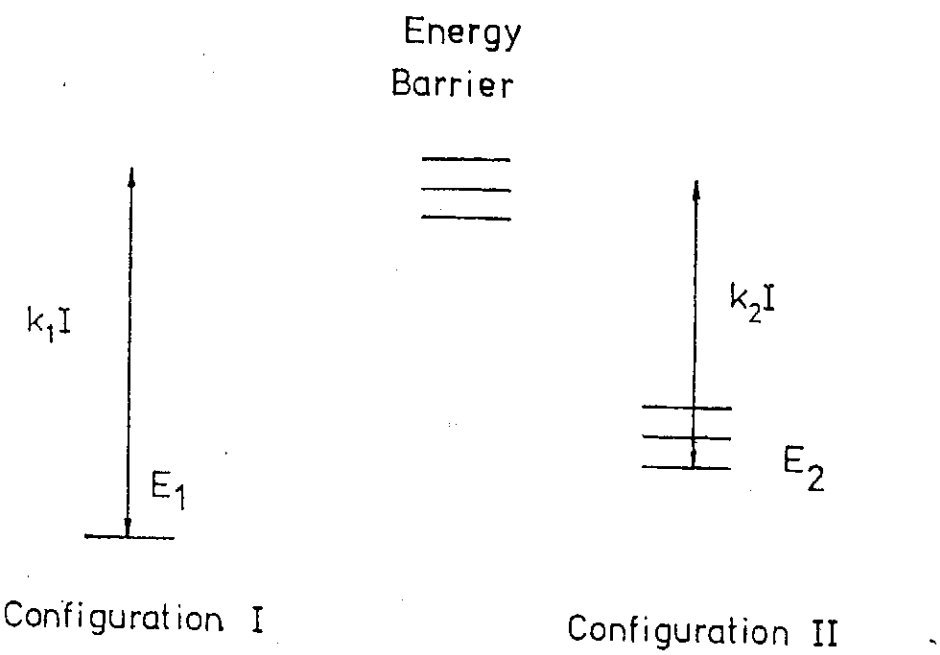

FIG. 1. Energy level of configuration I, configuration II and the barrier. The energy level of the configuration II and the barrier may be varied by the ON process.

k_1 and k_2 are constant. The elevation of the energy by the current is due to the fact that the kinetic energy of the current may dissipate and excite the respective configuration within the film. What essentials in this model are (i) there are two stable and reversible configurations exist in approximately equilibrium in the amorphous film, (ii) the conductivity of configuration II is much higher than that in configuration I, (iii) the energy level of the configuration I and II may be elavated by current I with the amount k_1 I and k_2 I respectively.

With above ideas, it can be seen that configuration I usually prevailes in the film together with a small number of configuration II, since E_1 is smaller. When passing current through the film, as $E_1 + k_1 I \ll E_2 + k_2 I$, namely, as long as the energy level of configuration I is smaller than the energy level of configuration II under electric excitation, then configuration I is more stable and prevails in the film. If configuration I is ohmic, then the V-I curve is linear as shown to be AB line in Fig. 2 (OFF state). With increasing current such that $E_1 + k_1 I \gg E_2 + k_2 I$ (this is possible at large current, since k_1 is larger than k_2), namely the energy level of configuration I is much higher than that of configuration II, then the atoms and electrons will be arranged in the form of configuration II, since it is this configuration which is favorable under electric excitation. Again, if it is ohmic and if the conductivity of configuration II is higher, then the V-I curve is shown as CD line in Fig. 2, and represents

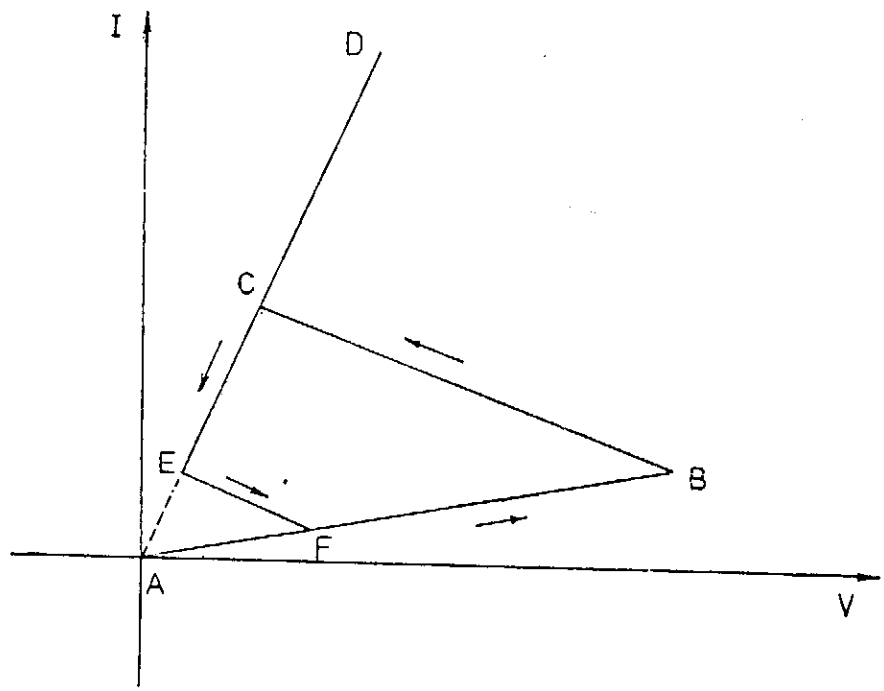

FIG. 2. I—V curve of the threshold switching and Memory state.

the ON state. If $E_1 + k_1 I = E_2 + k_2 I$, namely the energy level of configuration I and configuration is comparable, then the population of configuration I and configuration II is approximately equal and is very sensitive to the current. Slightly increasing of the current will shift the equilibrium and increases the population of configuration II significantly. Since the conductivity of configuration II is higher than that of configuration I, the "voltage drop" for the same amount of current passing through configuration II will be lower than that passing through configuration I, thus the voltage decreases as the current increases in the switching region as shown to be the BC line in Fig. 2. The minimum current which initiates the significant change is the threshold current and the corresponding voltage the threshold voltage (point B).

If the arrangement of atoms in configuration II is rigid and configuration II feels a constant envioroment, then the energy level and potential barrier of configuration II is fixed and assumed a unique value, then the switching from the ON state to OFF state will follow DCBA line which is exactly the reverse of the path from the OFF state to ON state. However, since there is drastic change of atomic and electronic arrangement during switching, configuration II feels different envioroment in ON state and OFF state, thus she energy level and the potential barrier will have different value; since large current passing through the film during switching and the temperature increases, thus the atoms or electrons may take a more optimum position with less geometrical strain,

thus the energy level and potential barrier of configuration II in theON state is smaller than that in the OFF state, namely, E_2 is smaller in ON state than in the OFF state, thus the current for which $E_1 + k_1 I = E_2 + k_2 I$ is smaller, thus the switching from ON state to OFF state follows DEFA line instead of DCBA line. The current corresponding to point E is called the holding current.

Suppose E_2 of configuration II after switching to ON state has decreased to E_1 or smaller than E_1, then configuration II is a more favorable state than configuration I, thus even the current decreases to zero, the film is still in the ON state with configuration II prevails in the film. This is the "memory" state. However, with a large sudden current pulse of either polarity, the optimum position of the atoms and electrons in configuration II is disturbed and they will be displaced to a more strained position, thus E_2 of configuration II increases again, which renders the configuration II unfavorable and the film switches to OFF state again, this is the erasing process. Experimently[12], it is often found that the newly deposited film initially requires holding current to keep the film in ON state, but after a few cycles, the film is in Memory state and does not require the holding current, this is due to the fact that after a few cycles, the enviorment gradually adjust for the configuration II to locate in a lower energy state with less bond strain which make it less probable to transform back to configuration I.

This model concisely explains the mechanism not only of the threshold switching process, but also the memory process. This model specifies the amount of current as the determinating factor, thus the changing of the polarity of the applied pulse should not appreciablly change the characteristics of the film as indeed observed by the experiment[2]. Following a similar mathematical treatment of organic thin film switching[6], a quantitative calculation of the above idea is possible and may show to be

$$V = \frac{d}{N} \frac{e^{(E_1+k_1|I|)/KT} + e^{(E_2+k_2|I|)/KT}}{g_2\, e^{(E_1+k_1 I)/KT} + g_1\, e^{(E_2+k_2 I)/KT}} I$$

where d is the thickness, N is the total number of atom units in the film and is constant in a given condition, g_1 and g_2 are conductivity per unit of configuration I and II respectively. The detailed calculation will report in other paper. It seems that no other electronic theory is able to derive a threshold switching equation yet.

REFERENCES

1. A. Szymanski, D. C. Larson and N. M. Labes, Appl. Phys. Lett. **14**, 88 (1968).
2. I. Balberg, Appl. Phys. Lett. **16**, 491 (1970).
3. M. Saji, C. H. Leung and K. C. Kao, J. Non-Crystalline Solids, **23**, 147 (1977).
4. W. Van Roosbroeck, Phys. Rev. Lett. **28**, 1120 (1972).
5. S. H. Lee and H. K. Henisch, Appl. Phys. Lett. **22**, 230 (1973).
6. C. Chiang, Appl. Phys. Lett. **31**, 554 (1977).
7. C. Y. Lee and C. Chiang, Bull. Math. Biol. **38**, 59 (1976).
8. C. Chiang, Bull. Math. Biol. **40**, 247 (1978).
9. M. Kastner, D. Adler and H. Fritzsche, Phys. Rev. Lett. **37**, 1504 (1976).
10. P. W. Anderson, Phys. Rev. Lett. **34**, 953 (1975).
11. R. A. Street, and H. F. Mott, Phys. Rev. Lett. **35**, 1293 (1975).
12. A. R. Elsharkawi, and K. C. Kao, J. Phys. Chem. Solids **38**, 95 (1977).
13. H. Carchano, R. Lacoste, and Y. Segui, Appl. Phys Lett. **19**, 414 (1971)

POLARIZED LIGHT AND VERTICAL SOLAR CELL

YU-TUNG YANG (楊 毓 東)

Institute of Physics, Academic Sinica
Nankang, Taipei, Taiwan, Republic of China

Abstract

Experiments show that a vertical solar cell made of plane junction prefers the absorption of plane polarized light. The electric power output is maximum when the E-wave of the incident monochromatic light $\vec{E}_{h\nu}$ is parallel to the built-in electrostatic field $\vec{E}_{in}$ of the solar cell, and becomes minimum when $\vec{E}_{h\nu}$ becomes perpendicular to $\vec{E}_{in}$.

In the case of a horizontal solar cell, the power output is maximum when the H-wave of the incident light, $\vec{H}_{h\nu}$, is perpendicular to $\vec{E}_{in}$ and it decreases gradually when $\vec{H}_{h\nu} \not\perp \vec{E}_{in}$. On the other hand, the power output is minimum when $\vec{E}_{h\nu} \perp \vec{E}_{in}$, and it increases when $\vec{E}_{h\nu} \not\perp \vec{E}_{in}$. Since the electric power output is directly related to the free electron-hole pair production probability and the latter is related to the light absorption coefficient α, therefore an analysis based on the "method of damped oscillator" is described. The analysis shows that the α for the free electron-hole pair production increases with the energy $h\nu$ of the incident light in an exponential manner and the α can not exist if $h\nu$ approaches the absorption edge from above.

(1) EXPERIMENTAL FINDINGS

If light is monochromatic and plane polarized and is shone on a vertical solar cell made of Si p-n junction, the electric power output is found maximum when the E-wave of the monochromatic light ($\vec{E}_{h\nu}$) is parallel to the built-in electrostatic field E_{in} of the solar cell, and minimum when $\vec{E}_{h\nu} \perp E_{in}$. Fig. 1 shows the relation between the open circuit voltage V_{oc} and the angle θ, where θ is the angle between $\vec{E}_{h\nu}$ and $\vec{E}_{in}$. Fig. 2 shows the relation between V_{oc} and θ when the illuminated spot is far away from the junction layer.

(2) EXPERIMENT

The source of light was the coherent light from a He-Ne laser. The frequency of the red light is $\nu = 4.740 \times 10^{14}$ sec^{-1}. ($\lambda = 6328$ Å). The image of the light beam is circular in shape without any noticeable ellipticity. The light emitted from the laser is unpolarized. A polarizer was used for producing the polarized light. The calibrated polarizer indicates the direction of the E-wave of the polarized light.

The solar cells were made in this laboratory by diffusion method. The dopants were BBr_3 and $POCl_3$, and the diffusion method described in the Runyan's book[1] was used. The V_{oc} obtained at AM1 is around 0.56 volt.

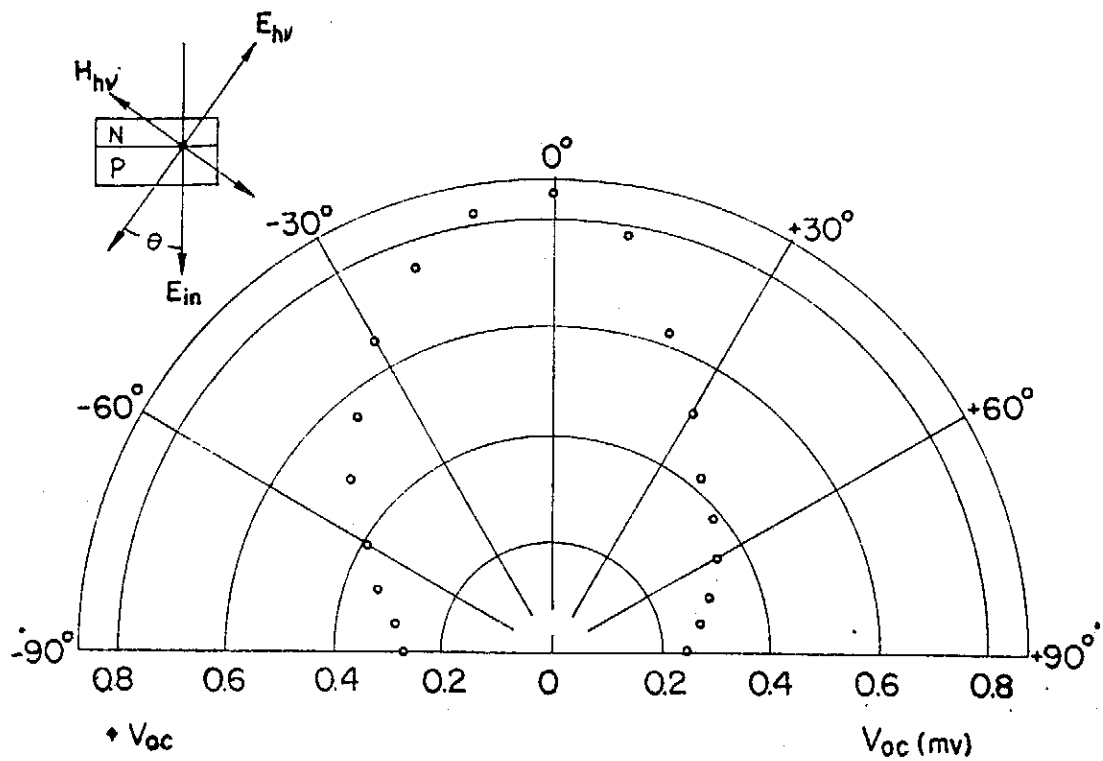

FIG. 1. V_{oc} vs. θ near the junction layer of a vertical solar cell. $\theta=0$ corresponds to $E_{in} \| E_{h\nu}$ and $\theta=\frac{1}{2}\pi$ corresponds to $\vec{E}_{in} \perp \vec{E}_{h\nu}$ The V_{oc} vs. θ curves were obtained by experiments using silicon diodes made by the diffusion method. The concentrations were: Boron: 10^{19} cm^{-3}, and Phosphorus: 10^{16} to 10^{17} cm^{-3}. Conventional ohmic contacts were applied.

For the purpose of local illumination, an instrument similar to the one described in my previous report[8] was used. The slit width of the instrument was adjusted to 10 μ. The diameter of the coherent light was 1.5 mm. Thus the area of illumination was 10 $\mu \times 1.5$ mm. Within such an area, the physical properties of the vertical solar cell was found relatively uniform. (Tested layer by layer by using an electric probe).

The adjustment for the strict alignment between the light beam and the plane of the vertical solar cell is important. The plane should be exactly perpendicular to the light beam. The location of the illuminated spot on the plane should remain unchanged during the rotation of the vertical solar cell around the normal of the plane passing through the center of the illuminated spot. The selection of the illuminated spot was done by adjusting the two perpendicularly oriented micrometer sticks. The position of the slit relative to the light beam was fixed. The vertical solar cell was placed near the center of the leveled round turn-table. The turn-table was used for the purpose of changing the angle θ between $\vec{E}_{in}$ and $\vec{E}_{h\nu}$. The simplified experimental arrangement is shown in Fig. 3.

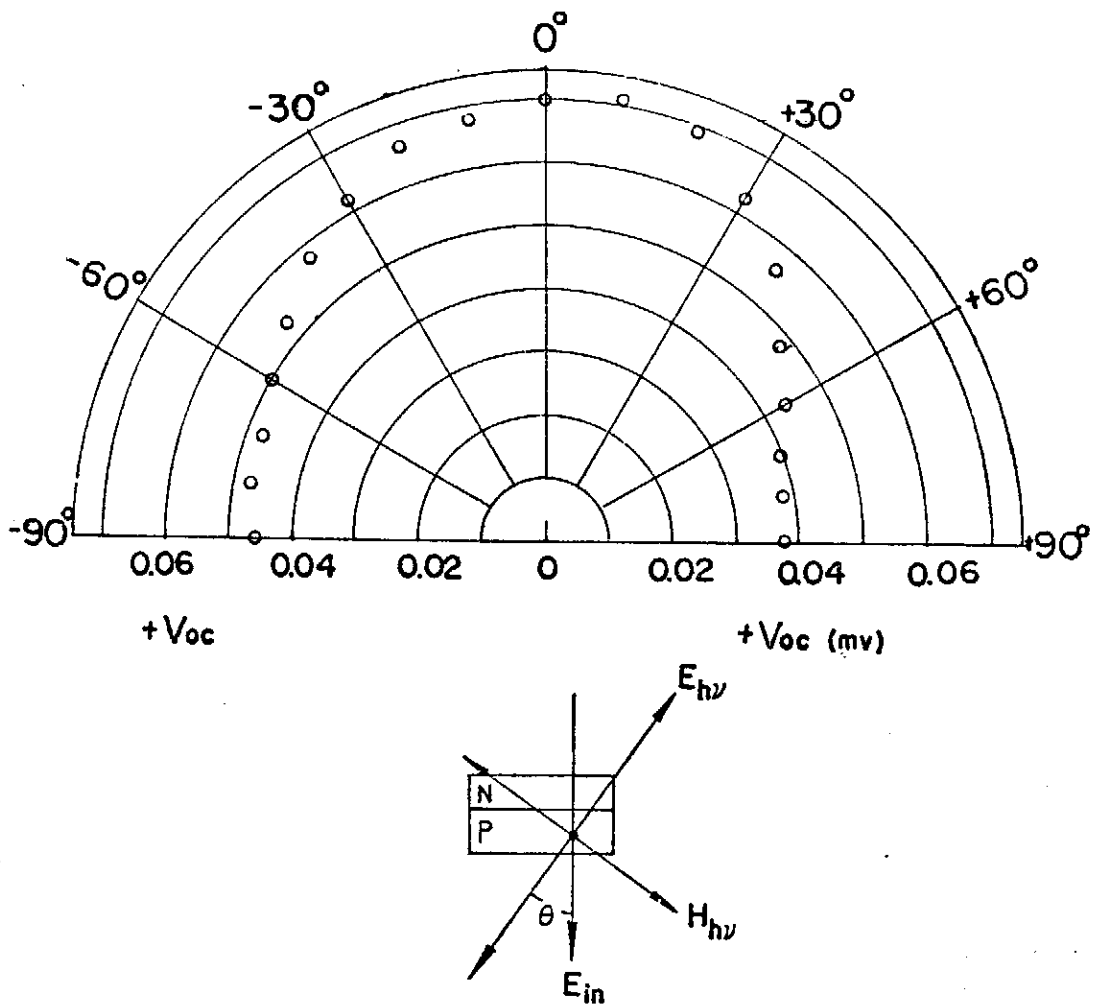

FIG. 2. V_{oc} vs. θ at a distance about 30 μ from the junction layer of the same vertical solar cell. The total thickness of the diode is about 0.5 mm. The junction depth is about 100 μ.

No such an angle-dependent-effect was observed in case of a horizontal solar cell, i.e., if a horizontal cell is rotated around the normal of the frontal plane by an angle ϕ, the output V_{oc} (as well as I_{sc}) will remain unchanged.

(3) A THEORETICAL EXPLANATION

A possible theoretical explanation of the above phenomena is proposed as follows. The theory is based on the method of damped oscillator.

(3a) The damping force and the photo-electrodynamic interaction

The Lorentz force due to an internal electrostatic field of the diode is

$$F = -e\, E_{in}, \qquad (1)$$

where E_{in} is the built-in electrostatic field of the diode. The effective force is possibly

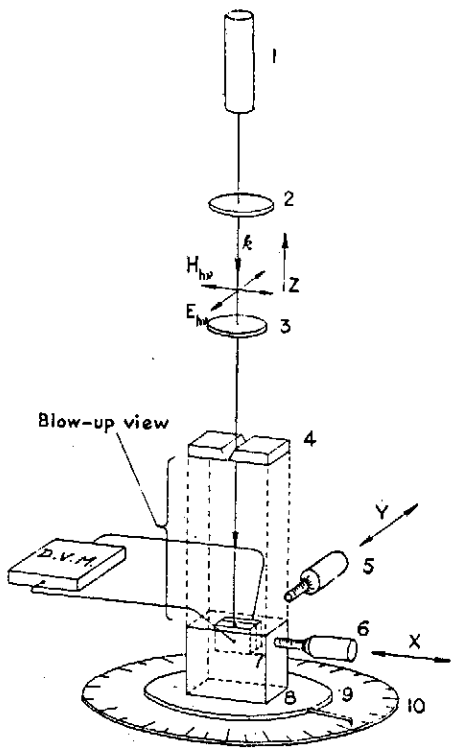

FIG. 3. Experimental arrangement. The basic instrument remains the same as shown in Ref. (8) except (1) He-Ne laser, $\lambda=6328$ Å. The diameter of the beam is 1.5 mm. (2) Polarizer which is fixed on the laser. (3) Pin-hole, 1.5 mm. (4) Slit, the width of which is 10 μ. The slit is placed very close to the surface of the solar cell yet the solar cell can still move in the x-y directions relative to the slit. The laser beam after passing through the slit is narrowed down to $10\mu\times1.5$ mm. (5) Micrometer stick for the y-movement of the solar cell adjustment. (6) Micrometer stick for the x-movement of the solar cell adjustment. (7) Solar cell which may either be a vertical or a horizontal one. (8) solar cell holder (a piece of black bakelite). (9) Turn-table, the center of the table is aligned with the laser beam and the plane of the table is perpendicular to the laser beam. (10) Fixed 360° plate. The D.V.M. stands for digital voltmeter. (Keithley model 160 multimeter).

$$F_e = -e\ E_{in}\left|\frac{v}{c}\right|, \qquad (2)$$

This is because $e\,|(v/c)|$ is the space component of the charge four-vector is $(e(\vec{v}/c),\ ie)$, such that[2]

$$\frac{\partial s_i}{\partial x_i}=0, \qquad (3)$$

where

$$s_i=\left(e\frac{\vec{v}}{c},\ ie\right). \qquad (4)$$

If $v \ll c$, the effective mass of the carrier m* may be introduced in (2), such that

$$F_e = -e\ E_{in}\left|\frac{m^*v}{m^*c}\right|. \qquad (5)$$

The above expression may represent the elecctrodynamic interaction scheme in a diode. The energy dissipation due to F_e may be

$$\varepsilon_{dis}=\vec{F_e}\cdot\vec{\ell}=\frac{-e\vec{E_{in}}\cdot\vec{\ell}\,|m^*v|}{m^*c}=\frac{-eE_{in}\,\ell\cos\theta}{m^*c}\,|p|\,, \tag{6}$$

where $\vec{\ell}\,\|\,\vec{E_{h\nu}}$, and ℓ is the magnitude of the oscillation of the carrier. θ is the angle between $\vec{E_{in}}$ and $\vec{E_{h\nu}}$ and $E_{h\nu}$ is the amplitude of the E-wave of photon.

If the momentum p of the oscillator is represented by an operator in terms of θ,

$$|p|\longrightarrow\frac{-i\hbar}{\ell}\frac{d}{d\theta}\,. \tag{7}$$

The kinetic energy in terms of p is then

$$\varepsilon_k=\frac{p^2}{2m^*}=\frac{-\hbar^2}{2m^*\ell^2}\frac{d^2}{d\theta^2}\,. \tag{8}$$

Assuming that ε is the energy mainly from photon for the excitation of the carrier, and if the wave function of the carrier is Θ, then the wave equation of the carrier in terms of θ may be written as

$$\frac{-\hbar^2}{2m^*\ell^2}\frac{d^2\Theta}{d\theta^2}+\left(\frac{eE_{in}\cos\theta}{m^*c}\right)i\hbar\frac{d\Theta}{d\theta}=\varepsilon\Theta\,, \tag{9}$$

which is a damped oscillator wave equation. (9) may be transformed into the Mathieu's equation in standard form. However, for the present semi-quantitative analysis, instead of considering the general solutions of (9), only two extreme cases are considered. Namely, (I) $\theta=\frac{\pi}{2}-\delta$, and (II) $\theta=0+\delta$, and in the limit, $\delta\to 0$. δ, instead of θ, is used as the variable for the semi-quantitative analysis in the extreme cases. (At the absorption edge, $\varepsilon=0$, $\ell\to\infty$, and the damping term does not exist, therefore the whole eq. (9) vanishes).

(3b) Case (I): $\theta=\frac{\pi}{2}-\delta$.

$$\cos\theta=\cos\left(\frac{\pi}{2}-\delta\right)=\sin\delta\approx\delta\,, \tag{10}$$

and

$$\frac{d}{d\theta}=-\frac{d}{d\delta}\,,\qquad\frac{d^2}{d\theta^2}=\frac{d^2}{d\delta^2}\,, \tag{11}$$

By substituting (11) into (9) and by rearranging the terms,

$$\frac{d^2\Theta}{d\delta^2}+\left\{\frac{\left(\frac{m^*c\varepsilon}{i\hbar eE_{in}}\right)+\delta\frac{d}{d\delta}}{\gamma^3}\right\}\Theta=0\,, \tag{12}$$

where

$$\gamma^3 = \frac{\hbar c}{2\, i\, eE_{in}\ell^2}\,.$$

γ is a dimensionless quantity. Let

$$p = \frac{\delta}{\gamma^3}\,, \text{ and } q = \frac{\left(\frac{m^* c\,\varepsilon}{ieE_{in}\hbar}\right)}{\gamma^3}\,, \tag{13}$$

then (12) becomes

$$\frac{d^2\Theta}{d\delta^2} + p\frac{d\Theta}{d\delta} + q\Theta = 0\,. \tag{14}$$

The solution of (14) is[3]

$$\Theta = \upsilon(\delta)\; e^{-\frac{1}{2}\int_0^\delta p d\delta'} = \upsilon(\delta)\; e^{-\frac{1}{4}\frac{\delta^2}{\gamma^3}}\,. \tag{15}$$

By substituting (15) into (14),

$$\frac{d^2\upsilon}{d\delta^2} + J(\delta)\;\upsilon(\delta) = 0\,, \tag{16}$$

where

$$J(\delta) = q - \frac{1}{2}\,\frac{d\,p(\delta)}{d\,\delta} - \frac{1}{4}\left\{p(\delta)\right\}^2\,. \tag{16a}$$

By substituting (16a) into (16),

$$\frac{d^2\upsilon}{d\delta^2} + (q - \frac{1}{2}B - \frac{1}{4}B^2\delta^2)\,\upsilon = 0\,, \tag{17}$$

where $B = \gamma^{-3}$. Let

$$D = q - \frac{1}{2}B = \frac{1}{\gamma^3}\left(\frac{m^* c\,\varepsilon}{i\hbar eE_{in}} - \frac{1}{2}\right), \tag{18}$$

and

$$K = B^{-2} \qquad = \gamma^3\,, \tag{19}$$

then (17) becomes

$$\frac{d^2\upsilon}{d\delta^2} + \left(\frac{KD - \frac{1}{4}\frac{\delta^2}{K}}{K}\right)\upsilon = 0\,. \tag{20}$$

Let a new variable be

$$\zeta = \frac{\delta}{K^{\frac{1}{2}}}\,, \tag{21}$$

and

$$\frac{d\zeta}{d\delta}=\frac{1}{K^{\frac{1}{2}}},\qquad \frac{d^2}{d\delta^2}=\frac{1}{K}\left(\frac{d^2}{d\zeta^2}\right). \tag{22}$$

then (20) becomes

$$\frac{d^2\upsilon(\zeta)}{d\zeta^2}+(KD-\frac{1}{4}\zeta^2)\ \upsilon(\zeta)=0, \tag{23}$$

where $\zeta=0$ is an ordinary point. The linear differential equation (22) is easily transformed into the "Weber's equation" in standard form[4], namely,

$$\frac{d^2\upsilon(\zeta)}{d\zeta^2}+(n+\frac{1}{2}-\frac{1}{4}\zeta^2)\ \upsilon(\zeta)=0, \tag{24}$$

and in which, in comparison with (23),

$$n=KD-\frac{1}{2}=\left(\frac{m^*c\,\varepsilon}{i\hbar eE_{in}}-1\right). \tag{25}$$

The solution of (23) is

$$\upsilon(\zeta)=w(\zeta)\ e^{-\frac{1}{4}\zeta^2} \tag{26}$$

where

$$w(\zeta)=a_0+a_1\zeta+a_2\zeta^2+\cdots\cdots \tag{27}$$

According to Weber, there could be two selections of the constant coefficients a_i: one set is $a_0=1$, $a_1=0,\cdots\cdots$, and the other set, $a_0=0$, $a_1=1,\cdots\cdots$. For the analysis, the second set is selected. Since ζ is very small if δ is, therefore,

$$w(\zeta)\approx\zeta. \tag{28}$$

From (26),

$$\upsilon(\zeta)\approx\zeta e^{-\frac{1}{4}\zeta^2}=\left(\frac{2ieE_{in}\ell^2}{\hbar c}\right)^{\frac{1}{2}}\delta\ e^{-\frac{1}{4}\left(\frac{2ieE_{in}\ell^2}{\hbar c}\right)\delta^2}. \tag{29}$$

and therefore from (15),

$$\Theta(\delta)=\upsilon(\delta)\ e^{-\frac{1}{4}\left(\frac{2ieE_{in}\ell^2}{\hbar c}\right)\delta^2}\approx\left(\frac{2ieE_{in}}{\hbar c}\right)^{\frac{1}{2}}\ell\delta\ e^{-\frac{1}{2}\left(\frac{2ieE_{in}\ell^2}{\hbar c}\right)\delta^2}. \tag{30}$$

The amplification probability is defined as

$$\Theta^*(\delta)\Theta(\delta)\approx\left(\frac{2eE_{in}\ell^2}{\hbar c}\right)\delta^2, \tag{31}$$

which is assumed proportional to the light absorption coefficient α, i.e., at $\theta=\frac{\pi}{2}-\delta$,

$$\alpha\rightarrow\alpha_{(\frac{\pi}{2}-\delta)}\propto\left(\frac{2eE_{in}\ell^2}{\hbar c}\right)\delta^2, \tag{32}$$

and

$$\alpha_{(\frac{\pi}{2})}=0 \text{ when } \delta=0, \quad \text{or } \theta=\frac{\pi}{2}. \tag{33}$$

(33) agrees qualitatively with the experimental fact.

(3c) Case (II): $\theta=0+2^{1/2}\delta$, $\delta \ll 1$.

In this case, $\cos\theta=\cos(0+2^{1/2}\delta) \longrightarrow (1-\delta^2)$. In this way, (9) becomes

$$\frac{d^2\Theta}{d\theta^2}+\frac{\left\{\frac{m^*c\ \varepsilon}{i\hbar eE_{in}}-(1-\delta^2)\frac{d}{d\theta}\right\}}{\gamma^3}\Theta=0. \tag{34}$$

Since

$$\frac{d}{d\theta}=\frac{1}{2^{\frac{1}{2}}}\frac{d}{d\delta}, \qquad \frac{d^2}{d\theta^2}=\frac{1}{2}\frac{d^2}{d\delta^2}, \tag{35}$$

therefore, (34) becomes

$$\frac{d^2\Theta(\delta)}{d\delta^2}+\left\{\frac{\left(\frac{2^{\frac{1}{2}}m^*c\ \varepsilon}{i\hbar eE_{in}}\right)-(1-\delta^2)\frac{d}{d\delta}}{\left(\frac{\gamma^3}{2^{\frac{1}{2}}}\right)}\right\}\Theta(\delta)=0, \tag{36}$$

which may also be put in the form[3]

$$\frac{d^2\Theta(\delta)}{d\delta^2}+p_1(\delta)\frac{d\Theta(\delta)}{d\delta}+q_1(\delta)\Theta(\delta)=0, \tag{37}$$

where

$$p_1(\delta)=-\frac{(1-\delta^2)}{\left(\frac{\gamma^2}{2^{\frac{1}{2}}}\right)}, \text{ and } q_1=\text{constant}=\frac{2^{\frac{1}{2}}m^*c\ \varepsilon}{i\hbar eE_{in}\left(\frac{\gamma^3}{2^{\frac{1}{2}}}\right)}. \tag{38}$$

$\delta=0$ is a regular point.

The solution of (36) may be written as

$$\begin{aligned}\Theta(\delta)&=\xi(\delta)\ e^{-\frac{1}{2}\int_0^\delta p_1(\delta')d\delta'}=\xi(\delta)\ e^{+\frac{1}{2}\left(\frac{2^{1/2}}{\gamma^3}\right)^{-1}\int_0^\delta(1-\delta'^2)d\delta'}\\&=\xi(\delta)\ e^{+\frac{1}{2^{1/2}\gamma^3}\left(\delta-\frac{\delta^3}{3}\right)}\approx\xi(\delta)\ e^{+\left(\frac{1}{2^{1/2}\gamma^3}\right)\delta}\end{aligned} \tag{39}$$

since $\delta^3 \ll \delta$ when $\delta \to 0$.

In (39) $\xi(\delta)$ satisfies

$$\frac{d^2\xi(\delta)}{d\ \delta^2}+L(\delta)\xi(\delta)=0, \tag{40}$$

where

$$L(\delta)=q_1-\frac{1}{2}\frac{dp_1}{d\delta}-\frac{1}{4}p_1^2=\frac{2^{\frac{1}{2}}m^*c\ \varepsilon}{i\hbar eE_{in}\left(\frac{\gamma^3}{2^{\frac{1}{2}}}\right)}-\frac{\delta}{\left(\frac{\gamma^3}{2^{\frac{1}{2}}}\right)}-\frac{1}{4}\left(\frac{2(1-\delta^2)^2}{\gamma^6}\right). \tag{41}$$

Since the last term on the right is much smaller than the other two terms (γ^3 is of the order of 10^{18}), and since the first term is usually the largest, therefore,

$$L(\delta) \approx \frac{2^{\frac{1}{2}} m^* c\ \varepsilon}{i\hbar e E_{in} \left(\frac{\gamma^3}{2^{\frac{1}{2}}}\right)} - \frac{\delta}{\left(\frac{\gamma^3}{2^{\frac{1}{2}}}\right)} . \tag{42}$$

The first term is real and the second term is purely imaginary. The first term is usually of the order of 10^5. Thus, (40) becomes

$$\frac{d^2\xi(\delta)}{d\ \delta^2} + \left(\frac{2^{\frac{1}{2}} m^* c\ \varepsilon}{i\hbar e E_{in} \left(\frac{\gamma^3}{2^{\frac{1}{2}}}\right)} - \frac{\delta}{\left(\frac{\gamma^3}{2^{\frac{1}{2}}}\right)} \right) \xi(\delta) = 0 . \tag{43}$$

Let a new variable be

$$\eta = \frac{A_1 - \delta}{T} = \frac{A_1}{T} - \frac{\delta}{T} , \tag{44}$$

where

$$A_1 = \frac{2^{\frac{1}{2}} m^* c\ \varepsilon}{i\hbar e E_{in}} \text{ and } T = \frac{\gamma}{2^{\frac{1}{6}}} , \tag{45}$$

then (43) becomes

$$\frac{d^2\ \xi(\eta)}{d\ \eta^2} + \eta\xi = 0 . \tag{46}$$

(46) is the Lommel equation in standard form[5], and the solution of (46) for large η is

$$\xi(\eta) \approx \eta^{-\frac{1}{4}}\ \exp\left(i\frac{2}{3}\eta^{\frac{3}{2}} \right) . \tag{47}$$

The second derivative of $\xi(\eta)$ is

$$\frac{d^2\ \xi(\eta)}{d\ \eta^2} = \left(\frac{5}{16\eta^{9/4}} - \eta^{\frac{3}{2}} \right) \exp\left(i\frac{2}{3}\eta^{\frac{3}{2}} \right) . \tag{48}$$

The absolute value of (48) is

$$\left| \frac{d^2\ \xi}{d\ \eta^2} \right| \approx - |\eta|^{\frac{3}{2}} , \quad |\eta| \gg 1 , \tag{49}$$

which shows the approximate validity of the solution (47).

If the standard formula (58.1) is applied, (see H. B. Dwight, "Tables of Integrals", p. 13), the equation (44) shows

$$\eta^{\frac{1}{2}} = (A + iB)^{\frac{1}{2}} = \left\{ \pm\sqrt{\frac{(A^2+B^2)^{\frac{1}{2}} - A}{2}} \pm i\sqrt{\frac{(A^2+B^2)^{\frac{1}{2}} + A}{2}} \right\} \approx$$

$$\pm\left\{ \left(\frac{B^2}{4A}\right)^{\frac{1}{2}} + i\left(A + \frac{B^2}{4A} \right)^{\frac{1}{2}} \right\} \approx \pm i\ A^{\frac{1}{2}}, \text{ if } A \gg \frac{B^2}{4A} , \tag{50}$$

where

$$A=\frac{2\ m^*\ \varepsilon\ c^{\frac{2}{3}}\ \ell^{\frac{2}{3}}}{e^{\frac{2}{3}}\ E_{in}^{\frac{2}{3}}\ \hbar^{4/3}},\qquad B=\frac{2^{\frac{1}{2}}\ e^{\frac{1}{3}}\ E_{in}^{\frac{1}{3}}\ \ell^{\frac{2}{3}}\ \delta}{\hbar^{\frac{1}{3}}\ c^{\frac{1}{3}}} \tag{51}$$

from (44) and (45).

(50) shows

$$\eta^{\frac{1}{4}}\approx\pm\ i^{\frac{1}{2}}A^{\frac{1}{4}}=\pm\frac{1+i}{2^{\frac{1}{2}}}A^{\frac{1}{4}}, \tag{52}$$

together with

$$\eta^{\frac{3}{2}}\approx\pm\left\{\sqrt{\frac{B^2}{4A}}+i\sqrt{A+\frac{B^2}{4A}}\right\}^3$$
$$=\pm\left\{\left(\frac{B^2}{4A}\right)^{\frac{3}{2}}+i\,3\frac{B^2}{4A}\sqrt{A+\frac{B^2}{4A}}-3\left(\frac{B^2}{4A}\right)^{\frac{1}{2}}\left(A+\frac{B^2}{4A}\right)-i\left(A+\frac{B^2}{4A}\right)^{\frac{3}{2}}\right\}. \tag{53}$$

In the above, only the imaginary part of $\eta^{\frac{3}{2}}$ is necessary for the evaluation of the photo absorption coefficient α (i.e., $\alpha_{\theta=0}$).

$$\mathrm{Im}\ \eta^{\frac{3}{2}}\approx\pm\ i\left\{\frac{3B^2}{4A^{\frac{1}{2}}}-A^{\frac{3}{2}}\right\}. \tag{54}$$

Using (54),

$$e^{i\frac{2}{3}\eta^{3/2}}\approx e^{\pm\left\{\frac{2}{3}\left(\frac{3B^2}{4A^{1/2}}\right)-\frac{2}{3}A^{3/2}\right\}}. \tag{55}$$

If we select the negative sign in (55),

$$e^{i\frac{2}{3}\eta^{3/2}}\approx\frac{e^{\frac{2}{3}A^{3/2}}}{e^{\frac{1}{2}\frac{B^2}{A^{1/2}}}}. \tag{56}$$

From (39), (47) and (52)

$$\Theta(\delta)\approx\xi(\delta)\ e^{\frac{\delta}{2^{1/2}\gamma^3}}\approx\frac{1}{\pm\ i^{\frac{1}{2}}\ A^{\frac{1}{4}}}\left(\frac{e^{\frac{2}{3}A^{3/2}}}{e^{\frac{1}{2}\frac{B^2(\delta)}{A^{1/2}}}}\right)e^{\frac{\delta}{2^{1/2}\gamma^3}} \tag{57}$$

in the above $B=B(\delta)$, and A is a real positive value inde pendent of δ. B is also a real positive value

At any angle θ

$$\Theta^*\Theta$$

is already an "amplification probability" therefore, it is not necessary to integrate $\Theta^*\Theta$. Except a constant of the dimension of (1/length) the photo absorption coefficient for electron-hole pair production α may be written as

$$\alpha \propto \Theta^{*}\Theta \approx \left(\frac{e^{\frac{2}{3}} E_{in}^{\frac{2}{3}} - \hbar^{4/3}}{2m^{*}c^{\frac{2}{3}} \varepsilon \ell^{\frac{2}{3}}}\right)^{\frac{1}{2}} \left[\frac{\exp\left\{\frac{2}{3}\left(\frac{2^{\frac{3}{2}} m^{*\frac{3}{2}} \varepsilon^{\frac{3}{2}} c\ell}{eE_{in}\hbar^{2}}\right)\right\}}{\exp\left\{\frac{1}{2^{\frac{1}{2}}}\left(\frac{eE_{in}\ell\delta^{2}}{m^{*\frac{1}{2}}\varepsilon^{\frac{1}{2}}c}\right)\right\}}\right], \qquad (58)$$

When $\delta = 0$, α becomes maximum, and such a maximum means the full utilization of light as a source of electric power.

$$\alpha_{max} = \alpha_{\delta=0}, \qquad \text{when } \delta = 0, \qquad (59)$$

and

$$\alpha_{max} \propto \left(\frac{e^{\frac{1}{3}} E_{in}^{\frac{1}{3}} \hbar^{\frac{2}{3}}}{2^{\frac{1}{2}} m^{*\frac{1}{2}} c^{\frac{1}{3}} \varepsilon^{\frac{1}{2}} \ell^{\frac{1}{3}}}\right) \exp\left\{\frac{4}{3}\left(\frac{2^{\frac{3}{2}} m^{*\frac{3}{2}} \varepsilon^{\frac{3}{2}} c\ell}{e E_{in}\hbar^{2}}\right)\right\}. \qquad (60)$$

The required constant of proportionality in (60) may be obtained from classical electrodynamics, namely a moving electron in the diode may be excited only when the electron is actually hit by light. If the light wave hits the electron within the area of πr_0^2 where $r_0 = e^2 m^* c^2$ (the classical radius of an electron), then the total cross-scction and the density of electron product may be defined as (for silicon)

$$\begin{aligned} \alpha_0 &= n\pi r_0^2 = 1.033 \times 10^{29}/m^3 \times 25 \times 10^{-30} m^2 \\ &= 2.58/m. \ (=0.0258/cm). \end{aligned} \qquad (60a)$$

In (60a) n is the particle number density of silicon. α_0 may be modified by (60) such that

$$\alpha_{max} \approx n\pi r_0^2 \left(\frac{e^{\frac{1}{3}} E_{in}^{\frac{1}{3}} \hbar^{\frac{2}{3}}}{2^{\frac{1}{2}} m^{*\frac{1}{2}} c^{\frac{1}{3}} \varepsilon^{\frac{1}{2}} \ell^{\frac{1}{3}}}\right) \exp\left\{\frac{4}{3}\left(\frac{2^{\frac{3}{2}} m^{*\frac{3}{2}} \varepsilon^{\frac{3}{2}} c\ell}{e E_{in}\hbar^{2}}\right)\right\}. \qquad (60b)$$

The eq. (60b) shows that α is a function of ε and ℓ, and ℓ is considered an amplitude of the carrier oscillator excited by light. Without light, $\varepsilon = 0$ and $\ell = \infty$. When $\ell = \infty$ there will be no oscillation. Such a conclusion may be seen in (9). ℓ may be determined from the known ε and α and (60b).

α is known from the optical experiments and

$$\varepsilon = \hbar\omega - \varepsilon_g \qquad (61)$$

where $\hbar\omega$ is the energy of the incident light and ε_g is the energy gap in a semiconductor. (For silicon, $\varepsilon_g = 1.1$ ev). The α vs. $\hbar\omega$ curve for silicon was reported by Dash and Newman.[6]

Since ε changes with $\hbar\omega$, therefore ℓ may also change with ε. Thus ℓ may change with both α and ε. If E_{in} is a constant in a diode, then the change of ℓ with ε is allowed in (9) because ℓ and θ are independent variables.

If $eE_{in} \approx 10^6$ eV/m *near the depletion layer* and is a constant, $m^* \approx 10^{-30}$ kg, $c = 3 \times 10^8$ m/s and $\hbar \approx 1.0 \times 10^{-34}$ J·s, then (60b) becomes

$$\alpha \approx \frac{0.0414}{\varepsilon_0^{\frac{1}{2}}\, \ell_0^{\frac{1}{3}}} \exp\,(18.923\ \varepsilon_0^{\frac{3}{2}} \ell_0)\,, \qquad (60c)$$

where $\varepsilon = \varepsilon_0 \times 1.6 \times 40^{-19}$ J,

and $\ell = \ell_0 \times 10^{-15.5}$ m.

were applied to (60b) for easy calculation.

For the purpose of demonstration, the dependence of ℓ on α and ε (with $\varepsilon = \hbar\omega - \varepsilon_g$) is shown in Table 1. The ε vs. ℓ curve obtained from (60c), (60d) and (60e) is shown in Fig. 4, (curve A). That curve shows ℓ decreases with increasing ε. Such a result is not surprising because if one compares the ℓ with the ℓ' of a free oscillator without damping under the same ε, one may easily recognize that the decrement of ℓ with increasing ε is a natural tendency.

TABLE 1. The light absorption coefficient α and the excited oscillator amplitude ℓ relation (From (60c))

$\hbar\omega$ (ev)	α(experi)ε_0		$\varepsilon_0^{1/2}$	$\varepsilon_0^{1/2}$	ℓ (m)
	(cm^{-1})	(ev)			
1.2	70	0.1	0.316	0.0316	$11.9\times10^{-15.5}$
1.4	600	0.3	0.5477	0.1643	$3.0\times$
1.6	1,000	0.5	0.7071	0.3535	$1.48\times$
1.9	3,650	0.8	0.8944	0.7155	$0.828\times$
2.6	14,500	1.5	1.2247	1.8371	$0.552\times$
3.0	50,000	1.9	1.3784	2.6190	$0.281\times$

The free oscillator energy balance equation is

$$\frac{\hbar^2\ (2\pi)^2}{2m^*\ \ell'^2} = \varepsilon\,. \qquad (62)$$

The ε vs. ℓ' curve obtained according to (62) directly is also shown in Fig. 4 (curve B).

One may wonder why for the same ε (of the order of 10^{-19} J), in the free oscillator case ℓ' is of the order of 10^{-10}m, but in the damped oscillator case ℓ is only of the order of $10^{-15.5}$ m. The answer may be found in (9). Using the numerical values shown previously, one may easily find that the value of the damping term $|(ieE_{in}\hbar/m^*c)\ (d\Theta/d\delta)|_{\delta=0} \approx 10^{-43}$ J, which may be neglected in comparison with the other terms in (9). Then, calculation shows

$$\left| \frac{-\hbar^2}{2m^*\ell^2} \frac{d^2\Theta(\delta)}{d\ \delta^2} \right|_{\delta=0} \approx \left| \varepsilon\Theta\,(\delta) \right|_{\delta=0} \approx 10^{-19}\ \text{J}\,. \qquad (63)$$

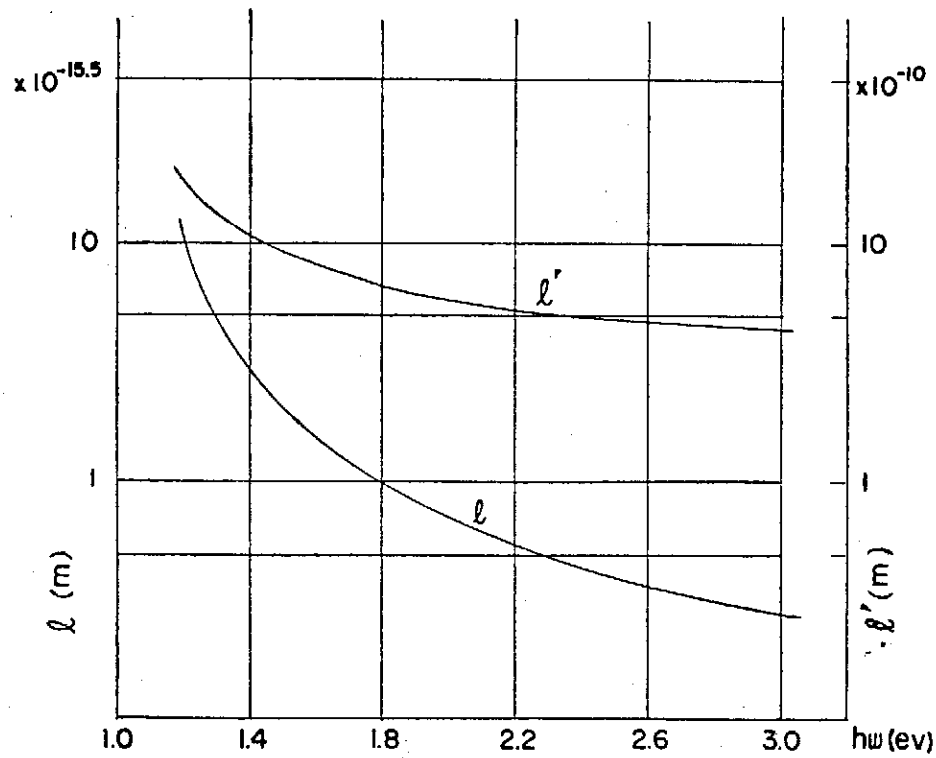

FIG. 4. Curve A: ε vs. ℓ curve calculated according to (61) with $\varepsilon = \hbar\omega - \varepsilon_g$ and the values of α are known from the published experimental curve of α vs. $\hbar\omega$ for Si crystal shown in Ref. 6. Curve B: ε vs. ℓ' curve calculated according to (62) for free oscillation without $\vec{E}_{in}$, or crystal potential.

The carrier wave function $\Theta(\delta)$ is shown in (57).

The difference between a homogeneous crystal without a junction and that with junction is the existence of the internal "lined-up" electrostatic field E_{in}. The E_{in} may also play the role of keeping the electrons and holes from recombination and for the power production. If E_{in} is not uni-directional, $<\cos\theta>=0$ in a sphere, therefore there is no damping. But, there is also no power production because the charge accumulation $q<\cos\theta>=0$. Therefore, there can be light absorption by a piece of homogeneous crystalline silicon but no electric power production ($\because q<\cos\theta>=0$).

(4) HORIZONTAL SOLAR CELL

In the casee of the horizontal solar cell (i.e., if the frontal surface of the solar cell is illuminated), the present expression of α may still be correct because if one considers that the $\cos\theta = \cos(0 + 2\frac{1}{2}\delta) \longrightarrow (1-\delta^2)$, then the final expression of α will remain the same as that shown in (60). θ is again the angle between $\vec{E}_{in}$ and $\vec{\ell}$ (which may be called $\vec{\Delta\ell}$ in this report). However, ℓ

is now presumably created by the $\vec{H}_{h\nu}$ – wave of the incident polarized light, The evidence of this argument is shown in Fig. 5. Fig. 5a shows if we let the $\vec{E}_{h\nu}$ vector of the incident polarized light be fixcd on the frontal surface of the solar cell and be normal to the "normal vector" of that plane, and if we rotate the plane around the "fixed" $\vec{E}_{h\nu}$ vector as the axis of rotation, then the angle between the "tangent" of the plane and the $\vec{H}_{h\nu}$ vector of the incident polarized light will change accordingly. (i.e., $\angle$(normal of plane, propagation vector of lighe $\vec{k}$) = $\angle$ (tangent of plane, $\vec{H}_{h\nu}$ vector of the incident light)). If the above angle of rotation of the plane is κ, then $\kappa = 0$ means normal incidence of light, and $\vec{\ell}$ of the excited carrier is parallel to the propagation vector $\vec{k}$ of the incident light and is also parallel to the $\vec{E}_{in}$ vector of the solar cell. Fig. 5a shows in the case of normal incidence of light, V_{oc} is maximum. α which is roughly prhportional to I_{sc} or V_{oc} may also reach maximum when $\vec{E}_{in} \perp \vec{H}_{h\nu}$. (i.e., $\vec{E}_{in} \parallel \vec{k} \perp \vec{H}_{h\nu}$).

When the angle $\kappa > 0$, the normal incidence becomes oblique incidence of light, and $\angle(\vec{E}_{in}, \vec{H}_{h\nu})$ becomes smaller than $\frac{1}{2}\pi$. However, $\angle(\vec{E}_{in}, \vec{E}_{\nu h})$ remains at $\frac{1}{2}\pi$ because $\vec{E}_{h\nu}$ of the incident light is along the axis of rotation of the

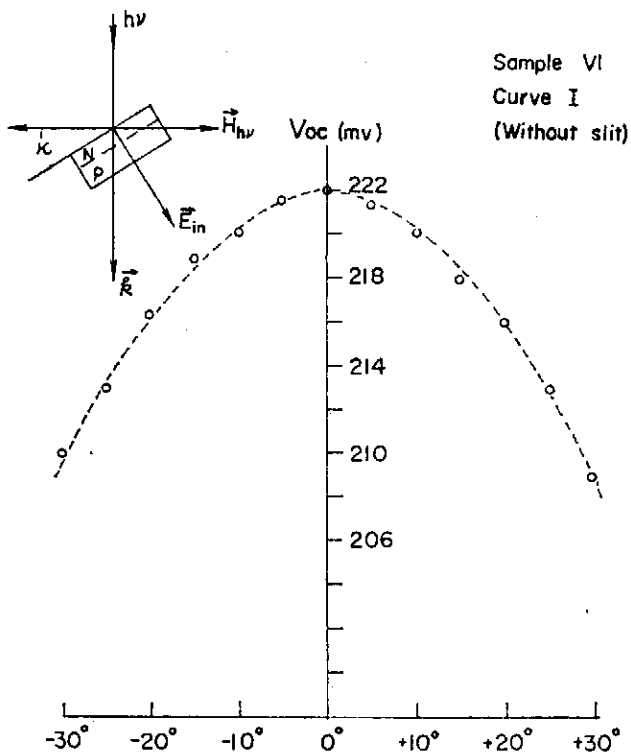

Fig. 5 (a)

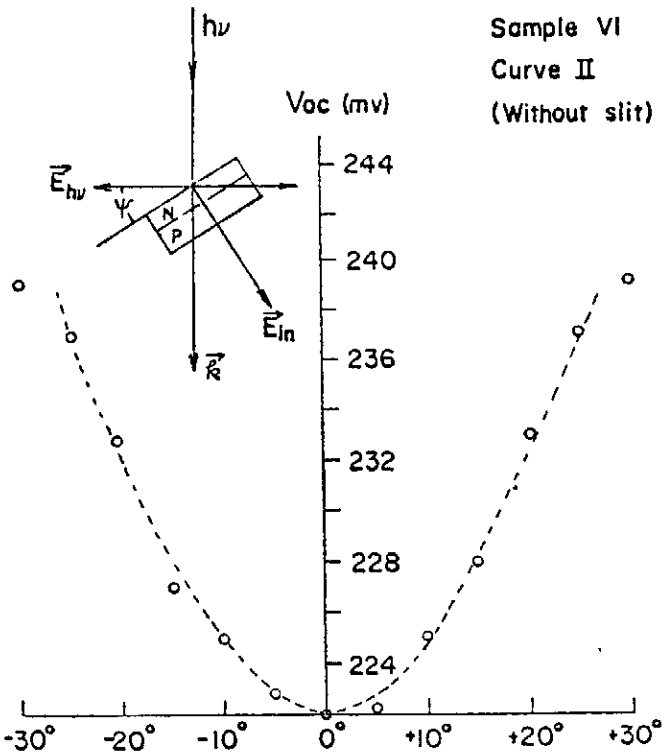

FIG. 5. (a) Curve I: V_{oc} vs. κ which is the angle of rotation of the frontal plane of the horizontal soalr cedaluor In $\vec{E}_{h\nu}$. $\vec{E}_{h\nu}$ is parallel to the axis of rotation and the axis of rotation is a tangent of the frontal plane. $\angle(\frac{1}{2}\pi - \kappa) = \angle(\vec{E}_{in}, \vec{H}_{h\nu})$, when κ increases $\angle(\vec{E}_{in}, \vec{H}_{h\nu})$ and V_{oc} decrease while $\angle(\vec{E}_{in}, \vec{E}_{h\nu})$ remains at $\frac{1}{2}\pi$. Thus the $\vec{H}_{h\nu}$ -wave may be responsible for the decrement of V_{oc}. α is therefore maximum when $\vec{E}_{in} \perp H_{h\nu}$.

(b) Curve II: V_{oc} vs. ψ which is the angle of rotation of the frontal plane of the horizontal solar cell around $\vec{H}_{h\nu}$. $\vec{H}_{h\nu}$ is now parallel to the axis of rotation and the axis of rotation is again a tangent of the frontal plane. $\angle(\frac{1}{2}\pi - \psi) = \angle(E_{in}, E_{h\nu})$, and when ψ increases $\angle(\vec{E}_{in}, \vec{E}_{h\nu})$ decreases but V_{oc} as well as I_{sc}), increases. Since $\angle(\vec{E}_{in}, \vec{H}_{h\nu})$ remains at $\frac{1}{2}\pi$, therefore, the $\vec{E}_{h\nu}$ -wave may become responsible for the increment of V_{oc}. α is therefore maximum when $E_{in} \parallel E_{h\nu}$, i.e., the horizontal solar cell is turned into a vertical solar cell by rotation around the $\vec{H}_{h\nu}$ vector. (For good experimental results, noise must be avoided by using coaxial cable, etc).

frontal plane of the horizontal solar cell. Since experimentally it was found that both the V_{oc} and I_{sc} decreased with $\angle(\frac{1}{2}\pi - \kappa) = \angle(\vec{E}_{in}, \vec{H}_{h\nu})$ while $\angle(\vec{E}_{in}, \vec{E}_{h\nu})$ remained at $\frac{1}{2}\pi$, therefore the $\vec{H}_{h\nu}$ – wave of the incident light might be responsible for the decrements of V_{oc} and I_{sc}.

The curve 5b shows that the V_{oc} increases with ψ (which is such an angle that $\angle(\frac{1}{2}\pi - \psi) = \angle(\vec{E}_{in}, \vec{E}_{h\nu})$) while the vector $\vec{H}_{h\nu}$ is alone the direction of the axis of rotation of the frontal plane of the horizontal solar cell. Since now $\angle(\vec{E}_{in}, \vec{H}_{h\nu})$ remains at $\frac{1}{2}\pi$, therefore the $\vec{E}_{h\nu}$ – wave may be responsible for

the increments of V_{oc} and I_{sc}. In this case, the maximum V_{oc} may be obtained when the angle $(\frac{1}{2}\pi - \psi) \to 0$, i.e., when a horizontal solar cell is changed into a vertical solar cell by rotation.

If we look at the Figs. 1 and 2 again, we may observe that the V_{oc} at $\theta = \frac{1}{2}\pi$ (i.e., $\vec{E}_{h\nu} \perp \vec{E}_{in}$) is not zero even-though it is usually much smaller than the maxmum V_{oc} found at $\theta = 0$. The reason for this is probably that there is always some incident light being scattered away from the original direction of incidence before being absorbed for the pair production. For instance, the carriers may be excited by the primary incident light first and the free electron hole pair is not formed but the excited carrier will re-emit a radiation with a component of $\vec{E}_{h\nu}'$ of the secondary radiation in the direction of $\vec{E}_{in}$, by quick deceleration in the direction of the original primary $\vec{E}_{h\nu}$ of the incident light. This process of scattering is allowed by the classical electrodynamic theory[7]. If the $\vec{E}_{h\nu}'$ component is in the direction of $\vec{E}_{in}$ and $E_{h\nu}' \approx E_{h\nu}$, then the absorption coefficient α_{bg} for the "background absorption" for the pair production may still be the expression shown in (60). Thus, the total absorption coefficient is

$$\begin{cases} \alpha_t(\lambda, \theta) = \alpha_{primary}(\lambda, \theta) + \alpha_{secondary}(\lambda), \\ \alpha_{bg} = \alpha_{secondary}(\lambda). \end{cases} \qquad ((64)$$

This may be so because α is considered a scalar quantity. $\alpha_{secondary}(\lambda)$ is considered the absorption coefficient of the scattered light and it is, on the average, independent of the angle θ (λ is the wave length of the incidnet light).

The experimental findings in the case of the vertical solar cells may indicate that if the vertical solar cell is properly designed technically, the efficiency may be substantially improved.

REFERENCES

(1) W. H. Runyan, "Silicon semiconductor technology", McGraw-Hill Co., New York, 1972, pp. 146-151

(2) C. Møller, "The theory of relativity", Oxford, New York, 1952, pp. 140-141

(3) E. T. Whittaker and G. N. Watson, "Modern analysis", 4th ed., Cambridge, New York, 1961, p. 194, equs. (A) and (B)

(4) H. Weber, Math. Ann., **1**, 29, 1869; also E. L. Ince, "Ordinary differential equations", Dover Publ. Inc., New York, 1956, p. 175

(5) E. Lommel, Math. Ann. **XIV**, 510, 1879; also G. N. Watson, "A treaties on the theory of Bessel functions" Cambridge, New York, 1958, p. 97, eq. (11)

(6) W. C. Dash and R. Newman, Phys. Rev., **99**, 1151, 1955

(7) W. K. H. Panofsky and M. Phillips, "Classical electricity and magnetism", 2nd ed., Addison-Wesley, Reading, Mass., 1962, Chapters 20-22. In particular, the equations (22-16), (22.22), and (22-72)

(8) Y. T. Yang, J. Appl. Phys., **50**(7), 5047, July, 1979

A SURFACE-ACOUSTICAL-WAVE BANDPASS FILTER AND ITS OPTICAL PROBING*

SHOU-YIH WANG, DAH-MIN HWANG**,
T.T. CHEN, C.S. LAI and YEON-FUH JIANG

Department of Physics, National Tsing Hua University
and
N. T. LIANG
Institute of Physics, Academia Sinica, Nankang,
Taipei, Taiwan, Rep. of China

Abstract

A wideband bandpass surface acoustical wave filter of center frequency 87 MHz with bandwidth 30 MHz has been designed and fabricated on a $LiNb0_3$ substrate. Measurements on the filter showed an insertion loss of approximate 28 dB and a time delay of 2 microseconds. Laser optical probing technique has been employed to study propagation characteristics of the surface acoustical waves. The resultant diffraction patterns expected features. These data agreed in general to existing literature, except that the sinx-x comb structure tended to generate energy profiles without strongly rising and falling edges across the transverse direction. Discussions on this point and others have been given.

I. INTRODUCTION

Surface acoustic waves (SAW), mainly Rayleigh waves, have been widely studied and developed to many applications. One feature of SAW is that the particles at the surface move in elliptical paths[1]. The SAW velocity in a semi-infinite medium is practically independent of frequency through the microwave range, and the particle motion decreases from its surface to small values at a depth about one wavelength. Hence, the SAW have much larger powes density than the elastic bulk waves. Since SAW velocities are roughly 10^5 times smaller than electromagnetic wave velocities, it is attrative to study the use of SAW in electronic devices, such as delay lines, filters, etc.. In section II, a SAW bandpass filter will be reported. The flexibility of the SAW design gives one vast freedom to choose time domain impulse response which has a desirable frequency transform.

In section III we describe the diffraction of light by SAW. To study the SAW on piezoelectric substrates by the method of optical probing is important to a SAW-device designer. The properties of SAW, such as propagation and steering effect, etc., can be obtained using a simple optical probing technique. The energy profiles of SAW filter were measured. Finally in section IV we will summarize the main results and discuss them.

* This work was financially supported by the National Science Council of the Republic of China.
** Current address: James Franck Institute, University of Chicago, Il1. 60637, U.S.A..

II. SAW BANDPASS FILTER

(A) General description

A widely adopted method of generation of SAW on piezoelectric substrates is to make use of an interdigital transducer (IDT). In these SAW devices, the frequency characteristic is determined by the finger spacing and finger width of the input and output IDT comb structure. The amplitude response is controlled by varying the lengths of the fingers. The delay time depends on the frequency and the distance between transmitter IDT and receiver IDT. Since the finger spacing and finger length are independent of each other, this feature allows us to design an IDT comb structure which could meet a predetermined frequency response.

The theory of the IDT may be described by some models, such as the equivalent circuit model[2], impulse model[3], and the so called δ-function model[4]. The design of SAW devices requires information about the dependence of the transfer function on electrode geometry and material parameters. In general, the frequency response of an isolated IDT comb structure is determined by the Fourier transform[5],

$$h(f)=K\int_{-\infty}^{\infty}A(x)\cos\left(2\pi\int^{x}\frac{dx'}{\Delta(x')}\right)e^{-2\pi jfx/v}\,dx \qquad (1)$$

where K is a constant, f is the frequency, x is the distance along the comb structure, v is the velocity of the SAM, A(x) is the length of the finger at x, $\Delta(x)$ is the spacing between adjacent finger.

Surface acoustical wave filters are generally treated as a two-port network. For a given impressed elastic excitation, the transmitting section generates a summation of plane waves radiating from the finger edges. The electric output in the receiver is a superposition of these transmitted waves as they traverse each finger. The filtering properties of these devices are completely determined by the process in conversion of electrical signal to acoustical energy, and vice versa, at the input and output interdigital transducers. The total transfer function of the device is the approximately given by[3, 6]

$$H(f)=\frac{V_{out}}{V_{in}}\cong h_{in}(f)e^{-j\omega\tau}\,h_{out}(f) \qquad (2)$$

where $h_{in}(f)$ or $h_{out}(f)$ is of the form of eq. (1) and τ is the delay time between the transmitter and receiver. Then the comb shape is the Fourier transform of the desired frequency response H(f).

(B) Design of a SAW bandpass filter

Suppose we desire a normalized $|H(f)|=1$, where $|f-f_0|\leq\frac{1}{3}f_0$, and f_0 is the center frequency. As given in section II(A), we would consider a case

where one IDT is unapodized (broad band, uniform) and one (sinx/x) apodized comb. On the unapodized transducer, the spectral amplitude response is nearly constant over the desired bandwidth Δf. Thus the frequency response is primarily determined by the sinx/x comb. In order to build the transducer of finite size, a finite impulse response is obtained by truncating the infinite spatial extent of sinx/x at the two tenth lobes on either side of the main lobe. There is a 180° phase change at each zero crossing of sinx/x, where the finger connection should be reversed. The input and output interdigital transducers are shown in Fig. 1. The transmitter has 121 fingers with the overlap function which has the finger lengths

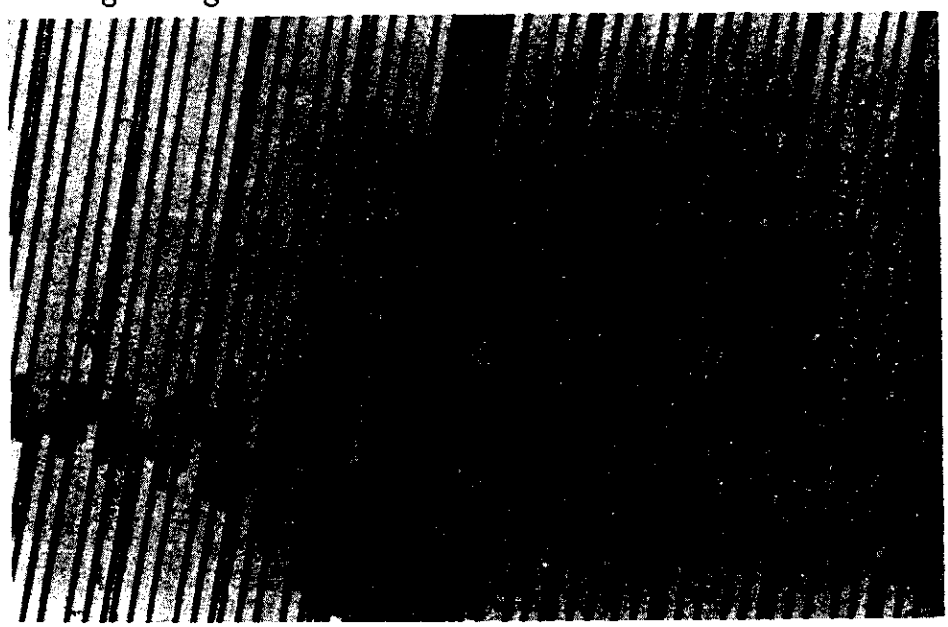

Fig. 1. (a)

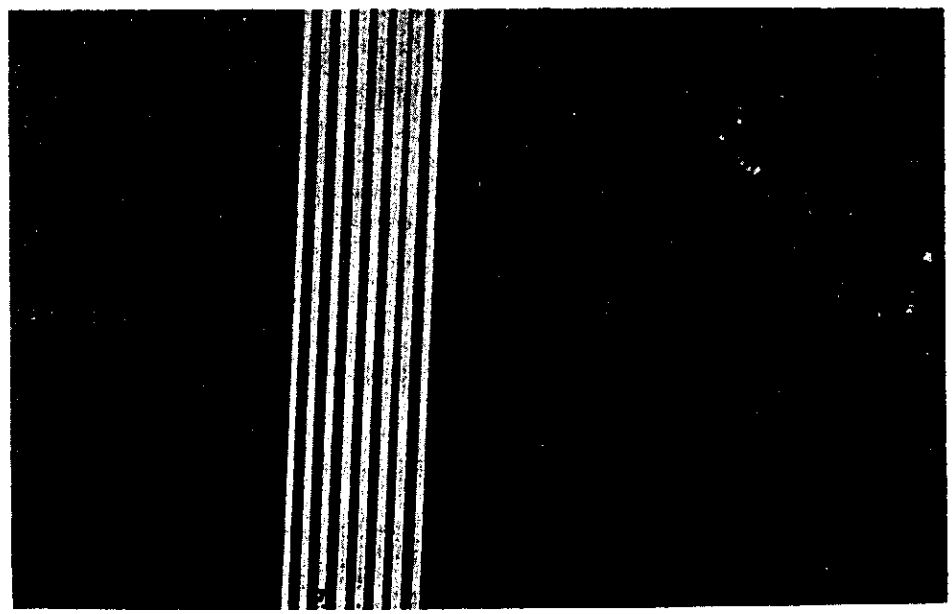

Fig. 1. (b)

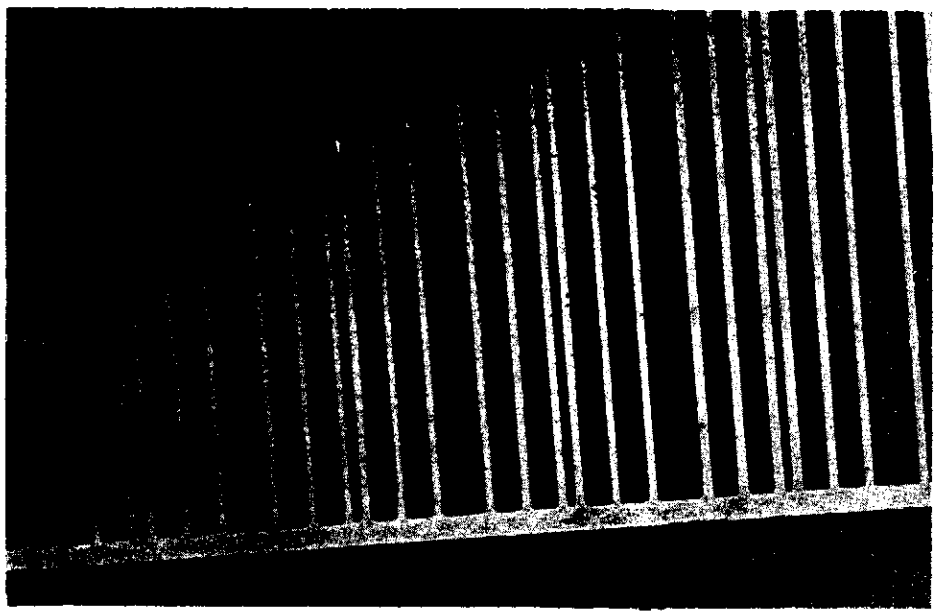

Fig. 1. (c)

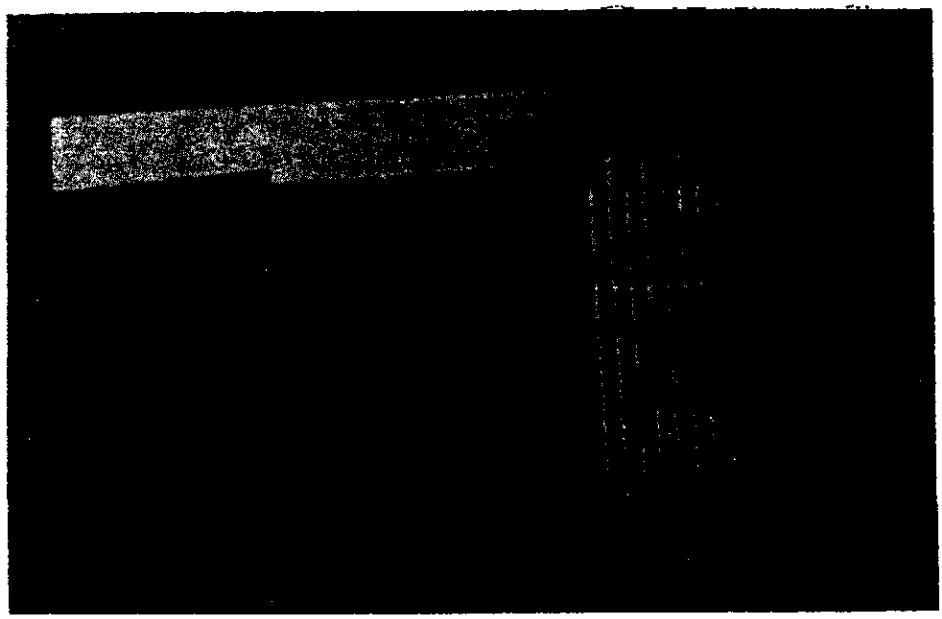

Fig. 1. (d)

FIG. 1. A part of photograph of a sinx/x comb is shown in Fig. 1(a). One broadband comb is shown in Fig. 1(b, d). The reversed connection at zero crossings of sinx/x comb is shown in Fig. 1(c).

$$A(x) = 3.6(\sin(\frac{\pi}{3}\frac{x}{\Lambda}))/(\frac{\pi}{3}\frac{x}{\Lambda}),$$

where $x = 0, \pm\frac{\Lambda}{2}, \pm\Lambda, \pm\frac{3}{2}\Lambda, \ldots, \pm 30\Lambda$. The acoustic beam width $a = 3.6$ mm and the acoustic wavelength $\Lambda = 40$ μm. The equal finger spacing and width $\Delta = 10$ μm. The receiver has 5 finger pairs with uniform overlap finger

length a = 3.6 mm. The distance between centers of transducers S = 0.68 cm. Consequently the filter will operate with center frequency $f_0 = 87$ MHz and with fractional band width 33%.

(C) Fabrication of the SAW filter on a piezoelectric substrate

The procedure required to prepare a filter on a $LiNbO_3$ substrate is listed as follows:

1. To comply with the design of SAW filter, a proportional 200 times enlargement of the final image of the desired IDT is scribed on a section paper.

2. Carefully cut the diagrams down on Rubylity.

3. Fabricate a photomask. It was done at the Semiconductor Research Center in National Chiao-Tung University.

4. Choose and clean a $LiNbO_3$ substrate.

5. Fabricate the IDT on $LiNbO_3$ by standard photolithographic technique in desired direction. The transducers are made of Al by vacuum evaporation with thickness about 2000 Å.

6. Bond the electrodes with silver bond.

In fig. 1 is shown the photographs of the structures of our IDTS.

(D) Measurement of the SAM filter

Because yz (y cut, z propagation) $LiNbO_3$ has maximum coupling coefficient, minimum steering effect and minimum insertion loss at fractional band width of about 30%, the yz $LiNbO_3$ was used as substrate. After the fabrication of SAW filter on $LiNbO_3$ was completed, the edges of $LiNbO_3$ were surrounded by an absorber (Q sealing compound) to eliminate the reflection of SAW.

The frequency response of the device was measured with AM signal. We saw the input and output signals with a YHF oscilloscope, TEKTRONIX 7603. To check whether the SAW was propagating through the substrate surface and not through the air, we tested with a drop of acetone on the substrate and watched the change in waveforms on the oscilloscope. Also, we can simultaneously record the input and output voltages. By definition, the insertion loss (IL) of a network is expressed in decibles as $IL = -20 \log H(f)$. The insertion loss of the unmatched SAW filter is shown in Fig. 2.

The delay time of the device can be seen with a 50 KHz modulated wave. It was found 2 μsec via an UHF oscilloscope. This agreed reasohably with the theoretical value of 1.95 μsec. The impulse response of the device can be seen when a narrow pulse is applied. The impulse response is shown in Fig. 3.

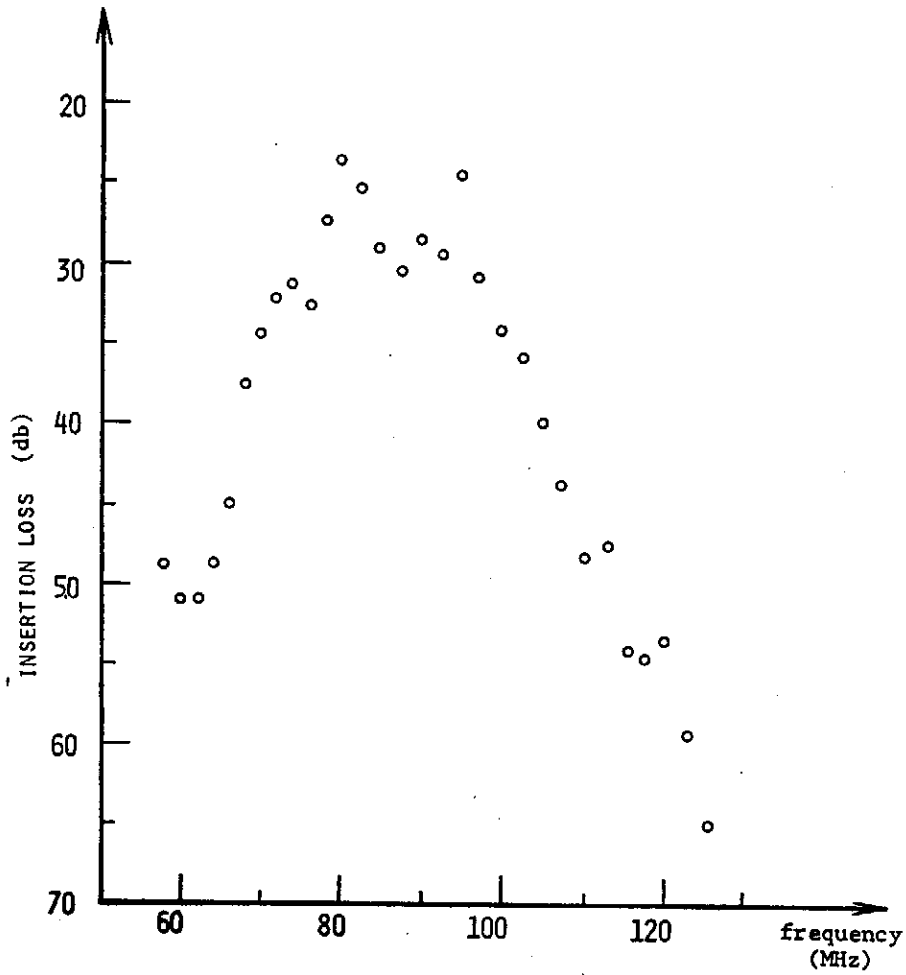

FIG. 2. Insertion loss of the SAW filter.

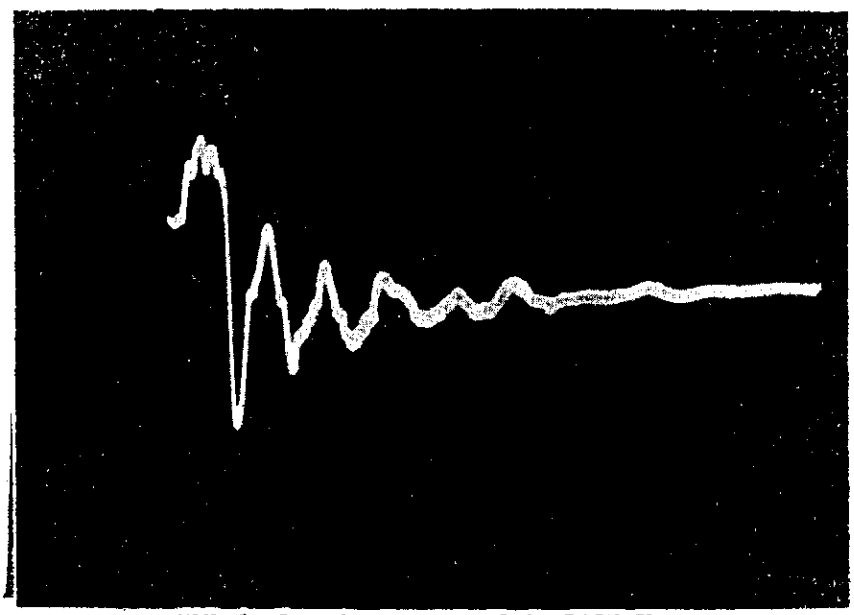

FIG. 3. Impulse response of the SAW filter.

III. OPTICAL PROBING OF SAW

(A) General description

A propagating Rayleigh wave produces both a surface deformation and a periodic variation of refractive index within the surface layer. It provides a moving phase grating for an incident laser light beam and thus diffracts the light into many side orders. For the reflected light beams only the surface deformation contributes to the light diffraction.

Assume the surface deformation to be sinusoidal. As the incident light is reflected, it produces a phase modulation and results in many interference peaks in the far field region. Then, a plane grating type of diffraction will be found. The angle of the m-th order diffraction is given by[6, 7]

$$\sin \theta_m = \sin \theta_o + m\lambda/\Lambda ; \qquad m = 0, \pm 1, \pm 2, \ldots .$$

where θ_m is the diffraction angle of the m-th order with respect to surface normal, θ_o is the angle of the incident light, λ is the optical wavelength and Λ is the acoustic wavelength.

The optical probing technique[7] serves to determine SAW propagating characteristics on an anisotropic substrate. This is based on the fact that the deflected light is directly proportional to the acoustic power of the surface wave. We can use the optical probing method to study the radiation pattern of an interdigital transducer. The energy profiles as a function of distance from the input transducer provide the information about diffraction loss and beam steering effect. These properties are very important in designing the microwave SAW devices.

(B) Experimental set-up and result

The propagation characteristics of SAW can be determined by directly probing the acoustic energy with a He-Ne gas laser. The SAW must be modulated. In this method, the surface wave deflects a small fraction of the incident light, which is detected with a photomultiplier tube (PMT) and a lock-in amplifier. The other instruments and experimental arrangement are shown in Fig. 4.

Because the first order diffracted light has higher intensity than other diffracted order, it is comparatively easy to be detected. To prevent the interference from other diffracted light, we detected the negative first order only. The recorder outputs of the first-order diffracted light at two different distances from the input IDT are shown respectively in Fig. 5(a) and (b).

IV. DISCUSSION AND CONCLUSION

In fig. 3, we showed the impulse response of the SAW filter. The waveform

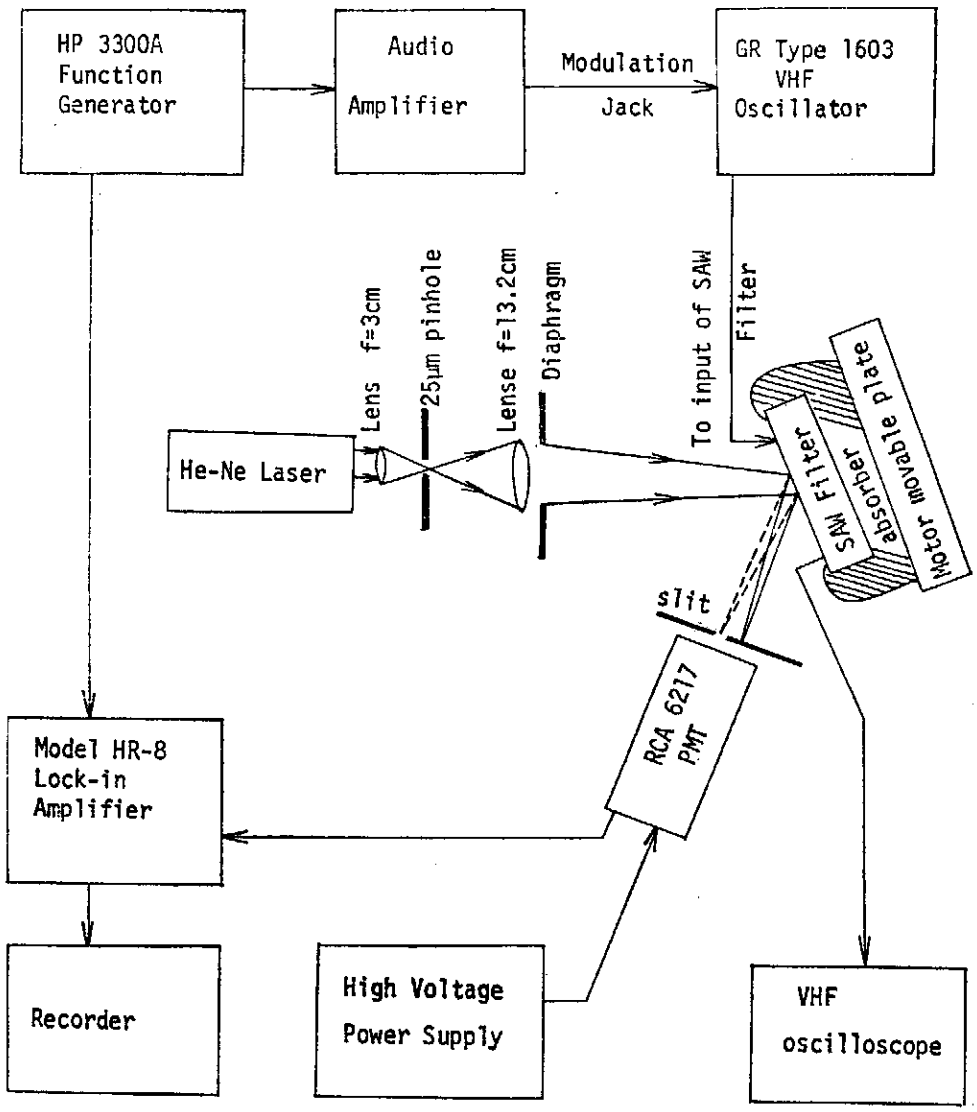

FIG. 4. The setup for optical probing of the energy distribution profiles of the SAW filter

behaves like a sinx/x truncated at the center. Since the transfer function of the device is the Fourier transform of the impulse response, the transfer function H(f) would behave like a gate function, i.e. an ideal band pass frequency dependence. The H(f) as observed in Fig. 2 indeed appears somewhat like a gate function except a number of diffraction peaks. This tends to demonstrate the Fourier transform relation between the sinx/x comb structure and the transfer function H(f). The truncation of sinx/x at its center is not understood. This might be due to improper triggering in using the VHF oscilloscope.

Impedance matching between the VHF oscillator GR type 1603 and the SAW filter input was not used, because as filter without matching network could

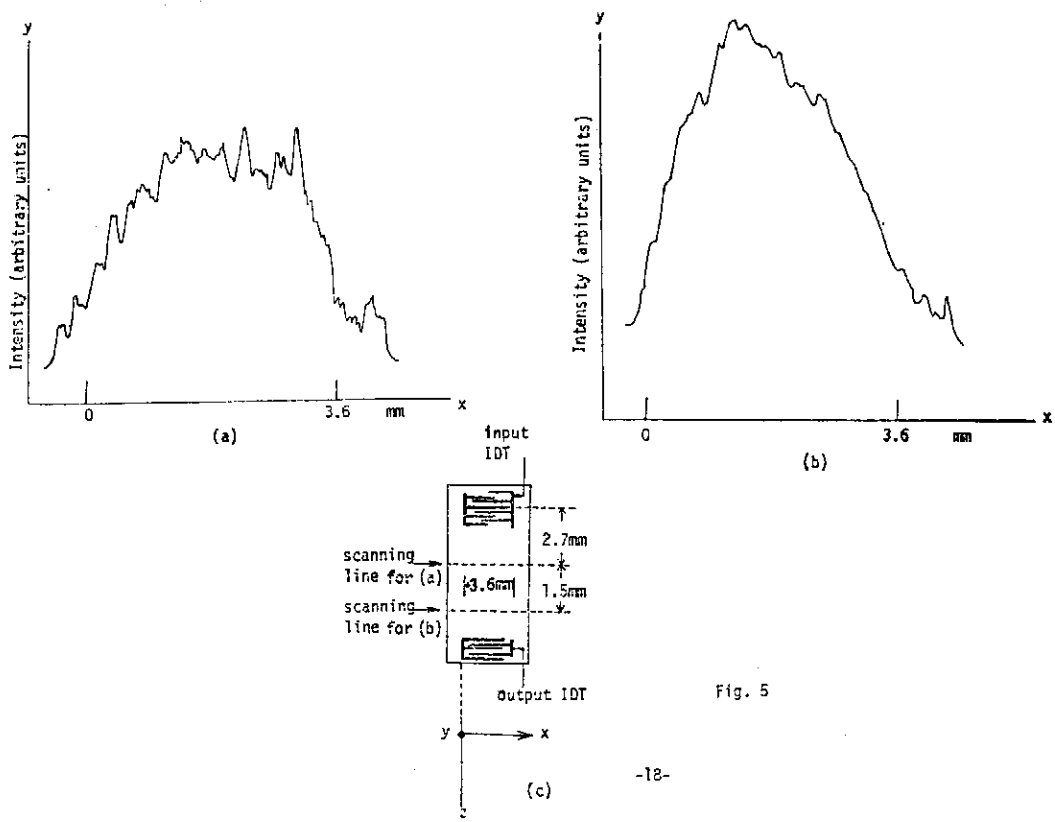

FIG. 5. The energy profile of SAW filter where the distance between scanning line and central finger is (a) 2.7 mm and (b) 4.2 mm, (c) shows the substrate and the scanning lines.

obtain its minimized triple transit echo due to unavoidable regenerations of unwanted signals at the network. In addition, transducers without matching would have lower electric Q-value of the circuit to meet our wideband requirement. Furthermore, via the aid of an admittance meter, the input impedance around the center frequency of the SAW filter was determined to be about 30 ohm pure resistance. This value was rather close to the idealized 50 ohm input impedance as required to match the 50 ohm output impedance of the VHF oscillator.

In the laser probing, the diffraction patterns of SAW generated by the sinx/x IDT at $z=2.7$ mm and $z=4.2$ mm have been detected and shown in Figs. 5(a) and (b) respectively. These intensity distributions appear qualitatively correct in their general shapes as compared to Fig. 12 of ref. (8). The pattern near the input IDT had wider full width of half maximum (FWHM) than that at farther distance. The position of the center of the pattern also shifted with the SAW propagation. The ripple peaks were rounded and decreasing in number at $z=4.2$ mm as compared with that at $z=2.7$ mm. These characteristics are in conformity with those in ref. (8).

The main differences of our results from the ref. (8) lie in two parts. One is that our pattern did not show strong rising and falling edges at two sides of the pattern as shown in Fig. 5. This would be caused by our sinx/x filter structure which had shorter overlap finger lengths along the center line of the two IDT's at the sidelobes of sinx x than those fingers middle of the comb. Here We remark that the interdigital transducer of in the ref. (8) is of uniform overlap which quite differs from sinx x. Another difference is the more pronouncing and sharper ripple peaks in our energy profiles. This effect could be made less pronouncing if the size of laser beam is suitably enlarged. The reason is that the optical probed diffraction pattern clearly is the result of the convolution of the local surface acoustical wave and the probing laser light. The above two differences could be quantitatively resolved if a computer computation is to be done. A numerical calculation based on Sommerfeld's diffraction integral with convolution of a Gaussian laser distribution would very possibly yield comparable theoretical diffraction patterns[9].

In conclusion, we designed and fabricated a bandpass SAW filter with satisfactory characteristics. Laser probing of the SAW exhibited features understandable and comparable with those of ref. (8) Clearly, this probing technique is very important in understanding the physics of diffraction of SAW and in optimizing the performance of the filter.

Acknowledgement: The authors are very grateful to Mr. L. C. Chu of Chung-Shan Research Institute, Dr. T. C. Liu, Professor C. Y. Che and C. S. Pang of the Electric Engineering Department of Chung Cheng Institute of Technology for their assistance and their VHF oscilloscope.

REFERENCES

1. B. A. Auld "Acoustic fields and waves in solids" Vol 11, Willey-Interscience 1973
2. W. Richard Smith, Henry M. Gerard and William R. Jones "Analysis and Design of Dispersive Interdigital Surface-Wave Transducers". IEEE Trans. Microwave Theory Tech. Vol. MIT-20, No. 7, July 1972 p. 458
3. Clinton S. Hartmann, Delamar T. Bell. Jr. and Ronald C. Rosenfeld "Impulse model Design of Acoustic Surface-Wave Filters" IEEE. Transasonics and ultrasonics, Vol. Su-20, No. 2, April 1973, p. 80.
4. R. H. Tancrell and M. G. Holland "Acoustic Surface Filters" Proceedings of the IEEE Vol. 59, No. 3 March 1971 p. 393
5. P. Hartemann and E. Dieulesaint "Intrinsic Compensation of Sidelobles in a dispersive acoustic delay line". Electronic letters 15th, May, 1969, Vol. 5, No. 10, p. 219
6. Melvin G. Molland, and Lewis, T. C. Laiborne "Practical Acoustic Wave Devices" Proceedings of the IEEE Vol. 62, No. 5, May, 1974, p. 582.
7. Eric E. G. Lean and Carl, G. Powell "Optical probing of Surface Acoustic Waves". Proceedings of the IEEE, Vol. 58, No. 12, December 1970, p. 1939
8. Andrew J. Slobodwik, Jr., "Surface Acoustic Waves and SAW Materials" Proceedings of the IEEE, Vol. 64, No. 5, May, 1976, p. 581.
9. Chia-Yu Ai, Chyr-Pwu Tzou, Shou-Yih Wang and Dah-Min Hwang "The Convergent Property of Surface Acoustic Waves Generated by Concave Transducers on Anisotropic Crystal Surfaces". Chinese J. of Phys., Vol. 17, No. 1, P. 12 (1979)

二維密度層變流通過障礙受阻的研究

黃　榮　鑑

中央研究院物理研究所

摘　　要

本文以實驗的方法探討有限深度之二維密度層變流場中，流體通過一系列半圓柱形及半橢圓形障礙物受阻的效應，背面波的形成與發展以及背面波流線不穩定的臨界狀況等現象。

實驗方法爲利用鹽水的填加，在實驗水槽中填製密度層變的流場，並引用對流場拍攝的技巧以追踪及記錄層變流場的流況發展與變化。經由一系列的變化流場的層變梯度、障礙物的大小以及流體的速度以進行實驗。實驗結果顯示，背面波的形成與發展除受 F, β 及 ϵ 因子影響外，因流體的粘滯性產生流線的分離亦爲重要的影響因素，特別在高深比 β 較小及障礙物高寬比 ϵ 較小時 R的影響至爲顯著。

壹、緒　　言

存在於地球表面及其周遭的自然界如海洋、大氣以及湖泊等的流體，其密度大抵爲穩定的層變性質：也就是流體的密度隨著高度的增加而減少。在密度層變之流場中，如遭受擾動，則有內重力波 (internal wave) 的發生。因此重力波的發生爲密度層變流場中的主要特性。而流體流經障礙物，因受阻所造成的干擾爲產生重力波最顯著的特例之一。當流場受阻形成內重力波（或稱背風波）後，其形成對於障礙體附近的流場有很大的影響及變化。

有關層變流通過障礙物的研究，當以 Long 氏一連串研究的貢獻爲最大[1-3]。在假設：(1)流場爲定量流 (steady flow)，(2)障礙物上游遠方之水平動能 $^1/_2\ \rho\ (z)\ U^2\ (z)$ 爲常數，亦即不受內重力波之干擾，(ρ 爲流體密度，U爲流體之水平流速) 。(3)無粘滯性之影響。Long 由非線性之 Euler 運動方程式，演譯導出線性的 Helmholtz 方程式，以探討二維層變流通過障礙物的流場，並利用適當的邊界條件得出 Long 氏模式 (Long's model)。由理論解析的結果，Long 氏指出：當 $F > \frac{1}{\pi}$，$F = \frac{U}{NH}$ (N 爲 Brunt Vaisala 頻率，H爲流場深度)，流場滋生之內重力

波爲穩定；當 $F<\frac{1}{\pi}$，如障礙體高度 h 大或高深比 $\beta=\frac{h}{H}$大時，則引生的內重力波會有翻滾或旋螺（overturning or rotor）的現象發生，而成爲不穩定。

隨後又有多人引用 Long 氏模式以進行二維層變流體通過不同形狀障礙物的流場解析。如 Miles 及 Huppert 氏對垂直板、半圓形柱體及半橢圓柱體等的一系列探討[4-6]；Davis 氏對垂直板及三角形柱體的解析[7]等。他們的研究結果指出：在層變流中，由於障礙體阻擋所產生的背面波(Lee wave)常因障礙體的高度、形狀及流場的 Richardson 數 $K=\frac{Nh}{U}$的不同而異，同時臨界穩定的情形也不同。當高寬比$\frac{h}{b}=\infty$（垂直板）時，$K_c=1.73$；$\frac{h}{b}=1$（半圓形柱體）時，$K_c=1.27$；$\frac{h}{b}\to 0$，時，$K_c=0.67$。這些解析的探討都假定流場的特性符合 Long 氏之假設（Long's hypothesis），也就是說阻擋物上游流場中沒有發生阻擋效應（upstream blocking effect），同時在障礙體上沒有因流線的分離（flow seperation）而滋生亂流尾流（turbulent wake）。

最近 Baines 氏曾對 Long 氏假設的眞實性加以探討[8]，由實驗記錄的流場狀況與 Long 氏模式解析的結果比較，他發現其吻合性並不好，主要由於阻擋效應常使上游區之流場發生變化，同時下游所發生之內重力波與旋螺也會向上游傳遞，而影響上游區的流況。因此 Long 氏其上游流場不變的假設並不能成立。此外，我們發現，在障礙體上發生流線分離所產生的尾流亦將影響內重力波之生成及穩定性，以及其旋螺區（rotor region）的特性。因此當密度層變流通過障礙體產生背面波時，在某些條件下其所受阻擋效應及粘滯性（引生流線分離）的影響不允忽視。

本文經由實驗以探討密度層流通過一系列柱體障礙物的流況變化情形。由對流場的觀測，分析流場的層變，障礙物的高度以及尾流區的形成對內重力波的生成及其穩定性的影響。同時，由對流場的記錄探討背面波形成的結構以及亂流尾流對於內重力波的影響。

貳、實驗裝置及其程序

實驗在一長 3.7 公尺，寬 0.3 公尺，深 0.3 公尺的壓克力水槽內進行。水槽中的層變流體以不同含鹽量之水充填，以產生高度向的密度層變。層變流體的密度梯

度由槽底至水面均爲常數。利用鹽水填加的方法[9]，在水槽中每 2 公分由下而上填加不同含鹽量之鹽水14層。水槽中鹽水之填加約需 5 小時。填妥之鹽水由於各層間之密度差異，在不受擾動下，由於分子運動的作用，將導致上下層間密度差的漸趨緩和。填妥後的水域靜置約18小時後，其密度層變將呈線性分佈。

水槽中水流通過障礙物的運動，係由移動障礙物的相對運動產生受阻之流場。如圖一所示，在水槽上方架二支平行於水槽兩側之鋼軌供臺車行走。臺車上裝置一由三組滑輪及一變速馬達組成的傳動系統，利用可變電壓器改變電源之電壓（40～110伏特），可使臺車在不同的速度（0.5～5.0公分／秒）下，極其穩定的前進。障礙物以四支細小連桿固定於臺車，置於水槽底部。因此由臺車的帶動，可使障礙體在層變流體中以所須的速度等速移動。

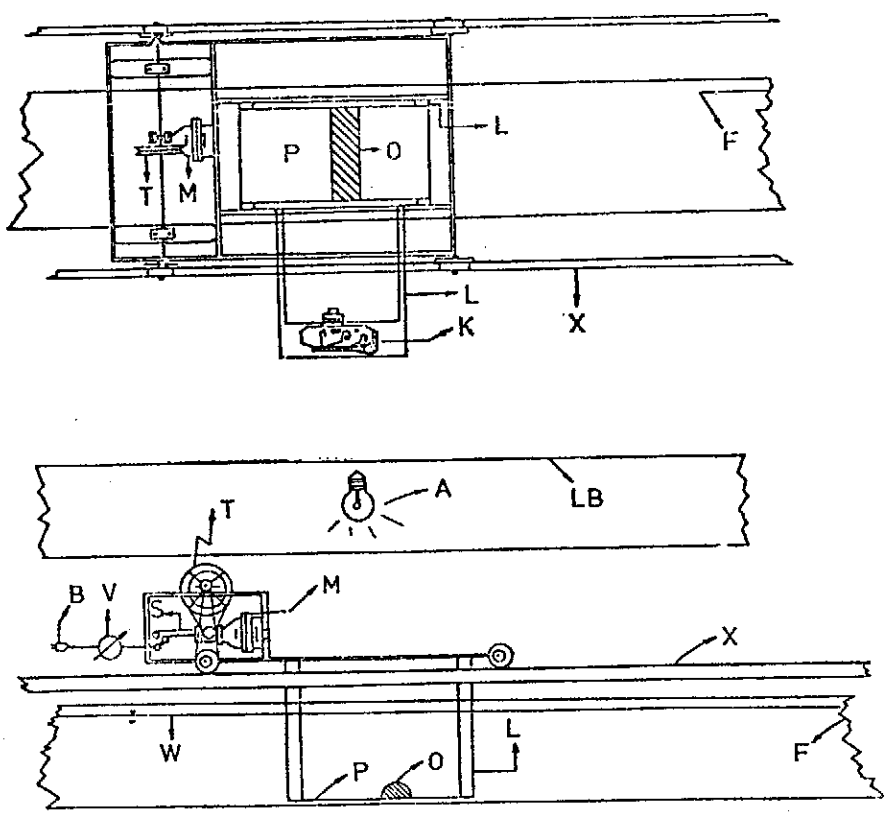

A 1kw 水銀燈
B 電源
F 水槽
K 相機
L 連桿
LB 光箱
M 馬達
O 障礙物
P 底板
T 傳動系統
V 電壓控制
W 水面
X 鋼軌

圖一　實驗裝置設備

流場的顯現，是利用架於水槽中段上方的光箱（長160公分，內置1瓩水銀燈一具）以 1 mm 寬之狹縫將光層射出，直接照射在懸浮於水中之細小白色塑膠顆粒（0.1～0.5 mm），再利用架於臺車側方（與臺車一同行進）的 Nikon F_2 50mm 鏡

頭之相機，由快門時間一秒，光圈 5.6，高感度黑白底片 ASA400，對流場作定時的拍攝，則流場的變化由顆粒的軌跡可清晰的被拍攝。而塑膠顆粒在層變流體靜止時，由於密度不同，穩定的懸浮於各層鹽水中。

實驗中，由於臺車行走的時間都在 200 秒內，因此肇因於流體粘滯效應在底部及水槽二側所形成之界面層 (Boundary Layer) 厚度 $(\nu t)^{1/2} \leq 1.4$ 公分，對於二維度及流況的影響十分微小，可予忽略。

參、結 果 與 討 論

二維層變流通過障礙體的實驗，經由一系列的變換障礙體形狀、大小、層變梯度及水理條件，如表一，藉對流場的拍攝獲致一系列的流況變化。經對流場的分析原觀察，發現流況與 F，β 及雷諾數 $R = \frac{Uh}{\nu}$ 有關。詳述如下：

表一　臨界流況附近之實驗數據。尾欄中○表示流況穩定，●表示不穩定。

RUN NO.	$\beta=\frac{h}{H}$	$R=\frac{Uh}{\nu}$	$F=\frac{U}{NH}$	U	ρ_{max}	$\frac{d\rho}{dy}$	$N=\sqrt{\frac{g}{\rho_{max}}\frac{d\rho}{dy}}$	
1—1	0.0893	148	0.0488	0.600	1.0152	0.000200	0.439	●
1—2	0.0893	178	0.0503	0.721	1.0077	0.000270	0.512	○
1—3	0.0893	235	0.0407	0.951	1.0192	0.000725	0.835	●
1—4	0.0893	279	0.0490	1.13	1.0192	0.000704	0.823	○
1—5	0.0893	294	0.0518	1.19	1.0192	0.000698	0.819	○
1—6	0.0893	324	0.0407	1.31	1.0373	0.00140	1.15	○
1—7	0.0893	331	0.0416	1.34	1.0373	0.00140	1.15	○
2—1	0.215	334	0.0700	0.968	1.0077	0.000251	0.494	●
2—2	0.215	354	0.0710	1.02	1.0077	0.000271	0.513	●
2—3	0.215	424	0.0546	1.23	1.0192	0.000671	0.803	●
2—4	0.215	481	0.0616	1.39	1.0192	0.000675	0.806	○
2—5	0.215	556	0.0512	1.61	1.0344	0.00132	1.12	●
2—6	0.215	591	0.0545	1.71	1.0344	0.00132	1.12	○
2—7	0.215	601	0.0551	1.74	1.0344	0.00135	1.13	○
3—1	0.214	687	0.0905	1.16	1.0077	0.00216	0.458	●
3—2	0.214	712	0.0943	1.20	1.0077	0.00213	0.455	○
3—3	0.214	717	0.0914	1.21	1.0077	0.00230	0.473	○
3—4	0.214	1057	0.0826	1.79	1.0155	0.000621	0.774	●
3—5	0.214	1058	0.0849	1.79	1.0155	0.000586	0.752	○
3—6	0.214	1068	0.0847	1.80	1.0155	0.000599	0.760	○
3—7	0.214	1426	0.0748	2.41	1.0344	0.00140	1.15	●

1. 背面波之形成與發展

內重力波的產生爲密度層變流場重要現象之一。在層變流場中，一旦受到擾動，則各層流體由於干擾所造成的移動將產生不平衡，再加上重力的影響使流體分子引生垂直向的運動，因而造成重力波[10]。 當層變流體通過障礙物時，在其下游區所產生的背面波爲最常見的一種重力波。背面波形成的發展受層變因素，動力因素以及障礙體的大小形狀的影響而有不同的現象。茲就本文實驗觀察所得敍述如下：

㈠阻擋效應：在密度層變流體中，當流體通過一障礙物時，由於底層流體之密度較大，因而在障礙物上游區常使部分流體無法隨主流移動而阻滯於障礙物前方，形成一阻滯區，如圖二。而由此阻滯所引起之效應稱爲阻擋效應 (blocking effect)

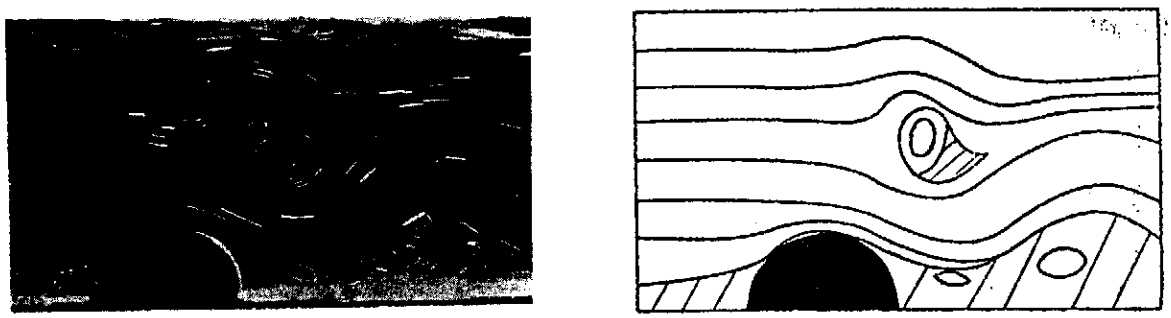

圖二　障礙物上游面阻滯區之形成。圖中 β=0.214, R=930, F=0.0719。

。影響阻滯區形成之因素，較重要的有障礙體之形狀大小，F及R等。起始之流場其流況近似勢能流，阻滯區不存在。隨著時間的增長而使阻滯區形成並向上游擴展，此種現象乃因慣性力不足以克服重力，且同時受到粘滯力的影響而成。在此時，障礙物所受之阻力很可能逐漸增加。當形成於下游之內重力波逐漸向上游傳遞時，阻滯區便開始逐漸回縮。而若波長過大時，其回縮之速度較緩；波長過小時，又不足以影響此區之行爲。通常R值及F值較大時其波長亦大，因此僅當R與F在一適當值時，方可見此區迅速回縮。另一影響因子則是波向上游傳遞之速度。通常R與F值較小時，其傳遞之速度較快，因而此區的回縮也較早發生。但若R與F之值過小，如圖三所示，其波長與振幅均小，故對此區之行爲影響很小。在當回縮之時，滯區變小，因此其阻力也可能逐漸降低。在此情況下阻滯區的形成受到壓制與破壞，而在上游形成一相當於背面波之擾動 (shear fronts or colunmnar disturbance mode's) 運動，其大小與障礙體之高度成正比。這現象

就是 Baines 氏評論 Long 氏模式缺失之主要論點（Long 氏假設上游流況不受阻擋效應之影響）。

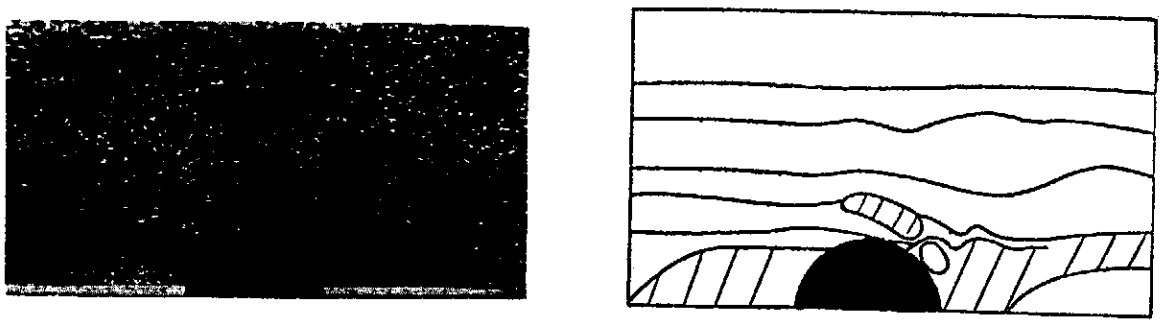

圖三　波長與振幅均小，對阻滯區之行爲影響較小，且其遠近二分離區相互重合
圖中 β=0.214, R=194, F=0.0104。

㈡流線分離區：當流體通過一障礙體時常在障礙體下游面產生流線的分離。在層變流場中，很少學者討論此區之變化，主要因爲目前有關背面波的特性研究多以 Long 氏之假設爲前題來探討。由於分離區的產生將消耗主流的能量，而影響主流場的流況，因而更使非粘性之假設理論（如 Loog 氏模式）與實驗結果不相符合。密度層變流體通過障礙物受阻的現象與均勻（Homogeneous）流體相異之處，乃在於前者由於受重力之作用，在通過障礙物後使流線急速下降，於近底床處再度躍起形成波浪狀。此外，由背面波之不穩定所形成之旋螺（rotor）更是層變流場的特性。

流體通過障礙物後，由於流域突然擴大，部分動能無法立即轉換爲壓能，因而在障礙體上便產生了流線的分離。流線分離後，除在近障礙物處形成與均勻流場相仿之分離區（稱近分離區）外，在第一（指障礙物下游第一個）波峯下也同時有擾流出現，稱之遠分離區。由於層變的效應，使近分離區較均勻流場中之分離區爲小。遠分離區其下限爲底床，上限爲波狀之流線。遠分離區首先形成於第一波峯之下，常作規則旋動後再復成爲擾流（Turbulence）。遠近兩分離區之關係直接受第一波長與第一振幅之影響。當 F 與 R 在某一中等大小值時，發現有時第一波谷與底床相接觸，而使此二區爲此波谷所隔離，如圖四。當 F 與 R 很小時，如圖三，第一波谷位於障礙物上，則此二分離區相互重合，此時由於流速較小，所携能量不大，此區之流體多呈靜止。又由圖五可看出當 F 與 R 值在某較大之值時，第一波谷形成於距底床某一距離處，而使此二分離區相互連接，形成一頭

尾皆大而中間小的分離區。至於分離區尾流之長度則與R值有關，R值越大，其長度越長。此外，如圖六所示，當R值較大且有旋螺出現時，在旋螺之後形成擾流，而與遠分離區相接。當然，第一波谷同樣會隨時間往上游移動，因此分離區的形狀也隨時間而改變。附帶一提的是：障礙體下游面之形狀與高度勢必影響分離區之性質。

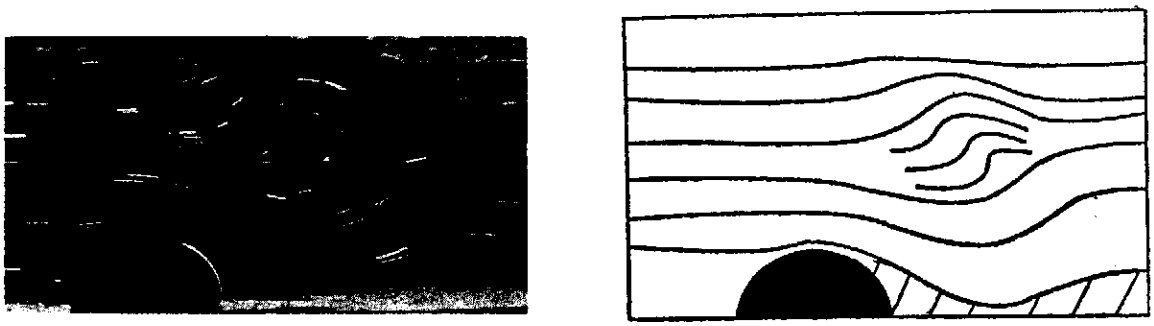

圖四　遠近二分離區相互隔離。圖中 β=0.214, R=997, F=0.0775。

圖五　遠近二分離區相互連接。圖中 β=0.214, R=930, F=0.0719。

圖六　旋螺後出現擾流。圖中 β=0.214, R=604, F=0.0775。

㈢旋螺之形成：層變流體通過障礙物受阻的流場，在起始時其流線與勢能流相仿，接著，流場受到障礙物的干擾，由於密度層變的作用，使得波長逐漸減小，振幅逐漸增大，因而在障礙體下游形成內重力波的運動。當F值小時，層變作用加大

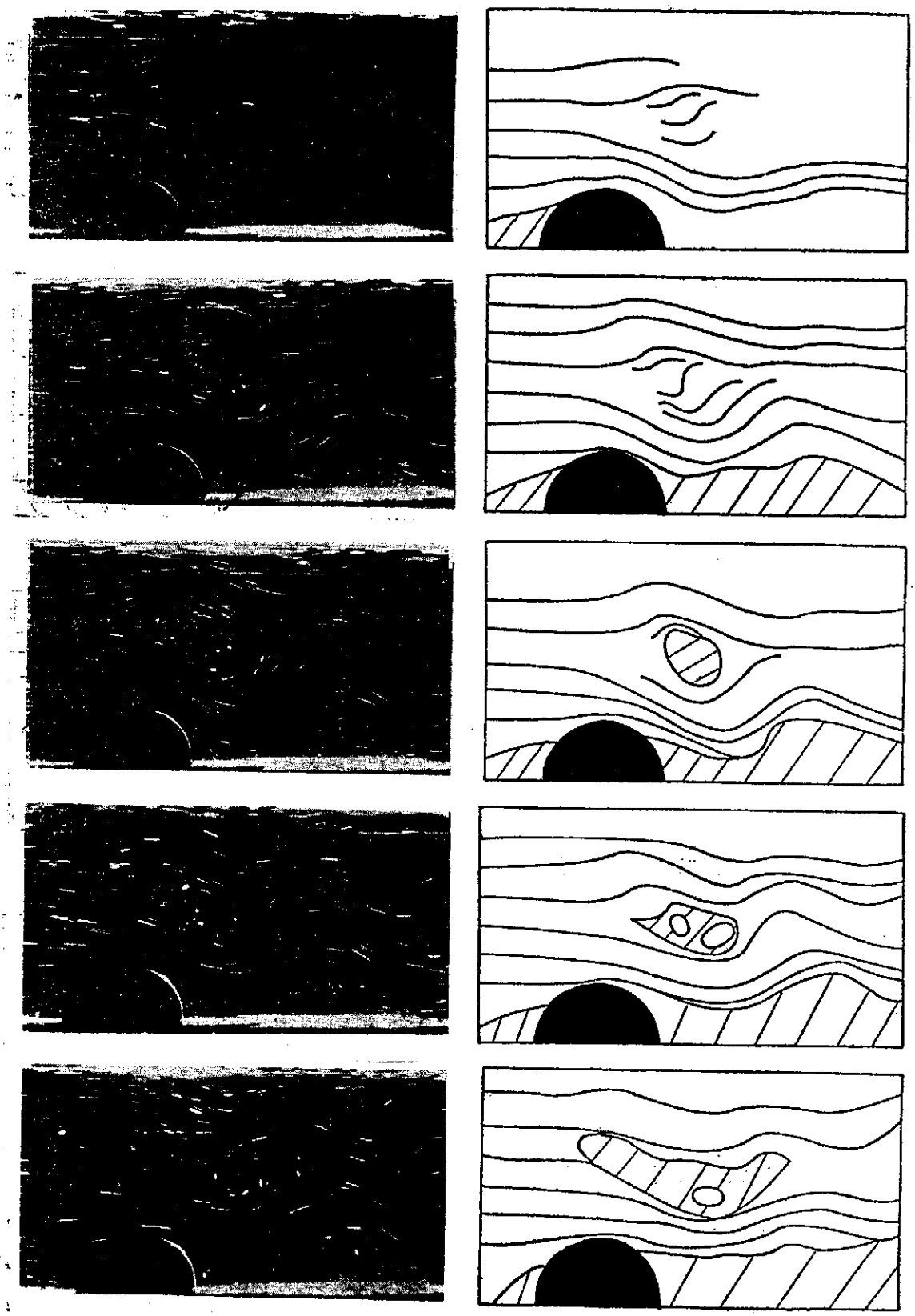

圖七　旋螺形成之一連串過程。圖中 β=0.214, R=829, F=0.0638。

，使得波長更爲減小，振幅更爲增大，而在某些地方使流線扭曲成S型，當此S型之流線中有部分與底床垂直時（或$\frac{\partial\delta}{\partial z}=1$，$\delta$＝流線在扭曲處之高度減去同條流線在上游遠方之高度，z爲高度向之座標），稱之爲內重力波或背面波不穩定的臨界狀況，當扭曲之S型流線超過臨界狀況時，便產生旋螺，使得流線發生翻轉的運動。旋螺的形成和水躍現象的發生有相似的成因。旋螺內常於上方先產生規則轉動，然後下方再呈規則轉動；在被拉長後，某區呈規則轉動，其他區則以擾流形態出現。由實驗結果可以看出：旋螺之長軸於發生時，略向前傾而接近垂直，接著隨著時間的變化其長軸逐漸增大且向前傾，有時甚至倒至水平狀態。旋螺於形成之後逐漸向上游移動，甚至可延伸至障礙物之前方。如圖七，爲旋螺發生與形成之一連串過程。此外，背面波之變化以及不穩定的發生皆與障礙物之高度（以$\beta=\frac{h}{H}$表示）寬度（以$\epsilon=\frac{h}{b}$表示）及受阻流場之R值有關。

2. 障礙物之形狀及其大小的影響

背面波之形成亦可由流場內渦度守恒（conservation of vorticity）方程式說明之。在層變流場中，由於浮昇重力產生的渦度（vorticity）爲$-(\partial\rho/\partial x)/\rho$，式中$\rho$爲流體密度，x爲水平流向，自左向右定爲正向。如果$\partial\rho/\partial x$爲正，表示在同一高度上右邊流體較左邊爲重，則較重之流體欲下沉而較輕者欲上昇，因而產生一負渦量（順時針旋轉）；相反地，如$\partial\rho/\partial x$爲負值，則將產生一正渦量（逆時針旋轉）。當層變流流經障礙體時，由於障礙體的阻擋作用，將迫使流體在其上游面爬昇（$\partial\rho/\partial x$爲正而在下游面下降（$\partial\rho/\partial x$爲負），因而在上游面滋生負渦量而在下游面產生正渦量。上游面之負渦量使流場形成阻滯區，下游面之正渦量使流體有逆時針轉動之趨勢而使流線上凹扭曲形成一波谷。當層變梯度越大，或障礙體越高，都會使其下游區所產生之正渦量越大，因而造成流線有更大的扭曲。當流線的扭曲超過臨界狀況（$\partial\delta/\partial z>1$）便產生背面波之不穩定而形成旋螺之紊動。

首先討論高寬比$\epsilon=\frac{h}{b}=1.0$之定值下，高深比$\beta=\frac{h}{H}$對流場的影響。圖八所示爲$F=0.065$，β，分別爲0.214和0.125二種流場中背面波形成之情形。由圖中可看出高障礙體（$\beta=0.214$）的流場，其背面波已呈不穩定狀況，而低障礙體（$\beta=0.125$）的流場，其背面波仍爲穩定狀況。圖九爲實驗中一系列改變β，流速及

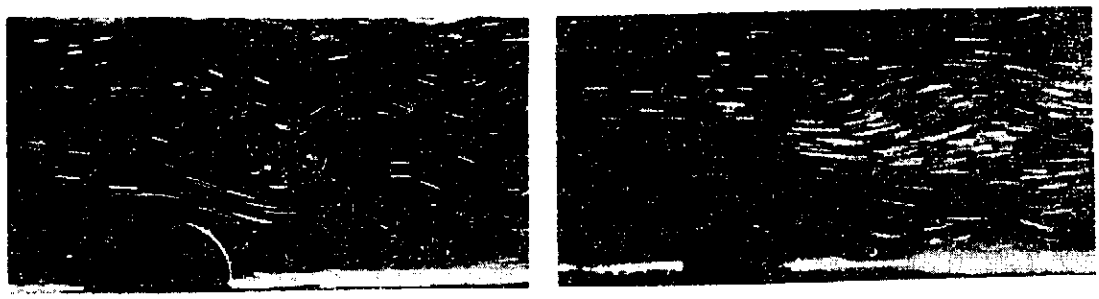

圖八　β 對背面波之影響，β=0.214 β=0.125 F=0.065

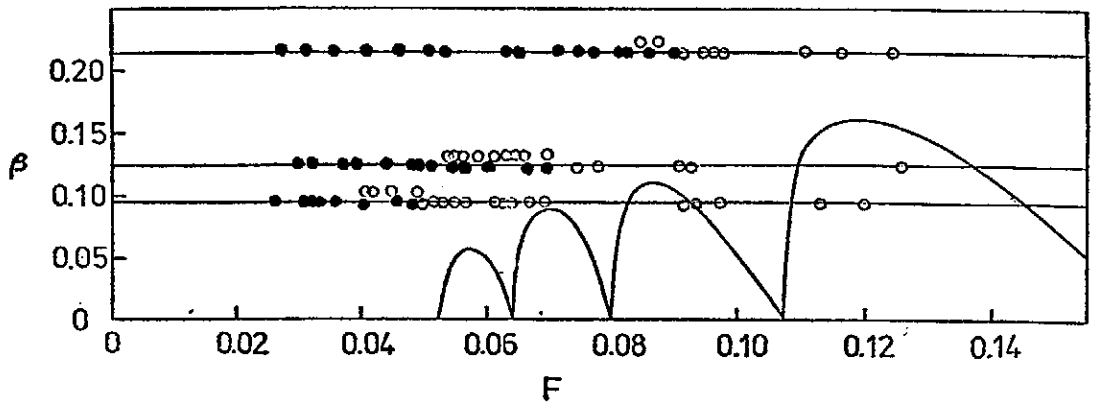

圖九　β 及 F 對穩定的影響。圖中○表示流況穩定，●表示不穩定，曲線爲 Long 氏模式之理論臨界曲線。

層變梯度所繪得之臨界線。圖中○表示背面波之流線變化未超過臨界狀況之穩定流況，●爲超過臨界狀況之不穩定流況。一般而言，當 β 值越大且 F 值越小時，背面波易於趨向不穩定，亦卽有旋螺之紊動發生。在 β 值大，F 值小且R值小的流場裏，背面波形成旋螺後發現旋螺有分裂的現象。如圖十所示爲 F＝0.0371，R＝330，β=0.214。時，背面波形成之一系列過程。旋螺於初形成時，其長軸較長，且其長軸前傾角度也較大。當旋螺之長軸前傾且逐漸向上游擴展延伸時，由於障礙體高度之影響，使旋螺被一分爲二，有如細胞之分裂過程。在此之後，由於原有之旋螺又逐漸向上游擴展延伸，因此我們相信此一分裂過程將持續進行，但分裂出之新旋螺尺度較小且强度較弱，也極易因主流中之粘度而被吞噬。旋螺形成之個數，在F及R值均小之極不穩定流況下，可能多達四個以上。當二旋螺形成之位置十分接近時，合而爲一之情況也會發生。

接著討論高深比 $\beta=\frac{h}{H}=0.125$ 之定值下，高寬比 $\epsilon=\frac{h}{b}$ 對流場的影響。圖十一之實驗結果顯示，在F值大時，高寬比小（較寬）的障礙體其背面波易於形成不

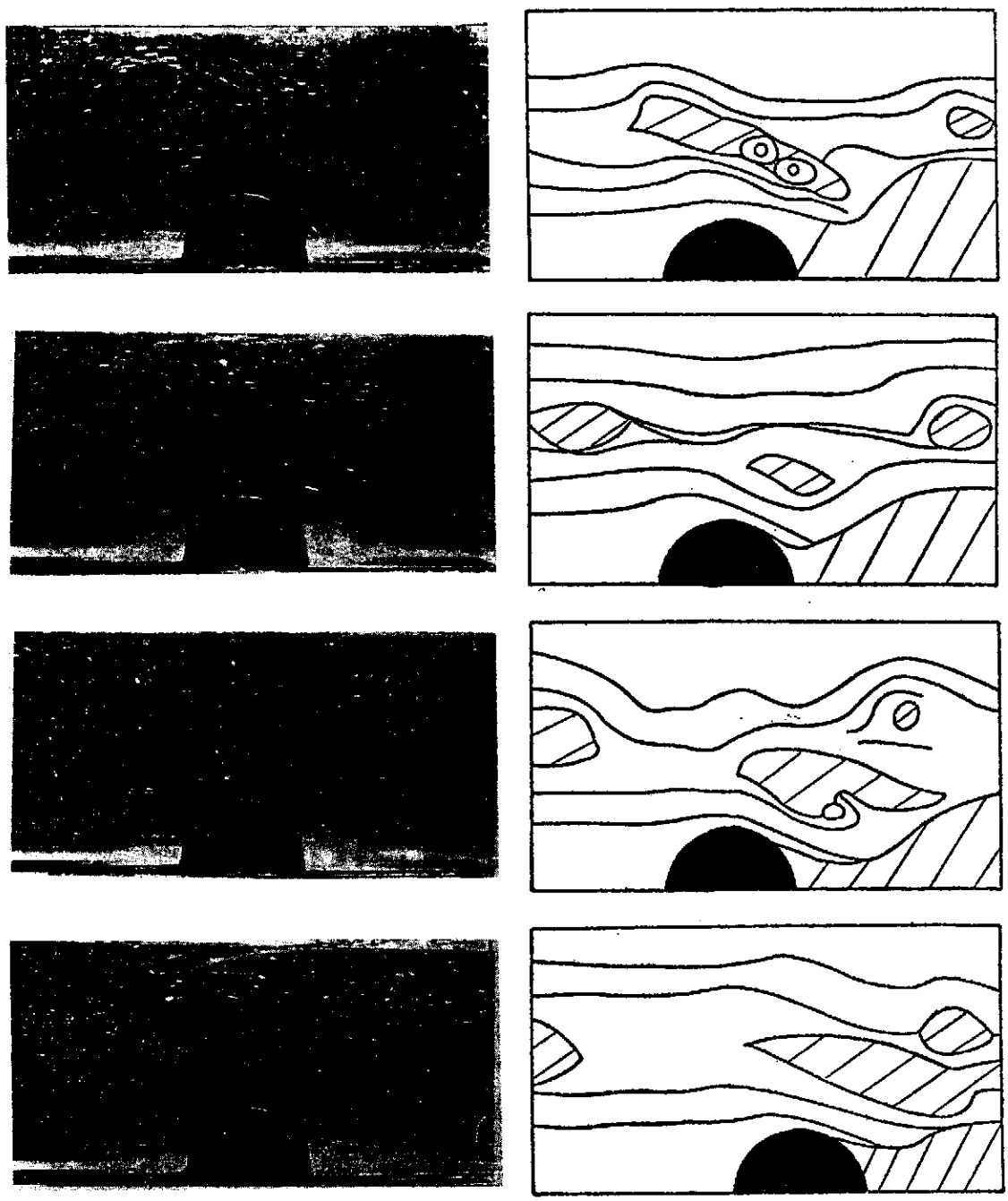

圖十　旋螺之分裂過程。圖中 β=0.214, R=332, F=0.0371。

穩定狀況的旋螺紊動。當層變流體通過障礙體時，障礙體寬度之增加，不僅加大流體爬越障礙體之時間與距離，而且減緩因形狀改變而產生的流況變化，使得界面層分離點延後發生，因而在障礙體下游流場形成較小的 $\partial\rho/\partial x$ （負值），從而引生較强之正渦量（逆時針向）亦卽流線將產生較激烈的上凹扭曲。圖十二所示爲 F=

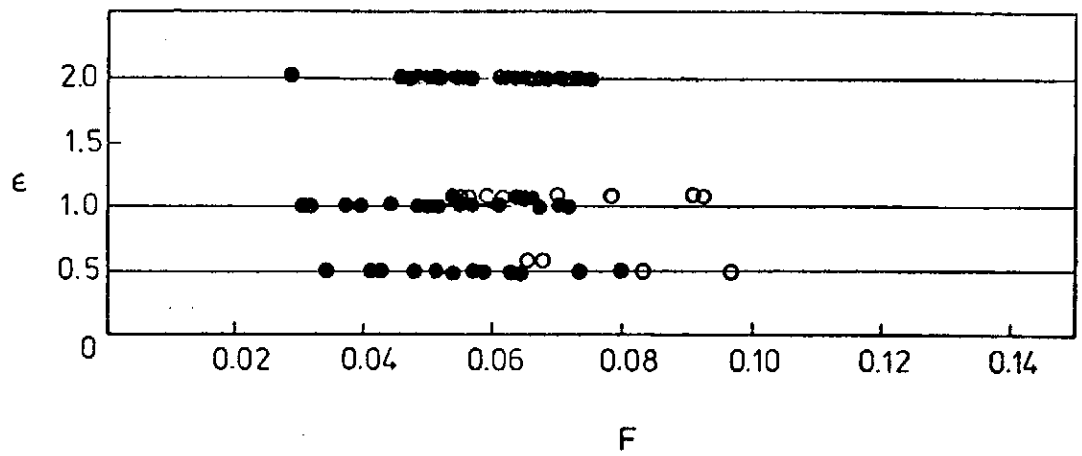

圖十一　ϵ 及 F對背面波穩定的影響。

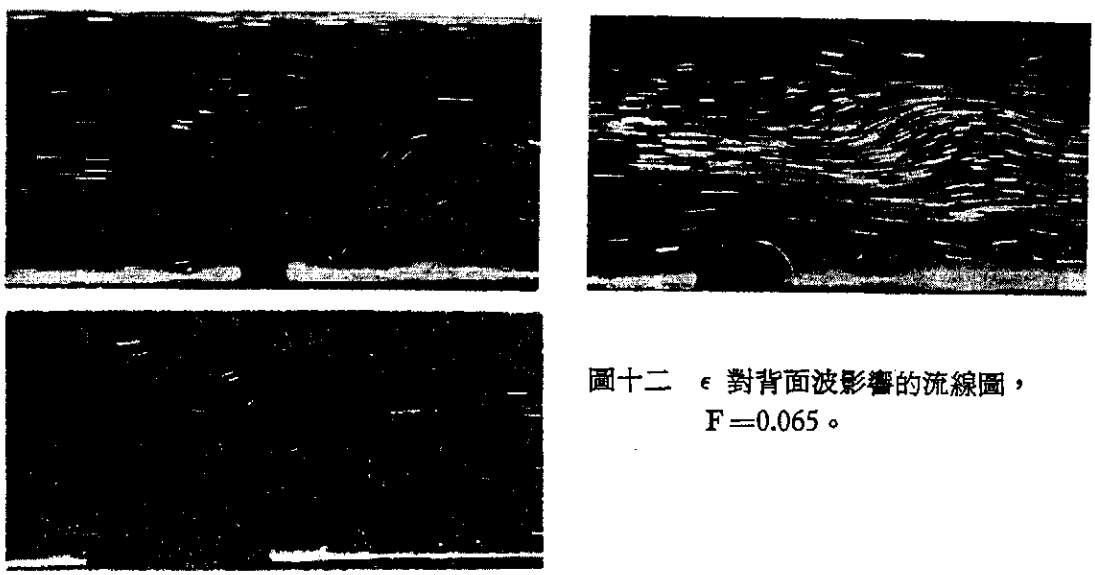

圖十二　ϵ 對背面波影響的流線圖，F=0.065。

0.065　$\epsilon=0.5$，1.0，2.0　三種不同寬度障礙體其背面波之情形。較寬的半橢圓體流場，其背面波已呈不穩定狀況，而較窄者其背面波仍爲穩定狀況。因此，一般而言，當層變因子一定時，減低流速及增加障礙體寬度，都會使背面波趨向於不穩定狀況之旋螺紊動。

3. 流場 R 值的影響致謝

在 Long 氏模式的計算裏，由於假設流體爲非粘滯性且沒有邊界層流線分離現象發生，因此背面波之形成與發展僅受 F 及高深比 β 影響。在本文一連串實驗研究中，發現當 β 及 ϵ 較小時，即高度低，寬度大之障礙體，流場中R值之影響不可

忽略。如圖十二及十四所示，一般而言，F值小，β 值大及 ϵ 值小時，流場中背面波之形成易呈不穩定狀況的旋螺紊動。但在圖中之實驗結果却可發現，當 β 值或 ϵ 值固定時，某些F值大的流場反較F值小的流場呈現不穩定的狀況。審視流場之水理條件，發現乃R值不相同之緣故，因而流場R值的大小對背面波形成之影響不容忽略。圖十五及十六分別爲 β，F，R及ϵ，F，R 對背面波的效應情形。 由圖中可發現，在 β 及 ϵ 值小時，流場R值之增加有助於背面波形成之穩定。因爲R值大時，障礙體上之邊界層分離點發生之位置將向上游移動，使得因流線分離所產生之尾流區範圍加大，而使爬越障礙體之流體無法充分下降，因而減低由於 $\partial\rho/\partial x$ 所引生的正渦量。同時分離區的增大，也消耗了主流更多的能量，因而使背面波振幅減小，波長增大，是故流線之扭曲更不易成垂直以形成旋螺，故流況較爲穩定。這些現象可由圖十七及十八看出，圖中所示皆爲 β 及F相同下，不同之R值。其背面波有不同狀況之形成。R值大時，其背面波爲穩定狀況，R值小時則爲不穩定狀況。因此，當 β 與 ϵ 值小時，流場中R值的變化對背面波的形成與發展有很大的影響。而當 β 及 ϵ 值增大時，由圖十五及十六可看出，背面波之形成受流場R值之影響逐漸減低。推測此乃因爲在 β 大時，液面的邊界影響超過因R值改變對流況引生

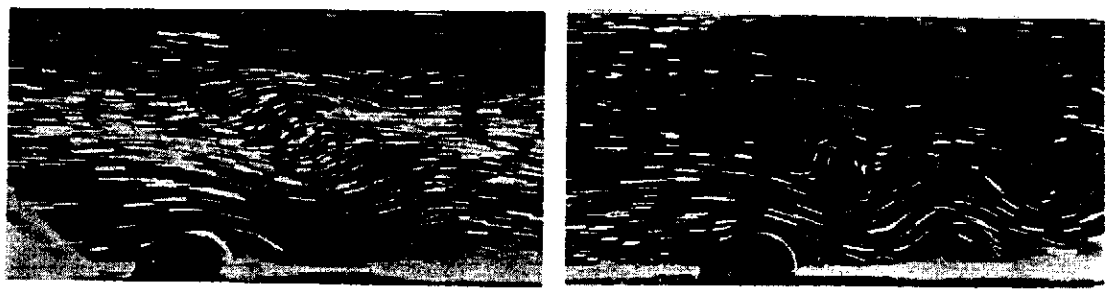

R=600　　R=420

圖十三　ϵ=1.0 β=0.125, F=0.055 的流場，R對背面波穩定性的影響。

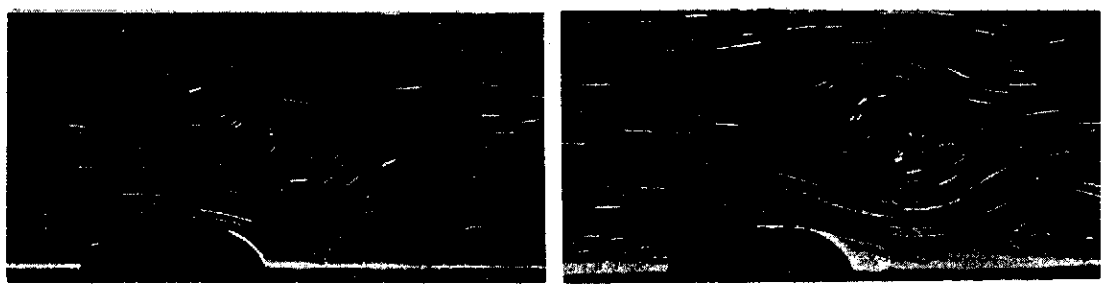

R=710　F=0.063　　R=680　F=0.080

圖十四　ϵ=0.5, β=0.125 的流場，R對背面波穩定性的影響。

之影響；同時，在 ϵ 值大時，障礙體上邊界層分離點的位置幾乎不變（即在障礙體之頂點），因此R值之增減，對於受阻流場之流況並無多大改變。因而背面波之形成，在 ϵ 值大之障礙體，受R之影響較少。

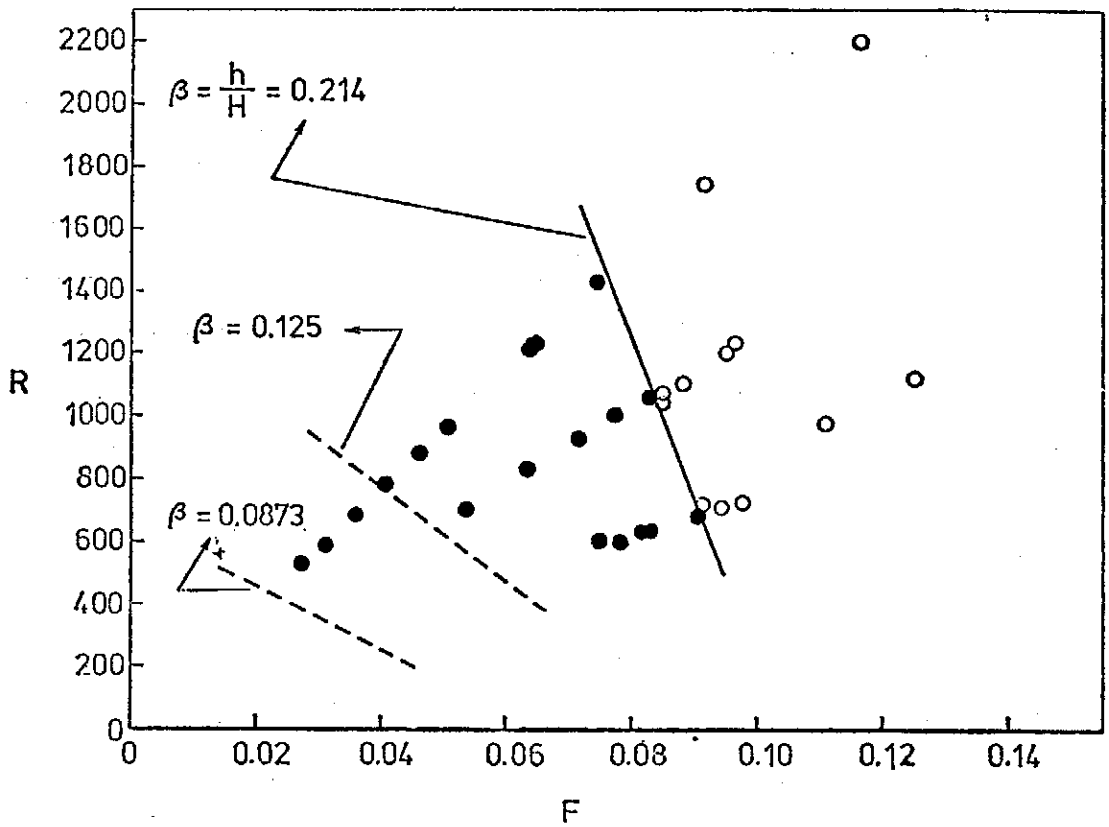

圖十五　R. F 及 β 對背面波流線穩定之影響。

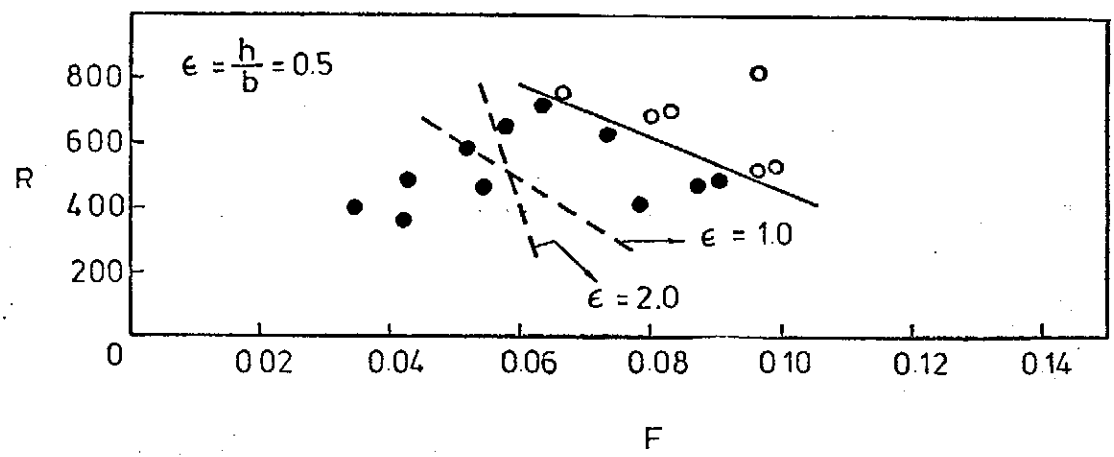

圖十六　R. F 及 ϵ 對背面波流線穩定之影響。

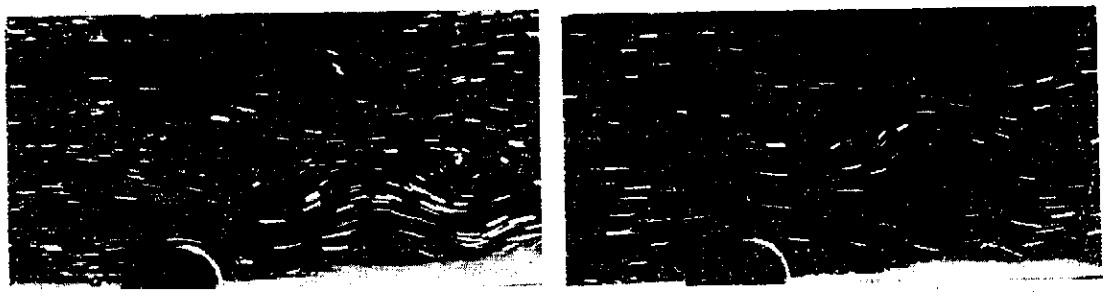

R=350　　R=550

圖十七　F=0.07 流場，R 對背面波形成之影響。

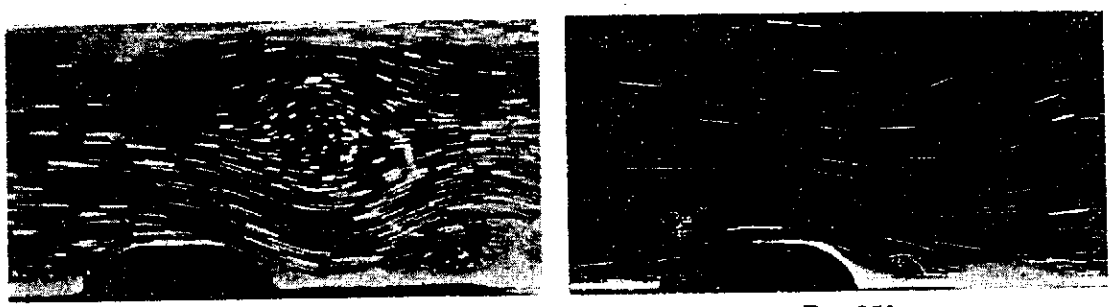

R=500　　R=850

圖十八　F=0.096, R 對背面波形成之影響。

值得一提的是，在圖十六中，$\epsilon=1.0$ 與 $\epsilon=2.0$ 二條臨界線相交，交點之R值約爲 600，因此二種不同寬度之障礙體所引生之流場在 R＞600 及 R＜600 情況下，對於背面波之形成與發展各有不同之趨勢與特性。在 R＜600 時，障礙體較窄者(ϵ 大者)其流況較爲穩定，而當 R＞600 時，障礙體較寬者（ϵ 小者）其流況反而較爲穩定。此種現象，經由對實驗流場之觀測，我們發現對於半圓形體（$\epsilon=1.0$），R值之增加會使其尾流迅速增大且紊流强度迅速增加；對於窄半橢圓體（$\epsilon=2.0$，R值之增加僅會使尾流緩慢增大且紊流强度緩慢增加。亦即 ϵ 值小者，其尾流之尺度與紊流之强度反應較爲敏感。R ＞ 600時，窄半橢圓體之分離區尺度較大，紊流强度較大，吸收主流能較多，因此其流況較爲穩定。R ＞ 600時，半圓形體所引生之波長增加較多，分離區尺度也增加較多，超過了窄半橢圓體，因此其流況反較窄半橢圓體爲穩定。圖十九爲二種障礙體在 F＝0.056，R＝620 相同的流場條件下，背面波之狀況。半圓形體產生之背面波，其波長較窄半橢圓體所產生之背面波爲長，因而使其流況爲穩定而未發生旋螺之紊動。

由實驗流場的觀測更可看出，當R值增大時，背面波之振幅與波長都隨之增大

。如圖二十爲 F＝0.068，R＝500, 760 二種背面波之情況。但是振幅與波長之比值則隨R之增大而減小，因此R值大者其波長隨時間收縮較緩。又由於R值大者，流場之流速較大，因此波向上游傳遞之速度較慢。這些現象都說明了R值之增大有助於背面波之形成保持穩定狀況。此外，當旋螺之紊動形成時，R值大者，其長軸前倒之速度較緩，且不易向上游延伸，擴展與傳遞，亦卽對上游流況之影響較爲緩慢，這些都是由於R值大時，慣性力之影響使得波向上游傳遞較慢之緣故。

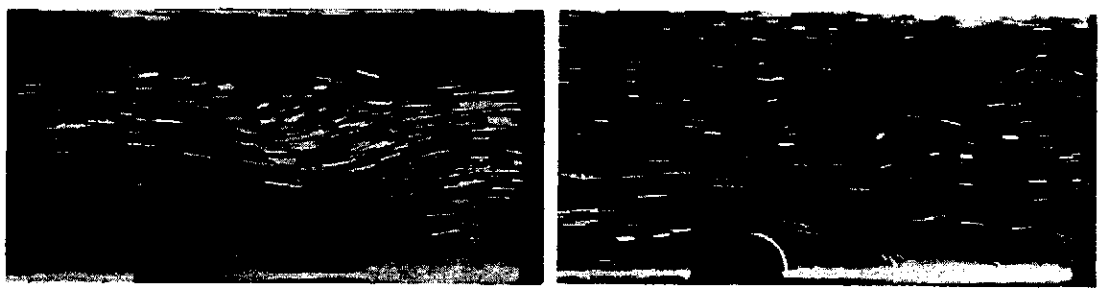

圖十九　障礙體形狀，ϵ 對背面波形成之影響。

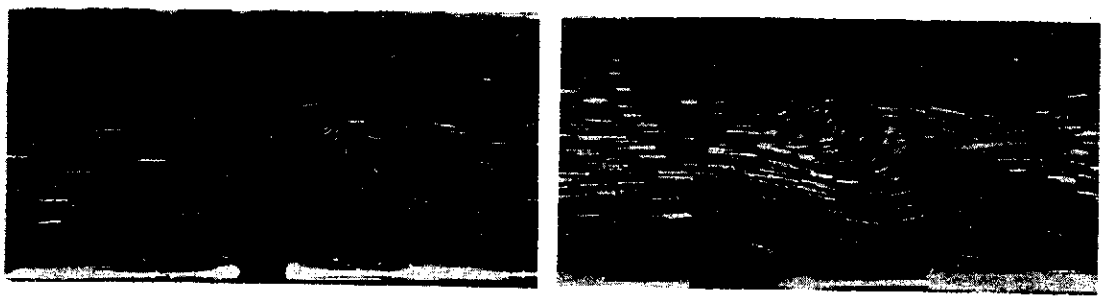

圖二十　流場R對背面波形成之影響。

肆、結　　論

本文以實驗方法探討二維密度層變流通過半圓形及半橢圓形障礙體的流場變化情形。經由一系列的變換流場層變因子、速度和障礙體的高度及寬度以進行研究。經由對流場的拍攝與分析，獲致下列的結果：

1. 障礙體的阻擋效應會影響上游的流況變化，尤其當F值小至某一適當之值時（太小時，其强度微弱）更爲劇烈。
2. 背面波之形成受F值、β 值及 ϵ 值之影響至鉅。F值小或 β 值大及 ϵ 值大時，易使背面波之流線產生旋螺紊動之不穩定狀況。
3. 當流線在障礙體上發生分離時，分離區之形成，影響背面波之流況。R值大時，

分離區較大且其强度較大，因此流況較趨穩定。

4.當 β 值小或障礙物高寬比 ϵ 小時，旋螺之形成與發展受R值之響影甚鉅。

本文之研究受中央研究院物理研究所及行政院國科會之支助，研究期間鄭仙偉與鄭永康君參與協助實驗，謹此一併致謝。

參 考 文 獻

(1) Long, R. R. 1953 Some aspects of the flow of stratified fluids; I. A theoretical investigation. Tellus, 5, 42.

(2) Long, R. R. 1954 Some aspects of the flow of stratified fluids; II. Experiments with two-fluid system. Tellus, 6, 97.

(3) Long, R. R. 1955 Some aspects of the flow of stratified fluids; III. Continuous density gradient. Tellus, 7, 341.

(4) Miles, John W. 1968 Lee waves in a stratified flow. Part 1. Thin barrier. J. Fluid Mech., 32 549.

(5) Miles, John W. 1968 Lee waves in a stratified flow. Part 2. Semicircular obstacles. J. Fluid Mech., 33, 803.

(6) Huppert, H. E. & Miles, J. W. 1969 Lee waves in a stratified flow. Part 3. Semi-elliptical obstacle. J. Fluid Mech., 35, 481.

(7) Davis, R. E. 1969 The two-dimensional flow of a stratified fiuid over an obstacle. J. Fluid Mech., 36, 127.

(8) Baines, P. G. 1977 Upstream influence and Long's model in stratified flows. J. Fluid Mech., 82, 147.

(9) Hwang, R. R. & Cheng, Y. K. 1979 Rise of Buoyant Jets in density-stratified environments—a laboratory study. Proc. of N.S.C., 3, 242.

(10) Turner, J. S. 1973 Buoyant Effects in Fluids. Cambridge University Press, 367 pp.

Annual Report of the Institute of Physics, Academia Sinica, Vol. 9, 1979

LEE WAVES IN A STRATIFIED FLOW OVER OBSTACLES-THE LABORATORY STRUDY

ROBERT R. HWANG
The Institute of Physics, Academia Sinica
Nankang, Taipei, R.O.C.

Abstract

This paper describes an experimental study of a stratified fluid of finite depth flowing over obstacles which flow seperation and turbulence are induced on the lee side and in which the inviscid model is no longer useful. Various properties of the flow field, such as the development of lee waves behind the obstacle, the blocking effect at upstream, the effect of viscosity, and in particular the criterion for the onset of gravitational instability in the lee-wave field, are observed and analyzed. The results show that lee waves produced by obstacles in a stratified flow depend on the internal Froude number, the ratio of the height of obstacles to the channel depth, the ratio of the height to the half width of obstacles, and Reynolds number of the flow. Therefore, it can be found that the existences of upstream influence and the flow seperation induced by the obstacle have great effect in some flow conditions on the development of the lee-wave field.

客觀分析程式對垂直速度計算的影響

曾 忠 一

中央研究院物理研究所
國立臺灣大學大氣科學系

摘 要

本研究從事氣象場的三種客觀分析，並計算其垂直速度場，以與主觀分析比較。本研究利用梅雨天氣資料來探討客觀分析程式對垂直速度計算的影響。研究結果顯示，客觀分析場能充分表現出主要的上升或下降運動系統，也能反映出實際的天氣情況。但是上升氣流和下降氣流中心的位置和强度仍和主觀分析場的垂直速度有顯著的差異。因此垂直速度計算對不同分析場的反應相當敏感。

壹、研究目的與有關文獻的檢討

近年來不論氣象作業單位或是研究機構均使用客觀分析法來從事氣象場的分析，把分佈不規則的測站上所測得的氣象資料內插到規則的網格點上，以作爲例行數值天氣預報的初值或作爲例行天氣分析之用。客觀分析法大約在一九五〇年代逐漸發展出來。Cressman (1959) 設計一種分析法，先把網格點周圍測站上的氣象變數值做加權平均以求得該變數在網格點上之值。Cressman 的權重是與測站到網格點間的距離有關。Inman (1970) 修改 Cressman 的權重，加重網格點上下風處的測站的影響力。Barnes (1973) 利用指數形式的權重來分析中幅度的大氣現象，並指出指數形式權重的優點。McFarland (1975) 合併了 Inman 權重和 Barnes 權重的優點，設計一種非均質、非等向性的權重來分析暴風氣流。我國氣象單位爲了將數值天氣預報納入預報作業內，近年來也積極研究客觀分析法。例如胡氏 (1977) 從事高空天氣圖客觀分析的研究，此項分析係由電子計算機一貫作業，業經中央氣象局採用，並納入電子計算機例行作業。曾氏 (1978a) 進行三種客觀分析程式的試驗，並與主觀分析比較。一般說來，在測站密集地區，客觀分析能準確定出高低壓中心以及冷區和暖區。在測站稀少，天氣資料缺乏地區，如西太平洋海面以及東南亞地區，很難得到正確的客觀分析場。

有時幾個主觀或客觀分析場之間看起來非常相似，由這些分析場計算出來的渦度，輻散或垂直速度是否也相似呢？這的確是值得研究的問題。客觀分析場的用途在於天氣分析與天氣預報，若某一客觀分析場得到的渦度，輻散或垂直速度與實際的天氣系統的環流型式不符合，則此客觀分析程式當然有嚴重的缺點。垂直速度在大氣大幅度運動中數值很小，不易由現有的觀測儀器直接求得，必須由其他觀測的氣象變數間接計算得到。而且垂直速度對不同的分析場的反應比較敏感，因此本研究探討不同的客觀分析程式對垂直速度計算的影響。垂直速度計算法大致說來有三種。第一種是運動學法，就是利用連續方程式由風的觀測值得到。第二種是絕熱法，就是利用熱力學方程式由風和溫度的觀測值求得垂直速度。第三種是動力學法，利用準地轉模式和平衡模式，只由等壓面上的高度求得垂直速度。最近幾年還發展出利用變分最佳化法的原理求得垂直速度的方法（見 McGinley 1973, McFarland 1975, Liang 1976, Liang 1977, 曾氏 1978b)。在垂直速度計算法的比較研究方面，Vincent 及其他人（1976）比較利用運動學法和準地轉模式求垂直速度的結果。他發現用運動學法來求垂直速度的結果較佳，用準地轉模式所得到的垂直速度場的分布並不與實際的天氣系統相符合，而且垂直運動相當微弱，僅及運動學法求得的垂直速度的五分之一。曾氏（1978b）對五種垂直速度進行比較研究，並且設計一種新的垂直速度計算法，利用一九七五年六月十日的梅雨資料探討這種方法的適用性。研究結果顯示，準地轉模式和平衡模式所求得的垂直速度在梅雨鋒面處非常微弱。可是在求中緯度天氣系統的垂直速度時，若不考慮潛熱的釋出只用絕熱的準地轉模式，仍能得到令人滿意的結果。Stuart（1974）利用四種不同的主觀分析和客觀分析的高度場輸入準地轉模式，以計算各個分析場的垂直速度，並做比較研究。他的研究結果指出，四個分析場的垂直速度均能與實際天氣系統的上升或下降運動符合。Smith 與 Lin（1978）對運動學法，準地轉模式和平衡模式所得的垂直速度進行比較研究。他們的研究結果顯示，比較垂直運動和降水量的相關係數，運動學法的結果較佳。此外準地轉模式所得的垂直速度比平衡模式的結果較佳。

本研究從事三種客觀分析，並計算其垂直速度場，以與主觀分析的結果互相比較。本研究利用一九七五年六月十日的梅雨天氣資料來探討客觀分析程式對垂直速度計算的影響。

貳、研 究 方 法

本研究首先利用三種客觀分析法，把測站上的天氣資料內插到網格點上，然後利用三種垂直速度計算法，以計算各個分析場的垂直速度。本研究使用的三種客觀分析程式均屬逐次校正法，分析的步驟大致相似，只是權重函數有所不同。氣象單位進行例行的客觀分析時，必須先對測站上的天氣資料，諸如高度、溫度和風等，進行統計檢定、靜水檢定以及靜力穩定度檢定，改正各種由於電訊傳遞、探空儀器結冰或人爲因素造成的錯誤，並且利用靜水關係式補充漏失的資料。本研究所使用的資料並未經這些自動的檢定處理，而是利用人工的方式仔細的改正各種錯誤。得到分析場以後，本研究亦曾進行靜水檢定和靜力穩定度檢定，以探討分析場在垂直方向是否維持內部一致。本研究使用的逐次校正法，其內容如下：

㈠基 本 分 析 法

假設 $D_k^{\mu-1}$ 是測站 k 觀測值與第 $\mu-1$ 次分析值之差，即

$$D_k^{\mu-1}=Z_k-Z_g^{\mu-1}$$

其中 Z_k 是測站 k 上的某氣象變數的觀測值，其值爲一定，$Z_g^{\mu-1}$ 是測站 k 上第 $\mu-1$ 次掃描時的分析，其值隨掃描次數而變動。某一網格點的校正值可由影響半徑內的 $D_k^{\mu-1}$ 值加權平均得到，

$$C_{ij}^{\mu}=\frac{\sum_{k=1}^{N} W_k D_k^{\mu-1}}{\sum_{k=1}^{N} W_k}$$

其中 C_{ij}^{μ} 是校正值，足號 ij 表示某一網格點，W_k 是測站 k 的權重函數，與該測站至某一網格點的間距有關，N 是使用的測站的數目。因此網格點上的新分析值爲

$$Z_{ij}^{\mu}=Z_{ij}^{\mu-1}+C_{ij}^{\mu}$$

得到新的分析值以後，可以照上述的方法重覆對所有的網格點進行掃描三次，就可以得到分析結果。

在進行下一次掃描之前，測站上的分析值必先加估計。網格範圍內的每個測站一定會落在四個網格點所包含的正方形中，因此測站上的分析值可由周圍四個網格點的分析值作線性內插得到（圖 1）

$$Z_s=Z_1+(Z_4-Z_1)\frac{\Delta x}{\Delta}+(Z_2-Z_1)\frac{\Delta y}{\Delta}-(Z_2-Z_3+Z_4-Z_1)\frac{\Delta x\Delta y}{\Delta^2}$$

其中各符號的定義見圖 1，Δ 是網格長度。觀測值的錯誤可以比較測站上觀測值和分析值之差而檢查出來。假如兩者之差的絕對值大於某一最大容許值，則我們可以判斷這測站上的觀測值有錯誤，也就是說當

$$|D_k^{\mu-1}| > \varepsilon$$

時，則測站 k 上的觀測值有錯。分析高度時，ε 可用 30m; 分析溫度和露點溫度時，ε 可定爲 3°；分析風速分量 u 和 v 時，ε 可定爲 5m/sec。在進行下一次掃描時，觀測值錯誤的測站資料原則上可以不再使用。在測站密集地區如發現觀測值和分析值相差太多，當然可以不再使用這個觀測值，不會影響分析結果。但是在測站稀少地區每個測站資料都很重要，只好再重新檢查測站資料，改正錯誤，然後再繼續從事分析。一般主觀分析也常用這種方法除錯，假如發現某一測站資料與周圍測站的資料相差過大或不一致時，改正此測站的資料。

(二)權 重 函 數

Cressman (1959) 使用的權重函數形式比較簡單，只與測站到某一網格點的距離有關，即

$$\begin{aligned} W_k &= \frac{R^2 - d_k^2}{R^2 + d_k^2} && d_k < R \\ &= 0 && d_k > R \end{aligned} \qquad (1)$$

其中R是影響半徑，是事先給定的，每次掃描都把R減小，以便較短波能重現在分析場上。d_k 是測站 k 至某一網格點的距離。由 (1) 式可知，距某一網格點愈遠的測站的資料對此一網格點的影響愈小。

Inman (1970) 修改 Cressman 的權重函數，加重網格點上風處和下風處測站資料的影響力，因此他的權重是

$$\begin{aligned} W_k &= \frac{R^{*2} - d_k^2}{R^{*2} + d_k^2} && d_k < R^* \\ &= 0 && d_k > R^* \end{aligned} \qquad (2)$$

其中

$$R^{*2} = R^2(1 + \beta \cos^2 \theta)$$

θ 是風向與網格點和測站方向角間的夾角（見圖 2）。β 可以控制 θ 對權重的影響，其值可由下式得到

$$\beta = \frac{bC}{C^*}$$

其中C是風速，C* 是一種最大風速，是常數，b 通常定爲 1。由 (2) 式看來，在網格點上下風處的測站資料權重較大，因此實際的影響區域是橢圓形的，而不是圓形的。在使用 Inman 權重時，第一次掃描時並無網格點上的風向與風速，因此在進行第一次掃描時，先使用 Cressman 權重進行風的分析，以得到網格點上的風向與風速，第二次掃描以後就可以使用 Inman 權重來進行客觀分析了。

Barnes (1973) 使用指數型式的權重，即

$$W_k = \exp\left(-\frac{d_k^2}{K}\right)$$

其中K是濾波參數，d_k 是測站至某一網格的距離。Barnes 指出，這種指數形式的權重具有下列優點：

1.因爲濾波參數K可以事先決定，因此反應函數亦可事先知道。

2.由於指數形式的權重函數隨着測站至網格點間距離的增加而漸近於零，因此測站上的資料可以影響到各處的網格點。

3.這種權重函數本身可以濾除雜波，而不需再使用濾波器。

4.用指數形式的權重在進行分析時只要掃描一次即可，可以節省許多計算時間。

McFarland (1975) 合併了 Inman 權重和 Barnes 權重的優點，設計一種非均質非等向性的權重函數

$$W_k = \frac{V}{V^*} \exp\left(-\frac{d_k^2}{K(1+\beta\cos^2\theta)}\right) \qquad (3)$$

其中

V　測站上的風速

V*　一種最大風速

K　濾波參數

β　非等向性參數

非等向性參數 β 的決定比較容易，β 愈大則上下風處測站資料的影響愈大。濾波參數K的值可以由數值實驗決定，本研究中選擇 $K = 0.8 \times 10^{-4}\ m^2$，這是以地圖上的距離來定的。若以地球上的距離來表示，則 $K = 18000\ km^2$，也就是我們假設測

站資料的影響幅度爲$\sqrt{18000}=130$ km。假如K值選擇過大，則會發生過度修勻的現象。假如K值定得過小，則 W_k 值可能會小於 10^{-99}，超出計算機所能處理的範圍。本研究中除了使用 Inman 權重 (2) 式和 McFarland 權重 (3) 式之外，也利用下列權重

$$W_k=\exp\left(-\frac{d_k^2}{K(1+\beta\cos^2\theta)}\right) \qquad (4)$$

這種權重的性質處於 Barnes 權重 (1) 式和 McFarland 權重(3)式之間，以下本文中稱爲改良式 Barnes 權重。

㈢初次估計值

初次估計值即 $Z_{ij}^{(0)}$ 與 $Z_s^{(0)}$，必須事先加以決定，才能進行分析。初次估計值可用氣候值，十二小時前的分析，或者是預報值。McDonell (1967) 曾對各種客觀分析的初次估計值加以比較。在某些情形下，初次估計值會嚴重影響客觀分析的品質，有時客觀分析場甚至不會收斂。本研究爲方便起見，各種氣象場分析時使用的初次估計值均爲零。

本研究利用三種方法來求主觀分析場和客觀分析場的垂直速度，即運動學法，準地轉模式以及線性平衡模式。運動學法是利用連續方程式

$$\frac{\partial u}{\partial x}+\frac{\partial v}{\partial y}+\frac{\partial \omega}{\partial p}=0 \qquad (5)$$

由風的觀測值 u, v 求得垂直速度 ω。這種等壓坐標面上的連續方程式所作的唯一的假設是靜水平衡。每一定壓層的 u, v 若已知，則可由底層往上積分，得到 ω 值。本研究的底層邊界定在 850mb，此處我們以 Chen and Tsay (1977) 梅雨報告中由摩擦和地形效應所求得的 850 mb 處的垂直速度爲邊界條件（圖 6），因此這層的垂直速度是本研究中三種垂直速度計算法所使用的底層邊界條件。運動學法的頂層邊界定在 10mb，該處的垂直速度定爲零。(5) 式中對 ω 而言是一階微分方程式，却有兩個邊界條件，因此由底層往上積分時，10mb 處的垂直速度不一定爲零，必須再加線性調整。運動學法的垂直網格結構如圖 3。所求得的垂直速度均位於兩定壓層的中間層，然後再線性內插到定壓層上。由運動學法得到的各層垂直速度均輸入準地轉模式和線性平衡模式中，以做爲邊界條件和初次估計值。

準地轉模式的垂直速度方程式形式如下 (Haltiner, 1971)

$$\sigma_s\nabla^2\omega+f_0^2\frac{\partial^2\omega}{\partial p^2}=\frac{\partial}{\partial p}J(\psi, f+\zeta)-\frac{1}{f_0}\nabla^2J\left(\varphi,\frac{\partial\varphi}{\partial p}\right) \qquad (6)$$

其中

f_0 平均科氏參數

σ_s 各層的平均靜力穩定度

φ 重力位

ζ 地轉渦度

其他符號與一般使用的相同。本研究中準地轉模式並未考慮摩擦和加熱的效應。(6)式中當 $\sigma_s > 0$ 時爲橢圓型偏微分方程式，可用緩和法來求解。在進行緩和法求解前，我們把運動學法求得的垂直速度當作準地轉垂直速度的初次估計值和邊界條件，如此可以減少計算時間。準地轉的垂直速度也是先在兩定壓層的中間層求得的，然後再內插到定壓層上。準地轉模式所使用的垂直網格結構如圖 4。

線性平衡模式的基本方程如下 (Haltiner 1971)

$$\nabla \cdot f \nabla \psi = \nabla^2 \varphi \tag{7a}$$

$$\nabla^2 \sigma\omega + f^2 \frac{\partial^2 \omega}{\partial p^2} = f \frac{\partial}{\partial p} [J(\psi, \zeta + f) + \nabla f \cdot \nabla \chi]$$

$$-\nabla^2 [J(\psi, \frac{\partial \varphi}{\partial p}) + \nabla \chi \cdot \nabla \frac{\partial \varphi}{\partial p}] - \nabla f \cdot \nabla \frac{\partial^2 \psi}{\partial p \partial t} \tag{7b}$$

$$\nabla^2 \frac{\partial \psi}{\partial t} + J(\psi, f + \zeta) + \nabla \chi \cdot \nabla f = f \frac{\partial \omega}{\partial p} \tag{7c}$$

$$\nabla^2 \chi + \frac{\partial \omega}{\partial p} = 0 \tag{7d}$$

其中

f 科氏參數

σ 靜力穩定度

ψ 流線函數

φ 重力位

ζ 渦度

χ 速度勢函數

其他符號與一般使用的相同。用 (7a) 可以由高度求得流線函數ψ。(7b)(7c)(7d)是 ω，$\frac{\partial \psi}{\partial t}$和 χ 的聯立方程式，必須用緩和法複作數次才能解出。平衡模式的垂直

網格結構和準地轉模式一樣，所用的ω的初次估計值和準地轉模式也一樣。線性平衡模式的解法詳見 Haltiner 1971。

參、研　究　結　果

本研究使用的資料取自一九七五年六月十日格林尼治時間零時的東亞地區各測站的天氣資料。此時天氣概況如圖 5, 8a, 9a, 10a, 11a, 12a, 13a。圖 5 是海平面氣壓，圖 8a, 9a, 10a, 11a, 12a, 13a 分別爲 850mb, 700mb, 500mb, 300mb, 200mb 和 100mb 的高度的主觀分析。當時副熱帶太平洋高壓與鄂霍次克高壓間的梅雨鋒面自日本向西南延伸，經過臺灣、琉球到達華南，蒙古高壓位於中國大陸北部。本研究考察的範圍大致包括以臺灣爲中心的東亞地區。本研究使用20×19個網格點，網格間距在一千五百萬分之一的地圖上爲 1.6 公分，也就是說在北緯 30° 處的網格間距爲 240 公里。在考察範圍測站的分布並不平均，東南亞地區以及琉球、臺灣、和菲律賓以東的西太平洋海面測站稀少，資料缺乏。其他如日本海和東海處測站也少，因此在這些地區比較不能得到正確的分析場。

本研究對高度、溫度、風速分量以及露點溫度均作三種客觀分析。此外高度場和溫度場分析完畢以後，亦曾進行靜水檢定和靜力穩定度檢定，以考察分析場在垂直方向是否保持內部一致。檢定結果顯示高度場和溫度場只有百分之五的網格點不能通過靜水檢定，溫度場也只有百分之六不能通過靜力穩定度檢定。所得到的結果比主觀分析場更令人滿意。 Inman 權重客觀分析的高度場分別在圖 8b (850mb), 9b (700mb), 10b (500mb), 11b (300mb), 12b (200mb), 13b (100mb)。改良式 Barnes 權重客觀分析高度場分別在圖 8c (850mb), 9c (700mb), 10c (500mb), 11c (300mb), 12c (200mb), 13c (100mb) 。McFarland 權重客觀分析高度場分別在圖 8d (850mb), 9d (700mb), 10d (500mb), 11d (300mb), 12d (200mb), 13d (100mb)。此外 500mb 以下各層的高度場圖中均有等混合比線，300mb 以上各層的高度場圖中均有等風速線。比較以上各圖我們可以發現，主觀分析與各種客觀分析的高低壓中心的位置均能互相符合，但客觀分析場的高低壓强度比較微弱，例如500mb的高度場中（圖10）位於中國東北的高壓和日本海的低壓在客觀分析場中就比主觀分析場微弱。中緯度地區的高低壓大致均能在客觀分析場中顯現出來，副熱帶高壓在客觀分析場中均較爲微弱，且向東退縮。在測站稀少，資料缺乏的東南亞

地區和西太平洋海面，比較不易得到正確的客觀分析場。此外，三種客觀分析得到的結果非常相似，相互間的差異很少超過 20 公尺。客觀分析場和主觀分析場之間差異也不大，大致在 30 公尺以內，相差最大的地方是在邊界附近，也就是測站稀少的地方。風速的分析場，客觀分析和主觀分析也很相近，強風地區和弱風地區的位置也能互相符合。

表一列出主觀分析和三種客觀分析的分析場和觀測值的根均方差。由此表中可以看出，主觀分析和測站觀測值的根均方差比客觀分析場的大。這可能是主觀分析時對測站原始資料修正過多，也可能是客觀分析使用的測站資料未能修正所有的錯誤所致。本研究亦曾對主觀分析進行靜水檢定和靜力穩定度檢定，發現主觀分析並不完全滿足靜水檢定和靜力穩定度檢定，尤其在高層的高度和溫度爲然，不能通過這兩種檢定的網格點超過百分之七。

計算出客觀分析場以後，接着進行主觀分析場和客觀分析的垂直速度計算。由於大氣大幅度運動中垂直速度是根據某些物理或數學的假設由其他的氣象變數得來。驗證各種垂直速度計算程式的優劣或正確性必須依靠它和其他氣象變數的相關以及天氣系統的環流型式來決定。本研究以主觀分析的垂直速度場爲基準，探討垂直速度對不同的客觀分析場的反應以及研究不同的客觀分析程式對垂直速度計算的影響。

通常上升運動大部分布在槽線的東方或南方，而下降運動通常在脊線的東南方，換句話說上升運動在槽線的前方，而下降運動分布在槽線的後方。本研究使用的天氣資料顯示，在中緯度槽線和梅雨槽線前後方共有四個主要的上升下降系統。主觀分析的垂直速度用三種計算法得到的結果大致合乎這個原理。由主觀分析計算的結果顯示（圖 14a 至 26a），上升運動主要分布在梅雨鋒面上，即由日本向西南延伸，經過琉球、臺灣以至於長江中下游。此外在中國大陸黃土高原以北，亦即在中緯度槽線的前方，也有强烈的上升氣流。海南島附近和日本海北部則有微弱的上升運動。下降運動主要分布在黃海及山東半島一帶，亦即梅雨槽線的後方，中國大陸西北地區也有强烈的下降氣流，這屬於中緯度槽線後方的下降運動系統。臺灣和呂宋島以東海面以及南海北部有微弱的下降運動。另一個微弱的下降氣流區域在雲貴高原。由三種垂直速度計算法得到的主觀分析場垂直速度顯示，各個主要的上升氣流和下降氣流的分佈型態相似。唯一不同的地方是由準地轉模式和線性平衡模式計

算出來的垂直速度比較微弱，尤其是梅雨鋒面處以及長江中下游的上升氣流非常微弱，僅及運動學法所得到的垂直速度的四分之一。這一點和實際的天氣狀況並不符合。由圖 7 的衛星照片得知，在梅雨鋒面處，即由日本琉球至臺灣和長江下游一帶，雲層很厚，此處應有强烈的上升運動。用運動學法求得的垂直速度場充分反應出這個事實。Danard (1964) 指出，若不考慮潛熱的釋出，在 600mb 以下各層，由準地轉模式所得到的垂直速度只有運動學的 ¼。由於在梅雨鋒面處降水很多，潛熱的釋出的物理過程變得非常重要，假如不考慮這一事實，則無法得到正確的垂直速度。本研究所使用的準地轉和線性平衡模式並未考慮潛熱的釋出，因此在降水豐富的梅雨鋒面處所得的垂直速度未能反映出實際的天氣情況。可是在求中緯度天氣系統的垂直速度時，本研究的結果顯示，若不考慮潛熱釋出的物理過程，只用絕熱的準地轉和線性平衡模式，仍能得到滿意的結果。此外比較地轉模式和平衡模式的垂直速度時，我們也可以發現，雖然平衡模式的物理假設比較嚴密，可是所得到的垂直速度場反而比準地轉模式得到的更不優良，而且上升運動和下降運動更加微弱，這點和 Smith 和 Lin (1978) 的結論一樣。

用運動學法計算出來的主觀分析和三種客觀分析的垂直速度場在圖14 (700mb)，圖15 (500mb)，圖16 (300mb)，圖17 (200mb) 和圖18 (100mb)。每一張圖中均有四個分析場的垂直速度，即主觀分析，Inman 客觀分析，改良式 Barnes 權重客觀分析，以及 McFarland 權重客觀分析。比較這些圖我們可以發現，客觀分析場的垂直速度相互間的差異較小，四個主要的上升氣流和下降氣流系統的中心位置相差均在兩個網格長度之內，零線的圖形和走向也很相似。若與主觀分析的垂直速度場比較，則有顯著的差異。在邊界上差異更大，例如各客觀分析的垂直速度圖中，在雲貴高原、菲律賓附近海面以及在日本南方海面上均出現相當大的垂直速度值，可是在主觀分析的垂直速度圖上並未出現。這個原因很明顯，由於這些地區測站比較稀少，風的分析非常不良，因此利用連續方程式由風計算出來的垂直速度誤差也就很大，而且這些地區又是在邊界附近，因此更不易計算出合理的風場和垂直速度場了。此外在北緯二十度線附近的下降運動也未充份表現出來。至於中緯度地區的四個上升下降運動，亦即中緯度槽線和梅雨槽線前後方的上升運動和下降運動，在三個客觀分析的垂直速度場中均能表現出來，但是上升或下降氣流中心的位置和强度與主觀分析的垂直速度場有少許的差異。不過在梅雨鋒面處的下降運動，若不

考慮邊界上的誤差，客觀分析的垂直速度場和主觀分析之間差異仍很明顯，例如700mb（圖14），500mb（圖15）的主觀分析垂直速度圖中，長江中下游處有兩個上升氣流中心，而且梯度很大，可是在客觀分析的垂直速度圖中均未能顯示出來。此外在改良式 Barnes 權重客觀分析的垂直速度圖中，200mb 處在黃土高原以北的垂直速度太大，也是不合理的現象。若要由於判斷何種客觀分析程式能得到較佳的垂直速度場誠屬不易。若仔細比較各圖，我們發現 McFarland 權重的客觀分析較優。我們可以發現，雖然主觀分析場和客觀分析場就其圖形比較起來非常相似，可是計算出來的垂直速度仍有很大的差異，尤其是在測站稀少，資料缺乏的地區爲然。客觀分析的垂直速度場大致仍能充分表現出中緯度地區的四個上升下降運動系統。一般說來，不論是主觀分析或是客觀分析，風的分析比高度場或溫度場的分析更難處理，觀測風若有錯誤也較難查出。因此各個分析場的垂直速度就會有顯著的差異。我們也可以發現，垂直速度對不同的分析場的反應相當敏感。

準地轉模式計算出來的垂直速度場在圖 19（700mb），圖 20（500mb），圖 21（300mb），圖 22（200mb）。同樣的，每張圖中均有四個分析場的垂直速度。準地轉模式的客觀分析垂直速度場在雲貴高原、日本南方太平洋海面以及菲律賓附近海面有不正常的上升或下降運動，這是因爲我們使用運動學法所得到的垂直速度當作邊界條件。中緯度槽線和梅雨槽線前後方的上升運動和下降運動均能充分表現出來。圖 19b, 20b, 21b, 22b 中我們可以發現，Inman 客觀分析垂直速度場在黃土高原以北地區的上升運動過於强烈，幾乎比同地區主觀分析垂直速大兩三倍，此外在中國大陸西北地區的下降運動也太强烈，因此 Inman 客觀分析場對垂直速度計算的影響十分不良。不談邊界附近不正常的上升或下降運動，則 Barnes 權重和 Mc Farland 權重客觀分析所得的垂直速度場比較合理。各客觀分析場之間的差異比較小，而且零線的圖形也比較相似。當然若比較準地轉模式和運動學法所得到的垂直速度兩者也有差異，這是因爲兩者的物理的假設完全不同。

線性平衡模式的垂直速度場在圖23（700mb），圖24（500mb），圖25（300mb）和圖26（200mb）。線性平衡模式的垂直速度場中，我們仍可以發現四個主要的上升和下降運動均能表現出來。雲貴高原，菲律賓以東海面以及日本南方海面仍有不正常的上升和下降運動。這也是因爲我們使用運動學法得到的垂直速度當作邊界條件。由圖 23 可知，Inman 權重客觀分析的垂直速度場在黃土高原以北處過大，而且

一直發展到 300mb，然後才逐漸減弱。在圖 25c, d 和 26c, d 中南方的邊界上出現很强烈的上升或下降運動，由此點看來改良式 Barnes 和 McFarland 的客觀分析場不及 Inman 權重的客觀分析場。此外在主觀分析垂直速度場中，北緯二十度線附近處有下降氣流，可是在客觀分析垂直速度場中不能表現出來。三種客觀分析場的垂直速度的零線和上升下降運動中心位置比較相近，尤其是改良式 Barnes 權重客觀分析和 McFarland 權重客觀分析的垂直速度場更爲接近。這是因爲兩者都屬於指數型式的權重。在琉球羣島的上升運動，由圖 23 至圖 26 看來，Inman 權重客觀分析場的垂直速度比其他兩種更能充分表現出來。因此在用線性平衡模式來計算垂直速度時，Inman 權重客觀分析場的結果較優。

肆、結　　語

本研究從事三種客觀分析，並計算其垂直速度場，以與主觀分析比較。本研究利用一九七五年六月十日的梅雨天氣資料來探討客觀分析程式對垂直速度計算的影響。研究結果顯示，雖然客觀分析相互間或客觀分析與主觀分析之間，就一般型態來看非常相似，可是對垂直速度場的計算有不同的影響。這是因爲垂直速度計算法對分析場的細微差異具有相當敏感的反應。由表一可知主觀分析場的根均方差比較大，這表示在進行主觀分析時，對原有的測站資料已做相當的修正，而客觀分析除了明顯的錯誤之外，均直接利用原始的測站資料內插到網格點上。儘管主觀分析和客觀分析的手法完全不同，但研究結果顯示，客觀分析場的垂直速度仍能充分表現出四個主要的上升或下降系統，即中緯度槽線和梅雨槽線前後方的上升和下降運動。三種客觀分析的垂直速度場中，在網格範圍的邊界處，出現反常的上升或下降運動，這是因爲在這些地區測站稀少，資料缺乏，不易得到合理的客觀分析高度場和風場。若略去邊界附近的垂直速度場，客觀分析的垂直速度場大致仍能反映出實際的天氣情況。三種客觀分析程式中，McFarland 權重客觀分析在用運動學法計算垂直速度時比較能得到合理的結果。用準地轉模式計算垂直速度時，改良式 Barnes 和 McFarland 權重客觀分析的結果較優良，此外垂直速度場若用線性平衡模式計算時用 Inman 權重客觀分析場比較能得到合理的結果。

致　　謝

本研究是在國家科學委員會 NSC-68M-0202-08(03)「亞洲地區氣象資料之蒐集檢定與分析及程式處理系統之研究」專案計畫支援下完成的。本所研究助理隋中興協助上機，使研究工作得以順利完成，特此致謝。

參　考　文　獻

Barnes, S. L., 1973: Mesoscale objective map analysis using weighted time series observations. NOAA-TM-ERL-NSSL-62, 60 pp.

Chen, T. J. and C. Y. Tsay, 1977: A detailed analysis of a case of Mei-Yu system in the vicinity of Taiwan. Tech. Rept. No. Mei-Yu-001, Dept. of Atmospheric Sciences, National Taiwan University, Taipei, 249 pp.

Cressman, G. P., 1959: An operational objective analysis systems. Mon. Wea. Rev., **87,** 367-374.

Danard, M, B., 1964: On the influence of released latent heat on cyclone development. J. Appl. Meteor., **3,** 27-37.

Haltiner, G. J., 1971: Numerical Weather Prediction, Wiley, New York, 317 pp.

胡仲英，1977：高空天氣圖客觀分析之研究。大氣科學，第四期，1—10，中華民國氣象學會。

Inman, R. L., 1970: Papers on operational objective analysis schemes used at NSSFC. NOAA-TM-ERL-NSSL-51, 91 pp.

Liang, W. J., 1976: The variational optimization of wind field for the estimation of vertical velocity. Ann. Rept. Inst Phys., Acad. Sin., **6,** 179-198.

Liang, W. J., 1977: Comparison of McGinley's and O'Brien's variational optimization formulation for the computation of vertical velocity. Atmospheric Science, **4,** 73-76.

McDonell, J. E., 1967: A summary of the first guess field used for operational analysis. ESSA-TM-WBTM-NMC-38, 17 pp.

McFarland, M. J., 1975: Variational optimization analysis of temperature and moisture advection in a severe storm environment. WEAT Rept. No. 16, Univ. of Oklahoma, Norman, Oklahoma, 86 pp.

McGinley, J. H., 1973: Environmental energy fields associated with severe storms. M. S. Thesis, University of Okbalnoma, Normon, 129 pp.

Smith, P. J. and C. P. Lin, 1978: A comparison of synoptic scale vertical motions computed by the kinematic method and two forms of the omega equation. Mon. Wea. Rev., **106,** 1687-1694.

Stuart, D. W., 1974: A comparison of quasi-geostrophic vertical motion using various analyses. Mon. Wea. Rev., **102,** 363-374.

曾忠一，1978a：三種客觀分析程式之比較研究。中央研究院物理研究所集刊，第 8 卷，155-175。
曾忠一，1978b：大氣垂直速度計算之研究。中央研究院物理研究所集刊，第 8 卷，127-154。
Vincent, D. G., K. E. Bossingham, H. J. Edmon, 1976: Comparison of large scale vertical motions computed by the kinematic method and quasi-geostrophic omega equation. Preprints of Papers, Sixth Conference on Weather Forecasting and Analysis, Albany, N. Y., 357-364.

	850mb	700mb	500mb	300mb	200mb	100mb
z 高度 m	9.1	7.9	15.9	24.2	36.2	44.9
T 溫度 °C	1.5	1.2	1.1	1.2	1.6	1.7
T_d 露點溫度 °C	1.6	2.5	2.7			
u 風速分量 m/sec	3.2	3.2	3.5	5.1	6.6	3.3
v 風速分量 m/sec	3.8	2.9	3.1	5.8	4.5	3.1

	850mb	700mb	500mb	300mb	200mb	100mb
z 高度 m	4.8	5.2	8.0	12.7	16.8	21.6
T 溫度 °C	0.7	0.6	0.7	0.7	0.7	1.0
T_d 露點溫度 °C	1.0	1.6	2.1			
u 風速分量 m/sec	1.7	1.9	1.9	2.0	2.5	1.5
v 風速分量 m/sec	1.8	2.0	1.6	2.8	1.9	1.8

	850mb	700mb	500mb	300mb	200mb	100mb
z 高度 m	7.1	8.0	12.1	19.3	24.4	31.7
T 溫度 °C	1.2	1.0	1.0	1.0	1.1	1.4
T_d 露點溫度 °C	1.6	2.7	3.2			
u 風速分量 m/sec	2.5	3.0	3.1	3.3	3.9	2.6
v 風速分量 m/sec	2.9	2.9	2.7	4.2	3.6	2.8

	850mb	700mb	500mb	300mb	200mb	100mb
z 高度 m	5.6	6.6	10.7	18.1	23.6	28.2
T 溫度 °C	0.9	0.8	0.9	0.9	1.0	1.3
T_d 露點溫度 °C	1.3	2.3	2.8			
u 風速分量 m/sec	1.4	1.6	2.0	2.3	2.9	2.0
v 風速分量 m/sec	2.2	2.4	2.2	3.6	3.2	2.2

表一　由上而下各表代表主觀分析，Inman 客觀分析，改良式 Barnes 客觀析分及 McFarland 客觀分析等分析場和觀測值的根均方差。

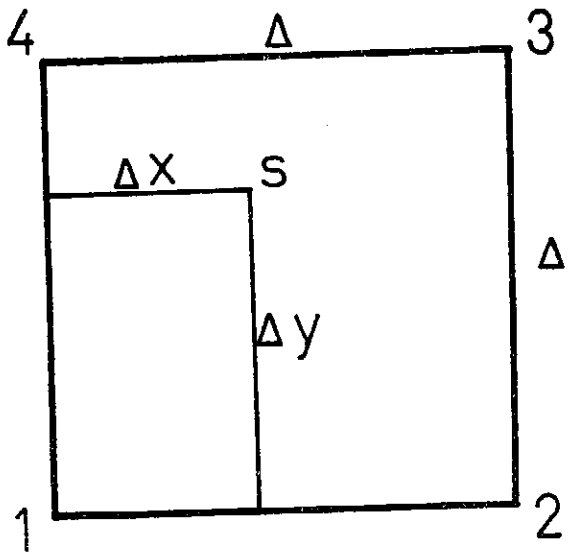

圖 1. 本圖說明測站上分析值的求法

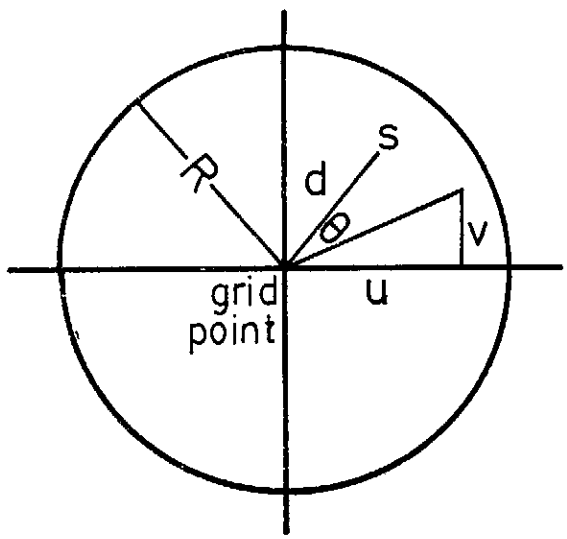

圖 2. 本圖說明各符號的定義

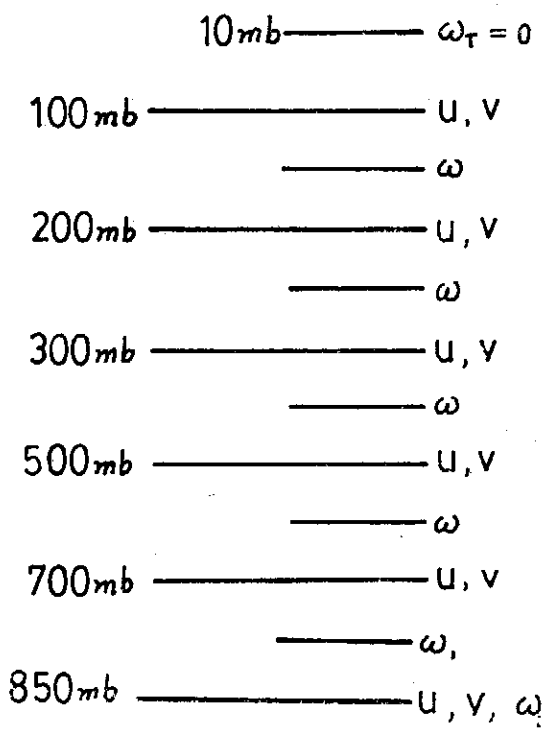

圖 3. 用運動學法求垂直速度時使用的垂直網格結構

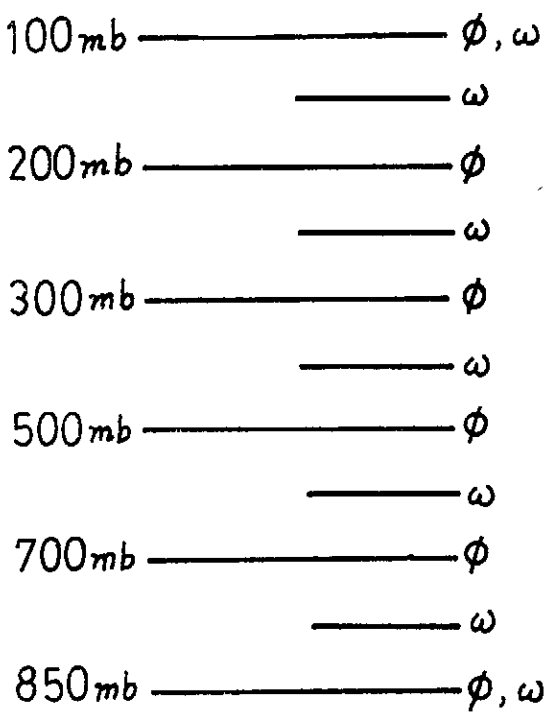

圖 4. 用準地轉和平衡模式求垂直速度時使用的垂直網格結構

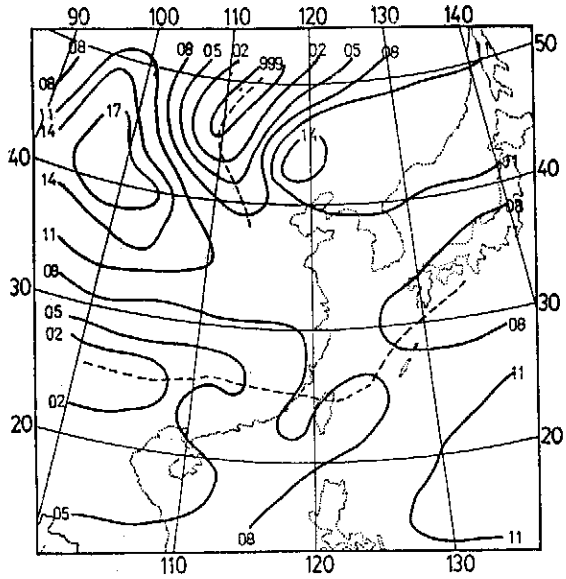

圖 5. 海平面氣壓，單位爲 mb 與鋒面（虛線）

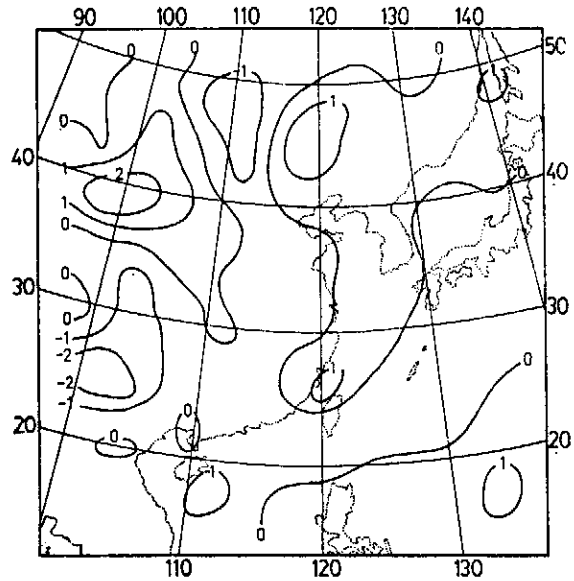

圖 6. 850mb 垂直速度場，單位爲 μb/sec.

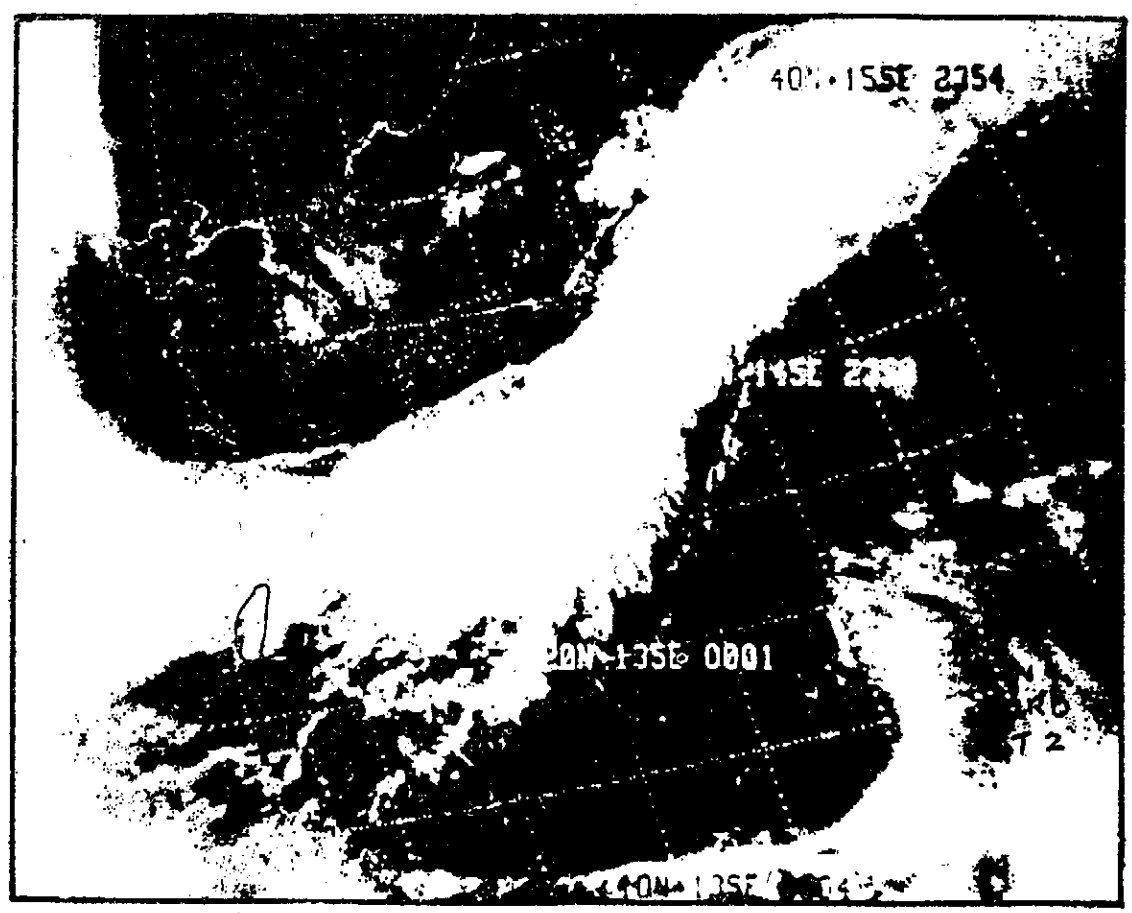

圖 7. NOAA-4 紅外光衛星照片，白色虛線表示經緯度以及海岸線，臺灣的位置用實線表示

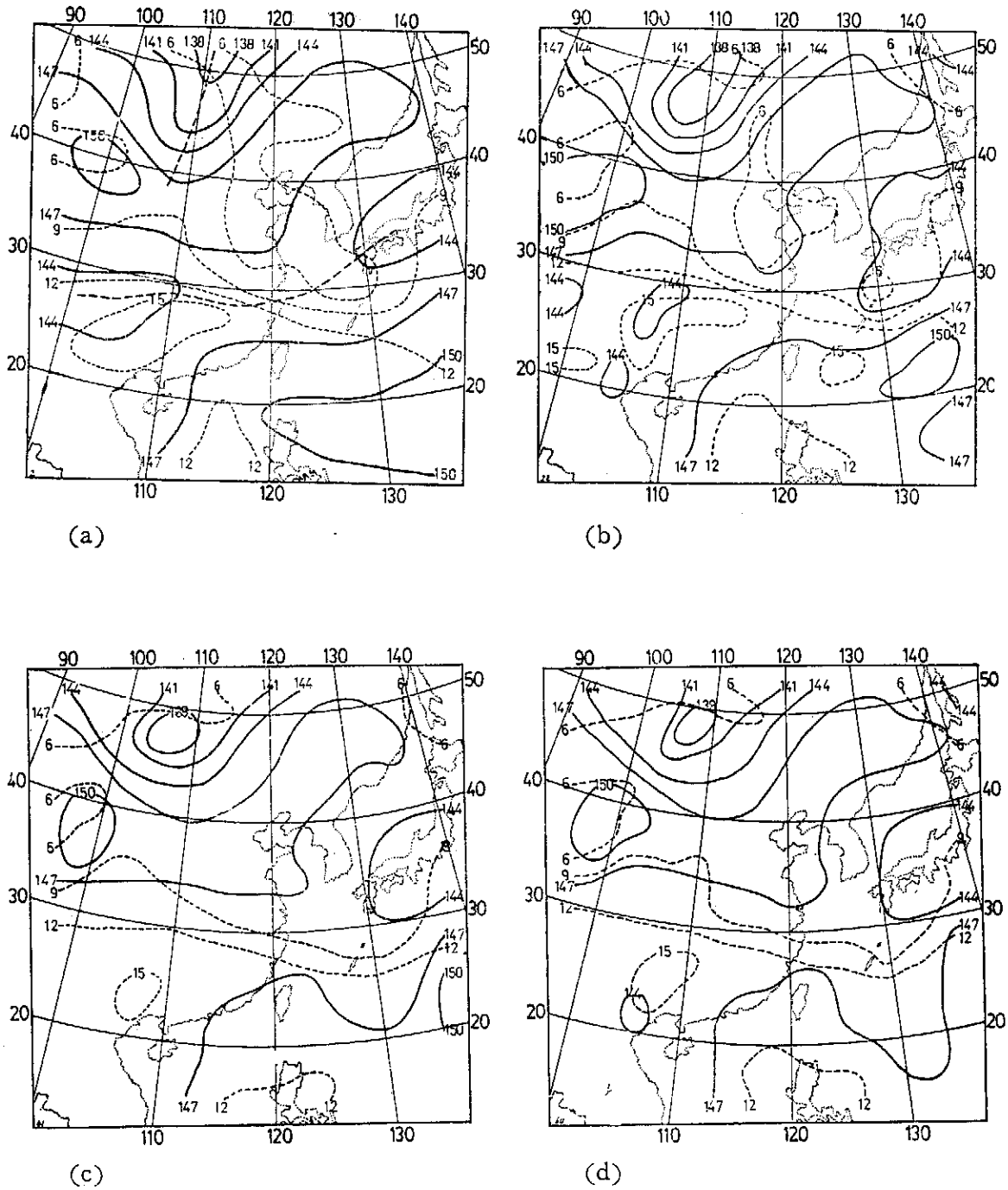

圖8. 850mb 高度場（實線）與混合比（虛線，單位爲 g/kg）(a) 主觀分析 (b) Inman 客觀分析 (c) 改良式 Barnes 客觀分析 (d) McFarland 客觀分析

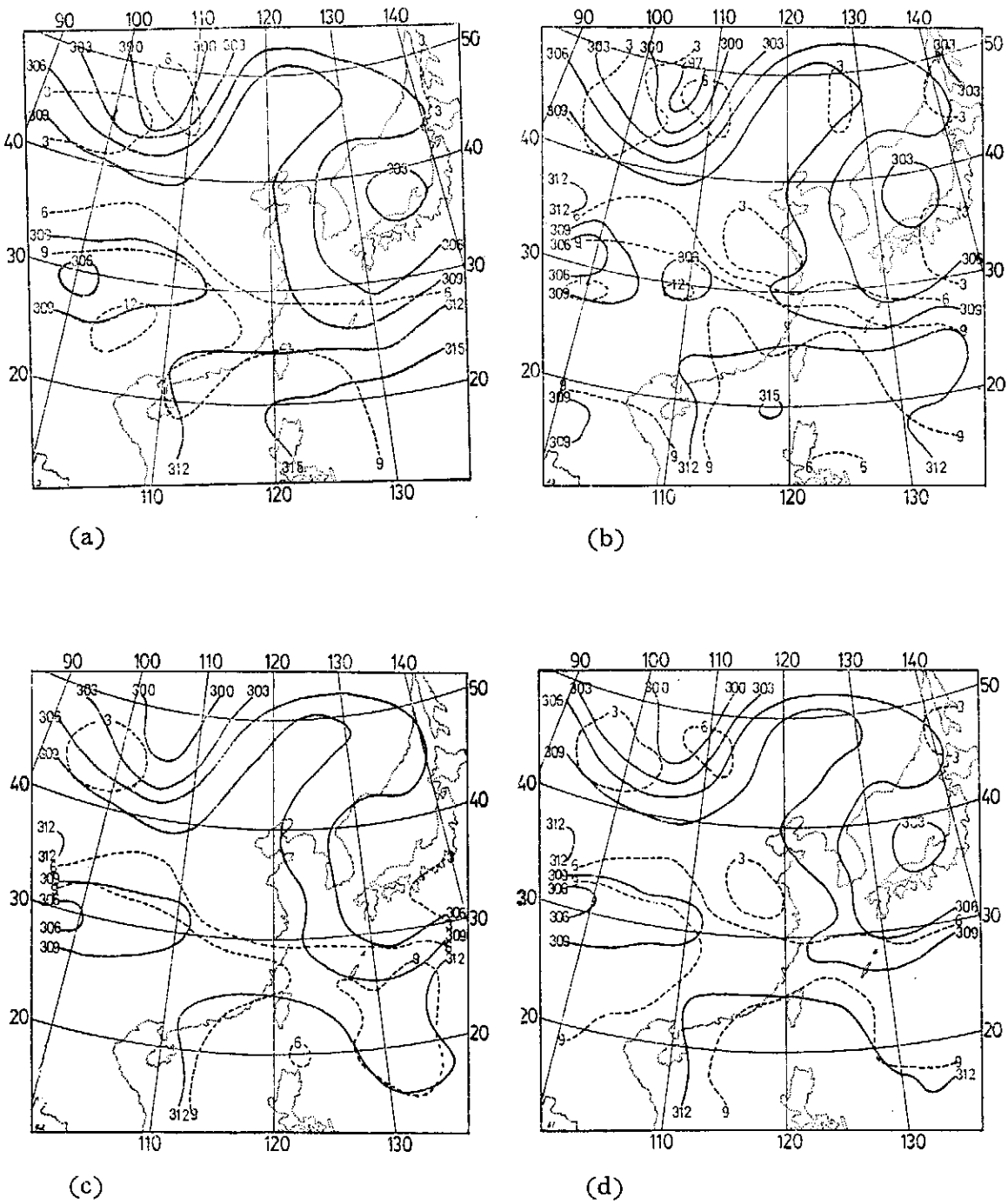

圖9. 700mb 高度場（實線，單位爲公尺）與混合比（虛線，單位爲 g/kg）(a) 主觀分析 (b) Inman 客觀分析 (c) 改良式 Barnes 客觀分析 (d) McFarland 客觀分析

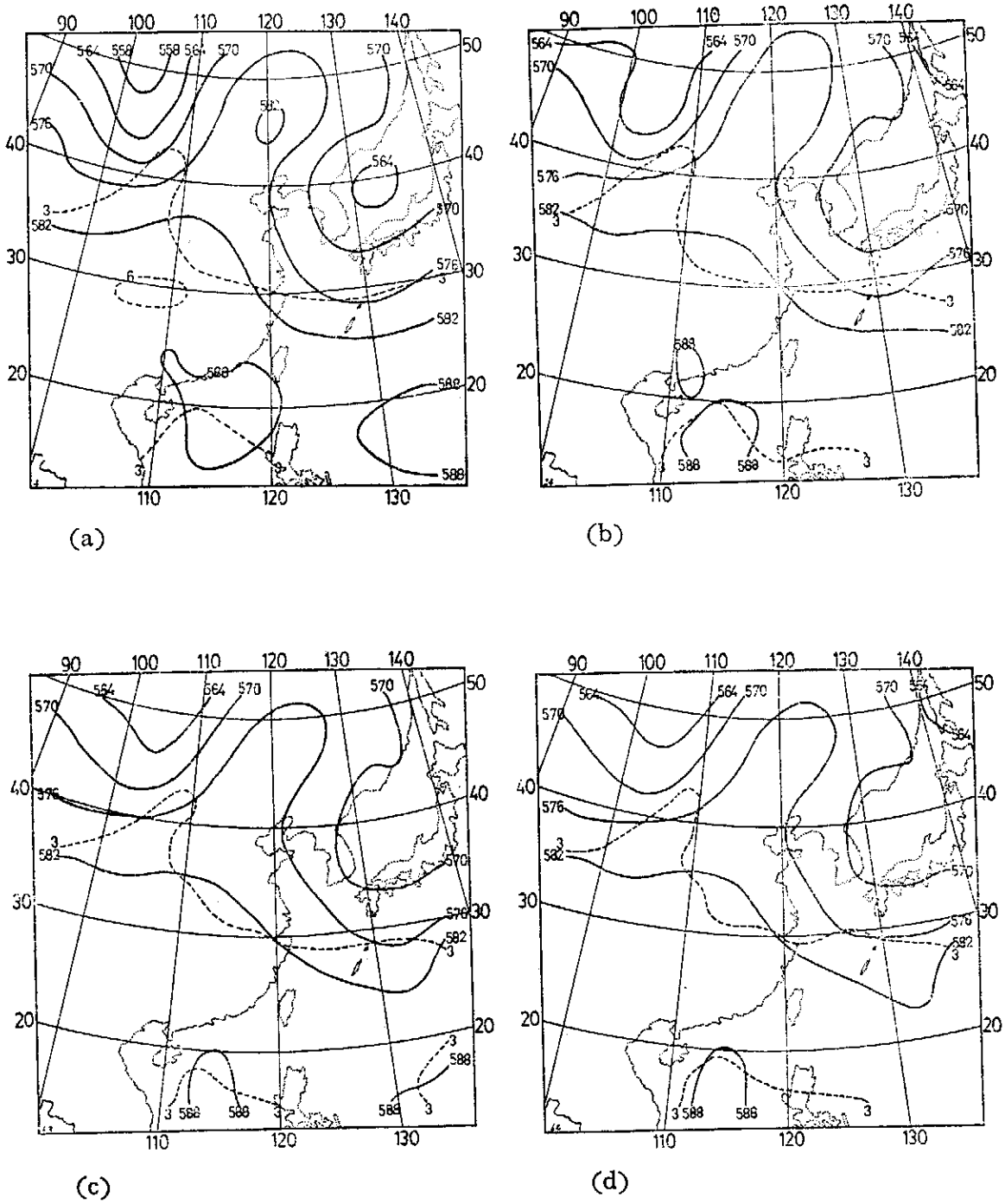

圖10. 500mb 高度場（實線，單位爲公尺）與混合比（虛線，單位爲 g/kg） (a) 主觀分析 (b) Inman 客觀分析 (c) 改良式 Barnes 客觀分析 (d) McFarland 客觀分析

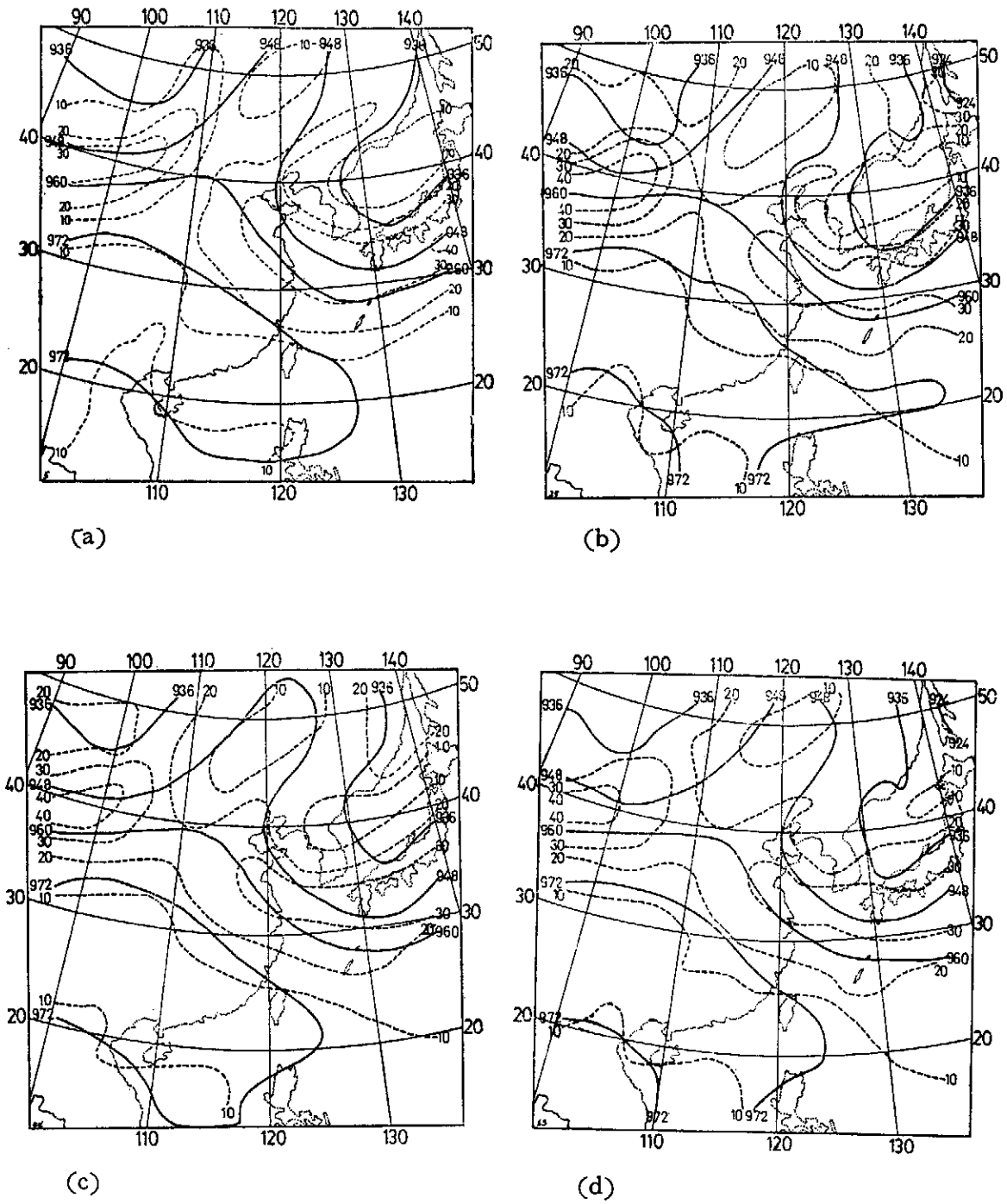

圖11. 300mb 高度場（實線，單位爲公尺）與風速（虛線，單位爲 m/sec） (a) 主觀分析 (b) Inman 客觀分析 (c) 改良式 Barnes 客觀分析 (d) McFarland 客觀分析

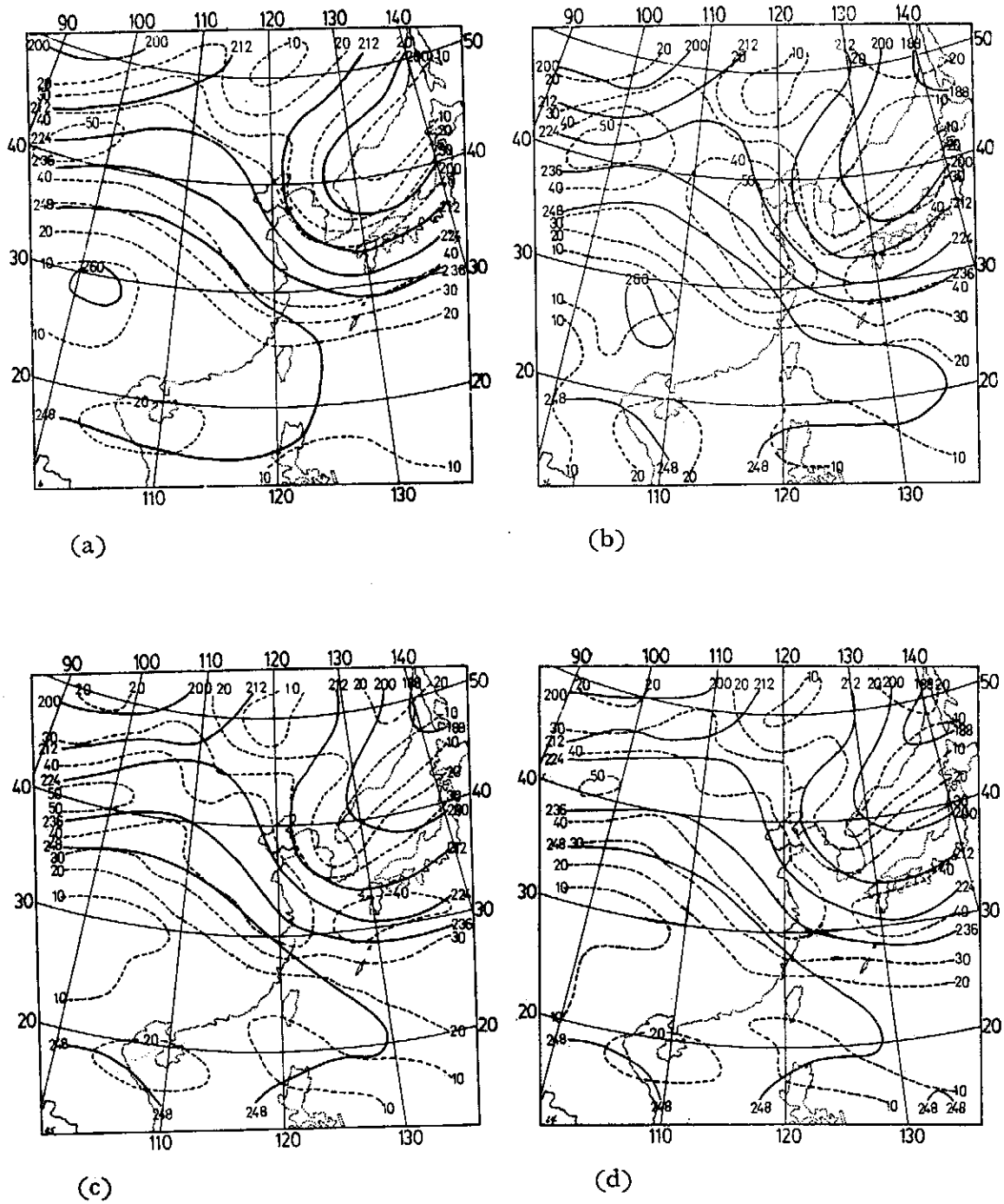

圖12. 200mb 高度場（實線，單位爲公尺）與風速（單位爲 m/sec） (a) 主觀分析 (b) Inman 客觀分析 (c) 改良式 Barnes 客觀分析 (d) McFarland 客觀分析

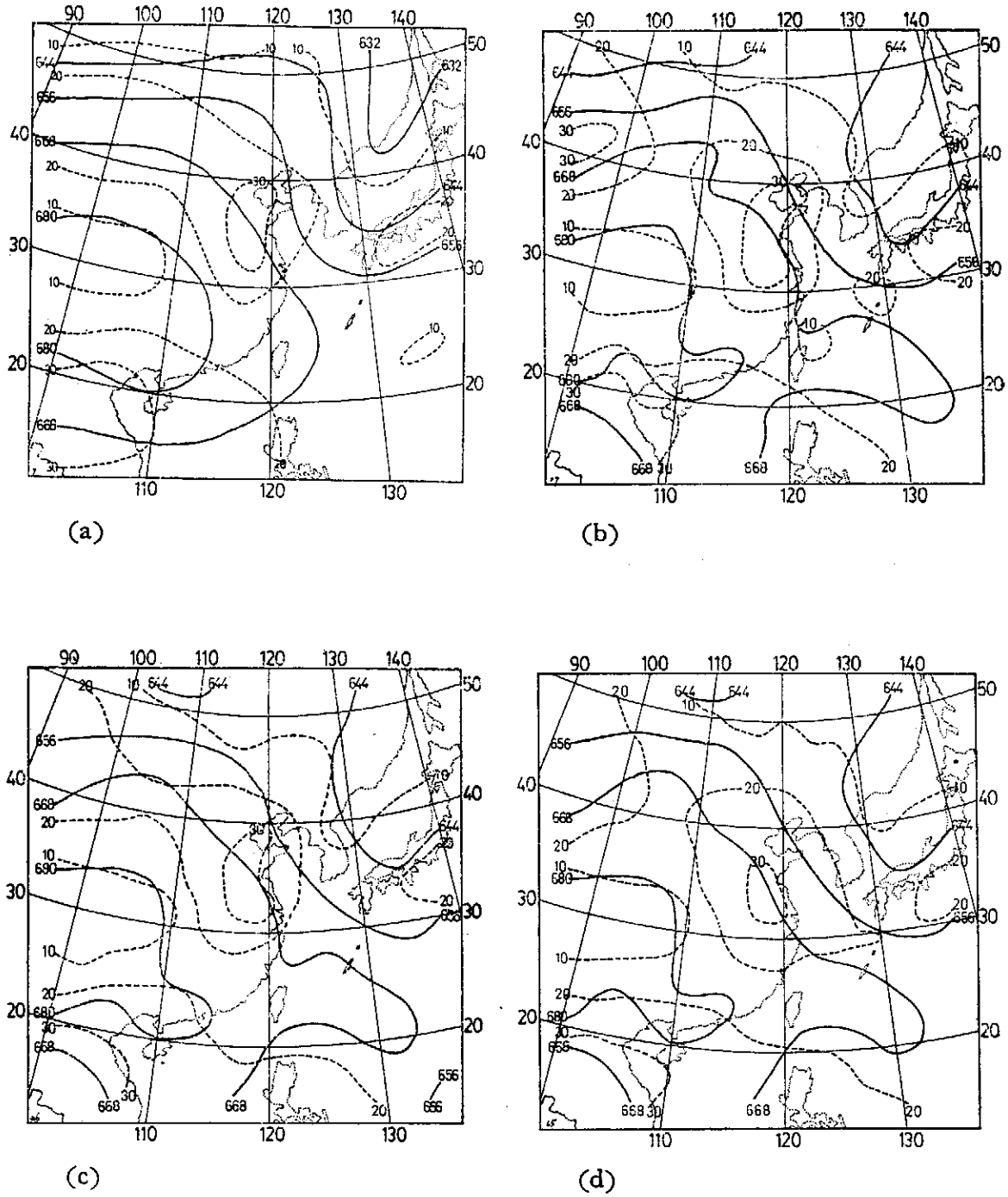

圖13. 100mb 高度場（實線，單位爲公尺）與風速（單位爲 m/sec） (a) 主觀分析 (b) Inman 客觀分析 (c) 改良式 Barnes 客觀分析 (d) McFarland 客觀分析

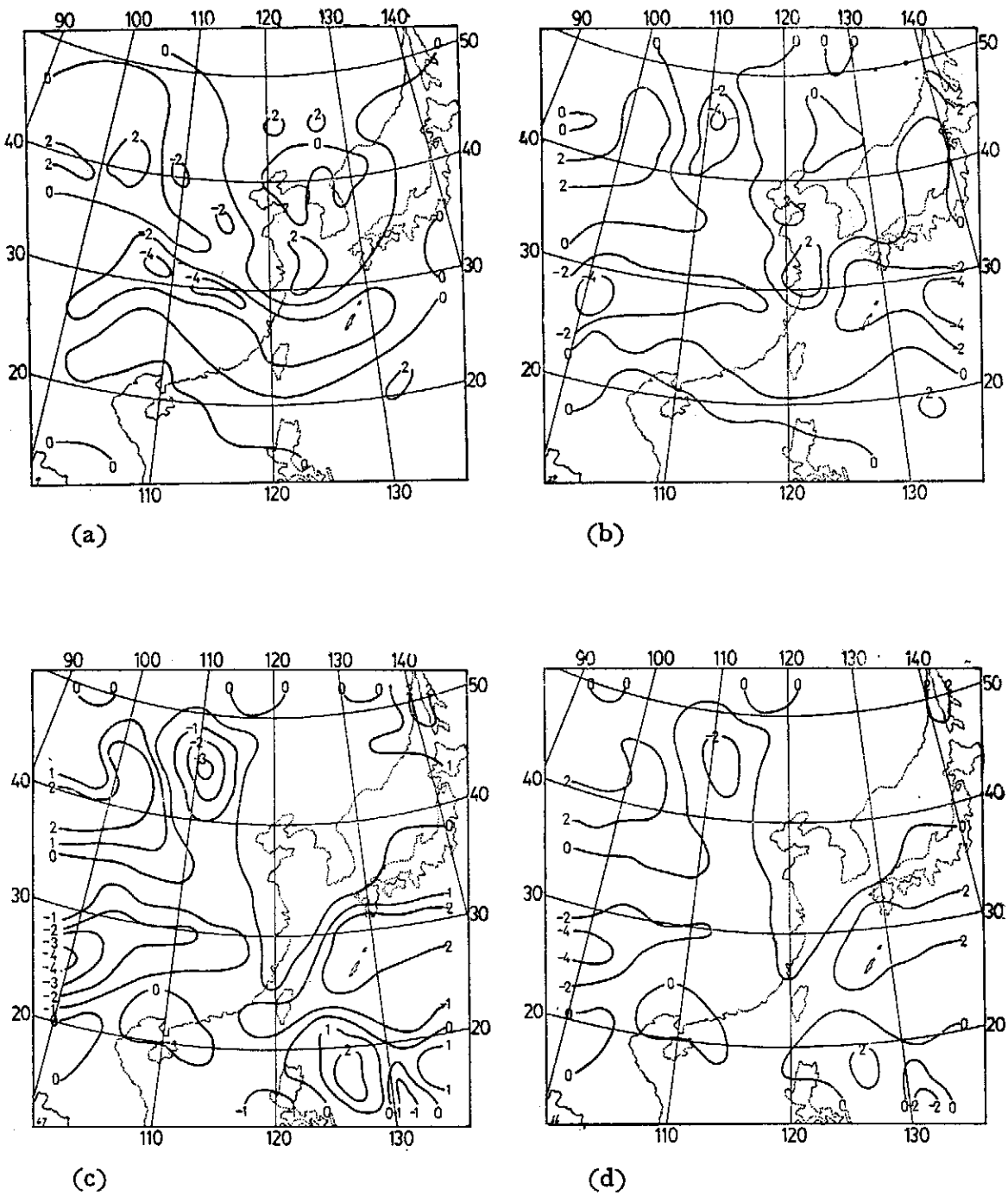

圖14. 用運動學法求得的 700mb 垂直速度，單位爲 μb/sec (a) 主觀分析 (b) Inman 客觀分析 (c) 改良式 Barnes 客觀分析 (d) McFarland 客觀分析

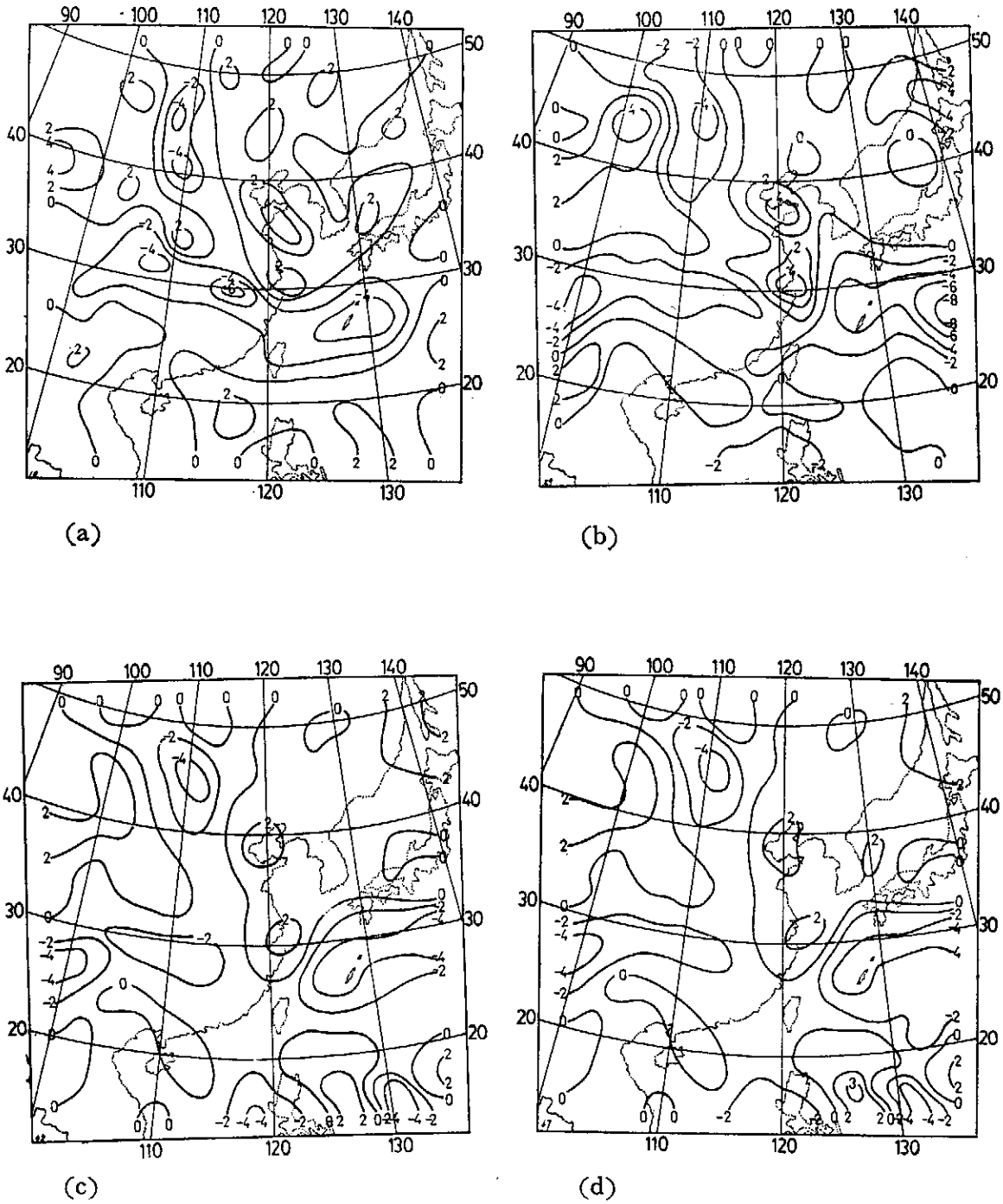

圖15. 用運動學法求得的 500mb 垂直速度，單位爲 μb/sec (a) 主觀分析 (b) Inman 客觀分析 (c) 改良式 Barnes 客觀分析 (d) McFarland 客觀分析

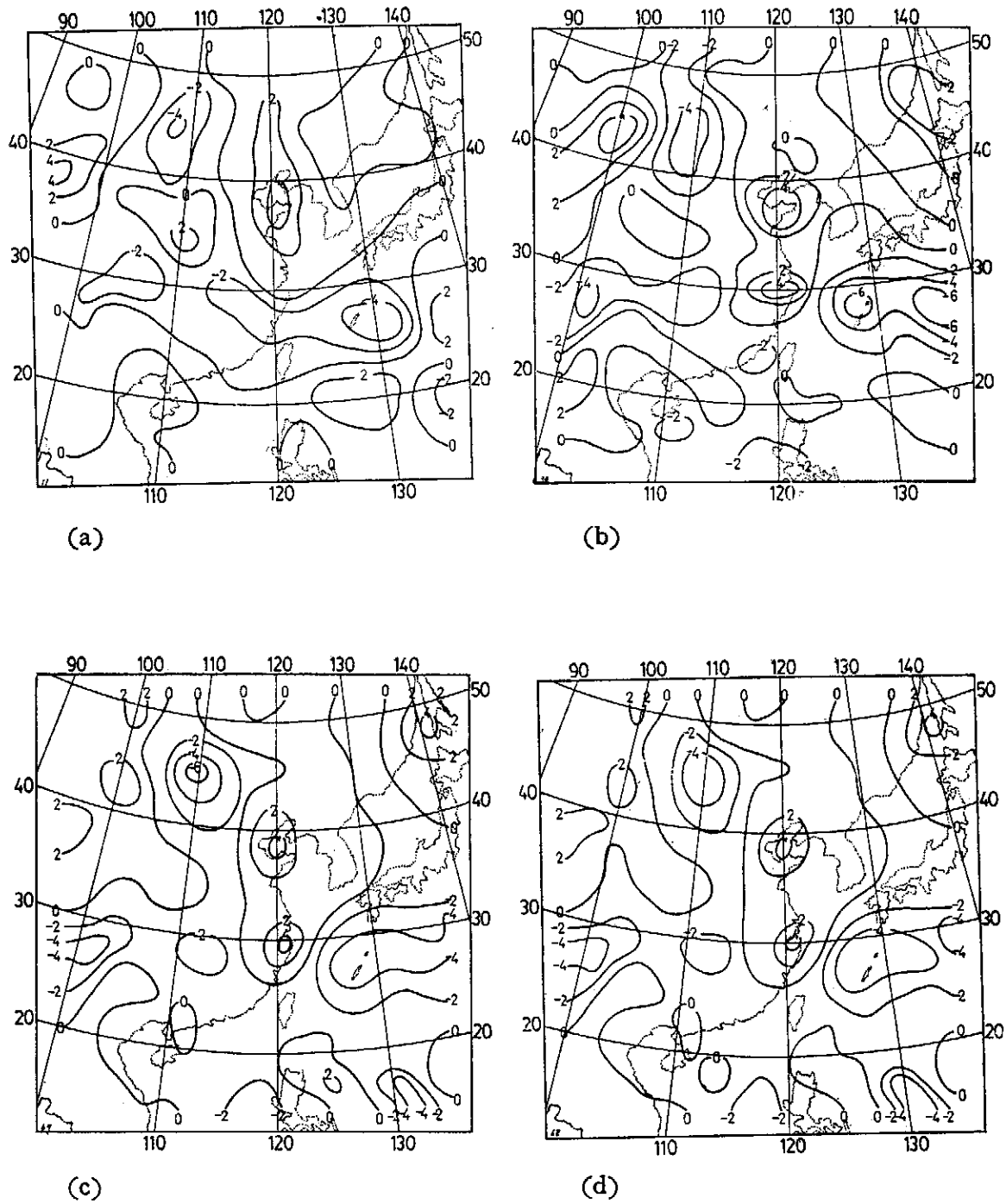

圖16. 用運動學法求得的 300mb 垂直速度，單位爲 μb/sec (a) 主觀分析 (b) Inman 客觀分析 (c) 改良式 Barnes 客觀分析 (d) McFarland 客觀分析

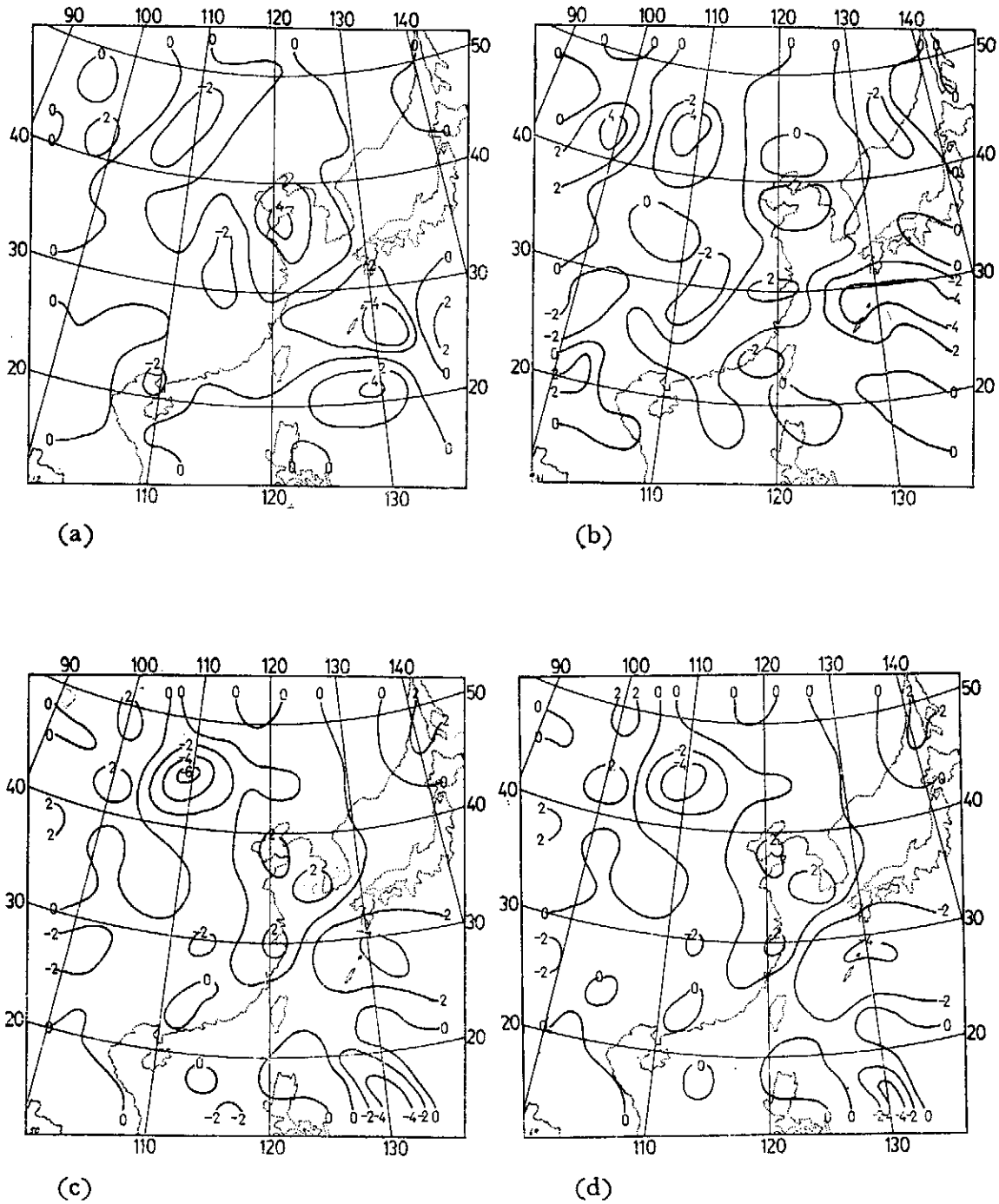

圖17. 用運動學法求得的 200mb 垂直速度，單位爲 μb/sec (a) 主觀分析 (b) Inman 客觀分析 (c) 改良式 Barnes 客觀分析 (d) McFarland 客觀分析

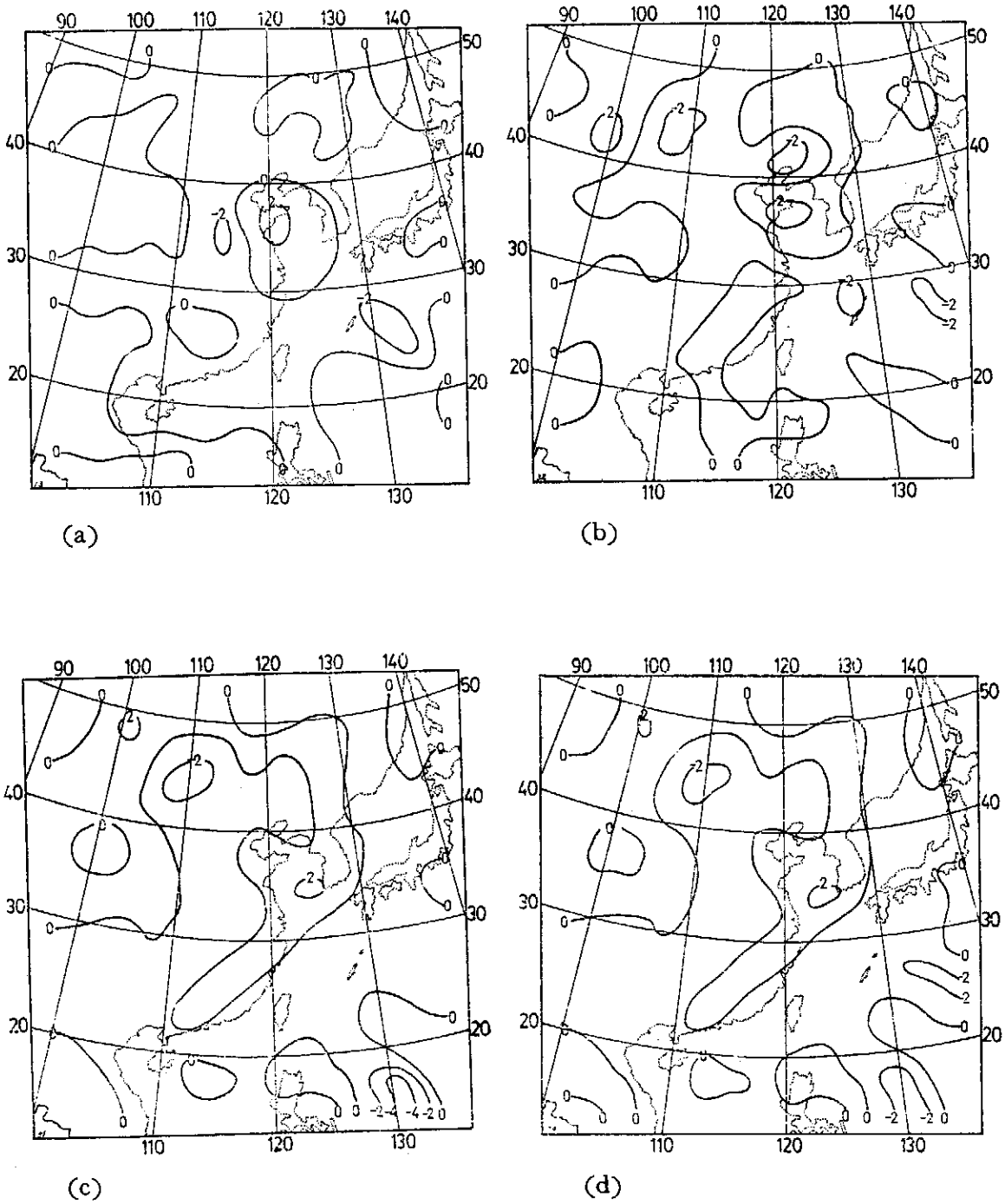

圖18. 用運動學法求得的 100mb 垂直速度，單位爲 μb/sec (a) 主觀分析 (b) Inman 客觀分析 (c) 改良式 Barnes 客觀分析 (d) McFarland 客觀分析

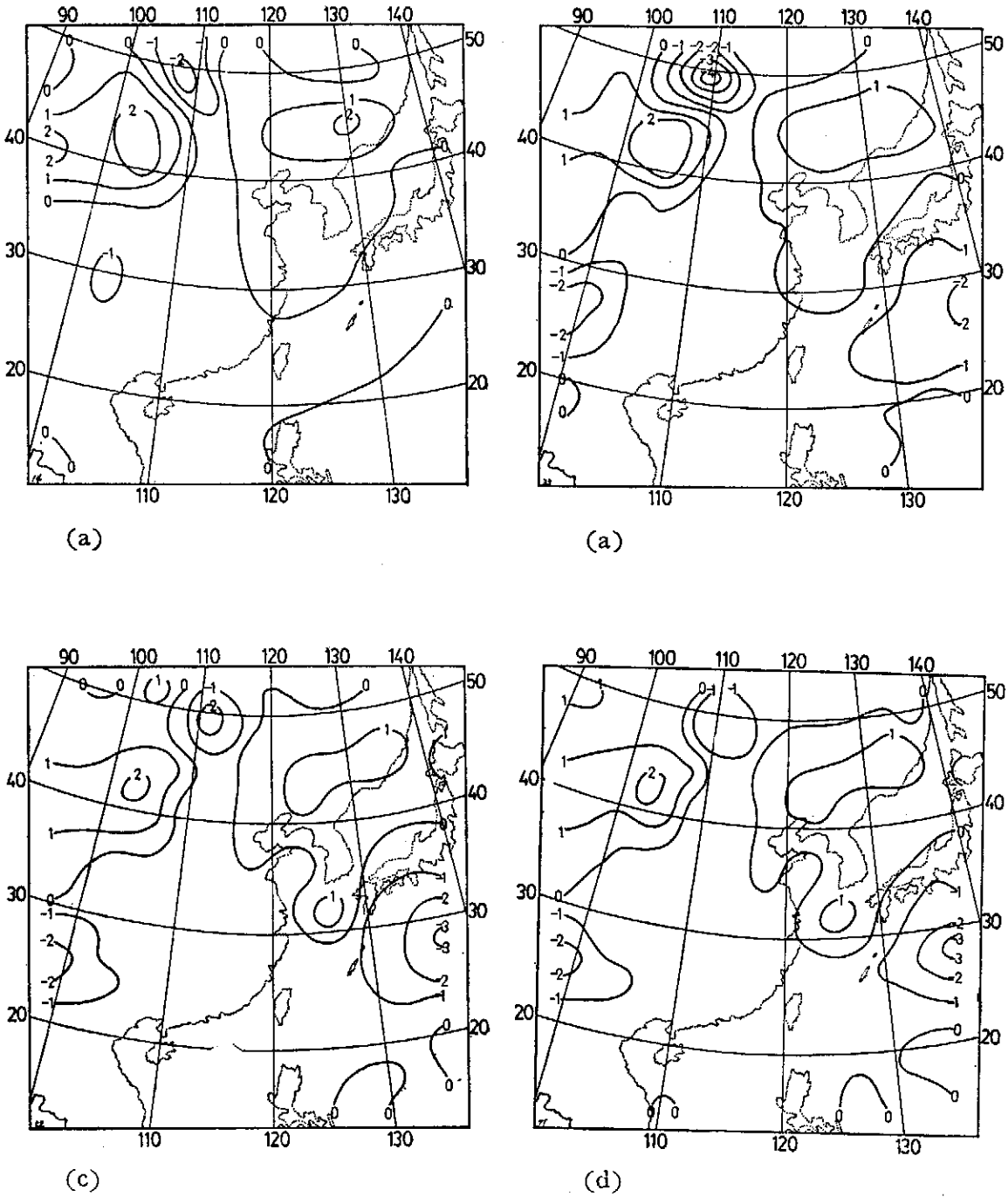

圖19. 用準地轉模式求得的 700mb 垂直速度，單位爲 μb/sec (a) 主觀分析 (b) Inman 客觀分析 (c) 改良式 Barnes 客觀分析 (d) McFarland

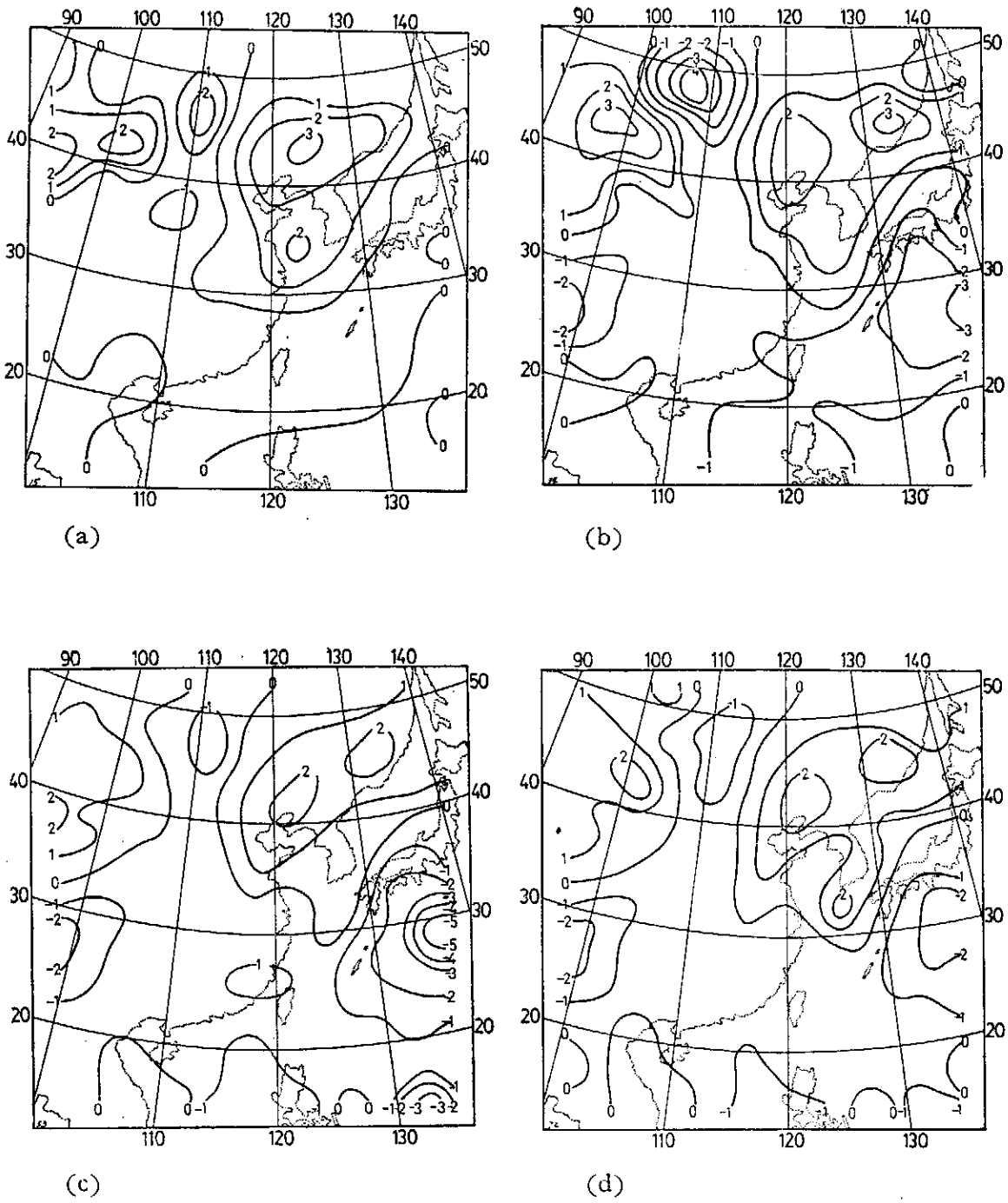

圖20. 用準地轉模式求得的 500mb 垂直速度，單位爲 μb/sec (a) 主觀分析 (b) Inman 客觀分析 (c) 改良式 Barnes 客觀分析 (d) McFarland 客觀分析

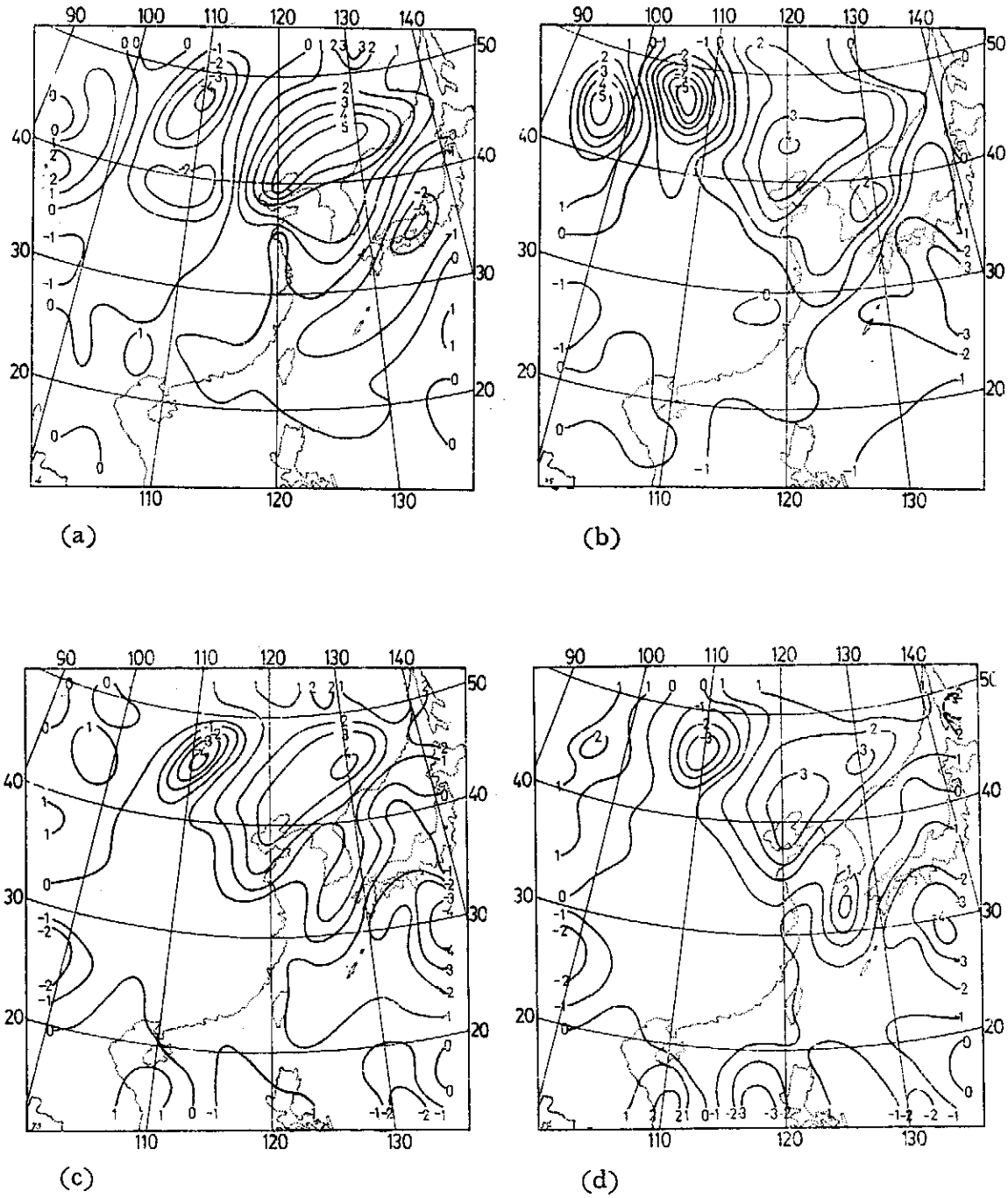

圖21. 用準地轉模式求得的 300mb 垂直速度，單位爲 μb/sec (a) 主觀分析 (b) Inman 客觀分析 (c) 改良式 Barnes 客觀分析 (d) McFarland 客觀分析

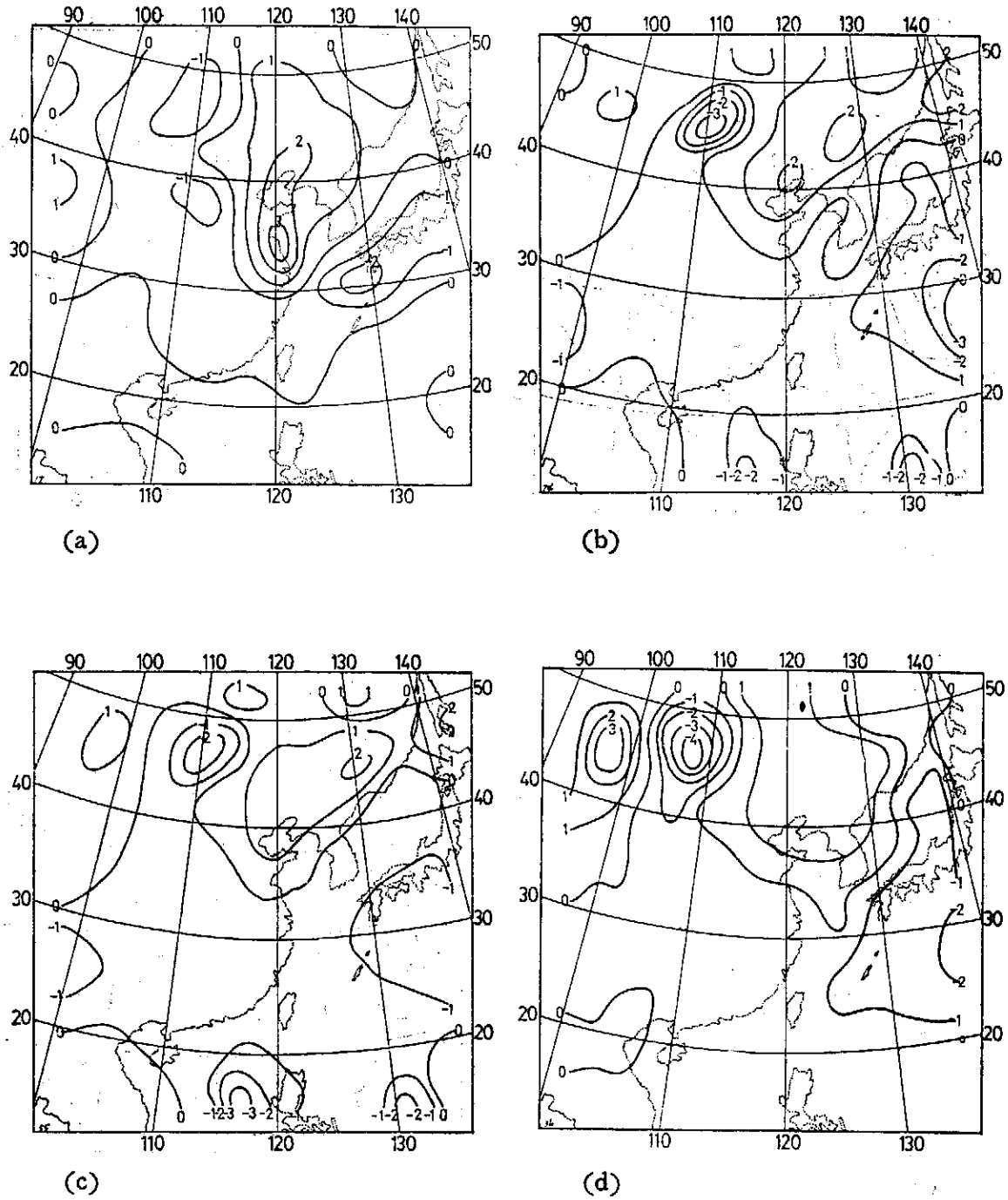

圖22. 用準地轉模式求得的 200mb 垂直速度，單位爲 μb/sec (a) 主觀分析 (b) Inman 客觀分析 (c) 改良式 Barnes 客觀分析 (d) McFarland 客觀分析

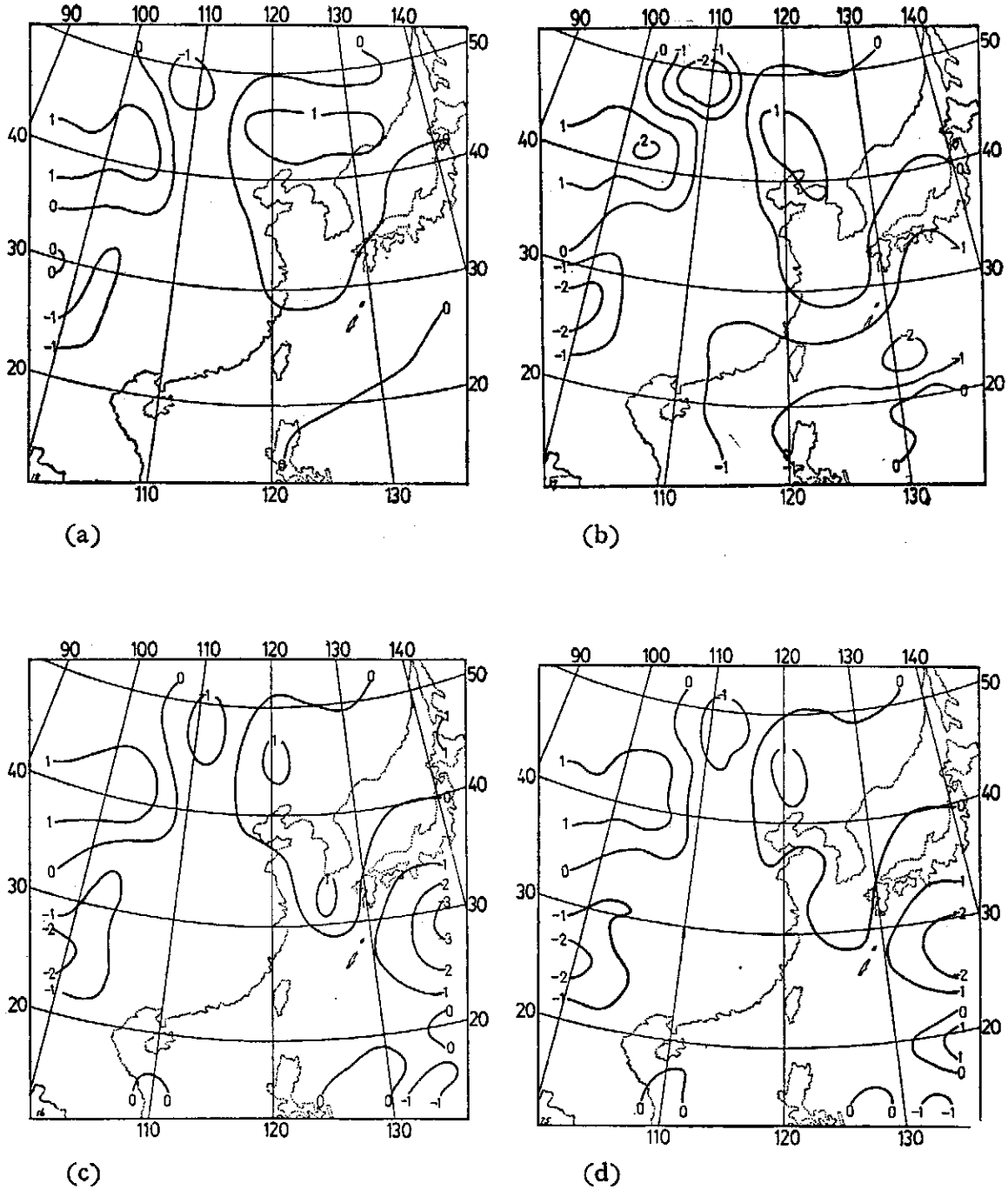

圖23. 用線性平衡模式求得的 700mb 垂直速度，單位爲 μb/sec (a) 主觀分析 (b) Inman 客觀分析 (c) 改良式 Barnes 客觀分析 (d) McFarland 客觀分析

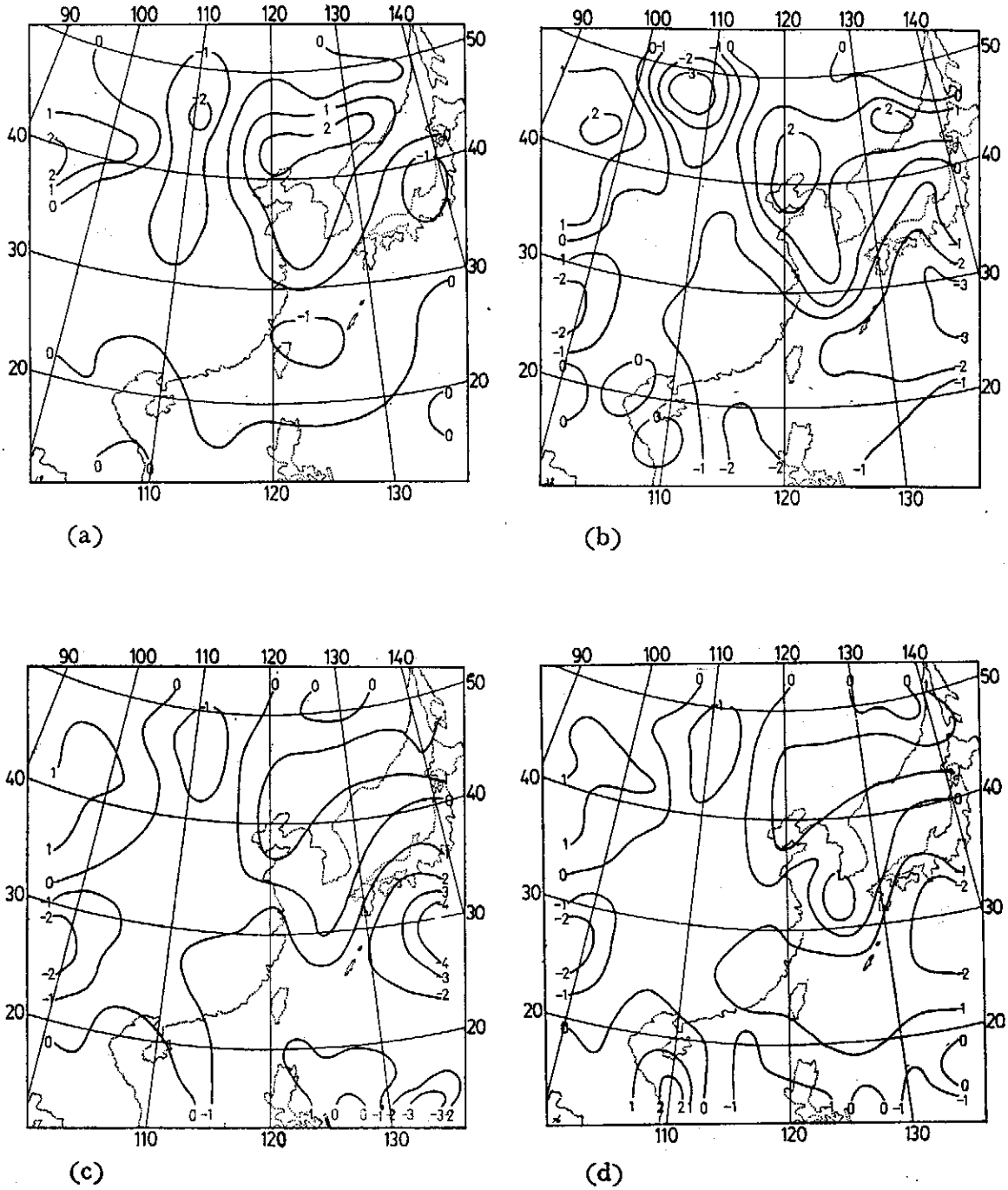

圖24. 用線性平衡模式得到的 500mb 垂直速度，單位爲 μb/sec (a) 主觀分析 (b) Inman 客觀分析 (c) 改良式 Barnes 客觀分析 (d) McFarland 客觀分析

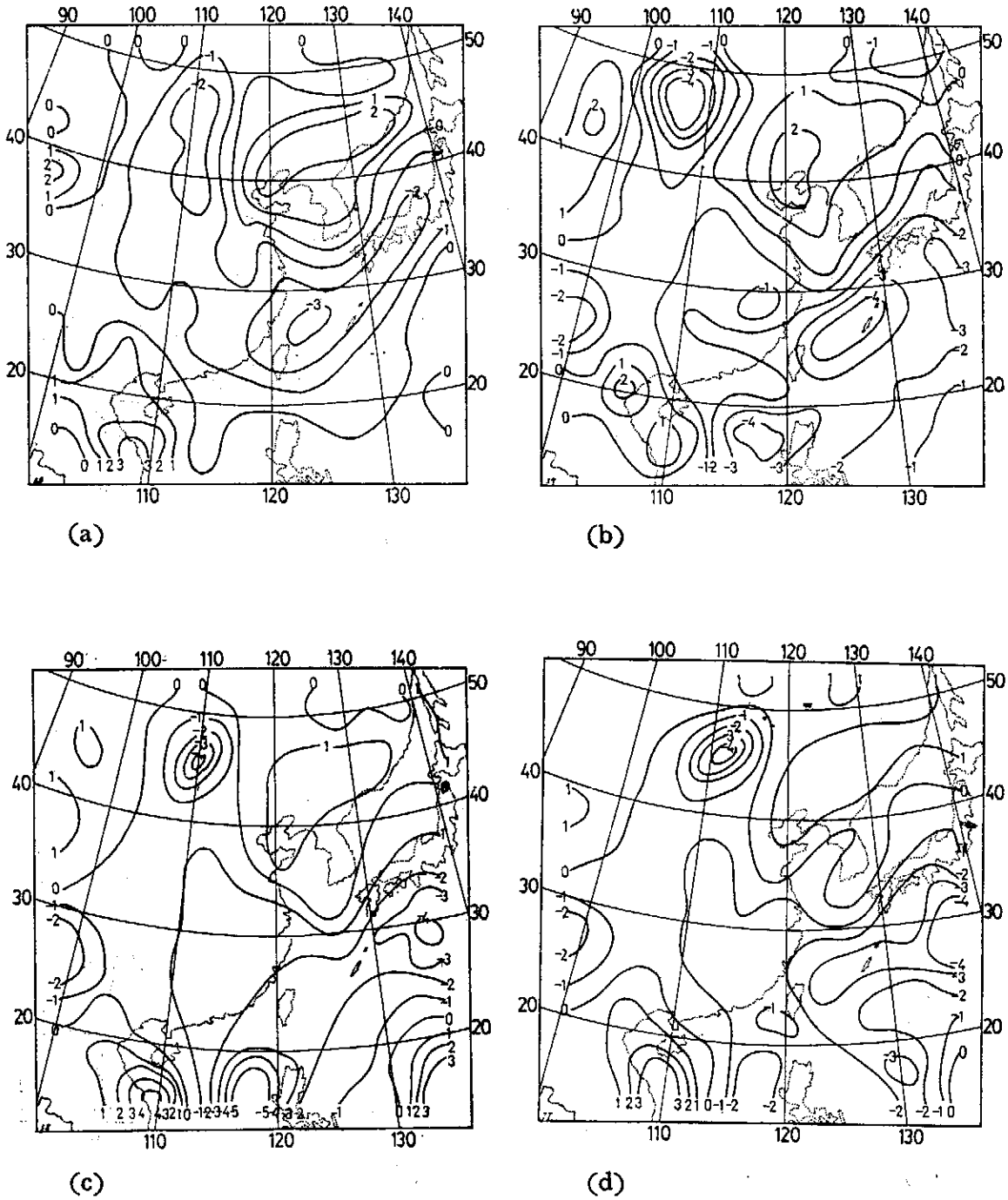

圖25. 用線性平衡模式得到的 300mb 垂直速度，單位爲 μb/sec (a) 主觀分析 (b) Inman 客觀分析 (c) 改良式 Barnes 客觀分析 (d) McFarland 客觀分析

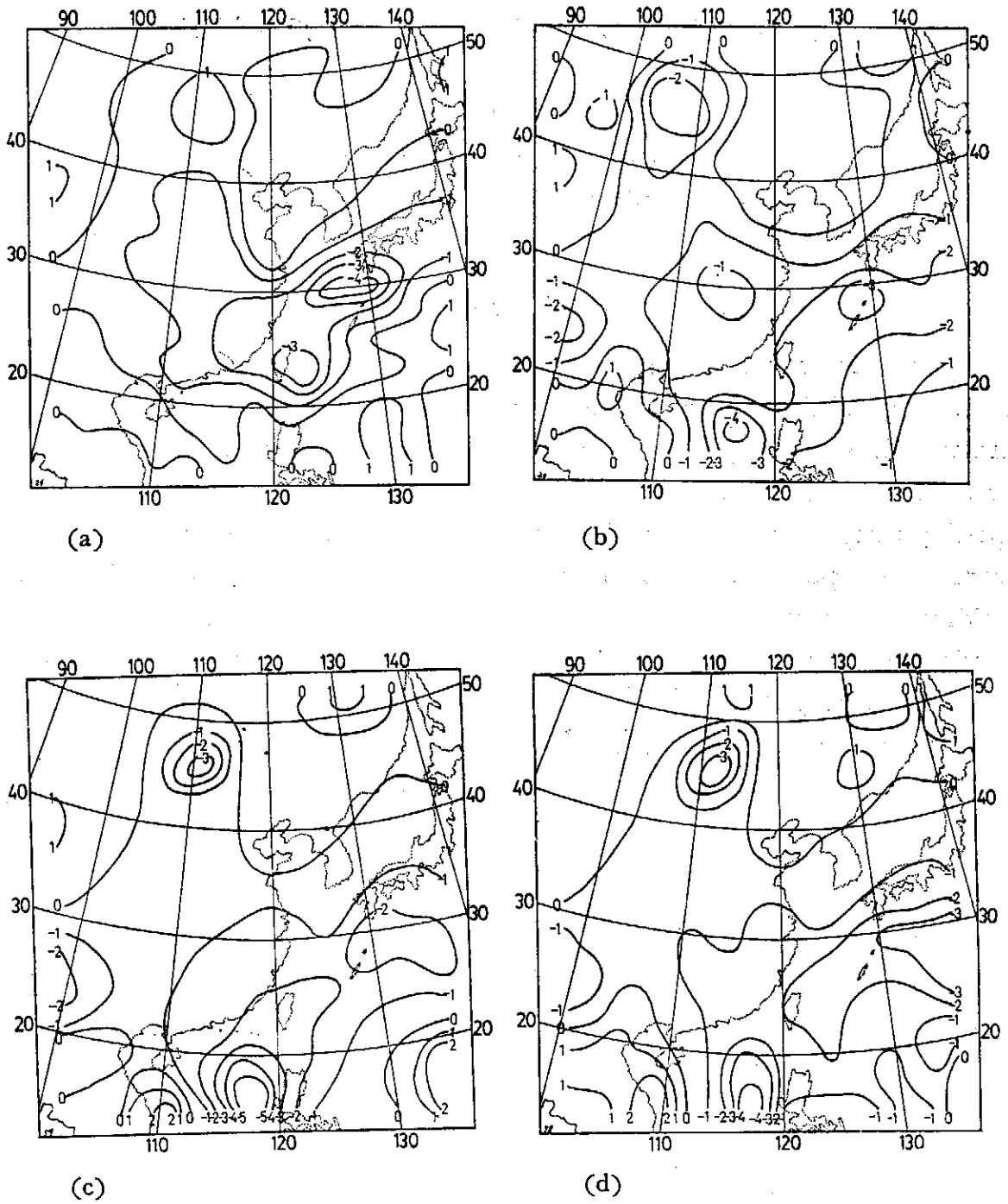

圖26. 用線性平衡模式得到的 200mb 垂直速度，單位爲 μb/sec (a) 主觀分析 (b) Inman 客觀分析 (c) 改良式 Barnes 客觀分析 (d) McFarland 客觀分析

Annual Report of the Institute of Physics, Academia Sinica, Vol. 9, 1979

EFFECT OF VARIOUS OBJECTIVE ANALYSIS SCHEMES ON VERTICAL MOTION COMPUTATION

CHUNG YI TSENG

Institute of Physics. Academia Sinica
Dept. of Atmospheric Sciences, National Taiwan University

Abstract

The effect of three objective analysis schemes on the vertical motion fields is investigated for a synoptic case over the East Asia area during the Mei-Yu season. Three objective analysis techniques are employed to prepare height and wind data. These data were used as input to the continuity equation, quasi-geostrophic omega equation and linear balance model to compute the vertical motion field. A comparison is made between these vertical motion fields using various analyses. It is found that the general patterns of the vertical motion field for each objective analysis technique are in good agreement with the middle-latitude synoptic weather system. The results of present study indicate that the vertical motion field is sensitive to the analysis techniques.

臺北市一氧化碳污染與偵測網之佳化評估

梁　文　傑

中央研究院物理研究所
國立臺灣大學機械工程研究所

李　克　堂

國立臺灣大學環境工程研究所

摘　　要

本文使用佳化理論來探討臺北市一氧化碳的污染情形。文中視車道爲有限線源，將高斯模式與測站上實際測定的濃度值相組合，以求出適合當地污染狀況的佳化排放源强度，再據而求出最能反映當地實況的一氧化碳佳化濃度分佈，並以佳化與未佳化模式在各測站的濃度計算值作統計特性的討論，以確知佳化結果的可信性，並根據佳化結果評估臺北市一氧化碳的污染狀況。此外，利用測站有效偵測圈與污染源分佈的關係，估計現有測站的偵測效率，又因夏季與冬季風向相異，故分別建議夏季與冬季增設測站的較佳位置與數目，估計其偵測效率，以作爲將來臺北市增設測站的參考。

壹、前　　言

空氣是人類生存的基本要素，人類必須從空氣中吸取氧而將氧化作用所產生的二氧化碳呼出體外，此種「呼」與「吸」實乃人類生命的基本現象，也是人類享有的基本權利與義務。由於吹風、下雨、沉澱、化學作用以及植物的吸收，人類所呼出的廢氣理應很容易的被稀釋與排除，然而隨著人類文明的進展，工業時代的來臨，工廠與車輛遍佈城市與鄉鎮的大街小巷，這些新時代的寵兒也同人類一樣必須從空氣中攝取氧以供氧化、燃燒及其他工業過程之由，而將產生的廢氣（包括氣體與固體）排至大氣中。所不同的却是它們驚人的排放量，就一輛小型汽車來說，每行一公里所排放的一氧化碳（約30公克），約需兩百萬公升的空氣才能稀釋到無害的濃度，而兩百萬公升的空氣正是兩百位成年人一天呼吸所需。換句話說，稀釋一輛

小型汽車行駛一天（每小時以60公里計）所排放的一氧化碳所需的空氣竟足以供應28萬8千位成年人一天呼吸之用！更由於工廠與車輛排放的廢氣有增無減，而空氣的體積及其排除作用的能力有限，使得這些污染物所帶來的不良影響日趨嚴重，而城市與工業區的污染問題便是其中最爲顯著的例子。

城市與工業區的污染源包含有點源、線源與面源三類，大工廠可視爲點污染源，而小工廠因其數目太多，若對每一個污染源的污染情形各別計算段不經濟，一般皆取其總污染量除以總面積而將之視爲面污染源，此外，車輛的污染可視公路、鐵路（或地下鐵道和隧道）等爲線污染源。城市污染問題首先在於了解市區的污染程度（亦即求取污染物濃度分佈圖），以作爲都市計畫或污染程度控制的依據，求得污染物濃度分佈的方法一般可分爲兩種，第一種是在選定的各量測點實際量測空氣中污染物的濃度，第二種是利用數學模式將所有污染源的污染情形算出，並據此繪出城市的濃度分佈曲線，理論上說，如果兩種方法都很理想，所求得的結果應該一致，但事實上由於量測與數學模式所牽涉到的許多問題，使得兩者之間出入頗大。就以第一種方法來說，量測地點不同，其結果大不相同，使得量測值的眞實意義不易確定。譬如，吹東風時（風由東向西吹），若測站在煙囪西邊則量得的濃度可能極高，若測站在煙囪的東邊，則量得的濃度可能爲零，Goldstein Bryan[2] 等人(1)藉各測站二氧化硫濃度的相關係數指出由一測站所測得的觀測值不一定可代表其周圍之污染情況，根據 Sasaki[4] 的研究，若要測知一地區的污染情況，每 0.65平方公里就需設一個測站，可是限於經濟與人力，實際作業下，測站的數目顯然無法滿足如此的要求，使得實際量測所繪出的濃度曲線無法眞實的反映出量測區域的污染狀況。因此各國各大都市與工業區都以第二種方法（數學模式）來作污染程度的評括，而第一種方法的結果僅用來作線性的統計校正（線性回歸）。但是由於污染源數目及其每一時刻的排放量都無法準確的知道，使得模式的計算不易精確，更由於氣象資料不齊、大氣紊流、城市地形與局部流動的複雜性、數值模式與數值方法的誤差等經常使計算結果與眞實情況出入頗大。換句話說，求取城市污染物濃度分佈曲線的兩種方法，雖然都能反映部分的眞實狀況，却也都包含相當程度的誤差，以致於簡單的線性回歸校正仍然無法使校正後的結果具有良好的代表性[3]，更精細的處理顯然是必要的。

其實，觀測資料與模式結果的代表性與一致性等問題並非空氣污染的評估，實

廣泛存在於各行各業中，而在氣象上更屬衆所週知的基本要題。一九五八年 Sasaki [4] 有見於此，首先以變微分法 (Calculus of Variation) 佳化氣象資料，以提高觀測資料的一致性，二十年來，由於氣象資料處理與天氣預報電腦化的需要日趨迫切，此法乃不斷的被深入的研究與廣泛的探討。近年來大氣污染程度的加重及人們對所處環境的關切，維護環境爲刻不容緩的要題， Heimbach 與 Sasaki[5] 遂將變微分法引用到空氣污染的評估上。然而 Heimbach 與 Sasaki 的方法僅限於測站數目多於污染源的數目，精確的說應爲測站數目多或等於污染源的數目減 1，但在實際情況下污染源必遠多於測站的數目，更有進者，將此法應用於實際資料時，所算出污染源的佳化排放值有許多負值出現，使得佳化濃度值亦爲負值。爲解決這些問題，作者之一[6]利用變微分法，重新發展適用於實際狀況的空氣污染佳化評估方法，此方法可適用於任何測站與污染源數目，並使污染源的佳化排放值爲正值，尤以測站稀少時（此爲一般實際情況）更具成效。

臺北地區位於臺灣本島西北端，包括臺北市及附近衛星城鎮。臺北市爲臺北地區的中心區域，爲我國自由地區第一大都市，人口近二百萬，工業發達，交通頻繁，住民的生活水準甚高，近年來由於人們對提高生活品質的要求日益强烈，此地區的工廠與車輛所產生的環境污染問題日漸被重視。臺北地區的工廠主要設於近郊與衛星城鎮，除幾個特殊區域（如松山地區）與特殊工廠（如鐵工廠）外，臺北市的主要污染來自一氧化碳，一氧化碳是含碳物質燃燒不完全的產物，臺北市空氣污染物百分之七十爲一氧化碳，而一氧化碳的污染百分之九十六來自車輛（參見表一），故研究臺北市空氣污染主要對象應爲機動車輛所產生的一氧化碳。研究機動車輛

表一、臺北市主要污染物與污染源之比較，最右一行為車輛在同類污染物中所佔的比率

空氣污染物 \ 數量	總量 (噸／年)	%	車輛 (噸／年)	%
粒狀物質	1513	1.84	460	30.4
硫氧化物	465	0.57	155	33.1
氮氧化物	4916	5.98	3073	61.3
碳氫化物	17616	21.44	16541	88.8
一氧化碳	57645	70.17	55109	95.6
合計	8.2×10^4	100	7.5×10^4	91.7

的污染，可視車道爲有限長度的線污染源，先做模式計算，再將計算結果與臺北市現有的污染測定站（五站）的測定值根據評估佳化理論作校正與組合以求得最能反映臺北市一氧化碳實際污染狀況的濃度分佈，作爲評估臺北市一氧化碳污染的依據。此外，本文並利用所得的結果，分多季與夏季分別討論一氧化碳測站的有效偵測範圍，建議設立最佳偵測網的位置與數目，以作爲臺北市將來增設測站的參考。

貳、佳化評估理論

本文採用(6)的佳化理論從事臺北市空氣污染實況的評估，有關佳化理論的詳細推導，已見於(6)中，本文僅簡述有關部份，然後將臺北市的實測資料代入模式中以求取臺北市的佳化濃度分佈。

假設有 n 個地面污染物濃度觀測值 $\{\tilde{C}_i\}$，$i=1,2,\cdots\cdots n$，並有 N 個排放源强度的觀測值爲 $\{\tilde{Q}_j\}$，$j=1,2,\cdots\cdots N$，另假設校正後的污染源佳化排放量爲 $\{Q_j\}$，$j=1,2,\cdots\cdots N$，由此佳化排放量代入模式算出之佳化濃度值爲 $\{C_i\}$，$i=1,2,\cdots\cdots n$；則濃度及排放源佳化前後的差異可以兩者差的平方和表示之：

$$E=\sum_{i=1}^{n}(C_i-\tilde{C}_i)^2+\sum_{j=1}^{N}(Q_j-\tilde{Q}_j)^2$$

爲了避免污染物濃度值的單位與排放源强度值單位的不同，將濃度值誤差項及排放源强度值誤差項予以尺度化（Scaling），且加入一誤差權重數（Error Weighting Factor），以 I 表示此誤差的平方和，則

$$I=\frac{\sum_{i=1}^{n}(C_i-\tilde{C}_i)^2}{\sum_{i=1}^{n}\tilde{C}_i^2\times n}+\beta^*\frac{\sum_{j=1}^{N}(Q_j-\tilde{Q}_j)^2}{\sum_{j=1}^{N}\tilde{Q}_j^2\times N}, \qquad 〔1〕$$

式中 $\overline{\sum_{i=1}^{n}\tilde{C}_i^2}$ 爲污染物地面濃度觀測值平方和的平均值，$\overline{\sum_{j=1}^{N}\tilde{Q}_j^2}$ 爲排放源强度值平方和的平均值。整理上式得

$$\overline{\sum_{i=1}^{n}\tilde{C}_i^2}\times n\times I=\sum_{i=1}^{n}(C_i-\tilde{C}_i)^2+\beta\sum_{j=1}^{N}(Q_j-\tilde{Q}_j)^2, \qquad 〔2〕$$

式中

$$\beta=\frac{\overline{\sum_{i=1}^{n}\tilde{C}_i^2}\times n}{\overline{\sum_{j=1}^{N}\tilde{Q}_j^2}\times N}\beta^*.$$

變微分法的原理乃是誤差的平方和要達到最小值，亦即

$$\delta I = 0 , \qquad 〔3〕$$

且 $\{C_i\}$ 與 $\{Q_j\}$ 滿足空氣污染的擴散模式

$$C_i = \sum_{j=1}^{N} F_{ij} Q_j . \qquad 〔4〕$$

本文取 F_{ij} 爲高斯分佈函數 (Gaussian Distribution Function，F_{ij} 爲距離的函數)。由〔2〕，〔3〕與〔4〕式可得

$$\sum_{i=1}^{n} F_{ji}^{T}(\sum_{k=1}^{N} F_{ik} Q_k) - \sum_{i=1}^{n} F_{ji}^{T} \tilde{C}_i + \beta(Q_j - \tilde{Q}_j) = 0.$$

令 $F = 〔F_{ij}〕$，$Q = 〔Q_j〕^T$，$\tilde{C} = 〔\tilde{C}_i〕^T$，$\tilde{Q} = 〔\tilde{Q}_j〕^T$，

則上式可化成下式之矩陣方程式

$$F^T F Q - F^T \tilde{C} + \beta (Q - \tilde{Q}) = 0 ,$$

或

$$Q = (F^T F + \beta J)^{-1} (\beta \tilde{Q} + F^T \tilde{C}) \qquad 〔5〕$$

式中 J 爲單位矩陣。〔6〕式所得之Q即爲利用觀測濃度校正後的佳化污染源强度值，而佳化濃度分佈可由〔5〕式之Q代入〔4〕式而得。

做佳化的目的是希望C與$\tilde{C}$完全相合，同時Q中的元素與$\tilde{Q}$中的元素相差愈小愈好。但從〔5〕式可看出，β 愈大，Q受$\tilde{Q}$的影響增大，β 愈小，Q受$\tilde{C}$的影響增大。即 β 愈大時，Q與$\tilde{Q}$的相差愈小，而 β 愈小，C與$\tilde{C}$愈接近。

如果强令C一定要完全等於$\tilde{C}$，而不管Q要做如何的變動，即令〔5〕式中的 β 等於0，將會造成測定站的 C_i 雖然與 $\tilde{C}_i$ 完全相同，但 Q中的元素不得不有些成爲負值，以符合 Q_j 對有影響的低濃度測站測定值，這樣在測站濃度誤差是很小了，却會出現不少的 Q_j 負值，負的 Q_j 在實際應用上並無意義，把這些 Q_j 代入高斯模式去求網格點的濃度分佈時，一定會有負的濃度值產生，不符合實際的狀況。β 值的加入可一方面佳化C一方面兼顧Q的變動，即恰使Q中的元素全爲正值的 β 值即爲本文所謂的最佳 β 值。此 β 值可以反覆法 (Iteration) 求得。

參、大氣擴散模式

一般常用的大氣擴散模式皆緣於 Pasquill[7]，此模式經過 Gifford[8]，Martin & Tikart[9] 等人的改良後，成爲 Air Quality Display Model (簡稱爲 AQDM 模

式)[10]，而廣泛應用於城市，工業區及工廠附近環境空氣品質的評估。

此模式主要係假定一個污染源，連續排放的污染物，在大氣中經紊流的擴散與稀釋作用，終將達到一個平衡狀態，此時污染物的濃度，在垂直於風向之截面上形成雙向高斯常態分布，由於紊流的擴散及稀釋作用與風速、風向及大氣熱力結構有關，而大氣熱力結構概要可爲溫度、穩定度及混合層高度所描述。因此爲確實模擬污染物在大氣中的擴散現象，模式中的係數及標準偏差應爲風速、風向、溫度、穩定度及混合層高度的函數。其中常態分布函數的標準偏差與穩定度與下風距離的關係採用 Parquill[11] 的關係曲線。

令一點污染源在 (0, 0, h) 處，並考慮地面反射，根據 ADQM 模式，在空間任何一點 (x, y, z) 處的污染濃度可以下式求得：

$$C=\frac{Q}{2\pi\sigma_y\sigma_z u}\exp\left[-\frac{1}{2}\frac{y^2}{\sigma_y^2}\right]\left\{\exp\left[-\frac{1}{2}\frac{(z-h)^2}{\sigma_z^2}\right]+\exp\left[-\frac{1}{2}\frac{(z+h)^2}{\sigma_z^2}\right]\right\}, \qquad [6]$$

式中 u 爲代表風速，Q爲點污染源强度（排放量），σ_y 與 σ_z 爲標準偏差，是 x 的函數因穩定度不同而異，可查圖而得[11]。當大氣有逆溫層 (Inversion Layer) 存在時，污染物在地面與此層間發生數次反射作用而逐漸趨於均勻分佈，此時地面濃度可由〔6〕式修改而得[12]：

$$C=\frac{Q\exp\left[-{}^1/_2(y^2/\sigma_y^2)\right]}{2\pi\sigma_y\sigma_z u}\cdot\sum_{j=1}^{5}\left[\exp\left(-\frac{1}{2}\frac{\lambda_1^2}{\sigma_z^2}\right)+\exp\left(-\frac{\lambda_2^2}{\sigma_z^2}\right)\right], \qquad [7]$$

式中 $\lambda_1=-H+2(j-3)H_m$，

$\lambda_2=H+2(j-3)H_m$，

H爲污染源高度，H_m 爲逆溫層高度（即混合層厚度）。

道路汽車排氣爲線污染源，視爲由許多點源所組成，令兩端點座標分別爲 (X_s, Y_s)，(X_e, Y_e)，其和X軸夾角爲 θ，路段平均强度爲Q，爲了避免混淆，以 Y 座標大者爲終點，當 $\theta=0$ 時以X座標大者爲終點，如圖一所示，而定長度線源對某一接收點 (receptor) 有影響之上、下限座標 (X_U, Y_U)，(X_L, Y_L) 可由線源落在對接收點有影響的扇形區域內的部份而求出，如圖二所示。則根據〔7〕式可導出線源的高斯分佈模式[13]：

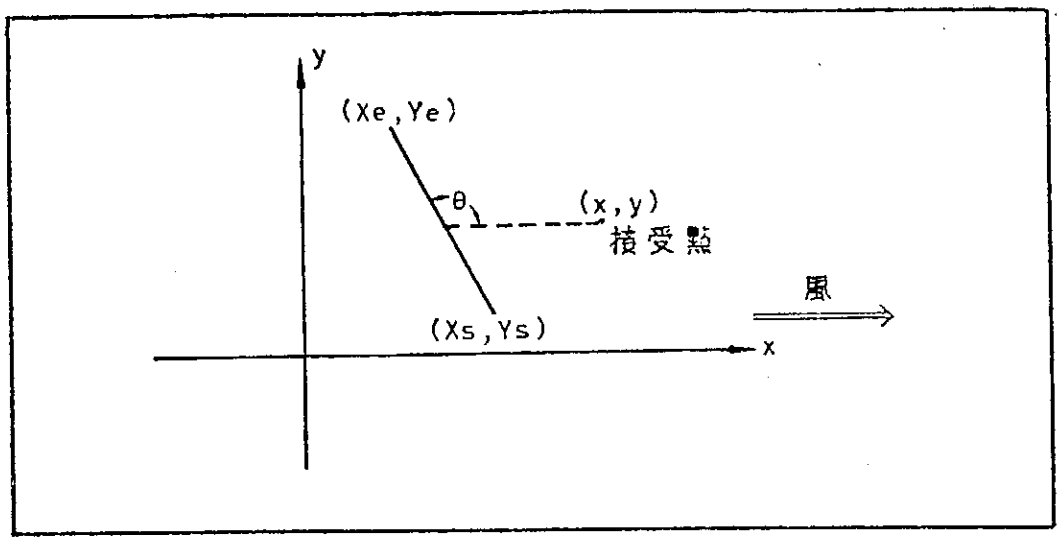

圖一、線源與接受點座標。X軸與風向同向，(X_s, Y_s) 爲線源起點，(X_e, Y_e) 爲線源終點。

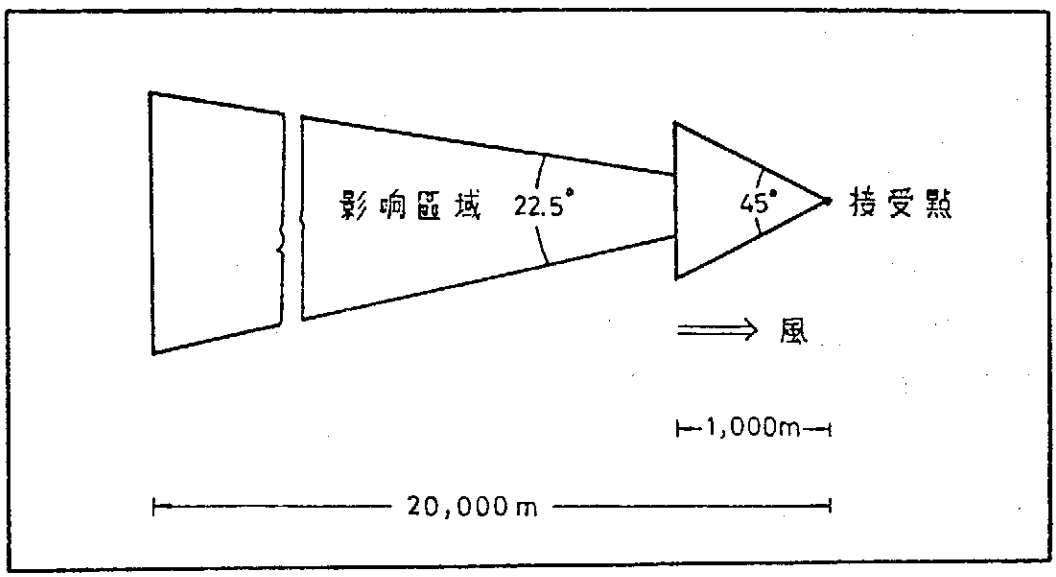

圖二、影響接受點的扇形區域。距接受點1,000公尺內取45度角，以外取22.5度角，最遠距離爲20公十。

當 $\theta \neq 90°$ 時

$$C(x, y, 0) = \int_{X_L}^{X_U} \frac{Q(1+\tan^2\theta)^{1/2}}{\pi\sigma_y\sigma_z u} \exp\left\{-\frac{1}{2}\frac{[(y-y_s)+(X_s-x_0)\tan\theta]^2}{\sigma_y^2}\right\} \cdot \cdot \sum_{j=1}^{5}\left\{\exp\left[-\frac{1}{2}\frac{\lambda_1^2}{\sigma_z^2}\right]+\exp\left[-\frac{1}{2}\frac{\lambda_2^2}{\sigma_z^2}\right]\right\} dx_0 , \quad [8]$$

當 $\theta=90°$ 時

$$C(x, y, 0)=\int_{UY}^{LY}\frac{Q}{\pi\sigma_y\sigma_z u}\times\exp\left[-\frac{1}{2}\frac{(y-y_0)^2}{\sigma_y^2}\right]\cdot$$

$$\cdot\sum_{J=1}^{5}\left\{\exp\left[-\frac{1}{2}\frac{\lambda_1^2}{\sigma_z^2}\right]+\exp\left[-\frac{1}{2}\frac{\lambda_2^2}{\sigma_z^2}\right]\right\}dy_0. \qquad [9]$$

實際積分時，將線源切成許多定長度的小段，而設每段中點爲强度集中的點源位置。

肆、結 果 與 討 論

一、資料來源與分析

本文爲了考慮交通流量調查、空氣污染測定站及氣象資料三者配合的完整性，特選取民國六十六年六月每日上午七時至八時之各項資料予以分析與計算。

1. 交通流量調查及線源強度估計

由新建工程處交通科提供的參考資料，分別有基準點調查19站、路段調查99站，交叉口調查 75 站等交通流量資料，除部份路段屬偏遠地區捨棄不用外，共選取 168 條主要線源爲臺北市街道代表。線源分段的原則主要視其方向或流量一致者爲一段，同一街道常因其各段流量不同或方向改變而分成數條線源。某些路段交通量無法直接知道需由前後、鄰近路段或交叉口資料加以推測、估計。

線源强度的估計，尙需由車輛類別（重型車、輕型車、機踏車）、使用燃料類別（柴油、汽油）、行馳速率與車輛維護狀況來估算一氧化碳的排放率，進而排算線源强度。一般對汽車污染物排放量的經驗計算是將每小時行經的重型車數（H）乘以1.6倍爲相當的輕型車數（L）。同理機踏車（B）乘以0.3換算成相當之輕型車數。假設每輛型車的污染物排放率（Emission Rate）E（單位爲：g/m/vehicle），其相當的總輕型車數爲每小時 $S=1.6H+L+0.3B$，則單位長度線源强度Q爲 $E\times S$（單位爲 g/m/hr），臺北市輕型車平均一氧化碳排放率依[13]的建議爲 0.0369g/m/vehicle，

即

$$Q=0.0369\ S, \qquad (g/m/hr),$$

$$=1.02\times10^{-5}\ S, \qquad (g/m/sec).$$

以此Q值代入模式中運算所得的 CO 濃度單位爲 g/m^3，20°C 時，CO 單位

換算爲每 1 g/m³ 爲 875 ppm，故

$$Q = 0.00869\ S, \qquad (\text{ppm. } m^3/m/sec). \qquad [10]$$

由S計算得Q，代入高斯模式中，所得濃度單位爲 ppm.，污染源高度即汽車排氣管高度設爲 1 公尺。

2.空氣污染偵測站及一氧化碳測定值

測站資料由臺北市環境清潔處提供。當時共有四個移動測站，以空氣污染測定車分別停靠在民權東路81號旁、敦化南路臺灣療養院旁、和平西路萬華戲院對面和中山南路市議會附近。二個固定測站，一在民權東路81號四樓，另一則在臺大土木系三樓，其各站觀測一氧化碳濃度值和測站座標如表二所示，除臺大土木系站在三樓，民權東路81號站（命名爲中山路）一樓與四樓都有測定站外，其餘各站皆在一樓，故臺大土木系三樓的測定值需轉換成爲一樓濃度，此值可由中山站的一樓與四樓的關係推算而得，亦即假設濃度值與高度的關係如下式：

表二、六十六年六月上午七時至八時臺北市一氧化碳測定站月平均濃度測定值與各測站的編號與位置，座標代表自原點向東與向北的位置

區（站號）	站名	實測濃度值 (ppm)	測站位置 (座標，米)
1	中山站	10.3	(3797, 6105)
2	八德路	5.0	(5911, 4492)
3	臺大	4.0	(5035, 1129)
4	萬華	6.1	(1103, 3000)
5	市議會	12.5	(3070, 4131)

$$\frac{C}{C_0} = \left(\frac{h}{h_0}\right)^b,$$

將中山站的濃度月平均值代入上式可得 b＝0.69，故臺大一樓月平均濃度值爲 4.0 ppm，各測站的位置如圖三所示。

3.氣 象 資 料

資料來自中央氣象局，採用時假設臺北市區的風速、風向、氣溫、相對濕度及穩定度都是均勻一致的。穩定度依當日上午 7 時 22.5分至 7 時 37.5分間風向的偏差來判斷，風向則以 7時至 8時的平均風向，混合層高可由氣溫和相對濕度來估計[14]。六月份的氣象狀況如（表三）所示。

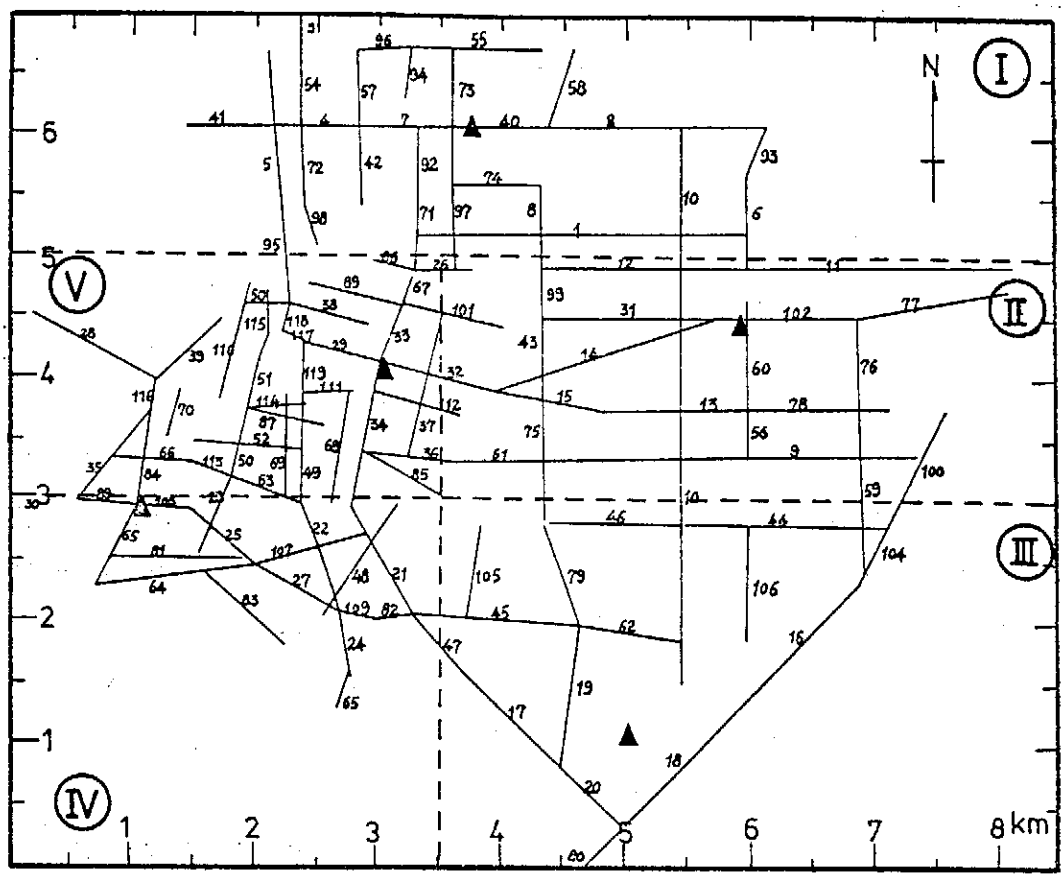

圖三、臺北市座標系統與百分之九十已知車道的分佈。虛線將臺北市分成五個分區。三角形代表污染測站位置。

表三、六十六年六月份上午七時至八時臺北市氣象狀況。風向，穩定度與風速皆以級數表示

風　向	穩定度	風　速	混合層高度(米)	發生頻率(天)
4	1	3	527	1
4	6	1	590	2
5	6	1	621	2
7	2	2	715	1
7	3	1	652	2
7	6	1	610	6
8	2	1	652	1
8	5	1	652	1
8	5	2	715	1
8	6	1	621	6
9	5	1	652	1
9	6	1	621	4
11	6	1	527	1
12	2	1	527	1

二、數 值 方 法

1.高 斯 模 式

求取長期累積平均濃度分佈時，需考慮風向、風速、溫度、穩定度、混合層高度對紊流擴散的影響，亦即在不同氣象狀況下污染物擴散分佈形態不同，今令：

$$C_i=\sum_{j=1}^{N}\sum_{ID=1}^{16}\sum_{IV=1}^{6}\sum_{IL=1}^{6}\text{Prob (ID, IL, IV) F(ID, IL, IV, XD) } Q_j$$

C_i ：接收點長期累積平均污染物濃度，

Q_j ：第 j 個染污源，其總數爲N，

ID ：風向，分十六向，

IV ：風速，分六級，

IL ：穩定度，分六級，

Prob (ID, IL, IV)：發生 ID 風向，IL 級穩定度，IV 級風速的概率，

X_D ：線源和接收點之距離，

F (ID, IL, IV, X_D)：在上述氣象條件下，距接收點 X_D 時的高斯分佈函數。

一般習慣將風劃分爲十六個方向（圖四），每一風向之範爲 22.5°，在此風向左

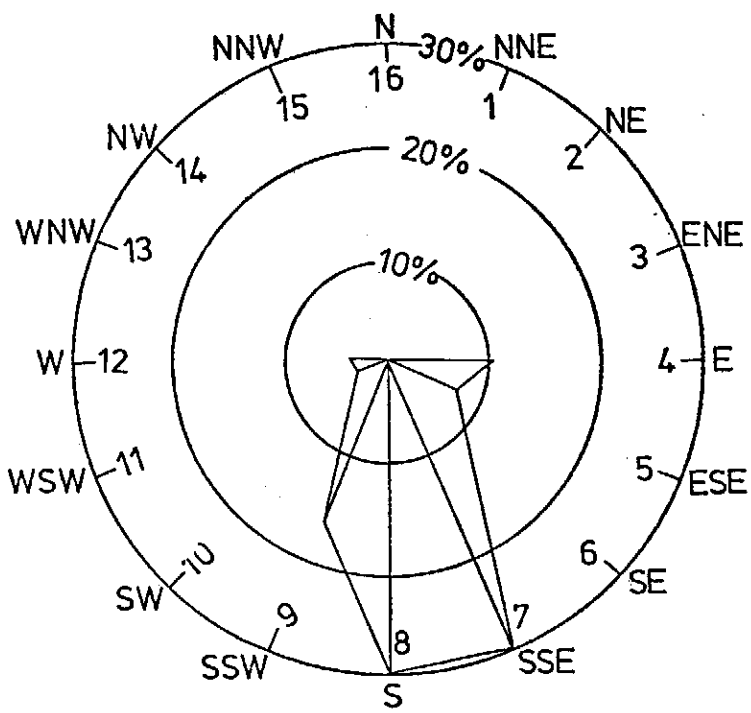

圖四、臺北市六月份早上七時至八時的風向玫瑰圖及風向分類標號。

右 11.25°範圍內卽以此風向爲代表，六月份風向玫瑰圖如圖四所示。爲了簡化計算，將風速分爲六級，其代表風速如表四所示。本文所用混合層高度爲同一氣象狀況下之平均混合層高度，卽在 ID, IV, IL 氣象條件下具相同之 H_m(ID, IL, IV) 以簡化計算。高斯模式計算所需 σ_y、σ_z 爲距離和穩定度的函數，本文取自 Turner[11] 文中 σ_y、σ_z 和水平距離與穩定度的關係曲線圖形。 此外由於日照與雲量的觀測資料不全，本文的穩定度改依 Stoner[15] 法， 由風向偏差求出， 而混合層厚度則依 Holzworth[16] 法利用東港探空資料，對露點差異作回歸分析獲得。

表四、風速等級分類及各級的代表風速值

級	風速範圍 (米/秒)	代表風速值 (米/秒)
1	0.0— 1.5	0.75
2	1.6— 3.3	2.45
3	3.4— 5.4	4.40
4	5.5— 7.9	6.70
5	8.0—10.7	9.35
6	10.7—	12.30

臺北市區座標系統如圖六所示，X 軸指向正東，Y 軸指向正北，並將選取之168個線源皆定起、訖點座標。網格點間距爲 500米，網格點共有 270點。爲配合計算需要，計算過程中座標軸需轉一個角度以使X軸與風向重合。積分上下限座標（X_U、Y_U）與（X_L、Y_L） 可由圖二求得，扇形以外地區，因其濃度甚低和扇形內相差甚大，故予忽略。線源積分運算用辛普森 (Simpson) 法則，積分分段區間爲20米，線源和接收點間用來決定 σ_y、σ_z 的距離 X_D，以每積分段中點和接收點X座標的差距代表。

2.佳化過程與佳化特性

依臺北市區所有的五個測站，將線源分爲五區，呈一「干」字形如圖六所示。線源的區屬以路段中點爲劃分的歸依，以便由各區選取一定百分比的染污源來運算時，能得到較均勻的分配。

爲改善各地區因污染源强度資料不全所引起的評估誤差，並瞭解模式評估的性能與簡單修正的可行性，我們求出測站的實測濃度值與模式在測站處的評估值的比值，分別爲 r_1，r_2，r_3，r_4 與 r_5 及平均值的比值，$\bar{r}$ ， 然後將污染源强度分別乘

以這些值，若乘 $\bar{r}$ 以則稱爲全區修正模式，若分區分別乘以對應的 r_1 至 r_5 則稱爲分區修正模式，以修正後的污染源排放量求得的評估值與其統計特性將於下文中詳細討論。

佳化的過程是將未修正或修正後的各污染源排放值與各測站的測定值代入〔5〕式中，以求得佳化排放量，有此佳化排放量便可借〔4〕式求得佳化濃度分佈。在此一系列的求解過程中，需先假定 β^* 值，換句話說，對應於每一個 β^* 值皆有一組佳化排放值，利用反覆法便可求得恰使佳化排放值皆爲正值的 β^* 值，此 β^* 值與其所對應的佳化放值便是所求之解。

由於臺北市車道分佈甚爲複雜，而臺北市興建工程處的車道與車輛流輛資料無法提供足够的資訊，許多車道的流量需以附近已知者參照估計而得，圖三是臺北市可知車道百分之九十的車道分佈圖，亦即每一區都是那一區可知車道的百分之九十，共計 119 條線源，附錄一是這些路段的編號與名稱。由圖三可知，即令是可知車道的百分之九十，與眞正的臺北市車道數目相較仍嫌不足，這些估計偏差可後下文的模式計算與測站測定值的差異看出，爲便於瞭解與查證各車道的污染實況，特將各車道（線源）强度的百分率以表五表示之。

圖五爲1977年 6 月份早上 7 至 8 時臺北市可知車道百分之九十（以下皆同）模

表五、臺北市已知線源百分之九十的線源強度百分率。第一行代表線源編號的十位數，第一列代表個位數

線源編號	1	2	3	4	5	6	7	8	9	10
0	2.34	1.93	1.66	0.98	0.95	0.76	0.76	0.72	2.84	2.65
1	1.93	1.44	1.40	1.06	1.06	1.13	1.13	1.06	0.95	0.91
2	1.06	0.64	0.60	0.57	0.57	0.42	0.42	1.66	1.17	0.91
3	0.91	0.91	0.83	0.79	0.64	0.57	0.49	0.45	0.45	0.72
4	0.64	0.64	0.98	0.91	0.83	0.76	0.42	0.34	0.45	0.45
5	0.45	0.42	0.42	0.53	0.49	0.45	0.45	0.45	0.76	0.76
6	0.72	0.64	0.34	0.34	0.30	0.42	0.42	0.42	0.38	0.30
7	0.45	0.45	0.42	0.38	0.72	0.64	0.57	0.53	0.60	0.57
8	0.26	0.26	0.26	0.30	0.26	0.26	0.26	0.26	0.23	0.23
9	0.23	0.38	0.34	0.34	0.30	0.26	0.26	0.26	0.53	0.53
10	0.45	0.42	0.34	0.49	0.49	0.42	0.26	0.26	0.23	0.23
11	0.19	0.19	0.49	0.19	0.19	0.19	0.19	0.19	0.19	

式計算的一氧化碳濃度分佈圖，圖中可看出三個主要污染區域分別爲新生南路與松江路交接處，臺視附近（即敦化北路、長安東路二段、八德路三段與南京東路三段交接處）及北門附近，而測站上的模式濃度計算值則如表六第五行所示。

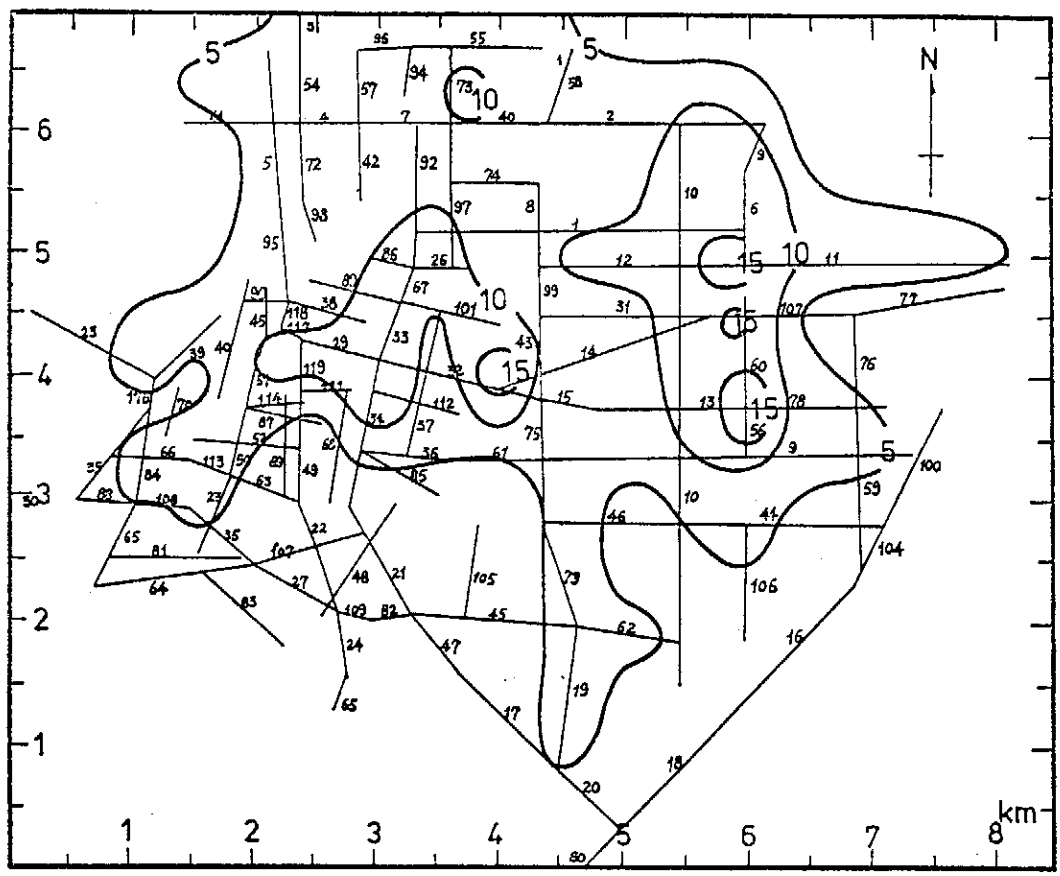

圖五、臺北市一氧化碳的模式（未修正未佳化）計算濃度分佈。圖中等濃度線上濃度值的單位爲 ppm。

爲瞭解模式的可靠性，本文分別以全變量 ET、污染源變量 EQ、濃度變量EC及污染源與濃度的平均誤差與標準偏差 $\overline{\Delta Q}$，$\overline{\Delta C}$，D(ΔQ)，D(ΔC) 來討論，各項定義如下：

$$ET = EC + \beta^{*2}\, EQ,$$

$$EQ = \sum_{n=1}^{N} (Q_n - \tilde{Q}_n)^2 \Big/ \sum_{n=1}^{N} \tilde{Q}_n^{\,2},$$

$$EC = \sum_{m=1}^{n} (C_m - \tilde{C}_m)^2 \Big/ \sum_{m=1}^{n} \tilde{C}_m^{\,2},$$

$$\overline{\Delta Q} = \sum_{n=1}^{N} \left(\frac{Q_n - \tilde{Q}_n}{Q_n} \right) / N,$$

$$\overline{\Delta C} = \sum_{m=1}^{n} \left(\frac{C_m - \tilde{C}_m}{\tilde{C}_m} \right) / n ,$$

$$D(\Delta Q) = \left[\sum_{n=1}^{N} \left(\frac{Q_n - \tilde{Q}_n}{\tilde{Q}_n} \right)^2 / N-1 \right]^{1/2} ,$$

$$D(\Delta C) = \left[\sum_{m=1}^{n} \left(\frac{C_m - \tilde{C}_m}{\tilde{C}_m} \right)^2 / n-1 \right]^{1/2} ,$$

而 β^* 則爲正常化 (Normalization) 後的 β 值，EC 與 EQ 兩項，分別以 $\sum_{n=1}^{N} \tilde{Q}_n$ 與 $\sum_{m=1}^{n} \tilde{C}_m$ 爲正常化尺度值。

未修正，全區修正與分區修正模式在測站上的一氧化碳濃度值及其統計特性分別列於表六與表七，由表七的第二行知模式值的平均誤差約爲 13.1%，濃度變量爲 12.4 %，可看出就全區而言模式的評估尚可接受，但若從濃度誤差的標準偏差的 38.3 %看來，模式並不穩定（就空間而言），也就是說整區的平均評估不錯，但詳細評估則差，這是一般模式評估最常見的情形。從表七的第三行可看出全區修正的濃度誤差就全區而言非常良好（ −2.0%），但其誤差的標準偏差則增大的 43.2%，故就各測站處而言，全區修正模式比原模式更不穩定。全區修正的污染源誤差值與變量分別爲12.8%與1.6%，由此可知原模式的污染源强度值與實際污染源强度值僅差 12.8，故就全區而言，原模式的污染源强度估計值（原估計爲可知的百分之九十）似甚正確。分區修正模式的全區平均誤差爲10.6%但變量與標準偏差則降爲2.3%與 15.1%，可見得分區修正除能有效的改進全區的平均濃度值外，對各測站處的濃度值也能有良好的評估，故分區修正顯然大大改進了模式的穩定性。

表六、臺北市各測站一氧化碳濃度觀測值與模式計算值的比較

(單位：ppm))

測站			觀測值	未修正模式值	全區修正模式值	分區修正模式值	佳化模式值
站號	名稱	座標					
1	中山	(3.8, 6.1)	10.3	13.5	15.2	12.6	10.3
2	八德路	(5.9, 4.5)	5.0	6.26	7.06	6.56	5.0
3	臺大	(5.0, 1.1)	4.0	1.93	2.18	4.0	4.0
4	萬華	(1.1, 3.0)	6.1	4.15	4.68	6.18	6.1
5	市議會	(3.1, 4.1)	12.5	7.77	8.76	12.3	12.5

表七、不修正、全區修正與分區修正模式的特性

(除最後一列外，皆以%為單位)

項目 \ 模式	不修正模式值	全區修正模式值	分區修正模式值
$\overline{\Delta Q}$	0	12.8	34.3
$\overline{\Delta C}$	13.1	− 2.0	10.6
D(ΔQ)	0	12.8	56.0
D(ΔC)	38.3	43.2	15.1
EQ	0	1.6	35.0
EC	12.4	14.0	2.3
Log (EC)	− 0.91	− 0.85	1.70

由分區修正模式對原模式在穩定性與平均濃度的改進可看出模式的修正需對各污染源分別給於修正，由於污染分佈的尺度 (Scale) 甚小，各處所需的修正差異頗大，任何籠統含混的修正方式並不能有效的改進評估的效果，比如，全區修正其結果甚不理想便是一例，而分區修正則需給與適當的選擇，此與測站地點、污染源分佈及氣象狀況有密切的關係，分區修正的極致便是對每一個污染源分別給與修正，佳化理論便是這種概念下所發展出來的。

不修正佳化、全區修正佳化、分區修正佳化的佳化值，其各變量 ET、EQ 與 EC 與 β^* 的變化分別如圖六、七、八所示，由於 β^* 愈小C與$\tilde{C}$愈相近，故 EC 與 ET 皆隨 β^* 的減小而減小，亦即 EC 與 ET 爲 β^* 的單向漸增函數，反觀 EQ，因Q與$\tilde{Q}$因 β^* 之增大而相近，故 EQ 隨 β^* 的增大而減小，亦即 EQ 爲 β^* 的單向漸減函數，從以上三圖可看出當 β^* 小至 10^{-13} 時，由於〔2〕式的污染源强度誤差項甚小至可忽略，亦即方程式系統漸轉變成不足擬定系統[6]，此時矩陣方程式〔5〕之係數矩陣 $F^TF+\beta J$ 的行列式值趨近於零，故圖六、七與八在 β^* 小於 10^{-13} 的區域不爲式〔5〕之解，僅由其大幅度之變化可印證當 β^* 趨近於零時佳化系統轉變爲不足擬定系統。

當 β^* 甚大時（比如大於100) EQ 趨近於零而 ET 與 EC 皆趨近於一定值，此定值即以不佳化之 Q 代入模式中算得之濃度值與觀測濃度值之變量值，分別爲 0.124，0.14與0.023 (取對數後爲−0.91，−0.85與−1.70)，如圖六、七、八與表七第7、8列所示。當 β^* 小於 10^{-3} 以後，EQ 幾乎保持定值，而 EC 與 ET 已甚小

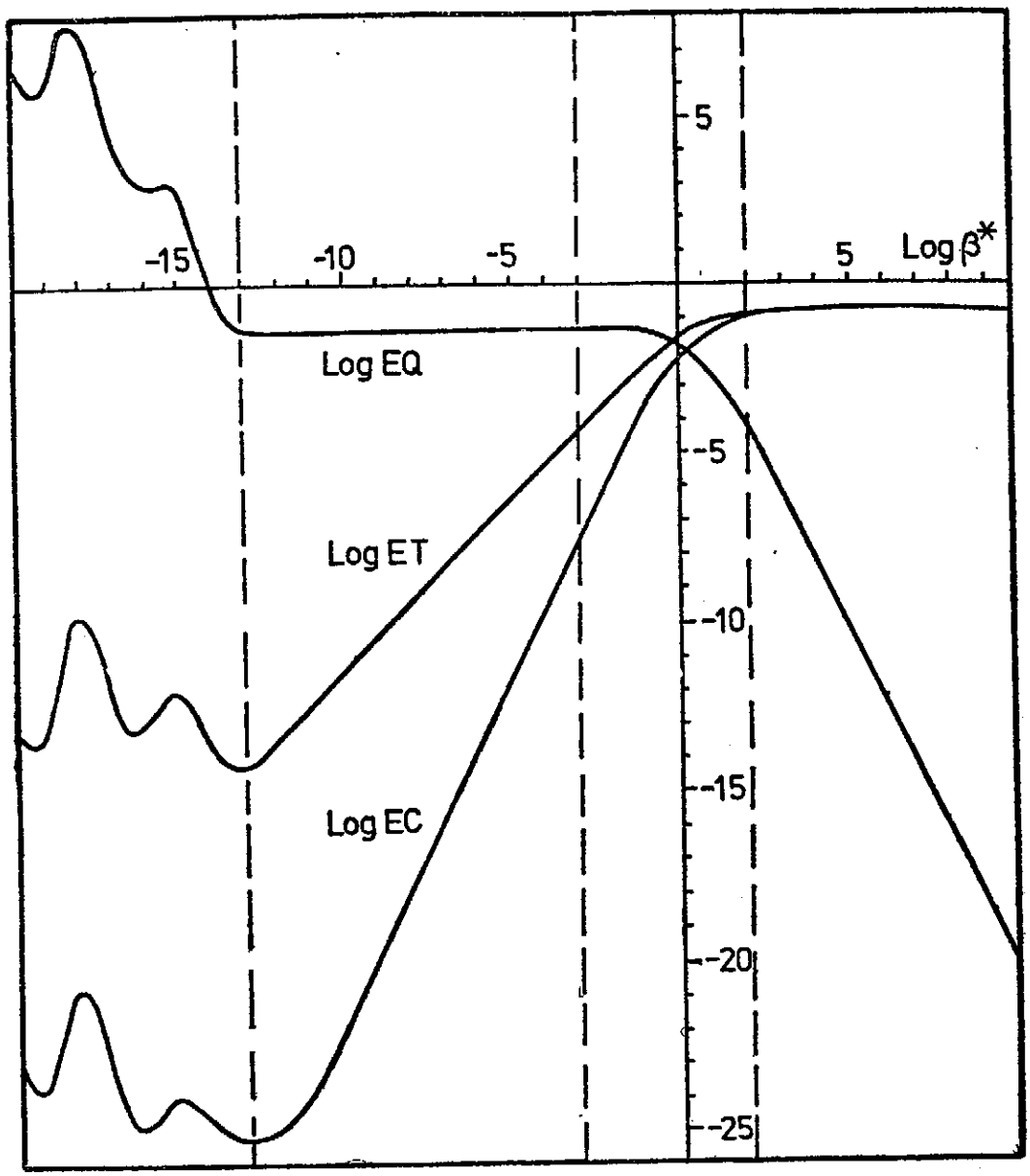

圖六、未修正的佳化過程。EQ 與 EC 分別表示污染源强度與濃度誤差變量，ET 則爲兩者的權商和。

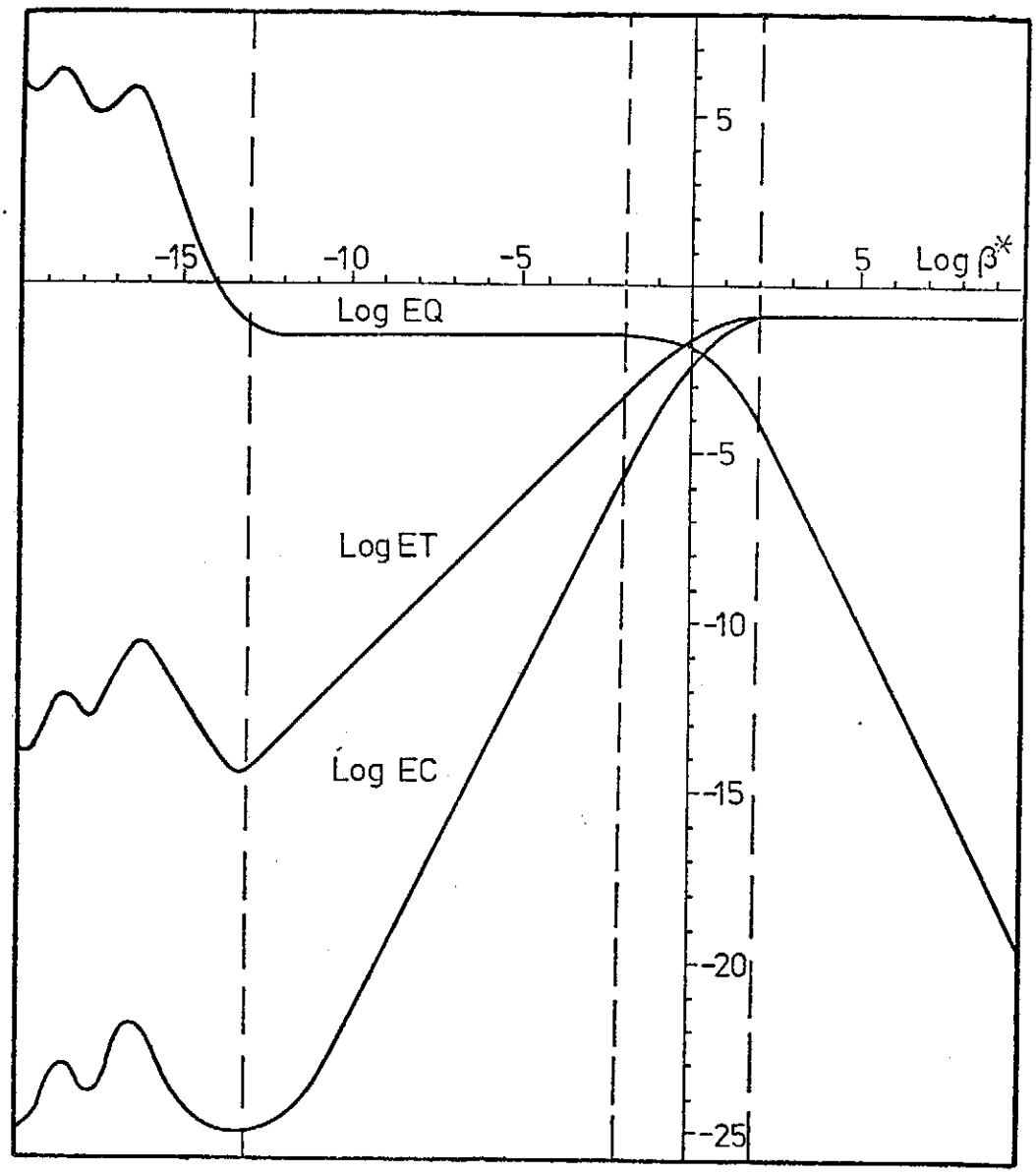

圖七、同圖六，唯係全區修正的佳化過程。

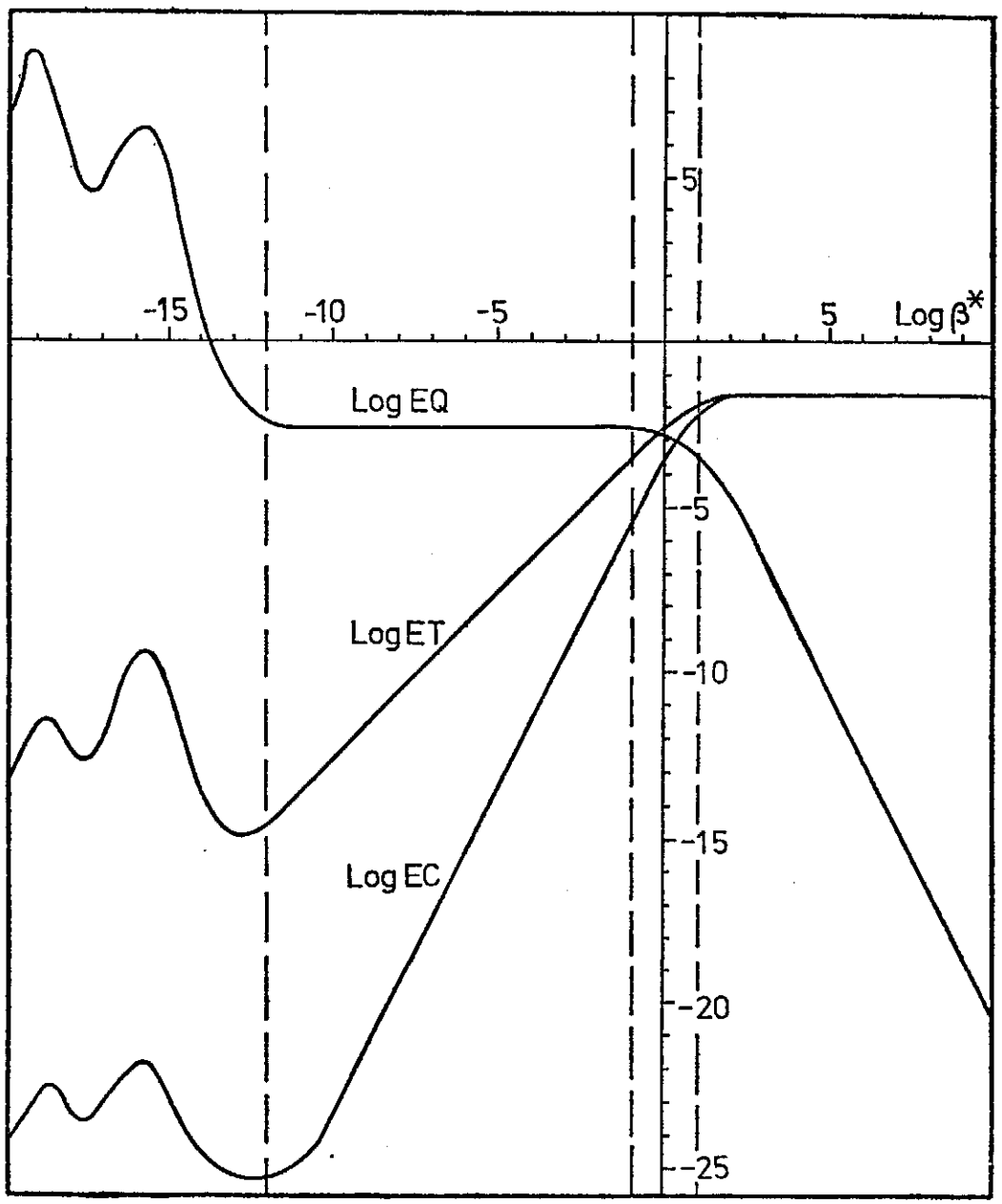

圖八、同圖六，唯係分區修正的佳化過程。

（就實際意義而言，可視爲零），故最佳 β^* 值實際上可取 β^* 爲 10^{-3} 至 10^{-12} 中之任何一值，此區間之寬廣表現出佳化法的穩定性，亦即 β^* 值與佳化值皆極易求得。

圖九顯示佳化過程中負污染源强度的變化與消失實況，由圖可知當 β^* 由甚小而趨近 10^{-13} 時，負污染源强度即漸消失，故 10^{-13} 理應爲最佳 β^* 值，但因此時 β^*太小，故式〔5〕之係數行列式值過小，致使所求得之解有相當程度之電腦計算誤差，此種誤差當 β^* 大於 10^{-12} 後便幾近消失，故最佳的 β^* 值乃以 10^{-12} 至 10^{-1} 區間任一值爲宜。

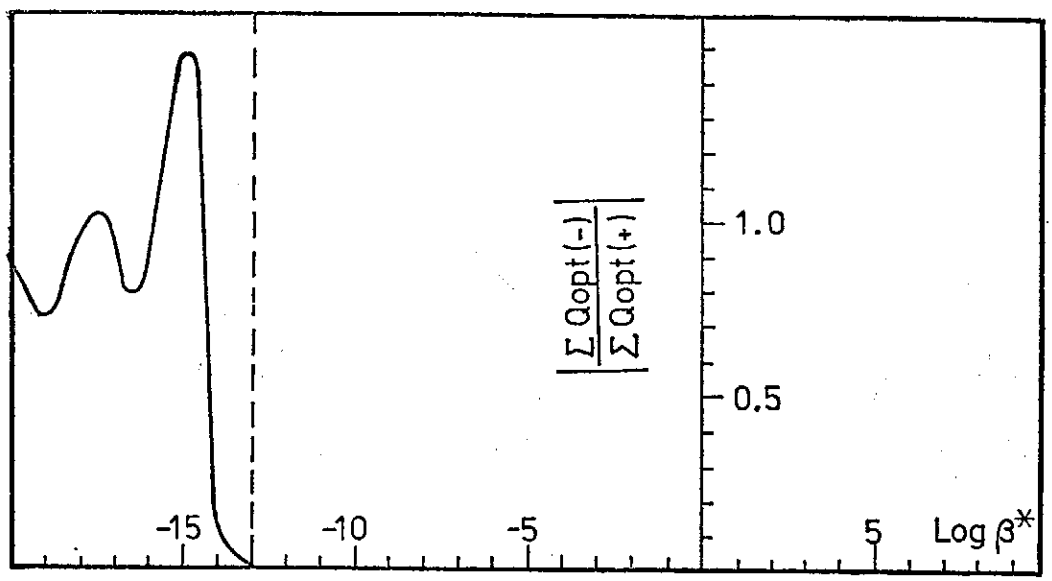

圖九、佳化過程中正與負污染源總强度比值對 β^2 值的變化。

圖十是全區修正後再從事佳化所得的佳化濃度分佈圖，在測站處模式值與測定值完全相同（稱爲完全佳化），從圖中可看出佳化濃度分佈除具有原模式的三個主要污染區外，又分別多出萬華地區、市議會地區、和平東路與新生南路交會區與辛亥路、基隆路交接處附近等四個主要污染區，很明顯的這些新污染區的出現與臺大、萬華、及市議會三個測站的量測值有良好的相關。由表可看出原模式或全區修正模式在此三測站的評估都有較大的誤差率，而佳化的效果既在對於這些偏差給予校正，則新主要污染區的出現與此三測站的相關性實爲顯而易見的結果。

3.污染與偵測網的佳化評估

六月份風向以南向來風爲主，其中南風佔9/30，南南東風佔9/30，南南西風佔

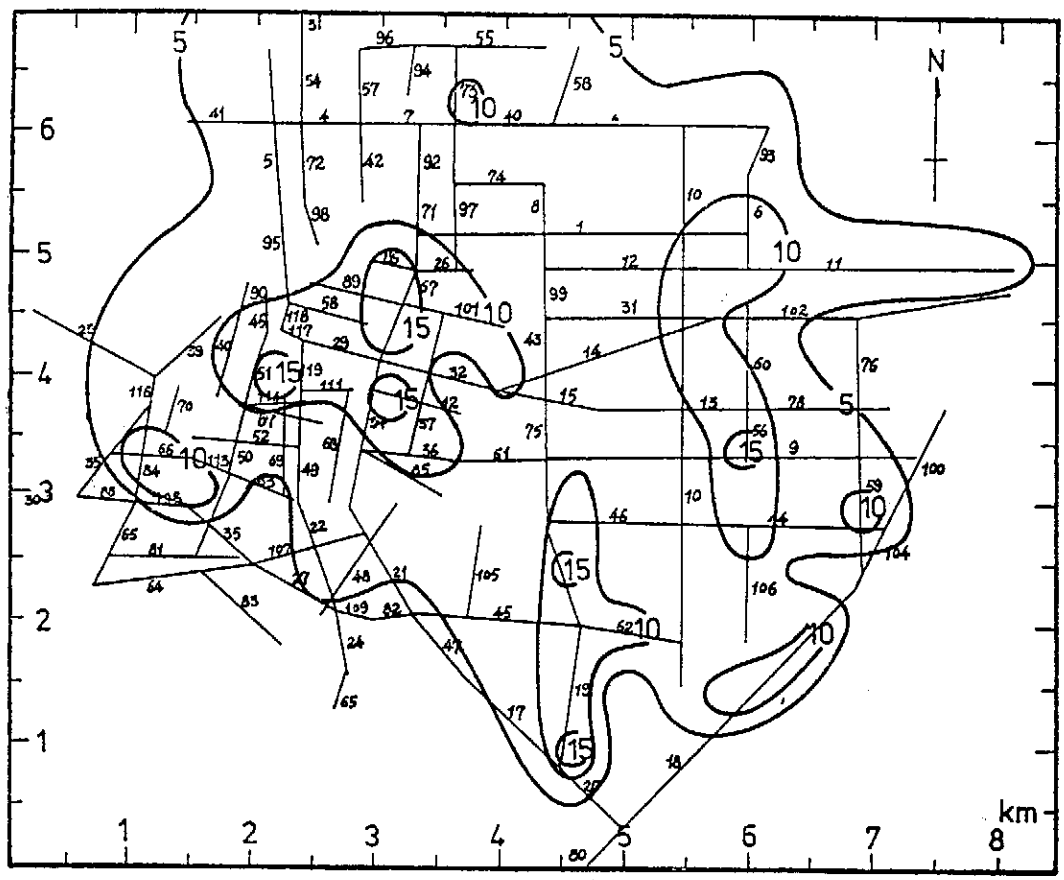

圖十、同圖五，唯係分區修正佳化的濃度分佈。

5/30，此 67.5°角內的來風合計約80%，由於風向集中，雖有 20 %的東、西南風，線源影響範圍仍然有限，部份地區濃度分佈圖形頗爲陡峻。

各分區線源佔全區總線源强度的百分率，及平均線源强度密度，如表八所示，密度是由該區總線源百分率除以網格點計算範圍內該區所佔之面積，單位爲 %/km²，密度大小依次爲四區、五區、二區、三區及一區。再由90%線源不做修正佳化前

表八、各分區線源佔全區總線源強度的百分率及
各分區的線源強度密度

項目 \ 分區編號	1	2	3	4	5
分區線源强度 (%)	20.3%	23.4%	17.7%	18.9%	19.7%
分區線源强度密度 (%/km²)	2.03	2.53	2.28	4.50	3.94

測站模式值(表六)得知各測站的 r_i 值分別爲 1.30，1.30，0.48，0.68，0.62，此第四、第五區模式值偏低的原因，顯然是排放率估計過低的緣故，蓋該兩區線源密度大，相對交通擁擠、行車緩慢，排放率應較其他三區爲高[13]，建議的臺北市汽車排放率 0.0369 g/vehicle-m，參考[15]資料中洛杉磯汽車行駛速率和一氧化碳排放率的關係，相當車速爲 54.7 km/hr，以此車速於上午七時八時在臺北市區行駛，尤其第四、五區是不太可能的。若設第四、五兩區的交通流量（Q）統計正確，則依其排放率應分別爲 0.0595 g/vehicle-m，0.0543 g/veqicle-m，相當車速各爲 28.3 km/hr，31.2 km/hr，於尖峯流量時間，此速應較合理。至於第三區模式值偏低，應該是羅斯福路四段和福和橋以南的線源捨棄的關係。

爲了探討臺北市氣空污染測站對線源污染影響掌握的實況，需先計畫出測站偵測的有效區域（稱爲有效偵測圖）。由六月份氣象狀況看來，平均穩定度屬第五級（E級），以最大濃度十分之一處與污染源的距離爲污染源影響距離，亦卽以測站爲中心，污染源影響距離爲半徑所劃之圓卽爲有效偵測圈，查[11]的圖可知有效偵測圈半徑爲 600 米，由於夏天與冬天風向相反，故有效偵測圈應爲半圓形（參見圖四），夏天爲北半圓，冬天爲南半圓。就夏天而言，由圖十一可看出已有測站的涵蓋地區以外，尙有許多重要污染源不在其影響範圍內。如要對這些污染源附近的污染狀況有所瞭解，勢必增加測站。由涵蓋區域的線源强度百分率的累積，知現有測站僅掌握90%線源分佈圖上，29.72%之線源强度，卽相當於全部線源强度的 18.71%。由於此保守估計的影響圈很少，若要對臺北市有通盤的瞭解，則需測站數目甚多，本文僅建議要掌握70%以上線源的資訊，應在那些重要污染源附近設測站。

由於夏季多吹南風，故測站位置選定主要在十字交叉口的北方。欲掌握70%以上線源的資訊，需多設的七個測站如下（圖十一）中以虛線半圓表示：

測站A：八德路一段和松江路交口北方，約在渭水街附近。

測站B：介於敦化北路和復興北路間的長春路北面路旁。

測站C：重慶南路一段和愛國西路交口，自由之家對西路旁。

測站D：仁愛路四段，延吉街口附近。

測站E：和平東路一段和新生南路二段交口處。

測站F：中華路一段和衡陽街交口，新聲戲院前。

測站G：重慶北路三段和民權西路交口北方。

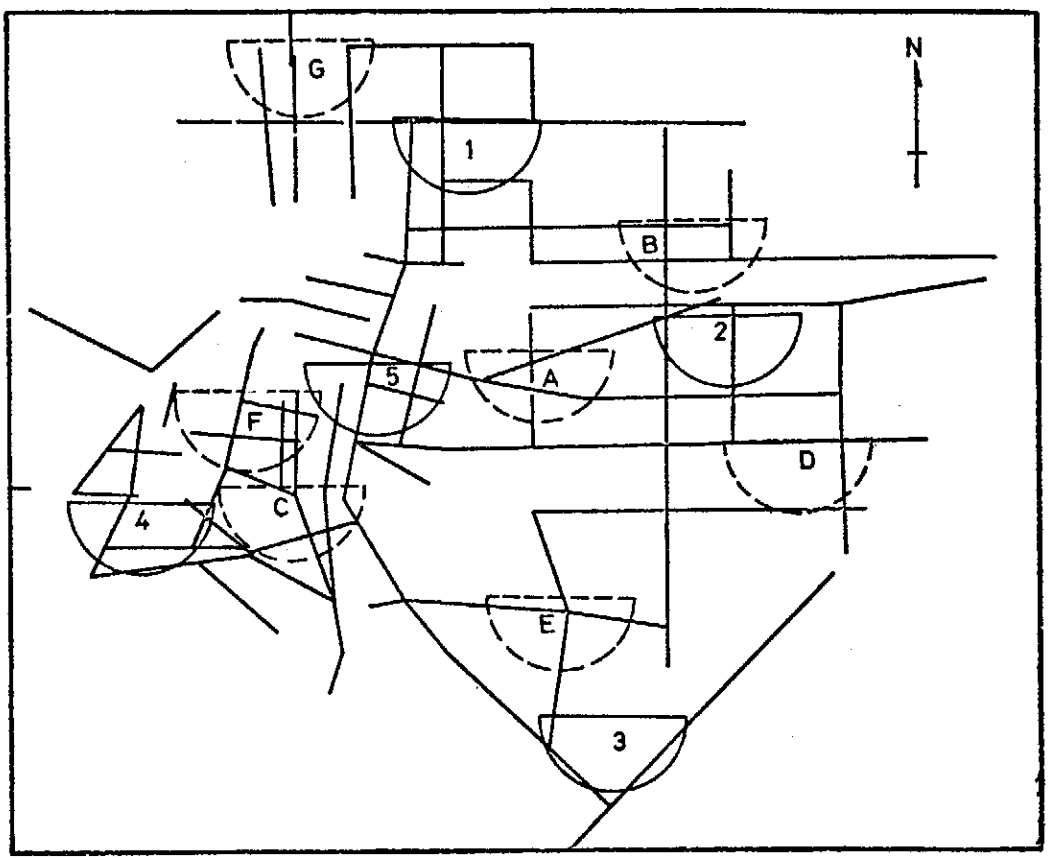

圖十一、夏季已有測站與建議增設測站的有效偵測圈及其有關的重要線源。實線半圓分別爲已有測站與建議增設測站的有效偵測圈。

各測站涵蓋下的線源强度的百分比及其總和如表九所示，所能掌握的線源總和提高至70.91%。

臺灣多季主要吹北或東北風，故有效偵測圈應爲 600 公尺半徑的南半圓，由圖十二可看出，多季時現有測站有效偵測圈涵蓋線源較多，五站所影響的線源强度總和提高至 36.77%，與夏季相較增加 7.05 %，測站A、E位置與夏季時相同，其他各增設站建議如下：

測站B：復興北路與民生東路交口南方。

測站C：移至自由之家前。

測站D：光復南路和仁愛路四段交叉口南方。

測站E：亦可移到原測站對面，和平東路旁。

測站F：復興南路和信義路三段交叉口南方。

總涵蓋污染源强度達73.93%，較夏季高出3.02%（表十）。此係因臺北市區街

表九、夏季已有各測站與建議增設測站有效偵測圈內的線源線編號（全區修正）強度，第三行為各測站有效偵測圈內的總線源強度

測站＼項目	線源編號與強度（括弧內爲強度值，%）	總企度（%）
1	7(0.99), 40(0.27), 73(0.83), 74(0.58), 92(0.99), 97(0.88).	4.54
2	10(0.60), 14(0.89), 31(0.96), 60(0.54), 102(1.0),	3.99
3	18(2.4), 19(0.98), 20(1.1).	4.48
4	23(1.1), 25(0.94), 64(1.1), 65(1.2), 81(2.0), 108(1.4).	7.74
5	32(1.2), 34(2.0), 37(2.0), 68(0.60), 111(0.97), 112(2.2).	8.97
A	13(0.96), 14(0.89), 15(0.96), 43(0.94), 75(0.95).	4.70
B	1(1.0), 6(0.99), 10(0.60), 12(1.0).	3.59
C	21(0.90), 22(0.85), 23(1.1), 34(2.0), 49(1.0), 53(1.0), 68(0.60), 69(0.99).	8.44
D	9(0.85), 44(0.69, 56(0.99, 59(1.0).	3.53
E	19(0.98), 45(0.89), 62(0.97, 79(1.0),	3.84
F	49(1.0), 50(0.98), 51(1.0), 52(0.96), 53(1.0), 69(0.99), 70(1.0), 87(1.1), 110(1.0,) 111(0.97, 113(0.99), 114(1.1).	12.09
G	3(1.0), 4(1.0), 5(1.0), 54(1.0), 57(1.0).	5.00

表十、同表九，唯係冬季的狀況

測站＼項目	線源編號與強度（括弧內爲強度值，%）	總強度（%）
1	40(0.27), 55(1.0), 58(1.0), 73(0.83).	3.10
2	6(0.99), 10(0.60), 11(1.0), 12(1.0), 14(0.89), 31(0.96), 60(0.54), 102(1.0).	6.98
3	10(0.60), 18(2.4), 19(0.98).	3.98
4	23(1.1), 25(0.94), 35(1.0), 66(1.0), 70(1.0), 81(2.0), 84(0.99), 108(1.4), 113(0.99).	10.42
5	29(1.0), 32(1.2), 33(0.99), 34(2.0), 38(1.0), 39(1.0), 67(0.99), 89(0.98), 101(0.93), 112(2.2).	12.29
A	13(0.96), 14(0.89, 15(0.96), 31(0.96), 43(0.94), 99(0.95), 101(0.93).	6.59
B	1(1.0), 2(1.0), 6(0.99), 10(0.60), 91(1.0).	4.59
C	21(0.90), 22(0.85), 34(2.0), 49(1.0), 50(0.98), 52(0.96), 53(1.0), 68(0.60), 69(0.99).	9.28
D	9(0.85), 59(1.0), 76(0.99), 78(0.94), 100(0.98).	4.76
E	19(0.98), 45(0.89), 62(0.97), 79(1.0).	3.88
F	9(0.85), 10(0.60), 44(0.69), 46(0.92).	3.06
G	3(1.0), 4(1.0), 5(1.0), 54(1.0), 57(1.0).	5.00

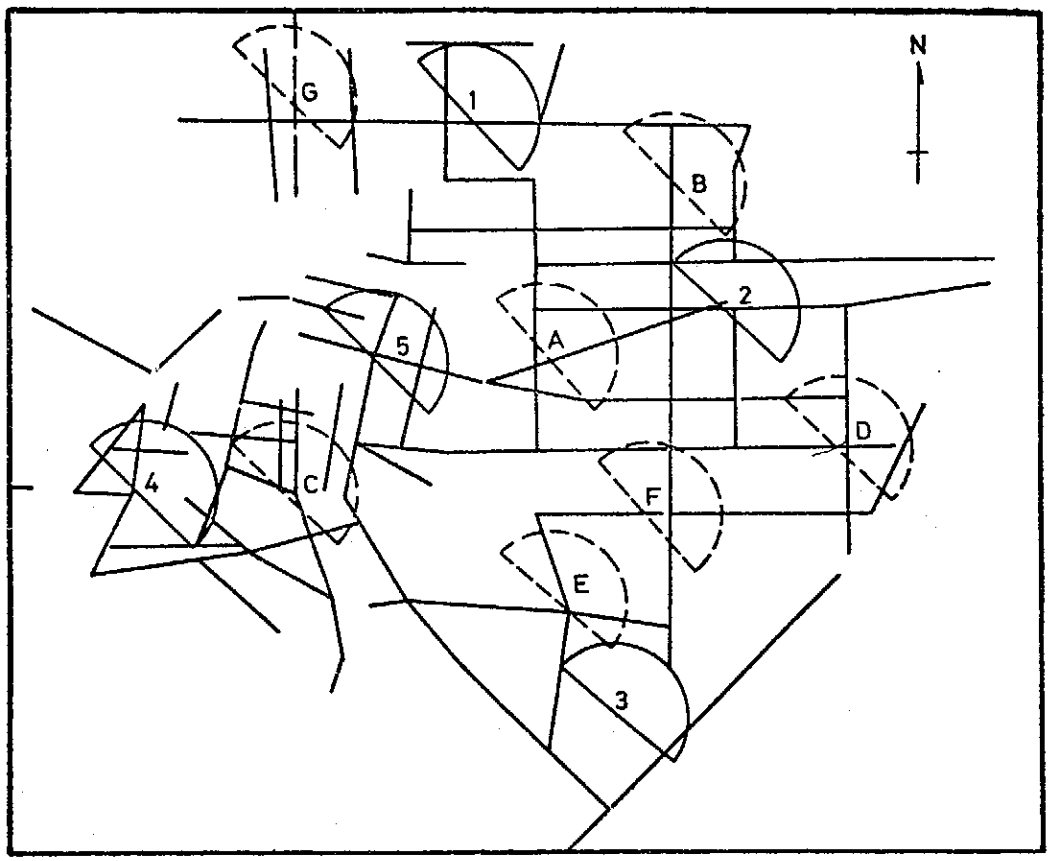

圖十二、同圖十一，唯係冬季的測站與有效偵測圈。

道多爲南北或東西向。尤其中山區和大安區多區間 (block) 呈東西向長，北南向短，對夏季測站的安排略有不利。

由以上討論可知，由於風向的差異，夏天與冬天需有不同的偵測網，爲達到最佳的經濟與人力的使用，可考慮多設移動性測站，作定期性的移動，補以適當的統計與模式的處理可使測站發揮最大的效力。

從修正佳化的結果看來，主要的一氧碳污染地區有七處，分別爲新生南路與松江路交口處。臺視附近、北門附近、萬華地區、市議會地區、和平東路與新生南路交口處、及辛亥路與基隆路交口處。這些主要污染區的一小時（早上七時至八時）月平均濃度都在 10 至 20ppm 間，根據中華民國環境空氣品質標準，就一氧化碳的規定如下（本標準不適用於慢車道、快車道，以及專供車輛停駐的場所）：

1.一小時的連續八小時平均值在 20ppm 以下。

2.一小時的全日平均值在 10ppm 以下。

3.在任何時間、地點，一小時值在 40ppm 以下。

由六十六年六月份的氣象資料可知，最大濃度值應爲月平均濃度值的二至三倍[11]，故早上七時至八時的一氧化碳濃度值在上述七個主要污染區應爲 30至 60ppm，亦即許多地區已超過我個設定的空氣品質標準，而今日國人購買力日益增强，新車供不應求，車輛數目的激增自可預期，故臺北市車輛排氣所造成的一氧化碳污染，實有待管制與改善，以維護居民的健康。

伍、結　　論

空氣污染問題的解決牽涉甚廣，但解決的過程不外乎觀察（或觀測）分析、評估、預測與控制，污染控制固爲污染問題解決的植本，但從觀察到預報這些過程却是污染控制的基礎，基礎不穩則控制的效果必然不彰，甚且事倍而功半，從國內公害防治的現況便可明白這個道理。

評估爲污染控制的先決條件，但作好評估並非易事，在實際作業時，由於經費、人力、時間與知識都極有限，而良好的評估却需建立在這些脆弱的條件上，則如何竭力發揮所有可能得到的資訊極爲重要。Heimbach 與 Sasabi[4] 利用測站上的實濃度以校正模式評估值，但其方法僅適用於測站數目多於污染源的數目加一，且其佳化後的污染源强度值常有負值出現，因此無法應用於實際狀況。本文利用(6)的佳化理論，使污染源强度值與污染濃度分佈值皆能爲正，且能適用於任何測站數目與污染源數目，從臺北市一氧化碳污染的評估可以看出 Heimbach 與 Sasaki 的方法顯然無法使用，本文使用佳化理論的佳化結果顯示佳化法確能有效的發揮觀測資料的資訊與我們對擴散現象的知識，而得到一個更具代表性的評估結果，對於未設測站的地方可以經由電腦程式利用佳化模式計算出濃度數值，這種效果絕非一般實測圖的線性內插所可比擬。

本文利用測站有效偵測圈對現有測站的偵測效果進行評估。因夏季與冬季風向不同，故分別建議增設站的數目與較佳位置，並估計出增設後的偵測效果，以作爲來日臺北市測站增設的參考。

總之，本文在經由佳化濃度分佈曲線與偵測站有效偵測圈的討論，希望能提供建立臺北市空氣污染評估系統的參考，並使對臺北市污染最嚴重的一氧化碳的影響實況有一個清晰的瞭解，對今後臺北地區執行空氣污染管制及保障住民健康盼望有實質上的益處。

附錄 1：臺北市路段編號查對表（90%）

編號	路段名稱	編號	路段名稱
1.	長春路	35.	環河南路（2北）
2.	民權東路（東）	36.	仁愛路（1）
3.	重慶北路（3北）	37.	林森南路（北）
4.	民權西路（西）	38.	鄭州路（東）
5.	延平北路（3，2北）	39.	環河南路（1北）
6.	敦化北路（南）	40.	民權東路（中）
7.	民權東路（東），民權西路（東）	41.	臺北大橋
8.	松江路（北）	42.	承德路（中）
9.	仁愛路（4，3）	43.	新生南路（1北），松江路（南）
10.	復興北路，復興南路（北）	44.	信義路（4）
11.	南京東路（5，4）	45.	和平東路（1）
12.	南京東路（3，2東）	46.	信義路（3）
13.	忠孝東路（4西，3東）	47.	羅斯福路（2南）
14.	八山路（2，1）	48.	林森南路（南）
15.	忠孝東路（3西，2）	49.	重慶南路（1南）
16.	基隆路（2南）	50.	中華路（1南）
17.	羅斯福路（3）	51.	中華路（1中）
18.	基隆路（3）	52.	貴陽街
19.	新生南路（3）	53.	愛國西路
20.	羅斯福路（4）	54.	重慶南路（3南）
21.	羅斯福路（1，2北）	55.	民族東路
22.	重慶南路（2南，3北）	56.	敦化南路（中）
23.	中華路（1南，2北）	57.	承德路（北）
24.	重慶南路（3南）	58.	松江路（北）
25.	和平西路（2西，3東）	59.	復興南路（南）
26.	南京東路（1，2西）	60.	敦化南路（北）
27.	和平西路（2東）	61.	仁愛路（2）
28.	中興大橋	62.	信義路（3）
29.	忠孝西路（1東）	63.	中正橋
30.	華江大橋	64.	西藏路
31.	長安東路（2）	65.	西園路（南）
32.	忠孝東路（1）	66.	桂林路（西）
33.	中山北路（1）	67.	中山北路（2南）
34.	中山南路	68.	公園路

附錄 1：臺北市路段編號查對表（90%）（續）

編號	路段名稱	編號	路段名稱
69.	博愛路	95.	延平北路（2南，1北）
70.	康定路（中）	96.	民族東路（西）
71.	中山北路（2南）	97.	林森北路（中）
72.	重慶北路（2北）	98.	重慶北路（2南）
73.	林森北路（北）	99.	松江路（中）
74.	民生東路（西）	100.	基隆路（1）
75.	新生南路（1中）	101.	長安東路（1）
76.	光復南路（北）	102.	八德路（3）
77.	八德路（4）	103.	新生南路（1南）
78.	忠孝東路（4東）	104.	基隆路（2北）
79.	新生南路（2）	105.	金山街
80.	福和大橋	106.	敦化南路（南）
81.	莒光路	107.	南海路
82.	和平西路（1東）	108.	和平西路（3中）
83.	中華路（2南）	109.	和平西路（1西）
84.	西園路（北）	110.	西寧北路（南），西寧南路（北）
85.	信義路（1）	111.	襄陽路
86.	南京西路（東）	112.	濟南（1，2）
87.	寶慶路	113.	桂林路（東）
88.	和平西路（3西）	114.	衡陽路
89.	長安西路	115.	塔城街
90.	鄭州路（西）	116.	環河南路（1南）
91.	中華路（1北）	117.	忠孝西路（1西）
92.	中山北路（2北）	118.	延平北路（1南）
93.	敦化北路（北）	119.	重慶南路（1北）
94.	中山北路（3）		

參 考 文 獻

1. Goldstein, I. F., and L. Landoritz, "Analysis of air Pollution Patterns in New York City. I. Can one station represent the large metropolitan area? II. Can one aerometric station represent the area surrounding it?", Atmos. Envir., Vol. 11, pp. 47-57, (1977).
2. Stern, A. C., Air Pollution, Academic Press, New York, pp. 425-436, (1968).
3. Gustafson S. A., K. O. Kortanek, and J.R. Sweigart, "Numerical Optimization Techniques in Air Quality Modeling: Objective Interpolation Formulus for the Spatial Distribution of Pollution Concentration", J. Appl. Meteor., vol. 16, pp. 1234-1255, (1977).
4. Sasaki, Y., "An Objective Analysis Based on the Variational Method", J. Meteor. Soc. Japan, Vol. 36, pp. 77-78, (1958).
5. Heimbach, J. A., and Y. Sasaki "A Variational Technique for Mesoscale Objective Analysis of Air Pollution", J. App. Meteor., Vol. 14, pp. 47-57, (1977).
6. 梁文傑，「空氣污染評估的佳化理論」，中國工程學刊，第三卷第二期，(1980)。
7. Pasquill, F., Atmospheric Diffusion. John Wiley and Sons, New York, New York. pp. 240-328 (1974).
8. Gifford, F. A., "Use of Routine Meterological Observations for Estimating Atmospheric Dispersion", Nuclear Safety, Vol. 2, pp. 47-51, (1961).
9. Martin, D. and J. A. Tikvart, "A General Atmospheric Diffusion Model for Estimating the Effects on Air Quality of One or More Sources" APCA paper No. 68-148, Washington, D. C., (1968).
10. Air Quality Display Model, U. S. Dept. of Health, Education, and Welfard, Cincinnati, Ohio, (1969).
11. Turner, D. B., Workbbok of Atmospheric Disperion Estimates. U. S. Department of Health, Education, and Welfare, Cincinnati, Ohio, (1970).
12. Bierly, E. W., and E. W. Hewson," Some Restrictive Meteorological Conditions to be considered in the Design of Stacks", J. Appl. Meteor., Vol. 1, pp. 383-390, (1962).
13. 宋志育，「用微擾動方法改進之一般性空氣污染擴散模型及其在臺北市之應用」，碩士論文，國立臺灣大學機械工程研究所，臺北市，(1975)。
14. 梁文傑、台世宗，「臺灣電力公司候選火力電廠廠址對周圍環境空氣品質影響之評估」，臺灣電力公司委託研究計畫研究報告，中央研究院物理研究所，臺北市，(1977)。
15. Rose, A. H., R. Smith, W. F. McMichael, and R. E. Kruse, "Comparison of Auto Exaust Emissions in Two Major Cities", J. Air Pollution Conrol Association, Vol. 15, pp. 362-366, (1965).

Annual Report of the Institute of Physics, Academia Sinica, Vol. 9, 1979

THE OPTIMIZATION EVALUATION OF CO AIR POLLUTION AND MONITOR NETWORK IN TAIPEI

WEN-JEY LIANG
Institute of Physics, Academia Sinica
and
Department of Mechanical Engineering
National Taiwan University

KEH-TARNG LEE
Institute of Environment Engineering
National Taiwan University

Abstract

The optimization theory of air pollution estimation is utilized to investigate the CO pollution in Taipei. Accordingly, the computed concentration from Gaussian dispersion model and the measured concentration data at monitor stations are combined to fine the optimized pollutant source strength and the optimized CO concentration distribution. In order to clarify the plausibilith of optimized results, the statistical properties of concentration at stations computed from optimized and non-optimized dispersion model are fully discussed. Employing the optimized results, the influence of pollution sources and the efficiency of the mornitoring stations of CO are carefully studied, and the optimal mornitor network is also suggested.

空氣污染評估的佳化理論

梁 文 傑

中央研究院物理研究所
國立臺灣大學機械工程學系

摘 要

本文利用變微分法發展出兩種空氣污染評估的佳化理論，分別爲强勢佳化理論與弱勢佳化理論，前者要求佳化值完全滿足擴散模式，後者只要求佳化值儘量滿足擴散模式。

由於佳化後的污染源强度值與地面濃度值必須爲正，拘束條件勢必同時包含等式與不等式，本文藉著一個簡單的控制機制，使不等式與佳化程序相關連，而此機制則由一個權重參數所制御。文中並以臺北市一氧化碳的污染評估爲例探討佳化理論的可信性及其優劣得失，結果顯示佳化法極其穩定，而佳化後的濃度值亦具有高度的代表性。

壹、前 言

空氣是人類生存的基本要素，人類必須從空氣中吸取氧而將氧化作用所產生的二氧化碳呼出體外，此種「呼」與「吸」實乃人類生命的基本現象，也是人類享有的基本權利與義務。由於吹風、下雨、沉澱、化學作用以及植物的吸收，人類所呼出的廢氣理應很容易的被稀釋與排除，然而隨著人類文明的進展，工業時代的來臨，工廠與車輛遍佈城市與鄉鎮的大街小巷，這些新時代的寵兒也同人類一樣必須從空氣中攝取氧以供氧化、燃燒及其他工業過程之用，而將產生的廢氣（包括氣體與固體）排至大氣中。所不同的却是它們驚人的排放量，就一輛小型汽車來說，每行一公里所排放的一氧化碳（約30公克），約需兩百萬公升的空氣才能稀釋到無害的濃度，而兩百萬公升的空氣正是兩百位成年人一天呼吸所需。換句話說，稀釋一輛小型汽車行駛一天（每小時以60公里計）所排放的一氧化碳所需的空氣竟足以供應28萬8千位成年人一天呼吸之用！更由於工廠與車輛排放的廢氣有增無減，而空氣的體積及其排除作用的能力有限，使得這些污染物所帶來的不良影響日趨嚴重，而城市與工業區的污染問題便是其中最爲顯著的例子。

城市與工業區的污染源包含有點源、線源與面源三類，大工廠可視爲點污染源

，而小工廠因其數目太多，若對每一個污染源的污染情形各別計算殊不經濟，一般皆取其總污染量除以總面積而將之視爲面污染源，此外，車輛的污染可視公路、鐵路（或地下鐵道與隧道）等爲線污染源。城市污染問題首先在於了解市區現在與將來可能的污染程度（亦即求取現在或預測將來的污染物濃度分佈），以作爲都市計畫或污染程度控制的依據，求得污染物濃度分佈的方法一般可分爲兩種，第一種是在選定的各量測點實際量測空氣中污染物的濃度，並據之作將來濃度值的推測，第二種是利用數學模式將所有污染源的污染情形算出，並據此繪出城市現在與將來可能的濃度分佈曲線，理論上說，如果兩種方法都很理想，所求得的結果應該一致，但事實上由於量測與數學模式所牽涉到的許多問題，使得兩者之間出入頗大。就以第一種方法來說，量測地點不同，其結果大不相同，使得量測值的眞實意義不易確定。譬如，吹東風時（風由東向西吹），若測站在煙囪西邊則量得的濃度可能極高，若測站在煙囪的東邊，則量得的濃度可能爲零，Goldstein 等人[1]藉各測站二氧化硫濃度的相關係數指出由一測站所測得的觀測值不一定可代表其周圍之污染情況，根據 Bryan[2] 的研究，若要測知一地區的污染情況，每 0.65 平方公里就需設一個測站，可是限於經濟與人力，實際作業下，測站的數目顯然無法滿足如此的要求，使得實際量測所繪出的濃度曲線無法眞實的反映出量測區域的污染狀況。因此各國各大都市與工業區都以第二種方法（數學模式）來作污染程度之評估與預報，而第一種方法的結果僅用來作線性的統計校正（線性回歸）。但是由於污染源數目及其每一時刻的排放量都無法準確的知道，使得模式的計算不易精確，更由於氣象資料不齊、大氣紊流、城市地形與局部流動的複雜性、數值模式與數值方法的誤差等經常使計算結果與眞實情況出入頗大。換句話說，求取城市污染物濃度分佈曲線的兩種方法，雖然都能反映部分的眞實狀況，却也都包含相當程度的誤差，以致於簡單的線性回歸校正仍然無法使校正後的結果具有良好的代表性[3]，更精細的處理顯然是必要的。

其實，觀測資料與模式結果的代表性與一致性等問題並非空氣污染的評估與預報所獨有，實廣泛存在於各行各業中，而在氣象上更屬衆所週知的基本要題。一九五八年 Sasaki 有見於此，首先以變微分法（Calculus of Variation）佳化氣象資料，以提高觀測資料的一致性與代表性，二十年來，由於氣象資料處理與天氣預報電腦化的需要日趨迫切，此法乃不斷的被深入的研究與廣泛的探討。近年來大氣污

染程度的加重及人們對所處環境的關切，維護環境爲刻不容緩的要題， Heimbach 與 Sasaki[4] 遂將變微分法引用於空氣污染的評估上。然而 Heimbach 與 Sasaki 的方法僅限於測站數目多於污染源的數目，精確的說應爲測站數目多或等於污染源的數目減 1，但在實際情況下污染源必遠多於測站的數目，更有進者，將此法應用於實際資料時，所算出污染源的佳化排放值有許多負值出現，就所試的各種結果顯示約有二分之一的污染源其佳化值爲負值，使得污染源附近的佳化濃度值亦爲負值，此種現象顯然極不合理，因此，若欲使用變微分法以佳化空氣污染的評估值極需作更深一層的研究與探討。

本文係以變微分法佳化空氣污染的評估值，爲使佳化理論可適用於任何測站與污染源數目，並使污染源的佳化排放值保持正值，佳化理論的動力拘束條件（Dynamic Constraints）同時包括等式與不等式；爲使不等式與佳化程序產生關連，本文於佳化函數中加入一個控制機制，而此機制則由一個權重參數所駕馭；文中並以臺北市的一氧化碳評估爲例探討佳化理論的可信性及其優劣得失。

貳、強勢佳化理論

令 $\{\tilde{C}_m \mid m=1, 2, \cdots\cdots, M\}$ 爲 M 個地面污染濃度觀測值，又令 $\{Q_n \mid n=1, 2, \cdots\cdots, N\}$ 爲 N 個已知排放源的排放值，一般來說，就測站點所在地，$\{\tilde{C}_m\}$值的可靠性高於由$\{Q_n\}$ 所求出的模式值，但就整個評估地區或預報地區而言，由$\{Q_n\}$所求出的濃度分佈曲線，其圖形（Pattern）的代表性實高於由有限個 $\{\tilde{C}_m\}$ 所繪出者，今欲求取一個最佳的地面濃度分佈函數 $C(x, y)$，使 $C(x, y)$ 爲位置變數 x 與 y 的連續函數，其值 $C(x_m, y_m)$ 儘量接近 $\{\tilde{C}_m\}$，而又能擁有模式圖形的特點，若以可重疊（Superposition）的擴散模式來求取污染濃度，則此種要求可簡示如下：

$$C(x, y)=\sum_{n=1}^{N} f_n(x, y)\, Q_n + C_b, \qquad 〔1〕$$

且使誤差 $(R_1)_m$：

$$(R_1)_m = C(x_m, y_m) - \tilde{C}_m$$

$$= C_m - \tilde{C}_m, \quad m=1, 2, \cdots\cdots, M,$$

的平方和爲最小，式中 $f_n(x, y)$ 爲擴散模式的擴散函數，C_b 爲背景污染濃度值（文中設爲常數）。爲便於數學式的推導，可令

$$Q_{N+1}=C_b\,, \qquad 〔2〕$$

$$f_{N+1}(x, y)=1\,, \qquad 〔3〕$$

則(1)式可改寫爲

$$C(x, y)=\sum_{n=1}^{N+1} f_n(x, y)\,Q_n. \qquad 〔4〕$$

由於觀測資料中除有M個濃度觀測值外，尚有N個污染排放值，若要充分利用這些資料使佳化的結果與觀測資料間具有最佳的一致性，則除了要求 $\{C_m\}$ 儘量接近 $\{\tilde{C}_m\}$ 外，亦應要求 $\{Q_n\}$ 儘量接近 $\{\tilde{Q}_n\}$，若令

$$(R_2)_n=Q_n-\tilde{Q}_n\,,\ n=1, 2, \cdots\cdots, N+1\,,$$

式中 $\tilde{Q}_1, \tilde{Q}_2, \cdots\cdots, \tilde{Q}_N$ 爲觀測值，而設 $\tilde{Q}_{N+1}$ 爲零，則綜合誤差的平方和應爲：

$$E=\sum_{m=1}^{M}(R_1)_m^2+\beta^2\sum_{n=1}^{N+1}(R_2)_n^2\,,$$

$$=\sum_{m=1}^{M}(C_m-\tilde{C}_m)_n^2+\beta^2\sum_{n=1}^{N+1}(Q_n-\tilde{Q}_n)^2 \qquad 〔5〕$$

此處 β 爲一誤差權重參數，其意義與作用將於下節詳述之。因此，所欲求取的最佳濃度分佈函數 $C(x, y)$ 必須滿足式〔1〕，並使 E 爲極小值。此外，爲了保證佳化的結果具有合理的物理意義 $\{Q_n\}$ 及 $\{C(x, y)\}$ 都必須爲正值。

由於我們擁有的訊息 (Information) 來源有三，即 $\{\tilde{C}_m\}$，$\{\tilde{Q}_n\}$ 與式〔1〕，而佳化後的 $\{C_m\}$ 與 $\{Q_n\}$ 既無法同時等於 $\{C_m\}$ 與 $\{Q_n\}$ 且滿足式〔1〕，權商其利弊，乃使所求的 $C(x, y)$ 與 $\{Q_n\}$ 儘量近似 $\{\tilde{C}_m\}$ $\{\tilde{Q}_n\}$ 與但式〔1〕却需完全被滿足，這種完全滿足式〔1〕的佳化理論，我們稱其爲强勢 (Strong) 佳化理論以與後來要討論的弱勢佳化理論有所區別，在弱勢佳化理論中 $\{C_m\}$ 與 $\{Q_n\}$ 僅要求儘量滿足式〔1〕。

E 的極小值可用變微分法的原理求得，爲便於運算可先將〔4〕式代入〔5〕式中：

$$E=\sum_{m=1}^{M}\Big(\sum_{n=1}^{N+1} f_{mn}\,Q-\tilde{C}_m\Big)^2+\beta^2\sum_{n=1}^{N+1}(Q_n-\tilde{Q}_n)^2\,, \qquad 〔6〕$$

式中 $f_{mn}=f_n(x_m, y_m)$，如此則上式中E的變數僅爲 $\{Q_n\}$。

今令

$$\delta E=0,$$

可得一矩陣方程式：

$$(F^TF+\beta^2 I)\ \vec{Q}=(F^T\vec{C}+\beta^2\ \vec{Q}) \qquad 〔7〕$$

式中

$$F=〔f_{mn}〕,$$

$$=\begin{vmatrix} f_{11}\ f_{12}\cdots\cdots f_{1N+1} \\ f_{21}\ f_{22}\cdots\cdots f_{2N+1} \\ \cdots\cdots\cdots\cdots\cdots\cdots \\ f_{M1}\ f_{M2}\cdots\cdots f_{MN+1} \end{vmatrix}$$

$$\vec{Q}=〔Q_1\ Q_2\cdots\cdots, Q_{N+1}〕^T,$$

$$\vec{\vec{C}}=〔C_1\ C_2\cdots\cdots C_M〕^T,$$

$$\vec{\vec{Q}}=〔\tilde{Q}_1\ \tilde{Q}_2\cdots\cdots\ \tilde{Q}_{N+1}〕^T,$$

而頂碼T代表矩陣的轉置，I代表單位矩陣。

式〔7〕可簡寫爲

$$A\vec{Q}=\vec{B}, \qquad 〔8〕$$

式中

$$A=F^T\ F+\beta^2\ I,$$

$$B=F^T\vec{\vec{C}}+\beta^2\ \vec{\vec{Q}}.$$

一般而言A的行列式不爲零故排放源的佳化排放量$\vec{Q}$可由式〔8〕求得：

$$\vec{Q}=A^{-1}\vec{B},$$

而佳化濃度分佈函數可由〔4〕式求得：

$$C(x, y)=\sum_{n=1}^{N+1} f_n(x, y)Q_n.$$

叁、誤差權重參數與控制機制

欲由式〔8〕解得排放源的佳化排放量$\vec{Q}$，必需先選定誤差權重參數β之值，一般在變微分法的佳化過程中，β 值常取爲 $\{\vec{C}_m\}$ 的誤差與 $\{\vec{Q}_n\}$ 的誤差的比值，一旦β值被選定，$\vec{Q}$及$\vec{C}$可依次求出。然而由於眞確的（True）排放量及濃度分佈無法知曉，$\{C_m\}$ 與 $\{Q_n\}$ 的誤差值無法準確的斷定，使得β值的選取陷入「任意」（Arbitrery）的圈套中。更有進者，當我們選定一個我們以爲適當的β值後，依式〔8〕所求得的$\vec{Q}$並不能保證必定爲正值，以致於由〔4〕式所求得的 C(x, y) 也無法保證爲正值。因此在進行求取佳化排放值與佳化濃度值之前，設法使

$$\vec{Q}\geq 0\,,$$

$$\vec{C}\geq 0\,,$$

兩不等式進入佳化的過程中，並以更肯定的準則來選取β值實爲首要之務。

就線性代數的理論來看，式〔4〕與〔5〕的眞實意義可由其相關的方程式系統的求解得到更進一層的瞭解：

$$\sum_{n=1}^{N+1} f_{mn}\,Q_n=\tilde{C}_m \qquad m=1,\ 2,\ \cdots\cdots,\ M\,, \tag{9}$$

$$Q_n=\tilde{Q}_n \quad n=1,\ 2,\ \cdots\cdots,\ N\,. \tag{10}$$

然而此方程式系統爲包含N個未知數 $\{Q_n\}$ 的 M+N 個方程式系統，由於方程式多於未知數，在線性代數上稱爲過度擬定系統（Over—determined System），此系統無準確解（Exact Solution），但若欲求者僅係近似解則〔6〕與〔7〕可對等於下列方程式系統：

$$\sum_{n=1}^{N+1} f_{mn}\,Q_n-\tilde{C}_m=(R_1)_m\,,\ m=1,\ 2,\ \cdots\cdots,\ M, \tag{11}$$

$$Q_n-\tilde{Q}_n=(R_2)_n\,,\ n=1,\ 2,\ \cdots\cdots,\ N+1\,, \tag{12}$$

$$E=\sum_{m=1}^{M}(R_1)_m^2+\beta^2\sum_{n=1}^{N+1}(R_2)_m^2\,, \tag{13}$$

$$\delta E=0\,. \tag{14}$$

將〔11〕與〔12〕代入〔13〕中即得式〔6〕，可見式〔4〕與〔5〕的佳化解實即式〔9〕與〔10〕的最佳近似解（就最小二乘方的意義而言）。

若 β 值爲零，式〔4〕與〔5〕卽與 Heimbach 與 Sasaki[4] 的方程式完全相同，故 Heimbach 與 Sasaki 的佳化解可視爲本文 β 值爲零時的特例。然而當 β 值爲零時，〔4〕與〔5〕式的相關代數方程式系統爲

$$\sum_{n=1}^{N+1} f_{mn} Q_n = \tilde{C}_m，m=1, 2, \cdots\cdots, M, \qquad 〔15〕$$

或

$$\sum_{n=1}^{N+1} f_{mn} Q_n - \tilde{C}_m = (R_1)_m，m=1, 2, \cdots\cdots \tilde{M}，\qquad 〔16〕$$

$$E_1 = \sum_{m=1}^{M} (R_1)_m^2 ，\qquad 〔17〕$$

$$\delta E_1 = 0 \qquad 〔18〕$$

〔15〕式的代數方程式系爲包含 N+1 個未知數 $\{Q_n\}$ 的 M 個方程式系統，若M大於 N+1，此系統爲過度擬定系統，此系統無準確解，但可由〔16〕～〔18〕的方程式系統求得最佳近似解，若 M 等於 N+1 則〔15〕有唯一的準確解，但若 M 小於 N+1 則式〔15〕爲不足擬定系統 (Under—determined System)，一般而言，具有無窮多個解，此中任何一個解都能滿足〔17〕式，此時〔16〕～〔18〕方程式系統實爲不恰當配置系統 (Ill-posed System)，故 Heimbach 與 Sasaki 的佳化法（亦卽 β 值爲零時）僅限於觀測站不少於污染源數目減 1 的情況，然而在一般實際作業系統中污染源數目皆遠多於觀測站，故式〔5〕中的 β^2 項實爲保證佳化法可使用於實際狀況的關鍵所在。

爲了瞭解 β 值的變化對佳化值的影響，我們先從 E 對 β^2 的第一階偏導式略窺端茅：

$$\frac{\partial E}{\partial \beta^2} = \left(\frac{\partial \vec{Q}}{\partial \beta^2}\right)^T \left[F^T F \vec{Q} - F^T \vec{\tilde{C}} + \beta^2 (\vec{Q} - \vec{\tilde{Q}})\right] + (\vec{Q} - \vec{\tilde{Q}})^2$$

$$= (\vec{Q} - \vec{\tilde{Q}})^2 \qquad 〔19〕$$

$$\geq 0$$

式〔19〕表明 E 值爲 β^2 值的單向逐增函數 (Monotonically increasing function)，故 β 值愈小，則 E 值愈小，其最小值係在 β^2 爲零處，由〔7〕式知此時的 $\vec{Q}$ 值爲：

$$\vec{Q} = (F^T F)^{-1} F^T \vec{\tilde{C}} \qquad 〔20〕$$

此 $\{\vec{Q}_n\}$ 不保證全爲正值。式〔20〕實爲 Heimbach Sasaki 與的佳化解。

由〔19〕式可看出E的最大值發生在 $\vec{Q}$ 與 $\tilde{\vec{Q}}$ 相等時，此時由〔4〕與〔5〕可知 C(x, y) 與E值分別爲：

$$C^*(x, y)=[C(x, y)]_{\vec{Q}=\tilde{\vec{Q}}},$$

$$=\sum_{n=1}^{N+1} f_n(x, y)\,\tilde{\vec{Q}}, \qquad [21]$$

$$E^*=[E]_{\vec{Q}=\tilde{\vec{Q}}},$$

$$=\sum_{m=1}^{M}(C_m-\tilde{C}_m)^2 \qquad [22]$$

顯然的，$C^*(x, y)$ 實即由觀測的排放量求出的模式計算值，而 E^* 則爲觀測排放量的模式值與觀測濃度值的誤差平方和，換句話說〔21〕與〔22〕表示出佳化解的誤差絕不大於沒有佳化的模式值。

爲了更瞭解 β 值的變化對E值的影響，我們可求取E爲 β^2 的第二階偏導式：

$$\frac{\partial^2 E}{\partial \beta^4}=2(\vec{Q}-\tilde{\vec{Q}})^T\frac{\partial \vec{Q}}{\partial \beta^2} \qquad [23]$$

由式〔7〕可求得 $\partial\vec{Q}/\partial\beta^2$ 的值如下：

$$(F^T F+\beta^2 I)\frac{\partial \vec{Q}}{\partial \beta^2}=-(\vec{Q}-\tilde{\vec{Q}}),$$

因此，

$$-(\vec{Q}-\tilde{\vec{Q}})^T(\frac{\partial \vec{Q}}{\partial \beta^2})=(\frac{\partial \vec{Q}}{\partial \beta^2})^T(F^T F+\beta^2 I)^T\ (\frac{\partial \vec{Q}}{\partial \beta^2})$$

在 $\{Q_n\}$ 全爲正值區域，上式右邊爲幾個正值矩陣的連乘，其元素必皆爲正，故由〔23〕式可知 E 對 β^2 的第二階偏導式在 $\{Q_n\}$ 全爲正值的區域必定爲負值，也就是說在此區域內不會有極小值發生，並且在 E 對 β^2 的曲線圖上斜率值爲單向逐減函數。且當 β^2 趨近無窮大時 $\partial^2E/\partial\beta^4$ 趨近於零，故此曲線以 $E=E^*$ 爲漸近線。

綜合以上所論，E 對 β^2 的曲線示意圖可以圖(一)表示之。由此圖可看出當 β^2 爲零時 E 值爲 E_1，此時 $\{Q_n\}$ 不保證全爲正值，當 β^2 值逐漸增加時 E 值亦逐漸增加，但其增加以 E^* 值爲極限，此時 $\{Q_n\}$ 值等於 $\{\tilde{Q}_n\}$ 值，故 $\{Q_n\}$ 全部爲正。既然 $\{Q_n\}$ 爲 β^2 值的連續函數，故當 β^2 值由零逐漸增加時必存在一個 β_0^2 值使得對應大或等於 β_0^2 值的 $\{Q_n\}$ 皆爲正值，此佳化值即爲所求的最佳正解。

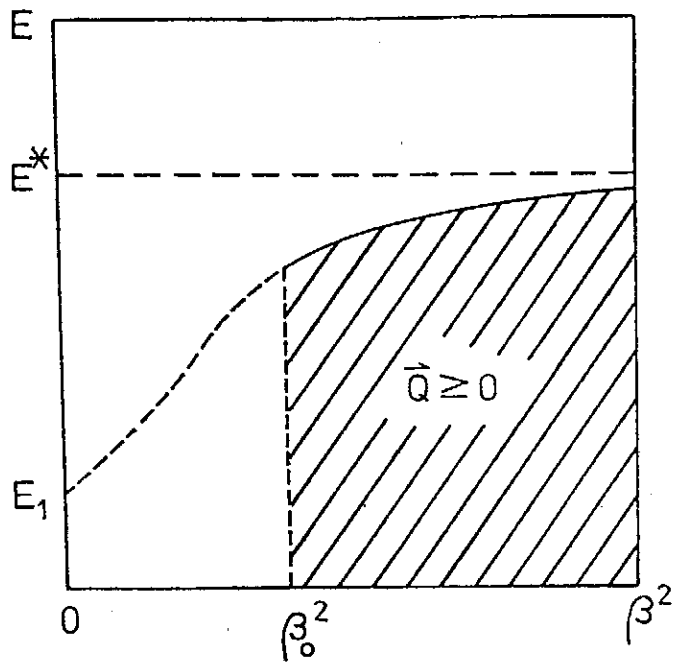

圖一　綜合誤差平方和E對控制參數 β^2 的關係

就變微分的理論來說，β^2 項代表一個控制機制，β^2 值爲此控制機制的控制參數，而 $\{\tilde{Q}_n\}$ 則爲此控制機制的基準，也就是說 β^2 項代表對 $\{Q_n\}$ 值的要求，此要求係以 $\{\tilde{Q}_n\}$ 爲基準，β^2 值的大小代表對此種要求的强弱程度，因此當 β^2 值趨近無窮大時，此種要求的强烈程度達到頂點，此時 $\{Q_n\}$ 被迫等於 $\{\tilde{Q}_n\}$。就本文而言，此種要求應儘量給與抑制，因爲此控制機制的目的僅在於使 $\{Q_n\}$ 值保證爲正，若 $\{Q_n\}$ 值已經爲正，則 β^2 值應儘量小以減少誤差函數E之值，也就是說，爲達到E值最小且 $\{Q_n\}$ 爲正的目的，β^2 值應取恰使 $\{Q_n\}$ 值全爲正時之值，此 β_0^2 值可以反覆法（Iteration）求得。

肆、弱勢佳化理論

如前所述，我們要求所求的佳化值 $\{C_m\}$ 與 $\{Q_n\}$ 必需滿足所使用的污染模式〔1〕，然而在許多情形下，式〔1〕並不比 $\{\tilde{C}_m\}$ 與 $\{\tilde{Q}_n\}$ 包含有更多的訊息（Information），亦即式〔1〕完全被滿足的需求，並非如此强烈與充分，更有進者，由於式〔1〕完全被滿足的要求使得 $\{C_m\}$ 與 $\{Q_n\}$ 無法足够的接近 $\{\tilde{C}_m\}$ 與 $\{\tilde{Q}_n\}$，比如，若式〔1〕完全不需要理會，則最小 E 值之解顯然爲 $\{C_m\}=\{\tilde{C}_m\}$，$\{Q_n\}$

$=\{\tilde{Q}_n\}$。因此，合理的放鬆式〔1〕的要求可使佳化解在 $\{\tilde{C}_m\}$、$\{\tilde{Q}_n\}$ 與式〔1〕間取得更好的協調，此種對 $\{\tilde{C}_m\}$、$\{\tilde{Q}_n\}$ 與式〔1〕三者皆採近似的佳化理論，我們稱其爲弱勢佳化理論。

依照上兩節的討論，弱勢佳化解可視爲下列方程式組的最佳近似解：

$$C_m=\tilde{C}_m\,, \qquad m=1,\ 2,\ \cdots\cdots,\ M\,,$$

$$Q_n=\tilde{Q}_n\,, \qquad n=1,\ 2,\ \cdots\cdots,\ N+1$$

$$C_m=\sum_{n=1}^{N+1} f_{mn}\ Q_n\,.$$

此方程式組爲含 $(M+N+1)$ 個未知數的 $(2M+N+1)$ 個方程式系統，是爲過度擬定系統，故無準確解，就最小兩乘方的意義來說，其最佳的近似解應爲：

$$e=\sum_{m=1}^{M}(C_m-\tilde{C}_m)^2+\beta^2\sum_{n=1}^{N+1}(Q_n-\tilde{Q}_n)^2+\lambda^2\sum_{m=1}(C_m-\sum_{n=1}^{N+1}f_{mn}\,Q_n)^2, \qquad 〔24〕$$

$$\delta e=0\,. \qquad 〔25〕$$

〔25〕式之解可以變微分法求得如下：

$$\vec{Q}=(F^T F+K^2\ I)^{-1}\ \ (F^T\tilde{C}+K^2\tilde{Q})\,, \qquad 〔26〕$$

$$\vec{C}=\frac{1}{1+\lambda^2}\ (\vec{\tilde{C}}+\lambda^2\ F\vec{Q})\,, \qquad 〔27〕$$

$$K^2=\frac{(1+\lambda^2)\beta^2}{\lambda^2} \qquad 〔28〕$$

由〔26〕式可看出 Q 對 K^2 的關係與强勢佳化解完全相同，只是此時 K^2 取代了 β^2 的角色而已，由〔28〕式可看出 β^2 不大於 K^2，若 λ^2 值甚大，此時式〔1〕的要求甚爲强烈，則 K^2 值趨近於 β^2 值，反之，若 λ^2 值甚小則 K^2 值遠大於 β^2 值，由於式〔26〕與式〔7〕完全相似，因此必存在一個 K_0^2 值使對應大或等於 K_0 值的 $\{\vec{Q}_n\}$ 值全部爲正，且此 K_0^2 值必定等於强勢佳化解的 β_0^2 值，若令

$$\beta_1^2=\frac{\lambda^2 K_0^2}{1+\lambda^2}\,,$$

且 λ^2 不爲零，則 β_1^2 必小於 K_0^2，亦即 β_1^2 值小於 β_0^2 值，由〔24〕式可知 β^2 值的減小表示 $\{Q_n\}$ 接近 $\{\tilde{Q}_n\}$ 的要求對 $\{C_m\}$ 接近 $\{\tilde{C}_m\}$ 的阻礙顯著的減小，此一事實可從〔27〕式看得更清楚，因〔27〕可改寫爲

$$\vec{C}-\vec{\tilde{C}}=\frac{\lambda^2}{1+\lambda^2}\left(F\vec{Q}-\vec{\tilde{C}}\right), \qquad 〔29〕$$

〔29〕式中（$F\vec{Q}-\vec{\tilde{C}}$）代表强勢佳化解對$\vec{\tilde{C}}$的偏差值，而（$C-\tilde{C}$）代表弱勢佳化解對$\tilde{C}$的偏差值，由〔29〕式可看出弱勢佳化解的濃度偏差值必小於强勢佳化解的濃度偏差值，兩者在 λ^2 趨近於無窮大時相等，而當 λ^2 值爲零時，弱勢佳化解的濃度偏差值爲零，亦卽此時$\vec{C}$全等於$\vec{\tilde{C}}$。

爲便於瞭解 λ^2 與 K^2 兩參數的作用與意義，可求 λ^2 對 β^2 與對 K^2 的第一階導式：

$$\frac{\partial\lambda^2}{\partial\beta^2}=\frac{1+\lambda^2}{K^2-\beta^2}\geq 0, \qquad 〔30〕$$

$$\frac{\partial\lambda^2}{\partial K^2}=-\frac{\lambda^2}{K^2-\beta^2}\leq 0, \qquad 〔31〕$$

〔30〕式顯示出當 λ^2 增大時 β^2 值必隨之增大，反之則隨之減小，也就是說，在K值不變的條件下，式〔1〕的要求欲高，$\{\tilde{C}_m\}$ 愈難接近 $\{\tilde{C}_m\}$ 值，使得濃度偏差值愈大。由〔31〕式可看出 λ^2 值愈大，K值亦隨之減小，而K值的減小增加 $\{Q_n\}$ 爲負的機會，可見得〔1〕式的要求一方面阻礙 $\{C_m\}$ 接近 $\{\tilde{C}\}$，另一方面也阻 $\{Q_n\}$ 礙爲正值，合理的放鬆〔1〕式的要求應有助於求得一個更具代表性的佳化解。

伍、佳化理論的應用

1. 資料與模式

佳化理論的各種特性在以上諸節中雖已有相當程度的討論，然而實際狀況常有出人意表者，因此，以實際資料置入理論中作檢驗應爲理論應用者不可省略的一步。理論應用的成效牽涉固廣，但就佳化理論而言，至少有三個主要因素關係到理論應用的效果，那便是測站上實測濃度的精確性，污染源調查的可靠性，以及污染模式的代表性，此三者相互關連，任何一個因素的不良（經過佳化過程後）都必需以其他因素精確性的犧牲來彌補，因此從佳化過程中各誤差值（如 R_1，R_2 與 R_3）的變化亦可看出資料的可信性與模式的可用性。

應用本文佳化理論的個案研究，由於牽涉極廣已有另文詳論之[5,6]，此處不擬作重複的詳述，僅以强勢佳化理論應用的一例來說明應用的效果。

本節係以一九七七年六月至七月臺北市車輛所排放的一氧化碳爲污染源，因此將車道視爲有限線源，各線源一氧化碳的排放强度需由車速[7]與車輛流量來決定（有關資料來自臺北市新建工程處交通科），由各項資料相互比較的結果採取輕型車輛排放率爲每輛每米 0.0369 克，而重型車輛與機踏車則分別取爲輕型車輛的 1.6 與 0.3 倍。由於臺北市車道分佈甚爲複雜，臺北市興建工程處的車道與車輛流量資料無法提供足够的資訊，許多車道的流量是以附近已知者參照估計而得，圖(二)爲臺北市可知車道百分之九十的車道分佈圖，附錄(1)則爲這些路段的編號與名稱，由圖(二)及附錄(1)可知即令是可知車道的百分之九十，與眞正的臺北市車道數目相較仍然不足，這些估計的偏差可從以上的模式計算值與測站量測值的差異看出，爲便於瞭解與查證各車道的污染實況，將各車道（線源）强度的百分率以表(一)表示之。

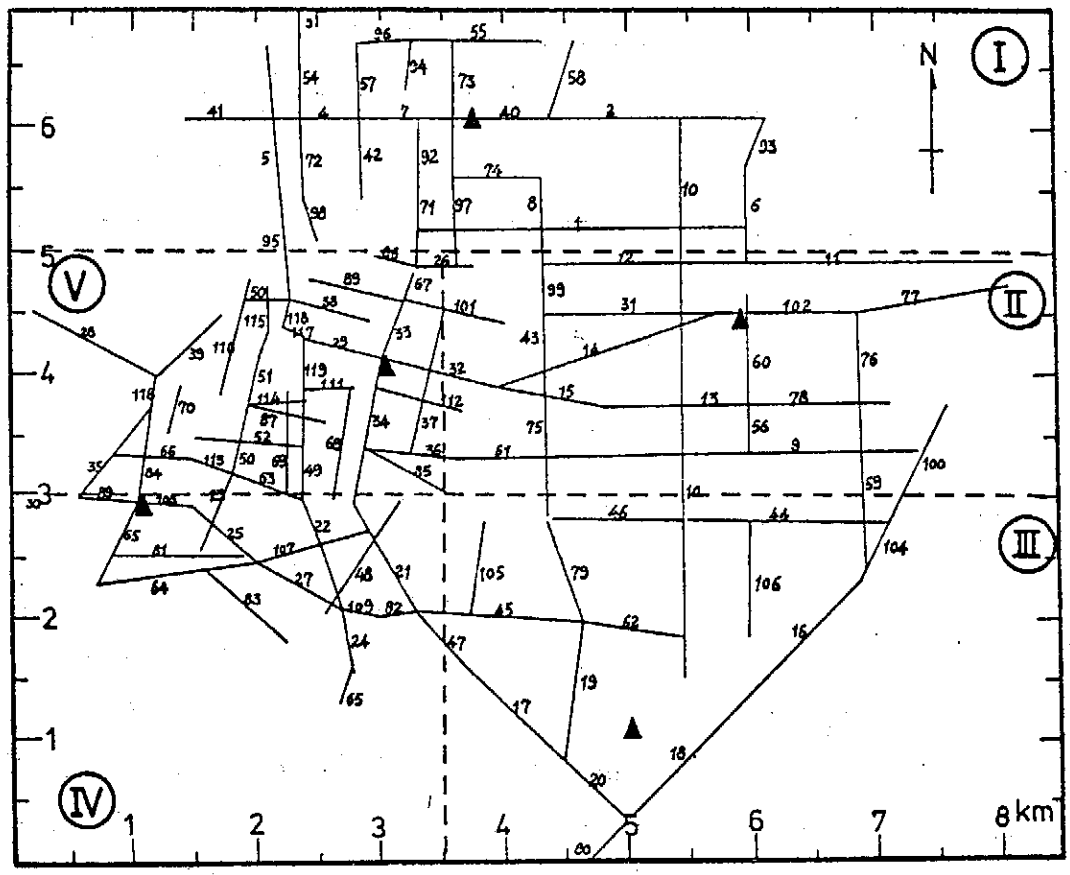

圖二　臺北市座標系統與百分之九十已知車道的分佈。虛線將臺北市分成五個分區。三角形代表污染測站位置。

表一、臺北市已知線源百分之九十的線源強度百分率。第一行代表線源編號的十位數，第一列代表個位數

線源編號	1	2	3	4	5	6	7	8	9	10
0	2.34	1.93	1.66	0.98	0.95	0.76	0.76	0.72	2.84	2.65
1	1.93	1.44	1.40	1.06	1.06	1.13	1.13	1.06	0.95	0.91
2	1.06	0.64	0.60	0.57	0.57	0.42	0.42	1.66	1.17	0.91
3	0.91	0.91	0.83	0.79	0.64	0.57	0.49	0.45	0.45	0.72
4	0.64	0.64	0.98	0.91	0.83	0.76	0.42	0.34	0.45	0.45
5	0.45	0.42	0.42	0.53	0.49	0.45	0.45	0.45	0.76	0.76
6	0.72	0.64	0.34	0.34	0.30	0.42	0.42	0.42	0.38	0.30
7	0.45	0.45	0.42	0.38	0.72	0.64	0.57	0.53	0.60	0.57
8	0.26	0.26	0.26	0.30	0.26	0.26	0.26	0.26	0.23	0.23
9	0.23	0.38	0.34	0.34	0.30	0.26	0.26	0.26	0.53	0.53
10	0.45	0.42	0.34	0.49	0.49	0.42	0.26	0.26	0.23	0.23
11	0.19	0.19	0.49	0.19	0.19	0.19	0.19	0.19	0.19	

表二、臺北市各測站一氧化碳濃度觀測值與模式計算值的比較

(單位：ppm)

測站號	測站名稱	測站座標	觀測值	未修正模式值	全區修正模式值	分區修正模式值	佳化模式值
1	中山	(3.8, 6.1)	10.3	13.5	15.2	12.6	10.3
2	八德路	(5.9, 4.5)	5.0	6.26	7.06	6.56	5.0
3	臺大	(5.0, 1.1)	4.0	1.93	2.18	4.0	4.0
4	萬華	(1.1, 3.0)	6.1	4.15	4.68	6.18	6.1
5	市議會	(3.1, 4.1)	12.5	7.77	8.76	12.3	12.5

臺北市一九七七的一氧化碳濃度測定站有五站，分別爲中山、八德路、臺大、萬華與市議會（如圖㈡之三角形所示），爲使污染源的分佈具代表性，將臺北市依上述的五個濃度測定站分別定爲一、二、三、四與五區，在選取污染源時儘可能使每一區的污染源比例相同，比如圖㈡爲可知車道的百分之九十分佈圖，亦即每一區都是那一區可知車道的百分之九十。本文僅擬以臺北市六月中早上七至八時一氧化碳的污染爲例，其測站的平均濃度得自臺北市環境清潔處的資料，如表㈡之第四行所示。

本文所用的模式爲高斯分佈模式，其中擴散的標準偏差 σ_y，與 σ_z 採自Turner[8]，所使用的公式及其推導詳見 Lamb[9]，Johnson 等人[10]，或宋[11]。氣象資料來自中央氣象局，氣象測站位於臺北市氣象局，氣象資料的內容、分析方法與處理過程詳見梁與呂[12]，表㈢爲六十六年六月上午七時至八時的氣象狀況，表中風向分爲16個方向（如圖㈢所示），穩定度分爲 6 級，風速分爲 6 級，每級的代表風速如表㈣所示，而風向玫瑰圖則如圖㈢所示。

表三、六十六年六月份上午七時至八時臺北市氣象狀況。

風向，穩定度與風速皆以級數表示

風　向	穩 定 度	風　速	混合層高度（米）	發生頻率（天）
4	1	3	527	1
4	6	1	590	2
5	6	1	621	2
7	2	2	715	1
7	3	1	652	2
7	6	1	610	6
8	2	1	652	1
8	5	1	652	1
8	5	2	715	1
8	6	1	621	6
9	5	1	652	1
9	6	1	621	4
11	6	1	527	1
12	2	1	527	1

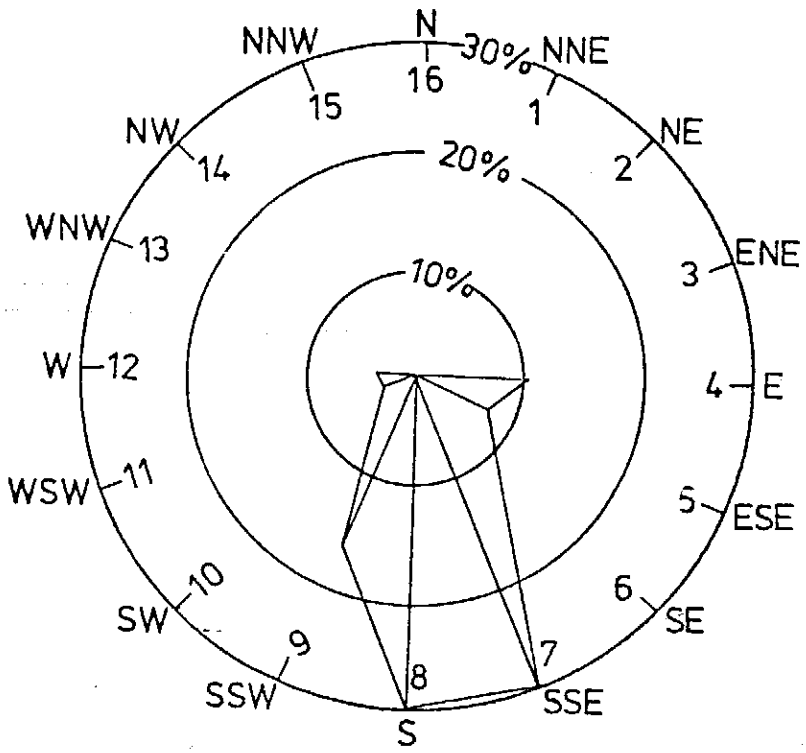

圖三　臺北市六月份早上七時至八時的風向玫瑰圖及風向分類標號。

表四、風速等級分類及各級的代表風速值

級	風速範圍（米／秒）	代表風速值（米／秒）
1	0.0— 1.5	0.75
2	1.6— 3.3	2.45
3	3.4— 5.4	4.40
4	5.5— 7.9	6.70
5	8.0—10.7	9.35
5	10.7—13.8	12.30

2. 結果與討論

圖㈣爲一九七七年六月份早上七至八時臺北市可知車道百分之九十（以下皆同）模式計算的一氧化碳濃度分佈圖，圖中可看出三個主要污染區域分別爲新生南路與松江路交接處，臺視附近（即敦化北路、長安東路二段、八德路三段與南京東路三段交接處）及北門附近，而測站上的模式濃度計算值則如表㈡第五行所示。

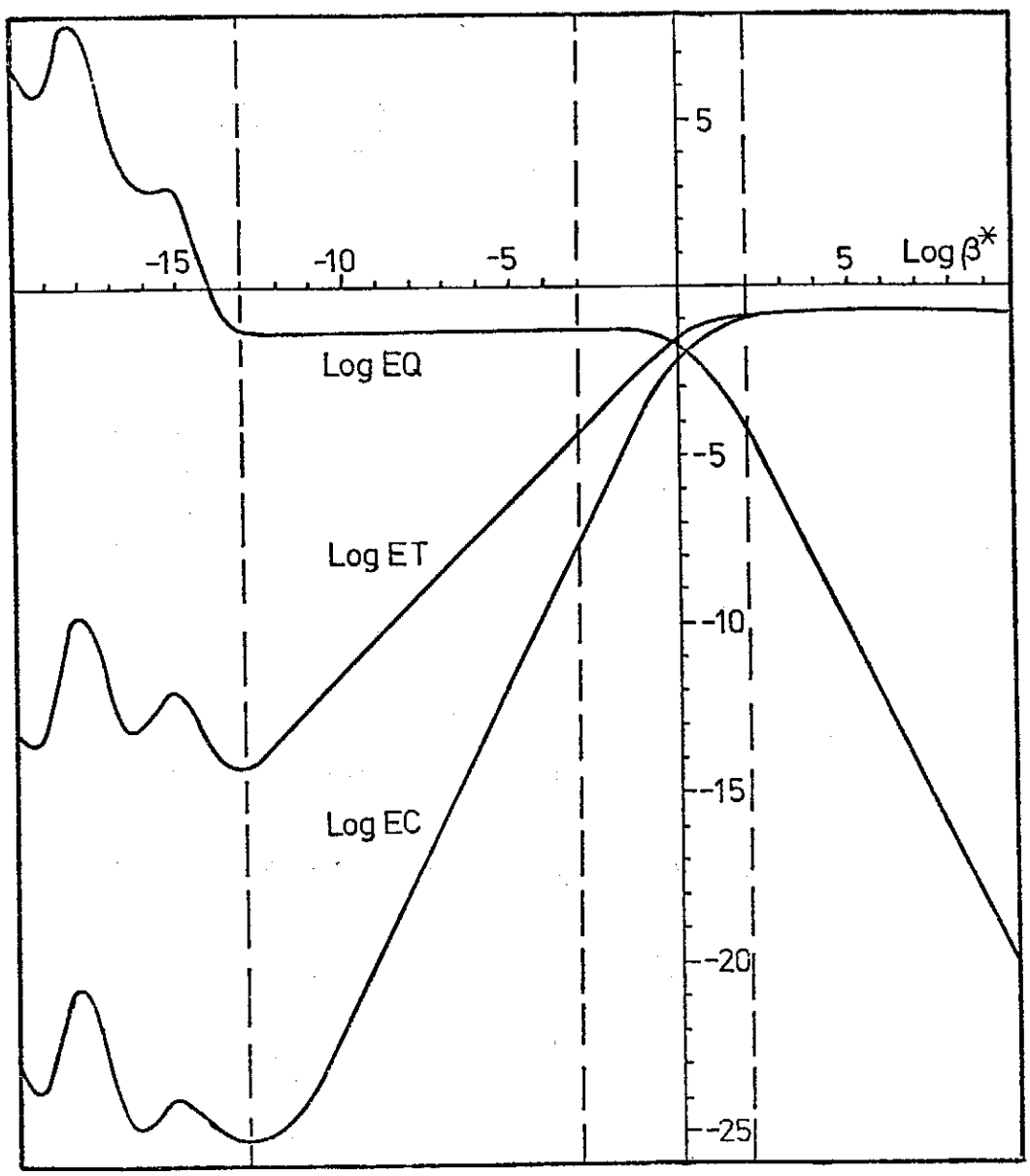

圖四　未修正的佳化過程。EQ 與 EC 分別表示污染源强度與濃度誤差變量，ET 則爲兩者之權商和。

爲瞭解模式的可靠性，本文分別以全變量 EF、污染源變量 EQ、濃度變量 EC 及污染源與濃度的平均誤差與標準偏差 $\Delta\overline{Q}$，$\Delta\overline{C}$，D(ΔQ)，D (ΔC) 來討論，各項定義如下：

$$ET = EC + \beta^* \ {}^2EQ,$$

$$EQ = \sum_{n=1}^{N} (Q_n - \tilde{Q}_n)^2 / \sum_{n=1}^{N} \tilde{Q}_n^2,$$

$$EC=\sum_{m=1}^{M}(C_m-\tilde{C}_m)^2/\sum_{m=1}^{M}\tilde{C}_m^2,$$

$$\Delta Q=\sum_{n=1}^{N}\left(\frac{Q_n-\tilde{Q}_n}{Q_n}\right)/N,$$

$$\Delta C=\sum_{m=1}^{M}\left(\frac{C_m-\tilde{C}_m}{C_m}\right)/M,$$

$$D(\Delta Q)=\left[\sum_{n=1}^{N}\left(\frac{Q_n-\tilde{Q}_n}{Q_n}\right)^2/N-1\right]^{1/2},$$

$$D(\Delta C)=\left[\sum_{m=1}^{M}\left(\frac{C_m-\tilde{C}_m}{C_m}\right)^2/M-1\right]^{1/2},$$

而 β^* 則爲正常化 (Normalization) 後的 β 值，EC 與 EQ 兩項，分別以 $\sum_{n=1}^{N}\tilde{Q}_n$ 與 $\sum_{m=1}^{N}\tilde{C}_m$ 爲正常化尺度值。

由表㈤的第五行知模式值的平均誤差約爲 13.1%，濃度變量爲 12.4%，可看出就全區而言模式的評估尚可接受，但若從濃度誤差的標準偏差的 38.3%看來，模式並不穩定（就空間而言），也就是說整區的平均評估不錯，但詳細評估則差，這是一般模式評估最常見的情形。

表五、不修正、全區修正與分區修正模式的特性

（限最後一列外，皆以%為單位）

項目 \ 模式	不修正模式值	全區修正模式值	分區修正模式值
$\Delta\overline{Q}$	0	12.8	34.3
$\Delta\overline{C}$	13.1	− 2.0	10.6
D (ΔQ)	0	12.8	56.0
D (ΔC)	38.3	43.2	15.1
EQ	0	1.6	35.0
EC	12.4	14.0	2.3
Log (EC)	− 0.91	− 0.85	1.70

爲瞭解模式評估的性能與簡單修正的可行性，我們求出測站濃度值與模式在測站處的評估值的比值，分別爲 r_1，r_2，r_3，r_4 與 r_5，及平均值的比值，$\bar{r}$，然後將污染源强度分別乘以這些值，若乘以 $\bar{r}$ 則稱爲全區修正模式，若分區分別乘以對應的 r_1 至 r_5 則稱爲分區修正模式，以修正後的污染源排放量求得的評估值，其統計特性分別列於表㈤中。從表㈤的第三行可看出全區修正的濃度誤差就全區而言非常良好（−2.0%），但其誤差的標準偏差則增大爲43.2%，故就各測站處而言，全區修正模式比原模式更不穩定。全區修正的污染源誤差值與變量分別爲12.8%與1.6%，由此可知原模式的全區平均濃度與全區實測平均濃度僅差 12.8%，故就全區而言，原模式的污染源强度估計值（原估計爲可知的百分之九十）似甚正確。分區修正模式的全區平均誤差爲 10.6%但變量與標準偏差則降爲 2.3%與 15.1%，可見得分區修正除能有效的改進全區的平均濃度值外，對各測站處的濃度值也能有良好的評估，故分區修正顯然大大改進了模式的穩定性。

由分區修正模式對原模式在穩定性與平均濃度的改進可看出模式的修正需就各污染源分別給於修正，由於污染分佈的尺度（Scale）甚小，各處所需的修正差異頗大，任何籠統含混的修正方式並不能有效的改進評估的效果，比如，全區修正其效果甚不理想便是一例，而分區修正則需給與適當的選擇，此與測站地點、污染源分佈及氣象狀況有密切的關係，而分區修正的極致便是對每一個污染分別給與修正，佳化理論便是這種概念下所發展出來的。

圖㈥是全區修正後再從事佳化所得的佳化濃度分佈圖，從圖中可看出佳化濃度分佈除具有原模式的三個主要污染區外，又分別多出萬華地區、市議會地區、和平東路與新生南路交會區與辛亥路、基隆路交接處附近等四個主要污染區，很明顯的這些新污染區的出現與臺大、萬華、及市議會三個測站的量測值有良好的相關。由表㈡可看出原模式或全區修正模式在此三測站的評估都有較大的誤差率，而佳化的效果既在於對這些偏差給與校正，則新主要污染區的出現與此三測站的相關性實爲顯而易見的結果。

不修正佳化、全區修正佳化、分區修正佳化的佳化值，其各變量 ET、EQ 與 EC 對 β^* 的變化分別如圖㈣、㈦、㈧所示，由於 β^* 愈小 $\vec{C}$ 與 $\vec{C}$ 愈相近，故 EC 與 ET 皆隨 β^* 的減小而減小，亦卽 EC 與 ET 爲 β^* 的單向漸增函數，反觀 EQ

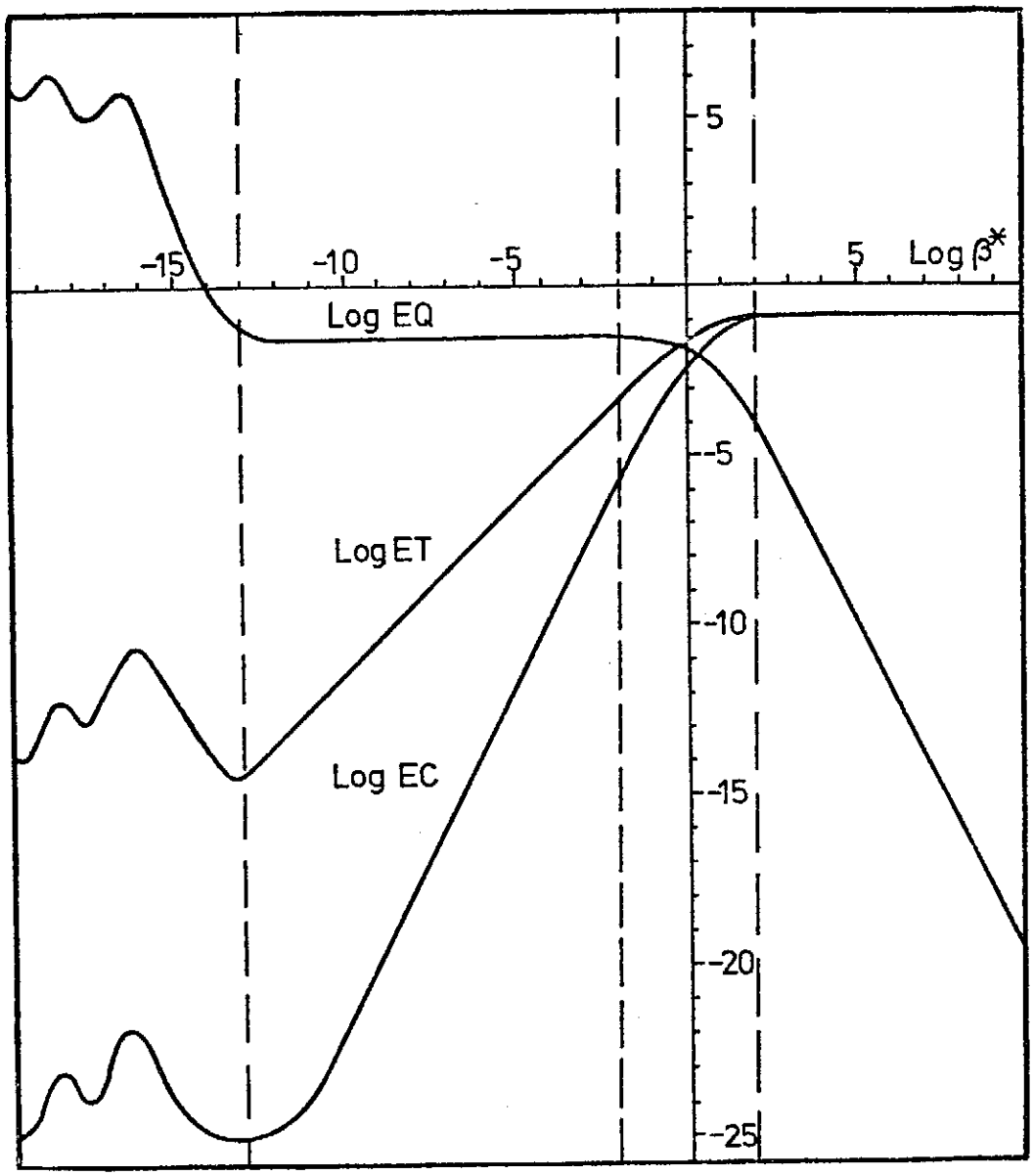

圖五　同圖四，唯係全區修正的佳化過程。

，因$\vec{Q}$與$\vec{\vec{Q}}$因 β^* 之增大而相近，故 EQ 隨 β^* 的增大而減小，亦即 EQ 爲 β^* 的單向漸減函數，從以上三圖可看出當 β^* 小至10^{-13}時，由於〔5〕式的 EQ 項甚小至可忽略，亦即方程式系統漸轉變成〔15〕至〔18〕，亦即近於不足擬定系統，此時矩陣方程式〔18〕之係數矩陣 A 的行列式值趨近於零，故圖(六)、(七)與(八)在 β^* 小於 10^{-13} 的區域不爲式〔8〕之解，僅由其大幅度之變化可印證當 β^* 趨近於零時佳化系統轉變爲不足擬定系統。

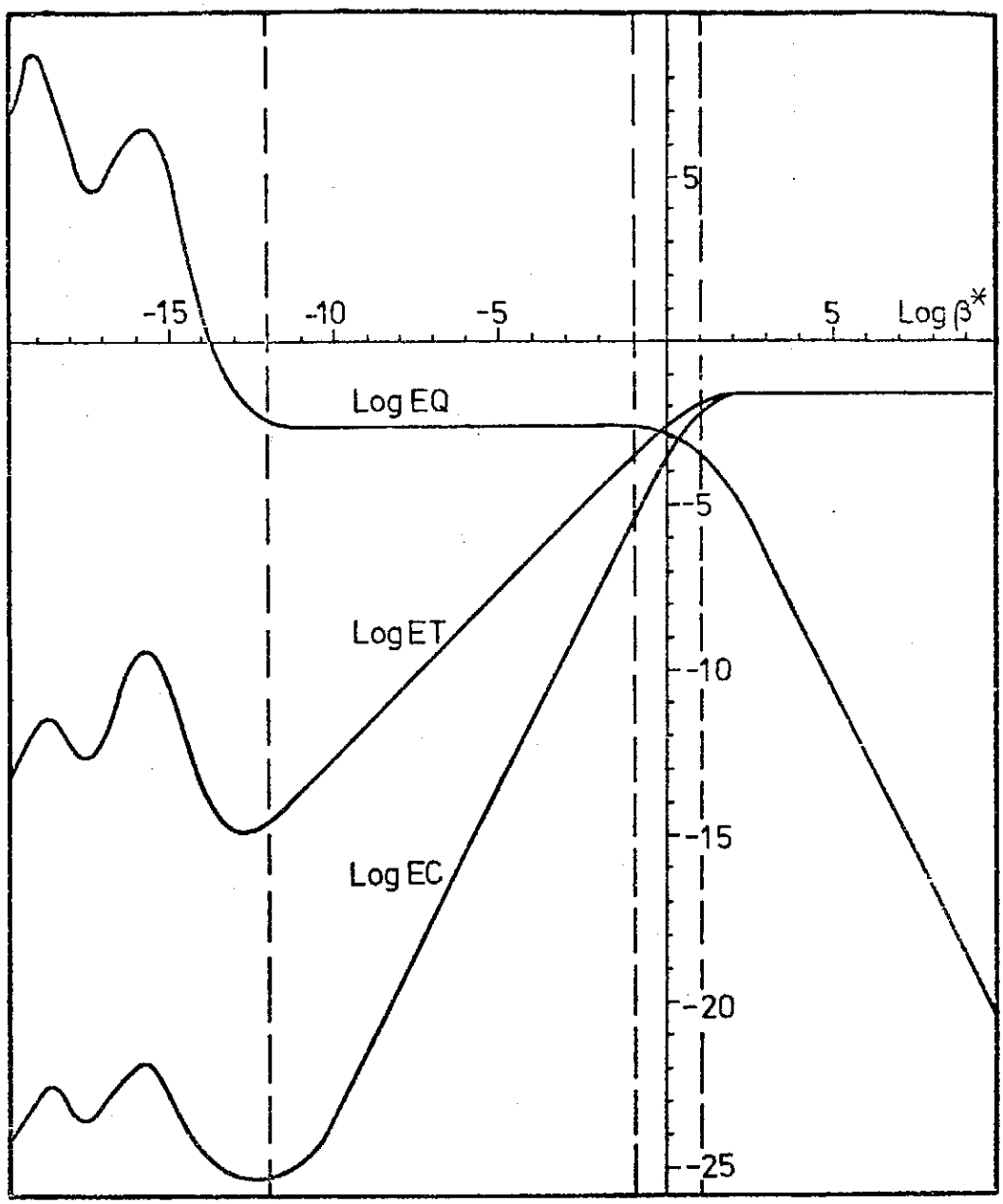

圖六　同圖四，唯係分區修正的佳化過程。

當 β^* 甚大時（比如大於100）EQ 趨近於零而 ET 與 EC 皆趨近於一定值，此定值卽以不佳化之 $\vec{Q}$ 代入模式中算得之濃度值與觀測濃度值之變量值，分別爲 0.124，0.14 與 0.023（取對數後爲 -0.91，-0.85與 -1.70），如圖(六)、(七)、(八)與表(五)第7、8列所示。當 β^* 小於 10^{-3} 以後，EQ 幾乎保持定值，而 EC 與 ET 已甚小（就實際意義而言，可視爲零），故最佳 β^* 值實際上可取 β^* 爲 10^{-3} 至 10^{-12}

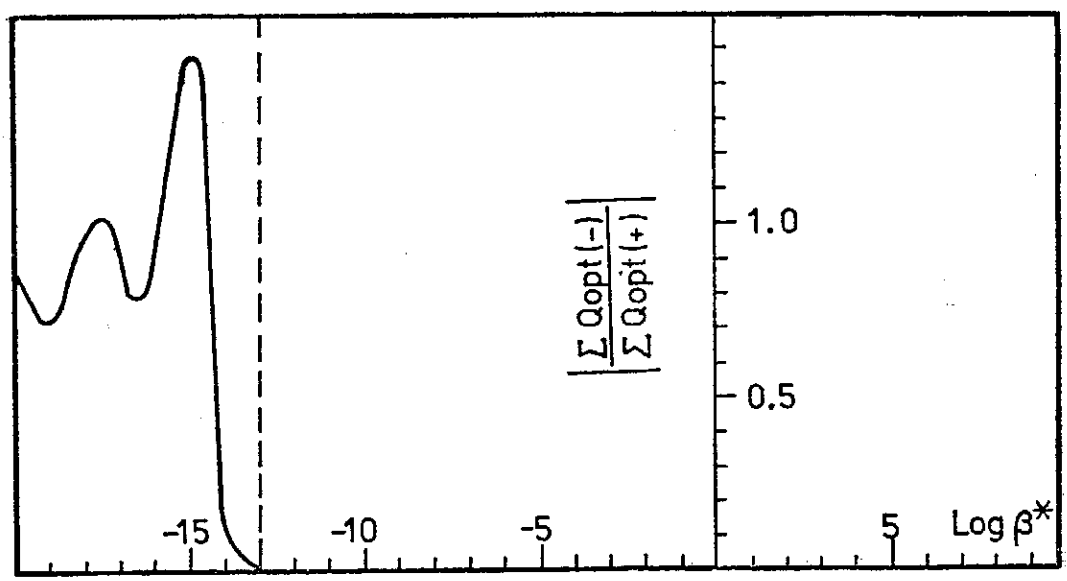

圖七　佳化過程中正與負污染源總强度比值對 β^2 值的變化。

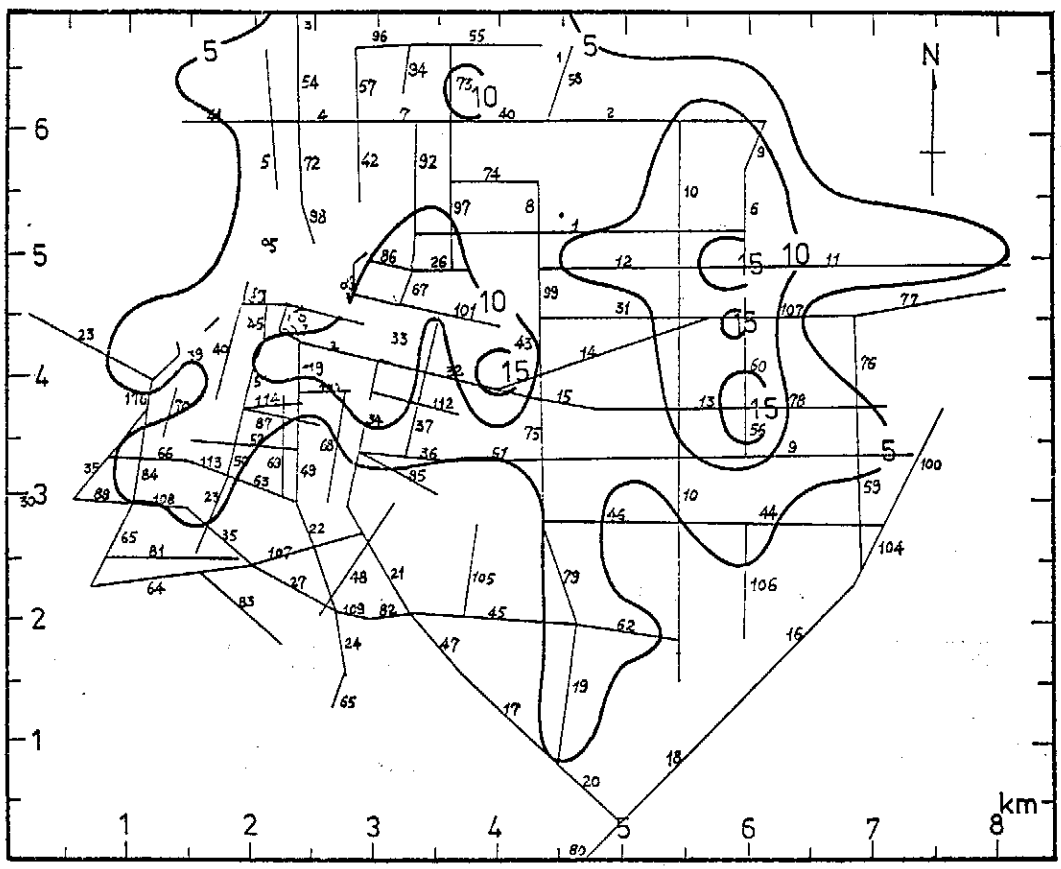

圖八　未修正未佳化的臺北市一氧化碳濃度分佈。圖中等濃度線上濃度值的單位爲 ppm。

中之任何一值，此區間之寬廣表現出佳化法的穩定性，亦即 β^* 值與佳化值皆極易求得。

圖(九)顯示佳化過程中負污染源强度的變化與消失實況，由圖可知當 β^* 由甚小而趨近 10^{-13} 時，負污染源强度即漸消失，故 10^{-13} 理應爲最佳 β^* 值，但因此時 β^* 太小，故式 (8) 之係數行列式值過小，致使所求得之解有相當程度之電腦計算誤差，此種誤差當 β^* 大於 10^{-12} 後便幾近消失，故最佳的 β^* 值乃以 10^{-12} 至 10^{-3} 區間任一值爲宜。

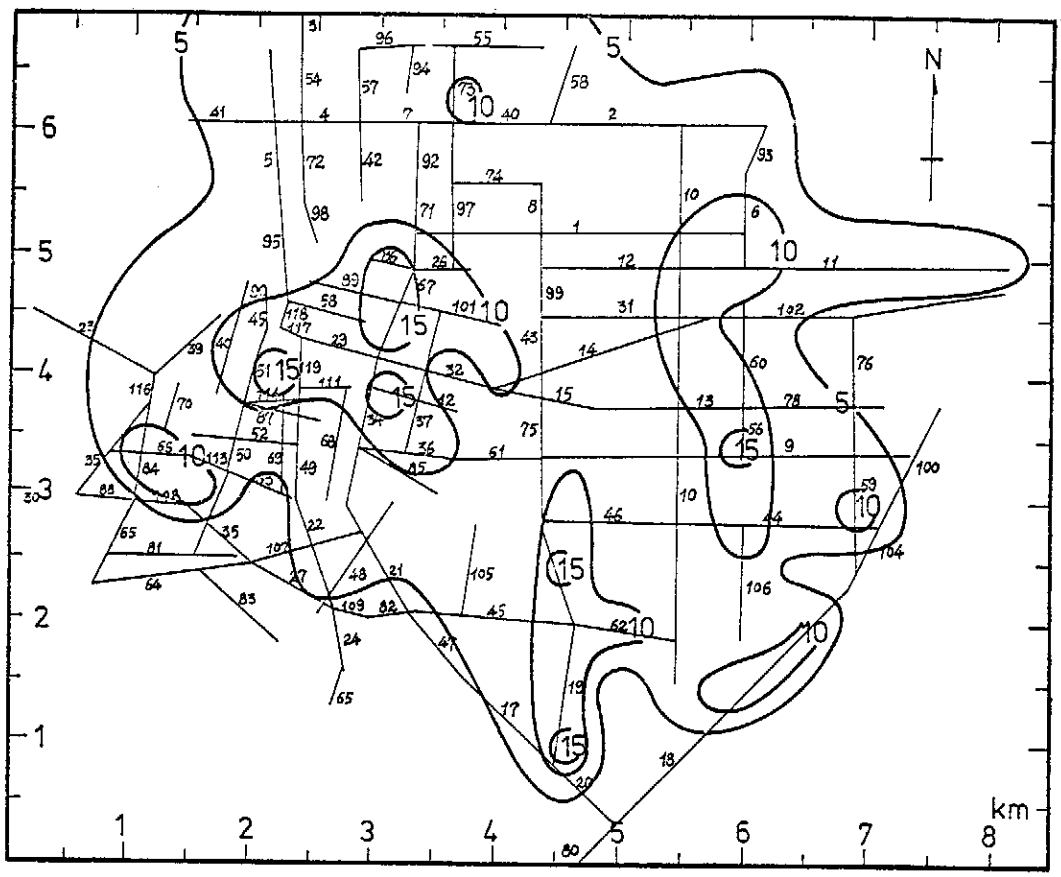

圖九　同圖八，唯係分區修正佳化的濃度分佈。

由於車道橫橫綜錯，有些地點雖在某兩條等濃度曲線間，但其濃度值並不一定在這兩個濃度值之間。由於網格點間距爲 500 公尺，許多更小尺度的分佈便被濾掉而無法表現在濃度分佈圖上，雖然如此，就臺北市現階段的一氧化碳污染實況而言，未佳化或佳化模式的計算結果都具有高度的代表性。

若要充分瞭解佳化理論（包括强勢佳化與弱勢佳化理論）在實際應用上的各種特性，因牽涉甚廣需另文詳細探討，但單從以上這個典型的例子可約略看出佳化理

論確能給與我們一個極具代表性的污染濃度分佈曲線，並有效的改進空氣污染評估的可靠性。

陸、結　　論

空氣污染問題的解決牽涉甚廣，但解決的過程不外乎觀察（或觀測）、分析、評估、預報與控制，污染控制固爲污染問題解決的根本，但從觀察到預報這些過程却是污染控制的基礎，基礎不穩則控制的效果必然不彰，甚且事倍而功半，從國內公害防治的現況便可明白這個道理。

評估與預報固爲污染控制的先決條件，但作好評估與預報並非易事，在實際作業時，由於經費、人力、時間與知識都極有限，而良好的評估與準確的預報却需建立在這些脆弱的條件上，則如何竭力發揮所有可能得到的資訊（Information）顯然是必需盡力去作的一件要事。在空氣污染的評估與預報上，最重要的資訊來源便是實測資料與評估或預報模式，可惜由於各種因素的限制，兩者之間並不一致，甚且出入頗大，互相調整的必要性使我們步入佳化（Optimization）的嘗試中。

Heimbach & Sasaki (4) 利用變微分法在實測濃度與評估模式間從事佳化，但其理論僅可用於測站數目多於污染源的數目加一，且其佳化後的污染源强度值常有負值出現，因此無法應用於實際狀況。本文借着一個簡單的控制機制，使污染源强度值與污染濃度分佈值皆能爲正，且能適用於任何測站數目與污染源數目，尤以測站數目稀少時（此爲一般實際情況）更具成效。

佳化理論分爲强勢佳化理論與弱勢佳化理論，前者要求佳化值完全滿足所使用的污染模式，後者則僅要求儘量滿足污染模式，從理論的觀點看來，後者應佳於前者，其佳化係數的選取需視實際資料的良否與所使用的模式的可靠性來決定。

從臺北市一氧化碳評估的實例中可以看出 Heimbach & Sasaki 的方法顯然無法使用，本文强勢佳化理論的佳化結果顯示佳化法確能有效的發揮觀測資料的資訊與我們對擴散現象的知識，而得到一個更具代表性的評估結果。

佳化理論應用於實際評估中的各種效果已有另文詳論之（5，6），而其在預報上的應用亦正在進行中，由於預報所牽涉的問題遠比評估複雜，其實際應用的效果尚有待試驗結果的評價。

參 考 文 獻

1. Goldstein, I. F., and L. Landoritz, "Analysis of air Pollution Patterns in New York City. I. Can one station represent the large metropolitan area? II. Can one aerometric station represent the area surrounding it?" Atmos. Envir., ll, pp. 47-57, (1977).
2. Stern, A. C., Air Pollution, Academic Press, New York, pp. 425-463, (1968).
3. Gustafson S. A., K. O. Kortanek, and J. R. Sweigart, "Numerical Optimization Techniques in Quality Modeling: Objective Interpolation Formulus for the Spatial Distribution of Pollution Concentration", J. Appl. Meteor., vol. 16, pp. 1243-1255, (1977).
4. Heimbach, J. A., and Y. Sasaki "A Variational technique for mesoscale objective analysis of air Pollution," J. App. Meteor., vol. 14, pp. 47-57, (1977).
5. 梁文傑、李克堂，「臺北市一氧化碳污染佳化評估的個案研究」，中央研究院物理研究所集刊，第八卷（待刊中），(1979)。
6. 梁文傑、李崇德，「高雄市二氧化硫污染佳化評估的個案研究」，中央研究院物理研究所集刊，第八卷（待刊中）。
7. Rose, A. H., Jr., R. Smith, W. F. McMichael, and R. E. Kruse, "Comparison of auto exhaust emissions in two Major cities", J. of Air Pollution Control Ass., Vol. 36, pp. 77-88, (1958).
8. Turner, D. B., Workbook of Atmospheric Diffusion Estimates. Nat. Air Pollution Control Agency, Cincinnati, pp. 8-9, (1969).
9. Lamb, R. G., "An air Pollution Model of Los Angeles", Master's Thesis Dept. of Meteor., Univ. of Calif., Los Angeles, Calif (1968).
10. Johnson, W. B., F. L. Ludwig, and A. E. Moon, "Development of a practical, multi-puropose urban diffuation model for carbon monoxide," Proc. of symposium on Multiple Sounes Urban Diffusion Model, Washigton D. C., (1970).
11. 宋志育，「用微擾動方法改進之一般性空氣污染擴散模型及其在臺北市之應用」，碩士論文，國立臺灣大學機械工程研究所，臺北市，(1975)。
12. 梁文傑、呂世宗，「臺灣電力公司候選火力電廠廠址對周圍環境空氣品質影響之評估」，臺灣電力公司委託研究計畫研究報告，中央研究物理研究所，臺北市，(1977)。

高雄地區二氧化硫污染與偵測網之佳化評估

梁　文　傑

中央研究院物理研究所
國立臺灣大學機械工程研究所

李　崇　德

國立臺灣大學環境工程研究所

摘　　要

本文使用變微分法，以高雄地區的 SO_2 爲研究對象，將高斯擴散模式與實際量測的資料組合，以求出適合當地污染狀況的最佳 SO_2 排放源，再據而求出最佳 SO_2 濃度分佈。接著更利用此最佳濃度分佈狀況，對當地的排放源加以評估，舉出影響重大的排放源，以做爲污染控制方面削減排放源强度的依據，同時又對量測站進行評估，分別列出不受影響的量測站及受相同排放源影響的量測站，使對於不需要的測站能加以裁撤以節省人力、物力，但却又能獲得等量的資料，而在多個排放源影響區域則建議設立測站，以獲得重要的污染資料，達到最佳偵測網之設計。

壹、前　　言

高雄地區位於臺灣本島西南端，東自高屏溪，北至路竹鄉，西、南二面面臨臺灣海峽，所域面積 438 平方公里。高雄市爲高雄地區工商業的精華地帶，亦爲我國自由地區第二大都市及首要港埠與工業中心。近年來因設置加工出口區及南部工業區，各方紛紛投資設廠，更促進該地區的繁榮與發展，然而隨伴來的廢水、廢物與廢氣的問題也日趨嚴重，使得這一個愛河河傍的都市終日籠罩在五花十色的迷煙綺霧之中。

國內巨型工廠大多集中在高雄地區。比如，中油高雄煉油廠、臺肥、臺鋁、臺碱、臺灣船舶廠、唐榮、臺糖農化廠、火力發電廠、臺灣造船、中鋼、中船及石油化學等，這些工廠所排出的廢氣都極其可觀，以大林火力發電廠爲例，六十四年耗油量 230萬公秉(1)，若以含游離硫量平均 3.5%計算，每日二氧化硫排放量便是 440

公噸，亦即每日有 670 公噸的硫酸（可能）降落下來。其他會發生空氣污染的尚有水泥廠、煉鋼廠及塑膠工廠等。爲維護生活環境，減少財物損失，確保國民健康，及時的防範與抑制已到刻不容緩的時候了。

高雄地區空氣污染問題的解決首先在於瞭解區域內各處的污染程度（亦即求取污染物濃度分佈）以作爲都市計畫或污染程度控制的依據，求取污染物濃度分佈的方法一般可分爲兩種，第一種是在選定的各量測站實際量測空氣中污染的濃度，第二種是利用數學模式將所有污染源的污染情形算出，據之繪出濃度分佈曲線。但限於人力與物力，平常作業時空氣污染測定站的數目甚少，由此少數測站所測得的濃度值顯然無法繪出具有全區代表性的濃度分佈曲線(2)。因此必需以第二種方法作污染程度的評估，而測站所得的結果僅用來作模式計算結果的檢驗與校正(3)。一般常用來作校正的方法爲線性回歸。然而由於實際情況的複雜性，簡單的線性回歸校正並無法使校正的結果具有良好的代表性(4)，更精細的處理顯然是必要的。

其實，觀測資料與模式結果的代表性與一致性等問題並非空氣污染評估所獨有，實廣泛存在於各行各業中，而在氣象上更屬衆所週知的基本要題。一九五八年 Sasaki (5)有見於此，首先以變微分法（Calculus of Variation）佳化氣象資料，以提高觀測資料的一致性與代表性，二十年來，由於氣象資料處理與天氣預報電腦化的需要日趨迫切，此法乃不斷的被深入的研究與廣泛的探討。近年來大氣污染程度的加重及人們對所處環境的關切，維護環境成爲刻不容緩的要題，Heimbach 與 Sasaki (6)遂將變微分法引用到空氣污染的評估上。然而 Heimbach 與 Sasaki 的方法僅限於測站數目多於污染源的數目，精確的說應爲測站數目多或等於污染源的數目減 1，但在實際情況下污染源必遠多於測站的數目，更有進者，將此法應用於實際資料時，所算出污染源的佳化排放值有許多負值出現，使得佳化濃度值亦爲負值。爲解決這些問題，作者之一(7)利用變微分法，重新發展適用於實際狀況的空氣污染佳化評估方法，此方法可適用於任何測站與污染源數目，並使污染源的佳化排放值爲正值。本文便是利用此法以測定站的污染物濃度測定值來校正並佳化空氣污染模式值，並將求得的佳化結果與行政院衛生署的「臺灣地區公害防治先驅計畫」密集測定所得的濃度分佈相比較。此外，本文亦利用佳化模式值檢討測站的較佳位置與站數，以作爲將來高雄地區測站設立的參考。

貳、佳化評估理論

本文採用(7)之佳化理論從事高雄地區空氣污染實況的評估，有關佳化理論的詳細推導，已見於(7)中，本文僅簡述有關部份，然後將高雄地區的實測資料代入模式中以求取高雄地區的佳化濃度分佈。

假設有n個地面污染物濃度觀測值 $\{\tilde{C}_i\}$，i＝1，2，……n，並有N個排放源強度的觀測值爲 $\{\tilde{Q}_j\}$，j＝1，2，……N，另假設校正後的污染源佳化排放量爲 $\{Q_j\}$，j＝1，2，……N，由此佳化排放量代入模式算出之佳化濃度值爲 $\{C_i\}$，i＝1，2，……n；則濃度及排放源佳化前後的差異可以兩者差的平方和表示之：

$$E=\sum_{i=1}^{n}(C_i-\tilde{C}_i)^2+\sum_{j=1}^{N}(Q_j-\tilde{Q}_j)^2 \qquad 〔1〕$$

爲了避免污染物濃度值的單位與排放源強度值單位的不同，將濃度值誤差項及排放源強度值誤差項予以尺度化（Scaling），且加入一誤差權重數（Error Weighting Factor），以I表示此誤差的平方和，則

$$I=\frac{\sum_{i=1}^{n}(C_i-\tilde{C}_i)^2}{\overline{\sum_{i=1}^{n}\tilde{C}_i^2}\times n}+\beta^*\frac{\sum_{j=1}^{N}(Q_j-\tilde{Q}_j)^2}{\overline{\sum_{j=1}^{N}\tilde{Q}_j^2}\times N}, \qquad 〔2〕$$

式中 $\overline{\sum_{i=1}^{n}\tilde{C}_i^2}$ 爲污染物地面濃度觀測值平方和的平均值，$\overline{\sum_{i=j}^{N}\tilde{Q}_j^2}$ 爲排放源強度值平方和的平均值。整理上式得

$$\overline{\sum_{i=1}^{n}\tilde{C}_i^2}\times n\times I=\sum_{i=1}^{n}(C_i-\tilde{C}_i)^2+\beta\sum_{j=1}^{N}(Q_j-\tilde{Q}_j)^2, \qquad 〔3〕$$

式中
$$\beta=\frac{\overline{\sum_{i=1}^{n}\tilde{C}_i^2}\times n}{\overline{\sum_{j=1}^{N}\tilde{Q}_j^2}\times N}\beta^*.$$

變微分法的原理乃是誤差的平方和要達到最小值，亦即

$$\delta I=0, \qquad 〔4〕$$

且 $\{C_i\}$ 與 $\{Q_j\}$ 滿足空氣污染的擴散模式

$$C_i=\sum_{j=1}^{N}F_{ij}\,Q_j. \qquad 〔5〕$$

本文取 F_{ij} 爲高斯分佈函數（Gaussian Distribution Function, F_{ij} 爲距離的函數）。由〔3〕，〔4〕，〔5〕式可得

$$\sum_{i=1}^{n} F_{ji}^{T}\left(\sum_{k=1}^{N} F_{ik}Q_k\right)-\sum_{i=1}^{n}F_{ji}^{T}\tilde{C}_i+\beta(Q_j-\tilde{Q}_j)=0\,.$$

令　　$F=[F_{ij}]$，$Q=[Q_j]^T$，$\tilde{C}=[\tilde{C}_i]^T$，$\tilde{Q}=[\tilde{Q}_j]^T$，

則上式可化成下式之矩陣方程式

$$F^TFQ-F^T\tilde{C}+\beta(Q-\tilde{Q})=0\,,$$

或

$$Q=(F^TF+\beta J)^{-1}(\beta\tilde{Q}+F^T\tilde{C})\,. \qquad 〔6〕$$

式中 J 爲單位矩陣。〔6〕式所得之Q即爲利用觀測濃度校正後的佳化污染源强度值，而佳化濃度分佈可由〔6〕式之Q代之〔5〕式而得。

做佳化的目的是希望C與$\tilde{C}$完全相合，同時Q中的元素與$\tilde{Q}$中的元素相差愈小愈好。但從〔6〕式可看出，β 愈大，Q受$\tilde{Q}$的影響增大，β 愈小，Q受$\tilde{C}$的影響增大。即 β 愈大時，Q與$\tilde{Q}$的相差愈小，而 β 愈小，C與$\tilde{C}$愈接近。

如果强令C一定要完全等於$\tilde{C}$，而不管Q要做如何的變動，即令〔6〕式中的 β 等於 0，將會造成量測站的 C_i 雖然與 $\tilde{C}_i$ 完全相同，但 Q 中的元素不得不有些成爲負值，以符合 Q_j 有影響的低濃度測站觀測值，這樣在測站濃度誤差是很小了，却會出現不少的 Q_j 負值，負的 Q_j 在實際應用上並無意義，把這些 Q_j 代入高斯模式去求網格點的濃度分佈時，一定會有負的濃度值產生，不符合實際的狀況。β 的加入便可一方面佳化C一方面兼顧 Q 的變動，即恰使 Q 中的元素全爲正值之 β 值即爲本文所謂的最佳 β 值。此 β 值可以反覆法（Iteration）求得。

叁、大氣擴散模式

一般常用之大氣擴散模式皆緣於 Pasquill (8)，此模式經過 Gifford (9)，Martin & Tikvart (10)等人的改良後，成爲 Air Quality Display Model（簡稱爲 AQDM 模式）(11)，而廣泛應用於城市，工業區及工廠附近環境空氣品質的評估。

此模式主要係假定一個污染源，連續排放的污染物，在大氣中經紊流的擴散與稀釋作用，終將達到一個平衡狀態，此時污染物的濃度，在垂直於風向之截面上形成雙向高斯常態分布，由於紊流的擴散及稀釋作用與風速、風向及大氣熱力結構有

關，而大氣熱力結構概要可爲溫度、穩定度及混合層高度所描述。因此爲確實模擬污染物在大氣中的擴散現象，模式中的係數及標準偏差應爲風速、風向、溫度、穩定度及混合層高度的函數。其中常態分布函數的標準偏差與穩定度與下風距離的關係採用 Parquill ⑿之關係曲線。

由於高雄地區二氧化硫的污染源百分之九十爲點源，故本文僅以點排放源求取月平均污染物濃度分佈，所使用的模式係綜合 ADQM，Turner 等人⒀與 Busse & Zimmerman ⒁等大氣擴散模式並給與適當之修正。據此，某一點的污染濃度 C_i 可以下式求得：

$$C_i = \frac{16}{2\pi} \sum_{m=1}^{N} \sum_{IV=1}^{6} \sum_{IL=1}^{6} \sum_{IT=1}^{8} \frac{Prob(K, IV, IL, IT) Q_m S(X_m, O; U_{IV}, IL)}{X_m} \qquad 〔7〕$$

式中各符號之定義如下：

C_i ：第 i 個測量點的平均污染物濃度。

m ：排放源個數的編號。

N ：排放源的總數。

IV ：風速的級數，共分爲六級。

IL ：穩定度的級數，共分爲六級。

IT ：溫度的級數，本文分爲八級。

Prob (K, IV, IL, IT)：發生第K個風向，第 IV 級風速，第 IL 級穩定度，第 IT 級溫度的概率。

Q_m ：第m個排放源的強度值。

X_m ：第m個排放源與量測點的距離。

U_{IV} ：第 IV 級風的代表風速。

σ_z ：Z 軸方向污染物濃度的標準偏差。

H ：煙流的有效高度。

$T^1/_2$ ：污染物在空氣中的半生期。

L ：混合層的高度。

〔7〕式中之 S，當 $\sigma_z \leqq 0.8$ L，或 $\sigma_z > 0.8$L，分別爲

$$S(X_m, O; U_{IV}, IL) = \frac{2}{\sqrt{2\pi}\, U_{IV}\, \sigma_z} \exp\left[-\frac{1}{2}\left(\frac{H}{\sigma_z}\right)^2\right] \exp\left(\frac{-0.692 X_m}{U_{IV}\, T^1/_2}\right)$$

或

$$S(X_m, O; U_{IV}, IL) = \frac{1}{U_{IV} L} \exp\left(\frac{-0.692X_m}{U_{IV} T^{1}/_{2}}\right).$$

當煙塵離開煙囪後，由於高熱浮力與初動量，煙塵會往上衝出一段 Δh 距離，然後才會在與其周圍的空氣具有相同溫度、速度下進行擴散。衝出的距離加上煙囪的實際高度，稱爲煙囪的有效高度。即

$$H = h + \Delta h$$

式中 H：煙囪的有效高度。

h：煙囪的實際高度。

Δh：煙流上衝的高度。

本文對於 Δh 的計算是依 Briggs 的 $^{2}/_{3}$ 定律求得[15]，即

$$\Delta h = 1.6B^{\frac{1}{3}}U^{-1}X^{\frac{2}{3}}, \quad X \leqq 3.5X^*$$

$$\Delta h = 1.6B^{\frac{1}{3}}U^{-1}(3.5X^*)^{\frac{2}{3}}, \quad X > 3.5X^*$$

式中

$$X^* = 14B^{\frac{5}{8}}, \quad B \leqq 55$$

$$X^* = 34B^{\frac{2}{5}}, \quad B > 55$$

$$B = gV_s R_s^2 [(T_s - T_a)/T_s]$$

g：重力加速度。

V_s：煙塵出口的速度。

R_s：煙囪的內徑。

T_s：煙塵的平均溫度。

T_a：煙囪周圍大氣的溫度。

U：風速。

X：排放源到量測點間的距離。

本文所欲求取者爲民國六十五年六月份二氧化硫的月平均濃度分佈，在進行濃度分佈的計算時，將風向分爲16個方向，每一風向的範圍爲22.5°。風速分爲 6級，每級的風速範圍與代表風速如表(一)所示。穩定度依 Stoner [16]分爲六級由風向偏差求得。而 σ_z 則取自 Turner [12]。

本文氣象資料來自梁、呂[17]，其煙囪有效高度處的風速，係依地球邊界層的冪次律求得，而冪次值是依據東港探空資料，對不同穩定度分類分析獲得。混合層高度則是依據 Holzworth 法，利用東港探空資料，對露點差異作回歸分析獲得。

表一、風速等級分類及各級的代表風速值

級	風速範圍 (米／秒)	代表風速值 (米／秒)
1	0.0— 1.5	0.75
2	1.6— 3.3	2.45
3	3.4— 5.4	4.40
4	5.5— 7.9	6.70
5	8.0—10.7	9.35
6	10.7—13.8	12.30

在〔7〕式求月平均濃度中，有一污染物半生期 $T^1/_2$，根據 Weber 發表的論文⑱指出此值隨著天氣狀況的不同而異，SO_2 的半生期大約是在20分鐘到 1個小時的期間，Busse 等人⑭將 SO_2 的半生期假設爲30分鐘，本文亦假設 SO_2 的半生期爲30分鐘。

本文將待測的高雄地區割分爲多個小網格點，以Y軸指向正北，X軸指向正東，每一小網格點的邊長爲 1 公里，涵蓋的區域在Y軸方向爲28公里，X軸方向爲15公里，所以總共有 420 個小網格點，如圖㈠所示。由於本文主要注重高雄地區 SO_2

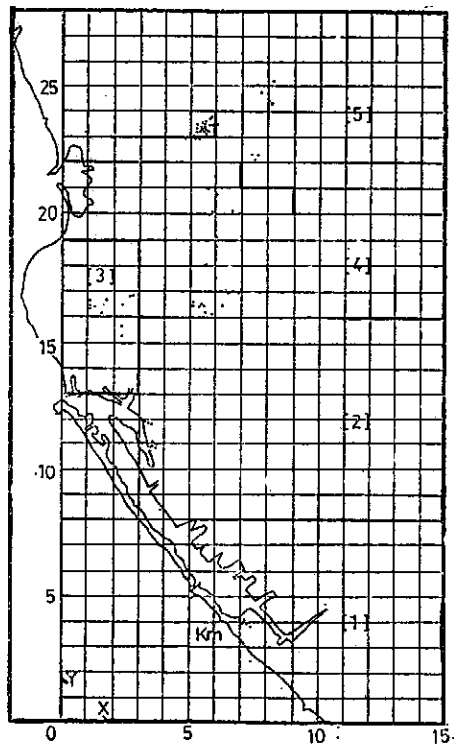

圖一：高雄地區79個排放源分佈狀況與分區方位圖。方括弧內的數字爲分區區號，橫座標爲Y軸（向東），縱座標爲X軸（向北）。

的濃度分佈狀況，因此對於海面上各網格點的濃度值並沒有加以求取。此地帶在濃度分佈圖上的座標爲X軸方向小於 3 公里及Y軸方向小於 7 公里。

排放源資料是得自前「臺灣地區公害防治先驅計畫工作專案小組」在高雄地區調查的結果。包括排放源所在的位置坐標，煙囪的高度，煙口的面積，排出的氣體體積，煙口排出氣體的溫度及排放源 SO_2 的强度值。

量測站濃度觀測資料亦得自前「臺灣地區公害防治先驅計畫工作專案小組」（行政院衛生署）在高雄地區量測的結果，包括量測站的位置及 SO_2 濃度觀測值。測定 SO_2 濃度使用的方法是鉛燭法，原資料的濃度值單位爲 $mgSO_3/100cm^2\ PbO_2/30$ days，本文根據附於原資料的廻歸方程式，將此單位換算爲月平均 ppm。

本文共集有 243 個點排放源，如果全部排放源都放入電腦程式計算，所求出的濃度分佈，當然是最能接近實際的濃度分佈，但如此將會佔用甚多的電腦時間，很不經濟；本文選取總點排放源80%的污染源來計算高雄地區的 SO_2 濃度分佈，由

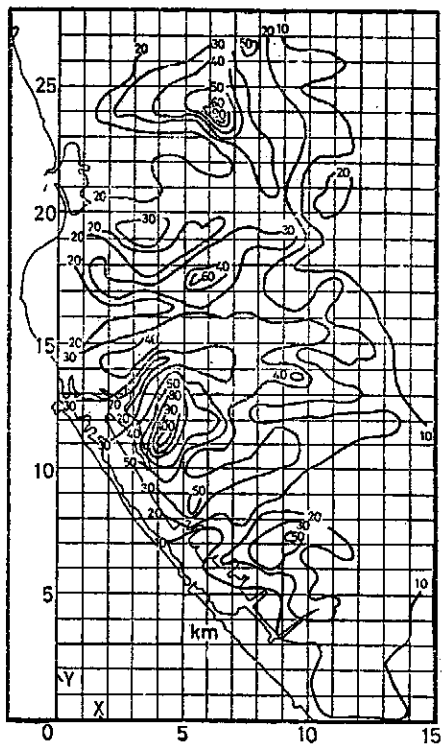

圖二：六十五六月高雄地區實際測定的二氧化硫月平均濃度分佈狀況（鉛燭法）。等值線區間爲 10mg $So_3/100cm^2\ PbO_2/30$ days 乘上 0.001 後約爲 1 ppm。

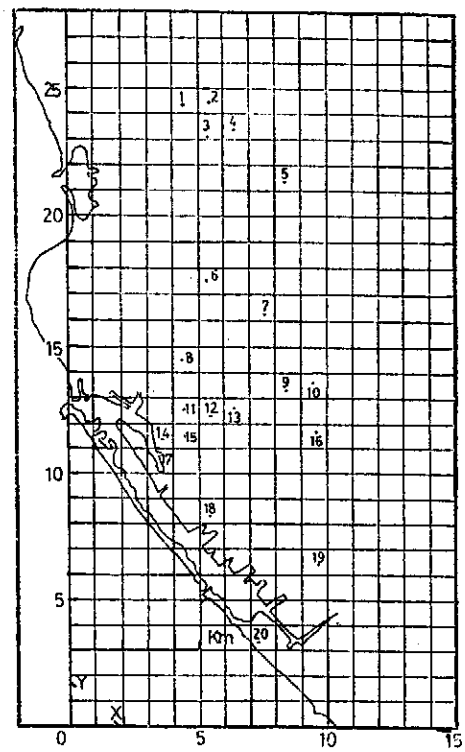

圖三：高雄地區用來作佳化評估的20個二氧化硫（鉛燭法）測定站分佈狀況。

於高雄地區 SO_2 的大排放源常集中在相近的地方，比如大林及南部兩個火力發電廠就佔了 SO_2 年排放量的 72.8 (1)，如果照排放源排放 SO_2 量的大小順序來選取80%總點排放量的排放源，則計算出的濃度分佈將會偏於一邊，在距離排放源相當遠處的濃度值將會發生少估的現象，因此本文依排放源集中的狀況，從南向北分爲五區，每區選取80%至85%的排放源，總共有79個點排放源。

對於量濃站濃度觀測值，本文根據實測的濃度分佈圖（如圖㈡）採取其中最具代表性的 20 個測站數值來做佳化。這些測站的位置分佈如圖㈢所示。

肆、佳化評估與佳化偵測網

1. 未佳化的濃度分佈

圖㈣是使用六十五年六月份的氣象資料所求出的未佳化濃度分佈圖，其型態與實測圖（參考圖㈡）有相當大的出入，除北部的高濃度區與實測圖一致外，其餘均

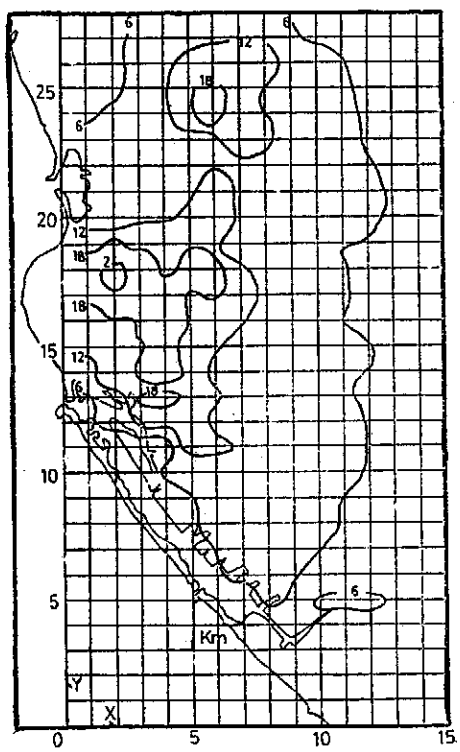

圖四：穩定度未減的高雄地區六十五年六月二氧化硫未佳化月平均濃度分佈圖。等值線區間爲 6×10^{-3} ppm。

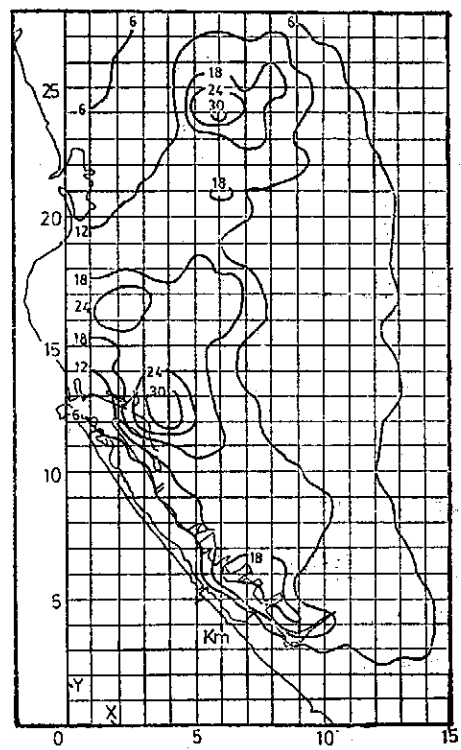

圖五：穩定度降低一級的高雄地區六十五年六月二氧化硫未佳化月平均濃度分佈圖。等值線區間爲 6×10^{-3} ppm。

有顯著的不同。鑑於都市地區由於較大的地面粗糙度及熱島效應，使得都市地區常較郊區不穩定，白天穩定度總在二、三級，而晚上則在四、五級[12]，從六月份的氣象資料來看〔參考表一〕，穩定度爲六級的佔了 53.5%，顯然由都市近郊的氣象資料求出的穩定度並不合於都市上空的實際穩定度狀況，因此本文進行將穩定度降低做比較，圖(五)爲穩定降低一級而其他氣象狀況不變的濃度分佈圖，與沒有降低的濃度分佈比較，發覺原在（3，5，13）的高濃度區向南方擴大，同時在數值上也比穩定度未減的濃度分佈增大，另外穩定度減一的分佈圖在南部（7.5，6）處顯出了一個高濃度區，這是穩定度未減的圖所沒有，而與實測濃度分佈的南部高濃度區有良好的相關與對應。

雖然穩定度降低一級後，模式所計算出的濃度分佈圖形與實測濃度分佈頗相似，但其濃度值却小甚多。此係由於所選的點排放源並不是 243 個總點源全部，而且 243 個總點源也不會是整個高雄地區的所有排放源，有些地方性的排放源很可能在調查時被忽略掉，而其污染效應却往往不容忽視。另外有些因素也可能造成模式計算出來的濃度偏低，如氣象狀況在實際上並不是均勻狀態，其擾亂度較大，促成污染物傳播不遠，而污染物在都市內由於高樓的阻擋往往無法擴散，再加上建築物有下衝（Downwash）的效應，且工廠自定的排放源强度數值一般都會比其實際排放的爲低，在都市地區更還有交通車輛排放出來的 SO_2，由於不會擴散太遠，造成地面量測濃度的加高，這些均有可能使模式的計算值較實際量測的爲低。

2. 佳化的通性

由於未佳化的模式計算結果與實測值相較，令人頗不滿意，顯示出佳化的必要性。佳化的過程是將具代表性的二十個測站的濃度測定值與七十九個排放源觀測（或調查）值代入〔6〕式中，以求得佳化排放量，有此佳化排放量便可借〔5〕式求得佳化濃度分佈。在佳化的過程中，對應於每一個 β^* 值皆有一組佳化排放值，利用反覆法便可求得恰使佳化排放值皆爲正值的 β^* 值，此 β^* 值與其對應的佳化排放值便是所求之解，圖(六)便是佳化過程中 β^* 變化的情形。圖中實線爲總誤差，虛線爲濃度誤差（分別爲〔2〕式中之 I 與右邊第一項之值），兩曲線間的差距爲排放源强度誤差乘以 β^* 值。從圖可以看出，總誤差或濃度誤差均隨著 β^* 的變小而減小；而且 β^* 值很大或很小時，總誤差或濃度誤差都會趨於一個定值，β^* 值愈大，Q_j 愈接近 $\tilde{Q}_j$。

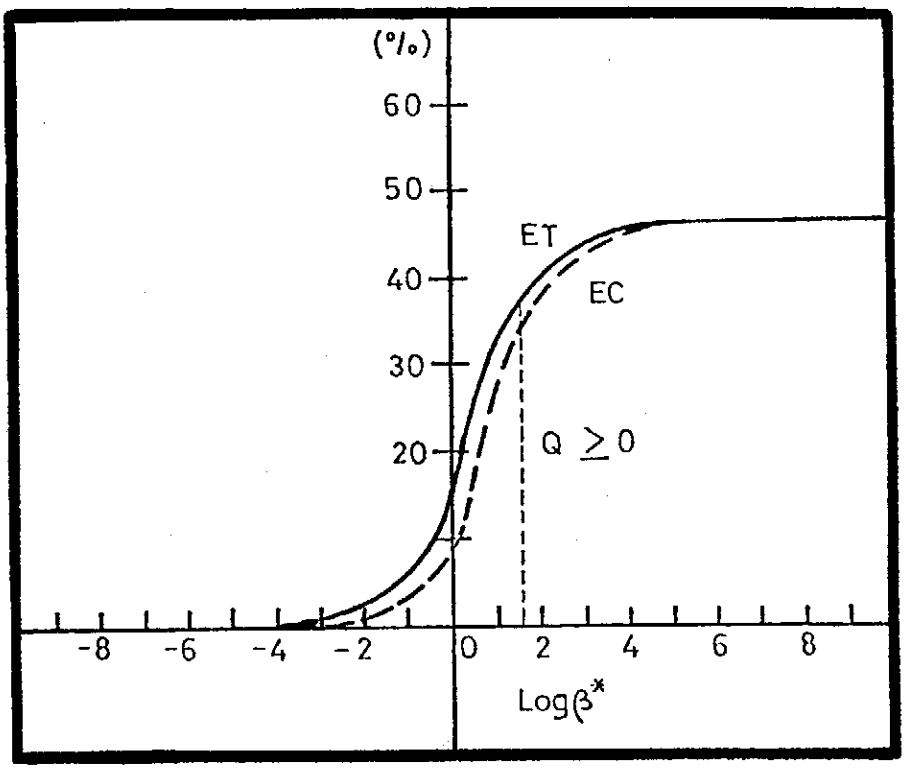

圖六：佳化過程中 β^* 與全誤差，ET，及濱度誤差，EC，的函數變化情形。虛線右邊爲Q值爲正區域，虛線處爲恰使Q值爲正處。

由佳化理論(7)可推知總誤差爲 β^* 的單向逐增函數，亦即 β^* 愈小，I 值愈小，其最小值發生在 β^* 爲零處，而最大值發生在Q與$\tilde{Q}$相等時，此時總誤差爲未佳化模式濃度值與測定濃度值的誤差平均和，換句話說，佳化解的誤差絕不大於未佳化的模式值。由圖(六)可看出總誤差確爲 β^* 的單向逐增函數，當 β^* 愈小時，其值亦愈小，就實際應用而言，當 β^* 小至 10^{-4} 時，總誤差已可視之爲零。當 β^* 漸大時，總誤差值亦漸增大，當 β^* 大至 10^5 時，總誤差已漸趨近於一定值，此一定值爲未佳化模式濃度值與測定濃度值之平方和，此時約爲 0.48。當 β^* 爲 41.5時，佳化排放值恰全爲正值，此時總誤差約爲 0.36。

3. 佳化濃度分佈

由於所選的七十九個排放源並不能代表全部污染源，使得未佳化模式值遠比實測濃度值爲低，就20個測定站而言兩者之平均比值爲 2.19。爲使模式值具有良好的代表性，佳化前先將各排放源的排放值分別乘以 2.19，然後將放大後的排放值與20個測定站的實測值置入佳化的程式中，所得的最佳 β^* 值爲 469，而總誤差則降爲

0.18，如此所得的佳化濃度分佈如圖(七)所示。

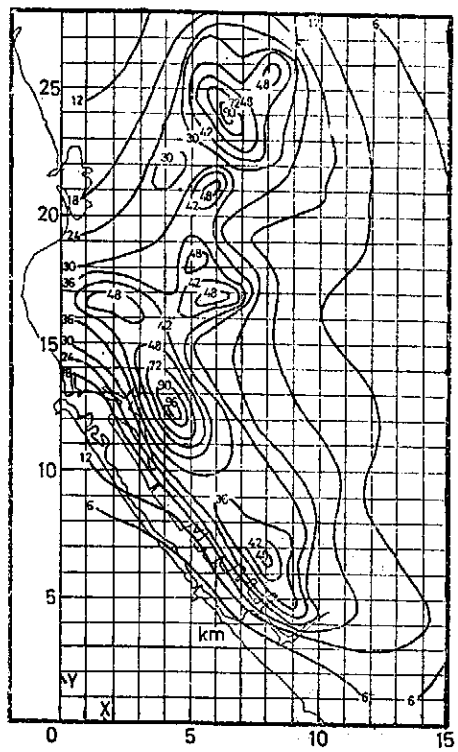

圖七：六十五年六月高雄地區二氧化硫的佳化月平均濃度分佈狀況。等值線單位爲 1×10^{-3} ppm。

由圖(七)可看出，最重要的三個高濃度污染中心分別位於北方（6，24），西岸（4，11.5）與南部地區（8，6），此三中心與實測濃度分佈圖相比較，不只位置極其相符，且濃度值亦極相近。其他各次要高濃度中心與實測濃度相比較亦皆互相對應且濃度值亦極相近。

4. 濃度分佈與測偵網之關係

在從事高雄地區污染評估前需先進行排放源影響區域的探討。爲簡便計，依 Holland 的公式(12)計算各污染源煙流的平均上衝高度 Δh：

$$\Delta h=\frac{V_s R_s}{U}\left(1.5+2.68\times10^{-3}\ P\frac{T_s-T_a}{T_s}R_s\right) \qquad [17]$$

Δh ：煙塵離開煙囪口後往上衝的距離，公尺。

V_s ：煙塵的出口速度，公尺／秒。

R_s ：煙囪的內徑，公尺。

U ：風速，$\frac{公尺}{秒}$。

P ：大氣壓力，毫巴。

T_s ：煙囪的平均出口溫度，°K。

T_a ：煙囪周圍大氣的溫度，°K。

其中風速採用最常發生的二級風（大約是平均風速級，參考表㈠），其代表風速爲 2.45$\frac{公尺}{秒}$。將 Δh 加上煙囪的實際高度後，得出煙囪的有效高度，取第四級穩定度爲計算的穩定度，且定最大濃度的 5%處爲煙塵的邊緣，由⑿的圖可查得某一風向的最大濃度發生地點及其與排放源的距離。因各種風向發生的概率不同，爲簡化起見，只做出四個最常發生的風向，即風向 7，8，14，2，此四風向的發生概率均約在10%，所以依上法求出風向發生概率10%的下風方向最大濃度發生處及10%風向發生概率的排放源影響邊緣，列於表㈡，再由此表以及測站位置圖（圖㈢）、排放源編組圖（圖㈣）作出排放源就測站的影響表（表㈢），其原則是只要測站是在排放源編組的影響範圍內，就列爲該排放源編組有影響的測站。

依此結果可看出測站 1，10，13，16，19，20 受已選用排放源在四個最常發生風向的影響並不重大，因此 9，10 站附近在實測圖上的高濃度區，應該是受未知的排放源或其他因素所造成。另外測站2，3均受到相同排放源的影響，因此實際上此二站中只須設立一站便可瞭解排放源的傳播情形。測站 8，11，12 也是只須設立一站即可。

但在排放源編組最大濃度交疊發生處則應設立測站，如（4～5，10～11）爲排放源編組 2，3，4 組的交疊影響區域，應設立性質優良的觀測站；（3～4，13～15）爲 2，3，6 組的影響區域也應設立良好的測站；而在三、四、五區，如果排放源傳播的距離不遠，測站的設立不能離排放源太遠，如此則當某一測站的濃度變動大時，影響此測站排放源必然有所變動，對於空氣污的防治及管制上很有助益。

因此就表㈢與以上的討論可知，欲偵測本文所使用的79個排放源所產生的污染實際僅需20個測站中的 7 個即可，換句話說，其中十三個測站並未能提供更多的資訊。由此可見良好的測站位置實具有極高的效用並可節省可觀的人力與物力，設站前不可不詳加評估。

表二、排放源編組及影響圈

排放源的編組	每組包含的排放源之排名	煙塵上衝距離 (Δh) (m)	有效煙囪高度 (H) (m)	每組的總排放源 (g/sec)	最大濃度發生處 (下風距離) (km)	排放源影響邊緣 (下風距離) (km)
1	1, 2, 3, 4	160	269	6481	14.00	26.00
2	7, 8, 9, 10	48	106	1215	3.00	9.50
3	12, 14, 15	22	59	337	1.20	3.10
4	13	38	86	120	2.20	6.00
5	160	47	82	2	2.10	5.80
6	54, 99	11	46	19	0.94	2.20
7	46, 71, 134, 148	3	20	34	0.35	0.85
8	125	3	28	4	0.52	1.30
9	157	0	7	2	0.12	0.27
10	109	1	16	5	0.25	0.54
11	104, 105	1	16	10	0.25	0.54
12	103, 113	3	32	9	0.62	1.40
13	124, 145, 158	4	17	8	0.27	0.60
14	85, 175	2	35	9	0.65	1.50
15	137	0	6	7	0.11	0.25
16	135, 166	5	13	5	0.21	0.45
17	162	5	43	2	0.90	2.20
18	119	2	12	4	0.20	0.40
19	182	3	18	2	0.31	0.70
20	161	8	38	2	0.76	1.70
21	136, 184	2	10	4	0.16	0.40
22	139, 140	13	48	5	1.00	2.60
23	102	1	21	5	0.37	0.82
24	180	5	38	2	0.76	1.70
25	84, 174	8	31	9	0.60	1.30
26	176	4	20	2	0.36	0.85
27	90	1	19	6	0.33	0.80
28	97	2	15	11	0.28	0.54
29	11, 19, 40	15	70	241	1.70	5.00
30	26, 30	7	65	81	1.30	3.40
31	36	7	25	29	0.42	1.00
32	27, 43	11	45	66	0.90	2.20
33	圖上小方塊	23	61	726	1.25	3.30

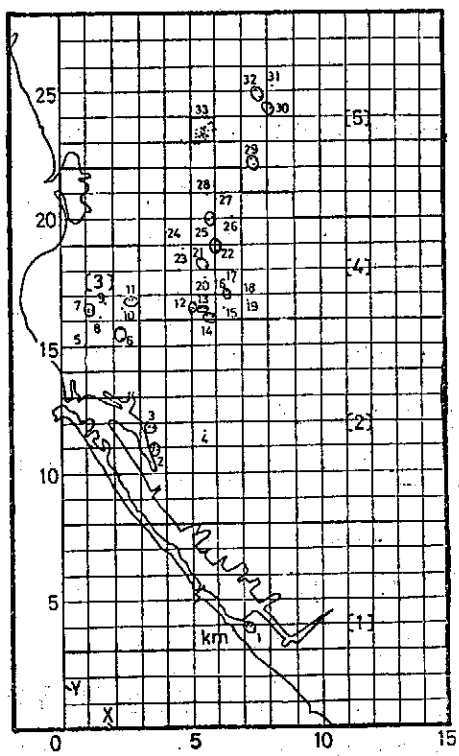

圖八：高雄地區79個排放源編組圖。圖上數字爲組號，方括弧內數字爲分區區號。

表三、排放源對測站影響

測站編號	在四個最大風向下對該測站有影響的排放源之編組	排放源的個數	總量（克／秒）
1			
2	33	22	726
3	33	22	726
4	32, 33	24	792
5	29	3	241.2
6	12, 20	3	11.3
7	17, 19	2	3.8
8	4	1	120.5
9			
10			
11	4	1	120.5
12	4	1	120.5
13			
14	2, 3	7	1552.1
15	3	3	336.8
16			
17	2	4	1215.3
18	1, 2	8	7696.8
19			
20			

5. 高雄地區的污染評估

由於修正佳化的濃度分佈圖與實測圖具有相當的一致性，鑑於佳化尚考慮到排放源的誤差，因此得出的濃度分佈應相當具有代表性，且因能對於選用的排放源加以評估，本文便以此圖做高雄地區 SO_2 分佈污染狀況的評估，對於排放源的最大濃度發生在高濃度區內則視爲主要污染源，對於排放源只是影響邊緣在高濃度區內者則視爲次要污染源。

首先看中心爲（6，24）的高濃度區，由排放源影響圈計算表（表二）可知，此高濃度區主要是受排放源編組第33的總共22個排放源所影響，這個地區絕大多數是中油的排放煙囪，在管制上將比較容易收到齊一的效果，此高濃度區的尖峯值爲 90×10^{-3} ppm 根據六十四年公佈的環境空氣品質標準的許可濃度[19]，一般地區要在 60mg $SO_3/100cm^2$ $PbO_2/30days$ 以下，工業區要在 90mg $SO_3/100cm^2$ $PbO_2/30days$ 以下，換算爲 ppm，即一般地區要在月平均 60×10^{-3} ppm 以下，而工業區要在月平均 90×10^{-3} ppm 以下，如果將此地區規劃爲工業區則尚合乎標準，但此高濃度區的範圍甚大，難免對附近居民的健康有所危害，因此應對此排放源加以削減，大約排放源減少33%，才可使濃度分佈在此區域降低至合乎環境品質的要求。

中心爲(8，25)的高濃度區其尖峯值爲 48×10^{-3} ppm，還合乎環境品質的要求，造成此處成爲高濃度區可能是排放源編組第30，31，32。第30組在發生南南東或南風時，其最大濃度發生於下風距離 1.3 公里，將造成此地區的污染。第31組在發生東北風時其最大濃度發生於下風距離 0.42公里，也是主要污染源。第32組則在吹西北風時，其最大濃度發生於下風距離 0.90公里造成污染較少。在這三組排放源中以第30組的排放源總量爲最多，南南東與南風又均能形成污染，因此第30組排放源(8，25) 處的污染效應最大，對此組排放源好好控制將可減少這一區的污染濃度。

接著是中心爲(5.8，21)的高濃度區，此區的尖峯值爲 40×10^{-3} ppm，合乎環境品質的要求。可能的主要排放源爲編組第28，26，25。其中第28，27組因10%風向發生概率的最大濃度下風距離爲 0.30公里，是本高濃度區的主要污染源；第26組其最大值發生處的下風距離爲 0.36公里，而影響圈的範圍在四個最大風向爲下風距離 0.85公里，將不對此區造成污染；第25組最大值發生處在其下風距雜 0.60公里，其影響圈的範圍爲下風距離 1.30公里 ， 因其排放量不少對於本區應 屬 於主要污染

源。

依次是中心爲（5.2，17.8）的高濃度區，此區的可能影響的排放源有第23組、22組、21組、20組、13組、12組。23組於吹西北風時會形成次要影響，22組於吹東北風時形成主要影響，第21組也是主要的影響源，第12組於吹南風時形成主要影響，第20、13組則不造成影響。

中心爲（5.8，16.5）高濃度區的可能影響污染源爲編組第12、14、15。12組於西北風時造成本區的污染，13組於西北風也會造成本區的污染，14、15組則對本區不造成污染。

中心爲（ 2，16）的高濃度區由於有水泥微粒的作用，在實際上不會造成如此的污染濃度，但可探討排放源對此區的影響狀況，編組第 8 是主要污染源，編組第7因總排放量甚大也應列於重要污染源，編組第6只有一排放源於吹南南東風向時會造成污染，應視爲次要污染源，編組第10於吹東北風向時可列爲次要污染源，第11組排放源則將不對本區造成影響。

中心爲（4.1，11.3）的高濃度區其尖峯值爲 102×10^{-3} ppm，超過環境品質標準，此地區又接近高雄市人口稠密的市中心，應嚴格加以管制，其中排放源編組第3爲臺鋁，編組第 2爲南部火力發電廠。編組第 3於吹西北風向造成本區的主要污染，編組第 2 雖然在吹南與南南東風向時，最大濃度發生在本高濃度區的邊緣，但因其排放量遠高於第 3 組，故亦應注意防範。另外本區因接近市中心，交通車輛排放的 SO_2 不容忽視，很可能也是造成本區高尖峯值的主要影響源。

最後，位於南部的編組第 1 的大林火力發電廠是整個高雄地區最大的排放源，雖然其煙囪高度很大，污染物能擴散很遠，可以獲得相當程度的稀釋，但對於如此大的排放源實在不能加以忽視，否則因氣象狀況的突然改變，造成空氣污染事件，其損失將是非常慘重。

從以上的評估可以看出六月份的高雄地區 SO_2 濃度分佈狀況，有些合乎環境空氣品質標準，有些則超出。對於超出地區的重要影響排放源進行排放源强度的削減，將是刻不容緩的事。而從以上的評估知曉高濃度區的重要影響排放源，於濃度突增或污染防治方面便有跡可尋，可以立即採取應變的措施，以保護高雄地區居民的健康。

五、結　　論

限於經濟與人力，在求一地區的污染物濃度分佈曲線時，往往無法將全部排放源代入程式中計算以求出數值；若依排放源大小取一定的百分率排放源去做計算必須顧慮到所取排放源的分佈是否均勻；分區選取某一百分率的排放源，然後再乘上修正係數，使得所選取的排放源在排放總量上與整個地區的總排放量大約相等，最後予以佳化應是良好的解決辦法。

對於氣象狀況的處理，在都市地區的大氣常較郊區不穩定，因此在作模式計算時，將穩定度級數降低，可得到符合實際狀況的濃度分佈。

在做變微分法佳化的程序中，β^* 及排放源誤差項的加入是必要的，否則雖然在測站方面的校正都很準確了，却造成排放源過大的變動，甚至出現負值，使得整個濃度分佈型態非常的不合理，β^* 的加入可兼顧濃度誤差最小及獲得全爲正值的排放源强度佳化值，如此得出的濃度分佈圖與實際量測圖在分佈型態相當一致，而且數值方面也很接近。修正佳化對於沒設測站的地方可以經由電腦程式計算而得出濃度數值，這種內插就不是一般實測圖的線性內插所可比擬。

本文利用排放源影響圈的範圍對測站進行評估，可找出不受所選定排放源影響的測站，這些測站便可以裁撤。而不受排放源影響的地方地不必設立測站，受同樣排放源影響的不同測站也可取消重複的測站，這樣並不會有損於對排放源傳播情形的了解。至於受多個排放源影響的地帶一定要設立測站，於發生嚴重污染事件時，能獲得可靠的資料，而作防治及控制的決策依據。

在對污染源的評估方面，由污染源的影響圈範圍，找出造成高濃度區的主要污染源及影響較少的次要污染源，可據而決定當爲適合環境品質要求而應減少排放源總量時，其應裁減的排放源順床。

總之，本文在經由佳化濃度分佈曲線的作出與污染排放源影響圈的計算後，希望能提供建立高雄地區空氣污染評估系統的參考，並使對高雄地區污染最嚴重的 SO_2 的影響實況有一個清晰的瞭解，對今後高雄地區執行空氣污染管制及保障住民健康都有實質上的益處。

參 考 文 獻

1. 行政院衛生署，臺灣地區公害防治先驅計畫工作報告，第39—188頁，臺北市，行政院衛生署，（一九七八）。
2. Goldstein, I. F., and L. Landovitz, "Analysis of Air Pollution Patterns in New York City—I. Can One Station Represent the Large Metropolitan Area? II. Can One Aerometric Station Represent the Area Surrounding it?", Atmos. Envir., Vol. 11, pp. 47-57, (1977)
3. Brier, G. W., "Validity of the air quality display model calibration procedure", Enviromental Protection Agency, Rep EPA-R4-73-017, Washington, D. C., (1973).
4. Gustafson, S. A., K. O. Kortanek, and J. R. Sweigart, "Numerical Optimization Techniques in Air Quality Modeling: Objective Interpolation Formulas for Spatial Distribution of Pollutant Concentration", J. Appl. Meteor., Vol. 16, pp. 1243-1255, (1977).
5. Sasaki, Y., "An Objective Analysis Based on the Variational Method," J. Meteor. Soc. Japan, Vol. 36, pp. 77-78, (1958).
6. Helmbach, J. A. and Y. Sasaki, "A Variational Technique for Mesoscale Objective Analysis of Air Pollution", J. Appl. Metero., Vol. 14, pp. 194-203, (1975).
7. 梁文傑，「空氣污染評估的佳化理論」，中國工程學刊，第三卷第二期（待刊中），（一九八〇）。
8. Pasquill, F., Atmospheric Diffusion. John Wiley and Sons, New York. New York. New York, pp. 240-328, (1974).
9. Gifford, F. A., "Use of Routine Meteorological Observations for Estimating Atmospheric Dispersion", Munclear Safety, Vol. 2, pp. 47-51, (1961)
10. Martin, D. and J. A. Tikvart, "A General Atmospheric Diffusion Model for Estimating the Effects on Air Quality of One or More Sources," APCA paper No. 68-148, Washington, D.C., (1968).
11. Air Quality Display Model, U.S. Dept. of Health, Education, and Welfard, U. S. Public Health Service, National Air Pollution Control Administration, TRW System Group, PB189194, Washington, D.C., (1969)
12. Turner, D. B., Workbook of Atmospheric Dispersion Estimates. U. S. Department of Health, Education, and Welfare, Cincinnati, Ohio, (1970).
13. Turner, D. B., J. R. Zimmerman, and A. D. Busses, "An Evaluation of some Climatological Dispersion Models", Proceedings of the Third Meeting of the Expert Panel on Air Pollution Modeling, Paris, (1972).
14. Busse, A. D., and J. R. Zimmerman, User's Guide for the Climatological Dispersion Model. Tech. Rep. EPA-4-73-024, National Environmental Research Center,

Washington, D. C., (1973).

15. Briggs, G. A., "Some Recent Analysis of Plume Rise Observation", Proceedings of the Second International Clean Air Congress, Academic Press, New York, (1971).
16. Stoner, R. R., "Procedures for Reduction of Meteorological Data". Environmental Safegards Division, NUS Corporation, Rockville, Maryland, (1971).
17. 梁文傑、呂世宗，臺灣電力公司候選火力電廠廠址對周圍環境空氣品質之評估。臺灣電力公司委託研究計畫研究報告，中央研究院物理研究所，臺北市，（一九七七）。
18. Weber, E., "Contribution to the Residence Time of Sulfur Dioxide in a Polluted Atmosphere", J. Geophys. Res., Vol. 75, No. 15, pp. 2909-2914, (1970).
19. 行政院衛生署，公害防治法令彙編。臺北市：行政院衛生署，第16頁，（一九七六）。

THE OPTIMIZATION EVALUATION OF SO_2 AIR POLLUTION AND MONITOR NETWORK IN KAO-HSUNG AREA

WEN-JEY LIANG
Institute of Physics, Academia Sinica
and
Department of Mechanical Engineering,
National Taiwan University

CHUNG-TE LEE
Institute of Environment Engineering,
National Taiwan University

Abstract

The optimization theory of air pollution estimation is utilized to investigate the SO_2 pollution in Kao-hsung area. Accordingly, the computed concentration from Gaussian dispersion model and the measured concentration data are combined to find the optimized pollutant source strength and the optimized SO_2 concentration distribution. The field studies of the SO_2 pollution in Kao-hsung area by National Health Administration during September, 1975 to June, 1977 are compared to clarify the plausibility of the optimized results. Employing the optimized results, the influence of pollution sources and the validity of the mornitoring stations of SO_2 are fully discussed, and the optimal mornitor network is also suggested.

TIME-DEPENDET SOLUTIONS OF THE VISCOUS INCOMPRESSIBLE FLOW PAST A CIRCULAR CYLINDER BY INVERSE TRANSFORMATION

L. C. CHIEN (簡 朱 成)

Institute of Physics, Academia Sinca, Taipei, Taiwan

Abstract

Inverse transformation is used to map the infinite domain exterior to the cylinder into an unit circle. The governing equations in terms of the vorticity and stream function are transformed and are solved using a hopscotch finite difference scheme and over relaxation procedure. Viscous layer considered vorticity and stream function obtained by the method of asymptotic expansion to the third order are employed as initial conditions for numerical integration. The time developed of the flow properties are obtained and plotted.

1. INTRODUCTION

The problem of viscous flow around a circular cylinder is a classical one with an extensive literature. Although there has been a large number of numerical computations on the flow over an impulsively started circular cylinder, the existing solutions agree neither quantitively nor qualitatively with one another.

Because the Navier-Stokes equations are non-linear, exact solutions are not available. The numerical method is one of the very few acceptable tools that is capable of making any contribution to engineering designs. Recent developments in high-speed digital computers make this approach both effective and popular. However, every numerical approach for a given physical problem requires both physical assumptions and mathematical approximations. We need to test a numerical method for its accuracy in the developing stage by applying it to a given problem. The flow over an impulsively started circular cylinder at relative low Reynolds numbers is one of the thoroughly investigated problem that can provide the basis for such study to test the numerical accuracy.

Because no analytical solution was the available, Payne (1958), and later others used potential flow as their initial conditions for numerical integration. They computed the vorticity on the cylinder for $t=0^+$ by using the stream function obtained from potential flow theooy. The finite difference formulation assumes a uniform thickness of one grid of vortex sheet around the cylinder. However, the vorticity already diffused 4 or 5 grids away from the cylinder surface for $Re=50$ at $T=0.02$ (Chien, 1977). Therefore, the potential flow started solution is a poor one near the singularity. Physically, the potential

flow started integration of the Navier-Stokes equations does not take into account the initial structure of the flow (Collins and Dennis, 1973). The solution is inaccurate initially. The effect of the inaccuracy on the later time probably leads to the lack of agreement among various investigations.

In this study, the viscus layer considered analytic solution obtained by inner-outer expansion to the third order (Chien, 1977) is used as initial conditions for numerical computation. The inverse transformation is used to map the computational field exterior to the cylinder into a unit circle. The hopscotch method solved the vorticity equation gave the accuracy and save the computer time. And the Poisson equation is solved by successive over relaxation method.

The problem of flow over an impulsively stated cirular cylinder has been investigated both experimentally and theoretically. In the present study, the case of Reynolds number 50 will be used for investigating the accuracy of the numerical method used.

2. MATHEMATICAL FORMULATION

The motion is referred to axes fixed in the cylinder. Consider the unsteady laminar flow of a viscous incompressible fluid with constant properties and subject to negligible body forces, past a circular cylinder of radius a when the flow starts at time $t=0$ with a constant velocity U in the direction of $\theta=0$ as shown in Fgure 1.

The equations of motion and equation of continuity in non-dimensional form in polar coordinates (Schlichting, 1979, p. 67) are

$$\frac{\partial u}{\partial t}+u\frac{\partial u}{\partial r}+\frac{v}{r}\frac{\partial u}{\partial \theta}-\frac{v^2}{r}=-\frac{\partial p}{\partial r}+\frac{1}{Re}\left[\frac{\partial^2 u}{\partial r^2}+\frac{1}{r}\frac{\partial u}{\partial r}+\frac{1}{r^2}\frac{\partial^2 u}{\partial \theta^2}-\frac{u}{r^2}-\frac{2}{r^2}\frac{\partial v}{\partial \theta}\right] \tag{1}$$

$$\frac{\partial v}{\partial t}+u\frac{\partial v}{\partial r}+\frac{v}{r}\frac{\partial v}{\partial \theta}+\frac{uv}{r}=-\frac{1}{r}\frac{\partial p}{\partial \theta}+\frac{1}{Re}\left[\frac{\partial^2 v}{\partial r}+\frac{1}{r}\frac{\partial v}{\partial r}+\frac{1}{r^2}\frac{\partial^2 v}{\partial \theta}+\frac{2}{r^2}\frac{\partial u}{\partial \theta}-\frac{v}{r^2}\right] \tag{2}$$

$$\frac{1}{r}\frac{\partial}{\partial r}(ru)+\frac{1}{r}\frac{\partial v}{\partial \theta}=0 \tag{3}$$

where (r, θ) are polar coordinates, (u, v) the velocity componens in radial and tangential directions, P the pressure and Re is the Reynolds number, based on radius.

The components (u, v) may be expressed in terms of dimensionless stream function $\psi(r, \theta, t)$ by the equations

$$u = \frac{1}{r}\frac{\partial \psi}{\partial \theta}, \quad v = -\frac{\partial \psi}{\partial r} \tag{4}$$

where the equation of continuity (1) is satisfied identically.

By differentiating the equation (1) with respect to θ, the equation (2) with respect to r and then eliminating between them the common term $\partial^2 P/\partial r \partial \theta$, we obtain the vorticity transport equation

$$\frac{\partial \omega}{\partial t} + \frac{1}{r}\left[\frac{\partial \psi}{\partial \theta}\frac{\partial \omega}{\partial r} - \frac{\partial \psi}{\partial r}\frac{\partial \omega}{\partial \theta}\right] = \frac{1}{Re}\left[\frac{\partial^2 \omega}{\partial r^2} + \frac{1}{r}\frac{\partial \omega}{\partial r} + \frac{1}{r^2}\frac{\partial^2 \omega}{\partial \theta^2}\right] \tag{5}$$

with
$$\omega = \frac{1}{r}\left[\frac{\partial (ru)}{\partial r} - \frac{\partial v}{\partial \theta}\right]. \tag{6}$$

Using equation (4) and (6), one obtains

$$\omega = \frac{\partial^2 \psi}{\partial r^2} + \frac{1}{r}\frac{\partial \psi}{\partial r} + \frac{1}{r^2}\frac{\partial^2 \psi}{\partial \theta^2} \tag{7}$$

The boundary conditions imposed upon the cylinder surface are the usual impermeability and no slip condition for all time,

$$\psi = \frac{\partial \psi}{\partial r} = 0, \quad \text{when} \quad r = 1. \tag{8}$$

On the surface of the cylinder, the stream function is zero, $\psi_{ij} = 0$, where i and j denote the locations in the θ and r directions, respectively. The stream function inside the cylinder surface, $\psi_{i,w-1}$, is assumed to be the mirror of the stream function around the cylinder, $\psi_{i,w+1}$, because of the zero gradient (Lin, Pepper and Lee, 1976; Roach, 1976). Consequently, the values of the vorticity on the surface of the cylinder can be written as

$$\omega_{i,w} = = \frac{2(\psi_{i,w+1} - \psi_{i,w})}{\Delta r^2}. \tag{9}$$

As the distance from the cylinder becomes very large, it is assumed that the flow will approach more and more that of a uniform stream (Son and Hanratty, 1969; Deffenbaugh and Marshall, 1976). Meta and Lavan (1975) considered the flow at the far boundary is constrained with the first-order differential equation obtained from the Navier-Stokes equations by dropping the tangential derivative of the pressure and viscous terms, i.e. at the outer boundary, the inertial terms are dominant

$$\frac{\partial \omega}{\partial t} = -\frac{1}{r}\left[\frac{\partial \psi}{\partial \theta}\frac{\partial \omega}{\partial r} - \frac{\partial \psi}{\partial r}\frac{\partial \omega}{\partial \theta}\right]. \tag{10}$$

And the stream function at the outer boundary is obtained by

$$\frac{\partial \psi}{\partial \rho} = -\frac{v}{\rho^2}, \tag{11}$$

where $\rho = r^{-1}$, and the velocity v is obtained by

$$\frac{\partial v}{\partial t} = -\left[\frac{1}{2r}\frac{\partial(u^2+v^2)}{\partial\theta} + u\omega\right] . \tag{12}$$

Since it is desirable to have a finer mech near the cylinder surface, Collins and Dennis (1973) took modified polar coordinates (ζ, θ) where $\zeta = \ln(r)$. In this study, the inverse transformation has been made, $Z = 1/\omega$, where $Z = x + iy = re^{i\theta}$ and $\omega = \rho e^{i\alpha}$, i.e.

$$r = \rho^{-1} , \qquad \theta = -\alpha . \tag{13}$$

Meta and Levan (1975) used the transformation mapped the exterior of the airfoil into a unit circle. We took the same transformation mapped the exterior of the cylinder into a unit circle. The computation domain is confined into $\rho_o \leq \rho \leq 1$. The domain bounded by $0 \leq \theta \leq 2\pi$ and $\rho_o \leq \rho \leq 1$ is transformed into a rectandular (Figure 2). If $\rho_o = \Delta\rho = 0.02$, one took 50 points in radial direction and got the domain of $1 \leq r \leq 50$, with finer grids near the cylinder surface. The defining equations (4), (5) and (7) then become

$$u = -\rho\frac{\partial\psi}{\partial\alpha} , \qquad v = \rho^2\frac{\partial\psi}{\partial\rho} , \tag{14}$$

$$\frac{\partial\omega}{\partial t} + \rho^3\left[\frac{\partial\psi}{\partial\alpha}\frac{\partial\omega}{\partial\rho} - \frac{\partial\psi}{\partial\rho}\frac{\partial\omega}{\partial\alpha}\right] = \frac{1}{Re}\left[\rho^4\frac{\partial^2\omega}{\partial\rho^2} + \rho^3\frac{\partial\omega}{\partial\rho} + \rho^2\frac{\partial^2 w}{\partial\alpha^2}\right] , \tag{15}$$

$$\frac{\partial^2\psi}{\partial\rho^2} + \frac{1}{\rho}\frac{\partial\psi}{\partial\rho} + \frac{1}{\rho^2}\frac{\partial^2\psi}{\partial\theta^2} = \frac{\omega^2}{\rho^4} . \tag{16}$$

The flow will be assumed to remain symmetrical about the front direction of the motion of the cylinder. Hence both the stream function ψ and vorticity ω are antisymmetrical about $\theta = 0$, i.e.

$$\psi = \omega = 0 \qquad \text{at} \quad \theta = 0 . \tag{17}$$

The boundary conditions on the surface of the cylinder, equations (8) and (9), are

$$\psi = \frac{\partial\psi}{\partial\rho} = 0 , \tag{18}$$

and

$$\omega_{i,w} = \frac{2(\psi_{i,w+1} - \psi_{i,w})}{\Delta\rho^2} , \qquad \text{at} \quad \rho = 1 . \tag{19}$$

The far field boundary conditions are

$$\frac{\partial\omega}{\partial t} = -\rho^3\left[\frac{\partial\psi}{\partial\alpha}\frac{\partial\omega}{\partial\rho} - \frac{\partial\psi}{\partial\rho}\frac{\partial\omega}{\partial\alpha}\right] , \tag{20}$$

$$\frac{\partial\psi}{\partial\rho} = \frac{v}{\rho^2} \tag{21}$$

and
$$\frac{\partial v}{\partial t} = -\left[\frac{1}{2}\rho\frac{\partial(u^2+v^2)}{\partial\theta} + u\omega\right] . \tag{22}$$

The quantities C_f and C_p are the friction and pressure drag coefficients. These coefficients together is the drag coefficient C_D, defined by $C_D = D/\rho U^2 a$, where D is the total drag. It is shown that

$$C_D = \frac{1}{Re}\int_0^{2\pi}\left(\omega + \frac{\partial\omega}{\partial\rho}\right)_{\rho=1}\sin\theta\ d\theta \tag{23}$$

where the first term in the integral corresponds to the friction drag coefficient and the second to the pressure drag coefficient.

3. NUMERICAL FORMULATION

The finite difference scheme is used to solve the vorticity equation (15) and stream function equation (16). Central differencei for space derivatives are used in the domain of calculation and at the outer boundary wherever possible. The domain bounded by $0 \leq \theta \leq 2\pi$ and $\rho_o \leq \rho \leq 1$ is divided into a rectangular network (Figure 2). The increments in θ, ρ and t are specified by $\Delta\theta$, $\Delta\rho$ and Δt with i, j and n as the correcponding indices. The scheme advances the solution from time $n\Delta t$ to time $(n+1)\Delta t$ consisting of calculating new values of the vorticity, ω_{ij}^{n+1} at all points via the vorticity equation (15) by finite difference approximation of the boundary conditions, the values of the vorticivy ω_{ij}^n and the stream function ψ_{ij}^n from the previous time step.

Hopscotch method, developed by Gourley (1970), is used to compute the vorticity at the new step. The method divides each time step calculation into two sweeps of the mesh. In the first and the subsequent oddnumber time steps, the points with i+j equal to odd are calculated based on the current values of neighboring points. For vorticity equation (15), the vorticity at the (n+1) time step ω_{ij}^{n+1} is give by

$$\omega_{i,j}^{n+1} = \omega_{i,j}^n + \Delta t\left[-\rho_j^3\left(\frac{\psi_{i+1,j}^n - \psi_{i-1,j}^n}{2\Delta\alpha}\,\frac{\omega_{i,j+1}^n - \omega_{i,j-1}^n}{2\Delta\rho} - \frac{\psi_{i,j+1}^n - \psi_{i,j-1}^n}{2\Delta\rho}\,\frac{\omega_{i+1,j}^n - \omega_{i-1,j}^n}{2\Delta\alpha}\right)\right.$$
$$\left. + \frac{1}{Re}\left(\rho_j^4\frac{\omega_{i,j+1}^n + \omega_{i,j-1}^n - 2\omega_{i,j}^n}{\Delta\rho^2} + \rho_j^3\frac{\omega_{i,j+1}^n - \omega_{i,j-1}^n}{2\Delta\rho} + \rho_j^2\frac{\omega_{i+1,j}^n + \omega_{i-1,j}^n - 2\omega_{i,j}^n}{\Delta\alpha^2}\right)\right]$$
$$\text{for}\quad i+j = \text{odd} \tag{24a}$$

The Second sweep at the same time level, the points of i+j equal to even is computed using the new values of the neighboring points obtained in the first sweep,

$$\omega_{i,j}^{n+1} = \omega_{i,j}^n + \Delta t\left[-\rho_j^3\left(\frac{\psi_{i+1,j}^n - \psi_{i-1,j}^n}{2\Delta\alpha}\,\frac{\omega_{i,j+1}^{n+1} - \omega_{i,j-1}^{n+1}}{2\Delta\rho} - \frac{\psi_{i,j+1}^n - \psi_{i,j-1}^n}{2\Delta\rho}\,\frac{\omega_{i+1,j}^{n+1} - \omega_{i-1,j}^{n+1}}{2\Delta\alpha}\right)\right.$$
$$\left. + \frac{1}{Re}\left(\rho_j^4\frac{\omega_{i,j+1}^{n+1} + \omega_{i,j-1}^{n+1} - 2\omega_{i,j}^{n+1}}{\Delta\rho^2} + \rho_j^3\frac{\omega_{i,j+1}^{n+1} - \omega_{i,j-1}^{n+1}}{2\Delta\rho} + \rho_j^2\frac{\omega_{i+1,j}^{n+1} + \omega_{i-1,j}^{n+1} - 2\omega_{i,j}^{n+1}}{\Delta\alpha^2}\right)\right]$$
$$\text{for}\quad i+j = \text{even} \tag{24b}$$

The first sweep consists of forward-time-contral-space differencing for the points of i+j odd, whilst the second sweep is fully implicit in the sense that the new values are required at (i, j), (i±1, j) and (i, j±1) but this implicitness involving no simultaneous algebraic solutions.

The stream function for the new time step $\psi_{i,j}^{n+1}$ is computed by the use of finite-diffence approximation of the stream function equation (16), the boundary conditions, the new values of vorticity $\omega_{i,j}^{n+1}$ and the old values of the stream function $\psi_{i,j}^{n}$. The most popular numerical method solving this elliptic equation is the successive over-relaxation method. The values of $\psi_{i,j}$ at the (n+1) th time step and the (k+1) th iteration were calculated by using the following relation

$$\psi_{i,j}^{k+1} = \psi_{i,}^{k} + \frac{\alpha}{2(1+\frac{\beta^2}{\rho_j^2})}\Big[\psi_{i,j+1}^{k}+\psi_{i,j-1}^{k}+\frac{\beta}{2\rho_j}(\psi_{i,j+1}^{k}-\psi_{i,j-1}^{k})$$

$$+\frac{\beta}{\rho_j^2}(\psi_{i+1,j}^{k}-\psi_{i-1,j}^{k})-2(1+\frac{\beta^2}{\rho_j^2})\psi_{i,j}^{k}-\frac{\Delta\rho^2}{\rho_j^4}\omega_{i,j}\Big] \qquad (25)$$

where $\beta=\Delta\rho/\Delta\alpha$, α is the over-relaxation factor. The successive over relaxation method consists of applying (25) at every internal mesh point in regular succession. The points are scanned row from left to right starting from the row next to the cylinder surface $\rho=1$ going up to the far field. This completes one iteration. The procedure is repeated until values of the stream function in two successive iterations satisfies the equation

$$\left|\frac{\psi_{i,j}^{k+1}-\psi_{i,j}^{k}}{\psi_{i,j}^{k+1}}\right| \leq 0.01 \ , \qquad (26)$$

at all interior grid points. The trancation error for the stream function equation (16) is $O[(\Delta\rho)^2+(\Delta\alpha)^2]$.

In the far field boundary conditions, (20), (21) and (22), the tangential derivative is replaced by a difference and normal derivative is appoximated by a three-point backward difference. The finite difference form for the vorticity residue at the outer boundary, equation (20), is chosen

$$\omega_{i,N}^{n+1} = \omega_{i,N}^{n} - \frac{\rho_N^3\,\Delta t}{4\Delta\alpha\Delta\rho}[(\psi_{i+1,N}-\psi_{i-1,N})\cdot(\omega_{i,N-3}^{n}-3\omega_{i,N-2}^{n}+3\omega_{i,N-1}^{n}-\omega_{i,N}^{n})$$

$$-(\omega_{i+1,N}^{n}-\omega_{i-1,N}^{n})(\psi_{i,N-3}-3\psi_{i,N-2}+3\psi_{i,N-1}-\psi_{i,N})] \qquad (27)$$

where N is the outer boundary grid number in the radial direction.

The outer boundary stream function is obtained from the finite difference of (21),

$$\psi_{i,N} = \psi_{i,N-2} + \frac{\Delta\rho}{\rho_j^2}\,v_{i,N-1} \qquad (28)$$

where $v_{i,N-1}$ is obtained by (22)

$$v^{n+1}_{i,N-1}=v^{n}_{i,N-1}-\left[\frac{\rho_{N-1}}{4}\frac{(u^{n}_{i+1,N-1})^2+(v^{n}_{i+1,N-1})^2-(u^{n}_{i-1,N-1})^2-(v^{n}_{i-1,N-1})^2}{\Delta\theta}+u^{n}_{i,N=1}\,\omega_{i,N-1}\right] \tag{29}$$

4. COMPUTATIONAL PROCEDURE

The initial values of the stream function and vorticity are obtained at the every grid point by the method of asymptotion expansion to the third order,

$$\begin{aligned}\psi(r,\theta,t)=\Big\{&r-\frac{1}{r}-4\sqrt{\frac{t}{\pi Re}}\left(\frac{1}{r}+\sqrt{\pi}\,\eta\ \mathrm{erfc}\ \eta-\exp(-\eta^2)\right)\\&-\frac{t}{Re}\left[\frac{1}{r}-(6\eta^2+1)\ \mathrm{erfc}\ \eta+\frac{6}{\sqrt{\pi}}\exp(-\eta^2)\right]\\&-2\left(\frac{t}{Re}\right)^{3/2}\left[\left(\frac{16}{3}\eta^3+\eta\right)\mathrm{erfc}\ \eta-\frac{1}{\sqrt{\pi}}\left(\frac{16}{3}\eta^2-\frac{1}{6}\right)\right.\\&\left.\exp(-\eta^2)-\frac{1}{6\sqrt{\pi}}\right]\Big\}\sin\theta\\&+8t\sqrt{\frac{t}{Re}}\left[\int_0^{\eta}f(\zeta)d\zeta-\frac{1}{\sqrt{\pi}}\left(1+\frac{4}{9\pi}-\frac{4\sqrt{2}}{3}\right)\left(\frac{1}{r^2}+2r-3\right)\right.\\&\left.+2\sqrt{\frac{t}{Re}}\int_0^{\eta}g_3(\zeta)d\zeta\right]\sin\theta\cos^2\theta\\&+16t^2\sqrt{\frac{t}{Re}}\left[\int_0^{\eta}F_3(\zeta)d\zeta\ \sin\theta\cos^3\theta-\int_0^{\eta}f_3(\zeta)d\zeta\ \sin^3\theta\right]\end{aligned} \tag{30}$$

where $f(\rho)$, $g_3(\rho)$, $F_3(\rho)$ and $f_3(\rho)$ are polynomials of error function.

Time is stepped by Δt, the new values of the vorticities are computed from (24) with stream function obtained by (30) and vorticity computed from (7). The new values of the stream function are computed by applying over relaxation methond (25) repeatedly until (26) is satisfied. The new values of vorticity at the boundary condition at the boundary condition at the cylinder surface are computed using (19). The new far field boundary values of vorticity and stream function are obtained by (27) and (28). The above precedure is repeated for successive Δt.

5. RESULTS

Calculations were carried out for the grids shown in Fig. 2. The computation domain was chosen with $\theta=0°(3°)360°$, and $\rho=0.02(0.02)1.00$. The grids represented an attempted to achieve the best compromise between the desired flow detail near the surface of the cylinder.

In this study, the case for $Re=50$, i.e. $Rd=100$ is surveyed to check the accuracy compared with the existing numerical solutions by Kawaguti and

Jain (1966), Collins and Dennis (1973) and experimental measurement by Honji and Taneda (1972).

The initial conditions for the numerical integration are the stream function and vorticity at $T=0.02$. The negative vorticity, corresponding to the negative of the stream function, was observed at $T=0.54$ located on the cylinder surface from $\theta=171°$ to 180° at the upper surface and 180° to 189° at the lower, where the angle is measured from the front stagnation point. We can infer that the initial separation time is about $t=0.52$. Comparing the results of the existins, solutions we see that present numerical solution agree excellently with these of Collins and Dennis (1973) with $t=0.513$.

The stream function and tangential velocity profile at early time, $t=0.2$, coincide with those obtained from the analytic solution and numerical solution with symmetric boundary conditions (Chien, 1977, 1978).

The development of the flow pattern at various time is shown in Figure 3. Figure 3(a) to 1(l) show that as time increases, the recirculation region is enlarged and the stream lines are displaced outward. The larger the time, the more negative becomes the stream function in the recirculation region. Consequently, the reverse tangential velocity becomes larger, Figure 4. As time goes on further, the staeam function and velocity profiles settle down to the steady-state solution. The vorticity diffused far away from the cylinder surface for larger timer, especially in the neighborhood of the rear stagnation point. The growth of the wake length with time is shown in Figure 6, where it is compared with the computation results of Kawaguti and Jain (1966), Collins and with the experiment of Honji and Taneda (1972). The greement is seen to be excellent between this study and the numerical solution of Collins and Dennis as well as the experiment measurement by Honji and Taneda. The results of the investigation of Kawaguti and Jain (1966) departs from the experimental measurement and the numerical computation of this study and of Collins and Dennis is due to inaccurate calculation for their coarse grid size.

The development of the vorticity distribution around the surface of the cylinder is shown in Figure 5. It is seen that the vorticity over the surface remains smooth up to $t=2.0$. A little bit time later, the curves show a kink in the separation region. The kink continues to be present as time increases. Although it never becomes sufficiently pronounced as it does for higher Reynolds number, (Son and Hanratty, 1969; Collins and Dennis, 1973; Chien, 1978). The vorticity within the separation region grows less negative and never increases to positive. This implies the second vortex does not exist in the flow field. As time increases further, the agrees with kink eventually becomes less

promounced until for $t=20$, and is more or less completely vanished. The vorticity distribution of the present solution at $t=20.3$ that of Collins and Dennis at $t=25$ and of Patel (1976) at $t=24.08$ is shown in Figure 6. The agreement is satisfactory.

6. CONCLUSION AND DECOMMFNDATION

It is necessary to examine the accuracy for the newly developed numerical scheme and inverse transforation solving the problem of viscous flow over an impulsively started cylinder. The analytic solution obtained by the method of matched asymptotic expansion to the third order is used as initial conditions fcr the numerical integration. In this study, we chose the case of $Re=50$ and compared our results with the experimental measurement of Honji and Taneda (1972), and the exiting solutions of Collins and Dennis (1973) and Patel (1976). The agreement of initial separation time, vorticity distribution on the cylindea surface and wake length are satisfactory.

We have solved the problem with satisfactory results for the case of $Re=50$ in this investigation. The numerical scheme can be applied to solve the problem of higher Reynolds number.

Acknowledgements: This research was supported by National Science Council of Republic of China, Contract NSC-68E-041-01-(01). The computations reported in this paper was carried out on cyber 74 at Control Data Taiwan Branch and IBM 3031 at Ministry of Accounting. The generous assistant of Dr. J. K. Lin, professor T. C. Tsao and professor C. C. Kuo is greatfully acknowledge.

REFERENCES

1. Chien, L. C. (1977). Impulsively Started Viscous Flow Over a Circular Cylinder. Ph. D. Dissertation, Department of Aerospace Engineering, University of Southern California.
2. Chien, L. C. (1978). Flow Past an Impulsively Started Circular Cylinder, Annual Report of Institute of Physics, Academia Sinica, Vol. 8, pp. 109-125.
3. Collins, W. M. and Dennis, S. C. R. (1973). Flow Past an Impulsively Started Circular Cylinder. Journal of Fluid Mechanics, Vol. 60, Part 1, pp. 105-127.
4. Deffenbauth, F. D. and Marshall, F. J. (1976). Time Dependent of the Flow about an Impulsively Started Cylinder, AIAA Journal, Vol. 14, pp. 908-913.
5. Gourely, A. R. (1970). Hopscotch: A Fast Second-order Pantial Ditterential Equation Solver. Journal of Institute of Mathematics and Applications, Vol. 6, pp. 375-390.
6. Honji, H. and Taneda, S. (1969). Unsteady Flow Past a Circular Cylinder. Journal of Physics Society of Japan, Vol. 27, pp. 1668-1677.

7. Honji, H. and Taneda, S. (1972). Starting Flow Past Spheres and Elliptic Cylinders, Report of Research Institute of Applied Mechanics, Kyushu University, Vol. 19, 265.
8. Jain, P. C. and Rao, K. S. (1969). Numberical Solution of Unsteady Viscous Incompressible Fluid Flow Past a Circular Cylinder, Physics of Fluids, Vol. 12, pp. II-57 to II-64.
9. Jain, P. C. and Goel, B. S. (1976). Shielding of Vortices Behind a Circular Cylinder. Computers and Fluids, Vol. 4, pp. 137-142.
10. Kawaguti, K. and Jain P. C. (1966). Numerical Study of a Viscous Fluid Past a Circular Cylinder. Journal of Physics Society of Japan, Vol. 21, pp. 2055-2062.
11. Lin, C. L., Pepper, D. W. and Lee, S. C. (1976). Numerical Methods for separated Flow Solutions around a Circular Cylinder, AIAA Journal Vol. 14, pp. 900-907.
12. Payne, R. B. (1958). Calculation of Unsteady Viscous Flow Past a Circular Cylinder, Journal of Fluid Mechanics, Vol. 4, pp. 81-86.
13. Panikker, P. K. G. and Lavan, Z. (1975). Flow Past Impulsively Started Bodies Using Green's Function. Journal of Computational Physics, Vol. 18, pp. 46-65.
14. Pantel, V. A. (1976). Time-dependent Solutions of the Viscous Incompressible Flow Past a Circular Cylinder by the Method of Series Trancation. Computers and Fluids, Vol. 4, pp. 13-27.
15. Roache, P. J. (1976). Computational Fluid Dynamics. Hermosa Publishers, New Mexico.
16. Schlichting, H. (1979). Boundary-layer Theory. McGraw-Hill Book Company, New York.
17. Son, J. S. and Hanratty, T. J. (1969). Numerical Solution of Flow Around a Cylinder at Reynolds Number of 40, 200 and 500. Journal of Fluid Mechanics. Vol. 35, Part 2, pp. 369-386.

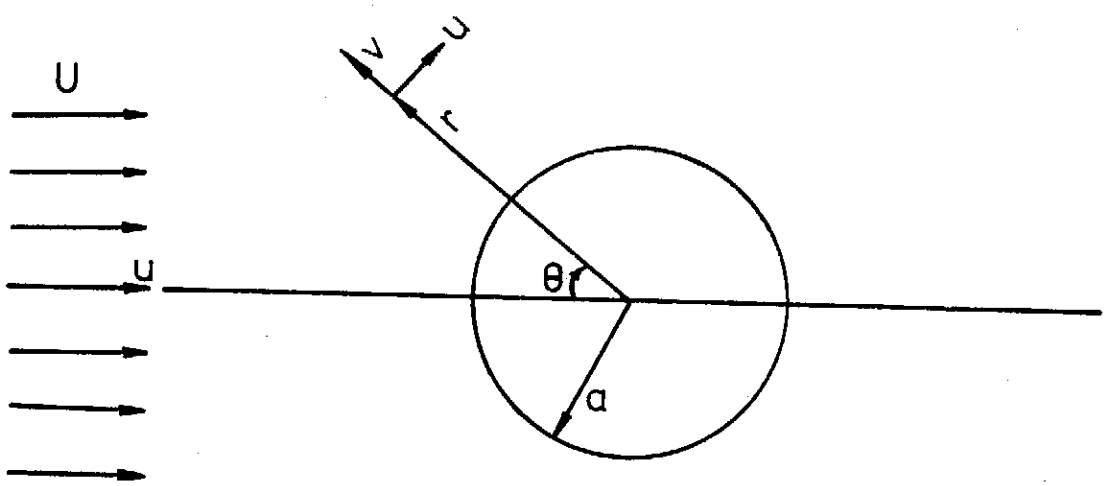

FIG. 1. Polar coordinate system.

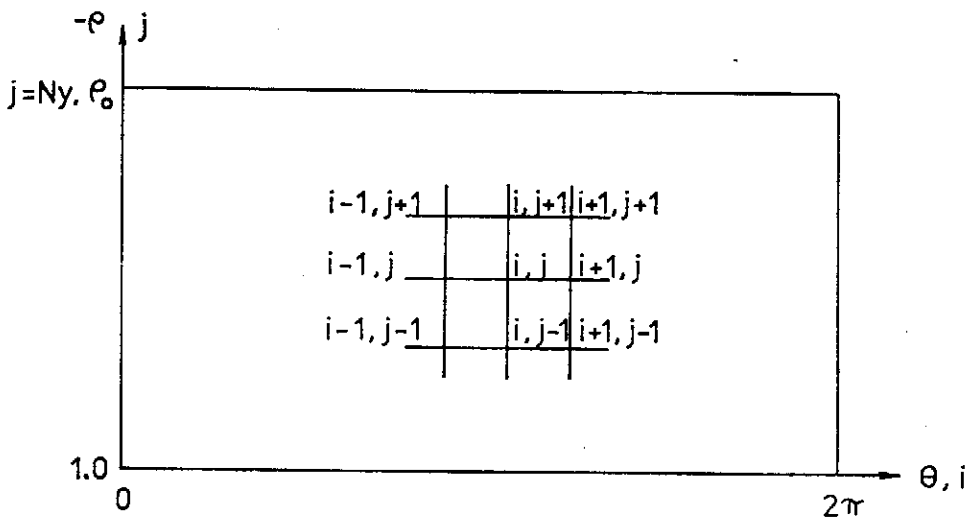

FIG. 2. Domain of calculation and grid notation.

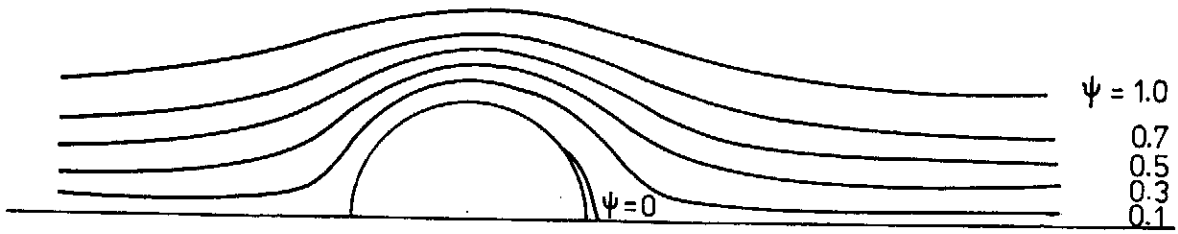

FIG. 3(a) Flow pattern at Re=50 for t=0.6.

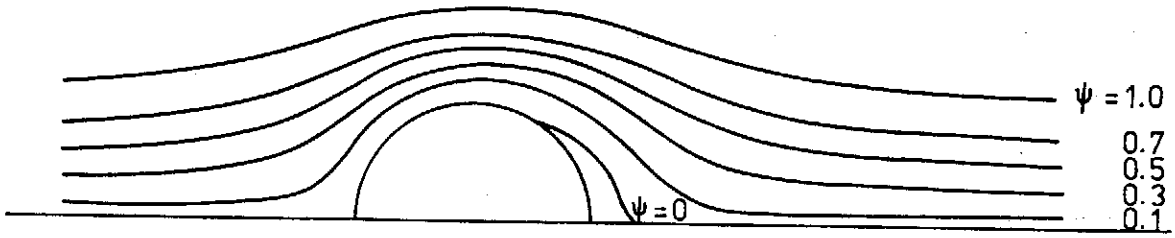

FIG. 3(b) Flow pattern at Re=50 for t=1.0.

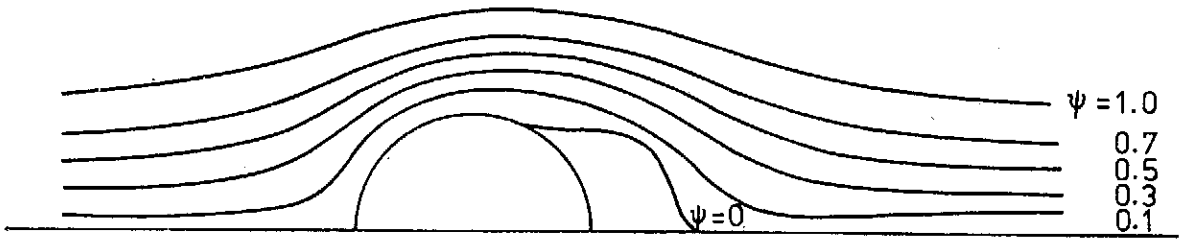

FIG. 3(c) Flow pattern at Re=50 for t=2.0.

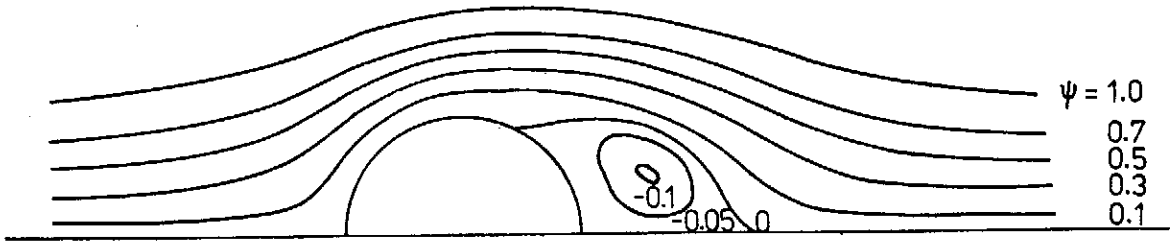

FIG. 3(d) Flow pattern at Re=50 for t=3.0.

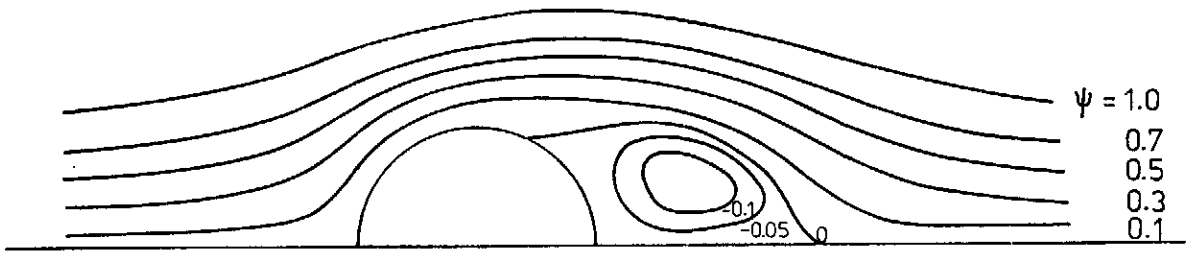

FIG. 3(e) Flow pattern at Re=50 for t=4.0.

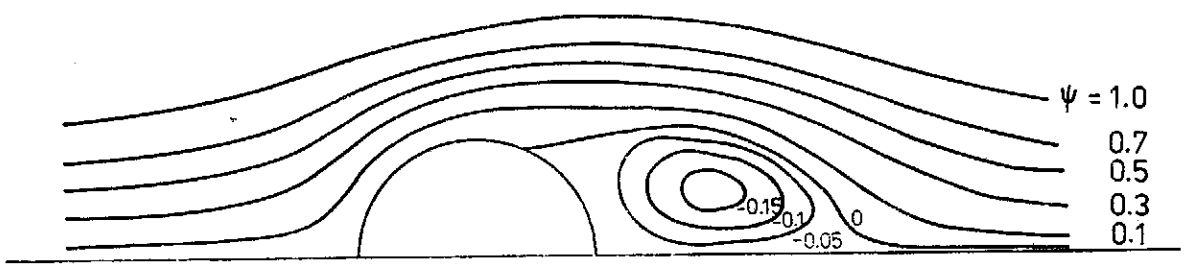

FIG. 3(f) Flow pattern at Re=50 for t=5.0.

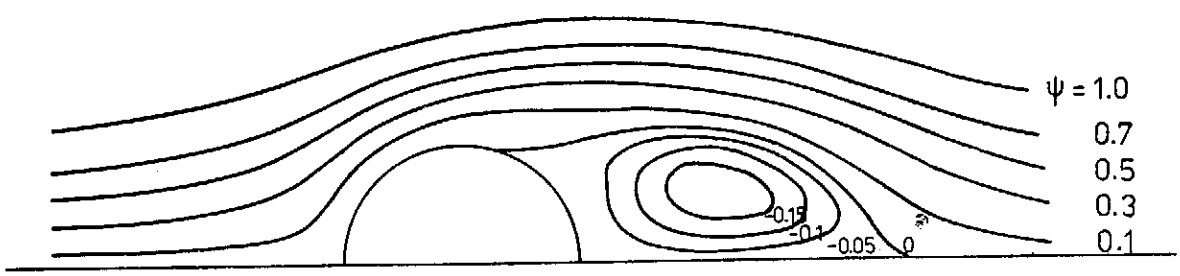

FIG. 3(g) Flow pattern at Re=50 for t=6.0.

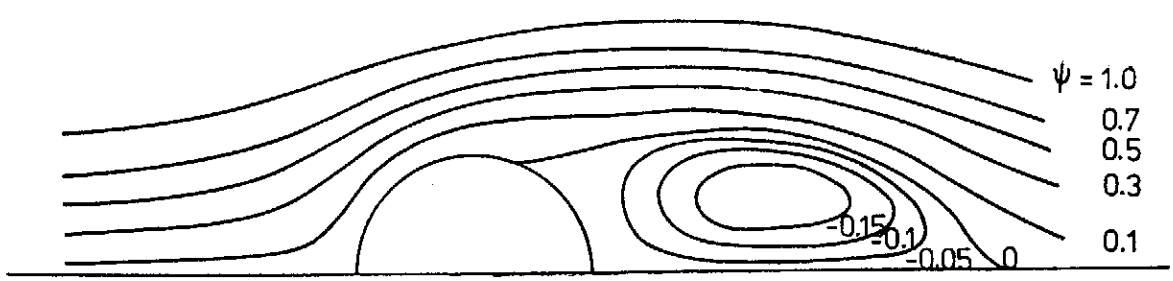

FIG. 3(h) Flow pattern at Re=50 for t=8.0.

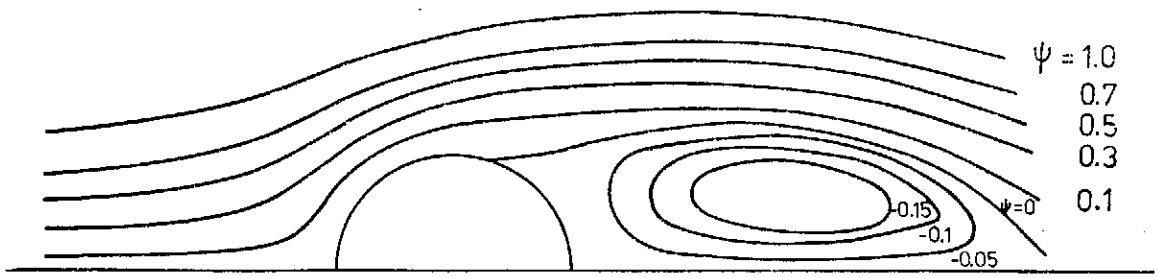

FIG. 3(i) Flow pattern at Re=50 for t=10.0.

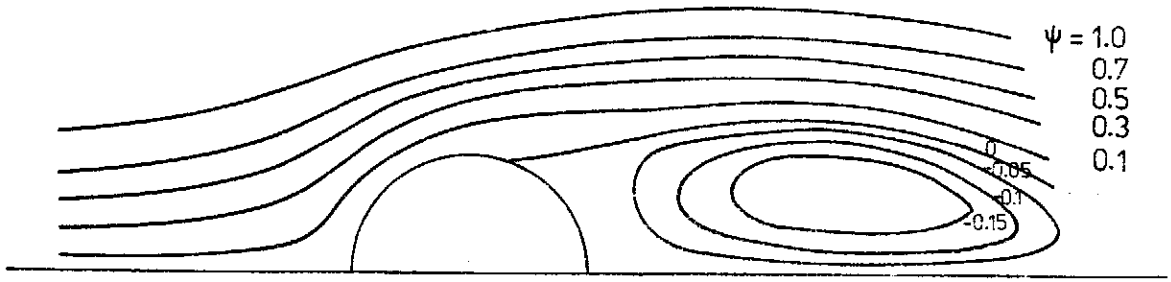

FIG. 3(j) Flow pattern at Re=50 for t=12.0.

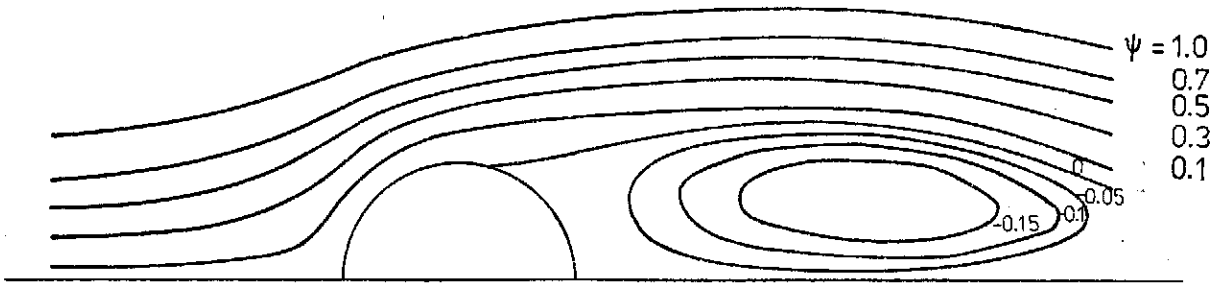

FIG. 3(k) Flow pattern at Re=50 for t=14.0.

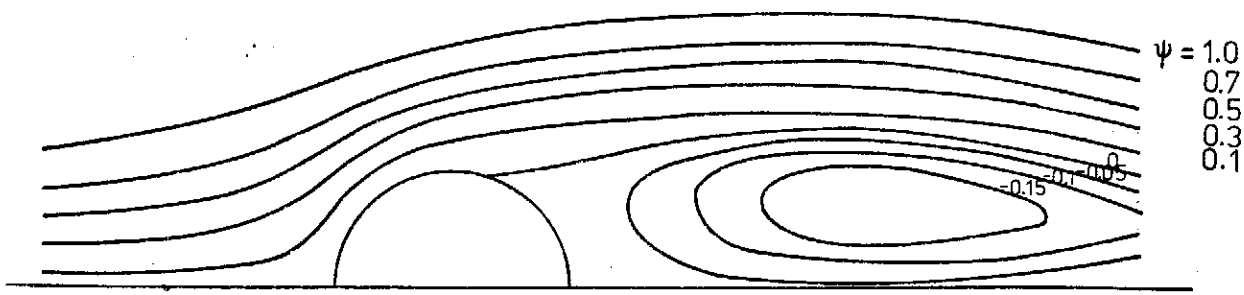

FIG. 3(l) Flow pattern at Re=50 for t=18.0

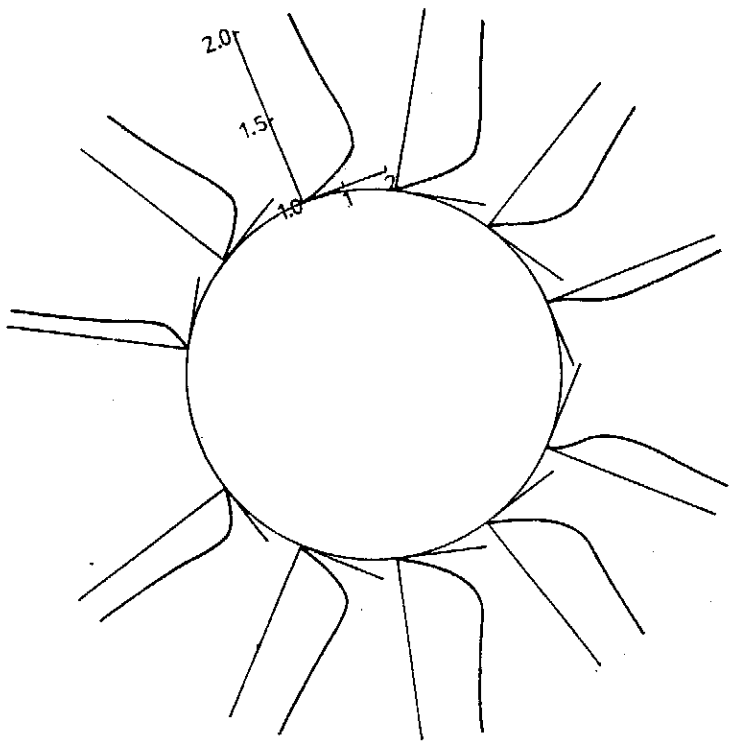

FIG. 4(a) Tangential velocity u_θ at Re=50 for t= 0.6.

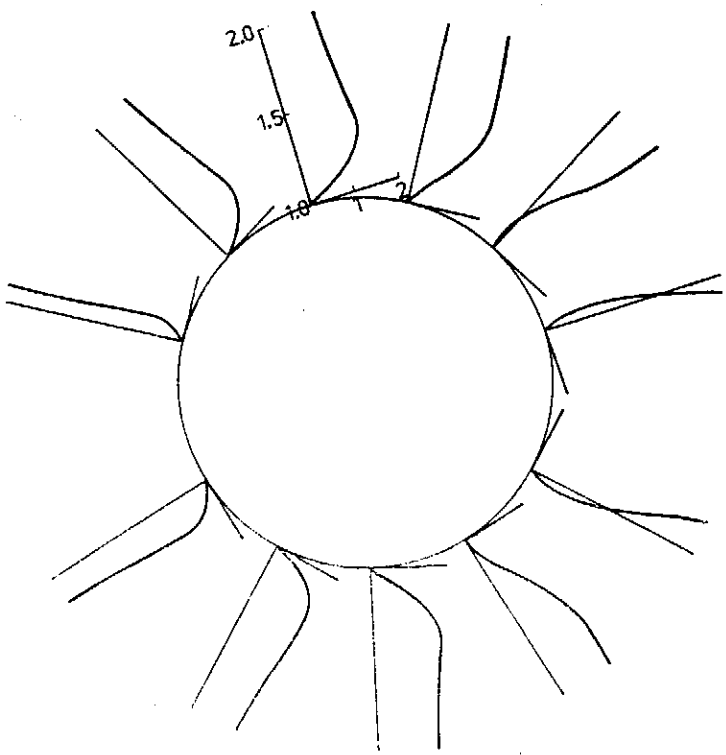

FIG. 4(b) Tangential velocity u_θ at Re=50 for t=1.0.

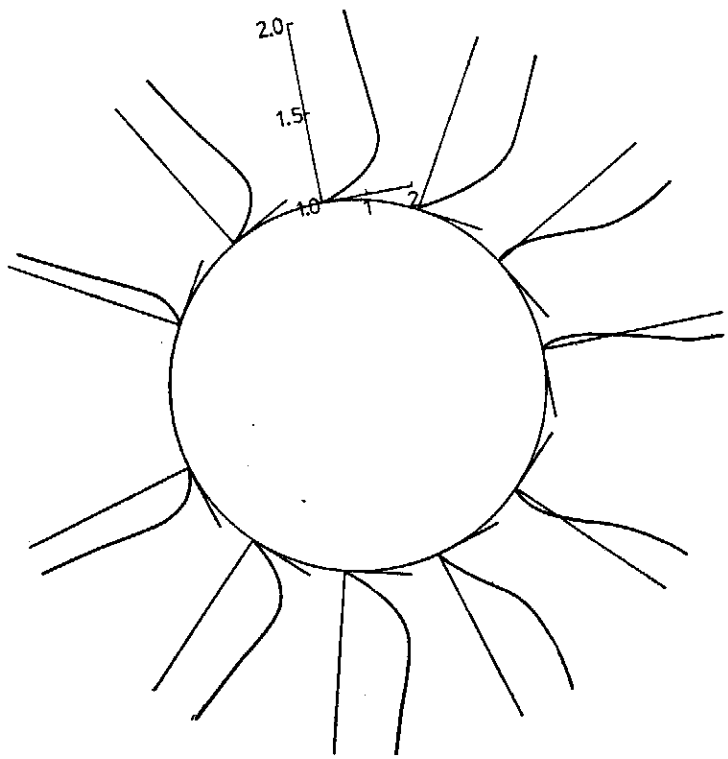

FIG. 4(c) Tangential velocity u_θ at Re=50 for t=2.0.

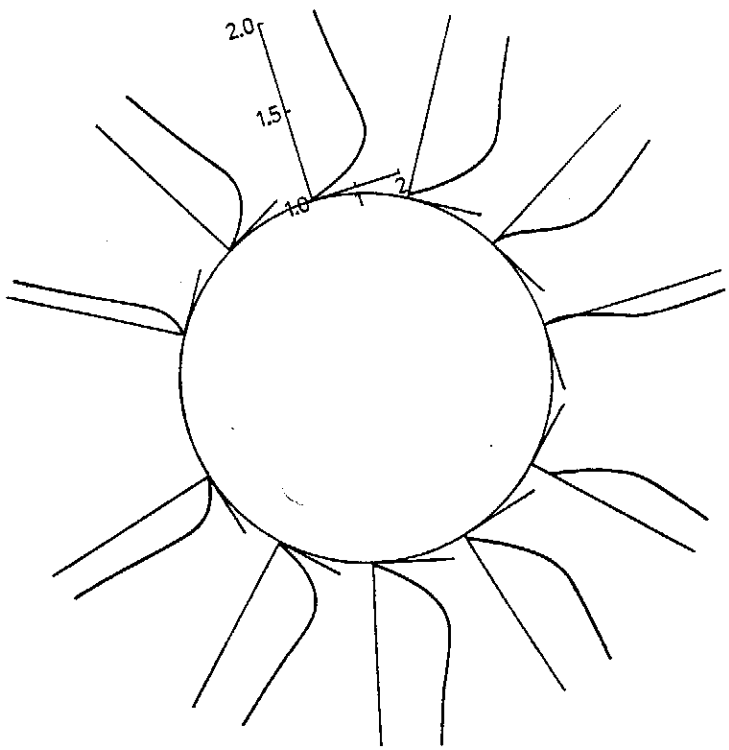

FIG. 4(d) Tangential velocity u_θ at Re=50 for t=3.0.

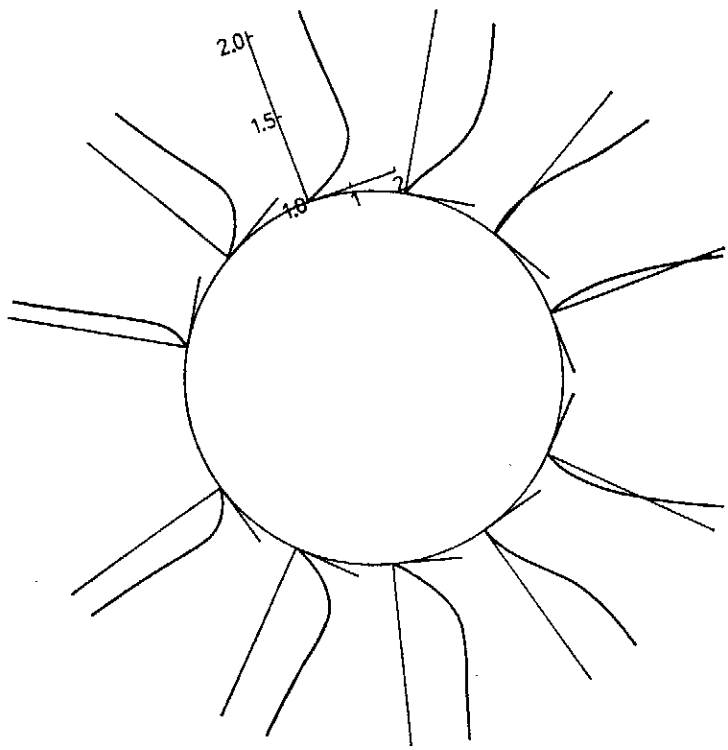

FIG. 4(e) Tangential velocity u_θ at Re=50 for t=4.0.

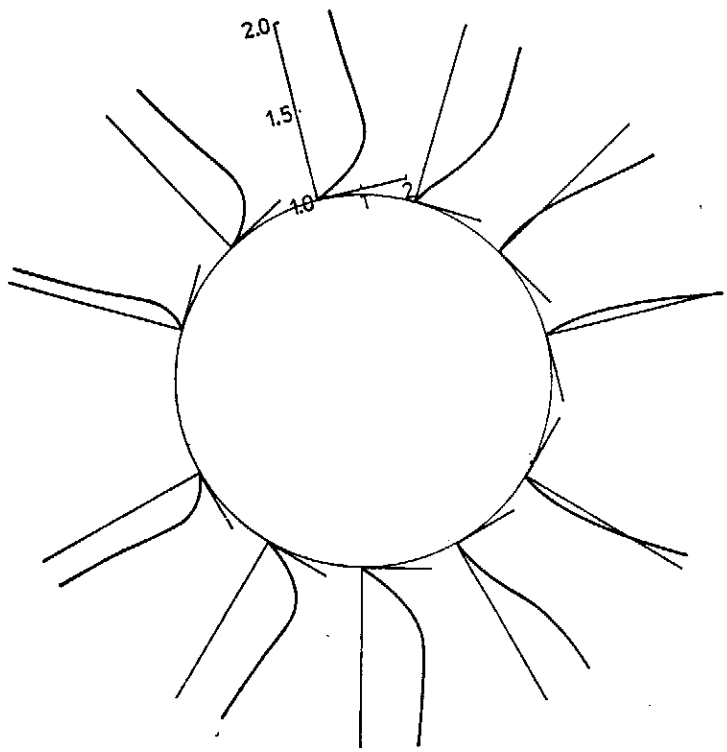

FIG. 4(f) Tangential velocity u_θ at Re=50 for t=5.0.

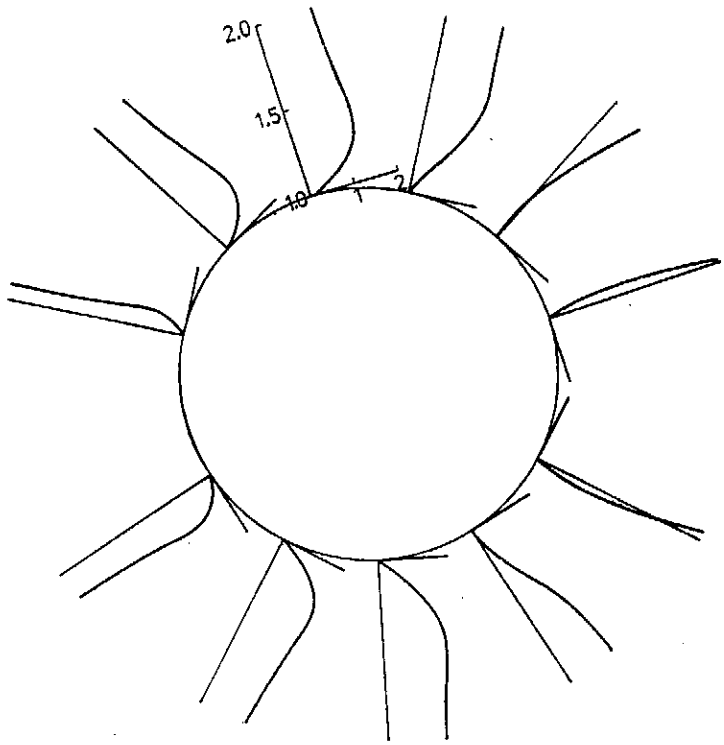

FIG. 4(g) Tangential velocity u_θ at Re=50 for t=6.0.

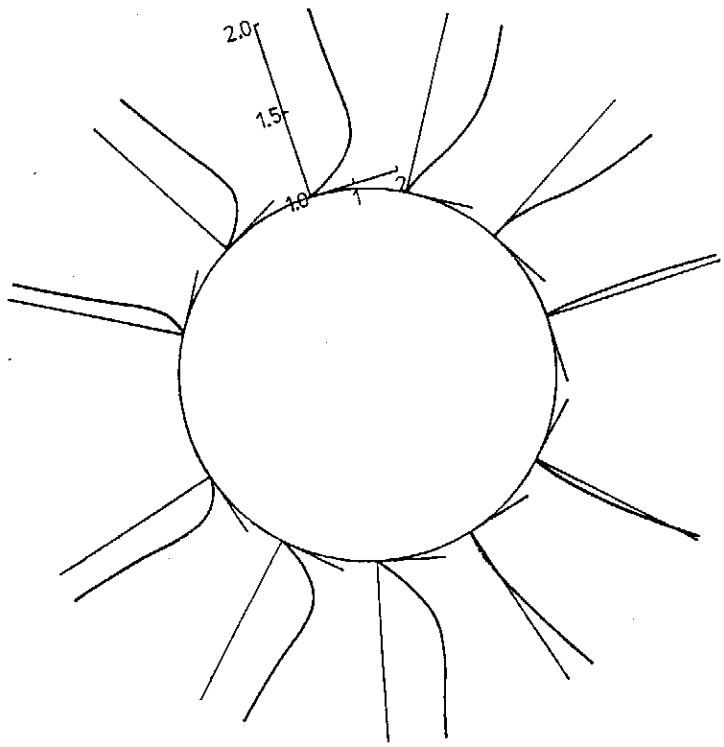

FIG. 4(h) Tangential velocty u_θ at Re=50 for t=8.0.

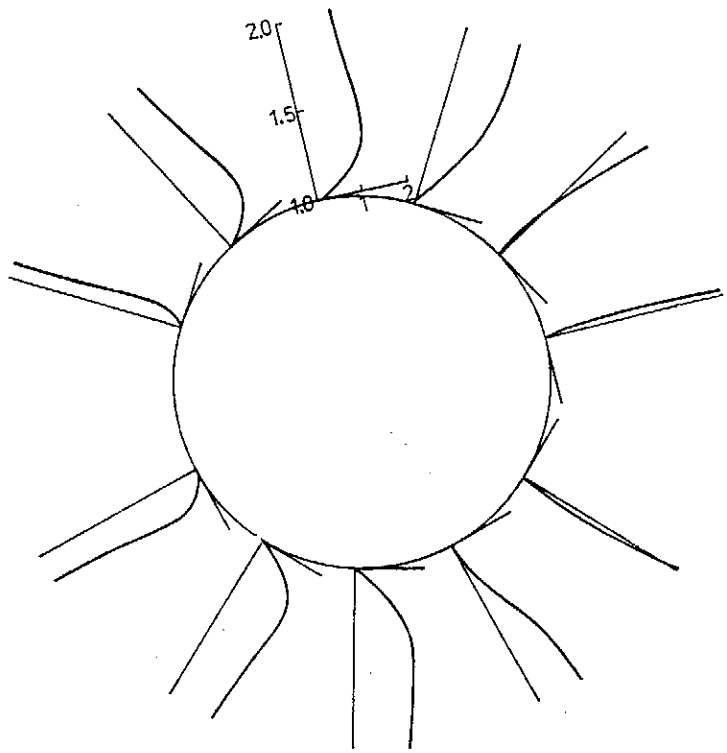

FIG. 4(i) Tangential velocity u_θ at Re=50 for t=10.0.

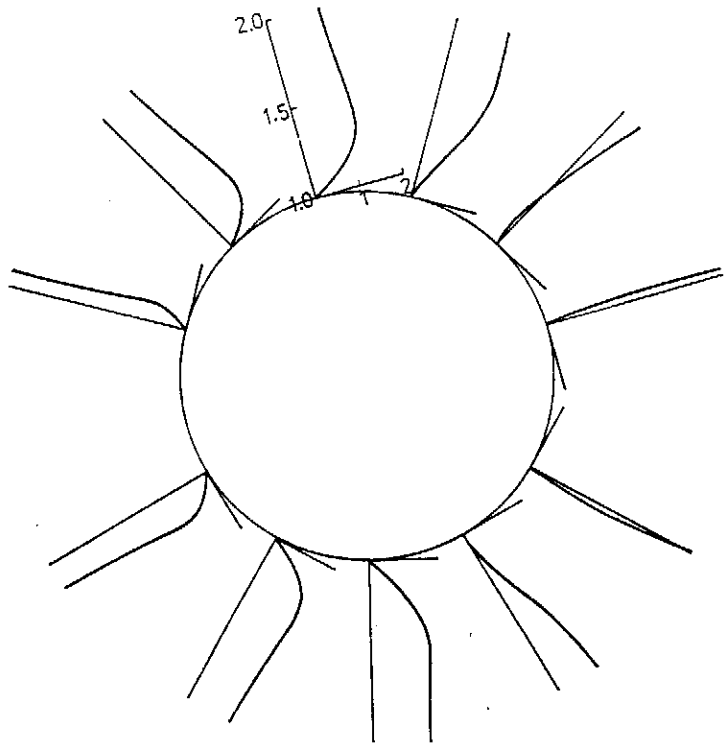

FIG. 4(j) Tangntiol velocity u_θ at Re=50 for t=12.0.

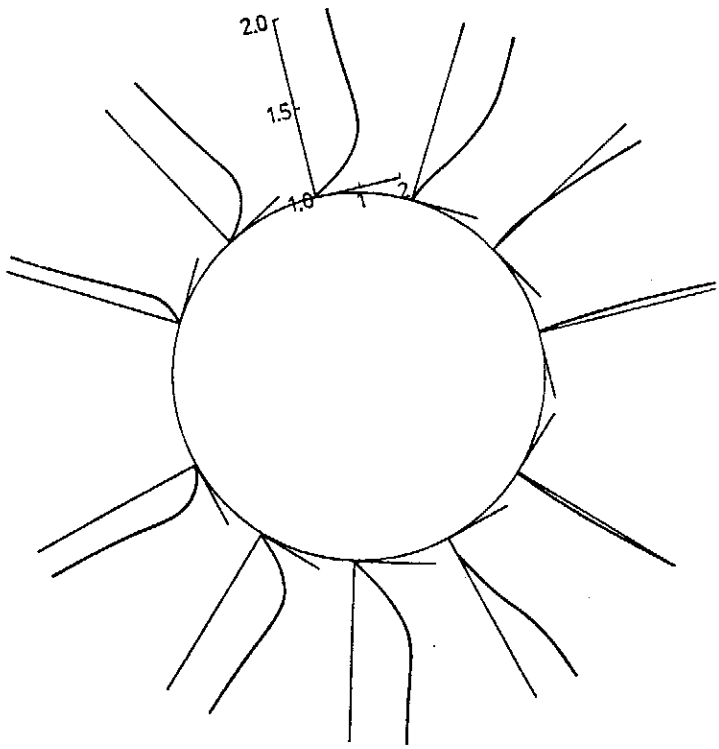

FIG. 4(k) Tangential velocity u_θ at Re=50 for t=14.0.

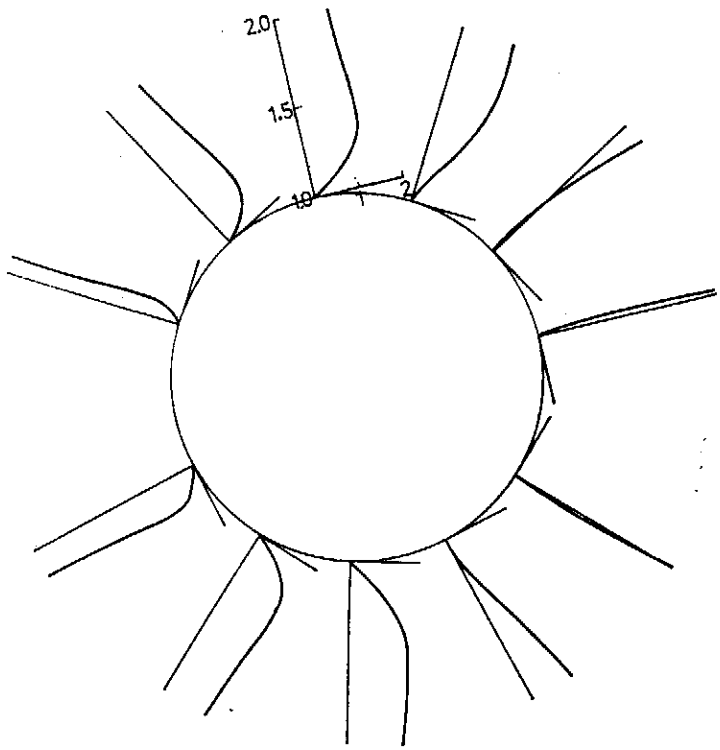

FIG. 4(l) Tangential velocity u_θ at Re=50 for t=18.0.

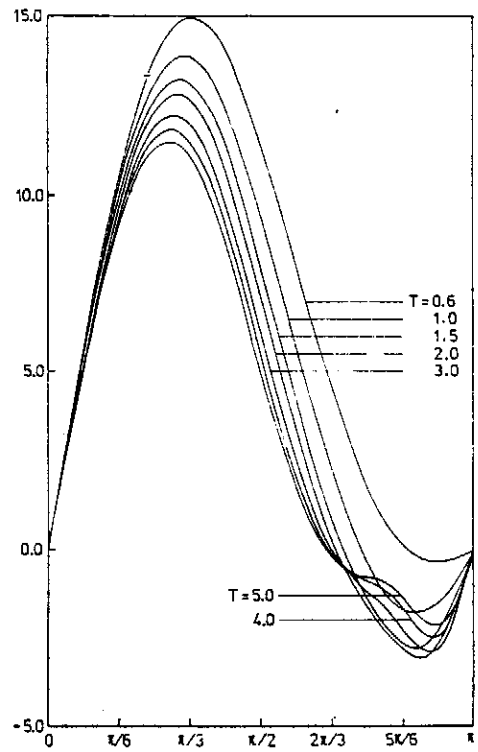

FIG. 5(a) Vorticity distribution on the cylinder at Re=50 for small time.

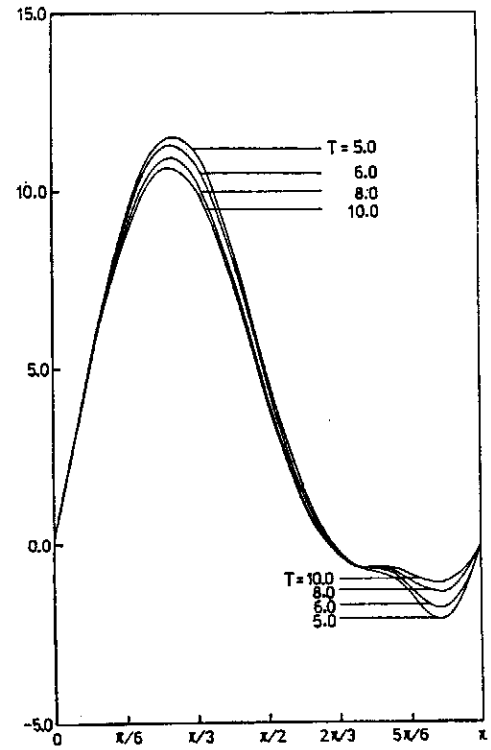

FIG. 5(b) Vorticity distribution on the cylinder at Re=50 for moderate time.

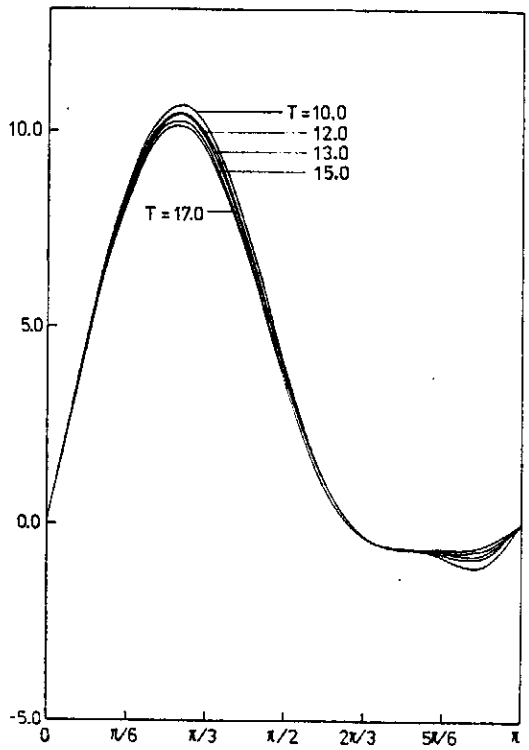

FIG. 5(c) Vorticity distribution on the cylinder at Re=50 for large time.

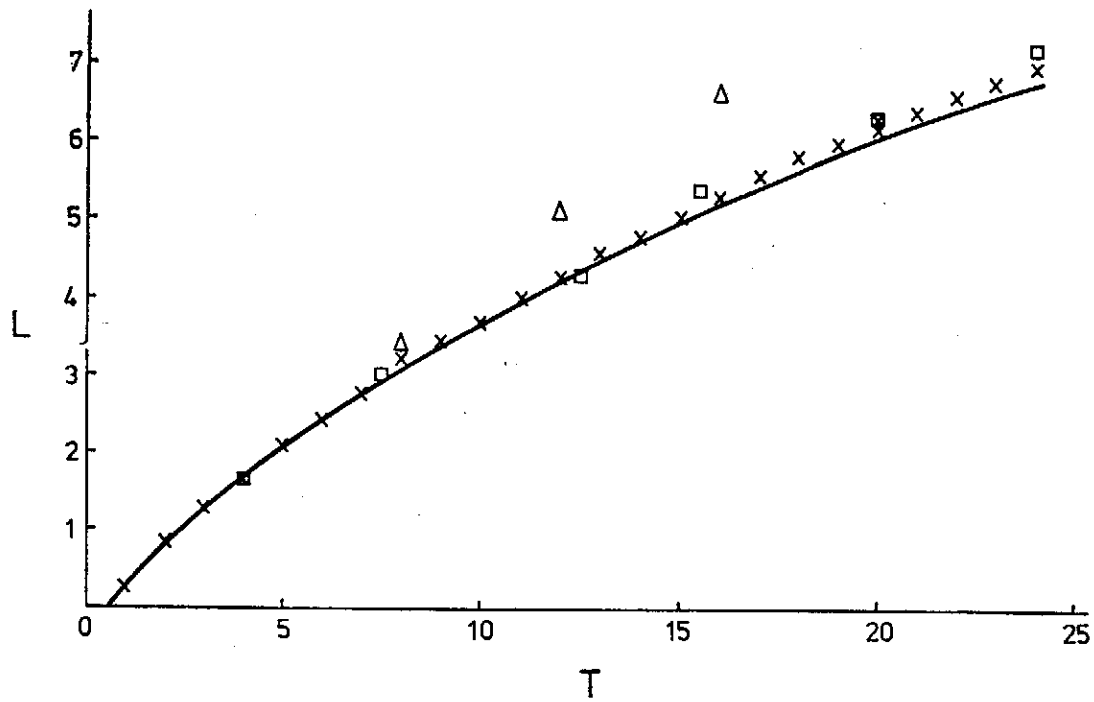

FIG. 6. Calculate and experimental values for the wake length at Re=50. Numerical solutions: △ Kawaguti and Jain (1966); x Collins and Dennis (1973); ——, thisstudy, Experimental measurement; □, Honji and Taneda (2972).

Temperature-Dependent Resistivity in Ni-Rich Alloys*

Y. D. YAO (姚永德)

Institute of Physics, Academia Sinica
Nankang, Taipei, Taiwan, R.O.C.

Abstract

An Analysis of experimental results obtained on nickel-titanium and nickel-copper alloys is used to show that the temperature-dependent part of the electrical resistivity of Ni-rich alloys follows a $T^{1.74\pm0.05}$ variation in the ferromagnetic region above 300 K and increases more slowly than T in the paramagnetic region.

* Published in Physica Status Solidi (Aug. 1, 1979).

Overlapping between Magnetic and $\alpha-\gamma$ Transitions in the FePd System*

Y. D. YAO (姚永德)

Institute of Physics, Academia Sinica
Nankang, Taipei, 115 Taiwan, R.O.C.
and
S. ARAJS
Department of Physics, Clarkson College of Technology
Potsdam, New York 13676 U.S.A.

Abstract

Electrical resistivity measurements of FePd alloys with 3.0 and 7.9 at.% Pd in the temperature range of 800-1200 °K are reported. Special attention is given to the hysteresis anomaly in the neighborhood of the ferromagnetic-paramagnetic-transition temperature. This anomaly is explained by the overlapping effect between magnetic and $\alpha-\gamma$ transitions.

* Published in Physics Status Solidi (Oct. 16, 1979).

Annual Report of the Institute of Physics, Academia Sinica, Vol. 9, 1979

The Electrical Resistivity of Polycrystalline Samarium and of Sm-3 At.% Dy Between 15 and 300 K*

Y. D. YAO, (姚 永 德) L. T. HO and C. Y. YOUNG

Institute of Physics, Academia Sinica
Nankang, Taipei, 115 Taiwan, R.O.C.

Abstract

The electrical resistivity ρ of polycrystalline samarium and of Sm-Dy containing 3 at.% Dy was measured as a function of the absolute temperature T between 15 and 300 K. On the basis of the criterion that $d\rho/dT$ is at a minimum at the Néel temperature T_N it was determined that the values of T_N are 105.8 ± 0.5 K and 102.8 ± 0.5 K for the hexagonal sites of samarium and Sm-3 at.% Dy respectively.

* Accepted for publishing in Journal of the Less-Common Metals.

A Theory of Threshold Switching in Amorphous Thin Films*

CHUN CHIANG (蔣 忻 儒)

Institute of Physics, Academia Sinica, Nankang, Taipei.

Abstract

Using the concept that two reversible forms exist in amorphous thin film and that the transition between them may be activated by the current, and these two forms have different conductivities, the threshold switching phonomenon may be explained. The threshold switching equation and time delay equation are also derived.

Mit der Annahme, daß zwei reversible Formen in dünnen amorphen Schichten existieren, der Übergang zwischen ihnen durch den Strom aktiviert werden kann, und diese Formen unterschiedliche Leitfähigkeiten besitzen, läßt sich das Phänomen des Schwellenschaltens erklären. Die Gleichung für das Schwellenschalten und die Zeitverzögerungsgleichung werden ebenfalls abgeleitet.

* This paper has been published in phys. stat. sol. (a) 54, 735 (1979).

Annual Report of the Institute of Physics, Academia Sinica, Vol. 9, 7979

A Model of a Human Recognition System with 'Thinking'*

CHUN CHIANG (蔣 忻 儒)

Institute of Physics, Academia Sinica, Nankang, Taipei, Taiwan, The Republic of China

Abstract

The human system of pattern recognition is explored. This system utilizes the method of syntactic feature comparison, activation of the patterns containing the feature, and sorting among the activated patterns. Both the pattern recognition process without thinking and with thinking are discussed, and examples are given. Contrary to the usual concept, the more complicated pattern has a better chance to be recognized correctly.

* Published in Biological Cybernetics 1980.

Laboratory Modeling of the Effects on Typhoon* When Encountering the Mountains of Taiwan

ROBERT R. HWANG (黃 榮 檉) and YANG-KANG CHENG

Abstract

The effects of mountainous island on a typhoon vortex during their encounter are of fundamental and practical importance for a better typhoon forcasting on its traveling track and its wind field. In this study laboratory experiments were performed by introducing an essentially two-dimensional concentrated vortex for studying the interaction between the typhoon vortex and Taiwan island. In pursuit of a more realistic modeling, the topography of the coastal area of the Chinese mainland and Philppine island was also included. Comparisons are made between the experimental results and field data during 1949-1976. It is found that the general behavior and the accompanying surface flow patterns of a typhoon vortex, when encountering with mountain area of Taiwan, can be reasonably simulated in the laboratory. It is also noted that the movement of the vortex as well as the typhoon is strongly affected by the approaching pathway of the vortex relative to the mountainous island. It is then suggested that laboratory modeling may provide a reliable and affective way for predicting the movement of a typhoon vortex when it is in the vicinity of the island.

* Journal of Civil and Hydraulic Engineering Vol. 6, No. 3, Paper No. 6-09 (P. 1~P. 12) (1979)

Annual Report of the Institute of Physics, Academia Sinica, Vol. 9, 1979

The Buoyant Rise of Plumes in a Linearly Stratified Environment*

ROBERT R. HWANG (黃 柔 煜)

Institute of Physics, Academia Sinica Taipei, Taiwan, R.O.C.

Abstract

The rise of a buoyant chimney plume in a possibly stratified atmosphere is a particularly complex phenomenon. Buoyancy and initial momentum of the plume will cause the rise of the buoyant plume vertically and the density gradient of the stratified environment will influence the establishment of the flow field. In a stably stratified environment, the jet first behaves like a buoyant jet and mixes with heavy bottom ambient producing a neutrally buoyant cloud. The density deficit of the jet will reduce continuously and becomes zero at a certain height (point of neutral buoyancy). The buoyancy force, from here-on, will be negative and the flow will be decelerated, turned down and spreaded sideway after reaching a maximum height.

This study is to obtain such a jet-rise formula from correlating a substantial series of experimental data of laboratory study according to simple theoretical considerations such as dimensional analysis. The height of rise was obtained in terms of the initial momentum and buoyancy of jet and the stratification of the surrounding environment. In the laboratory experiments, a filling salt solution process is designed to produce a linearly stratified environment and a photographic technique is used to trace the development of the flow. It is found that the maximum rise of a plane buoyant jet is proportional to $F_0^{2/3}$ and $S^{1/2}$, in which F_0 is the initial Froudes number and S, the stratification parameter.

* This paper has been published in Proc. 3rd Engineering Mechanics, ASCE, p. 830 (1979).

Annual Report of the Institute of Physics, Academia Sinica, Vol. 9, 1979

Hopscotch Integration Scheme for Numerical Weather Prediction in Mei-Yu Season*

LAI-CHEN CHIEN (簡 來 成) and CHUN-TSUNG WANG (汪群從)

Institute of Physics Academia Sinica
Taipei, Taiwan Republic of China

Abstract

An efficient computational process, hopscotch method, has been applied to four-level baroclinic quasi-geostrophic diabatic model for 24-hour forecasting in Mei-Yu season over the East Asia. Numerical integrations of vorticity equation and energy equation are carried out by making use of this scheme. The method uses explicit and implicit finite difference schemes at alternate mesh points to solve the partial differential equations. Each time step is calculated in two sweeps of the mesh. In the first and subsequent odd-numbered time steps, the grid points with $i+j$ odd (i is the row number, j the column number) are calculated based on current values of the neighboring points. For the second sweep at the same time level, the computation is excuted at points with $i+j$ even, using the known advanced values of neighboring points calculated in the first sweep. The first sweep is explicit, the second is fully implicit with no simultaneous algebraic solution. The method, equivalent to Peacemen-Rachford procedure with coefficient matrix split in a novel way, is unconditionally stable and allowing arbitrarily large time step and is 3 to 4 time faster. This algorithm is very efficient with regard to storage requirement and ease of programming. For comparison, computations were made for the same initial and boundary conditions by applying both explicit method and the present method with triple and quadruple time increment. The results show that 24-hour predicted Z-field ageres excellently to 3 significant figures in both methods.

* This paper has been published in Proc, Natl, Sci, Counc. ROC, Vol. 3, No. 4, 1979, pp 356-363.

† Presented at American Meteorogical Society Twelfth Technical Conference on Hurricanes and Tropical Meterogy, at New Orleans, Louisiana, April 24-27, 1979.

Annual Report of the Institute of Physics, Academia Sinica, Vol. 9, 1979

北迴鐵路長大隧道通風問題之研究*

呂秀雄　梁文傑　簡來成
廖世平　邱國益　陳石法

摘　要

第一篇：火車經過隧道時速度及通風之實驗分析

模擬北廻鐵路的草嶺隧道和南澳隧道（分有通風道和無通風道），利用微處理系統和熱線風速計以獲得隧道內各位置的速度變化情形，由此推知隧道內穩定風速和火車車速比爲常數，此值隨隧道之增長而降低。火車通過量測位置負風速的平均值與車速之比亦爲常數，但隨隧道之增長而增加（絕對值）。火車通過隧道所推出的空氣量爲常數，單位體積的通風量隨隧道之增長而降低。有通風道的隧道其通風量可大幅增加。本實驗之例增加48%。本文的結論和實地量測及理論的結果很類似。

第二篇：火車通過時隧道中之速度場與壓力場

以特徵線數值方法模擬隧道中火車通過時之壓力場及速度場，利用計算機求出其一維 (One-dimension)、可壓縮、不穩定流之數值解 (Numerical Solution)。分析車長、車速及隧道長度對風速和壓力的影響，並分析設了通風道之隧道中壓力場和速度場。結果顯示，火車前面之風速最大，車旁之風速最小，隨隧道的增長，隧道內之風速漸低，壓力則漸高。隧道中之壓力分佈以車前最高，而以車後爲最低（大氣壓力以下）。空氣速度與車速之比值爲一定值，而火車於隧道中之時間內進入隧道之總空氣量不隨車速而增加，但火車在隧道內的時間隨車速增加而減少，因此有利於通風，另一方面，車速增加提高了隧道內的壓力。車長的增加雖然也可增加進氣量，但是也增加火車的負荷。

設了通風道後可減小隧道內的高壓力部分，減少火車前後的壓力差，進入隧道之總空氣量增加，就全部隧道而言，設了通風道後應可減小平均污染濃度，但是由於通風道的關係，火車以外之區段風速較低如此可能影響該部分污染物之排除。

第三篇：火車通過時隧道中之污染問題

研究火車通過隧道時產生的污染問題，利用數值分析中的第二逆流法來探討污染物的分佈狀況。文中分別取320，640，1200，2400，4800，7680公尺長的隧道加以分析。根據分析，一千公尺以內的隧道靠著火車本身產生的速度場就可將污染物攜出；隨著隧道長度的增加，火車後面會產生較長的均勻濃度區域，當火車距離隧道時，污染物無法全部排出，而積聚在出口端附近。在連續班車行駛中，若兩車方向相同，則可繼續將殘留污染物由出口排出；但若兩車方向相反，則

污染物會被推回隧道內。通風道的開設可以在連續班車行駛時改善污染情形，經過文中的分析，通風道開設的數目愈多效果愈好，其位置愈靠近中央或長度愈短污染物濃度就愈低，污染程度也較輕微。至於火車在隧道中途停車，不但增加曝露時間且會提高污染物濃度，造成嚴重的污染問題。

* 本文已發表於中國工程師學會會刊，第54卷第三期，第四期，與第五期。並獲六十八年度中國工程師學會論文獎。